Fluid Dynamics in Complex Fractured-Porous Systems

Boris Faybishenko, Sally M. Benson, and John E. Gale
Editors

AGU American Geophysical Union

WILEY

Geophysical Monograph Series

164 **Archean Geodynamics and Environments** *Keith Benn, Jean-Claude Mareschal, and Kent C. Condie (Eds.)*

165 **Solar Eruptions and Energetic Particles** *Natchimuthukonar Gopalswamy, Richard Mewaldt, and Jarmo Torsti (Eds.)*

166 **Back-Arc Spreading Systems: Geological, Biological, Chemical, and Physical Interactions** *David M. Christie, Charles Fisher, Sang-Mook Lee, and Sharon Givens (Eds.)*

167 **Recurrent Magnetic Storms: Corotating Solar Wind Streams** *Bruce Tsurutani, Robert McPherron, Walter Gonzalez, Gang Lu, José H. A. Sobral, and Natchimuthukonar Gopalswamy (Eds.)*

168 **Earth's Deep Water Cycle** *Steven D. Jacobsen and Suzan van der Lee (Eds.)*

169 **Magnetospheric ULF Waves: Synthesis and New Directions** *Kazue Takahashi, Peter J. Chi, Richard E. Denton, and Robert L. Lysak (Eds.)*

170 **Earthquakes: Radiated Energy and the Physics of Faulting** *Rachel Abercrombie, Art McGarr, Hiroo Kanamori, and Giulio Di Toro (Eds.)*

171 **Subsurface Hydrology: Data Integration for Properties and Processes** *David W. Hyndman, Frederick D. Day-Lewis, and Kamini Singha (Eds.)*

172 **Volcanism and Subduction: The Kamchatka Region** *John Eichelberger, Evgenii Gordeev, Minoru Kasahara, Pavel Izbekov, and Johnathan Lees (Eds.)*

173 **Ocean Circulation: Mechanisms and Impacts—Past and Future Changes of Meridional Overturning** *Andreas Schmittner, John C. H. Chiang, and Sidney R. Hemming (Eds.)*

174 **Post-Perovskite: The Last Mantle Phase Transition** *Kei Hirose, John Brodholt, Thorne Lay, and David Yuen (Eds.)*

175 **A Continental Plate Boundary: Tectonics at South Island, New Zealand** *David Okaya, Tim Stem, and Fred Davey (Eds.)*

176 **Exploring Venus as a Terrestrial Planet** *Larry W. Esposito, Ellen R. Stofan, and Thomas E. Cravens (Eds.)*

177 **Ocean Modeling in an Eddying Regime** *Matthew Hecht and Hiroyasu Hasumi (Eds.)*

178 **Magma to Microbe: Modeling Hydrothermal Processes at Oceanic Spreading Centers** *Robert P. Lowell, Jeffrey S. Seewald, Anna Metaxas, and Michael R. Perfit (Eds.)*

179 **Active Tectonics and Seismic Potential of Alaska** *Jeffrey T. Freymueller, Peter J. Haeussler, Robert L. Wesson, and Göran Ekström (Eds.)*

180 **Arctic Sea Ice Decline: Observations, Projections, Mechanisms, and Implications** *Eric T. DeWeaver, Cecilia M. Bitz, and L.-Bruno Tremblay (Eds.)*

181 **Midlatitude Ionospheric Dynamics and Disturbances** *Paul M. Kintner, Jr., Anthea J. Coster, Tim Fuller-Rowell, Anthony J. Mannucci, Michael Mendillo, and Roderick Heelis (Eds.)*

182 **The Stromboli Volcano: An Integrated Study of the 2002–2003 Eruption** *Sonia Calvari, Salvatore Inguaggiato, Giuseppe Puglisi, Maurizio Ripepe, and Mauro Rosi (Eds.)*

183 **Carbon Sequestration and Its Role in the Global Carbon Cycle** *Brian J. McPherson and Eric T. Sundquist (Eds.)*

184 **Carbon Cycling in Northern Peatlands** *Andrew J. Baird, Lisa R. Belyea, Xavier Comas, A. S. Reeve, and Lee D. Slater (Eds.)*

185 **Indian Ocean Biogeochemical Processes and Ecological Variability** *Jerry D. Wiggert, Raleigh R. Hood, S. Wajih A. Naqvi, Kenneth H. Brink, and Sharon L. Smith (Eds.)*

186 **Amazonia and Global Change** *Michael Keller, Mercedes Bustamante, John Gash, and Pedro Silva Dias (Eds.)*

187 **Surface Ocean–Lower Atmosphere Processes** *Corinne Le Quèrè and Eric S. Saltzman (Eds.)*

188 **Diversity of Hydrothermal Systems on Slow Spreading Ocean Ridges** *Peter A. Rona, Colin W. Devey, Jérôme Dyment, and Bramley J. Murton (Eds.)*

189 **Climate Dynamics: Why Does Climate Vary?** *De-Zheng Sun and Frank Bryan (Eds.)*

190 **The Stratosphere: Dynamics, Transport, and Chemistry** *L. M. Polvani, A. H. Sobel, and D. W. Waugh (Eds.)*

191 **Rainfall: State of the Science** *Firat Y. Testik and Mekonnen Gebremichael (Eds.)*

192 **Antarctic Subglacial Aquatic Environments** *Martin J. Siegert, Mahlon C. Kennicut II, and Robert A. Bindschadler*

193 **Abrupt Climate Change: Mechanisms, Patterns, and Impacts** *Harunur Rashid, Leonid Polyak, and Ellen Mosley-Thompson (Eds.)*

194 **Stream Restoration in Dynamic Fluvial Systems: Scientific Approaches, Analyses, and Tools** *Andrew Simon, Sean J. Bennett, and Janine M. Castro (Eds.)*

195 **Monitoring and Modeling the *Deepwater Horizon* Oil Spill: A Record-Breaking Enterprise** *Yonggang Liu, Amy MacFadyen, Zhen-Gang Ji, and Robert H. Weisberg (Eds.)*

196 **Extreme Events and Natural Hazards: The Complexity Perspective** *A. Surjalal Sharma, Armin Bunde, Vijay P. Dimri, and Daniel N. Baker (Eds.)*

197 **Auroral Phenomenology and Magnetospheric Processes: Earth and Other Planets** *Andreas Keiling, Eric Donovan, Fran Bagenal, and Tomas Karlsson (Eds.)*

198 **Climates, Landscapes, and Civilizations** *Liviu Giosan, Dorian Q. Fuller, Kathleen Nicoll, Rowan K. Flad, and Peter D. Clift (Eds.)*

199 **Dynamics of the Earth's Radiation Belts and Inner Magnetosphere** *Danny Summers, Ian R. Mann, Daniel N. Baker, and Michael Schulz (Eds.)*

200 **Lagrangian Modeling of the Atmosphere** *John Lin (Ed.)*

201 **Modeling the Ionosphere-Thermosphere** *Jospeh D. Huba, Robert W. Schunk, and George V Khazanov (Eds.)*

202 **The Mediterranean Sea: Temporal Variability and Spatial Patterns** *Gian Luca Eusebi Borzelli, Miroslav Gačić, Piero Lionello, and Paola Malanotte-Rizzoli (Eds.)*

203 **Future Earth - Advancing Civic Understanding of the Anthropocene** *Diana Dalbotten, Gillian Roehrig, and Patrick Hamilton (Eds.)*

204 **The Galápagos: A Natural Laboratory for the Earth Sciences** *Karen S. Harpp, Eric Mittelstaedt, Noémi d'Ozouville, and David W. Graham (Eds.)*

205 **Modeling Atmospheric and Oceanic Flows: Insights from Laboratory Experiments and Numerical Simulations** *Thomas von Larcher and Paul D. Williams (Eds.)*

206 **Remote Sensing of the Terrestrial Water Cycle** *Venkat Lakshmi (Eds.)*

207 **Magnetotails in the Solar System** *Andreas Keiling, Caitríona Jackman, and Peter Delamere (Eds.)*

208 **Hawaiian Volcanoes: From Source to Surface** *Rebecca Carey, Valerie Cayol, Michael Poland, and Dominique Weis (Eds.)*

209 **Sea Ice: Physics, Mechanics, and Remote Sensing** *Mohammed Shokr and Nirmal Sinha (Eds.)*

Geophysical Monograph 210

Dynamics of Fluids and Transport in Complex Fractured-Porous Systems

Boris Faybishenko
Sally M. Benson
John E. Gale
Editors

This Work is a co-publication between the American Geophysical Union and John Wiley and Sons, Inc.

AGU
American Geophysical Union

WILEY

This Work is a co-publication between the American Geophysical Union and John Wiley & Sons, Inc.

Published under the aegis of the AGU Publications Committee

Brooks Hanson, Director of Publications
Robert van der Hilst, Chair, Publications Committee

Published by John Wiley & Sons, Inc., Hoboken, New Jersey
Published simultaneously in Canada

Library of Congress Cataloging-in-Publication Data is available.

ISBN: 978-1-118-87720-3

Cover images: Large illustration: Dynamics of fluids in fractured rocks, Box Canyon, adjacent to the Big Lost River, Idaho, in the Eastern Snake River Plain near the city of Arco, Idaho © Boris Faybishenko. Inset illustration: Dry Lake Fluid Flow Path 03-02-14 © Yohann Ropers.

Printed in the United States of America

10 9 8 7 6 5 4 3 2 1

CONTENTS

CONTRIBUTORS

Jacob Bensabat
Environmental & Water Resources Engineering Ltd.
Haifa, Israel

Sally M. Benson
Department of Energy Resources Engineering, School of Earth Sciences, Stanford University
Stanford, California, USA

Eric Boomsma
Department of Physics and Astronomy,
Purdue University
West Lafayette, Indiana, USA

Sarinya Charoenwongsa
Colorado School of Mines
Golden, Colorado, USA

Inci Demirkanli
The Cadmus Group, Inc.
Arlington, Virginia, USA

Christine Doughty
Earth Sciences Division, Lawrence Berkeley National Laboratory
Berkeley, California, USA

Maria Inés Dragila
Department of Crop and Soil Science, Oregon State University
Corvallis, Oregon, USA

Perapon Fakcharoenphol
Colorado School of Mines
Golden, Colorado, USA

Boris Faybishenko
Lawrence Berkeley National Laboratory
Berkeley, California, USA

R. Allan Freeze
Surrey, British Columbia, Canada

John E. Gale
Fracflow Consultants Inc.
St. John's, Newfoundland, Canada

Junichi Goto
Nuclear Waste Management Organization of Japan
Mita, Tokyo, Japan

Hai Huang
Idaho National Laboratory
Idaho Falls, Idaho, USA

John A. Hudson
Imperial College
London, UK

Da Huo
Department of Energy Resources Engineering, School of Earth Sciences, Stanford University
Stanford, Caliofrnia, USA

Iraj Javandel
Lawrence Berkeley National Laboratory
Berkeley, California, USA

Dan Kaplan
Savannah River National Laboratory
Aiken, South Carolina, USA

Kenzi Karasaki
Lawrence Berkeley National Laboratory
Berkeley, California, USA

Hossein Kazemi
Colorado School of Mines
Golden, Golden, Colorado, USA

Basak Kurtoglu
Marathon Oil Company
Houston, Texas, USA

Hui-Hai Liu
Aramco Research Center
Houston, Texas, USA

Siamak Malek-Mohammadi
Bradley University
Peoria, Illinois, USA

Fred Molz
Environmental Engineering and Earth Sciences, Clemson University
Anderson, South Carolina, USA

Uri Nachshon
Environmental Hydrology and Microbiology, ZIWR, BIDR, Ben Gurion University of the Negev
Beer-Sheva, Israel

Shlomo P. Neuman
Department of Hydrology and Water Resources, University of Arizona
Tucson, Arizona, USA

Auli Niemi
Department of Earth Sciences, Uppsala University
Uppsala, Sweden

John R. Nimmo
U.S. Geological Survey
Menlo Park, California, USA

Celia T. Onishi
U.S. Geological Survey
Menlo Park, California, USA

Brian Powell
Environmental Engineering and Earth Sciences, Clemson University
Anderson, South Carolina, USA

Laura J. Pyrak-Nolte
Department of Physics and Astronomy, Department of Earth and Atmospheric Sciences, and School of Civil Engineering, Purdue University
West Lafayette, Indiana, USA

Eunjeong Seok
Fracflow Consultants Inc.
St. John's, Newfoundland, Canada

Prabhakar Sharma
Department of Earth Sciences, Uppsala University
Uppsala, Sweden
School of Ecology and Environment Studies, Nalanda University
Rajgir, Nalanda, Bihar, India

Shannon Thompson
US Nuclear Regulatory Commission, Office of Research
Rockville, Maryland, USA

Chin-Fu Tsang
Earth Sciences Division, Lawrence Berkeley National Laboratory
Berkeley, California, USA

Michael C. Tsenn
ExxonMobil Upstream Research Company
Houston, Texas, USA

Joseph S. Y. Wang
Lawrence Berkeley National Laboratory
Berkeley, California, USA

Noam Weisbrod
Environmental Hydrology and Microbiology, ZIWR, BIDR, Ben Gurion University of the Negev
Beer-Sheva, Israel

Philip H. Winterfeld
Department of Petroleum Engineering, Colorado School of Mines
Golden, Colorado, USA

Thomas Wood
University of Idaho, Center for Advanced Energy Studies
Idaho Falls, Idaho, USA

Yu-Shu Wu
Department of Petroleum Engineering, Colorado School of Mines
Golden, Colorado, USA

PREFACE

Prof. Paul A. Witherspoon (1919–2012)

Even after many years of study, predicting fluid flow, heat, and chemical transport in fractured-porous media remains a challenge for scientists and engineers worldwide. This monograph is the third in a Geophysical Monograph Series on fluid and transport dynamics in fractured rock to be published by the American Geophysical Union. The first two monographs followed the Witherspoon's Symposiums held in Berkeley, California, USA, in 1999 (*Geophysical Monograph Series*, Vol. 122, 2000; see http://www.agu.org/books/gm/v162/) and 2004 (*Geophysical Monograph Series*, Vol. 162, 2005; see http://www.agu.org/books/gm/v122/). This monograph draws primarily from the presentations given at Session H071, "Dynamics of Fluids and Transport in Fractured Porous Media," of the Fall 2012 AGU Meeting, held in San Francisco in December 2012.

The intent of this monograph is to honor the late Dr. Paul A. Witherspoon (1919–2002), for his outstanding, lifelong contribution to the field of hydrology, and his seminal influence on the development of ideas and methodologies for contemporary fractured rock hydrogeology. His work has influenced our approaches to such fundamental and applied challenges as environmental remediation, exploitation of oil, gas, and geothermal resources, disposal of spent nuclear fuel, and geotechnical engineering. In 1957, Paul Witherspoon became Professor of the University of California at Berkeley, and in 1977 he was appointed the first Director of the newly organized Earth Sciences Division (ESD) of Lawrence Berkeley National Laboratory (LBNL).

The monograph addresses many fundamental and applied scientific questions, and in doing so may help many scientists and practitioners bridge gaps in current scientific knowledge. Specifically, the volume begins with a chapter that for the first time introduces complex systems approaches to describe flow and transport in fractured-porous media. The chapter goes on to apply this approach to the analysis of fluid dynamics and transport in fractured-porous media, based on the papers* published in this volume, along with the presentations given at Session H071 of the Fall 2012 AGU Meeting.

The section "*Methods of Field Measurements and Experiments*" (chapters 2–4) includes a discussion of recent multidisciplinary studies and activities in underground research laboratories (URLs) related to radioactive waste storage and disposal, as well as repository design; a methodology for characterizing the hydrologic properties of a fault in a complex fractured system; and the application of a flowing fluid electrical conductivity (FFEC) logging method in deep boreholes to estimate the hydraulic properties of an aquifer.

The section "*Collective Behavior and Emergent Properties of Complex Fractured Rock Systems*" (chapters 5–10) includes a review of the development and application to fractured rock studies of the well-recognized cubic law, and its extension, for understanding the behavior of fractured rock masses. The chapters within this section include, respectively, (1) experimental results and a theoretical model demonstrating that swarm transport in a fracture is affected by the topology of the fracture, specifically the size and spatial variation in aperture; (2) a discussion of simultaneous measurements of stress-dependent permeability and fracture aperture distributions, demonstrating that both the aperture and effective fracture roughness are stress-dependent and hysteretic; (3) a new approach using the optimality principle to derive a unified form of conductivity relationship for two different flow systems, landscapes and unsaturated soils; (4) a method for evaluating the permeability of partially cemented fractures; (5) the results of experimental and numerical modeling studies indicating that osmotic pressure promotes countercurrent flow of oil from both the water-wet and oil-wet segments of shale; and (6) a discussion

*Some papers within this monograph were prepared using U.S. government funding. As such, the government retains a nonexclusive, royalty-free, worldwide license to use those articles for internal government purposes. Questions regarding individual abstracts should be directed to the respective author(s).

focused on the longstanding and often debated idea of representative volume elements (RVE), which plays a central role in the mechanics and physics of random heterogeneous materials and their effective properties.

The section "*Connection to the Surrounding Environment*" (chapters 11 and 12) includes the results of studies of advective gas transport via vadose zone fractures driven by surface-wind and vadose zone thermal gradients, as well as an approach to quantifying water flow and retention in an unsaturated fracture-facial domain, using a three-domain matrix-microcavity-film model.

The final section of the monograph, "*Multidisciplinary Research for Different Applications*" (chapters 13–15), presents the results of modeling thermo-hydro-mechanical (THM) processes in fractured and porous media, using (1) the momentum equation relating mean stress pore, pressure, and temperature, (2) the results of studies involving the biochemical behavior of plutonium in soil-plant systems, and (3) a description of an integrated experimental and modeling study of episodic air-water two-phase flow in fractures and a fracture network.

We expect that the readers of this book will include researchers, engineers, and professionals within academia, federal agencies, and private industry, as well as graduate and undergraduate students involved in theoretical, experimental, and numerical modeling studies of fluid dynamics and reactive chemical transport. Such studies could of course pertain to a wide range of scientific and practical applications in the field of flow and transport in fractured-porous media.

ACKNOWLEDGMENT

The Editors would like to express their deep gratitude to the Earth Sciences Division of Lawrence Berkeley National Laboratory for the support of publication of this Monograph, and to Dr. Donald DePaolo, LBNL Associate Director, and Dr. Susan Hubbard, Earth Sciences Division Director, for their encouragement of the development of this Monograph. The Editors are very much thankful to all presenters at the Fall 2012 AGU Special Session H071 and contributors of Chapters to this Monograph.

Boris Faybishenko, *Lawrence Berkeley National Laboratory, Berkeley, California, USA*
Sally Benson, *Stanford University, Stanford, California, USA*
John Gale, *Fracflow Consultants Inc., St. John's, Newfoundland and Labrador, Canada*

INTRODUCTION

Paul Witherspoon and the Birth of Contemporary Fractured Rock Hydrogeology

R. Allan Freeze[1], Iraj Javandel[2], and Shlomo P. Neuman[3]

ABSTRACT

Paul Witherspoon has been a seminal influence on the development of ideas and methodologies related to the hydrogeology of fractured rocks. His interest in the topic grew from his earliest studies on caprock integrity for underground gas storage, through his midcareer emphasis on the role of aquitards in hydrogeological systems, to his later work on thermohydrologic and hydromechanical couplings in geothermal systems and nuclear waste isolation.

EARLY INFLUENCES

It is possible that Paul Witherspoon's interest in deep fractured-rock hydrogeology may have been piqued as early as his teenage years in Dormont, Pennsylvania. Paul's father was a civil engineer who worked for a time for the Carnegie Coal Company. Paul took his first trips underground into the Carnegie coal mines with his father, where he was fascinated by the mining methods and surveying procedures used in the underground operations. A few years later, Paul's father founded his own business, drilling for natural gas, and Paul found himself serving as a tool dresser on his father's cable-tool rigs. There is little doubt that these early experiences led Paul to major in petroleum engineering when he entered the University of Pittsburgh in 1937. He graduated with a BS degree in 1941.

From 1941 to 1949 Paul worked in various capacities for the Phillips Petroleum Company in Oklahoma, Texas, and Kansas, but the further he advanced in his career, the more he felt the need to improve his background in mathematics, engineering, and geology. In the fall of 1949, at the age of 30, already married and a father, he left Phillips and enrolled at the University of Kansas. He graduated in 1951 with an MSc in petroleum engineering physics.

Paul's doctoral studies were carried out in a far different manner than were most of ours. He successfully completed his program at the University of Illinois while simultaneously holding down a full-time position as head of the Petroleum Engineering Division at the Illinois State Geological Survey. His PhD was awarded in 1957. His thesis topic involved the role of clay minerals and colloidal particles on the movement of oil and water through reservoir rocks. Even at this earliest stage of his research career he seemed more interested in subsurface barriers to flow than in the more popular studies of high-permeability aquifers and reservoirs.

UNDERGROUND GAS STORAGE

While working at the Illinois Survey, Paul became involved in a project to store natural gas in an aquifer near Herscher, Illinois. Depleted gas fields had been safely converted to storage operations for many years, but this represented the first attempt to use a relatively shallow aquifer that was not a proven trap for oil and gas. Early operations had to be curtailed because of leakage through the overlying caprock. It was this experience that led Paul to begin investigating improved methodologies for assessing caprock integrity.

[1]*Surrey, British Columbia, Canada*

[2]*Lawrence Berkeley National Laboratory, Berkeley, California, USA*

[3]*Department of Hydrology and Water Resources, University of Arizona, Tucson, Arizona, USA*

Dynamics of Fluids and Transport in Complex Fractured-Porous Systems, Geophysical Monograph 210, First Edition.
Edited by Boris Faybishenko, Sally M. Benson, and John E. Gale.

Paul joined the faculty in the Department of Mineral Technology at the University of California at Berkeley in 1957. There, aided by a large grant from the American Gas Association, he continued his work assessing the tightness of caprocks for underground gas storage [*Witherspoon et al.*, 1967]. There is little question that it was these studies that set him on a lifelong quest to better understand low-permability formations.

AQUITARDS

In the early 1960s, prodded by some reorganization at the university, Paul turned his attention away from petroleum engineering toward full-time research on hydrogeological topics. His background in gas storage studies led to his early recognition of the importance of aquitards in hydrogeological systems. His work with Allan Freeze showed that the location, geometry, and continuity of low-permeability formations has a controlling influence on the nature of regional groundwater flow systems [*Freeze and Witherspoon*, 1966]. His work with Shlomo Neuman led to the development of improved pump-testing methodologies for complex aquifer/aquitard systems [*Neuman and Witherspoon*, 1968]. He and Iraj Javandel provided a very early application of finite-element modeling in hydrogeology to assess flow in multilayered aquifers [*Javandel and Witherspoon*, 1969]. In 1971, he organized a seminal conference at Monterrey, California, that was the first to bring attention to the issue of the role of aquitards in groundwater flow systems.

GEOTHERMAL ENERGY

In 1977, Paul moved "up on the hill" to become the first director of the new Earth Sciences Division at Lawrence Berkeley National Laboratory (LBNL). During this period, and later as leader of the Reservoir Engineering and Hydrogeology Group, Paul saw LBNL take its place as one of the world's leading research institutes in the applied earth sciences.

In the 1970s and 1980s, there was considerable national interest in investigating alternative energy sources other than coal and petroleum. The LBNL group was involved in several projects to assess the potential of geothermal energy. The work included reservoir engineering, production engineering, geochemical and geophysical studies, and land subsidence investigations [*Gringarten et al.*, 1975; *Preuss et al.*, 1982].

NUCLEAR WASTE ISOLATION

Paul was well ahead of his time in realizing that a hydrological understanding of rock mass properties was going to be needed for purposes other than just withdrawing fluids from aquifers. His emphasis on the role of aquitards was a precursor to the issues that would soon arise in connection with nuclear waste isolation, geothermal energy production, and contaminant transport problems.

In the late 1970s, Paul was asked by the U.S. Energy Research and Development Agency to organize a workshop on low-permability rocks in Austin, Texas. The workshop was attended by a representative of the Swedish Nuclear Fuel Safety Program, who told Paul about their plans to carry out an underground testing program in an abandoned iron ore mine near Stripa, Sweden. The upshot was a cooperative research program between Sweden and the United States with LBNL taking the lead American role. At Stripa the joint teams developed new methods of fractured-rock characterization, and applied them to the hydrogeologic assessment of alternative waste-emplacement strategies. The Stripa studies set the standard for the investigation of nuclear waste repositories, and were among the first comprehensive studies of flow and transport in fractured rocks at depth [*Witherspoon et al.*, 1981; *Witherspoon*, 2000b].

The LBNL team also played a prominent role in the assessment of rock conditions at the proposed nuclear waste disposal site at Yucca Mountain, Nevada. Starting in 1991, Paul became the prime mover in producing a series of comprehensive reviews of the developing technology in nuclear waste isolation [cf. *Witherspoon and Bodvarsson*, 2006]. In 1996, Paul chaired a peer review of the thermohydrologic modeling and testing program at Yucca Mountain [*Witherspoon et al.*, 1996].

FRACTURED ROCK HYDROGEOLOGY

From his earliest work on caprock integrity, through his mid-career emphasis on aquitard hydrogeology, to his later work on geothermal energy production and nuclear waste isolation, an overarching theme in Paul's life was to understand the physics of flow through low-permeability media. In the early work, low-permeability formations were still treated as homogeneous units rather than as discretely fractured media, but he and his students and colleagues soon moved on to treatments of discrete fracture systems, initially based on parallel plate models (influenced by the earlier work at Berkeley by David Snow [1969]), then on interconnected three-dimensional fracture networks [*Long and Witherspoon*, 1985], and eventually on dual porosity representations of fracture systems embedded in more traditional porous media. The paper by *Witherspoon et al.* [1981] on the "Validity of cubic law for fluid-flow in a deformable rock fracture" is one of the most influential papers in the field of fractured rock hydrogeology [*Zimmerman*, 2012]. For a summary of this intellectual journey, see *Witherspoon* [2000a] and *Neuman* [2005].

Paul and his team were among the first to recognize the many coupled interactions between fluid flow, heat flow, and the stress/strain field that will occur at geothermal and nuclear waste sites in fractured rock. They were

responsible for some of the earliest treatments that integrated the thermohydrologic and hydromechanical couplings in subsurface environments [*Wang et al*., 1981; *Tsang and Witherspoon*, 1981].

Paul was one of the first hydrogeological researchers to recognize the potential of computer-based mathematical modeling in hydrogeology, but he was adamant throughout his career that it is also critical to get underground and carry out large-scale in-situ testing of hydrogeological conditions. He felt that the complete hydrogeological engineer must understand and integrate field measurement technology, laboratory experimentation, and mathematical modeling expertise (both analytical and numerical).

PAUL WITHERSPOON'S LEGACY

Paul was widely honored for his work. He and Shlomo Neuman were awarded both the Horton Award from the American Geophysical Union and the Meinzer Award from the Geological Society of America (GSA). Paul also received the Horton Medal from AGU and the Distinguished Service Award from GSA. In 1989, he was elected to the National Academy of Engineering for "pioneering work in geothermal energy, underground storage, hydrogeology, and the flow of fluids in fractured and porous rocks." In 2001, he was elected as a Fellow in the World Innovation Foundation.

Perhaps Paul's greatest legacy are his students and colleagues, who benefited from his generous mentorship, and a lifelong friendship of inestimable value. To show their appreciation, they honored him with three memorable research conferences at LBNL on the occasions of his 60th, 70th, 80th, and 85th birthdays. The proceedings of two of these events were published by the Geological Society of America [*Narasimhan*, 1982] and the American Geophysical Union [*Faybishenko et al.*, 2000; 2005].

To learn more about Paul Witherspoon in his own words, a videotaped interview that he gave in 2007 is posted on the website of the International Association of Hydrogeologists (timecapsule.iah.org). A biographical article based on the interview was also published by IAH [*Freeze and Javandel*, 2008]. Paul died on February 10, 2012, at the age of 93.

REFERENCES

Faybishenko, B., P. A. Witherspoon, and S. M. Benson (eds.) (2000), Dynamics of fluids in fractured rock, *Am. Geophys. Union, Geophysical Monograph*, *122*, 400 pp.

Faybishenko, B., P.A.Witherspoon, and J.Gale (eds.) (2005), Dynamics of Fluids and Transport in Fractured Rock, Geophysical Monograph Series, Vol. 162.

Freeze, R. A., and I. Javandel (2008), Hydrogeologist time capsule: Paul Witherspoon, *Hydrogeology Jour*., *16*, 811–815.

Freeze, R. A., and P. A. Witherspoon (1966), Theoretical analysis of regional groundwater flow: 1. Analytical and numerical solutions to the mathematical model, *Water Resources Res., 2*, 641–656.

Gringarten, A. C., P. A. Witherspoon, and Y. Ohnishi (1975), Theory of heat extraction from fractured hot dry rock, *Jour. Geophys. Res., 80,* 1120–1124.

Javandel, I., and P. A. Witherspoon (1969), A method of analyzing transient fluid flow in multi-layered aquifers, *Water Resources Res., 5,* 856–869.

Long, J. C. S., and P. A. Witherspoon (1985), The relationship of the degree of interconnections to permability in fracture networks, *Jour. Geophys. Res., 90*(B4), 3087–3098.

Narasimhan, T. N. (1982), Recent trends in hydrogeology, *Geol. Soc. Am. Special Paper 189,* 448 pp.

Neuman, S. P. (2005), Trends, prospects and challenges in quantifying flow and transport through fractured rocks, *Hydrogeology Jour., 13,* 124–147.

Neuman, S. P., and P. A. Witherspoon (1968), Theory of flow in aquicludes adjacent to slightly leaky aquifers, *Water Resources Res., 4,* 103–112.

Preuss, K., G. S. Bodvarsson, R. C. Schroeder, and P. A. Witherspoon (1982), Model studies of the depletion of two-phase geothermal reservoirs, *Soc. Pet. Engrs. Jour., 22,* 280–290.

Snow, D. T. (1969), Anisotropic permeability of fractured rock, *Water Resources Res., 5,* 1273–1289.

Tsang, Y. W., and P. A. Witherspoon (1981), Hydromechanical behavior of a deformable rock fracture subject to normal stress, *Jour. Geophys. Res., 18*(B10), 9287–9298.

Wang, J. S. Y., C. F. Tsang, N. G. W. Cook, and P. A. Witherspoon (1981), A study of regional temperature and thermohydrologic effects of an underground repository for nuclear wastes in hard rock, *Jour. Geophys. Res., 86*(B5), 3759–3770.

Witherspoon, P. A. (2000a), Investigations at Berkeley on fracture flow: From the parallel plate model to chaotic systems, in B. Faybishenko, P. A. Witherspoon, and S. M. Benson (eds.), *Dynamics of Fluids in Fractured Rock*, Am. Geophys. Union, Geophysical Monograph *122*, 1–72.

Witherspoon, P. A. (2000b), The Stripa project, *Intern. Jour. Rock Mechanics and Mining*, Neville Cook Special Issue, 385–396.

Witherspoon, P. A., and G. S. Bodvarsson (eds.) (2006), *Geological Challenges in Radioactive Waste Isolation: Fourth Worldwide Review*, Lawrence Berkeley National Laboratory, Report 59808, 283 pp.

Witherspoon, P. A., N. G. W. Cook, and J. E. Gale (1981), Geologic storage of radioactive waste: Field studies in Sweden, *Science, 211*(4485), 894–900.

Witherspoon, P. A., R. A. Freeze, F. A. Kulacki, J. N. Moore, F. W. Schwartz, and Y. C. Yortsos (1996), *Peer Review Report on Thermohydrologic Modeling and Testing Program, Yucca Mountain Site Characterization Project*, Department of Energy, Office of Civilian Radioactive Waste Management, 117 pp.

Witherspoon, P.A., J.S.Y. Wang, K. Iwai, and J.E. Gale (1980), Validity of cubic law for fluid-flow in a deformable rock fracture, *Water Resour. Res*., 16,1016–1024.

Witherspoon, P. A., I. Javandel, S. P. Neuman, and R. A. Freeze (1967), *Interpretation of Aquifer Gas Storage Conditions from Water Pumping Tests*, American Gas Assn.

Zimmerman, R.W. (2012), The history and role of the cubic law for fluid flow in fractured rocks, Fall AGY Session H071: Dynamics of Fluids and Transport in Fractured Porous Media, 3 December 2012.

1

A Complex Systems Approach to Describing Flow and Transport in Fractured-Porous Media

Boris Faybishenko[1], Sally M. Benson[2], John E. Gale[3], and Fred Molz[4]

1.1. INTRODUCTION

The study of complex systems has become recognized in recent years as a new scientific discipline. The primary goal of this chapter is to introduce an approach for the study of flow and transport in fractured-porous media through the use of complex systems theory. This approach will be based on (1) a review of complex systems theory, and (2) an analysis of the papers presented in this monograph, along with presentations given at the Fall 2012 AGU meeting session "Dynamics of Fluids and Transport in Fractured-porous Media," as well as other publications. Specifically, we would like to show that a fractured rock system may exhibit an emerging behavior resulting from interactions of its components.

The structure of the chapter is as follows: We will begin with the description of the general idea of the field of complex systems (including terminology), the general approach to the study of complex systems, central properties of complex systems, and the idea of emergence. Then, we will present the concept of a fractured-porous medium as a complex system, using a review of chapters included in this book, as well as abstracts of the presentations given at Session H071, "Dynamics of Fluids and Transport in Fractured-porous Media," of the Fall 2012 AGU Meeting held in San Francisco in December 2012. Our conclusion to the chapter will summarize the concept of a complex fractured rock system as one of the emerging trends in the field of hydrological science and technology, and answer the question whether the complexity sciences approach can benefit the field of flow and transport in fractured-porous media.

1.2. THE FIELD OF COMPLEX SYSTEMS

Adjectives such as *complicated, intricate, interconnected, interwoven, self-organizing*, and others are often used to describe complex systems, frequently in a qualitative sense. Despite much research on complex systems within different scientific fields, many such systems are not fully understood; there is no concise definition of a complex system [*Ladyman et al.*, 2013]. In a general sense, a complex system may be defined as a system consisting of a large number of interacting components, which are described by a set of dependent variables and parameters requiring measurement, whose total behavior in space and time is nonlinear and cannot be derived from the summation (i.e., linear superposition) of individual component activities. This definition applies to complex systems from a wide array of scientific disciplines, and interdisciplinary research is often necessary for the study of complex systems. *Whitesides and Ismagilov* [1999] defined a complex system as"one whose evolution is very sensitive to initial conditions or to small perturbations, one in which the number of independent interacting components is large (three or more), or one in which there are multiple pathways by which the system can evolve. Analytical descriptions of such systems typically require nonlinear differential equations. A second characterization is more informal; that is, the system is 'complicated' by some subjective judgment and is not amenable to exact description, analytical or otherwise."

Werner [1999] explained that the complexity in natural landform patterns is "a manifestation of two key characteristics. Natural patterns form from processes that are nonlinear, those that modify the properties of the

[1] *Lawrence Berkeley National Laboratory, Berkeley, California, USA*
[2] *Stanford University, Stanford, California, USA*
[3] *Fracflow Consultants Inc., St. John's, Newfoundland, Canada*
[4] *Clemson University, Anderson, South Carolina, USA*

Dynamics of Fluids and Transport in Complex Fractured-Porous Systems, Geophysical Monograph 210, First Edition.
Edited by Boris Faybishenko, Sally M. Benson, and John E. Gale.

environment in which they operate or that are strongly coupled; and natural patterns form in systems that are open, driven from equilibrium by the exchange of energy, momentum, material, or information across their boundaries."

Complexity theory is generally used to characterize systems with many parts (variables) that interact with each other in multiple and complex ways. When such interactions are understood thoroughly, then the overall system may be represented by coupled sets of nonlinear ordinary or partial differential equations. Because complete understanding of these complex linkages is often lacking, experimental and theoretical studies with complex systems theory in mind are often the main goal of research in different fundamental and applied scientific fields, such as computer science, mathematics, sociology, physics, philosophy, chemistry, psychology, economics, and biology. However, despite great interest in studies of complex systems, universal laws governing all such systems have not been developed.

The main characteristics and common principles of complex systems are illustrated in Figure 1.1 (developed at the New England Complex Systems Institute, http://www.necsi.edu/about/). Figure 1.1 illustrates that a complex system is composed of many parts that interconnect in complicated ways, and that the complexity of the system is related to the number and nature of the interconnections. In this chapter, we will show how these concepts can be linked to real examples of flow and transport in fractured-porous media.

1.2.1. General Approach to the Study of Complex Systems

Complex systems can be studied using a unified framework of theories and methods from all scientific and engineering disciplines. Complex system studies, in the first place, include research on how parts of a system give rise to the collective behavior of the system and how the system interacts with its environment, with the focus on both direct and indirect relationships between parts and the whole system. In 1948, Warren Weaver suggested two forms of complexity: disorganized complexity and organized complexity [*Weaver*, 1948]. In Weaver's view,

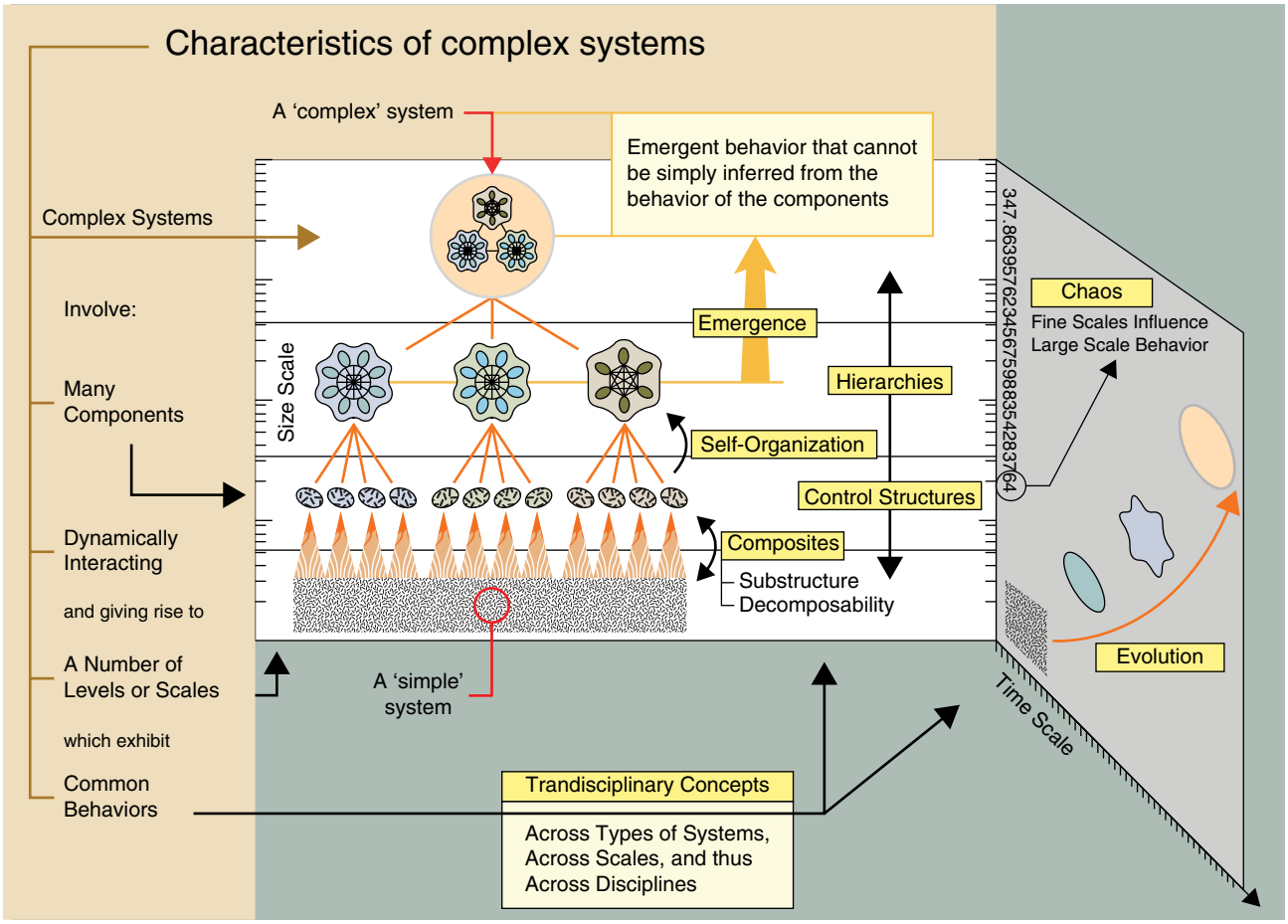

Figure 1.1 Main characteristics of a complex system. (Source: The New England Complex Systems Institute (NECSI), http://www.necsi.edu/projects/mclemens/sysrep.gif)

phenomena of disorganized complexity are treated using probability theory and statistical mechanics, whereas organized complexity deals with phenomena that escape such approaches and confront "dealing simultaneously with a sizable number of factors which are interrelated into an organic whole." Weaver's paper has influenced subsequent thinking about complexity.

As with simple systems, the nature of a complex system is intrinsically related to the behavior of its parts [*Bar-Yam*, 1997], but the emergent behavior of the complex system cannot be inferred directly from the behavior of individual components alone (http://www.necsi.edu/visual/systems.html).

To understand the behavior of a complex system, we must understand the concept of *dynamic interaction*. In other words, we must recognize the dynamic behavior of not only the system's parts but also how they act together to form the collective behavior of the whole system. The collective behavior of complex systems depends on many dependent and independent types of information and processes. It is also apparent that we cannot describe the whole system without describing its parts, and each part must be described in relation to other parts, which is the reason why complex systems are coupled and difficult to understand.

Describing the relationships among complex system parts is difficult, because the relationships are typically nonlinear. Moreover, a complex system is composed of groups of parts whose relationships (their nature, their degree) are more often than not poorly known or understood. Therefore, the emergent behavior of the system is difficult, if not at all possible, to predict, even though the behavior of individual components may be known, readily predictable, and observable.

Based on the theory of systems analysis, the behavior of an entire complex system cannot be understood by close study of its individual parts by themselves. Thus, experiments that isolate one part of a system while holding the other parts constant [*Smolin*, 2014] do not produce any real knowledge. It is necessary to look at parts in the context of the whole system, including the interaction with their surrounding environment, and account for these patterns in predictions using mathematical models. The notion of dynamic complexity can be applied to studies of different categories of complex systems, such as hydrodynamics (fluid flow, weather), climate, soil, composite materials, and earthquakes.

1.2.1.1. Emergent complexity and emergent simplicity of complex systems

Another property of complex systems is the phenomenon of emergence. This refers to a unique property that "emerges" (or appears) when the system components interact to develop a higher-level aggregate object, with a novel (often useful in a practical sense) property. A simple and well-understood example would be the development of a hive from the interaction of many individual bees. Presumably, no particular insect has the complete hive architecture in mind, but somehow it emerges from their many interactions (see http://dictionary.reference.com/browse/emergent+property).

In studies of complex systems, it is important to determine how the complexity of the entire system is related to the complexity of its parts, and vice versa. However, collective behavior of a complex system is not readily understood from the behavior of the parts. Individual components of a complex system are often complex systems themselves, so it seems reasonable to assume that a collective behavior of the complex parts would also be complex. Still, even if a system were composed of simple parts, the collective behavior of these simple parts may become complex, which is called *emergent complexity*.

Another type of emergent behavior is *emergent simplicity*. A system composed of complex parts may exhibit a simple collective behavior, which is called *emergent simplicity*. A simple example is a planet, such as Earth, orbiting around a star, while the Earth itself is a complex system. This example illustrates that the collective system and its parts may behave *differently* at different scales. In other words, the system (and the system's components) may behave in a complex way on a smaller scale, but on a larger scale multiple complex details may not be relevant.

The following hydrogeological examples may be used to illustrate the concept of emergent simplicity and the difference between local emergence (when collective behavior appears within a small part of the system) and global (i.e., systems) emergence (when collective behavior relates to the whole system). For example, in the study of gas transport in fractured-porous subsurface media, two emergent properties of a gas are its pressure and temperature. These properties are emergent because they do not naturally arise out of the description of individual particles. Pressure and temperature become relevant to thermodynamic studies only when many particles are combined together, so that pressure and temperature can become local emergent properties of media. The pressure and temperature are local properties of the gas phase in the subsurface, and hydraulic pressure is a local property of the water in the subsurface. In physics, these local emergent properties are called *intensive*.

Phase transitions (e.g., solid to liquid and liquid to vapor) represent collective dynamics that are visible on a macroscopic scale but that can be seen in a microscopic sample as well, using modern detection methods (such as advanced spectroscopic, microscopic, and tomographic characterization techniques) to study biogeochemical interfaces in porous media (e.g., *Rennert et al.*, 2012).

Another example of a local emergent property is the formation of water from atoms of hydrogen and oxygen.

The properties of water are not apparent in the properties of oxygen or hydrogen gases, nor does an isolated water molecule reveal most properties of water. However, a microscopic amount of water is sufficient. In the study of complex systems (such as fractured rock), we are mainly interested in global emergent properties, which also depend on the surrounding environment.

1.2.1.2. Self-organization and feedback loops

Self-organized criticality, the spontaneous development of systems to a critical state, is the first general theory of complex systems with a firm mathematical basis. This theory describes how many of the seemingly disparate events of the world, from stock market crashes to mass extinctions, avalanches to solar flares, all share a set of simple, easily described properties.

The collective behavior and the emergence of a real complex system can spontaneously lead to the system's *self-organization* [*Peak and Frame*, 1994] and self-organized criticality, a feature of a complex system, related to an emergency [*Bak et al*., 1987]. Self-organization is a process in which some form of global order or coordination arises out of the local interactions between the components of an initially disordered system. This process is spontaneous: it is not directed or controlled by any agent or subsystem inside or outside of the system; however, the laws followed by the process and its initial conditions may have been chosen or caused by an agent. It is often triggered by random fluctuations that are amplified by positive feedback. The resulting organization is wholly decentralized or distributed over all the components of the system.

The original "principle of the self-organizing dynamic system" [*Ashby*, 1947] states that any deterministic dynamic system would evolve toward a state of dynamic equilibrium (or in the terms of nonlinear dynamics and chaos, an attractor), so that the further evolution of the system is constrained to remain within the attractor. The presence of the attractor implies a mutual dependency or coordination between system components, with each component adapting to a state affected (to different degrees) by all other components.

The component adaptation is developed through a process that occurs in a feedback loop, including both positive feedback and negative feedback. *Positive feedback* is an influence on the process that enhances or amplifies the response of the system, when a small disturbance on a system increases in magnitude. Positive feedback loops normally do not cause endlessly increasing growth but rather have limited effects over time and space, resulting, for example, in the system's explosion, erosion, or collapse.

The positive feedback loops are often followed by a negative loop [*Meadows*, 1999]. *Negative feedback* occurs when the output of a system, process, or mechanism is fed back as a system (or one of its components) input to reduce the system's output growth or fluctuations, which may lead to instability. Negative feedback generally reduces the effects of perturbations, promotes system's stability, and stimulates a state of equilibrium and stability.

Feedback loops in the emergent system result in coevolution, which in turn lead to further iterations of the system [*Main et al*., 1994].

The complexity of a system must be a decreasing function of scale, because the information needed to describe a system on a larger scale must be a subset of the information needed to describe the system on a smaller scale: any finer-scale description contains the coarser-scale description. (The Earth orbiting the sun is a relatively simple example.) In general, the complexity of system parts is described by the complexity of the system evaluated on the scale of the parts. When the behavior of the system depends on the behavior of its parts, the complexity of the whole must involve a description of the parts, thus it is large. The complexity of the entire system increases when the complexity of the smaller parts of the system is included.

1.2.1.3. Mathematical models: General approach

In classical mathematical theory, a model of any system is formed from simple elements whose states are correlated to a certain degree. Without correlations, emergent behavior is impossible. A model must be sufficiently rich in order to capture the phenomenon of global emergent behavior. The quantitative study of both simple and complex systems is based on the use of modeling using differential equations. Differential equations, like the equations that describe the relation between pressure and water flow, assume that a system is essentially uniform. The equations include effective parameters because the local-scale details are not important for the behavior of the system at larger scales.

However, such assumptions may not be generally valid for complex systems and may lead to significant uncertainties or errors in predictions. Alternative models such as fractals, percolation models, and nonlinear dynamical models may reduce such predictive uncertainty or error.

1.3. FRACTURED ROCK AS A COMPLEX SYSTEM

The goal of this section is to present the principal properties and characteristics of complex systems, described in the preceding section of this chapter, as they are related to fractured rock.

1.3.1. Methods of Field Measurements and Experiments

A fractured rock system is a complex system containing many interdependent parts. These parts need to be studied using different types of field and laboratory tests

and experiments, using various monitoring techniques. Over the past 20–30 years, multiple surface and subsurface geophysical methods have been developed to characterize fractured rock and sediments. The most commonly employed methods include the heat pulse flow meter, the electromagnetic flow meter, and hydrophysical (or FEC) logging [*Pedler*, 2012]. These methods have been successfully applied in all types of hydrogeologic systems, including fractured bedrock, fractured sandstones, alluvium, massive and fractured clays, karst, and volcanic, for various practical applications, including remediation, geotechnical, mining, and water supply.

Karasaki et al. [2015, this volume] report on conducting a series of pump tests in isolated sections of two inclined ~200 m long boreholes, which were separated by a distance of ~130 m from each other. The boreholes penetrated the Wildcat Fault, a semivertical strike slip fault and a member of the Hayward Fault System, situated in the Berkeley Hills. The geology encountered in the boreholes was predominantly that of the Claremont formation, with extensively fractured and alternating sequences of chert, shale, and sandstone. The authors analyzed the drawdowns in four isolated sections within a vertical borehole (WF-1) and drilled adjacent to the fault at distances of ~45 m and ~95 m from each of the inclined boreholes. The permeability of the fault plane was found to be two orders of magnitude higher than that of the protolith, and anisotropic, with a ~10-fold higher permeability in the near-horizontal direction, which is somewhat expected for a strike slip fault. Buildup analysis suggests that the fault is asymmetric with higher permeability along the east side of the fault plane and lower along the west side. The results of this paper indicate that the field pumping tests provide an evaluation of the effective hydrogeological parameters on the scale of tens of meters, which relates to the idea of an emergent simplicity on a larger scale.

Wang and Hudson [2015, this volume] raise the question of how to determine the geometrical and hydrogeological properties of fractures in a specific rock mass, how to establish the link between hydrogeological fracture properties and other variables (such as the *in situ* stress state), and how to validate the results of experimental investigations at the full scale. The authors describe their progress in developing underground research laboratories (URLs) in both hard and soft rock, in housing large halls for particle detections at great depths, and in testing the energy and resource recovery capacities and waste disposal potential through borehole complexes.

Hawkins et al. [2012] present the results of an experiment in which the effect of channelized flow on fluid/rock heat transfer is measured using fiber optic distributed temperature sensing (DTS) and ground-penetrating radar. They showed that between wells with good hydraulic connection, heat transfer followed a classic dipole sweep pattern. However, between wells with poor hydraulic connection, heat transfer was skewed toward apparent regions of higher transmissivity (or larger aperture). The saline tracer test between the same wells confirmed that flow channeling significantly impacts heat transfer efficiency, even in single bedding plane fractures. The flow-channeling concept is similar to the idea of preferential flow in fractured rock.

In their studies of preferential flow paths in waste rock piles, *Broda et al.* [2012] demonstrate the importance of studies of various forms of unsaturated localized preferential flow processes, such as flow in macropores and fractures, and flow at heterogeneity-driven and gravity-driven unstable high velocity (with local hydraulic conductivity of several dozen meters per day).

Chan et al. [2012] demonstrate the need to use a variety of field tests, including saltwater tracer tests, hydraulic tests, and heat-pulse flowmeter tests, to locate the permeable fractures and detect the hydraulic connections between boreholes. Tracer cross-borehole tests included injection of zero-valent iron tracer with a magnet array specifically to locate permeable fractures and determine connectivity. *Howar and Wohnlich* [2012] use a series of push-pull tests, also known as single-well injection-withdrawal (SWIW) tests, with an application of tracer-cocktails consisting of fluorescent tracers (Uranine, Amidorhodamine G and Tinopal CBS-X) with different diffusion and sorption properties to characterize the fractured-porous media. *Le Borgne et al*. [2012] report on conducting a series of thermal and solute tracer tests to characterize the fractured crystalline aquifer of Ploemeur, France. Thermal tracer tests were performed by injecting continuously 50° C water in a fracture located at a 50 m depth. The breakthrough curves measured in an adjacent borehole show a significant time lag between the thermal and solute breakthrough due to the large coefficient of heat diffusion compared to molecular diffusion. Combining heat and solute tracer tests allows measuring tracer dispersion with Peclet numbers varying over orders of magnitude, thus providing important constraints on effective transport behavior [*Klepikova et al.*, 2011].

DePaolo [2012] describes an application of isotopic and trace element sensors for fluid flow, heat- and mass transport in fractured rocks, including examples of useful analytical models and applications to available data from fluid-rock systems for helium and helium isotopes, Sr-O-H isotopes, uranium isotopes, U decay series isotopes, and radiocarbon. The application of these methods will allow scientists to better understand the nature of heat and mass transport in hydrothermal systems in fractured rock. Isotopic methods are used as a supplement to directly measuring flow and transport properties in fractured rock, taking into account mineral-fluid chemical reactions and transport in the interfracture rock matrix. *Ellis et al*. [2012]

report on studying the leakage of CO_2 acidified brine, resolving and accounting for spatial variations in mineralogy along these leakage pathways, which is needed to improve the predictive models used to estimate the permeability evolution through reactive caprock fractures. *Menke et al.* [2012] studied CO_2 and H_2O leakage rates from the injection zone to overlying units as a result of geologic sequestration, and found that the water-leakage rate through the fault increases with decreased CO_2 injection rate. This inverse relationship is attributed to the complex relationships between relative permeability, saturation, pressure, and capillarity. Both papers on CO_2 transport are an illustration of the need to study the properties of complex systems in relation to the surrounding environment, along with coupled processes affecting the systems' emergent behavior.

1.3.1.1. Collective behavior, emergent complexity, and emergent simplicity of complex fractured rock systems

Ellis et al. [2012], in their studies of mineral spatial heterogeneity of a limestone fracture, determine that a doubling in fracture volume may overestimate the calculated values of permeability by as much as 40%, when dissolution is assumed to occur uniformly along the fracture. The authors indicate the importance of studies of bands of less reactive minerals perpendicular to the direction of flow, which restrict flow along the fracture, serving to control fracture permeability. These bands are a demonstration of the need to study different parts of the complex fractured rock, which may influence the behavior of the whole system.

Mourzenko et al. [2012] investigate the percolation and permeability of fracture networks in excavated damaged zones (EDZ) at the Mont Terri underground rock laboratory (Switzerland). This work is performed to study the characteristics of Opalinus Clay to assess its capacity to serve as a low-permeability formation for hosting radioactive waste repository sites [*Mourzenko et al.,* 2011]. The authors found that the fracture density is an exponentially decreasing function of the distance to the wall of the EDZ with a characteristic length of about 0.5 m. They also found that the fracture orientation is anisotropic, most fractures are subparallel to the tunnel walls, and this can be approximated by a Fisher law. They demonstrate that a heuristic power-law model can accurately describe the results for the percolation threshold over the whole investigated range of heterogeneity and anisotropy, and a simple parallel flow model can be used to describe fractured rock transmissivity. The latter demonstrates the idea of conversion of the emerging complexity regarding the individual parts of the system, into an emerging simplicity, when the flow can be described using a simple parallel flow model.

To study the overall thermo-hydro-mechanical properties of the rock, *Ezzedine et al.* [2012] focus on how within fractured-porous rock, micropores and microfractures and their interactions affect the cumulative behavior of effective mechanical, thermal, and hydrological rock properties. The results are then used to infer uncertainty associated with the physical and chemical aggregates of tight shale rock and their parameterization, using brute-force Monte-Carlo method. *Sun and Carrigan* [2012] also demonstrate the results of modeling of uncertainty in predictions of gas transport in fractured rock. Both papers confirm that uncertainty is an inherent feature of complex systems.

Field tests at various scales (1 to 100 m) demonstrate that the dynamics of multiphase flow in fracture networks is highly complex because of the coupling of inertial and viscous forces, gravity, surface tension, and wettability of fracture walls, as well as fracture intersections. Moreover, fracture intersections act as flow integrators and switches of flow pathways [*Wood and Huang*, 2015, this volume].

In their studies of candidate sites for radioactive-waste disposal, *Geier et al.* [2012] find many similarities and differences, which can be attributed to regional and local conditions such as stress fields, rock types, fractured-rock hydrodynamics, and paleohydrogeology. For example, while having broadly similar redox and pH conditions, there is more dissolved methane and lower sulfate below 300 m depth at the Olkiluoto site in Finland than at the Forsmark site in Sweden, although both sites are in hard crystalline rock (migmatite gneiss and metagranite, respectively) with groundwater flow mainly via fractures. Water-rock reaction modeling does not explain these and other differences in groundwater compositions and secondary minerals at the two sites. The conclusion, from the standpoint of complex system theory, is that the studies of individual parts of the complex system are insufficient for understanding the behavior of the entire system, or for understanding the relationships among the specific components of the system.

Boomsma and Pyrak-Nolte [2015, this volume] present the results of studies regarding the collective behavior of transport in fractured media, which is a manifestation of the emergent properties of the fractured rock system. The authors create a synthetic fracture-network model, using an Objet Eden 350V 3D printer, to build a network of fractures and show that the ability to transport cohesive swarms through the fracture network is a function of the flow rate and swarm volume. These experiments demonstrate conditions under which colloidal-size contaminants can be driven through a fracture network. High-speed transport of cohesive swarms depends on the volume of the swarm and the ambient flow rates that provide a balance of forces, preventing significant loss of particles from the swarm or deposition of particles along the flow path. Swarms that are transported cohesively travel along a highly localized path through a fracture network. The result of this

investigation is clear evidence of collective, emergent behavior in the fractured rock system, which may occur in fractures in the subsurface as a result of both natural and anthropogenic/industrial processes (such as synthetic nano- and micro-particles from consumer products, chemical and mechanical erosion of geologic material, and hydraulic fracturing proppants). The degree of localization and speed of transport of such particles depends on the transport mechanisms, the chemical and physical properties of the particles and surrounding rock, and the flow-path geometry through the fracture. This chapter is an excellent example of the need to study the collective behavior of parts of the system.

Another example of collective behavior is given by *Fakcharoenphol et al.* [2015 (this volume)], who reported the results of experimental and numerical modeling studies conducted to evaluate the potential of low-salinity waterflooding of oil reservoirs in shales. The authors find that osmotic pressure, caused by a salinity contrast, can cause countercurrent flow of water and oil, both in oil-wet and water-wet shale formations, and showed that in conventional oil reservoirs, low salinity oil-recovery improvements of carbonate formations might be partly attributable to osmotic pressure induced by salinity contrast. The mathematical/numerical model includes osmotic pressure, gravity, and capillary effects, thus illustrating the need for consideration of the collective behavior at the field scale.

1.3.1.2. Upscaling is manifestation of emergent simplicity

The idea of upscaling is relevant to the notion of emergent simplicity. *Karimi-Fard et al*. [2012] present an application of discrete fracture modeling (DFM) and upscaling techniques to complex fractured reservoirs, including DFM techniques developed by *Karimi-Fard et al*. [2004], in turn based on an unstructured finite-volume discretization. The mass flux between two adjacent control volumes is evaluated using an optimized two-point flux approximation. The method is designed for general purpose simulators, and any connectivity-based simulator can be used for flow simulations. The DFM technique can be used as a stand-alone or as part of an upscaling technique. Such upscaling techniques are required for large reservoirs, wherein the explicit representation of all fractures and faults is not possible [*Karimi-Fard et al*., 2006]. Using an empirical finite-sized scaling approach to understand the hydromechanical relationship of single fractures, *Petrovitch et al*. [2012] find that fluid flow can be represented at all scales by a single universal scaling function.

Using the results of air permeability measurements in vertical and inclined boreholes spanning a $30\times20\times30$ m^3 site in unsaturated fractured tuff near Superior, Arizona, *Neuman et al.* [2012] show that a hierarchical structure of fractured rock renders their attributes scale-dependent. The authors show that this behavior is consistent with sub-Gaussian random fields subordinated to truncated (monofractal) fractional Brownian motion (tfBm). Using the scaling theory, the authors develop a consistent statistical relationship between fracture length, aperture, density, and log permeability.

1.3.1.3. Feedback loops, hysteresis, and variations of parameters

In their study of stress-dependent permeability in fractured-porous media, *Huo and Benson* [2015 (this volume)] provide compelling evidence that flow and transport in fractured-porous media meets the criteria of a complex system, specifically self-organized criticality and forward feedback. Using a series of core flood experiments, the authors show that hysteretic behavior in both permeability and fracture aperture is due to repeated cycles of compression and decompression. When fractured rock is compressed axially, the fracture aperture is compressed, resulting in effective pressure increases and an exponential decrease in permeability, as expected from stress-dependent permeability theory. However, when the fractured rock is decompressed, permeability increases but does not follow the compression path to the original value. In other words, the phenomenon of hysteresis indicates the irreversible deformation of fracture asperities and friction between asperities, and corroborates the idea of forward and negative feedbacks in complex fractured rock systems.

Lee et al. [2012] study the evolution of the dispersion coefficient in the single rough-walled fracture before and after circulated flow near the wall. They show that dispersion in the variable-aperture fractures occurs by the combined effects of molecular diffusion, macro-dispersion, and Taylor dispersion. In particular, Taylor dispersion is proportional to the square of the velocity, while macro-dispersion is proportional to the velocity. The results of the experiments conducted using a rough-walled fracture model show distinct dispersion regimes in different parts of the fracture and for different Reynolds numbers. For example, in the range of $\mathrm{Re} < 2.78$, the dispersion coefficient was proportional to the power of n from 1 to 2, which corresponds to previously published data. However, the calculated dispersion coefficient decreased for $\mathrm{Re} > 2.78$, which the authors explain by the generation of circulated flow near the fracture wall. It is the opinion of the authors of this chapter that Lee et al.'s experimental results correspond to the idea of forward feedback in flow through fractures.

Tsenn [2015 (this volume)] studies the effect of contact area on fracture permeability, based on the notion that chemical processes could alter both the contact-area fraction and the pattern of the fracture surface and fracture aperture. The author conducts numerical Monte-Carlo

modeling, using the boundary-element method to assess the fracture pressure and flux, and shows that (1) contact-area fraction has a much greater effect on fracture permeability than the contact-area pattern, (2) a near-linear relationship exists between contact-area fraction and normalized fracture permeability when the contact-area fraction is less than 0.2, (3) as the contact-area fraction increases, normalized fracture permeability decreases, with the spread of values possibly up to one order of magnitude, and (4) flow through fractures could be blocked for the contact-area fraction greater than 0.7. Moreover, these results show that the calculated fracture permeability based on the parallel-plate model may overestimate the fracture-network permeability by over one order of magnitude. Another important conclusion is that dynamic data, such as pressure transient tests, are needed to assess the equivalent hydraulic aperture or hydraulic conductivity for fractures in the fracture network. Tsenn's chapter provides an example of when an emergent complexity of the system on a small scale can be presented using a set of effective parameters, i.e., by means of emergent simplicity.

Petrovitch et al. [2012] present the idea of universal scaling of fracture hydraulic properties, based on the results of nonintrusive geophysical techniques. While seismic techniques have been developed to probe the mechanical properties of fractures, e.g., fracture-specific stiffness, there are no techniques by which to remotely characterize their hydraulic properties. In this study, an empirical finite-sized scaling approach was used to understand the hydromechanical relationship of single fractures. This paper is an example of reducing the level of complexity in the measurements of fractured rock properties by measurements of seismic and hydraulic properties, or the consideration of a more simple level of emergency.

Liu [2015 (this volume)] develops a hydraulic conductivity relationship for unsaturated water flow based on minimized energy dissipation, using the optimality principle. The basic idea of the optimality principle is that natural processes organize themselves in such a way that their functioning is optimal under given external forcing and steady state conditions. The optimality principle has been widely used in many scientific fields, including constraining hydrological models [*Kleidon and Schymanski*, 2008; *Westhoff and Zehe*, 2013]. Based on the assumption that a flow field will tend toward a minimum energy dissipation rate, *Liu* [2015 (this volume)] derives an unsaturated hydraulic conductivity function and shows that the ratio of water flux to water head (energy) gradient is a power function of water flux. Empirical evidence supports the validity of this relationship under gravity-dominated conditions. The finding that the hydraulic conductivity depends not only on capillary pressure (or saturation) but also on the water flux confirms a long-standing hypothesis developed for structured soils (e.g., *Rode*, 1965).

Seok and Gale [2012] address the long-standing idea of representative volume elements (RVE), which plays a central role in the mechanics and physics of random heterogeneous materials when predicting their effective properties. The authors conduct an experiment using one cubic meter of granitic rock with a single natural fracture, which is characterized by strong spatial variability in permeability and porosity. The experimental results were compared with those from simulations of flow, using average and spatially variable permeability in a discrete fracture. The comparison also includes the results of water injection tests in seventeen boreholes, both individually and in groups, to assess the local permeability and hydraulic head distributions over the fracture plane as a function of normal stress.

In *Seok and Gale* [2015 (this volume)], the authors present fracture pore space data, from coupled stress-flow experiments, that had been measured using a resin technique on the scale of the fracture apertures over the entire 200 mm × 300 mm area of a fracture plane sample. Using these pore space data, which essentially constitute a fully characterized part of one piece of the complex system, the authors were able to determine how much data were required to obtain a reasonable match between the measured flow rates and the numerical-model-simulated flow rates, when the complexity of the spatial variability of the fracture pore space was embedded in the numerical fracture-flow models. In addition, the fully characterized fracture pore space allows us to evaluate how the inherent spatial variability in just one part of the complex fracture-flow system affects the fluid velocities (and hence solute transport) in fracture planes with highly variable fracture-aperture or pore-space distributions. The results of these experimental and 3D numerical modeling studies demonstrate that the complex flow and transport phenomena in fractured media can be simulated based on the idea of statistically similar RVE, using effective properties of heterogeneous media. This chapter [*Seok and Gale*, 2015 (this volume)] is another manifestation of the concept of RVE and effective parameters corresponding to the concept of emergent simplicity used in the theory of complex systems.

1.3.1.4. Connection to the surrounding environment

A complex adaptive system, such as a soil or fractured-porous system, responds by varying its behavior depending on its surrounding environment. *Dragila et al*. [2015 (this volume)] addressed the phenomena of complexity in gas exchange between the Earth's upper crust and the atmosphere, which controls to a large extent many important processes, such as the Earth-atmosphere water cycle, agricultural activities, and greenhouse gas emissions. Although diffusion was conventionally considered the main mechanism of gas exchange between the atmosphere

and vadose zone, driven by gas concentration gradients, laboratory and field-scale studies have shown that advective gas transport mechanisms are governing these fluxes in fractured rocks and cracked soils. Convection driven by thermal gradients (free convection) and wind induction (forced convection) were found to play a major role in Earth-atmosphere gas exchange.

Nimmo and Malek-Mohammadi [2015 (this volume)] attempt to quantify water flow and retention in a partially saturated fracture-facial domain, using a three-domain flow model. Two of the domains are assumed to characterize water flow and water storage in a fracture-facial region, and the third domain is assumed to characterize the matrix water. The flow domain is modeled with a source-responsive preferential flow model, the roughness-storage domain is modeled with capillary relationships applied to the fracture-facial area, and the matrix domain is modeled using traditional unsaturated flow theory. The authors test the proposed model to characterize the hydrology of the Chalk formation in southern England, linking hydrologic data including recharge estimates, streamflow, water table fluctuation, imaging by electron microscopy, and surface roughness. The authors indicate that the concept of unsaturated roughness storage is the collective effect of all microcavities in unsaturated media, which is one of the main features of complex systems.

The chapter by *Sharma et al*. [2015 (this volume)] is an illustration of long-term temporal changes in local flow rates in a brine formation composed of multiple layers with different transmissivities over a period of months or years, for instance, as a result of seasonal or climatic changes, owing to the connection to the atmosphere. The chapter also illustrates the effect of self-organization and a feedback loop (both forward and negative feedbacks), as a consequence of supercritical CO_2 storage in the deep subsurface. The results of investigations show how the local flow pattern of the storage formation will be disturbed and may change over time, as low-density and low-viscosity CO_2 enters into the transmissive layers and interacts with water and rock.

1.4. MODELS AND APPROACHES: MODEL SIMPLIFICATIONS

Zimmerman [2012] reviews the history and role of the cubic law for fluid flow in fractured rock, starting from the seminal paper "Validity of Cubic Law for Fluid Flow in a Deformable Rock Fracture" by Witherspoon et al [1980]. The idea of the cubic law was initially developed based on the model of hydraulic transmissivity of a channel bounded by two smooth parallel walls separated by an aperture h, for which transmissivity is exactly equal to $h^3/12$. However, the walls of actual rock fractures are rough and are in contact at discrete asperities that correspond to local regions of zero aperture. The presence of spatially varying apertures led to the development of the theory of hydraulic aperture or the evaluation of effective mean aperture, to account for the effect of aperture variability and contact area by suitable multiplicative factors. Zimmerman also emphasizes that normal stress will reduce the aperture in a nonuniform manner, so that the three factors, mean aperture, aperture variability and contact area, will influence the manner in which the transmissivity changes due to normal stress. Although the cubic law holds for flow between parallel walls up to the laminar-turbulent transition that occurs at Reynolds numbers of about 2000, deviations from a linear relationship between pressure drop and flow rate in a rough-walled fracture occur at much lower Reynolds numbers, on the order of about 10, during laminar flow. Zimmerman's paper provides an example of the case in which positive feedback in fractured rock is followed by a negative feedback, leading to stability of the system.

Broda et al. [2012] simulate such flow patterns using a numerical 3D fully integrated surface/subsurface flow model HydroGeoSphere, in which material heterogeneity is represented by means of (1) the dual continuum approach, (2) discrete fractures, and (3) a stochastic facies distribution framework using TPROGS. The results of this paper demonstrate the need for an application of multiple models and corresponding observations on different scales.

Leube et al. [2012] perform a model reduction and multiscale simulations for solute transport in fractured-porous media, based on the application of the multirate mass transfer model (MRMT) with model block upscaling. Modeling also includes the application of temporal moments for generating the MRMT equations, which were used to analyze the multiscale arrival time statistics in fractured media, taking into account fracture network properties, matrix properties, heterogeneity, and mass transfer that leads to non-Fickian transport behavior.

Willmann and Kinzelbach [2012] develop a new stochastic particle-tracking method to model transport explicitly in both fractures and matrix. Contrary to the existing flow simulations using a superposition of two separate domains, the fracture and matrix domains with exchange particles between them, the authors use a model in which a particle stays in a fracture before being released again to the matrix, depending on the fracture aperture, with the matrix flux perpendicular to the fracture, and a molecular diffusion component. This stochastic model also takes into account weighted random choice at fracture intersections as well as a random component of molecular diffusion. The model is applied to assess a fractured sedimentary formation in Northern Switzerland, which is currently under investigation as a host rock formation for nuclear waste disposal.

van Genuchten et al. [2012] show that complex flow and transport processes at a uranium mining site having

granular and fissured aquifers underneath can be simulated using Richards equation with a dual-porosity numerical model for variably saturated water flow and contaminant transport. In this model simulation, the composite (effective) unsaturated hydraulic conductivity function is used to account for the separate effects of the fracture and matrix domains, while uranium transport is simulated using a full dual-porosity formulation.

1.4.1. Multidisciplinary Hydrological, Geochemical, and Microbiological Research for Different Applications

Kahler [2012] presents a technique to promote mixing in dead-end pores to improve a pump-and-treat remediation approach, which is among the most common methods to remediate contaminated groundwater. A series of numerical and laboratory experiments illustrate that a change in pressure is needed to promote the pore-cleaning mechanism. The physical mechanisms of mixing were previously discussed in a number of publications (e.g., *Ottino*, 1990; *Weeks and Sposito*, 1998). *Faybishenko* [2005] showed that in fractured rock, mixing and dispersion of fluids result from two types of complex interactions between flow processes (even for small Reynolds numbers) on different scales: (1) drop length-scales, such as breakup, coalescence, and hydrodynamic interactions; and (2) agglomerate length-scales, such as surface erosion, fragmentation, and aggregation [*Ottino*, 1990], which are also caused by chaotic regimes in fractured-porous media [*Faybishenko*, 2003].

Winterfeld and Wu [2015 (this volume)] study geomechanically coupled processes in unconventional oil and gas reservoirs, showing that fracture networks provide highly permeable flow paths that allow for access to tight matrix blocks. Using as an example the results of water injection in Bakken, the authors illustrate how stress changes during water injection could induce microfractures that further extend the fracture network into the matrix. The stress change is calculated using equivalent mechanical properties for fractured rock, assuming that the deformation of fractured rock is the sum of the deformation of intact rock and fractures. The authors also apply the Hoek-Brown failure criterion to calculate when matrix rock fails. Simulation results indicate that viscous displacement and spontaneous imbibition processes are negligible because they cannot penetrate into the tight matrix block. Once matrix blocks are cracked via thermally induced stresses on the matrix surface, these processes become more pronounced and can improve oil production from the cracked tight matrix. The results of this paper are indicative of the sequence of positive and negative feedback processes in fractured media.

Peng et al. [2012] address the problem of reduced gas recovery in fractured Barnett shale, finding that the average first-year decline reported was 64%, which is attributed to the coupled physical (such as tortuous flow pathways) and chemical (such as desorption) processes in the low permeability shale nano-porous matrix. Similar results of the long-term decline of gas production in shale were reported by *Patzek et al.* [2013] and *Monteiro et al.* [2012].

Mullally and Lowell [2012] investigate boundary layer flow, heat, and chemical transfer near an internally heated vertical borehole or borehole array emplaced in a homogeneous water-saturated porous medium, as a means of developing a large-scale hydrothermal experiment at the DUSEL site in the Homestake Mine, South Dakota, or elsewhere. The authors use a scale analysis to determine the relationships between vertical fluid velocity, boundary layer thickness, and the Rayleigh number, for both a single borehole maintained at constant temperature and a linear array of boreholes maintained at a constant heat flux. Based on the scale analysis, it is determined that thermoelastic stresses generated by heating the rock near the boreholes do not significantly impact the permeability for a low initial porosity of ~5%, or when the initial crack aspect ratio is less than or equal to 10^{-2}. The scale analysis is also used to assess mineral dissolution within the boundary layer adjacent to the boreholes.

Molz et al. [2015 (this volume)] describe a decade long multidisciplinary research project, including field, laboratory, and modeling of plutonium (Pu) transport, first in field lysimeter soil, then in field soil containing grass roots, and finally in the roots and stems of corn (a type of grass) grown in laboratory pots. The overall system studied was certainly complex, involving natural climatic conditions driving variably saturated flow, coupled to oxidation and reduction of Pu species, species interaction with chelating agents secreted by plants and microbes, then rapid uptake by plant roots followed by transport in the transpiration stream and into the surrounding plant tissues. Many of the sub-processes occurred at very different time scales, but emerged simplicity was evident in several of these sub-processes. Downward transport of Pu in soil was dominated by the highly adsorbed oxidized Pu species, with only a couple of cm movement during the 11 year field period. A tiny fraction of Pu that was reduced on particle surfaces and released, in a repetitive manner, moved downward more rapidly. Pu uptake and movement in plants was millions of times faster than oxidized Pu in the soil, about 58 cm in 10 to 20 min. based on laboratory experiments. This rapid transport was probably due to Pu uptake by the biochemical apparatus of plants that was evolved to facilitate iron (Fe) uptake, an essential nutrient that is often held tightly to soil surfaces. In the lysimeter experiments, upward movement in the transpiration stream resulted in Pu being deposited on the soil surface due to grass dieback in the winter. Thus, biologically based complexation appears essential to the accelerated Pu and Fe movement in the soil-plant system. In this sense, a plant root in soil demonstrates some of the rapid transport features associated with a fracture in

rock. Throughout the study, experiments motivated model development and modeling results motivated the performance of additional experiments, what the authors call computer-aided thinking due to microbiological activities in soils.

1.5. CONCLUSION: CAN COMPLEXITY SCIENCES BENEFIT THE FIELD OF FLOW AND TRANSPORT IN FRACTURED-POROUS MEDIA?

We apply the concepts of complex systems theory to the analysis of papers published in this volume and the papers presented at the Fall 2012 AGU Meeting, at the session titled "Dynamics of Flow and Transport in Fractured-Porous Media." Our analysis shows that fractured-porous media can be defined as a complex system formed out of many components with an emergent behavior. Certain properties of complex systems appear to be inherent to fractured-porous media, such as collective behavior, emergence, coevolution with their environment, connectivity of the fractured-porous media parts, feedback mechanisms, and self-organization. Moreover, all of these properties are intrinsically related to one another through multiple dynamic processes. Complex behavior is due to nonlinear dynamical effects, which under certain conditions may lead to the physically based phenomenon of chaos in natural systems (not due to numerical effects).

The relationships between different parameters and variables measured in the field are very complicated because the subsurface is composed of a hierarchy of structures and processes that span a large range of spatial and temporal scales. We show examples of both emergent complexity and emergent simplicity in the behavior of fractured-porous media. Due to the collective behavior of the components of a fractured rock system, the whole-system behavior cannot be simply inferred from the behavior of its components. Because the causes and effects in fractured rock are not obviously related, the problems of flow and transport in fractured rock are difficult to solve and are often hard to understand. In this perspective, the study of fractured rock as complex systems, based on the results of experimental field or laboratory investigations and modeling, is a new endeavor that strives to improve our ability to understand the processes of flow and transport, when a system is highly complex. Examples of fractured rock as complex systems that undergo guided developmental processes as part of their formation include infiltration tests or pumping and injection tests/experiments. During these tests, system developmental processes are guided by the boundary conditions.

The flow of fluids through fractured rock is critically important in many practical applications, including remediation, nuclear waste disposal, hydrothermal systems associated with geothermal energy production, base metal ore deposits, gas and oil recovery, and global geochemical cycles. The nature of mass, heat, and chemical transport in fractured rock systems is determined by the physical (spacing and volume) properties of fractures, the nature of chemical transport between fractures and matrix blocks, and the dissolution and precipitation rates of minerals in matrix blocks and on fracture walls. Fractured-porous media meet all criteria of the complex systems.

ACKNOWLEDGMENT

The work of the first author was partially supported by the Sustainable Systems Scientific Focus Area (SFA) program at LBNL, supported by the U.S. Department of Energy, Office of Science, Office of Biological and Environmental Research, Subsurface Biogeochemical Research Program, through Contract No. DE-AC02-05CH11231 between Lawrence Berkeley National Laboratory and the U. S. Department of Energy.

REFERENCES

Ashby, W. R. (1947), Principles of the self-organizing dynamic system, *Journal of General Psychology, 37,* 125–128.

Bak, P., Tang, C. and Wiesenfeld, K. (1987). Self-organized criticality: An explanation of 1/*f* noise, *Physical Review Letters*, *59*(4), 381–384.

Bar-Yam, Y. (1997), *Dynamics of Complex Systems*, Addison-Wesley, 865 p.

Boomsma, E., and L. Pyrak-Nolte (2015), Particle swarms in fractures, in B. Faybishenko, S. M. Benson, and J. E. Gale (eds.), *Dynamics of Fluids and Transport in Complex Fractured-Porous Systems*, AGU and Wiley, Washington, D.C.

Dragila, M. I., U. Nachshon, I. Bersheba, and N. Weisbrod (2015), Fractures as advective conduits at the Earth atmosphere interface, in B. Faybishenko, S. M. Benson, and J. E. Gale (eds.), *Dynamics of Fluids and Transport in Complex Fractured-Porous Systems*, AGU and Wiley, Washington, D.C.

Fakcharoenphol, P., B. Kurtoglu, H. Kazemi, S. Charoenwongsa, and Y. S. Wu (2015), The effect of chemical osmosis on improve oil recovery from fractured shale formations, in B. Faybishenko, S. M. Benson, and J. E. Gale (eds.), *Dynamics of Fluids and Transport in Complex Fractured-Porous Systems*, AGU and Wiley, Washington, D.C.

Faybishenko, B. (2003), Nonlinear dynamics in flow through unsaturated fractured-porous media: Status and perspectives, *Reviews of Geophysics*, RG2003, doi:10.1029/2003RG000125.

Faybishenko, B. (2005), Chaotic processes in flow through fractured rock: Field and laboratory experiments revisited, in *Subsurface Contamination Remediation: Accomplishments of the Environmental Management Science Program, 904*, ACS Symposium Series, 183–228.

Huo, D, and S. Benson (2015), An experimental investigation of stress-dependent permeability and permeability hysteresis behavior in rock fractures, in B. Faybishenko, S. M. Benson, and J. E. Gale (eds.), *Dynamics of Fluids and Transport in Complex Fractured-Porous Systems*, AGU and Wiley, Washington, D.C.

Karasaki, K., C. T. Onishi, and J. Goto (2015), Anisotropic permeability of a strike slip fault, in B. Faybishenko, S. M. Benson, and J. E. Gale (eds.), *Dynamics of Fluids and Transport in Complex Fractured-Porous Systems*, AGU and Wiley, Washington, D.C.

Karimi-Fard, M., L. J. Durlofsky, and K. Aziz (2004), An efficient discrete-fracture model applicable for general-purpose reservoir simulators, *SPE Journal*, *9*(2), 227–236.

Karimi-Fard, M., B. Gong, and L. J. Durlofsky (2006), Generation of coarse-scale continuum flow models from detailed fracture characterizations, *Water Resources Research, 42*(10), W10423.

Kleidon, A., and S. Schymanski (2008), Thermodynamics and optimality of the water budget on land: A review, *Geophys. Res. Lett.*, *35*, L20404, doi:10.1029/2008GL035393.

Klepikova, M., T. Le Borgne., O. Bour, and P. Davy (2011), A methodology for using temperature-depth profiles under ambient, single and cross-borehole pumping conditions to estimate fracture hydraulic properties, *Journal of Hydrology*, *407*, 145–152.

Ladyman, J., J. Lambert, and K. Wiesner (2013), What is a complex system? *European Journal for Philosophy of Science*, *3*(1), 33–67.

Liu, H.H (2015), An emergent conductivity relationship for unsaturated water flow based on minimized energy dissipation: From landscapes to unsaturated soils, in B. Faybishenko, S. M. Benson, and J. E. Gale (eds.), *Dynamics of Fluids and Transport in Complex Fractured-Porous Systems*, AGU and Wiley, Washington, D.C.

Main, I. G., P. G. Meredith, J. R. Henderson, and P. R. Sammonds (1994), Positive and negative feedback in the earthquake cycIe: The role of pore fluids on states of criticality in the crust, *Annali Di Geofisica (Annals of Geophysics)*, *37*(6).

Meadows, D. (1999), Leverage points: Places to intervene in a system, available at http://www.donellameadows.org/archives/leverage-points-places-to-intervene-in-a-system/.

Molz, F., I. Demirkanli, D. Kaplan, and B. Powell (2015), Plutonium transport in soil and plants: An interdisciplinary study motivated by lysimeter experiments at the Savannah River site, in B. Faybishenko, S. M. Benson, and J. E. Gale (eds.), *Dynamics of Fluids and Transport in Complex Fractured-Porous Systems*, AGU and Wiley, Washington, D.C.

Monteiro, P. J. M., C. H. Rycroft, and G. I. Barenblatt (2012), A mathematical model of fluid and gas flow in nanoporous media, *Proc Natl Acad Sci U S A*, *109*(50):20309–20313.

Mourzenko, V. V., P. M. Adler, C. Nussbaum, and P. Pinettes (2011), Faults and fractures in the Gallery 04 of the Mont Terri rock laboratory: Characterization, simulation and application, *Engineering Geology*, *117*, 39–51.

Nimmo, J., and R. S. Malek-Mohammadi (2015), Quantifying water flow and retention in an unsaturated fracture-facial domain, in B. Faybishenko, S. M. Benson, and J. E. Gale (eds.), *Dynamics of Fluids and Transport in Complex Fractured-Porous Systems*, AGU and Wiley, Washington, D.C.

Ottino, J. M. (1990), Mixing, chaotic advection, and turbulence, *Annual Review of Fluid Mechanics*, *22*, Palo Alto, CA, 207–253.

Patzek, T. W., F. Male, and M. Marder (2013), Gas production in the Barnett Shale obeys a simple scaling theory, *PNAS*, *110*(49), 19731–19736.

Peak, D., and M. Frame (1994), *Chaos Under Control: The Art and Science of Complexity,* Freeman & Co, New York.

Rennert, T., K. U. Totsche, K. Heister, M. Kersten, and J. Thieme (2012), Advanced spectroscopic, microscopic, and tomographic characterization techniques to study biogeochemical interfaces in soil, *Journal of Soils and Sediments*, *12*(1), 3–23.

Rode, A. A. (1965), *Background of the Theory of Soil Moisture, Vol. 1*, Gidrometeoizdat, Leningrad, 663 pp.

Seok, E., and J. Gale (2015), Comparison of simulated flow in a discrete fracture laboratory sample based on measured average and spatially varying permeability, in B. Faybishenko, S. M. Benson, and J. E. Gale (eds.), *Dynamics of Fluids and Transport in Complex Fractured-Porous Systems*, AGU and Wiley, Washington, D.C.

Sharma, P., C.-F. Tsang, C. Doughty, A. Niemi, and J. Bensabat (2015), Feasibility of long-term monitoring of deep hydrogeology with flowing fluid electric conductivity logging method, in B. Faybishenko, S. M. Benson, and J. E. Gale (eds.), *Dynamics of Fluids and Transport in Complex Fractured-Porous Systems*, AGU and Wiley, Washington, D.C.

Smolin, L. (2014), *Time Reborn: From the Crisis in Physics to the Future of the Universe*, Mariner Books.

Tsenn, M. C. (2015), Permeability of Partially-Cemented Fractures, in B. Faybishenko, S. M. Benson, and J. E. Gale (eds.), *Dynamics of Fluids and Transport in Complex Fractured-Porous Systems*, AGU and Wiley, Washington, D.C.

Wang, J. S., and J. A. Hudson (2015), Laboratory and field studies of fracture flow and its extension in underground settings, in B. Faybishenko, S. M. Benson, and J. E. Gale (eds.), *Dynamics of Fluids and Transport in Complex Fractured-Porous Systems*, AGU and Wiley, Washington, D.C.

Weaver, W. (1948), Science and complexity, *American Scientist*, *36*(4), 536–544, PMID 18882675, Retrieved 21 Nov 2007.

Weeks, S. W., and G. Sposito (1998), Mixing and stretching efficiency in steady and unsteady groundwater flows, *Water Resources Research*, *34*(12), 3315–3322.

Werner, B. T. (1999), Complexity in natural landform patterns, *Science*, *284*, 102–104.

Westhoff, M. C., and E. Zehe (2013), Maximum entropy production: Can it be used to constrain conceptual hydrological models? *Hydrol. Earth Syst. Sci.*, *17*, 3141–3157.

Whitesides, G. M., and R. F. Ismagilov (1999), Complexity in chemistry, *Science*, *284*, 89–92.

Winterfeld, P., and Y. S. Wu (2015), Simulation of THM processes in fractured reservoirs, in B. Faybishenko, S. M. Benson, and J. E. Gale (eds.), *Dynamics of Fluids and Transport in Complex Fractured-Porous Systems*, AGM and Wiley, Washington, D.C.

Witherspoon, J. S., Y. Wang, K. Iwai, and J. E. Gale (1980), Validity of cubic law for fluid flow in a deformable rock fracture, *Water Resources Research*, *16*, 1016–1024.

Wood, T., and H. Huang (2015), Experimental and modeling studies of episodic air-water two-phase flow in fractures and fracture networks, in B. Faybishenko, S. M. Benson, and

J. E. Gale (eds.), *Dynamics of Fluids and Transport in Complex Fractured-Porous Systems*, AGU and Wiley, Washington, D.C.

Papers presented at Session 071, "Dynamics of Fluids and Transport in Fractured-Porous Media," of the Fall 2012 AGU Meeting, San Francisco, California, December 2012.

Broda, S., D. Blessent, and M. Aubertin (2012), Conceptual model suitability for reproducing preferential flow paths in waste rock piles.

Chan, W., L. Chung, T. Lee, C. Liu, Y. Chia, and M. Teng (2012), Tracer tests in the fractured rock to investigate preferential groundwater flow.

DePaolo, D. J. (2012), Isotopic and trace element sensors for fluid flow, heat- and mass transport in fractured rocks.

Ellis, B. R., J. P. Fitts, and C. A. Peters (2012), Mineral spatial heterogeneity constrains permeability evolution in a limestone fracture.

Ezzedine, S. M., O. Vorobiev, and F. J. Ryerson (2012), Investigation of the thermo-hydro-mechanical effective properties of tight fractured porous rock.

Geier, J. E., O. Stephansson, and A. Luukkonen (2012), Comparison of Olkiluoto (Finland) and Forsmark (Sweden) candidate sites for radioactive-waste disposal.

Hawkins, A., M. W. Becker, and G. P. Tsoflias (2012), Field measurement of fracture/matrix heat exchange using fiber optic distributed temperature sensing.

Howar, J., and S. Wohnlich (2012), Push-pull tests for the estimation of flow and transport processes in a fractured porous sandstone.

Kahler, D. M. (2012), Novel technology to promote mixing in dead-end pores could improve pump-and-treat.

Karimi-Fard , M., A. Lapene, and L. Pauget (2012), Application of discrete fracture modeling and upscaling techniques to complex fractured reservoirs.

Le Borgne T., M. Klepikova, P. Goderniaux, O. Bour, T. Read, R. Hochreutener, V. Boschero, N. Lavenant, and V. Bense (2012), Thermal tracing of flow and transport in fractured media.

Lee, S., K. Lee, I. Yeo, and T. Le Borgne (2012), Evolution of dispersion coefficient in the single rough-walled fracture before and after circulated flow near the wall.

Leube, P., W. Nowak, and X. Sanchez-Vila (2012), Model reduction and multi-scale simulation for solute transport in fractured porous media.

Menke, H. P., J. E. McCray, A. Sitchler, and R. M. Maxwell (2012), CO2 and H2O leakage rates from the injection zone to overlying units as a result of geologic sequestration.

Mourzenko, V., J. Thovert, P. M. Curie, and P. M. Adler (2012), Percolation and permeability of fracture networks in excavated damaged zones.

Mullally, D. M., and R. P. Lowell (2012), Boundary layer flow, heat, and chemical transfer near vertical heated boreholes in water- saturated rock: A mechanism for developing a large scale underground hydrothermal experiment (DUSEL).

Neuman, S. P., A. Guadagnini, and M. Riva (2012), Scaling of fractured rock properties.

Pedler, W. H. (2012), Borehole fluid logging methods for hydrogeologic characterization: What have we learned in twenty-five years?

Peng, S., Q. Hu, and R. P. Ewing (2012), Gas recovery in fractured Barnett shale.

Petrovitch, C., L. J. Pyrak-Nolte, and D. D. Nolte (2012), Universal scaling of single fracture hydromechanics.

Seok, E., and J. Gale (2012), Comparison of simulated flow in a discrete fracture laboratory sample based on measured average and spatially varying permeability.

Sun, Y., and C. R. Carrigan (2012), Uncertainty quantification of barometric driven gas transport in fractured rock.

van Genuchten, M., E. Pontedeiro, J. Su, M. Batalha, and C. R. Bezerra (2012), Numerical analysis of a subsurface uranium pollution problem.

Willmann, M., and W. K. Kinzelbach (2012), New stochastic particle tracking approach for fractured sedimentary formations.

Zimmerman, R. W. (2012), The history and role of the cubic law for fluid flow in fractured rocks.

Part I
Methods of Field Measurements and Experiments

2

Fracture Flow and Underground Research Laboratories for Nuclear Waste Disposal and Physics Experiments

Joseph S. Y. Wang[1] and John A. Hudson[2]

ABSTRACT

Basic studies of fracture flow, such as the cubic law, have been widely cited for over three decades and used in understanding processes in fractured media. We first review the cubic law and its extension in the literature, which contributes to understanding the behavior of fractured rock masses. Laboratory, theoretical, and field studies greatly enhance our capabilities for various engineering, earth resources, and sustainability applications related to fluid flow through fractured rocks. We then discuss recent activities in underground research laboratories (URLs) for radioactive waste storage and disposal, repository design, and the multidisciplinary studies associated with deep physics detector halls, with examples of energy and environmental evaluations through borehole investigations. Many countries in Asia, Europe, North America, and the southern hemisphere have URLs and deep physics facilities established or planned in different rock formations. The International Society for Rock Mechanics (ISRM) has formed the Commission on URL Networking to promote collaborations and interdisciplinary interactions for optimal uses of underground settings, and this review is based on the work of that commission.

2.1. INTRODUCTION

The Earth Sciences Division of the Lawrence Berkeley National Laboratory was founded in 1977 by Paul A. Witherspoon. In 1980, Witherspoon and his coauthors published two papers [*Witherspoon, Cook, et al.*, 1980; *Witherspoon, Wang, et al.,* 1980] that have had great impacts and are the initial focus of our current article. The paper on the cubic law for fracture flow [*Witherspoon, Wang, et al.*, 1980] has been cited extensively in literature on laboratory characterization of discrete fractures, on modeling of fractured rock masses, and on the understanding of coupled thermo-hydrological-mechanical-chemical processes. The other paper, on the Stripa Underground Research Laboratory [*Witherspoon, Cook, et al.*, 1980], influences the development of underground research laboratories (URLs) worldwide in hard crystalline rocks, and later to softer and more absorbing medium with matrix contributing to retardation and other processes. This article discusses the development and impact of both fracture flow and URL papers on geotechnical engineering, earth sciences, and other fields.

Section 2.2 of this chapter is on the cubic law and associated literature on the characterization of fractured rock masses. Section 2.3 is on radioactive waste URLs, deep physics facilities for rare event detections, and examples of boreholes drilled for energy, resource, and environmental evaluations. Section 2.4 presents concluding remarks.

2.2. CUBIC LAW FOR FRACTURE FLOW AND LITERATURE ON FRACTURED ROCK MASS CHARACTERIZATION

Witherspoon, Wang, et al. [1980] evaluated the validity of the cubic law for single fracture flow. This cubic law paper was cited by 782 other papers and reports (up to 31 October 2013), based on a Google scholar search. (Note that such searches are dynamic in nature, with citation numbers increasing in time. As time proceeds,

[1] *Lawrence Berkeley National Laboratory, Berkeley, CA*
[2] *Imperial College, London, UK*

Dynamics of Fluids and Transport in Complex Fractured-Porous Systems, Geophysical Monograph 210, First Edition.
Edited by Boris Faybishenko, Sally M. Benson, and John E. Gale.

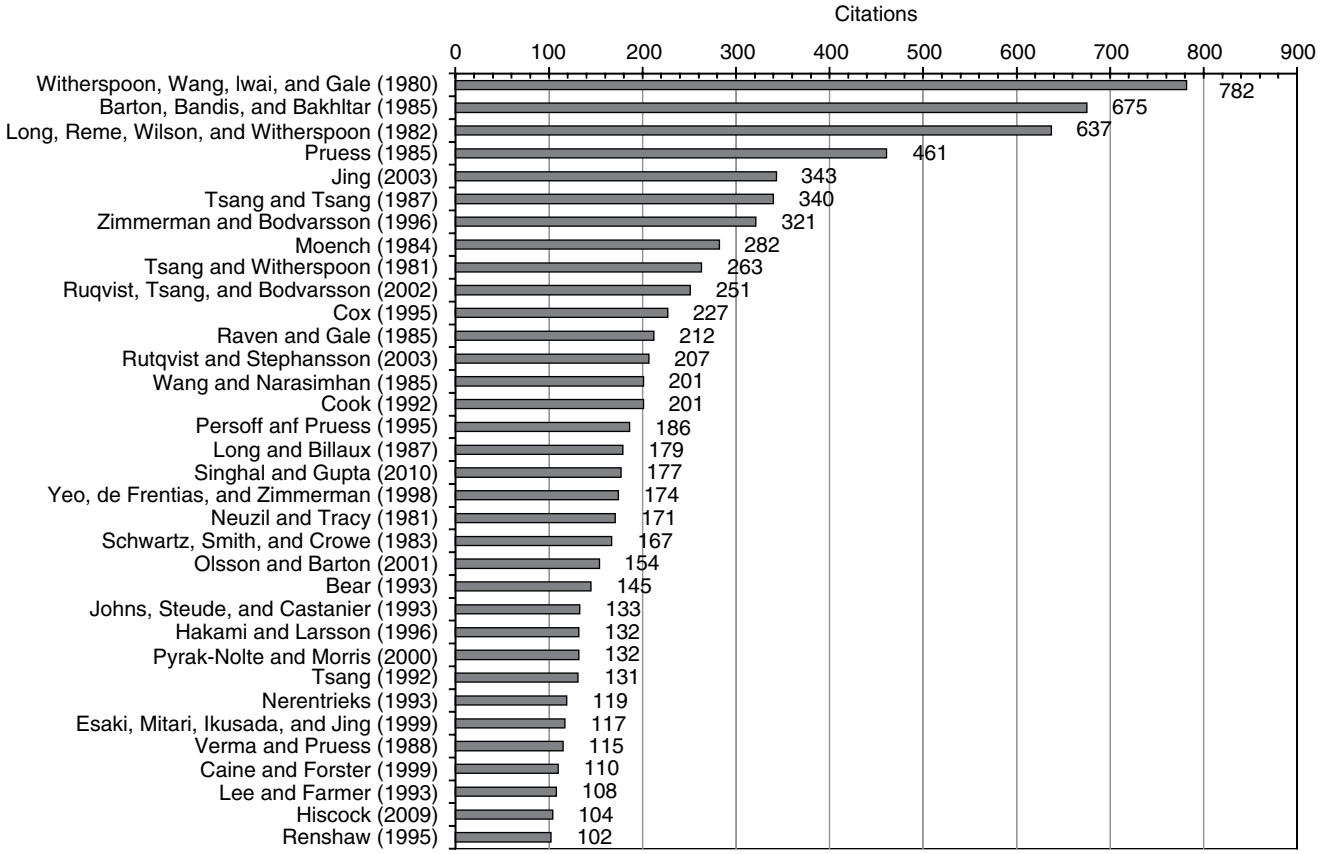

Figure 2.1 Number of citations for key references related to fracture flow and fractured rock masses (to October 2013).

this representation can be periodically updated.) We first presented our search results at the AGU in 2012 [*Wang and Hudson*, 2012] when the number of citations on 5 October 2012 was 624. The significant difference between 624 and 782 citations over one year is one indication that the cubic law is continuing to be referenced as an approximation for fracture flow. Citing citation numbers is one simple way to identify key references for flows and other related coupled processes not only through single discrete fractures but also through fractured rock masses. Figure 2.1 lists citation numbers of both the cubic law paper and 33 other papers that have cited the cubic law paper. Papers from similar technical topics are grouped in the following subsections. Within each subsection of literature reviews, we follow mainly references with large citation numbers listed in Figure 2.1. This approach does place more emphasis on early historical papers, but we hope it identifies relevant papers that may be influential for early developments of conceptual understandings for fracture flows. We do try to combine citations from same authors and coauthors if the topics are similar in technical matters. We also include examples of recent related papers.

Subsection 2.2.1 is mainly on single fracture flow and fracture aperture characterization. We emphasize references for the evaluation of the validity of the cubic law. Subsection 2.2.2 focuses on differences between hydraulic apertures and mechanical apertures, and discusses mechanical modeling. We then review various approaches to model fractured rock masses in subsection 2.2.3, including developments of different conceptual approaches. Subsection 2.2.4 presents a general summary of the literature reviews of fracture flows.

2.2.1. Single Fracture Flows and Aperture Characterization

The cubic law paper [*Witherspoon, Wang, et al.*, 1980] is on both opened and closed fractures, with closed fracture having fracture surfaces in contact and the fracture aperture decreased under normal stress. Tension fractures were artificially induced from homogeneous samples of granite, basalt, and marble, and flow tests were conducted in both radial and straight geometries. Apertures ranged from 250 to 4 μm, with normal stress up to 20 MPa. The cubic law was derived by assuming laminar flow through

a smooth-walled parallel plate gap, for open and modestly closed fractures. The validity of the cubic law over orders of magnitude range in aperture and flow rate was analyzed and showed for all granite and basalt samples, and over most of the range for marble sample. Figure 2.2 reproduces the analysis for radial flow through marble. Deviations from the cubic dependence, near the maximum stress, minimum aperture, and lowest flow rate limits, were shown graphically in *Witherspoon, Wang, et al.* [1980]. The deviations were discussed in this subsection, focusing on detailed mechanisms and extensions beyond the cubic law approximation.

Cook [1992] gave a Jaeger Lecture on mechanical, hydraulic, and seismic behavior and properties of natural joints in rock under normal stress. Many results were presented, including using liquid metal porosimetry (with woods metal) to measure the void space between two rough joint surfaces, defining a specific stiffness for the joint under stress, and discussion of the validity of the cubic law. The marble results mentioned above at high stress were further characterized. *Pyrak-Nolte and Morris* [2000] studied the relation between fracture specific stiffness and fluid flow. *Pyrak-Nolte and Cook* [1988] described woods metal images, fluid percolation through single fractures, and deviations from the cubic law. *Pyrak-Nolte et al.* [2011] discussed the particle swarm transport in fracture networks. *Pyrak-Nolte* [2013] presented fracture toughness as a link (NEXUS) between hydrology, geomechanics, and geophysics through a scaling relationship of length scales to fracture flux flow. *Nolte et al.* [1989] studied the fractal geometry of flow paths in natural fractures and the approach to percolation. *Wang et al.* [1985] derived the aperture correlation of a fractal fracture.

Tsang and Witherspoon [1981] developed a physical model to understand the effect of normal stress on fluid flow through a single fracture, with roughness along the fracture walls being taken into account. Appropriately weighted averages of aperture cubes were shown to provide a better and more basic understanding of factors controlling the flow of fluids through fractures. Granite and basalt data were used to test the theory. *Hakami and Larsson* [1996] presented aperture measurements and flow experiments on a single natural fracture. *Tsang* [1992] discussed the usage of equivalent apertures as derived from hydraulic and tracer tests.

Raven and Gale [1985] used cores of different sizes from the same natural fracture to evaluate the effects of changes of sample size on fluid flow under normal stress. *Gale* [1982, 1987] presented results from both induced and natural fracture under uniaxial compression up to 30 MPa, and compared coupled fracture deformation and fluid flow models with direct measurement of fracture pore structures and stress-flow properties.

Zimmerman and Bodvarsson [1996] discussed the single-phase flow through a rough-walled fracture, within the context of Navier-Stokes equations for laminar flow between parallel plates to the Hele-Shaw lubrication equations to account for tortuosity effects due to walls which are in contact. Reasonably accurate predictions of hydraulic conductivity could be characterized by the first two moments of the aperture distribution functions and the fraction of contact area. *Yeo et al.* [1998] tested the effect of shear displacement on the aperture and permeability of a rock fracture. *Zimmerman* [2012] also discussed the history and role of the cubic law.

There are several books that cite the cubic law. *White* [1988] has many citations on the geomorphology and

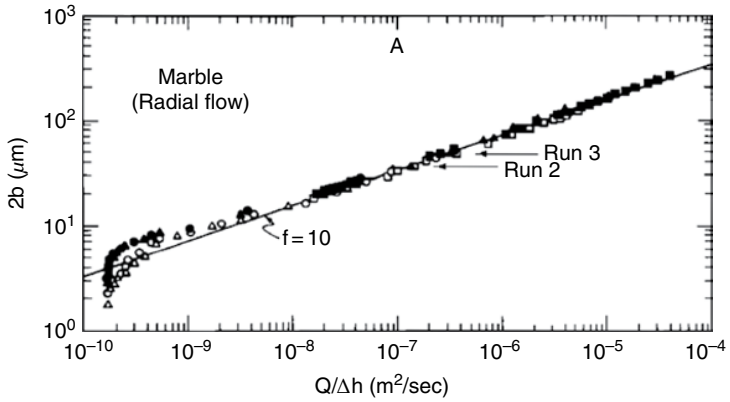

Figure 2.2 Comparison of experimental results for radial flow through tension fracture in marble with cubic law. Three different experimental runs are represented by different symbols. In the range below 10^{-8} for the ratio between flow rate Q and pressure head difference Δh with small fracture aperture 2b under high stress loading, deviations from the cubic law are noted (f = 1 line, indicating cubic law without including a correction with a fitting factor f) [*Witherspoon et al.*,1980b].

hydrology of karst terrains. *Singhai and Gupta* [2010] is a general applied hydrogeology book including discussion of the cubic law. *Bear* [1993] and *Neretniks* [1993] were the first two (out of nine) chapters of a conference proceedings on flow and transport through fractured rocks. *Lee and Farmer* [1993] also discusses the validity of the cubic law. *Hiscock* [2009] is on the principle and practice of hydrogeology.

2.2.2 Mechanical and Hydraulic Apertures, Mechanical and Coupled Processes

Barton et al. [1985] described a strength-deformation-conductivity coupled joint behavior model, with the joint roughness coefficient (JRC) presented as one of the parameters required for joint characterization. Among many results described and summarized in this paper, differences between measured mechanical apertures and the hydraulic apertures (derived from the cubic law) for six tension and natural fractures were discussed. The differences were from flow losses due to tortuosity and surface roughness under normal loading. This Barton Model with the associated methods of joint characterization is popular among geotechnical engineers and earth scientists to characterize fractured outcrops, tunnel walls, and borehole cores. *Olsson and Barton* [2001] described an improved version of the Barton model for hydro-mechanical coupling during shearing of granite rock joints. This improved model has the same appearance as the original model, using both mechanical and hydraulic apertures and the JRC. *Renshaw* [1995] analyzed the relationship between mechanical and hydraulic apertures in rough-walled fractures. *Barton* [2002] presented some Q-value correlations for site characterization and tunnel design.

Jing [2003] reviewed techniques, advances and outstanding issues of numerical modeling for rock mechanics and rock engineering. Various numerical models, methods to obtain necessary parameters for the models, and couplings between thermal, hydraulic, and mechanical processes were discussed. *Hudson et al.* [2011] presented the status of the DEvelopment of COupled models and their VALidation against EXperiments (DECOVALEX) project. The DECOVALEX project since 1996, and especially the phase through to 2011, was discussed. *Kolditz et al*. [2013] discussed the coupled thermal-hydro-mechanical-chemical (THMC) processes in a DECOVALEX book and in an openGeoSys Benchmark book. *Jing et al.* [2013] summarized conceptual understanding, testing, and mathematical modeling of the coupled stress-shear-fluid flow-solute transport THMC processes by the authors since 2004 in crystalline rock fractures. *Esaki et al.* [1999] developed a shear-flow apparatus and determined coupled properties for a single rock joint. *C. F. Tsang* [1991] reviewed coupled THMC processes in rock fractures. *Polak et al.* [2003] measured permeability reduction of a natural fracture under net dissolution by hydrothermal fluids. *Yasuhara et al*. [2013] tested THMC processes that induce evolution of rock permeability under hydrothermal and stressed conditions.

Rutqvist et al. [2002] presented the methodology of linking two computer codes, TOUGH2 and FLAC3D, for coupled thermal-hydrologic-mechanical (THM) analysis of multiphase fluid flow, heat transfer and deformation in fractured and porous rock media. TOUGH2 code for multiphase flows is summarized in the next subsection. FRAC3D dictates changes in effective stress (stress − pressure) as a function of multiphase pore pressure and thermal expansion, and TOUGH2 corrects porosity, permeability, and capillary pressure for changes in stress. The capability of the linked simulator was demonstrated in problems related to injection and storage of CO_2 in aquifers and to disposal of nuclear waste in unsaturated fractured porous media. *Rutqvist and Stephansson* [2003] reviewed the role of hydromechanical coupling in the fractured rock engineering context. *Rutqvist and Tsang* [2003] analyzed the THM behavior near an emplacement drift at Yucca Mountain. *Rutqvist* [2011] presented the geomechanical aspects of CO_2 sequestration and modeling of the in Salah CO_2 storage project in Algebra, which is 1.8–1.9 km deep. The ground surface uplift and microseismic events were shown to be caused by tensile opening of faults intersecting the injection zone.

Witherspoon and Gale [1977] discussed mechanical and hydraulic properties of rocks related to induced seismicity. *Brace* [1980] noted that the permeabilites of crystalline rocks were harder to be related to borehole measurements than were those of argillaceous rocks, as fractures played a more significant role. *Cox* [1995] studied faulting processes at high fluid pressures with fault valve behavior in a fault in Australia. Various coupled processes were expected during faulting at high temperature near 300°C, fluctuations in stress and in overpressuring, with hydrothermal sealing and slip over ~800 m, and in displacement with a maximum of 50 m. The faulting was believed to occur at low shear stresses and in near-lithostatic fluid pressure regime. *Caine and Forest* [1999] evaluated fault zone architecture and fluid flow from field data and numerical modeling. *Engelder and Scholz* [1981] evaluated fluid flow along joints at effective pressures up to 200 MPa.

2.2.3. Fracture Network and Multiphase Modeling of Fractured Rock Masses

Long et al. [1982] developed a fracture network model with an equivalent porous medium permeability tensor constructed through specifications of fracture center locations, orientations, sizes, and shapes of facture sets. The cubic law was used for the fracture flows. The variables in

the fracture network model are randomly distributed according to available field data analyzed. The transition from discrete fracture network to equivalent continuum porous medium behavior can be evaluated by this model. *Long and Billaux* [1987] described a technique for processing field data for the fracture network model and analyzed data from the Fanay-Augeres mine in France using both drift mapping and borehole testing data. *Schwartz et al.* [1983] developed a stochastic modeling technique to investigate mass transport in a network of discrete fractures. *Neuzil and Tracy* [1981] described a model with a set parallel plate opening with different aperture, and the model led to a modified Poiseuille equation for flow. *Haimson and Doe* [1983] tested the state of fractures, permeability, and stress in a 1,600-m-deep pre-Cambrian granitic borehole in Illinois. *Doe* [2011] described the compartmentalized fracture systems from studies in different radioactive waste research laboratories.

Pruess [1985] presented the multiple interacting continua method, which is the basis of the TOUGH family of simulators for heat and multiphase fluid flows and other coupled processes in multidimensional fractured porous media. Approximate thermodynamic equilibrium within each computational volume element was assumed at all times and led to the use of nested elements through the integrated finite difference method. The transient flow of heat and fluid between fractures and porous matrix were treated with a numerical method. The TOUGH models have been applied to geothermal reservoirs, petroleum production, radioactive waste storage, and lately to both CO_2 sequestration and shale "fracking," plus other multiphase problems. This method is a generalization of the well-established double-porosity concept. *Persoff and Pruess* [1995] described a flow apparatus to visualize and measure two-phase gas/liquid flows in natural rough-walled rock fractures. *Johns et al*. [1993] used X-ray computed tomography to nondestructively measure fracture aperture in crystalline rock cores. *Verma and Pruess* [1988] evaluated thermodynamic conditions and silica redistribution near emplaced high-level wastes. *Pruess et al.* [1990] performed simulation studies on thermohydrologic conditions near high-level nuclear wastes emplaced in partially saturated fractured tuff, with explicit fractures taken into account. *Pruess and Narasimhan* [1982] evaluated the fluid reserves and the production of superheated steam from fractured, vapor-dominated geothermal reservoirs. *Bodvarsson and Tsang* [1982] considered injection and thermal breakthrough in fractured geothermal reservoirs.

Tsang and Tsang [1987] presented a channel model for fractured rocks in terms of flows through channels of variable apertures. The channels are characterized by a probabilistic aperture density distribution and a spatial correlation length. Calculated tracer breakthrough curves were constructed by way of a number of channels, with geometrical characteristics of the channels from comparison to measurements of fracture surfaces, and model validation through comparison with tracer field test data. *Moreno et al*. [1988] presented a stochastic model and its relation to field observations. *Anderson and Woessner* [1992], *Gerke and van Genuchten* [1993], *Cacas et al.* [1990], *Berkowitz* [2002], and *Neuman* [2005] reported on various aspects of flow, transport, and modeling, recognizing the channeling nature of flow.

Moench [1984] modified the double-porosity model to incorporate effects of a thin skin, i.e., a layer of low-permeability material presented at fracture-matrix block interfaces as result of mineral deposition or alteration. Resistance to flow at fracture-block interfaces was assumed to reduce spatial variation of hydraulic head gradients within the blocks and justified the assumption of pseudo-steady block-to-fissure flow. Results from Laplace inversion were used to develop dimensionless type curves for analyzing well testing data of the fractured volcanic rock terrace of the Nevada Test Site. *Elsworth and Bai* [1992] presented a constitutive model of flow-deformation response of dual-porosity media. *Bai and Elsworth* [1994] investigated the modeling of subsidence and stress-dependent hydraulic conductivity for intact and fractured porous media. *Capuano* [1993] presented evidence of fluid flow through micro-fractures in geopressured shales, Texas.

Wang and Narasimhan [1985] presented a conceptual model for hydrologic mechanisms governing fluid flow in a partially saturated, fractured, porous medium. The fractures were shown to desaturate first during the drainage processes, and the bulk of fluid flow would then be through interconnected pores in the matrix. The residual liquid would be held by capillary force to regions around fracture contact areas. Normal to the fracture surfaces, liquid flow from one matrix block to another matrix block would be through the reduced effective area enclosing the contacts. Precipitations on fracture surfaces were used to quantify the contact area fractions and matrix-to-matrix flows. The schematics of matrix-to-matrix flow normal to the fracture surfaces was reproduced in Figure 2.3 (see also *Freeze and Cherry*, 1979). *Nitao and Buscheck* [1991] considered infiltration of a liquid front in an unsaturated, fractured porous medium. *Rangel-German and Kovscek* [2002] studied multidimensional imbibition in fractured porous media.

2.2.4 General Summary of the Literature Reviews of Fracture Flows

In summary for this section, the literature review presented is on fluid flow, solute transport, and coupling to mechanical and thermal processes in single fractures and in fractured rock masses. References are mainly from

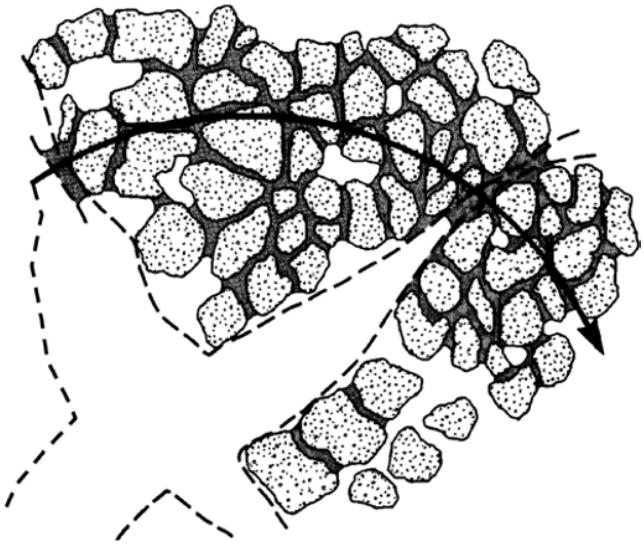

Figure 2.3 Conceptual model of partially saturated, fractured, porous medium showing schematically the flow lines moving around the dry portions of the fractures [*Wang and Narasimhan*, 1984].

citations to the cubic law paper of *Witherspoon, Wang, et al.* [1980] over three decades. The development of an improved understanding of discrete fractures has enabled extensions to account for fracture surface roughness in retarding flow and transport, inducing tortuous flow paths, channeling fluid and solute, differences between mechanical and hydraulic apertures, fractal representation/correlation for the apertures, matrix-to-matrix flow through fracture contact areas, and fracture toughness controlling mechanical responses and seismic wave transmission.

In the range that fracture apertures can be measured, quantified, or derived from hydrological tests, the literature reviews indicate that the cubic law has sustained the tests of time over three decades. In underground settings that fractured flows dominate, the laminar conditions and parallel-plate approximation are generally valid, and the cubic law is used extensively. Stress states are likely within the range of validity tested. The conceptual simplicity of the cubic law and the range tested are likely responsible for the popularity of the cubic law paper of *Witherspoon, Wang, et al.* [1980]. While there are literatures addressing the generalization of the cubic law at high stresses and portions of fracture surfaces are in contact and not amendable to flow and transport, local aperture distributions over the active flow paths are still used to quantify the fractured flows.

Fracture networks and fracture rock mass representations and models usually use the cubic law approximation for the discrete fracture flows in studies of equivalent porous behavior and couplings to mechanical, thermal, chemical, geological, and other processes. The agreements with measured responses of coupled processes intrinsically validate the use of the cubic law to describe the fractured flows through discrete fractures and through fractured rock masses. The simple literature reviews so far indicate that there are continuing efforts for better quantifications of both single fractures and in fracture rock masses. With better quantifications and more fundamental studies, we can address the key question of whether the cubic law held the test of time. We do believe that the cubic law is valuable as an approximation in applications.

The state of the art in understanding fracture-related phenomena has steadily improved over decades and is expected to progress in the future with better experimental techniques, both in laboratories, in analytic and numerical simulations, and in field testing and measurement techniques. In addition to laboratory and theoretical references, some field applications are mentioned in this section for applications in groundwater aquifers, in radioactive waste assessments, in petroleum and natural gas fields, in geothermal systems, and in CO_2 sequestration. These topics will be further discussed in the next section on underground studies.

2.3. UNDERGROUND RESEARCH LABORATORY, FACILITY, BOREHOLE STUDIES, AND THE ISRM NETWORKING COMMISSION

Witherspoon, Cook, et al. [1980] and reports from the American-Swedish Cooperative Project starting in late 1970s focus on the underground research laboratory (URL) in Stripa, Sweden. The Stripa iron mine, closed in 1977 for mineral production, was made available for additional drifting into a nearby granite body, and the Stripa URL was established for fractured hard rock investigations of hydrological and thermal mechanical processes for research in radioactive waste assessments. Many URLs have since been established worldwide. Worldwide reviews of URLs for radioactive wastes and nuclear waste programs were published with the fourth world review by *Witherspoon and Bodvarsson* [2006] covering 24 countries and 3 chapters on multinational repositories, education and training, and science and technology. In addition to experiments that have been since generalized in many other URLs, the efficiency of deploying the setup within a few months was inspirational for decades. For example, *Wang* [2001] presented the Stripa URL operation as an example to promote interdisciplinary international collaborations in underground sciences in the U.S. effort to establish a deep underground science and technology laboratory (DUSEL).

The Stripa URL provided important test examples in terms of fracture hydrology and thermo-mechanical heater induced measurements. Three long inclined boreholes were

drilled and instrumented from the ground surface for hydrological characterization of the surrounding fractured rock mass in the vicinity of the URL. The full scale and scaled heater tests formed the examples for many heater tests deployed by other URLs. The Stripa project generated important technical findings which were the basis for nearly a decade-long international corporation at that site. This type of international cooperation continues at the Swedish Äspo Hard Rock Laboratory and has had an influence on the Finnish program and many URLs in hard rocks and other softer rocks.

We will divide this section into three subsections. Subsection 2.3.1 is on URLs for radioactive assessments. Subsection 2.3.2 is on deep physics facilities with emphasis on excavation of large cavities to house rare particle detectors. Subsection 2.3.2 discusses example of borehole complexes mainly for energy and environmental studies. These activities are the basis and reason for the formation of an International Society for Rock Mechanics (ISRM) Commission on URL Networking, which has been active in recent years. Instead of citing key technical references, as in the last section, we discuss studies over three decades on underground laboratories, facilities, boreholes, and underground settings location by location, alphabetically following countries in Asia, Europe, North America, and the southern hemisphere continents. The infrastructure aspects of underground facilities are described in this section.

We count mainly on websites to monitor the progress made in each URL. Most of the URLs maintain and update each website periodically. We also update the ISRM website of the ISRM URL Networking Commission about twice a year. Most websites can be reached by search engines and will not be treated as references in this chapter. The ISRM URL website is periodically updated and presented to the ISRM Council. We also plan to include in the website topical discussions by commissioners and other speakers and authors in URL workshops and meetings. One workshop is in 2011 (with 22 presentations in five sessions, I–V), associated with the 12th ISRM Congress. Because the ISRM congresses are worldwide events every four years, we plan to have either a meeting, a workshop, or an international conference every four years. We also will organize field trips, meeting sessions, and workshops in between the congresses. In 2013, we had sessions associated with the SINOROCK and the EUROROCK (three presentations each), and with the AGU Fall Meeting. In the past several years, there were AGU Hydrology, Natural Hazard, and Union sessions. We also attended American Rock Mechanics Association (ARMA), ISRM, and other topical conferences to evaluate progress in different laboratories, facilities, and borehole complexes. Relevant presentations in workshops, meetings, and conferences are the main sources of references in this section.

2.3.1. Radioactive Waste Assessment URLs

Hudson [2010] provided an overview of rock mechanics contribution to underground radioactive waste disposal. In situ rock stress, intact rock properties, thermal properties, fractures, and hydrological aspects were reviewed. The reproducibility of numerical modeling and associate technical auditing were discussed. Existing and future URLs are required for in situ experiments to support design premises which need thorough and relevant suitable checking to ensure all aspects of design are included and appropriately accommodated.

Note that while URLs exist in different countries, there is yet to be a civilian high-level nuclear waste repository licensed and constructed. For the existing used nuclear fuels or wastes, there is a strong need to develop underground radioactive waste disposal facilities. We focus here on recent progress in various planned and new excavations and selected experiments in URLs.

In Asia, there are an increasing number of nuclear power plants on line for electric power production. China has a relatively recent nuclear waste program. *Ju Wang* [2010] provided an overview of China's plan to handle nuclear waste problems, with underground in-situ testing likely at the Beishan site in northeast China which is being considered for an URL, to be constructed in 2021–2040. This is a granite site with currently deep vertical boreholes drilled for site characterization. There are geological and hydrological investigations, in-situ stress and permeability measurements, engineered barrier studies, THMC testing in Gaomiaozi benetonite, and mechanical testing of Beishan granite.

In Japan, there are currently two URLs: one at Honorobe in northern Japan and the other at Mizinami in central Japan, both with the Japan Atomic Energy Agency (JAEA). *Tsusaka et al.* [2011] presented the status and plan of the investigation of rock mechanics at the Horonobe URL which was established in 2001 in sedimentary formations. After rock properties and initial stress evaluations, the excavation disturbed zone was investigated, and further testing of the zone and the engineered barrier system (EBS) were planned. Two access shafts, one ventilation shaft, four gallery levels (at the 140-, 260-, 360-m, and later to the 500-m level) in Horonobe were used to access in-situ experiments and to measure and monitor stress distributions. *Sugita and Nakama* [2012] presented an EBS experiment as Task B of the DECOVALEX-2105 project (www.decovalex.org). The Mizunami URL in crystalline rocks is described by the Tono Geoscience Center, JAEA, which has hosted the URL for over 30 years of research. By 1 November 2013, the main shaft and the ventilation shaft reached 500 m depth, with the excavations planned for 1000 m. Geoscience investigations were conducted between shaft-sinking (drill, blast, and mucking) and shaft-lining cycles.

The Korea Atomic Energy Research Institute (KAERI) was established in 1959 and a 500-m-deep URL in crystalline rock was mentioned by *Feng* [2011]. *Kwon and Choi* [2006] analyzed thermo-mechanical stability for a multilevel radioactive waste disposal concept. *Kwon et al.* [2013] studied the 3D thermal and mechanical behavior of engineered barriers and rock mass, including swelling pressure effects, thermal expansion, and failure criteria.

Russia has a closed nuclear city, Zhelenogorsk, near Krasnosyarsk in Siberia, where it was approved in 2012 at a public environmental meeting that a URL could be constructed. Engineered barriers and thermodynamics of underground chambers, shafts, and geologic layers were planned to be studied. In the 1950s to 1960s, underground reactors were built near the city to produce electricity and to provide hot water and heat. Also the Kola Peninsula, among other locations, has a long-term facility for storing reactor vessels and radioactive waste.

In Europe, there are more URLs established. While we mostly focus on URLs for high-level wastes, some sites for low and intermediate wastes are mentioned. In Belgium, HADES of the European Underground Research Infrastructure for Disposal of Nuclear Waste in Clay Environment (EURIDICESCE) is the URL in Boom clay. *X. Li* [2011] presented the role of the Belgian program on radioactive geological disposal since 1974. The URL is through two shafts connected with a test gallery at a depth of 225 m. There were several experiments, including the PRACLAY gallery instrumented since 2007 for a heater experiment. *Sneyers and Li* [2012] mentioned that the temperature at the lining-rock interface will be held at 80°C during a 10-year heating phase. *X. Li et al.* [2012] described the status of HADES and the thermo-hydro-mechanical-chemical state of the art around PRACLAY and in Boom clay. *Wouters et al.* [2013] presented evidence of diverse and active microbial community in borehole water around HADES.

In Denmark, a decision was made by the Danish Parliament to find a site for a final repository on Danish land territory, excluding Greenland. *Nilsson et al.* [2012] discussed the site selection progress since 2003 for a radioactive waste repository site to replace temporal disposal at the nuclear facility.

Finland has the ONKALO URL of POSIVA in crystalline rocks, gneiss, and pegmatite. *Siren and Johnsson* [2011] discussed the ONKALO as a second generation URL and its role in POSIVA's repository development program. The ONKALO, proceeded by many deep exploratory boreholes, started in 2004 and has reached the potential repository depths of 430–440 m through a 4,780-m-long ramp. There are also one personal and two ventilation shafts being raise bored. *Hudson et al.* [2013] included an update of ONKALO activities and discussed risk assessment in URLs.

France has the Meuse/Haute-Marne URL of the French Radioactive Waste Management Agency (ANDRA) in eastern France, 420–550 m deep in the Callovo Oxfordien claystone. *Armand* [2011] presented the status of the URL with galleries and experiment sites continuously excavated by roadheaders, starting at 1999 until at least 2016. Impacts of digging and lining methods and thermo-hydro-mechanical processes around high-level waste cell were among studies evaluated. *Delay et al.* [2007] discussed the methodology applied at the 445-m and 490-m-deep area for monitoring geomechanical changes associated with construction, thermodynamic changes in circulating gases and fluids, and testing the concept of the excavation disturbed zone through a cross-cutting technique.

Germany has considered the Gorleben salt dome as a site for a potential high-level repository. There are drifts at the 860-m level for testing and also consideration of boreholes 870–1,170 m for emplacement of fuel element canisters. *Heusermann et al.* [2013] presented three-dimensional modeling of high-level waste emplacement in the salt dome. Two models were performed for a time period of 10,000 years. Barrier integrity was also analyzed. *Fahland and Heusermann* [2013] also presented geomechanical analyses of the low and immediate waste repository at the Marsleben repository, in a salt and potash mine.

Hungary has the national low- and intermediate-radioactive waste repository site at Bataapati with two parallel 1.7-km inclined exploratory tunnels excavated in 2005, with a 10% inclination to reach 170 m. *Gaich et al.* [2012] described the high-resolution 3D photographic imaging during the construction of the ramps between drill and blast excavation cycles. *Deak et al.* [2013] discussed the excavation damaged zones at the Bataapati repository.

Sweden has the Äspo Hard Rock Laboratory (HRL) of the Swedish Nuclear Fuel and Waste Company (SKB) excavated in crystalline rocks. *Svemar et al.* [2011] discussed the status and future activities of SKB's HRL. The URL reached a depth of 460 m through 4 km of tunnel loops. The URL also has a shaft for access. Sweden has over 30 years of URL experience, starting in the 1970s with the Stripa mine and since 1986 with construction and operation phases at the HRL. Many experimental sites are distributed between 220 and 460 m depth. The HRL was extended into an international R&D facility. A Nova R&D platform was founded by the municipality of Okharshamn and SKB, with focus also on aspects outside the spent nuclear fuel program. Among many experiments, the rock spalling in canister borehole and pillar stability under thermal stress were evaluated. *Hakami and Christiansson* [2012] discussed the use of induced borehole breakouts as a method for stress orientation determination in hard

crystalline rocks, tested at Äspo and to be applied at Formark and other sites.

Switzerland has two URLs: the Grimsel Test Site (GTS) of NAGRA since 1984 in crystalline hard rocks and the Mont Terri underground rock laboratory by Swisstopo since 1996 in Opalinus clay. *Vomvoris* [2011] described many experiments and compared the feature/event/process, construction, evaluation, and demonstration in these two URLs. *Blechschmidt and Martin* [2012] presented in-situ tracer tests using radioactive elements and presented models developed to understand flow paths in a shear zone at the GTS. *Nussbaum and Bossart* [2012] presented the research program and key results of the Mont Terri laboratory. *Gaus* (2012, presented by Garitte) was on the fifth in-site heater experiment, HE-E, for task B of the DOCOVALEX-2015 project. Note that this experiment, together with Task A at the Tourmemire URL in France, described by *Barnichon and Millard* [2012], and Task C at the Bedichov tunnel in Czech Republic, described by *Hokr* [2012], are three DECOVALEX test cases sited along horizontal tunnels. The Honorobe URL in Japan, as described above for Task B Test Case, is accessible through vertical shafts. The access to URL, through horizontal, slanted, or looped tunnels, and vertically through shafts, is one of the operation considerations in instrumenting and testing in different URLs.

In North America, in Canada during 1968–1988 there was the Whiteshell URL of Atomic Energy of Canada, Limited (AECL) in hard rock at depths of 220–420 m, which closed in 2010 after flooding. Examples of contributions to hard rock geotechnical engineering and geophysics included tunnel stability and tunnel shape from circular to eye-shaped configuration, depending on stress orientation, and the characterization of excavation-disturbed zones from acoustic emission signals. *Martin and Young* [1993] is an example of papers from Whiteshell URL. *Marklund et al.* [2009] and *Jensen* [2009] presented aspects of the site characterization program in southern Ontario for a low- and intermediate-level waste repository.

In the United States, the Yucca Mountain Exploratory Study Facility (ESF) reached a depth of 300 m, and its testing program operated during 1997–2006. The ESF loop was horizontally excavated through 600-m-thick unsaturated tuff. *Wang and Bodvarsson* [2003] summarized the evolution of the ESF and associated cross-drift for seepage testing in both hard welded tuff units and softer lithophysal cavity-rich nonwelded tuff units. *Flint et al.* [2001] described the evolution of the conceptual model for Yucca Mountain hydrology. *Tsang et al.* [2009] reviewed the single heater test and the drift scale test, with four-year heating and four-year cooling periods. *Alley and Alley* [2013a, b] discussed decades of evolution in the U.S. nuclear waste disposal program and the demise of the Yucca Mountain project, which was closed in 2009. *Newbury and Simmons* [2012] and *Dyer* [2012] presented overviews of the post–Yucca Mountain perspective.

The Waste Isolation Pilot Plant (WIPP) is the world's first and only operating repository since 1999 for transuranic wastes. *Bauheim and McKenna* [2009] summarized the conceptual-based site characterization of the bedded salt at WIPP. *Hansen* [2013] described the tests conducted at WIPP with a plan for excavation for an additional heater experiment. Germany-U.S.A. collaborations for the salt URL were discussed. *Myers and Elkins* [2004] proposed to site both a nuclear power plant and a nuclear waste repository at the same salt site underground. We are evaluating whether the underground nuclear plant, including consideration of dry cask storage for spent fuel and wastes onsite, could be feasible for the next generation of nuclear power plants, for small- and medium-scale advanced reactors and for conventional reactors. The ISRM currently has a commission on the underground siting of nuclear power stations, www.isrm.net.

In 2001, The International Atomic Energy Agency (IAEA) had formed a network of Centres of Excellence for training and demonstration of waste disposal technologies. This project continues today and detailed programs have been developed to reflect the needs of all the member states in the network. At all technical meetings, the input and needs of members were discussed by network participants. The 2012 meeting was held at Albuquerque with a field trip to WIPP led by *Van Luik* [2012], with visitors from 19 member states including Belgium, Canada, Czech Republic, Germany, Japan, Kazakhstan, Philippines, South Africa, South Korea, Switzerland, Ukraine, United Kingdom, and United States.

There have been several proposals for regional and international repositories for disposal of high-level nuclear wastes. The concept was endorsed by the IAEA. European Commission funded studies to assess the feasibility of European regional waste repositories, and similar initiatives were expected for the Mideast, North Africa, and Southeast Asia. Even the Australian outback was identified with appropriate characteristics for an international deep geological disposal by the Pangea Resources. *McCombie and Chapman* [2004] presented an expert discussion on nuclear fuel cycle concepts.

2.3.2. Deep Facilities for Physics Rare Event Detections

Bettini [2007] presented a review of world underground physics facilities, including ones in Finland, France, India, Italy, Spain, Russia, Ukraine, United Kingdom, and United States. *Bettini* [2011] described recent world underground scientific laboratories and facilities and projects for new ideas. General considerations for cost and design were also given. *Coccia* [2010, 2011], *Bettini* [2012, 2013], and *Smith* [2013] discussed different physics experiments and

updates of the infrastructure of existing and new halls recently built or planned. This subsection supplements the overviews given in these papers and focuses mainly on multidisciplinary studies in different underground physics laboratories in Asia, Europe, North America, and southern-hemisphere countries.

As in other fields, astrophysics, particle physics, and nuclear science use many nomenclatures for experiments, detector techniques, and for project collaborations with many researchers. Detectors for rare events and particles use water, water doped with chemical elements (scintillators), solid crystal or components (usually at cryogenic conditions for most of the chargeless particles), and electronic signals for particles with charges. Particles are detected by lights, radiations emitted, or other particles generated in the detector medium. Water and liquid detectors are large in volume, currently approaching kiloton and million ton scales, with surrounding photo-multipliers and other devices to measure particle velocities and energies. Solid detectors of kilogram weights are approaching ton scale and deploying water and other solids for better shielding. The time projection chamber (TPC) with parallel wires under high voltages is an alternative sensor technique used. The detector trends typically toward requiring larger laboratory spaces, deeper locations for shielding from cosmic rays, and other radiations. Neutrinos and anti-neutrinos are chargeless with masses (only mass differences but not the absolute mass values known in the past decade) and different favors associated with electron, muon, and tau particles. Dark matter searches and neutrino-less double beta decays are popular experiments, with other rare events including proton decay, detection of supernovae, gravity wave, or even dark energy signals. Measurements of neutrinos from the Sun (solar neutrinos from nuclear fusion), from the reactors (from nuclear fission), and from the Earth's core and crust (geoneutrinos from U, Th, or K radioactive decays) are also carried out by different laboratories. Newly constructed or planned laboratories place more emphasis on these infrastructure needs.

In this article, we will present some infrastructural information and mention some well-known detector and experiment names. The physics experiments are mentioned for information and for inputs to determine if new laboratories and excavations are needed, and for designs for next generations of physics experiments. Geotechical and design-related activities for the construction of experimental halls are mentioned if the information is available. We also mentioned available information on geoscience and multidisciplinary studies associated with these relatively deep facilities.

In Asia, there are underground physics laboratories in China, India, and Japan. The China JinPing Laboratory is the deepest underground physics laboratory, constructed when the JinPing tunnels were excavated. *Feng* [2011] described the excavation of China's JinPing tunnels for hydropower production. The maximum tunnel overburden is 2,525 m through the marble rock mass, having maximum principal stress value of 70 MPa. Four headrace tunnels, two auxillary tunnels, and one water drainage tunnel were excavated with an average length of 16.7 km. The diameters of the headrace tunnels excavated ranged from 12.4 to 13 m. Test tunnels with smaller diameters (2.2–8 m) were excavated between the east-west main tunnels. Acoustic wave apparatus for the single and cross-hole method, a sliding micrometer, and a digital borehole camera were used to measure the evolution of the surrounding rock induced by the excavation, first by the tunnel boring machine and later by the drill and blast methods. Geological structure, elastic wave, deformation, fractures, and rockburst/rock spalling data were collected. Both the excavation *disturbed* zone associated with microfracturing inferred by acoustic emission microseismic signals and sliding micrometer measurement, and the excavation *damaged* zone associated with new fractures (with aperture > 0.2 mm) observed by a digital borehole camera, were observed and quantified. Both the immediate and the time-delay types of rock bursts were observed, with the immediate type being mainly associated with tension failures and the time-delay type associated with shear failures. The rockburst risks were numerically analyzed via a "vulnerability" index. The data and models of tunnels and excavations were valuable for the development of the design methodology, the main topics of the ISRM Design Methodology Commission, as summarized by *Hudson and Feng* [2013]. Four papers in *Feng et al.* [2013] are on various aspects of the JinPing tunnels.

Yue [2011], *J. Li* [2011], and *Wong* [2013] described the China JinPing Laboratory (CJPL) hall and the CDEX dark matter experiment with a Ge solid crystal detector. The other dark matter experiment PANDIX with a two-phase Xe liquid detector was described by *Liu* [2011] and *Ni* [2013]. *Yang* [2011] indicated that additional experimental support would be developed in China's next five-year plan, which is expected to start in 2016. *J. Li* [2013a, b] presented the second phase of CJPL (CJPL-II), with eight additional halls, each designed as 12 m wide, 10 m high, and more than 30 m long. The total volume for CJPL-II, 96,000 m^3, is more than 40 times the original CJPL, with its volume of 4,000 m^3, 6.5 m wide, 6.5 m high, 40 m long. The radon emission measurements, the radiation background, and regional earthquake events were also presented. With such a large increase in laboratory volume, it is possible to site more physics and multidisciplinary experiments beyond the one-ton extensions of CDEX and PANDEX at CJPL-II. *J. Li et al.* [2013] discussed next-generation neutrino-less double decay, solar neutrino, and infrastructure requirements of other physics experiments. *Wang and Li* [2013] discussed general geophysics investigations,

rockburst monitoring in deep tunnel excavations, and multidisciplinary co-location/collaboration studies, including the $[SQUID]^2$ sensor for global magnetic-earthquake monitoring, as described by *Waysand* [2006], and the SIMPLE detector for bubble-chamber-type fluorine-based superheated liquid dark matter search, by *Girard* [2012].

India has the Indian Neutrino Observatory (INO) approved for excavation in 2013. *Dighe* [2013] described this URL with Cavern 1 having dimensions $26 \times 32.5 \times 132$ m^3 to host a magnetized iron calorimeter with solid Fe plates of 50–100 kton for atmospheric neutrino studies. There are three other smaller caverns planned for other dark matter and double beta experiments, all located at ~1,000 m deep, accessible through a horizontal tunnel to be excavated.

Japan has the Kamioka mine with many physics observatories and experiments: Super-KAMIOKANDE, KamLand for reactor neutrino and geoneutrino experiments, CLIO and its extension LCGT for gravity wave detection, KMASS, CANDLES, NewAGE, and other dark matter and double beta decay experiments. There are also a laser strainmeter and superconducting gravity meter installed for geophysics studies. The Kamioka Observatory was established in 1983 at 1,000 m deep, via horizontal access, well-known for the 1987 supernova neutrino detections by KAMIOKANDE (19 m in diameter, 22.5 m high, 6,000 m^3). The Super-KAMIOKANDE cavern (40 m in diameter, 55 m high, 96,000 m^3) currently houses the world largest water Cherenkov detector. There is also a neutrino beam from Tokai to Kamioka (T2K) over 295 km for neutrino oscillation experiments. *Yamatomi* [2013] presented the design for Hyper-KAMIOKANDE at Tochibora mine at 370 m deep (8 km from Kamioka), the next-generation million-ton water detector, with a twin-cavern configuration having lengths ~ 250 m, truncated egg-shape cross-section with 50 m width and 56 m height. Nearly 30-m-long rock bolts were considered in the design. The total volume to be excavated was estimated to be 1.6×10^6 m^3.

OTO-Cosmo Observatory in Japan has ^{48}Ca and CaF_2 laboratories with ~100 m^2 space for dark matter and double beta decay experiments, at 470 m depth, through a horizontal tunnel with natural wind ventilation.

Korea has the Yang Yang Underground Laboratory (Y2L) since 2003 associated with a pumped storage power plant at a depth of 600 m accessible through a horizontal tunnel. CsI, Ge, and $CaMoO_4$ crystal detectors were used for dark matter and double beta decay experiments. The possibility of expansion of laboratory space is being explored, from the existing 100 m^2 to 800 m^2.

In Europe, there are underground laboratories in Finland, France, Russia, Spain, Ukraine, and the United Kingdom. Finland has the Centre for Underground Physics at Pyhasalmi (CUPP), with available space over 1,000 m^2 in the old mine from the 95- to 980-m levels (500 m^2 occupied by the EMMA experiment for over a decade) and possible laboratory space at the 1,450-m-deep level in the new mine. *Nuijten* [2012, 2013] discussed the LAGUNA-LBNO project with the design of an LBNO liquid argon detector 64 m wide, 51 m high, and 103 m long. This is bigger than the 60-m span of the Gjovik Olympic Cavern at 40 m deep in Norway. LAGUNA was Europe's long baseline neutrino beam project for which seven laboratories, mines, and sites in different European countries were evaluated, for consideration to receive neutrino beams from the CERN in Switzerland. Three types of detectors were considered by LAGUNA: MEMPHIS for water Cherenkov, GLASIER for liquid argon, and LENA for liquid scintillator technologies.

France has the Laboratoire Souterrain de Modane (LSM) since 1982, at a maximum depth of 1,700 m, the deepest European laboratory with ~400 m^2 space. EDELWEISS Ge and NEMO ^{100}Mo detectors were used in the main dark matter and double beta decay experiments. *Piquemal* [2012, 2013] described these and other scientific activities, including using gamma spectroscopy for dating wines, environmental, oceanography, retro-observation, and other multidisciplinary applications. A Deep Observatory for Multidisciplinary Underground Sciences was funded for future excavation in a new laboratory hall sited next to the existing laboratory and between two roadway tunnels.

Italy has the Laboratori Nationali del Gran Sasso (LNGS), the largest in the world in volume, with three halls each 20 m wide, 18 m high, and 100 m long, excavated and operated since 1987 together with the construction of highway tunnels. The total excavated area is 17,300 m^2 and total excavated volume 180,000 m^3, at a depth of 1,400 m. In 2013, there were experiments on dark matter search (CRESST, DAMA/LIBRA NaI annual modulation, DARKSIDE, WRAP Xe Ar, XENON Xe), double beta decay (COBRA CdZnTe, CUORE $^{130}TeO_2$, GERDA ^{76}Ge), supernova (LVD scintillator with neutrino from gravitational stellar collapse), solar and geoneutrino (BOREXINO), nuclear astrophysics (LUNA), long base line 730 km from CERN (ICARUS liquid Ar-TPC, OPERA tau neutrino emulsion cloud chamber), and other physics experiments (VIP validation of Pauli exclusion principle) in the three halls, and two 90-m Michelson interferometers and other earth science experiments (CRYO STEM biological evolution, EMRES ^{222}Rn–^{14}C–^{3}He, GIGS crustal deformation, PULEX2 radiation on living matter, TULLUS electromagnetism-plasma-charged particles, UNDERSEIS seismic). All experiments are planned to last for finite periods determined through an international committee. *Plastino* [2012] summarized environmental radioactivity monitoring of radon in air, uranium in water, noble gas, and other measurements at Gran Sasso and worldwide associated with earthquakes.

Russia has the Baksan Neutrino Observatory (BNO), the world's oldest physics facility, established in 1966, with two 4-km railroad tunnels to access and reach the BUST hall ($24 \times 24 \times 16$ m^3 near the tunnel entrance) and SAGE hall ($10 \times 12 \times 60$ m^3 under 2,100 m). A plan to excavate a larger and deeper hall of 40,000 m^3 for solar neutrino research was started in 1990 and stopped in 1992.

Spain has the Laboratorio Subterraneo de Canfranc (LSC) with the old lab ~100 m^2 created in the 1980s and the new lab ~1,000 m^2 since 2008, accessible through two tunnels at a depth of 850 m. The lab has Hall A 15 m wide, 12 m high, 40 m long; Hall B 10 m wide, 8 m high, 15 long; and three other rooms. The approved physics experiments since 2008 include BiPo for SuperNEMO on double beta decay, ArDM for Ar TPC dark matter search, ANAIS NaI for annual modulation of neutrino signals, ROSEBUD (BGO, sapphire, LiF, etc.), NEXT ^{136}Xe TPC, and SUPER Gd screening. *Diaz* [2012] described an earth science GEODYN observatory, with seismographs and laser strainmeters on ground surfaces and underground tunnel locations to monitor the entire geodynamical spectrum.

Ukraine has the Solotvina Underground Laboratory (SUL) since 1984, 430 m deep in a salt mine accessed through a mine cage, and ~1,000 m^2. SUL evaluated ^{116}Cd WO_4, $CaWO_4$, $ZnWO_4$, $PbWO_4$, and $CaMoO_4$ detectors for double beta decay and dark matter experiments.

The United Kingdom has the Boulby Palmer Laboratory (BUL) developed in 1998 with ~1,500 m^2 at 1,100 m depth in potassium chloride. *Paling* [2012] gave an overview of the DRIFT physics experiment and other cosmic rays, climatic, muon tomography, geomicrobiology/astrobiology, environmental, geology, and geoscience studies conducted there. *Cockell et al*. [2012] discussed the conversion of the Palmer Lab facility (where ZEPLINE and other physics experiments used to be located) to a UK Center of Astrobiology and engaged in the search for life on Mars, which is covered in salt. The Boulby International Subsurface Astrobiology Lab hosted a workshop with NASA to explore Boulby as an extraterrestrial analogue.

Canada has North America's deepest laboratory, Sudbury Neutrino Observatory (SNO) with the SNO+ experiment and the newly completed SNOLab, at a depth of 2,000 m. The heavy water SNO detector, 1,860 m^2, has been converted into a liquid scintillator SNO+ detector for geoneutrino studies. The new space in SNOLab, 5,360 m^2, has a cube hall, a linear ladder lab, and a barrel-shaped cryopit, 18 m in diameter, 20 m high. *Sinclair* [2013] presented the status of experiments at SNOLab, with the ladder lab space occupied and only the cryopit space remaining to be assigned. DEAP, MiniCLEAN, DAMIC, and HALO are in the cubic hall and in the HALO stub. PICASSO, COUP, and SuperCDMS are in the ladder lab. *Sherwood Lollar et al.* [2012] discussed microbiology searches at SNOLab, in Canadian shield, and in other URLs (in Sweden and Finland). *Kaiser et al.* [2011] discussed mines in Sudbury, in Canada, and in Australia and the United States toward a networked deep mine observatories.

The United States has four underground laboratories: KURF, SUL, SURF, and WIPP. *Link and Vogelaar* [2013] described the Kimbalton Underground Research Facility (KURF) in the Kimbalton mine, with spiraling drive-in access to reach six experiments (mini-LENS, neutron spectrometer, excited state double decay, HPGe screening, MALBEK, 39Ar depleted argon) in the 14th level, and the experiment Watchboy project in the 2nd level. Watchman is on spallation isotope production for reactor monitoring by neutrinos.

The Soudan Underground Laboratory (SUL) has two halls with a total volume of 2,300 m^2 at a depth of 700 m. One hall contained the CDMS-II experiment for dark matter search. The other hall had the MINOS Fe plate detector for the neutrino beam from Fermi National Accelerator Laboratory (FNAL) near Chicago. SUL uses a slightly inclined shaft for access. *Marshak* [2013] described the NUMI neutrino beam, 735 km from FNAL to Soudan, the dark matter searches with CDMS and CoGeNt, low background counting, and geology/geochemistry/goemicrobiology earth sciences.

Homestake gold mine has a long history, with the Davis hall excavated for the famous solar neutrino Cl experiment from 1965 to 2001. *Lesko* [2013] described the Sanford Underground Research Facility (SURF) with two experiments held at the 1,450 m (4,850 ft) level, in Yates campus for the Large Underground Xenon (LUX) dark matter experiment in the expanded Davis hall (11 m wide, 13 m high, 18 m long), and the MAJORANA double beta decay experiment in a newly excavated hall (16 m wide, 5 m high, 43 m long). There is also the Long Baseline Neutrino Experiment (LBNE) planned to have a neutrino beam from Fermi Lab to Homestake, ~1,300 km, with the detector preferably built underground. Before SURF, there were efforts to convert the Homestake mine, closed in 2001, to a Deep Underground Science and Engineering Laboratory (DUSEL). *Elsworth* [2012] discussed the evolution of bio-geo-engineering efforts in ecohydrology, faulting processes, CO_2 sequestration, THMCB coupled processes, large cavity, low background counting, seismic imaging, TM HPPP testing, $[SQUID]^2$ magnetic earthquake monitoring, and gravity measurements. *Moser* [2011] and Wang [2013] discussed microbiology studies at Homestake and other URLs. These bio-geo-engineering experiments were located in many levels in the mine. *Wang and Laughton* [2010] discussed the use of multiple levels for studies at DUSEL and other URLs. *Laughton* [2011] discussed geotechnical challenges including cost, safety, and interaction with industry. *Vardiman* [2012] and *Roggenthen*

[2013a, b] described and geotechnical and hydrological site investigations of SURF in levels at Homestake.

WIPP has a science area located away from the transuranic waste storage area, at a depth of 600 m. The detector for the Enriched Xenon Observatory (EXO) was installed in 2010. The detector observed the slowest process in the universe, with a decay half-life 200 billion times the age of the universe. The WIPP URL for radioactive waste storage and research is described above in subsection 2.3.1. WIPP is for both physics and radioactive waste research.

In South America, between Argentina and Chile, the ANDES underground laboratory is being planned to be built along the Agua Negra tunnel, under 1,750 m of overburden. *Bertou* [2012] and *Dib* [2013] presented the evolving design for ANDEA, with halls of different configurations (rectangular, elliptical) being considered. The size of ~4,000 m^2 and 65,000 m^3 is in seven halls which are expected to open in 2019–2020. DAMA/LIBRA yearly modulation is one physics experiment to be investigated in the southern hemisphere if the modulation is due to dark matter. Also planned are the third-generation dark matter experiment, CCD detection techniques, geoneutrinos, superNEMO, and a geophysics laboratory for seismograph, magnetic, and gravimeter studies.

In South Africa, there are renewed interests in underground physics experiments. *Wyngaardt* [2013] described the possible location of a closed tunnel next to a highway tunnel for establishing an underground laboratory. South Africa also has many gold mines over 3 km deep with a history of siting physics experiments and for microbiology studies.

Two Nobel Prizes in Physics were granted for neutrino research in underground laboratories. In 1965, atmospheric neutrinos were observed at the East Rand Proprietary mines in South Africa at 3.2 km depth and in the Kolar gold mine in India at 2.7 km, followed by wider and shallower experiments at Utah and Ohio, leading to the 1995 prize to Frederick Reines, shared with Martin Perl. The neutrino oscillation solar neutrino experiment at Homestake and the KAMIOKANDE supernova observations at Kamioka mine led to the 2002 prize to Raymond Davis and Masatoshi Koshiba, shared with Riccardo Giacconti. Future discoveries, observations, and explanations of dark matter, neutrino-less double decay, proton decay, and dark energy will likely be found, with underground laboratories further contributing to such physics research. The history evolutions are reviewed by many papers, including *Wang* [2011].

2.3.3. Examples of Borehole Complexes for Energy, Resources, and Environmental Research

This subsection is on energy resources and environmental research in underground settings, using borehole complexes and excavations other than those discussed above for radioactive waste assessments in subsection 2.3.1 and for physics research in subsection 2.3.2. We first discuss general assessments of energy resource production and then present examples for solid waste disposal and CO_2 sequestration.

Brinkman [2012] showed that reduction of CO_2 by 50% could be achieved by substituting natural gas for coal, and U.S. energy consumptions from 2010 to 2035 could see increases from 7% to 11% in renewables, 1% to 4% in liquid biofuels, 25% to 26% in natural gas, no changes at 9% in nuclear energy, decreases from 21% to 20% in coal, and 37% to 32% in petroleum and other liquids. *Hitzman et al*. [2012], *Hitzman* [2012], and *Tester* [2012] discussed critical elements for energy production, as needed for renewable solar and wind energy and for car batteries, geothermal resources for electric generation and for district heating, and shale gas production through hydraulic fracturing and the associated environmental concerns. *Shephard* [2013] discussed the development of shale reserves and water use strategies for a sustainable future. *Elsworth* [2013] discussed the uncertainties in sustaining energy recovery and the roles of underground experiments and URLs in resolving the issues.

The development of shale gas and oil depends on hydraulic fracturing (or fracking) along mainly horizontal wells. *Tutuncu* [2011] presented site characterization and injection/withdrawal assessment of a proposed in situ laboratory in shale gas and shale oil. *Zoback et al.* [2010] showed that hydraulic fracturing at the Barnet shale occurred at depth ~ 2 km. *Dusseault* [2013] presented the theory, reality, and uncertainty of hydraulic fracturing operations. Hydraulic fracturing was also used in deep slurried solid injections. *Dusseault* [2011] explained that saline water and sold slurry injection practices into deep fractured and porous layers had been used in oilfields for more than 20 years, could be practiced in China in identified areas, occurred at Alberta Canada in 1996, had a zero discharge oil field solid injection site in Indonesia, and applied to municipal biosolids in Los Angeles since 2009.

Wakimoto [2013] presented impacts on energy production from storms, hurricanes, earthquakes, tsunamis, and melting of the Arctic ice. *Uhle* [2012] described the aftermath of the Fukushima Daiichi Nuclear Power Plant in Japan and the associated regulatory concerns. The 15-m tsunami associated with the 2011 magnitude 9 earthquake exceeded the site design protection for the reactor buildings. *McNutt* [2012] discussed other kinds of challenges in energy and resource recovery. The National Petroleum Reserve and the National Wildlife Refuge Area in Alaska were shown to have great potential for undiscovered oil and gas reserves and coastal erosion on the north coast of Alaska from 2011 to 2014 were shown as examples for concerns. Perhaps underground sitings with dry cask waste storage near existing coastal nuclear power plants

as discussed in subsection 2.3.1 will be one solution to nuclear energy and waste problems.

Duffaut [2007, 2011, 2013] pointed out that many hydropower plants were excavated underground worldwide; extensive studies occurred in 1960–1978 on underground nuclear power plants in Norway, Switzerland, France, Sweden, and studies in Canada. The accidents at Three Mile Island, Chernobyl, and Fukushima have slowed down the development of nuclear energy since then. There were 439 nuclear power reactors operating in 31 countries as of January 2013. Since some of reactors are over the typical 40-year design operation period, the future of nuclear energy may depend on siting the nuclear power plants underground, by excavating into hills near existing and licensed locations or in shallow cavities to be covered by dirt to protect from natural hazards and terrorism. There also has to be a co-located source of cooling water.

All these energy and environment assessments in underground setting are multidisciplinary in nature, as shown for most of the different URLs and deep physics facilities. One underground laboratory is unique in practicing and promoting interdisciplinary deep underground science and technology under low noise conditions. *Gaffet* [2012, 2013] described the Laboratoire Souterrain a Bas Bruit (LSBB) in France at a depth of 500 m. There are seismic sensors on the ground surface and along underground horizontal tunnel segments, with the MIGA project for matter wave laser interferometer, CRITEX for water resource in a carbonic aquifer, MAXWELL, HPPPCO$_2$, LINES for rock properties/CO$_2$ sequestration, EEG, ERI-4D, EM3D in collaboration with University of British Columbia, EPHRAT on energetic charged particles above thunder storms, in addition to the SIMPLE detector for dark matter search and [SQUID]^2 detector mentioned in subsection 2.3.2. *Waysand et al.* [2010] presented the azimuthal polarization analysis of the 2008 Sichuan, China, earthquake and 2009 sprite observation in the Gulfe de Lyon (see also *Wang and Waysand*, 2010). *Fourie et al.* [2013] presented (by Samuel Henry) the first simultaneous magnetic measurements of low-frequency signals associated with earthquakes in the global network with both South Africa and France, following the detection of magnetic signals associated with the 2008 Sichuan earthquake in China. *Guglielmi* [2011] and *Guglielmi et al.* [2012] discussed the development and application to fault zone hydro-mechanical testing at LSBB, in fractured aquifer sites, and the applicability to other URLs. A step-rated injection method for fracture in-situ properties (SIMFIP) was accepted in 2013 as one of the ISRM Suggested Methods, as discussed in *Wang et al.* [2013].

All these underground research activities are evaluated by the ISRM URL Networking Commission, with its scope including radioactive waste URLs, deep physics facilities, and borehole complexes for energy resource and environmental evaluations. The commission currently has 18 commissioners, with six representing radioactive URLs; five representing deep physics facilities four representing energy, environment, and interdisciplinary research; and three for managing and as ex-officios for the commission. Additional commissioners will be added in the future to expand the reach and in order to form a multidisciplinary network.

2.4. CONCLUDING REMARKS

In memory of Paul A. Witherspoon, we reviewed the impacts of two 1980 papers authored by Witherspoon and his colleagues. One is on the cubic law for fracture flow [*Witherspoon, Wang, et al.*, 1980], widely cited for over three decades and used in understanding processes in fractured media. The fracture flow cubic law and its extension in fracture media and coupled processes play important roles in our studies of different underground settings. We evaluated the fracture flow law implications and its extensions. The understanding of fluid flow through fractured rocks is important for progress in the many existing and proposed engineering projects. Moreover, the characterization of this understanding is crucial during the use of the supporting computer modeling, which is becoming ever more ambitious and ubiquitous. The calculations and resultant outputs need to be validated, both in order to ensure appropriate engineering decisions and because there is increasing emphasis on the use of the Earth's resources and their sustainability, as well as on more accountability of engineers' decisions.

Within this context, there remain many unknowns. We conducted the literature review to address in part the following questions: How do we establish the geometrical and hydrogeological properties of fractures in a specific rock mass? How do we establish the link between the hydrogeological fracture properties and other variables, such as the in situ stress state and changes in temperature? Critically, how do we validate the results at the full scale? We realize that there are fundamental challenges in quantifying fractures under stress and in exploring applications, especially in the field scales.

Concurrently with the laboratory and numerical studies of fracture flows, we have made progress in developing underground research laboratories (URLs), following the pioneer work of *Witherspoon, Cook, et al.* [1980] in hard rocks and later generalized to softer rocks. We further discuss the housing of large halls for particle detectors at great depths, and in testing the energy and resource recovery capacities and the waste disposal potentials through borehole complexes. In addition to existing worldwide networks for radioactive wastes, we initiate preliminary comparisons of different underground laboratories and facilities, including physics laboratories and borehole complexes.

Site characterizations, evaluations of the excavation disturbed and damaged zones, flow and tracer transport experiments, and engineered barrier experiments existed in most radioactive waste URLs. Heater experiments and coupled process studies are also common in all radioactive waste URLs. Note that the heat transfer processes are relatively slow, and heater tests usually need years and decades to be carried out. This represents a major challenge in planning, execution, funding, management, and safety concerns. For deep physics halls, excavations of large spaces, especially ones with wider spans, represent challenges mainly for rock mechanics and geotechnical engineering. There is growing interest, currently mainly in Europe, to tackle multidisciplinary research. Geosciences are likely included in new physics laboratories. We also present examples for borehole studies, mainly along deep boreholes for energy and environmental research. We hope that networking among different underground studies contributes to addressing common concerns and leads to improvements, saving, and exchanges of scientific knowledge. Networking can contribute to solving many common concerns.

This article supplements early papers and presentations compiled by *Wang et al.* [2010]. The findings since 2011 of a Commission for the International Society for Rock Mechanics on URL Networking are summarized. Side drifts off roadway tunnels, dedicated facilities with tunneling and shafting to reach desired depths, and levels in active and recently deactivated mines, are well-established examples of URLs for radioactive assessments and for rare-event detector housings. Many dedicated facilities also have boreholes drilled for site characterization. Examples of borehole complexes for energy and environment research and development have been included in our comparisons.

ACKNOWLEDGMENTS

We thank Boris Faybishenko and two anomalous reviewers for support and comments. Suggestions to the early draft led to improvements in this manuscript. Recent inputs from the ISRM commissioners and authors are invaluable for the technical topics addressed and reviewed in this article. The support for author J.S.Y. Wang as an affiliate of the Earth Sciences Division of Lawrence Berkeley National Laboratory is acknowledged. This manuscript has been authored by an author at Lawrence Berkeley National Laboratory under Contract No. DE-AC02-05CH11231 with the U.S. Department of Energy. The publisher, by accepting the article for publication, acknowledges that the U.S. Government retains a nonexclusive, paid-up, irrevocable, worldwide license to publish or reproduce the published form of this manuscript, or allow others to do so, for U.S. Government purposes.

REFERENCES

Alley W. M., and R. Alley (2013a), Challenges in uncertainty and the science of nuclear waste disposal, Abstract U21A-03 presented at 2013 Fall Meeting, American Geophysical Union, San Francisco, 9–13 December.

Alley, W. M., and R. Alley (2013b), *Too Hot to Touch*, Cambridge University Press, 370 pp.

Anderson, M. P., and W. W. Woessner (1992), *Applied Groundwater Modeling: Simulation of Flow and Advective Transport*, Google book, Academic Press, New York.

Armand, G. (2011), Status of the Meuse/Haute-Marne Underground Research Laboratory, Presentation III-5, URL Workshop, 12th ISRM Congress, Beijing, 17 October, 20 slides.

Bai, M., and D. Elsworth (1994), Modeling of subsidence and stress-dependent hydraulic conductivity for intact and fractured porous media, *Rock Mechanics and Rock Engineering*, *27*(4), 209–234.

Barnichon, J. D., and A. Millard (2012), Task A: The SEALEX IN-site experiments, 33 slides, DECOVALEX-2015 Workshop, 34 slides, Berkeley, CA, 17–19 April.

Barton, N. (2002), Some new Q-Value correlations to assist in site characterization and tunnel design, *International Journal of Rock Mechanics and Mining Sciences*, *39*, 18–206.

Barton, N., S. Bandis, and K. Bakhtar (1985), Strength, deformation and conductivity coupling of rock joints, *International Journal of Rock Mechanics and Mining Sciences & Geomechanics Abstracts, 22*(3), 121–140.

Bauheim, R. L., and S. A. McKenna (2009), Conceptual-model-driven characterization of the Culebra dolomite at the waste isolation pilot plant, *EOS Transaction AGU*, *90*(22), Joint Supplement Abstract IA33A-02.

Bear, J. (1993), Modeling flow and contaminant transport in fractured rocks, in J. Bear, C.-F. Tsang, and G. de Marsily (eds.), *Flow and Contaminant Transport in Fractured Rock*, Google Books, Academic Press, New York, pp. 1–38.

Berkowitz, B. (2002), Characterizing flow and transport in fractured geological media: A review, *Advances in Water Resources*, *25*(8–12), 861–884.

Bertou, X. (2012), The ANDES Underground Laboratory, focus point on underground science laboratories, edited by S. Bettini, *European Physical Journal Plus*, September, *6* pages.

Bettini, A. (2007), The world underground scientific facilities, a compendium, *Topics in Astrophysics and Underground Physics* (TAUP), *33* pp.

Bettini, A. (2011), The world underground physics laboratories, Paper I-3, URL Workshop, 12th ISRM Congress, Beijing, 17 October, 20 pp.

Bettini, A. (2012), The world deep underground laboratories, *European Physical Journal Plus*, *127*, 114.

Bettini, A. (2013), New underground laboratories, *Topics in Astrophysics and Underground Physics (TAUP) International Conference*, *34* pp.

Blechschmidt, I., and A. J. Martin (2012), In-situ tracer tests and models developed to understand flow paths in a shear zone at the Grimsel test site, Switzerland, Abstract H33J-1472 presented at 2012 Fall Meeting, American Geophysical Union, San Francisco, 3–7 December.

Bodvarsson, G. S., and C.-F. Tsang (1982), Injection and thermal breakthrough in geothermal reservoirs, *Journal of Geophysical Research: Solid Earth, 87*(B2), 1031–1048.

Brace, W. F. (1980). Permeability of crystalline and argillaceous rocks, *International Journal of Rock Mechanics and Mining Sciences & Geomechanics Abstracts, 17*(5), 241–251.

Brinkman, W. F. (2012), Energy independence with sustainability, Abstract U24A-01 presented at 2012 Fall Meeting, American Geophysical Union, San Francisco, 3 December.

Cacas, M. C., E. Ledoux, G. De Marsily, B. Tillie, A. Barbreau, E. Feuga, and P. Peaudecent (1990), Modeling fracture flow with a stochastic discrete fracture network: Calibration and validation, 2. The transport model, *Water Resources Research*, *26*(3), 479–489.

Caine, J. S., and C. B. Forest (1999), Fault zone architecture and fluid flow: Insights from field data and numerical modeling, in W. C. Haneberg, P. S. Mozley, J. C. Moore, and L. B. Goodwin (eds.), *Faults and Subsurface Fluid Flow in a Shallow Crust*, American Geophysical Union.

Capuano, R. M. (1993), Evidence of fluid flow in micofractures in geopressured shale, *AAPG Bulletin*.

Coccia, E. (2010), Underground laboratories today, *Acta Physica Polonica B, 41*(7), 1693–1707, Cracow Epiphany Conf. Phys. Underground Laboratories & Its Connection with LHC, Cracow, Poland, 5-8, January.

Coccia, E. (2011), Interdisciplinary research in underground laboratories, ASPERA Workshop, Zaragoza, Spain, 30 June–2 July, 57 slides.

Cockell, C., S. Paling, D. Pyrus, D. McLuckie, et al. (2012), Boulby International Subsurface Astrobiology Laboratory (BISAL), ASPERA-2, Duhram, 17–19 December, 22 slides.

Cook, N. G. W. (1992), Natural joints in rock: Mechanical, hydraulic and seismic behavior and properties under normal stress, Jaeger Memorial Dedication Lecture, *International Journal of Rock Mechanics and Mining Sciences & Geomechanics Abstracts, 29*(3) 198–223.

Cox, S. F. (1995), Faulting processes at high fluid pressures: An example of fault valve behavior from the Wattle Gully Fault, Victoria, Australia, *Journal of Geophysical Research: Solid Earth, 100*(B7), 12841–12859.

Deak, F., L. Kovacs, and B. Vasarheyl (2013), Modeling the excavation damaged zones in the Bataapati Radioactive Waste Repository, EUROCK, Wroclaw, 21–26 September.

Delay J., A. Vinsot, J.M. Krieguer, H. Rebours, and G. Armand (2007), Making of the Underground Scientific Experimental Programme at the Meuse/Haute-Marne Underground Research Laboatory, North Eastern France. *Physics and Chemistry of the Earth* 32, 2–18, doi:10.1016/j.pce.2006.04.033.

Diaz, J. (2012), GEODYN: A geodynamic facility at Canfranc Laboratory, ASPERA-2, Duhram, 17–19 December, 52 slides.

Dib, C. (2013), ANDES: An underground laboratory in South America, 13th International Conference on Topics of Astroparticle and Underground Physics (TAUP), Asilomar, 12 September.

Dighe, A. (2013), Physics and status of INO, DAE-BRNS HEP Symposium, Santiniketan, India, January, 41 pages.

Doe, T. (2011), Thirty years of contributions to fracture flow from underground radioactive waste research laboratories, Presentation IV-1, URL Workshop, 12th ISRM Congress, Beijing, 17 October, 14 slides.

Duffaut, P. (2007), Safe nuclear power plants shall be built underground, 11th ACUUS Conference, 207–212, Athens, 10–13 September.

Duffaut, P. (2011), Large caverns, design and construction, Paper I-3, URL Workshop, 12th ISRM Congress, Beijing, 17 October, 4 pp.

Duffaut, P. (2013), State of art of underground nuclear power plant, Underground Nuclear Power Plant/URL meeting, EUROROCK, Wroclaw, September.22.

Dusseault, M. (2011), Deep sedimentary basin solids placement, Presentation IV-4, URL Workshop, 12th ISRM Congress, Beijing, 17 October, 34 slides.

Dusseault, M. (2013), Hydraulic fracturing: Theory—reality—uncertainty, Distinguished Scientist Lecture, Berkeley, 15 March.

Dyer, J. R. (2012), Overview of the Yucca Mountain Scientific Investigation Program, Presentation 73-2, Geological Society of America meeting, Minneapolis, 9–12 October.

Elsworth, D. (2012), DUSEL Interdisciplinary Science Studies: Geoscience and Geoengineering @ DUSEL, Presentation V-1, ASPERA-2, Duhram, 17–19 December, 27 slides.

Elsworth, D. (2013), Resolving key uncertainties in energy recovery: One role of in-situ experimentation and URLs, Abstract H31G-09 presented at 2013 Fall Meeting, American Geophysical Union, San Francisco, 9–13 December.

Elsworth, D., and M. Bai (1992), Flow-deformation response of dual-porosity media, *Journal of Geotechnical Engineering, 118*(1), 107–124.

Engelder, T., and C. H. Scholtz (1981), Fluid flow along very smooth joints at effective pressure up to 200 megaparscals, *Mechanical Behavior of Crustal Rock: The Handin Volume, Geophysical Monograph, 24*, 127–152.

Esaki, T., S. Du, Y. Mitani, K. Ikusada, and L. Jing (1999), Development of a shear-flow test apparatus and determination of coupled properties for a single rock joint, *International Journal of Rock Mechanics and Mining Sciences, 36*(5), 641–650.

Fahland, S., and S. Heusermann (2013), Geomechanical analysis of the integrity of waste disposal areas in the Morsleben Repository, in X.-T. Feng, J. A. Hudson, and F. Tan (eds.), *Rock Characterization, Modeling and Engineering Design Methods*, pp. 345–350, Proceedings of the 3rd ISRM SINOROCK Symposium, Shanghai, 18–20 June.

Feng, X.-T. (2011), From Sweden to China's competent, sparsely fractured sites and deep tunnels, Presentation I-2, 39 slides, URL Workshop, 12th ISRM Congress, Beijing, 17 October.

Feng, X.-T., J. A. Hudson, and F. Tan (2013), Rock characterization, modeling and engineering design methods, Proceedings of the 3rd ISRM SINOROCK Symposium, Shanghai, 18–20 June, 915 pp.

Flint, A. L., L. E. Flint, G. S. Bodvarsson, E. M. Kwicklis, and J. Fabryka-Martin (2001), Evolution of the conceptual model of undaturated zone hydrology, *Journal of Hydrology, 247* (1–2), 1–30.

Fourie, C., J. Van Vuuren, E. T. Lockner, C. Kwisanga, P. Febvre, E. Pozzo de Borgo, G. Waysand, D. Gouws, Sauderson, T. Matladi, and S. Henry (2013), Abstract

NH31B-1606, presented by S. Henry at 2013 Fall Meeting, American Geophysical Union, San Francisco, 9–13 December.

Freeze, A., and J. A. Cherry (1979), *Groundwater*, Prentice-Hall, 604 pp.

Gaffet, S. (2012), LSBB Underground Research Laboratory: A new platform for fundamental & applied low background noise, Inter-Disciplinary Underground Science & Technology, ASPERA-2, Duhram, 17–19 December, 20 slides.

Gaffet, S. (2013), A new platform for fundamental & applied low background noise, Inter-Disciplinary Underground Science & Technology, URL Meeting, EUROROCK, Wroclaw, 22 September, 12 slides.

Gaich, A., F. Deak, and M. Potsch (2012), High resolution 3d imaging during the construction of national radioactive waste repository from Bataapati, Hungary, Abstract H33J-1473 presented at 2012 Fall Meeting, American Geophysical Union, San Francisco, 3–7 December.

Gale, J. E. (1982), The effects of fracture type (induced versus natural) on the stress-fracture closure-fracture permeability relationships, 23rd US Symposium on Rock Mechanics, ARMA 82-290, Berkeley, 25–27 August.

Gale, J. E. (1987), Comparison of coupled fracture deformation and fluid flow models with direct measurements of fracture pore structure and stress-flow properties, 28th US Symposium on Rock Mechanics, ARMA 87-1213, Tucson, 29 June–1 July.

Gaus, I. (2012), Introduction to Task B of DECOVALEX 2015: HE-E experiment: In-situ heater test, DECOVALEX-2015 Workshop, Berkeley, 17–19 April, 38 slides.

Gerke, H. H., and M. T. van Genuchten (1993), A dual-porosity model for simulating the preferential movement of water and solutes in structured porous medium, *Water Resources Research, 29*(2), 305–319.

Girard, T. A. (2012), A Phase IV SIMPLE Search for Astroparticle Dark Matter, 2 parts, ERC Advanced Grant Research Proposal, 25 pp.

Guglielmi, Y. (2011), Hydro-mechanical coupled tests and induced seismicity, URL Workshop, 12th ISRM Congress, Beijing, 17 October, 15 slides.

Guglielmi, Y., F. Cappa, B. Derode, P. Jeanne, and J. Rutqvist (2012), Underground testing of permeability and earthquake nucleation in fault zones, Abstract H32G-05 presented at 2012 Fall Meeting, American Geophysical Union, San Francisco, 3 December.

Haimson, B. C., and T. W. Doe (1983), State of stress, permeability, and fractures in the Precambrian granite of North Illinois, *Journal of Geophysical Research: Solid Earth, 88*(B9), 7355–7371.

Hakami, E., and R. Christiansson (2012), Using induced bolehole breakouts as a method for stress orientation determination in hard crystalline rocks, EUROCK ISRM International Symposium, Stockholm, 28–30 May.

Hakami, E., and E. Larsson (1996), Aperture measurements and flow experiments on a single natural fracture, *Journal of Geophysical Research: Solid Earth, 98*(B2), 1889–1900.

Hansen, F. D. (2013), Underground salt research laboratory at the waste isolation pilot plant, SAND 2103-0356C, Sandia National Laboratories, Albuquerque, 8 pp.

Heusermann, S., R. Eickemeier, N. K Nipp, and S. Fahland (2013), Three-dimensional thermomechanical modeling of high-level emplacement in a salt dome, in X.-T. Feng, J. A. Hudson, and F. Tan (eds.), *Rock Characterization, Modeling and Engineering Design Methods*, pp. 647–652, Proceedings of the 3rd ISRM SINOROCK Symposium, Shanghai, 18–20 June.

Hirscock, K. (2009), *Hydrogeology: Principles and Practice*, Google Book, 389 pp.

Hitzman, M. (2012), Necessity for industry-academic economic geology collaborations for energy critical minerals research and development, Abstract H32G-02 presented at 2012 Fall Meeting, American Geophysical Union, San Francisco, 3 December.

Hitzman, M., J. W. Tester, and M. D. Zoback (2012), Opportunities for fundamental university-based research in energy and resource recovery, Abstract H32G-06 presented at 2012 Fall Meeting, American Geophysical Union, San Francisco, 3 December.

Hokr, M. (2012), Bedrichov Tunnel test case proposal for DECOVALEX 2015, DECOVALEX-2015 Workshop, 34 slides, Berkeley, 17–19 April, 52 slides.

Hudson, J. A. (2010), Underground radioactive waste disposal: The rock mechanics contributions, ISRM International Symposium, 6th Asian Rock Mechanics Symposium, New Delhi, 23–27 October, 18 pages.

Hudson, J. A., and X.-T. Feng (2013), Risk in rock engineering: Key issues and the work of the ISRM Design Methodology Commission, in X.-T. Feng, J. A. Hudson, and F. Tan (eds.), *Rock Characterization, Modeling and Engineering Design Methods*, pp. 49–60, Proceedings of the 3rd ISRM SINOROCK Symposium, Shanghai, 18–20 June.

Hudson, J. A., J. S. Y. Wang, and L. Jing (2013), The value of underground research laboratories in reducing rock engineering risk, URL Meeting, SINOROCK Symposium, Shanghai, 17 June, 33 slides.

Hudson, J. A., J. C. Andersson, L. Jing, and C.-F. Tsang (2011), Studies of coupled THMC problems in the DECOVALEX Project with support from URL field experiments, Paper V-2, URL Workshop, 12th ISRM Congress, Beijing, 17 October, 8 pages.

Jensen, M. (2009), Ontario's power generation's proposed deep geological repository, Tiverton, Ontario, Canada, *EOS Transaction AGU, 90*(22), Joint Supplement Abstract IA33A-04.

Jing, L. (2003), A review of techniques, advances and outstanding issues in numerical modeling of rock mechanics and rock engineering, *International Journal of Rock Mechanics and Mining Sciences, 40*(3), 283–354.

Jing, L., T. Koyama, Zhao, and B. Li (2013), Stress and shear effects on fluid flow and solute transport in rock fractures, in X.-T. Feng, J. A. Hudson, and F. Tan (eds.), *Rock Characterization, Modeling and Engineering Design Methods*, 33–44, Proceedings of the 3rd ISRM SINOROCK Symposium, Shanghai, 18–20 June.

Johns, R. A., J. S. Steude, L. M. Castanier, and P. A. Roberts (1993), Nondestructive measurements of fracture aperture in crystalline rock cores using X ray computed tomography, *Journal of Geophysical Research: Solid Earth, 98*(B2), 1889–1900.

Kaiser, P. K., D. Duff, and B. Valley (2011), Smart underground monitoring and integrated technologies in networked deep

mining observatories, Paper IV-3, Presentation 14 slides, URL Workshop, 12th ISRM Congress, Beijing, 17 October, 6 pages.

Kolditz, O., U.-J. Gorke, H. B. Shao, W. Wang, H. Shao, J. A. Hudson, and X.-T. Feng (2013), Thermo-hydro-mechanical-chemical processes in fractured rock, in rock fractures, in X.-T. Feng, J. A. Hudson, and F. Tan (eds.), *Rock Characterization, Modeling and Engineering Design Methods*, 45–48, Proceedings of the 3rd ISRM SINOROCK Symposium, Shanghai, 18–20 June.

Kwon, S., and J.-W. Choi (2006), Thermo-mechanical analysis for a multi-level radioactive waste disposal concept, *Geotechnical and Geological Engineering, 24*, 361–377.

Kwon, S., J.-W. Choi, and J. O. Lee (2013), An analysis of the thermal and mechanical behavior of engineer barriers in a high-level radioactive repository, *Nuclear Engineering and Technology, 45*(1), 41–52.

Laughton, C. (2011), Underground research laboratories: Siting criteria and engineering design considerations. A rock engineer's top ten list, Paper I-3, URL Workshop, 12th ISRM Congress, Beijing, 17 October, 4 pp.

Lee, C.-H., and I. W. Farmer (1993), *Fluid Dynamics, Rocks, Permeability*, Chapman & Hall, 169 pp.

Lesko, K. (2013), The Sanford Underground Research Facility (SURF), 13th International Conference on Topics of Astroparticle and Underground Physics (TAUP), Asilomar, 12 September.

Li, J. (2011), The status and plan of China JinPing Underground La (CJPL), Presentation II-2, presentation II-2, 14 slides, URL Workshop, 12th ISRM Congress, Beijing, 17 October, 25 slides.

Li, J. (2013a), China JinPing Underground Lab, radiation background measure, URL Meeting, SINOROCK Symposium, Shanghai, 17 June, 26 slides.

Li, J. (2013b), The status and plan of China JinPing Underground Laboratory (CJPL), 2nd Phase China JinPing Laboratory Town Meeting Associated with 13th International Conference on Topics of Astroparticle and Underground Physics (TAUP), Asilomar, 8 September, 85 slides.

Li, J., X. Ji, W. Haxton, and J. S. Y. Wang (2013), The second-phase development of the China JinPing Underground Laboratory, 13th International Conference on Topics of Astroparticle and Underground Physics (TAUP), Asilomar, 12 September, 33 slides.

Li, X. (2011), The roles of the URL HADES in the Belgian RD & D program on Radwaste geological disposal, Presentation III-6, URL Workshop, 12th ISRM Congress, Beijing, 17 October, 26 slides.

Li, X., G. Volckaert, and W. Bastiaen (2012), R & D at the Underground Research Laboratory, HADES, Belgium and the state of art on THMC behavior of boom clay, Abstract H33J-1471 presented at 2012 Fall Meeting, American Geophysical Union, San Francisco, 3–7 December.

Link, J. and B. Vogelaar (2013), Kimbalton Underground Research Facility, Deep Underground Research Association meeting, Palo Alto, 5 March, 35 slides.

Liu, X. (2011), Shielding of PANDIX experiment and cosmogenic activation of Cu sample, Cosmogenic Activity and Backgrounds Workshop, Berkeley, 13–15, April, 21 slides.

Long, J. C. S., and D. M. Billaux (1987), From field data to fracture network modeling: An example incorporating spatial structure, *Water Resources Research, 23*(7), 1201–1216.

Long, J. C. S., J. S. Remer, C. R. Wilson, and P. A. Witherspoon (1982), Porous media equivalents for networks of discontinuous fractures, *Water Resources Research, 18*(3), 645–658.

Marklund, L., S. Xu, and A. Worman (2009), Characterization of the discharge areas of radionuclides originating from nuclear waste repositories, EOS Transaction AGU, 90(22), Joint Supplement Abstract IA33A-01.

Marshak, M. (2013), The Soudan Underground Laboratory, Deep Underground Research Association meeting, Palo Alto, 5 March, 37 slides.

Martin, C. D., and P. R. Young (1993), The effect of excavation-induced seismicity on the strength of La du Bonnet granite, in P. R. Young, Bakema (eds.), *Rockbursts and Seismicity in Mines*, pp. 367–372.

McCombie, C., and N. Chapman (2004), Nuclear fuel cycle centres: An old and new ideas expert group report, Symposium of World Nuclear Association, London, 8–10 September.

McNutt, M. K. (2012), The frontiers of resource-related scientific research, Abstract U24A-02 presented at 2012 Fall Meeting, American Geophysical Union, San Francisco, 3 December.

Moench, A. F. (1984), Double-porosity models for a fissured groundwater reservoir with fracture skin, *Water Resources Research, 20*(7), 831–846.

Moreno, L., Y. W. Tsang, C. F. Tsang, F. V. Hale, and I. Neretnick (1988), Flow and tracer transport in a single fracture, *Water Resources Research, 24*(12), 2033–2048.

Moser, D. (2011), (Micro)biology at Sanford Lab, Deep Underground Research Association meeting, Batavia, Illinois, 19 January, 20 slides.

Moser, D. (2011), Update of Biology at SURF, Deep Underground Research Association meeting, Palo Alto, 11 January, 20 slides.

Myers, A., and N. Elkins (2004), Underground nuclear parks and the continental SuperGrid, SuperGrid 2 Conference, 25–27 October, 34 slides.

Neretniks, I. (1993), Solute transport in fractured rocks: applications to nuclear waste repositories, in J. Bear, C.-F. Tsang, and G. de Marsily (eds.), *Flow and Contaminant Transport in Fractured Rock*, Google Book.

Neuman, S. P. (2005), Trends, prospects and challenges in quantifying flow and transport through fractured rocks, *Hydrogeology Journal, 13*, 124–147.

Neuzil, C. E., and J. V. Tracy (1981), Flow through fractures, *Water Resources Research, 17*(1), 191–199.Newbury, C. M., and A. M. Simmons (2012), The past Yucca Mountain project-advancing science and technology for the future: Was it worth the cost? Presentation 73-1, Geological Society of America meeting, Minneapolis, 9–12 October.

Ni, K. (2013), Status and plans of the PandaX experiment at CJPL, Session PA-6, Cosmic Frontier Workshop, Palo Alto, 6–8, March, 15 slides.

Nilsson, B., P. Gravesen, S. S. Petersen, and M. Binderup (2012), Final Repository for Denmark's Low- and Intermediate Level Radioactive Waste, Abstract H33J-1475 presented at 2012 Fall Meeting, American Geophysical Union, San Francisco, 5 December.

Nitao, J. J., and T. A. Buscheck (1991), Infiltration of a liquid front in an unsaturated, fractured porous medium, *Water Resources Research, 27*(8), 2099–2112.

Nolte, D. D., L. J. Pyrak-Nolte, and N. W. Cook (1989), The fractal geometry of flow paths in natural fractures in rock and the approach to percolation, *Pure and Applied Geophysics, 131*(1/2), 111–138.

Nuijten, G. (2012), Underground synergies with astro-particle physics: Multi-disciplinary studies in the world deep science facilities, ASPERA-2, Duhram, 17–19 December, 105 slides.

Nuijten, G. (2013), LUGANA, URL Meeting, EUROROCK, Wroclaw, 22 September, 30 slides.

Nussbaum, C. O., and P. J. Bossart (2012), Mont Terri Underground Rock Laboratory, Switzerland: Research program and key results, Abstract H32G-06 presented at 2012 Fall Meeting, American Geophysical Union, San Francisco, 3 December.

Olsson, R., and N. Barton (2001), An improved model for hydromechanical coupling during shear of rock joints, *International Journal of Rock Mechanics and Mining Sciences, 38*, 317–329.

Paling, S. (2012), Boulby Underground Science Facility: Status & future plans, ASPERA-2, Duhram, 17–19 December, 21 slides.

Persoff, P., and K. Pruess (1995), Two-phase flow visualization and relative permeability measurement in natural rough-walled rock fractures, *Water Resources Research, 31*(5), 1175–1186.

Piquemal, F. (2012), Modane Underground Laboratory, ASPERA-2, Duhram, 17–19 December, 48 slides.

Piquemal, F. (2013), Activities at Modane Underground Laboratory, 13th International Conference on Topics of Astroparticle and Underground Physics (TAUP), Asilomar, 12 September.

Plastino, W. (2012), Environmental radioactivity monitoring for earth sciences at Gran Sasso National Laboratory, Italy, ASPERA-2, Duhram, 17–19 December.

Polak, A., D. Elsworth, H. Yasuhara, A. S. Grader, and P. M. Halleck (2003), Permeability reduction of a natural fracture under net dissolution by hydrothermal fluids, *Geophysical Research Letters, 30*(20), SDE I-1-4.

Pruess, K. (1985), A practical method for modeling fluid and heat flow in fractured porous media, *Society of Petroleum Engineering (SPE) Journal, 25*(1), 14–26.

Pruess, K., and T. N. Narasimhan (1982), On fluid reserves and the production of superheated steam from fractured, vapor-diminated geothermal reservoirs, *Journal of Geophysical Research: Solid Earth, 87*(B11), 9329–9339.

Pruess, K., J. S. Y. Wang, and Y. W. Tsang (1990), On thermohydrologic conditions near high-level nuclear wastes emplaced in partically saturated fractured tuff: 1. Simulation studies with explicit consideration of fractured effects, *Water Resources Research, 26*(6), 1235–1248.

Pyrak-Nolte, L., J. (2013), DSSS: The Critical Link: Fracture Stiffness as Nexus, Distinguished Scientist Lecture, Berkeley, 25 October–March.

Pyrak-Nolte, L. J., and N. G. W. Cook (1988), Fluid percolation through single fractures, *Geophysical Research letters, 15*(11), 1247–1250.

Pyrak-Nolte, L. J., and J. P. Morris (2000), Single fractures under normal stress: The relationship between fracture stiffness and fluid flow, *International Journal of Rock Mechanics and Mining Sciences, 37*, 245–262.

Pyrak-Nolte, L. J., T Mackin, and E. Boomsma (2011), Particle swarm transport in fracture network, Abstract H14A-02 presented at 2012 Fall Meeting, American Geophysical Union, San Francisco, 3 December.

Rangel-German, E. R., and A. R. Kovscek (2002), Experimental and analytical study of multidimensional imbibition in fractured porous media, *Journal of Petroleum Science and Engineering, 32*(1/2), 45–60.

Raven, K. G., and J. E. Gale (1985), Water flow in natural rock fracture as a function of stress and sample size, *International Journal of Rock Mechanics and Mining Sciences & Geomechanics Abstracts, 22*(4), 251–261.

Renshaw, C. E. (1995), On the relationship between mechanical and hydraulic apertures in rough-walled fractures, *Journal of Geophysical Research: Solid Earth, 100*(B12), 24629–24636.

Roggenthen, W. (2013a), Geotechnical monitoring on laboratory levels at Sanford, Deep Underground Research Association meeting, Palo Alto, 5 March, 11 slides.

Roggenthen, W. (2013b), Overview of the hydrogeologic systems of the former Homestake mine, SD, Abstract H31G-08 presented at 2013 Fall Meeting, American Geophysical Union, San Francisco, 9–13 December.

Rutqvist, J. (2011), Geomechanical aspects of CO_2 sequestration and modeling, Presentation IV-3, URL Workshop, 12th ISRM Congress, Beijing, 17 October, 21 slides.

Rutqvist, J., and O. Stephansson (2003), The role of hydromechanical coupling in fractured rock engineering, *Hydrogeology Journal*, *7–40*.

Rutqvist, J., and C.-F. Tsang (2003), Analysis of thermal-hydrologic-mechanical behavior near an emplacement drift at yucca mountain, *Journal of Contaminant Hydrology, 62*/63, 637–652.

Rutqvist, J., Y.-S. Wu, C.-F. Tsang, and G. Bodvarsson (2002), A modeling approach for analysis of coupled multiphase fluid flow, heat transfer, and deformation in fractured porous rock, *International Journal of Rock Mechanics & Mining Sciences, 39*, 429–442.

Schwartz, F. W., L. Smith, and A. S. Crowe (1983), A stochastic analysis of macroscopic dispersion, *Water Resources Research, 19*(5), 1253–1265.

Shephard, L. (2013), Developing America's shale reserve: Water strategies for a sustainable future, Abstract U21A-02 presented at 2013 Fall Meeting, American Geophysical Union, San Francisco, 9–13 December.

Sherwood Lollar, B., T. C. Onstott, E. Van Heerden, and T. L. Kieft (2012), Life in inner space: Subsurface microbiology investigations in underground research laboratories and deep mines, Abstract H32G-04 presented at 2012 Fall Meeting, American Geophysical Union, San Francisco, 3 December.

Sugita, Y., and S. Nakama (2012), Task B EBS Horonobe Experiment, DECOVALEX-2015 Workshop, Berkeley, 17–19 Apri, 34 slides.

Sinclair, D. (2013), The SNOLAB Science Programme, 13th International Conference on Topics of Astroparticle and Underground Physics (TAUP), Asilomar, 12 September.

Singhai, B. B. S., and R. P. Gupta (2010), *Applied Hydrogeology of Fractured Rocks*, Google e-Book, 428 pp.

Siren, T., and E. Johnsson (2011), ONKALO—On-site, second generation URL: Its role in POSIVA's repository development program, Paper III-2, URL Workshop, 12th ISRM Congress, Beijing, 17 October, 6 pages.

Smith, N. (2013), Status update of non-U.S. deep underground facilities, Deep Underground Research Association meeting, Palo Alto, 5 March, 42 slides.

Sneyers, A., and Li, X. (2012), Update on the Belgian programme, IAEA URL Network Partners and Annual Meeting, Albuquerque, 3–7 December.

Svemar, C., R. Christansson, M. Ohlsson, T. Eng, and M. Laaksoharju (2011), Paper III-3, URL Workshop, 12th ISRM Congress, Beijing, 17 October, 7 pages.

Tester, J. W. (2012), The potential of geothermal as a major supplier of U.S. primary energy using EGS technology, Abstract H32G-01 presented at 2012 Fall Meeting, American Geophysical Union, San Francisco, 3 December.

Tsang, C.-F. (1991), Coupled hydromechanical-thermochemical processes in rock fractures, *Review of Geophysics, 29*(4), 537–551.

Tsang, Y. W. (1992), Usage of "equivalent apertures" for rock fractures as derived from hydraulic and tracer tests, *Water Resources Research, 28*(5), 1451–1455.

Tsang, Y. W., J. T. Birkholzer, and S. Mukhopadhyay (2009), Modeling of thermally-diven hydological processes in partially saturated fractured rocks, *Review of Geophysics, 47* (3), RG3004, 30 pp.

Tsang, Y. W., and C.-F. Tsang (1987), Channel model for flow through fractured media, *Water Resources Research, 23*(3), 467–479.

Tsang, Y. W., and P. A. Witherspoon (1981), Hydromechanical behavior of a deformable rock fracture subject to normal stress, *Journal of Geophysical Research: Solid Earth, 86*(B10), 9287–9298.

Tsusaka, K., Y. Sugita, D. Inagai, M. Nakayama, S. Yabuuchi, H. Yokata, and T. Tokiwa (2011), Japan investigation of rock mechanics at Horonobe underground research laboratory project—Present status and future plan, Paper III-4, URL Workshop, 12th ISRM Congress, Beijing, 17 October, 8 pages.
Tutuncu, A. N. (2011), Shale gas and shale oil reservoir site characterization and fluid injection/withdrawal assesment, Presentation IV-2, URL Workshop, 12th ISRM Congress, Beijing, 17 October, 9 slides.

Uhle, J., L. (2012), External hazard research at the U.S. Nuclear Regulatory Commission, Abstract U24A-03 presented at 2012 Fall Meeting, American Geophysical Union, San Francisco, 3 December.

Van Luke, A. (2012), The world is watching: IAEA-sponsored group visits WIPP, *TRU Team Work*, *5* pp. 17 December.

Vardiman, D. (2012), Sanford Underground Research Facility: The United States' deep underground research facility, 18 slides, Abstract H32G-07 presented at 2012 Fall Meeting, American Geophysical Union, San Francisco, 3 December.

Verma, A., and K. Pruess (1988), Thermohydrological conditions and silica redistribution near high-level nuclear wastes emplaced in saturated geological formations, *Journal of Geophysical Research: Solid Earth, 93*(B2), 1159–1173.

Vomvoris, S. (2011), Overview and highlights of the activities in the two international URLs in Switzerland, Paper III-1, 13 pp., URL Workshop, 12th ISRM Congress, Beijing, 17 October.

Wakimoto, R. M. (2013), Energy infrastructure and extreme events, Abstract U21A-01 presented at 2013 Fall Meeting, American Geophysical Union, San Francisco, 9–13 December.

Wang, J. S. Y. (2001), Earth science workshop summary for national underground science laboratory, 30 slides, Plenary Session, Underground Science Conference, Lead, 4–7 October.

Wang, J. S. Y. (2011), Physics-geoscience-engineering interactions in deep underground laboratories, ARMA 11-159, 45th U.S. Rock Mechanics Symposium and 5th U.S.-Canada Rock Mechanics Symposium, San Francisco, 26–29 June.

Wang, J.S.Y. (2013), Multidisciplinary Microbiology Studies, Deep Underground Research Association meeting, Palo Alto, 5 March, 21 slides.

Wang, J. S. Y., and G. S. Bodvarsson (2003), Evolution of the unsaturated zone testing at Yucca Mountain, *Journal of Contaminant Hydrology, 62*/63, 337–360.

Wang, J. S. Y., Y. Guglielmi, J. A. Hudson, and X.-T. Feng (2013), Progress in interactions among underground research laboratories, ARMA 13-718, 8 pp., 47th U.S. Rock Mechanics/ Geomechanics Symposium, San Francisco, 23–26, June.

Wang, J. S. Y., and J. A. Hudson (2012), Laboratory and field studies of fracture flow and its extension in underground settings, Abstract H14A-03 presented at 2012 Fall Meeting, American Geophysical Union, San Francisco, 3 December.

Wang, J. S. Y., and C. Laughton (2010), Use of levels in underground research laboratories for earth sciences and geotechnical studies, ARMA 10-276, 4 pp., 44th U.S. Rock Mechanics Symposium and 5th U.S.-Canada Rock Mechanics Symposium, Salt Lake City, 27–30 June.Wang, J. S. Y., and S. Li (2013), Geophysics opportunities at depths > 2 km, 31 slides, 2nd Phase China JinPing Laboratory TownMeeting associated with 13th International Conference on Topics of Astroparticle and Underground Physics (TAUP), Asilomar, 8 September.

Wang, J. S. Y., and T. N. Narasimhan (1985), Hydrologic mechanisms governing fluid flow in a partially saturated, fractured, porous medium, *Water Resources Research, 21*(12), 1861–1874.

Wang, J. S. Y., T. N. Narasimhan, and C. H. Scholz (1985), Aperture correlation of a fractal fracture, *Journal of Geophysical Research: Solid Earth, 93*(B3), 2216–2224.

Wang, J. S. Y., P. H. Smeallie, X.-T. Feng, and J. A. Hudson (2010), Evaluation of underground research laboratories for formulation of interdisciplinary global networks, 18 pp., 6th Asia Rock Mechanics Symposium, New Dehli, 23–27 October.

Wang, J. S. Y., and G. Waysand (2010), Observations of magnetic signals in underground research laboratories, 22 slides, Electromagnetic Studies for Earthquakes and Volcanos, Orange, 4–6 October.Wang, Ju (2010), High-level radioactive waste disposal in China: Update 2010, *Journal of Rock Mechanics and Geotechnical Engineering, 2*(1), 1–11.

Waysand, G. (2006), The low noise underground laboratory at Rustrel-Pays d'Apt, *Journal of Physics Conference Series, 39*, 157–159.

Waysand, G., E. Pozzo di Borgo, S. Soule, M. Pyee, J. Marfaing, M. Yedlin, R. Blancon, P. Barroy, and A. Cavaillou (2010), Azimuthal analysis in $[SQUID]^2$ analysis for mesopause and sprites excitations, i-DUST Conference, Apt, 2 pp.

White, W. B. (1988), *Geomorphology and Hydrology of Karst Terrains*, Oxford Press, 464 pp.

Witherspoon, P. A., and G. S. Bodvarsson (2006), Geological challenges in radioactive waste isolation fourth worldwide review, LBL-59808, Lawrence Berkeley National Laboratory, 295 pp.

Witherspoon, P. A., N.G.W. Cook, and J. E. Gale (1980a), Geologic storage of radioactive waste: Field studies in Sweden, *Science, 211,* 894–900.

Witherspoon, P. A., and J. E. Gale (1977), Mechanical and hydraulic properties of rocks related to induced seismicity, *Engineering Geology, 11*(1), 23–55.

Witherspoon, P. A., J. S. Y. Wang, K. Iwai, and J. E. Gale (1980b), Validity of cubic law for fluid flow in a deformable fracture, *Water Resources Research, 16*(6), 1016–1024.

Wong, H. T. (2013), TEXONO-CDEX: Dark matter searches with sub-keV germanium detectors, Session PA-5, Cosmic Frontier Workshop, Palo Alto, 6–8 March, 12 slides.

Wouters, K., H. Moors, P. Brown, and N. Leys (2013), Evidence and characteristics of a diverse and metabolically active microbial community in deep subsurface clay borehole, in F. J. de Bruijn (ed.), *Molecular Microbial Ecology of the Rhizosphere*, FEMS Microbiology Ecology, on-line, doi: 10.1111/1574-6941.12171.

Wyngaardt, S. (2013), Toward a South Africa underground laboratory, 13th International Conference on Topics of Astroparticle and Underground Physics (TAUP), Asilomar, 12 September.

Yamatomi, J. (2013), The Hyper-KAMIOKANDE project in the Kamioka mine, Japan, URL Meeting, SINOROCK Symposium, Shanghai, 17 June, 15 slides.

Yang, C. (2011), Underground lab in China, presentation II-3, URL Workshop, 12th ISRM Congress, Beijing, 17 October, 29 slides.

Yasuhara, H., M. Takahashi, K. Koshida, and S. Nakashima (2013), Chemo-mechano coupling processes inducing evolution of rock permeability under hydrothermal and stressed conditions, Abstract H31G-01 presented at 2013 Fall Meeting, American Geophysical Union, San Francisco, 9–13 December.

Yeo, I. W., M. H. de Freitas, and R. W. Zimmerman (1998), Effect of shear displacement on the aperture and permeability of a rock fracture, *International Journal of Rock Mechanics & Mining Sciences, 35*(8), 1051–1070.

Yue, Q. (2011), China JinPing Underground Laboratory (CJPL) and cosmogenic background measurement, Cosmogenic Activity and Backgrounds Workshop, Berkeley, 13–15 April, 37 slides.

Zimmerman, R. W. (2012), The history and role of the cubic law for fluid flow in fractured rock, Abstract H13H-04 presented at 2012 Fall Meeting, American Geophysical Union, San Francisco, 3 December.

Zimmerman, R. W., and G. S. Bodvarsson (1996), Hydraulic conductivity of rock fractures, *Transport in Porous Media, 23*, 1–30.

Zoback, M., S. Katasei, and B. Copithorn (2010), Addressing environmental risks from shale gas development, Briefing Paper No. 1, Worldwide Watch Institute, Stanford University, July.

3

Permeability Structure of a Strike-Slip Fault

Kenzi Karasaki[1], Celia T. Onishi[2], and Junichi Goto[3]

ABSTRACT

A study is being conducted on the Wildcat Fault in Berkeley, California, to develop a methodology for characterizing the hydrologic properties of a fault. The geologic setting of the San Francisco Bay Area is intertwined with some of the most complex and active geology in the world. The rocks are extensively sheared and fractured. The Wildcat, a strike-slip fault, appears to consist of multiple fault planes. That the exact location of the main fault is still in dispute among participating researchers highlights the fact that it is very difficult to uniquely characterize such a complex fault zone. The hydrologic characteristics of the Wildcat Fault zone suggest a dual nature, with high permeability along the direction of the fault zone and low permeability across it. Data from cross-hole pumping tests conducted in the high permeability zone along the fault plane exhibit 10:1 near-horizontal anisotropy, which we think is consistent with the fact that the Wildcat is a strike-slip fault. The main philosophy behind our overall approach to the hydrologic characterization of such a complex fractured system is to let the system present its own average property by performing large-scale tests and conducting long-term monitoring, instead of collecting a multitude of data at small length and time scales, or at a discrete fracture scale and to "up-scale," which is extremely tenuous at best.

3.1. INTRODUCTION

3.1.1. Background

Faults often have major influence on the groundwater flow and transport in their surroundings. Thus, correct characterization of fault zone hydrology is crucial to the success of many environmental undertakings, including nuclear waste isolation, geologic sequestration of CO_2, groundwater remediation, and geothermal energy production. However, hydrologic parameters of faults have rarely been directly measured. Instead, overly conservative or guess values are often used in predictive modeling of groundwater flow, whose outcome is often dictated by the parameters chosen for the faults.

Faults are usually subvertical with contrasting properties of very low and very high permeability zones juxtaposed to each other. Thus, a standard characterization approach developed for horizontal aquifers using vertical borehole measurements may not be applicable for characterizing the fault zone hydrology. Development of an accurate fault zone characterization technology is acutely needed.

To this end, the Nuclear Waste Management Organization of Japan (NUMO) and the Ernest Orlando Lawrence Berkeley National Laboratory (LBNL), one of the U.S. Department of Energy's (DOE) National Laboratories, have been collaborating to develop a methodology for characterizing the hydrology of fault zones, recognizing that reliable characterization of faults is crucial to the safe geologic isolation of nuclear wastes.

The Wildcat Fault (Figure 3.1) in the East Bay Hills, which is a predominantly strike-slip fault and a member of the Hayward Fault system, was chosen to be the target fault of the field study. Wildcat runs through the LBNL property, within and around which surface-based

[1] *Lawrence Berkeley National Laboratory, Berkeley, California, USA*

[2] *U.S. Geological Survey, Menlo Park, California, USA*

[3] *Nuclear Waste Management Organization of Japan, Mita, Tokyo, Japan*

Dynamics of Fluids and Transport in Complex Fractured-Porous Systems, Geophysical Monograph 210, First Edition.
Edited by Boris Faybishenko, Sally M. Benson, and John E. Gale.

Figure 3.1 Location of Lawrence Berkeley National Laboratory (LBNL) and the Wildcat Fault relative to the major faults in San Francisco Bay Area.

investigations have been conducted, most of which were concentrated in an approximately 1 km^2 area. A total of five trenches were excavated. Surface geophysical investigations were conducted using electrical resistivity survey and seismic reflection/refraction profiling along five lines on the north, in the middle and to the south of the LBNL site. Five 150~200 m deep boreholes were drilled including two inclined boreholes, in which hydraulic tests and long-term monitoring have been conducted. A hydrogeologic model of the site was constructed and numerical simulations of groundwater flow were performed. The results of the investigation have so far been intriguing, and in some ways contrary to our expectations [*Kiho et al.*, 2012; *Karasaki et al.*, 2012]. We encountered a formation on the west side of the Wildcat that was not expected based on the previously published literature [*LBNL and Parsons*, 2000].

3.1.2. Area Geology and the Wildcat

The geologic setting of the San Francisco Bay Area is intertwined with some of the most complex and active geology in the world. The oldest rock in the Bay Area region is from the Jurassic to Cretaceous age (200–65 Ma) Franciscan assemblage, which was originally deposited in a deep marine environment and trench deposits. It was subsequently accreted during a plate subduction along the coast of Northern California. Over more than 100 million years of subduction, accretion brought together many types of Mesozoic rock that we now see in the Bay Area. Extensive tectonic activity uplifted and folded the Franciscan mélanges, which consisted of exotic blocks of basalt, chert, and limestone embedded in a matrix of sheared greywacke and shales.

The Wildcat Fault is considered to be a secondary splay fault associated with the Hayward fault. It cuts late

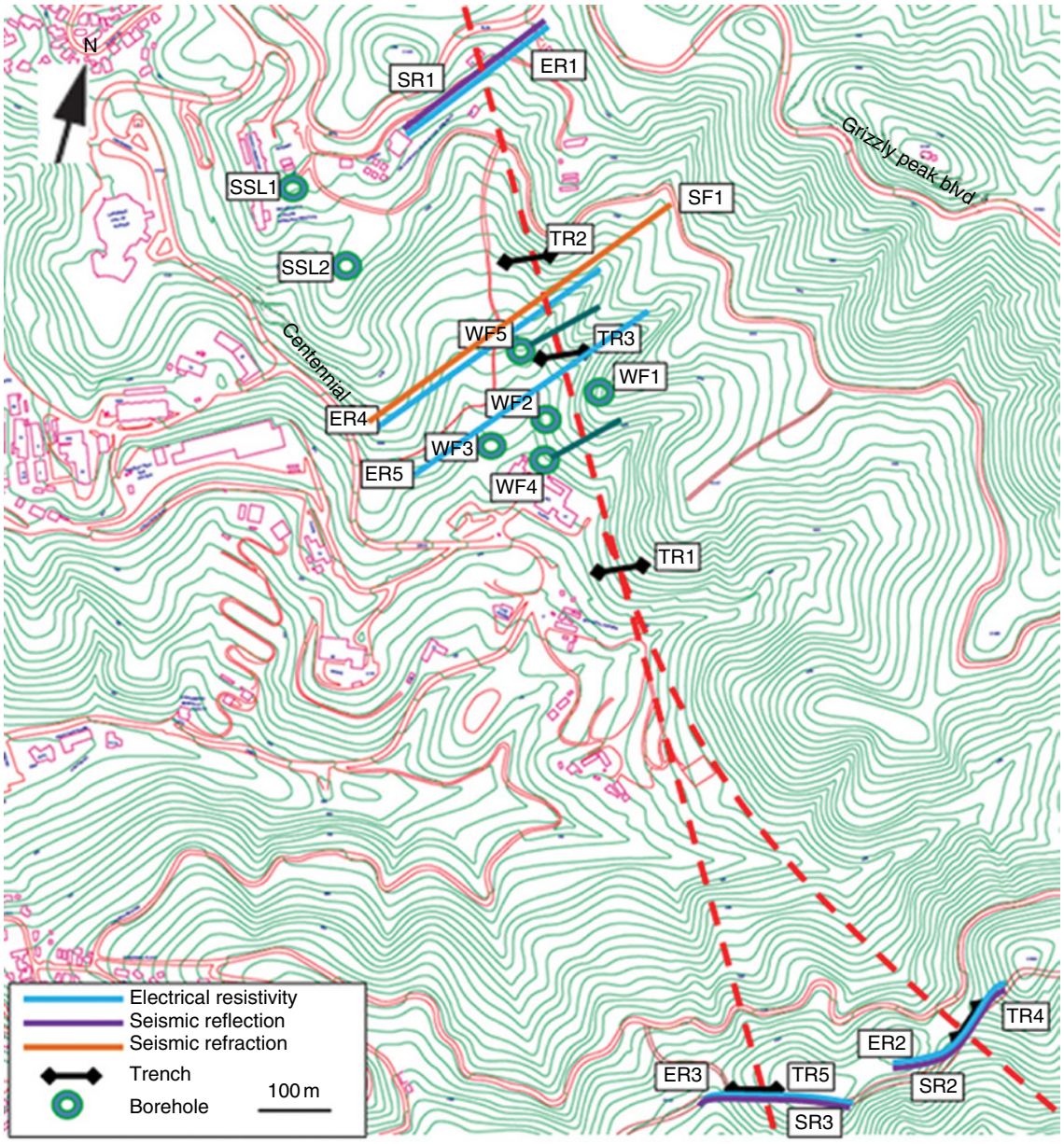

Figure 3.2 Map showing the location of surface geophysical survey lines, trenches, boreholes, and inferred trace of the Wildcat Fault (red broken lines).

Cenozoic strata, striking subparallel to the Hayward Fault. The fault, which runs about one and one-half kilometers east of the Hayward Fault, has been considered as part of the San Andreas Fault system, but no clear evidence of activity in the Quaternary has been identified [*LBNL and Parsons*, 2000]. Wildcat passes along the eastern margin of LBNL and runs from Oakland to Richmond. Regionally, the fault is difficult to map throughout its length and appears to be discontinuous, although it clearly truncates and offsets strata at many locations.

At the regional scale, the fault shows right-lateral strike-slip movement [*Curtis*, 1989], and local reverse movement has also been observed and described [*Jones and Curtis*, 1991]. According to *Bishop et al.* [1973], the Wildcat Fault eventually joins the Hayward Fault in the north near the city of San Pablo and in the south in Oakland [*Graymer*, 2000].

3.1.3. Trenching and Geophysical Surveys

A total of five trenches have been excavated, crosscutting the fault, to investigate the deformation structure of the fault in the bedrock (Figure 3.2). The locations were chosen based on the literature and evidence from

road/building construction, as well as additionally conducted geological surveys. The TR-4 trench was 60 m long, dug as deep as 4.5 m, with a width of 1 m. At least one to (as many as) several faults were observed in all five trenches, although it is yet to be determined whether any of the trenches have intersected the "main" fault. It is possible that there are numerous small faults in the area and that one or more fault(s) may be found no matter where we cut a trench. Trench studies are effective when the location of a fault is known and the thickness of the alluvium above the bedrock is not very thick; however, because the observation is near surface, the properties of the fault may be affected by stress release and weathering. Thus, care must be taken when inferring properties at depth.

Five electrical resistivity tomography (ERT) surveys, three reflection seismic surveys, and one refraction survey using P- and S-wave sources were conducted at five separate locations across the fault trace. Figure 3.2 shows the locations of these geophysical survey lines, which were chosen to cross the fault perpendicularly while maintaining a straight line (as much as possible in the extremely hilly terrain). We also had to be selective in choosing ERT lines to avoid anthropogenic noises such as high-voltage lines, buried cables, and guard rails.

Although it was possible to infer the existence of multiple discontinuities from the results of seismic reflection analysis and ERT surveys, the geophysical survey results were largely inconclusive in locating and defining the fault. This is probably because the geology of the Berkeley Hills is very complex: The Claremont formation is extensively folded, fractured, and faulted, with no clear reflective horizons. There is a large paleo-landslide in the area as well.

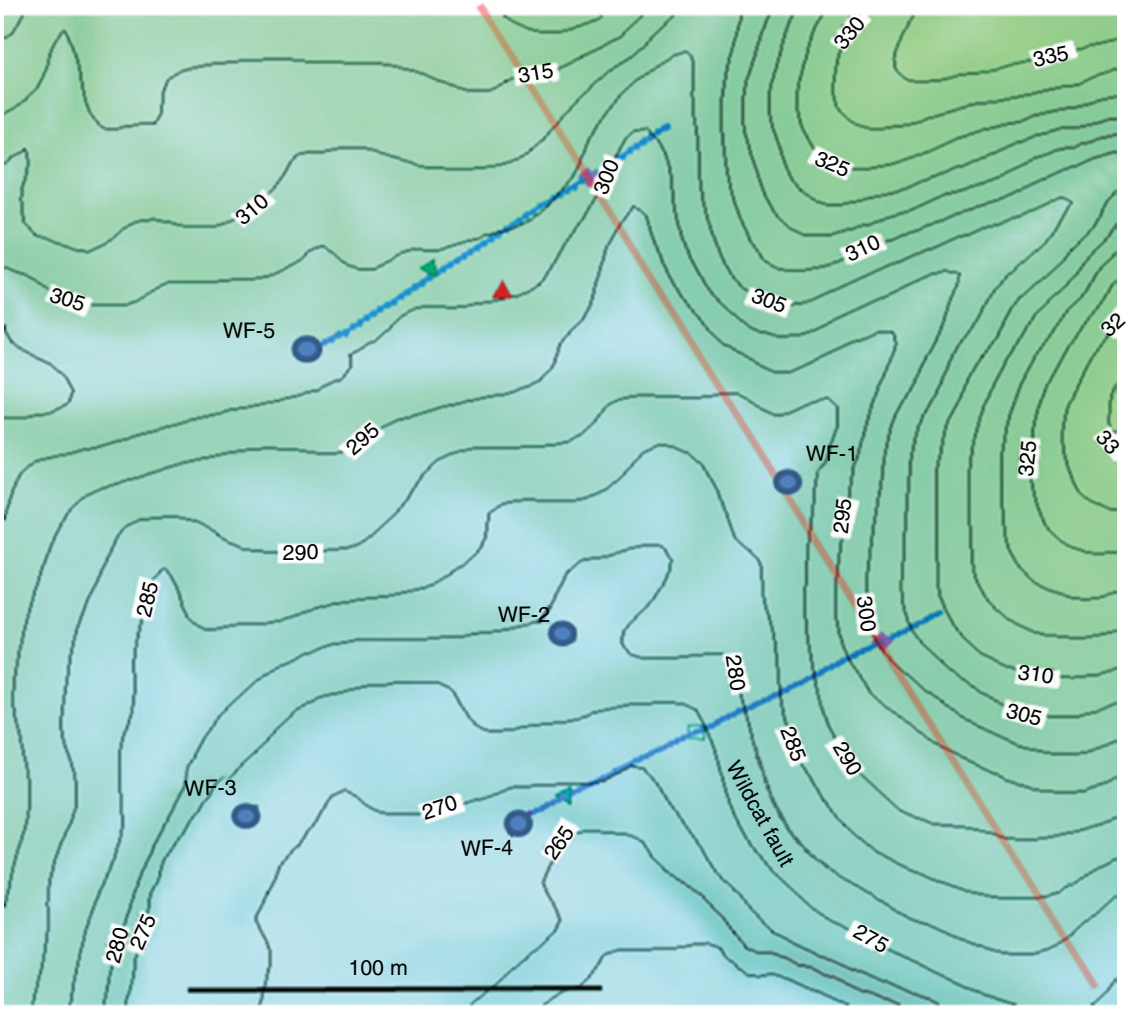

Figure 3.3 Relative location of Wildcat Fault (WF) boreholes. WF-4 and WF-5 are inclined at 60° from horizontal and penetrate the Wildcat. WF-1 is just adjacent to the fault.

3.1.4. Borehole Drilling and Logging

Five boreholes were drilled, each to an approximate depth of 150 m by mud-rotary with full coring. Figure 3.3 shows the relative location of these boreholes, WF-1~WF-5. Several shear zones and fault gouges were observed in all five boreholes, in addition to several hundred fractures. Two inclined boreholes, WF-4 and -5, were drilled to penetrate the Wildcat, believed to run between WF-1 and -2. As the drilling of WF-4 progressed, first the monitoring intervals in WF-2 and later those in WF-1 showed pressure responses, indicating that there are hydraulic connections in the SE-NW direction parallel to the fault.

In both inclined boreholes, many problems were encountered with frequent collapses and core-losses. In both boreholes a 5-ft drop of drill bit occurred: near the bottom of WF-4 and in the middle of WF-5. A line that connects the two locations is arguably believed to be the trace of the main fault plane, which was created by the youngest of multiple movements of the Wildcat. In analyzing pump tests in these boreholes, we assume that the pumping interval is located at the fault location and is 5 ft long in both boreholes, although the packed off intervals are much longer.

Borehole geophysical logs including caliper, SP, gamma, resistivity, acoustic televiewer, sonic, and suspension logs were conducted in the boreholes. None of the logs, including core logs (Figure 3.4), were able to be used to correlate features from hole to hole or to groundwater flow. In addition to these conventional logs, flowing fluid conductivity logs (FFEC) were conducted in each hole. FFEC logs can identify inflow points caused by the electric conductivity contrast artificially created between the formation fluid and that of the borehole under a pumping condition [Doughty et al., 2008]. The results of FFEC logs show that the fracture density is not a good indicator for flow. For example, in WF-2, only one inflow point was identified, which is located at a depth where fracture density is at its lowest. Similar results were obtained in all the other boreholes (Figure 3.4).

The question arises whether these flowing fractures have special attributes (dip and orientation) that we have not been able to identify thus far. It may be more logical to assume that the flowing fractures were created (opened) by faults along preexisting weak planes such as the bedding (Claremont Fm. is heavily folded.) but otherwise have no special attributes. Thus, they are more or less random fractures that happened to be intersected by a borehole.

3.2. HYDRAULIC TESTS

We conducted numerous hydraulic tests in and around the Wildcat Fault. Slug tests, injection tests, and pumping tests were conducted in each borehole immediately after the completion of drilling to estimate the transmissivity of each borehole. Although the rock is highly fractured and the flow is fault/fracture controlled, no attempts were made to measure the permeability of discrete fractures. This is because (1) our scale of interest is over 100 m and (2) we do not believe that "scaling up" of small-scale measurements to predict large-scale properties will work in this geologic environment. In this chapter we focus on the analysis of the cross-hole pumping tests conducted between boreholes that are 45~95 m apart.

After conducting single-hole hydraulic tests, five zones were isolated in each of the WF-1~3 boreholes with a pressure and temperature sensor in each zone packed with sand, which was separated by grout from each other. It is believed that there is little hydraulic communication between WF-1, WF-2, and WF-3: No pressure responses were observed in WF-1 or WF-2 boreholes during the drilling of WF-2 and WF-3, respectively. The heads observed in the intervals of WF-1 are higher than those in WF-2 and WF-3, even after the elevation differences are factored in.

Cross-hole pump tests were performed in the isolated sections of two inclined ~200-m-long boreholes that are ~130 meters apart from each other (WF-4 and WF-5 in Figure 3.3). Both sections were believed to be straddling the Wildcat Fault as shown in Figure 3.3 and Figure 3.5. The horizontal distance from WF-4 and WF-5 to WF-1 is ~45 m and ~95 m, respectively. The WF-4 and WF-5 boreholes were isolated into three zones by packers. Groundwater was pumped first from the bottom section of WF-4 at 3 GPM for approximately 4 days and the recovery was monitored over 10 days. Another pumping test was performed from the middle section of WF-5 at 2 GPM for ~7 days, followed by more than two weeks of recovery monitoring.

During the pumping of WF-5, the bottom interval of WF-4 as well as the WF-1 intervals showed pressure responses (Figure 3.6). There were no responses observed in WF-2 or WF-3, although WF-2 is closer to the pumping interval than WF-4. The pressure disturbance created by the pumping is assumed to have been mainly confined within or along the fault plane.

Responses were observed in the bottom two intervals in WF-2 during the pumping of the bottom section of WF-4. However, it is believed that the pressure drop was propagated along the borehole to the interval above the pumping zone and ultimately to WF-2 along the hydraulic connection observed during the drilling of WF-4, presumably because the packers in WF-4 were not completely separating the bottom two zones.

Isolating zones by packers in a fractured formation is very difficult. When there is a pressure communication between adjacent intervals, it is almost impossible to

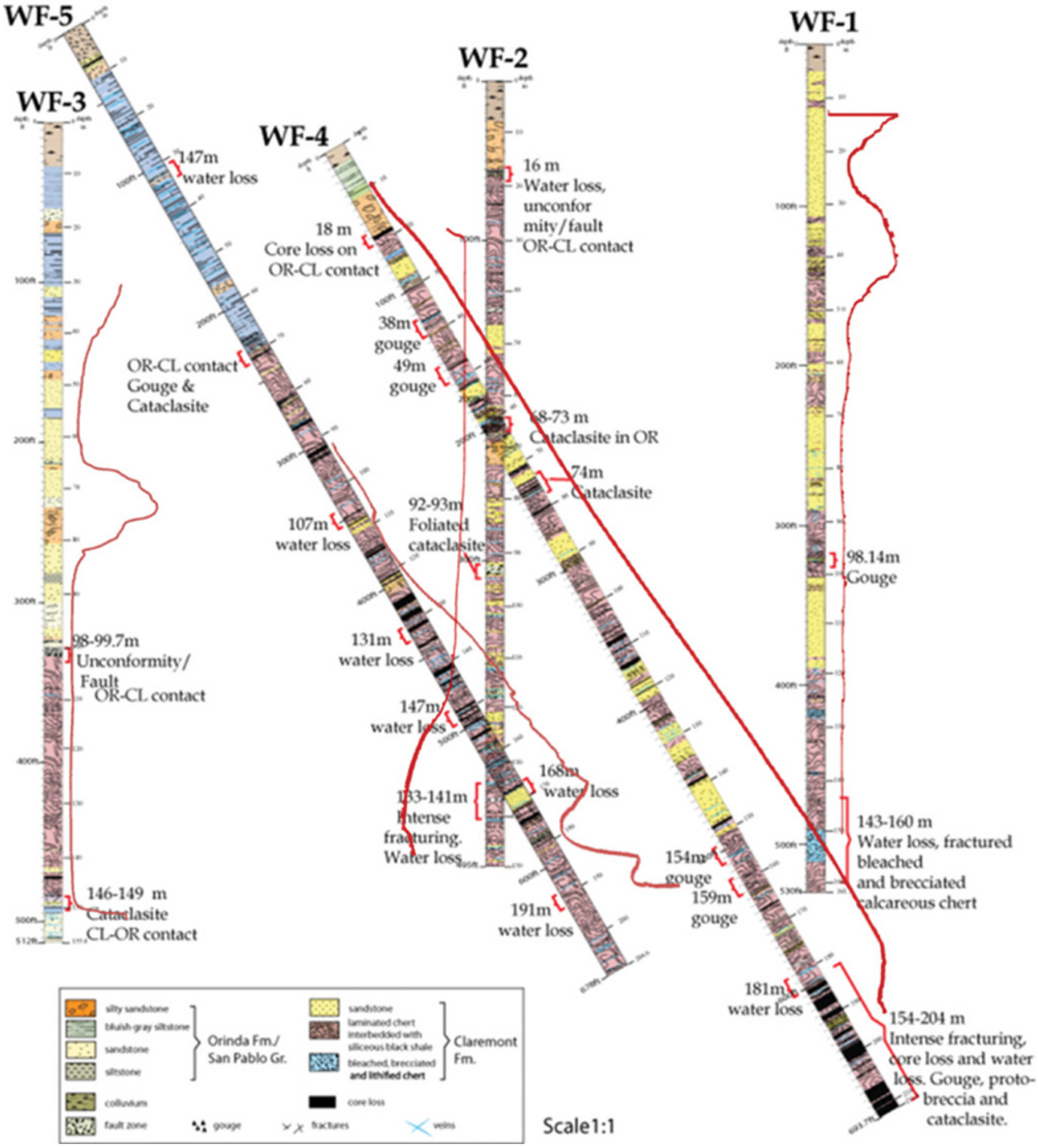

Figure 3.4 Core logs of WF-1~WF-5 boreholes shown in 2D. Note that there is little borehole to borehole correlation. Black colors indicate core loss sections. Superimposed are the FFEC log results in red curves along the boreholes.

know the exact cause of it. It could be because packers are not seated well due to rough walls or through hydraulically connected fractures. In fact, using ordinary short packers to isolate sections in a long borehole results in long open sections. In a fractured formation, this can be problematic: such long open sections create artificial permeable paths that can short-circuit pressure or mix groundwaters otherwise separated.

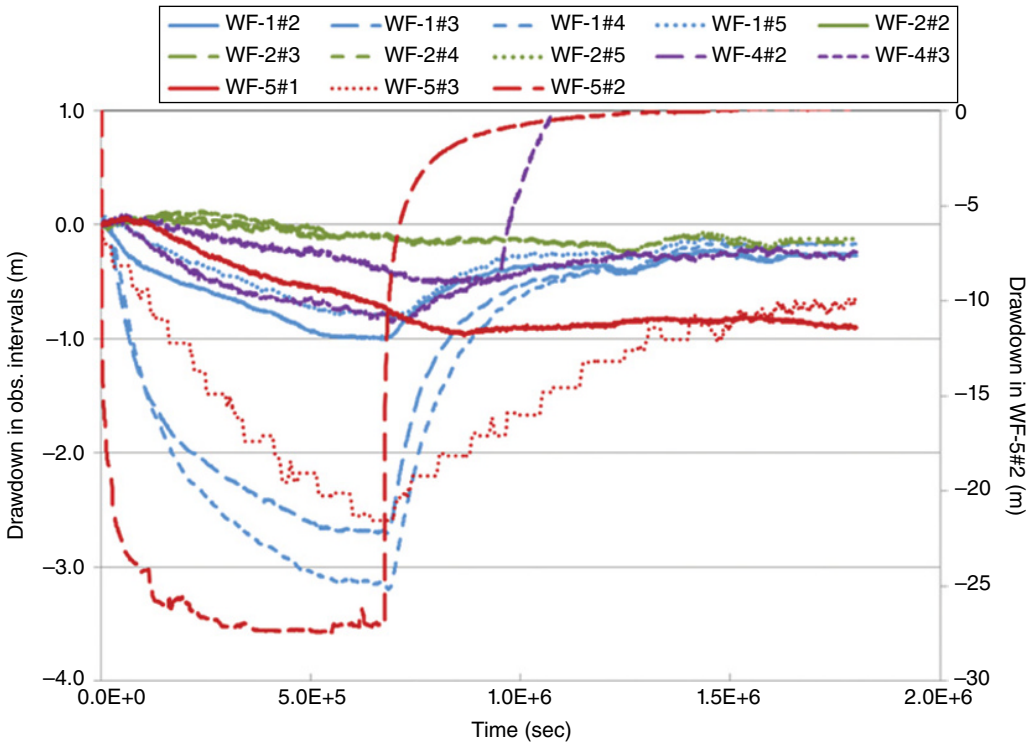

Figure 3.5 Geometric configuration between WF-1, WF-4, and WF-5 boreholes in relation to the suspected main fault. The vertical WF-1 is believed to be adjacent to the fault. (Figure not to scale.)

3.3. DRAWDOWN ANALYSIS

3.3.1. Distance Between Intervals

Assuming a continuum, the distance between a pumping zone and a monitoring interval to be used for interference analysis is the shortest distance between two line segments, i.e., interval lengths. For vertical boreholes it is straightforward to calculate the distance: merely the distance between the boreholes. However, it is not so simple in our case because WF-4 and WF-5 are inclined and WF-1 is vertical, and because the lengths of the sand-packed sections in WF-1 vary from 12 m to 60 m.

The distances between the pumped interval in WF-4 and WF-5 and the monitoring intervals in WF-1 are listed in Table 3.1. The algorithm described by *Allen et al.* [1993] and coded in FORTRAN by *Vesely* [2002] for calculating the minimum distance between two line segments was used. Also listed are the drawdowns observed in the intervals in WF-1 at the end of two pumping tests. Note that the distances from WF-5#2 to the zones in WF-1 are approximately the same, but the drawdown values differ. Although the packed off intervals are as long as 60 m, for the calculation we assumed that the length of the pumping interval is 5 ft and coincides with the location where the drill bit dropped, i.e., the location of the fault plane itself or the associated damage zone. Nonetheless, assuming different interval lengths does not alter the overall distances significantly.

The magnitudes of drawdown in WF-1 intervals were correlated with the distance in the vertical direction (elevation difference) as shown in Table 3.1, in which the drawdowns at the end of each pumping test are also listed. The WF-1#1 interval was considered as nonresponding to either pumping test.

3.2.2. Dimensionless and Normalized Drawdown

It is straightforward to compare the drawdowns in WF-1 during WF-5 pumping, because the 3D distance is almost the same for all four intervals (#2, #3, #4 and #5), as can be seen in Table 3.1. However, the 3-D distances from the fault intersect in WF-4 to WF-1 intervals vary. Thus, the drawdowns cannot be directly compared as they are. Comparison of the drawdowns between those during the WF-5 pumping to those during the WF-4 pumping cannot be directly compared either. The drawdowns have to be normalized to the pumping rate and time using the arithmetic manipulations described in the Appendix. Then the responses at different distances and flow rates at different time lengths can be compared

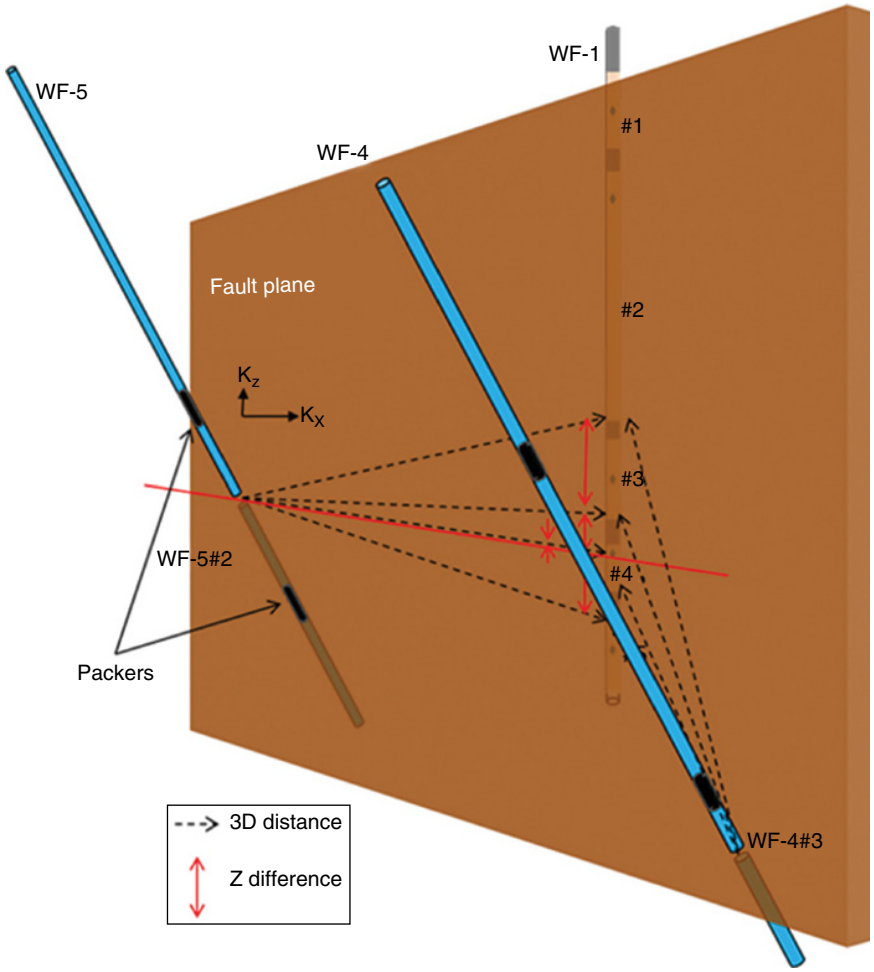

Figure 3.6 Drawdown responses in the monitoring zones in WF-1, 2, 4, and 5 during the pumping from WF-5#2 zone. Blue lines are for WF-1, green for WF-2, purple for WF-4, and red for WF-5. The sensor in WF-4#2 failed after 1×106 seconds. Note that the drawdown in the pumping zone, WF-5#2, is on the right axis.

Table 3.1 Comparison of the distance from two pumping zones to the monitoring zones, drawdown, and h_D, the dimensionless normalized drawdown.

Pump zone	Monitor Zone	3D Distance	Elevation Difference (m)	Δh (m)	h_D
WF-4#3	WF-1#2	95.1	84.1	0.18	0.63
	WF-1#3	74.9	60.3	1.00	0.61
	WF-1#4	62.0	43.3	2.40	0.77
	WF-1#5	48.4	19.2	5.70	1.32
WF-5#2	WF-1#2	94.8	29.4	1.00	0.62
	WF-1#3	90.3	5.6	2.70	1.16
	WF-1#4	90.1	−0.2	3.10	1.30
	WF-1#5	91.9	−18.0	0.80	0.52
	WF-4#3	145.2	−54.7	0.80	0.92

assuming a developed radial flow in the plane of the fault, as shown in Figure 3.7.

Equation 3A.4 in the Appendix was used to nondimensionalize the drawdowns in WF-1 intervals responding to the pumping in WF-4 and WF-5. Equation 3A.6 was then used to calibrate the dimensionless drawdowns at WF-1 intervals during each pump test, using a reference radius. For the WF-4#3 pump test, we chose the distance to

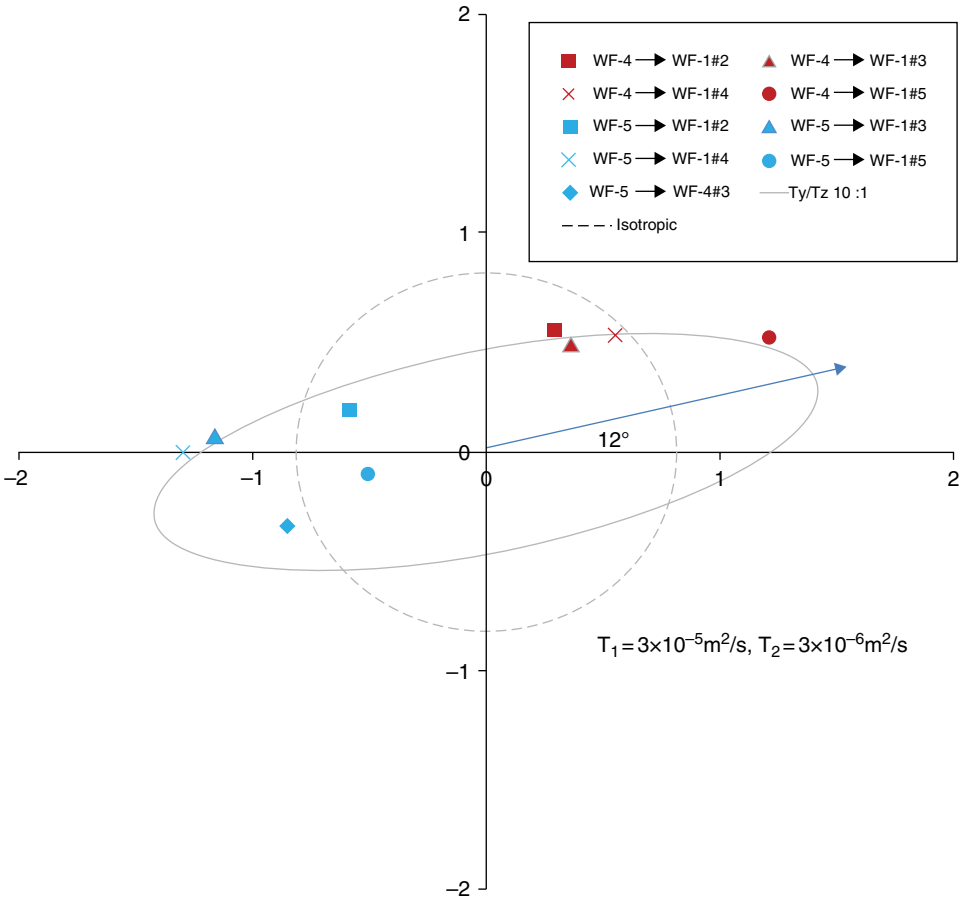

Figure 3.7 Normalized dimensionless drawdowns in WF-1 in response to the pumping from WF-4 and WF-5. Note the permeability anisotropy is 10:1 and the long axis is tilted at 12°.

WF-1#5, 48.4 m, as the reference distance and used Equation 3A.4. The calibrated dimensionless drawdown can be seen in the last column in Table 3.1.

Equation 3A.5 was used to calibrate the drawdowns at WF-1 during the WF-5 pump test so that the drawdowns are at the same t/r^2 value, as shown in Table 3.1. Now, the values in the rightmost column can be plotted together in the relative direction from the pumping interval, as shown in Figure 3.7. In this plot, if the medium is isotropic, all drawdowns at t_D = 6.5 would plot on a circle of radius $log_{10}6.5 = 0.8$. Note that the value of 6.5 is not quite large enough for *Cooper and Jacob's* [1946] logarithmic approximation. However, the errors are considered to be minor. As can be seen in the figure, the drawdown distribution in WF-1 intervals can be explained assuming that the fault zone is a planar feature with 10:1 permeability anisotropy, with the principal axis tilted by 12° from the horizontal axis. That the fault has near-horizontal anisotropic permeability is consistent with the fact that the Wildcat is a right lateral strike slip fault with a slight reverse thrust. Most of the many slickensides we observed in the cores from WF boreholes were indeed near horizontal. Thus, it is not surprising that the permeability is enhanced in the direction of the fault movement.

3.3. CONCLUSIONS

The static head distribution and the pressure responses to the drilling of an inclined borehole indicate that the Wildcat Fault is low permeability in the direction perpendicular to the fault and is high permeability along the strike direction of the fault. Cross-hole pump tests were conducted in two inclined boreholes that penetrate the fault plane and the drawdown data were analyzed. The pressure disturbance created by the pumping was assumed to be mainly confined in the fault plane. Drawdowns observed in the four intervals in a vertical borehole that was drilled adjacent to the fault were analyzed after the drawdown values were calibrated by nondimensionalizing and normalizing by the distance, pumping rate, and time duration so that the drawdown data of two pumping tests from different boreholes can be plotted on a single polar plot. We found that a permeability ellipse of a 10:1 anisotropy ratio with the principal axis tilted by 12° from

the horizontal axis fits the data well. This near-horizontal anisotropic permeability is considered consistent with the fact that the Wildcat is a strike-slip fault.

ACKNOWLEDGMENTS

This work was supported by Nuclear Waste Management Organization and performed under Contract No. DE-AC02-05CH11231.

APPENDIX

Assuming a developed radial flow, when the *Cooper and Jacob* [1946] equation can be applied, the drawdown in an isotropic medium can be written as

$$\Delta h = \frac{2.3Q}{4\pi T} log \frac{2.25Tt}{r^2 S} \tag{3A.1}$$

where Δh, Q, T, S, r and t are the drawdown, flow rate, transmissivity, storativity, radius, and time, respectively. In the x-z coordinate system, $x = r \cdot cos\theta$ and $z = r \cdot cos\theta$, where θ is the angle to the positive x direction. If the medium is anisotropic and the axis of anisotropy is rotated by α from the coordinate axis, the transformation is

$$\begin{pmatrix} x' \\ z' \end{pmatrix} = \begin{pmatrix} \cos\alpha & -\sin\alpha \\ \sin\alpha & \cos\alpha \end{pmatrix} \begin{pmatrix} x \\ z \end{pmatrix} \tag{3A.2}$$

If the anisotropy ratio of principal direction to minor direction is T_1/T_2, the coordinate system x′ and z′ can be replaced with x′′ and z′′, where x′′ = x′ and $z'' = z'\sqrt{T_1/T_2}$.

Thus, in the transformed x′′–z′′ coordinate system, Equation 3A.1 is still valid. The dimensionless drawdown can be expressed as

$$\Delta h = \frac{2.3Q}{4\pi \sqrt{T_1 T_2}} log \frac{2.25\sqrt{T_1 T_2}\, t}{r^2 S} \tag{3A.3}$$

The dimensionless drawdown h_{D1} at radius r_1 can be expressed as

$$h_{D1} = \frac{\Delta h_1}{\left(\frac{2.3Q}{4\pi T}\right)} = log \frac{2.25Tt_1}{r_1^2 S} \tag{3A.4}$$

Then the difference of the dimensionless drawdowns at r_1 at t_1 and r_2 at t_2 can be written

$$h_{D1} - h_{D2} = log \frac{2.25Tt_1}{r_1^2 S} - log \frac{2.25Tt_2}{r_2^2 S} = \log\left({}^{t_2 r_1^2}\!\!\diagup\!\!{}_{t_1 r_2^2} \right) \tag{3A.5}$$

If the drawdown is measured at the same length of time, Equation 3A.3 further reduces to

$$h_{D1} = h_{D2} + 2\log\left({}^{r_1}\!\!\diagup\!\!{}_{r_2} \right) \tag{3A.6}$$

Thus, the dimensionless drawdown at r_1 can be expressed in terms of the dimensionless drawdown at r_2.

REFERENCES

Allen, M. P., G. T. Evans, D. Frenkel, and B. M. Mulder (1993), Hard convex body fluids, *Adv. Chem. Phys.*, *86*, 1–166.

Bishop, C. C., R. D. Knox, R. H. Chapman, D. A. Rodgers, and G. B. Chase (1973), *Geological and geophysical investigations for Tri-Cities seismic safety and environmental resources study: California Division of Mines and Geology preliminary report, 19*, 44 p.

Cooper, H. H., Jr., and C. E. Jacob (1946), A generalized graphical method for evaluating formation constants and summarizing well field history., *Trans. Amer. Geophys. Union*, *27*, 526–534.

Curtis, G. H. (1989), Late Cenozoic volcanic rocks of the central Coast Range, in C. Wahrhaftig and D. Sloan, *Geology of San Francisco and Vicinity, Field Trip Guidebook T 105*, Washington, D.C., American Geophysical Union, 33–35.

Doughty, C., C. F. Tsang, K. Hatanaka, S. Yabuuchi, and H. Kurikami (2008), Application of direct fitting, mass integral, and multirate methods to analysis of flowing fluid electric conductivity logs from Horonobe, Japan, *Water Resour. Res.*, *44*, W08403, doi:10.1029/2007WR006441.

Graymer, R. W. (2000), Geologic map and map database of the Oakland metropolitan area, Alameda, Contra Costa and San Francisco Counties, California, *USGS Miscellaneous Field Studies MF3242g*, Version 1.0.

Jones, D. L., and G. Curtis (1991), Guide to the geology of the Berkeley Hills, Central Coast Ranges, California, in *Geologic Excursions in Northern California: San Francisco to the Sierra Nevada,* California Department of Conservation, Division of Mines and Geology, Special Publication *109*, 63–73.

Kiho, K., K. Ueta, T. Miyakawa, T. Hasegawa, H. Ito, M. Hamada, H. Nakada, S. Tanaka, and K. Tsukuda (2012), *CRIEPI Technical Report, Survey and Analysis related to Development of Hydrologic Characterization Technology of Fault Zones IV*.

Karasaki, K., C.T. Onishi, C. Doughty, M. Conrad, E. Gasperikova, P. Cook, and C. Ulrich (2012), *Development of Hydrologic Characterization Technology of Fault Zones*, LBNL-5862E, NUMO-LBNL-CRIEPI Collaboration Research Project.

LBNL and Parsons (2000), RCRA Facility Investigation Report for Lawrence Berkeley National Laboratory Environmental Restoration Program, A Joint Effort of Environment, Health and Safety Division and Earth Sciences Division LBNL, UC Berkeley and Parsons Engineering Science, Inc.

Vesely, F. J. (2002), Shortest distance between two line segments, http://homepage.univie.ac.at/franz.vesely/notes/hard_sticks/hst/hst.html.

4

Feasibility of Long-Term Passive Monitoring of Deep Hydrogeology with Flowing Fluid Electric Conductivity Logging Method

Prabhakar Sharma[1,2], Chin-Fu Tsang[1,3], Christine Doughty[3], Auli Niemi[1], and Jacob Bensabat[4]

ABSTRACT

The flowing fluid electrical conductivity (FFEC) logging method has been used in deep boreholes to obtain estimates for the transmissivity, salinity of formation water, hydraulic head, and formation water flow rate of hydraulically conducting layers. In this chapter we propose a modified FFEC logging procedure, involving a setup of a string of EC/T probes in the borehole, to passively monitor long-term temporal changes in local flow rates in a brine formation composed of multiple layers with different transmissivities over a period of months or years. The local flows in the layers can vary over time, for instance, as a result of seasonal or climatic changes. In the case of supercritical CO_2 storage in the deep subsurface, the local flow pattern of the storage formation will be disturbed; furthermore, it may change with time as the low-density and low-viscosity CO_2 enters more and more into the transmissive layers and interacts with in situ water and rock. The present chapter explores the possibility of using the FFEC method for such long-term monitoring in an observation well. The feasibility is demonstrated with field data from the Outokumpu test site in Finland.

4.1. INTRODUCTION

Knowledge of hydraulic structures and locations of hydraulically conductive zones in deep subsurface formation is important for understanding flow and transport behavior of regional groundwater and solutes. Such hydraulic information is usually obtained through established geophysical and hydrological methods applied to deep boreholes, such as straddle-packer tests [*Walton*, 1970], gamma and neutron logging [*Keys*, 1986; *Mendoza et al.*, 2010], borehole image logging [*Zemanek et al.*, 1970; *Paillet*, 1991], cross-well geophysical imaging [*Jardani et al.*, 2013], high-resolution flow logging [*Molz et al.*, 1989], and flowing fluid electrical conductivity (FFEC) logging [*Tsang et al.*, 1990; *Doughty and Tsang*, 2005; *Doughty et al.*, 2005; *Doughty et al.*, 2013]. Among all these methods, the FFEC logging has been suggested as an efficient method that can identify the locations of inflow zones and evaluate their hydraulic conductivity and fluid salinity as a function of depth along the borehole, using a standard conventional EC/T probe (electric conductivity and temperature probe; e.g., *Robertson Geologging*, 2014; *Mount Sopris*, 2014].

Measurements of local flow in a subsurface formation penetrated by a well have also been made with different methods, such as point dilution of radioisotopes [*Drost et al.*, 1968], tracer dilution analysis [*Brainerd and Robbins*, 2004], cross-well time-lapse tomography [*Jardani et al.*, 2013], and the FFEC logging method [*Doughty and Tsang*, 2005; *Doughty et al.*, 2013]. The understanding of slow water flows through transmissive layers or fracture zones and their change with time is important in the study of injection/pumping of fluids (such as petroleum products, supercritical CO_2 storage, etc). In cases where the flow in a transmissive layer at a monitoring well varies

[1] *Department of Earth Sciences, Uppsala University, Uppsala, Sweden*

[2] *School of Ecology and Environment Studies, Nalanda University, Rajgir, Nalanda, Bihar, India*

[3] *Earth Sciences Division, Lawrence Berkeley National Laboratory, Berkeley, California, USA*

[4] *Environmental and Water Resources Engineering Ltd., Haifa, Israel*

Dynamics of Fluids and Transport in Complex Fractured-Porous Systems, Geophysical Monograph 210, First Edition.
Edited by Boris Faybishenko, Sally M. Benson, and John E. Gale.

with time over a long time period, the changes in "regional" flow rate cannot be easily measured in a monitoring mode by methods such as that proposed by *Drost et al*. [1968], which requires an active testing procedure each time the measurement is made.

Not many simple methods are available for passive long-term monitoring of hydrologic processes of the subsurface. Pressure sensors are often used to monitor well pressures, but the pressure values are averaged over the whole depth of the well. For many applications, there is a need for information on flows and pressures as a function of depth in the monitoring well. Fiber optics–based high–spatial resolution temperature measurements have been found very useful in monitoring detailed depth-dependent temperature changes [*Freifeld et al*., 2008]. The optical fiber can be emplaced all along the well casing and used for long-term monitoring. Although changes in temperature can indicate certain flow processes, they are less useful in yielding flow details because of the high thermal diffusivity.

In this chapter, we propose that the FFEC method may be able to provide, in a continuous and passive way, the monitoring of water flow through the individual fractures/layers in a deep formation over a long time period. We investigate, through modeling, the possibility of monitoring flow rates in the individual layers of the storage formation at a monitoring well. In the next section, motivation in the context of CO_2 geological storage is presented. Then the FFEC logging method is described, followed by an investigation of its use for long-term flow monitoring. A partial demonstration of this approach is then presented through a preliminary analysis of a set of three-year FFEC field data from the Outokumpu test site in Finland.

4.2. MOTIVATION AND PROBLEM DEFINITION

In one of the main concepts of geosequestration of CO_2, supercritical CO_2 ($ScCO_2$) is injected deep underground into a hydraulically conductive brine formation at a depth of around 1000 m. At such depth, the $ScCO_2$ has a compressibility an order of magnitude larger than that of in-situ brine, a low density (0.47 g/cm^3), and a viscosity that is about 10% that of water [*Colina et al*., 2003; *Beckman*, 2004]. The brine formation, into which $ScCO_2$ is injected and stored, is typically heterogeneous and often displays a layered structure.

An example is the geologic carbon storage project at Heletz test site in Israel, where it happens that the natural groundwater flow in the storage formation of interest is very small. The storage formation is composed of three conductive layers with different values of hydraulic conductivities. As $ScCO_2$ is injected into the aquifer, it pushes the ambient water away from the injection well. An appropriately positioned monitoring well can be used to measure these induced "natural" or "regional" flow velocities in the three layers and serve as a means to monitor the development of flow into the transmissive layers due to $ScCO_2$ injection.

With three transmissive layers of different hydraulic conductivities, the flow rates in the three layers will be different. The partitioning of the injected $ScCO_2$ among the three layers would be useful information in modeling the behavior of the CO_2 storage system. Recent studies [*Rasmusson et al*., 2014] have shown that, because of buoyancy effects operating in the injection well coupled with the transmissive layers of the storage formation, flows into the layers do not follow the simple ratios of hydraulic transmissivities of these layers but are also a function of the relative depths and actual transmissivity values of these layers.

Furthermore, if $ScCO_2$ enters one layer more than the other two, the effective hydraulic conductivity of this layer may become larger because $ScCO_2$ has a larger compressibility, a lower density than water, and a much lower viscosity. This means that the flow of $ScCO_2$ and formation water in this layer may change with time, with corresponding changes in $ScCO_2$ flow into the other two layers, assuming a constant total injection rate. Such temporal changes in flow rates in the three layers may be very useful information for understanding and modeling of $ScCO_2$ injection and storage. Other processes, such as $ScCO_2$ dissolution into brine, mineral trapping of $ScCO_2$, and leakage from the storage formation, may also cause flow changes in the storage brine formation over the time period of injection storage, which can be 30–50 years. Thus, long-term monitoring of flow rate changes in the conductive layers of the storage formation would yield very useful information to characterize the development and movement of the $ScCO_2$ being stored and also to detect potential leakage.

Seasonal or longer-term changes in groundwater recharge and discharge may also change flow rates in subsurface hydraulic conductive formations. Additionally, varying formation water flow rate is also expected during long-term pumping/injection of groundwater, which is a very common scenario for the purpose of drinking and irrigation water as well as the treatment of contaminated water. If the pumping and injection rates are not held constant, the flow rates in those transmissive layers can be varying in the surrounding area.

4.2.1. Approach of FFEC Method

This section gives a brief summary of data collection and analysis methods using the FFEC logging, followed by a proposed modification to adapt it for long-term monitoring. Further details of the data collection method may be found in *Tsang et al*. [1990] and *Doughty et al*. [2005], and details of the analysis method may be found in *Doughty and Tsang* [2005].

In the FFEC logging method, the water in a wellbore is first replaced by water of a constant salinity significantly different from that of the formation water. This may be accomplished, for example, by injecting deionized water or drinking water through a tube to the bottom of the wellbore at a constant rate, while simultaneously pumping from the top of the well at the same rate (wellbore water replacement phase). In the normal FFEC logging method, the well is then pumped at a low constant rate and the FFEC profiles are measured for a series of times by moving an electrical conductivity probe down and up the wellbore. The profiles will exhibit peaks at depth levels where formation water enters the borehole. At successive times, the peaks will increase in size corresponding to the increase in inflow rate times the salinity concentration. The peaks will also tilt up or down the borehole depending on the flow velocity being up or down the borehole, respectively. Thus, these profiles can be analyzed to obtain the inflow into the well and its salinity at different depths [*Doughty and Tsang*, 2005].

For our present purpose of monitoring the temporal changes in formation water flow rates at a monitoring well, a modified FFEC logging procedure is proposed. Instead of the moving electric conductivity probe, a series of electrical conductivity and temperature probes at one- or two-meter intervals are attached onto an injection tubing and installed in the monitoring well. The series of probes should cover a depth range containing the transmissive layers of interest. They can then be used for continuous monitoring of fluid electrical conductivity (FEC) values with time due to formation water flow passing through the well, as a function of depth. Data from these probes are collected via a data scanner and sent to a surface data logger through a cable. This is illustrated by Figure 4.1. Suppose we would like to monitor the flow

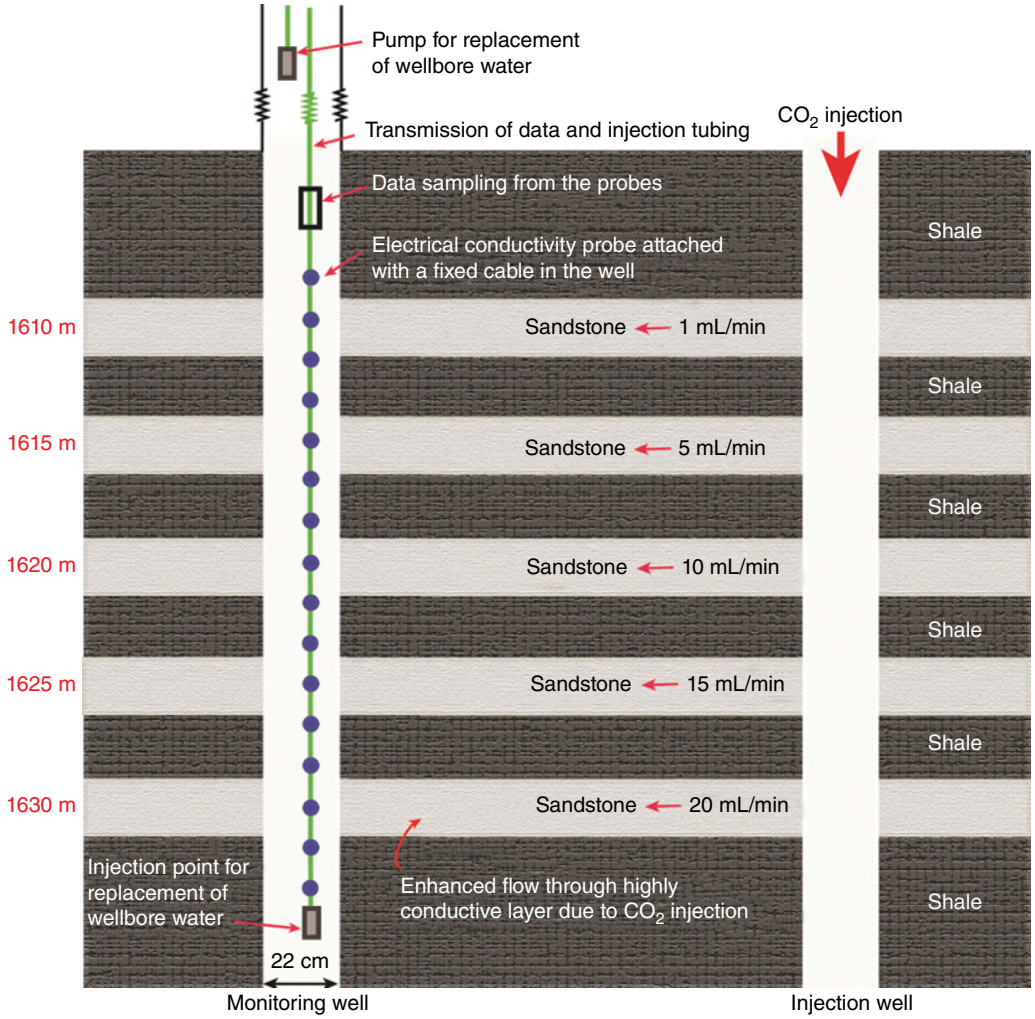

Figure 4.1 An example of FFEC logging arrangement for replacement of wellbore water (with pumping point at the top of the well and injection point at the bottom) and for monitoring temporal formation water flow rates during CO_2 injection at a monitoring well located 50 m away from the injection well.

rates in the transmissive layers after one month, six months, one year, or three years, which we may call the monitoring time, t_m, followed by a monitoring period typically of a few days. At the starting time t_m, water with salinity significantly different from that of the formation water is injected to the bottom of the wellbore, while the well is pumped at the same rate at the top (wellbore water replacement). This is stopped when the probes in the depth interval of interest record a constant FEC value similar to that of the injected water. Then the data from the probes at successive times, $t_m + \Delta t$, $t_m + 2\Delta t$, $t_m + 3\Delta t$, …… (where Δt can be 1, 2, 10, 20 hours) can be downloaded, extracted, and analyzed as described below. Note that the proposed method allows the monitoring of temporal change in FEC of the wellbore water as a function of depth continuously over a long period of time in a passive mode, without the need for any further instrument emplacement or adjustment after the initial setup.

To explore the feasibility of FFEC logging for monitoring natural flows in different transmissive layers and their changes, calculations of FFEC profiles as a function of depth are first made (forward calculation) by assuming that, in each layer intercepted by the well, there is inflow into the well from one side, with simultaneous outflow of an equal rate at the opposite side, thus representing the process of "regional" flow crossing the well (similar to *Doughty et al.*, 2013). The formation water entering through the wellbore will mix with borehole water before exiting the wellbore, at a mixing strength controlled by a dispersion parameter D_w of water salinity along the wellbore. By keeping the salinity differences relatively small but still significant, the density-driven mixing of wellbore water can be assumed to be negligible. The FFEC logs will then display peaks at the depth locations where the formation water enters and exits the wellbore at different rates as shown in Figure 4.2. In this figure, we consider five depth locations with formation water flow crossing the well, and the resulting five peaks of salinity in mg/L are found to grow with time. The salinity value is related to the measured electric conductivity in μS/cm by an equation also dependent on the local water temperature [*Tsang et al.*, 1990]:

$$FEC = 1870C - 40C^2 \tag{4.1}$$

where C is salinity of formation fluid (in g/L) and FEC is fluid electric conductivity (in μS/cm) corrected for temperature dependence to be that at 20°C by using the following equation [Tsang et al., 1990]:

$$FEC(20°\text{C}) = \frac{FEC(T°\text{C})}{1 + S(T°\text{C} - 20°\text{C})} \tag{4.2}$$

where $S = 0.024°\ \text{C}^{-1}$.

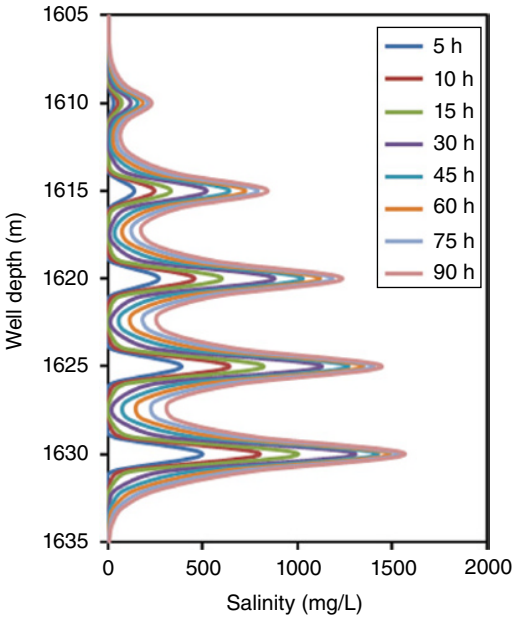

Figure 4.2 The FFEC profiles in the well as a function of depth at different times from 5 h to 90 h after replacement of wellbore water at beginning of the monitoring time t_m. Flow rates in individual layers from top to bottom are V_1: 1 mL/min, V_2: 5 mL/min, V_3: 10 mL/min, V_4: 15 mL/min, and V_5: 20 mL/min.

The peaks shown in Figure 4.2 will grow with time symmetrically in the wellbore direction across the inflow/outflow point in the absence of pumping, with the peak height depending on D_w. At long times, the peak heights reach a constant value when they reach the salinity of the corresponding formation layers.

Now for the inverse problem, we can fit these FFEC logs to the one-dimensional advection-dispersion numerical model, so that the position of inflow points, the water flow rates, and the salinity of the formation water can be obtained. We accomplish this by using the BORE-II code developed by *Doughty and Tsang* [2005]. The BORE-II code estimates the inflow/outflow locations and flow rates by examining the early time FFEC profiles and by assigning the inflow salinity and flow rates in a trial and error procedure until an acceptable match is achieved.

4.3. RESULTS AND DISCUSSION

4.3.1. Water Flow Rates Constant with Time

Figure 4.2 shows that the FFEC profiles (salinity of wellbore water as a function of depth for several times after the start of monitoring time t_m) cover five hydraulically conductive layers (from top to bottom: L_1, L_2, L_3, L_4, and L_5) having a range of formation water flow rates (1, 5, 10, 15, and 20 mL/min) in these layers. The parameters are chosen similar to those of the Heletz test site

where $ScCO_2$ injection of 3.5 tons/hour is being planned. We have conducted the study of FFEC method in a monitoring well 50 m away from the injection well by considering the probes to be at 1-m intervals for simplicity and by considering the five layers each having a single depth point for formation water flowing into and out of the well. Each inflow point was separated by 5 m from its neighbors in this simulation (Figure 4.2). The uppermost layer at 1610 m depth was the lowest conductive fracture with only 1 mL/min of induced flow rate at the monitoring well, while the lowermost layer at 1630 m depth was the highest conductive fracture with 20 mL/min flow rate. All inflows have the same salinity of 2 mg/L. A series of conductivity profiles are plotted at 5 h, 10 h, 15 h, 30 h, 45 h, 60 h, 75 h, and 90 h after t_m, as shown in Figure 4.2. It is noticed that the peaks in the profiles increase at a decreasing rate after 45 h due to the increased mixing of well water with influx from natural water flow. These results show a clear difference in the peaks of the FFEC profiles, demonstrating that the FFEC logging may actually be used to distinguish the different "regional" flow rates in different transmissive layers.

Next we calculate the total masses of salt under each peak corresponding to the individual layers as a function of time. After some exploratory study, we found that the total salt mass displays a consistent linear trend in a log-log scale of total mass of salt (M) with time (t) over the first part of time period for each conductive layer (see Figure 4.3a). This linear trend is given as

$$\log M = a + b \log t \tag{4.3}$$

where a and b are constant coefficients. The total salt that enters through formation water to the monitoring well (from the end of recirculation period with deionized water) increases as a power law with time, however, different coefficients a and b varies for the different flow rates (Figure 4.3a). The linearity with log of time is thus a signature that the formation water is passing across the well at a constant rate. This linearity is however expected to be invalid as the salinity in the wellbore at the inflow/outflow zone becomes saturated to be the salinity value of the formation water at the corresponding depth. Then the increase of mass in the borehole will be less and less until it becomes equal to the dispersion of salinity up and down the borehole.

4.3.2. Varying Water Flow Rates

To evaluate the effect of changes in formation water flow on the FFEC logging profile during the monitoring time period, a study is made by an increase or decrease of the flow rates through three different conductive zones, V_1, V_3, and V_5, at a prescribed time of 45 h (after t_m) of constant local water flow. As expected, it is found that a decrease in local flow (from 1 to 0.5 mL/min) at t = 45 h decreases the salt mass inflow rate suddenly (sharp drop at changing point) and then stabilizes to be parallel to the original flow of 1 mL/min, and similarly a sharp rise in salt mass was observed with enhanced local water flow from 1 to 5 mL/min. However, for a case of high initial local water flow rate of 20 mL/min, an increase to 30 mL/min at 45 h causes relatively small deviation from the linear trend. It is due to the fact that the wellbore water was nearly saturated with formation water at 45 h under such a high regional flow rate, so that the enhanced water flow did not cause much increase in salt concentration in the monitoring well, especially in a log-log plot.

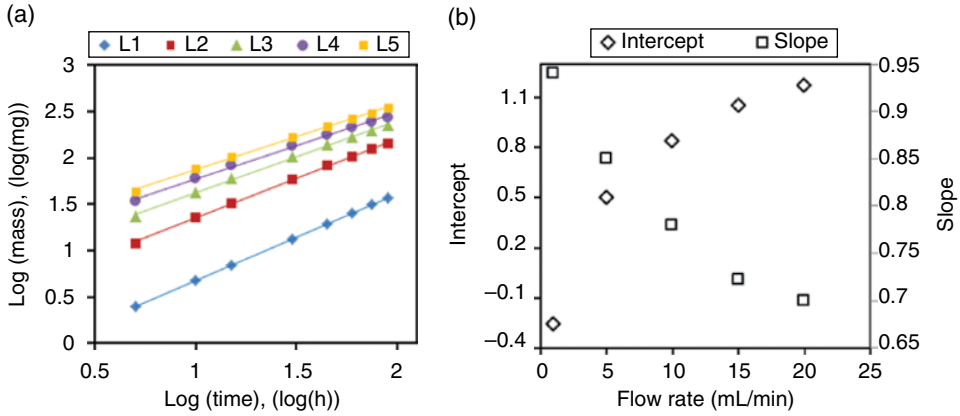

Figure 4.3 (a) Total salt mass present in the well as a function of time during the monitoring period (in log-log scale) for different flow rate in the individual layers: L1: 1 mL/min, L2: 5 mL/min, L3: 10 mL/min, L4: 15 mL/min, and L5: 20 mL/min. The solid points show the calculated values and the lines show the linear fitting. (b) Intercept and slope of linear fits of log-log plots of total salt mass with time.

4.3.3. Feasibility of Determining the Local Flow Rates at Different Times from the FFEC Log Profiles

In order to understand the rate of increase in salt mass with time for different flow rates of formation water surrounding the monitoring well, two plots were made: first a plot of the intercept of the mass-time log-log plot versus the flow rate, and second a plot of the slope of the mass-time log-log plot versus the flow rate (Figure 4.3b). Figure 4.3b indicates that the intercept a in Equation 4.3 increases with an increase in flow rate (i.e., the intercept is higher for high transmissive layers). It shows that the slope b in Equation 4.3 decreases with an increase in flow rate. This can be understood since the entering rate of formation water into the well through a highly transmissive zone is much faster in the beginning (i.e., just after the replacement of wellbore water with deionized water), but that rate decreases with time. However, the responses of formation water flow into the well through less transmissive zones are slower in the beginning, which might have improved after the stabilization of the entrance of formation water through higher transmissive layers (Figure 4.2). Now, we can use the FFEC log profile at 45 h and subtract that from the later FFEC profiles at the new flow rate (we call this the normalized case). The new profiles thus obtained can be analyzed as before in terms of a plot of log M versus log t, where t is now measured from the changed time of 45 h. This observation suggests an alternative analysis procedure for cases of flow rate changes within the monitoring period.

4.3.4. Sensitivity Analysis

The analysis method has been tested for the impact of wellbore diameter of the monitoring well. It was found that the saturation time for wellbore water is increased for larger wellbore diameter. Thus, for the FFEC method, a larger well diameter will allow the measurement of higher flow rates and its temporal change. Other engineering considerations along this line will be explored in an ongoing study to evaluate and improve the possible range of local flow rates that can be conveniently monitored by the FFEC logging method for the Heletz test site.

We also tested the effect of dispersion coefficient (D_w) within the borehole, which controls the mixing of inflow water from the formation with the wellbore water. Figure 4.4 shows the effect of D_w on the total salt mass as a function of time in the monitoring well. The simulations are performed in a single conductive layer by assuming a constant flow rate and three different D_w values, namely, D5: 4×10^{-5} m^2/s, D6: 4×10^{-6} m^2/s, and D7: 4×10^{-7} m^2/s. The results (Figure 4.4) indicate that for early time the effect of D_w is not so important, and therefore the comparison of intercept and slope in Figure 4.3b is not sensitive to the dispersion of salt along the length of the monitoring well over a range of three orders of magnitude in the dispersion parameter.

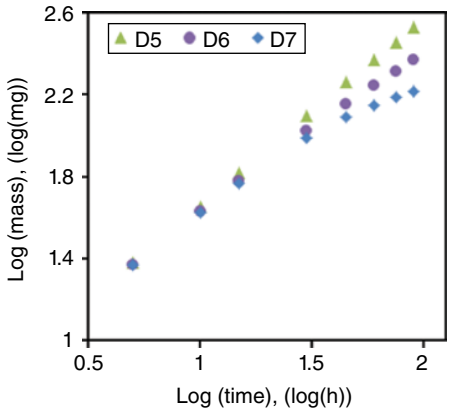

Figure 4.4 Comparison of total salt mass in the well versus time in a single layer on a log-log plot for different values of dispersion coefficient: D5: 4×10^{-5} m^2/s, D6: 4×10^{-6} m^2/s, and D7: 4×10^{-7} m^2/s.

The sensitivity of the method in determining flow rates and their changes can be demonstrated by the analysis of data from a field case as presented in the next section.

4.3.5. Partial Demonstration of the Feasibility of the Approach Based on Field Data

It may be noted that up to now, FFEC logging has been used to provide profiles of fluid electric conductivity in the borehole at successive time intervals over a period of only one or two days for obtaining the hydraulic information of deep and shallow boreholes at field and commercial scale [*Doughty et al.*, 2008; *Doughty et al.*, 2013]. Thus, the FFEC method has not yet been tested for long-term monitoring of the natural flow of surrounding formation water through a wellbore. However, some long-term FFEC logging data are available from a deep borehole at Outokumpu, Finland, which was drilled primarily for geothermal studies by the Geological Survey of Finland and their partners. The borehole is 2516 m in depth and penetrates into Palaeoproterozoic metasedimentary, igneous, and ophiolite rocks, and studies were conducted to systematically understand the temperature variation over depth (in the range of 6°C to 38°C corresponding to the land surface to a depth of 2.5 km) and the heat flux due to long-term paleoclimatic disturbances, groundwater flow, and structural effects [*Kukkonen et al.*, 2011]. During this investigation, four electrical conductivity logs at different times over more than three years were also obtained [*Ahonen et al.*, 2011; *Kukkonen et al.*, 2011]. This data set, though not obtained according to our proposed long-term logging method, provides us an opportunity to

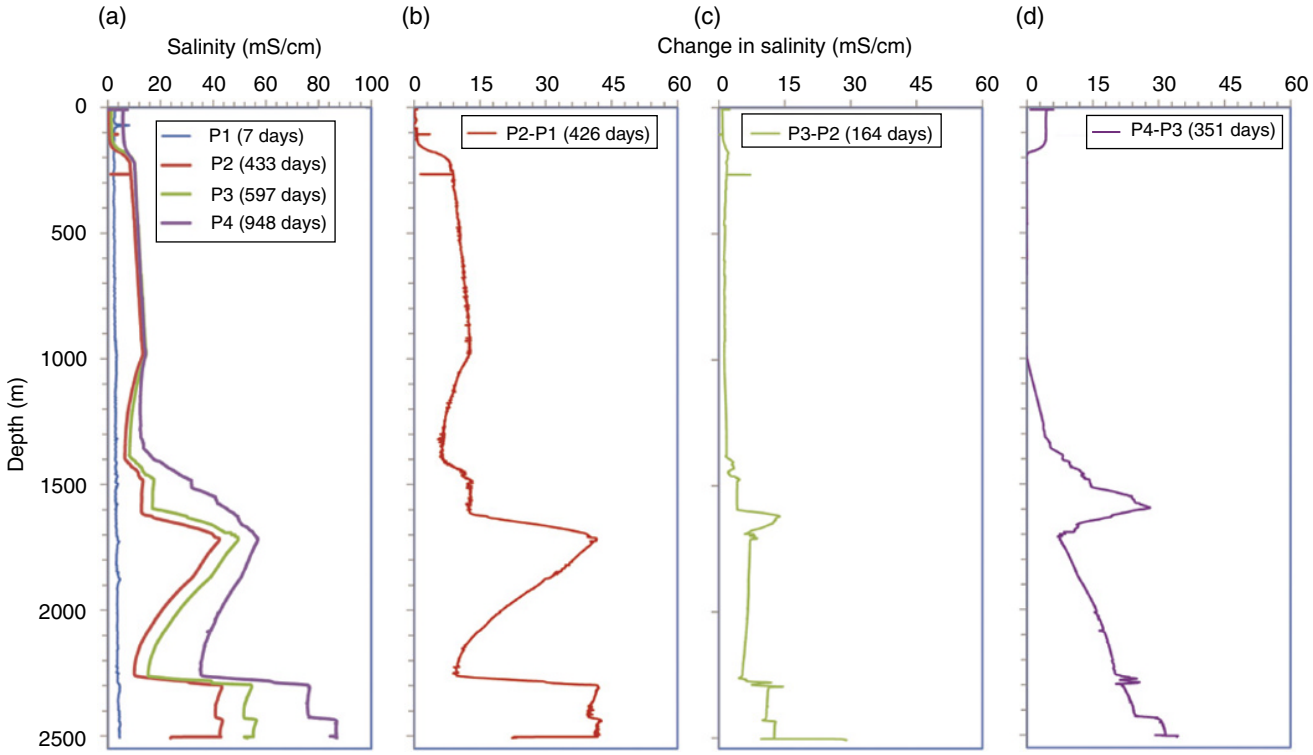

Figure 4.5 (a) Long-term (from February 2005 to September 2008) fluid electrical conductivity profiles (P1, P2, P3, and P4) in a deep borehole at the Outokumpu site during geothermal studies; differences between two adjacent profiles are shown in (b) P2-P1, (c) P3-P2, and (d) P4-P3.

demonstrate the feasibility of our approach for using FFEC logging to monitor change in formation water flow rate over a period of three years.

Figure 4.5a shows four FEC profiles (P1, P2, P3, and P4) from 8 m to 2516 m in a well at Outokumpu test site at 7 days, 433 days, 597 days, and 948 days, respectively, after drilling. A careful study of Figure 4.5a unveils that, in this case, inflows and outflows occur at different depths along the well. Further, it is found that the salinity of borehole water was already stabilized from well-top to 1000 m sometime between 7 and 433 days, but it was still increasing with time in the deeper part of the well. In this particular case, multiple fixed probes were not used (as we proposed in our method), but the FEC profiles were obtained using a moving probe to scan the well. First, these data demonstrate that consistent FEC profiles can be measured in the field over a long time period. Then we proceed to analyze the data. As only four profiles were obtained over the three and half year period, their analysis using FFEC method was challenging. A preliminary analysis of these FEC profiles is summarized below.

In order to understand the inflow and outflow locations, change in water flow rates, and change in salinity of formation water along the well depth, we obtained the difference between two adjacent profiles (P2-P1, P3-P2, and P4-P3), as shown in Figure 4.5 parts b, c, and d. A study of the FEC profiles and the "differences" profiles indicates the occurrence of inflow points representing high conductive layers or fractures at the locations of the peaks. It is also possible to see that though the inflow zones may exist continuously at a shallower part of the well (<1000 m), the profile stabilized as wellbore water salinity was approaching to the formation water salinity after about one year (433 days). In addition, we could observe a linear increase in salinity with depth of the well (see profile P4-P3 for depth below 1000 m), which may imply a constant rate of (relatively smaller) background salinity diffusion from the formation water to the borehole over an extended interval of the well.

After accounting for the background salinity diffusion along the well, and assuming a depth-dependent salinity of formation water that is constant with time (ranging from 12 mS/cm near the land surface to 300 mS/cm at the depth of the bottom of the well), we were able to simulate all the FEC peaks and their respective development by fitting using the BORE II code (Figure 4.6). The results on inflow locations of the peaks, their flow rates, and salinity of formation water are presented in Table 4.1. The calculated results for the peak flow rates were constant with time for the peaks of the profiles P2-P1, P3-P1, and P4-P1, except

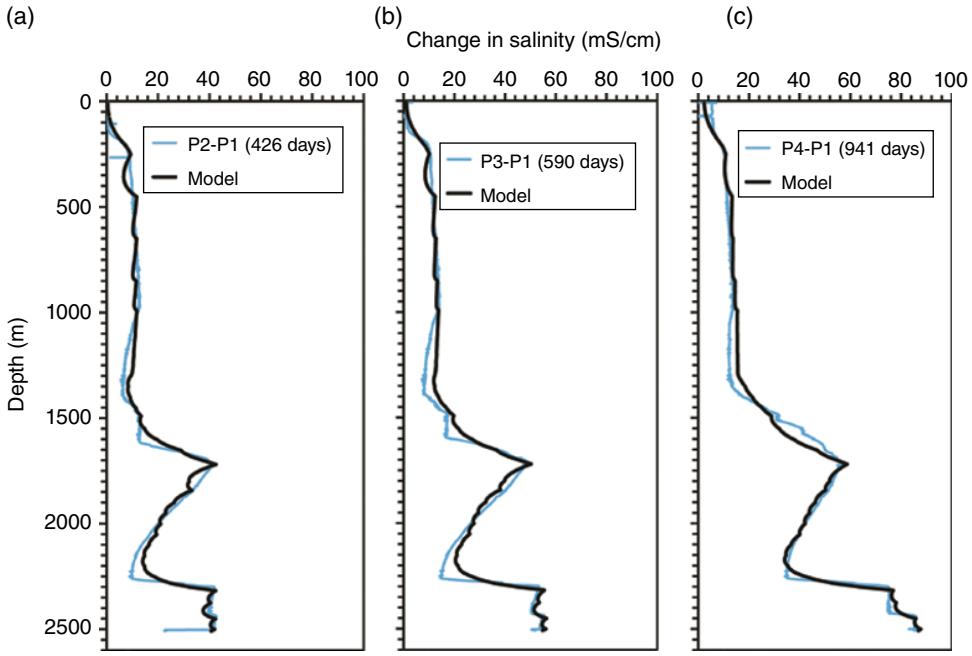

Figure 4.6 Application of FFEC analysis method to the profiles from the Outokumpu site after considering the first profile (P1) as a baseline. The figures show the data and model fit for (a) P2-P1, (b) P3-P1, and (c) P4-P1.

Table 4.1 Results of a preliminary analysis of long-term FFEC data in a deep borehole of Outokumpu site. Flow rates in bold face indicate cases where flow rates changed over the different time intervals.

		Flow Rate (mL/min)		
Well Depth (m)	Salinity (mS/cm)	P2-P1 (426 days)	P3-P1 (590 days)	P4-P1 (941 days)
200	12	OF	OF	OF
250	12	35	35	35
450	15	45	45	45
650	15	40	40	40
850	18	30	30	30
990	25	14	14	14
1300	50	OF	OF	OF
1490	90	**2**	**3**	**3**
1650	120	3	3	3
1718	140	**7**	**7**	**6**
1718	140	OF	OF	OF
1840	160	**3**	**2**	**2**
2300	250	OF	OF	OF
2315	260	**4**	**5**	**6**
2450	280	2	2	2
2500	290	2	2	2
2550	300	OF	OF	OF

OF = outflow from the wellbore.

for the four inflow points at 1490 m, 1718 m, 1840 m, and 2315 m (Table 4.1). At these four depths, the changes in flow rate for the time interval between the two adjacent FEC profiles are shown in Table 4.2, which shows the

Table 4.2 Changes in flow rates at different well depths from data over different time intervals.

		Flow Rate (mL/min)		
Well Depth (m)	Salinity (mS/cm)	P2-P1 (426 days)	P3-P2 (164 days)	P4-P3 (351 days)
1490	90	2	4	3
1718	140	7	7	4
2315	260	4	7	8
2450	280	2	2	3

average flow rates at these depths over the first 426 days, then over the next 164 days, and finally over the next 351 days. Thus, Table 4.2 indicates a decreasing flow rate at 1718 m but increasing flow rates at 2315 m and 2450 m. The flow rate appears to increase and then decrease at 1490 m. The preliminary analysis of these long-term data demonstrates the feasibility of our proposed approach of using FFEC logging data to monitoring salinity changes, from which to obtain the long-term temporal flow rates changes in the formation. The results in Tables 4.1 and 4.2 also show that the sensitivity of the method in determining the local inflow rates is down to a few mL/min.

4.4. CONCLUDING REMARKS

It has been shown that the FFEC logging method for long-term (about three years) monitoring of FEC in a deep borehole is possible [*Kukkonen et al.*, 2011], and

that these data can be successfully analyzed using the FFEC analysis method. In this chapter, a modified FFEC logging procedure is suggested for passive, long-term monitoring of the flows of formation water across the well through different transmissive layers and their temporal changes over a long time period. The modified procedure may be summarized as follows. (1) A series of electrical conductivity probes can be attached onto an injection tubing and installed in a monitoring well. (2) A data scanner connecting all the probes can be placed just above the series of probes to collect data from the probes in series. (3) The scanner would transmit data to a surface data logger at any time as demanded by a signal from the surface. (4) At a monitoring time t_m (which could be months or years), the borehole water is replaced by simultaneous injection to well bottom and pumping at well top at the same rate. (5) The display and analysis of data can be performed at selected times after wellbore water replacement, at $t_m + \Delta t$, $t_m + 2\Delta t$, $t_m + 3\Delta t$, etc., where Δt can be minutes or hours. (6) Finally, the profiles obtained from these collected data can be analyzed using our model. The results and sensitivity analyses presented in this chapter show that the amount of formation water entering into the monitoring well during the monitoring period, in a log-log plot, increases linearly with time if there are no temporal flow rate changes. Changes in "regional" water flow during this period can also be monitored by analyzing the deviation from linearity of the log-log plot. The appropriate range of flow rates that can be monitored is dependent on the wellbore diameter among other engineering parameters. Plans for testing and optimizing the proposed FFEC method for monitoring "regional" water flow rates are being developed for field validation for the large-scale $ScCO_2$ injection to be conducted at the Heletz test site, during which the range of flow rates that can be monitored as a function of design parameters will be further studied.

ACKNOWLEDGMENTS

We would like to acknowledge the funding from European Community's Seventh Framework Programme FP7/2007-2013 under Grant Agreement No. 227286 (as part of MUSTANG project) for supporting this research. We would like to thank Dr. Ilmo T. Kukkonen, Geological Survey of Finland (currently at the University of Helsinki), for providing the well logging data used in Figure 4.5a in this chapter. The second and third authors would also like to express their appreciation to Paul A. Witherspoon, for his mentoring over many years and for his generous encouragement to new ideas.

REFERENCES

Ahonen, L., R. Kietäväinen, N. Kortelainen, I. T. Kukkonen, A. Pullinen, T. Toppi, M. Bomberg, M. Itävaara, A. Nousiainen, M. Nyyssönen, and M. Oster, M. (2011), Hydrological characteristics of the Outokumpu deep drill hole, in I. T. Kukkonen (ed.), *Outokumpu Deep Drilling Project*, Special Paper *51*, 151–168.

Beckman, E. J. (2004), Supercritical and near-critical CO2 in green chemical synthesis and processing, *J.Supercritical Fluids*, *28*, 121–191.

Brainerd, R. J., and G. A. Robbins (2004), A tracer dilution method for fracture characterization in bedrock wells, *Ground Water*, *42*, 774–780.

Colina, C. M., C. G. Olivera-Fuentes, F. R. Siperstein, M. Lisal, and K. E. Gubbins (2003), Thermal properties of supercritical carbon dioxide by Monte Carlo simulations, *Molecular Simulation*, *29*, 405–412.

Doughty, C., S. Takeuchi, K. Amano, M. Shimo, and C. F. Tsang (2005), Application of multi-rate flowing fluid electric conductivity logging method to Well DH-2, Tono Site, Japan, *Water Resour. Res.*, *41*, W10401, doi:10.1029/2004WR003708.

Doughty, C., and C. F. Tsang (2005), Signatures in flowing fluid electric conductivity logs, *J. Hydrol.*, *310*, 157–180.

Doughty, C., C. F. Tsang, K. Hatanaka, S. Yabuuchi, and H. Kurikami (2008), Application of direct-fitting, mass integral, and multirate methods to analysis of flowing fluid electric conductivity logs from Horonobe, Japan, *Water Resour. Res.*, *44*, W08403, doi:10.1029/2007WR006441.

Doughty, C., C. F. Tsang, S. Yabuuchi, and T. Kunimaru (2013), Flowing fluid electric conductivity logging for a deep artesian well in fractured rock with regional flow, *J. Hydrol*., *482*, 1–13.

Drost, W., D. Klotz, A. Koch, H. Moser, F. Neumaier, and W. Rauert (1968), Point dilution methods of investigating ground water flow by means of radioisotopes, *Water Resour. Res.*, *4,* 125–146.

Freifeld, B. M ., S. Finsterle, T. C. Onstott, P. Toole, and L. M. Pratt, (2008), Ground surface temperature reconstructions: Using in situ estimates for thermal conductivity acquired with a fiber-optic distributed thermal perturbation sensor, *Geophys. Res. Lett., 35*, L14309, doi:10.1029/2008GL034762.

Jardani, A., A. Revil, and J. J. Dupont (2013), Stochastic joint inversion of hydrogeophysical data for salt tracer test monitoring and hydraulic conductivity imaging, *Adv. Water Resour.*, *52*, 62–77.

Keys, W. S. (1986), Analysis of geophysical logs of water wells with a microcomputer, *Ground Water*, *24*, 750–760.

Kukkonen, I. T., V. Rath, L. Kivekäs, J. Safanda, and V. Cermak (2011), Geothermal studies of the Outokumpu deep drill hole, Finland: Vertical variation in heat flow and palaeoclimatic implications, *Physics of the Earth and Planetary Interiors*, *188*, 9–25.

Mendoza, A., C. Torres-Verdin, and B. Preeg (2010), Linear iterative refinement method for the rapid simulation of borehole nuclear measurements: Part I. Vertical wells, *Geophysics*, *75*, E9–E29.

Molz, F. J., R. H. Morin, A. E. Hess, J. G. Melville, and O. Guven (1989), The impeller meter for measuring aquifer permeability

variations: Evaluation and comparisons with other tests, *Water Resour. Res.*, *25*, 1677–1683.

Mount Sopris (2014), Mount Sopris Instruments, Temperature-Fluid Conductivity probe: http://mountsopris.com/products/downhole-probes/item/q40ftc-b-1000.

Paillet, F. L. (1991), Use of geophysical well logs in evaluating crystalline rocks for siting of radioactive waste repositories, *The Log Analyst*, *32*, 85–107.

Rasmusson, K., Y. Tsang, C. F. Tsang, L. Pan, and A. Niemi (2014), Partitioning of injected supercritical CO_2 into a double-layer brine formation, paper to be submitted to *Water Resources Research*.

Robertson Geologging (2014), Robertson Geologging Borehole logging systems and services. Temperature-Conductivity probe:http://www.geologging.com/slimhole-logging/temperature-conductivity/.

Tsang, C. F., P. Hufschmied, and F. V. Hale (1990), Determination of fracture inflow parameters with a borehole fluid conductivity logging method, *Water Resour. Res.*, *26*, 561–578.

Walton, W. C. (1970), *Groundwater Resource Evaluation*, McGraw-Hill, New York, 664 pp.

Zemanek, J., E. E. Glenn, L. J. Norton, and R. L. Caldwell (1970), Formation evaluation by inspection with the borehole televiewer, *Geophysics*, *35*, 254–269.

Part II
Collective Behavior and Emergent Properties of Complex Fractured Rock Systems

5

Particle Swarms in Fractures

Eric Boomsma[1] and Laura J. Pyrak-Nolte[1,2,3]

ABSTRACT

Particle swarms confined in an uniform aperture fracture travel farther and faster prior to destabilization, for an optimal range of apertures, than in an open tank. Experiments were performed to image swarm evolution, maintenance, and destabilization in fracture samples with uniform and variable apertures. Two competing mechanisms affect swarm evolution in a fracture, namely, tangential drag from the wall, which decelerates the swarm, and a normal force from the wall that prevents swarm expansion. In apertures less than the swarm radius, the tangential drag dominates, causing a swarm to decelerate and reducing the destabilization length. For fractures with apertures 10 times greater than the swarm diameter, swarms behaved as though released in an open tank, where the swarm is free to evolve, expand, and bifurcate. However, when a swarm was released in fractures with apertures within the optimal range, $1 < \frac{\text{aperture}}{\text{swarm diameter}} < 10$, the swarm traveled 1.5 to 2.5 times faster than swarms released in an open tank, and bifurcations were suppressed. In this range, confinement forces maintain the swarm density by preventing swarm expansion, inhibiting and delaying swarm destabilization. In variable aperture fractures, swarms speed and topology change in response to both local expansion and constrictions in aperture as well as global variations in resistance.

5.1. INTRODUCTION

Recently, research efforts have focused on the development of nano- and microsensors to deploy into the subsurface to probe rock formations and the fluids contained in them [*Durham*, 2011; *Prodanovic et al.*, 2009; *Yang et al.*, 2011]. Current development of subsurface sensors can be categorized into sensors that [*Durham*, 2011] (1) augment electromagnetic, acoustic, or other physical properties to delineate the spatial distribution of fluids; (2) exhibit irreversible changes upon exposure to variations in physical and chemical conditions; and (3) continuously measure physical and/or chemical properties and store/transfer data back to a wellbore. No matter the type, sensor mobility is a major challenge for any innovation that relies on the introduction of nano- or microparticles into the subsurface. Sensor mobility depends critically on the complexity of the flow paths in the rock, the size, shape, and functionality of the sensors, and the chemical interaction among the sensors, fluids, and rock surfaces. A potential method for sensor deployment is the use of sensor swarms, i.e., groups of nano- or microsensors that are maintained as a coherent group to enable targeted emplacement in fractures, sensor-to-sensor communication, and/or coherent transmission of information as a group. A fundamental understanding of the physical processes that affect swarm transport in fractures in rock is required to control the deployment of sensor swarms. Fractures are the likely pathways along which sensors will be distributed in the subsurface, because these flow paths are usually more conductive than the rock matrix.

Particle swarms are collections of nano- to micrometer-scale particles in dilute concentrations (1%–4% by mass)

[1] *Department of Physics and Astronomy, Purdue University, West Lafayette, Indiana, USA*

[2] *Department of Earth and Atmospheric Sciences, Purdue University, West Lafayette, Indiana, USA*

[3] *School of Civil Engineering, Purdue University, West Lafayette, Indiana, USA*

Dynamics of Fluids and Transport in Complex Fractured-Porous Systems, Geophysical Monograph 210, First Edition.
Edited by Boris Faybishenko, Sally M. Benson, and John E. Gale.

Table 5.1 Experimental parameters from the literature. Compare to Table 5.2.

Parameter	*Adachi et al.* [1978]	*G. Machu et al.* [2001a]	*Pignatel et al.* [2011]	*Metzger et al.* [2007]	*Mylyk et al.* [2011]
Bulk fluid material	glycerol-water	glycerin-water	UCON oil & water	UCON oil & water	glycerol-water
Bulk fluid viscosity (*mPa•s*)	186, 984	1	9.2–295	1170	110
Bulk fluid density (kg/m^3)	1230	1200	1011–1062	1030	1224
Swarm fluid material	glycerol-water	glycerin	UCON oil & water	UCON oil & water	glycerol-water
Bead material	glass	glass	glass, polystyrene	glass	glass
Bead density (kg/m^3)	2500	2400	2490, 1178	2450	2400
Bead radius (μm)	14, 30	25	75, 156	67, 154	25
Particle concentration (%)	0.1, 0.4, 1 (mass)	1–15 (volume)	2–50 (volume)	4–20 (volume)	10 (volume)
Container parameters (cm)	Cylinder (5 × 70)	Box (5 × 25 × 50)	Box (4 × 10 × 100)	Box (4 × 10 × 120)	not given

that coherent group behavior. The number of particles in a swarm depends not only on the mass concentration but also the size of the particles and the relative densities of the particles and the fluid in which they are contained. Past work (Table 5.1) has used swarms containing as few as ~1,000 to as many as ~1,000,000 particles in fluids with viscosities ranging from 10 mPas to 200,000 mPas. The behavior of the particles composing the swarm are often described by Stokeslets [*Adachi et al.*, 1978; *Bosse et al.*, 2005; *Ekiel-Jezewska et al.*, 2006; *Nitsche and Batchelor*, 1997; *G. Machu et al.*, 2001a; *Metzger et al.*, 2007], because of their small size and low velocities. The Stokeslet approximation is a series of simplifications to the far more complex Navier-Stokes equation (Equation 5.1).

$$\rho f\left(\frac{\partial \mathbf{v}_f}{\partial t}+\mathbf{v}_f\cdot\nabla\mathbf{v}_f\right)=-\nabla P+\mu\nabla^2\mathbf{v}_f+\mathbf{F}_f \qquad (5.1)$$

In this and all subsequent equations, **F** is the force acting on a particle or the fluid, P is pressure, μ is the dynamic viscosity of the fluid, ρ is the density of the fluid or particle and **v** is the velocity of the particle or fluid. All variables with the subscript p represent particle properties and variables with the subscript f represent fluid properties. The simplifications (Equation 5.2) are additional conditions on the fluid motion that include time independence and fluid incompressibility [*Happel and Brenner*, 1965]. When applied to the motion of a particle these simplifications result in the well known Stokes law for fluid drag (Equation 5.3).

$$\nabla P-\mu\nabla^2\mathbf{v}_f=\mathbf{F}_f \qquad (5.2)$$

$$\mathbf{F}_p=-6\pi\mu a\mathbf{v}_p \qquad (5.3)$$

Here, a is the radius of the particle. It is important to note that this approximation is only valid as long as the fluid is non-inertial as quantified by the condition of a sufficiently small Reynolds number (equation 5.4).

$$\mathrm{Re}=\frac{\rho_f vL}{\mu} \qquad (5.4)$$

Here L is the characteristic length (particle diameter, hydraulic diameter, traveled distance, etc.) and v is the relevant velocity (fluid or particle). While the Reynolds number requirements for laminar flow can vary greatly with the geometry of the boundaries, up to Re = 2100 for circular ducts [*Happel and Brenner*, 1965], the conditions for Stokes flow are far more demanding. Stokes flow only occurs when $Re << 1$.

Investigators have studied particle swarms both experimentally and numerically in the past few decades [*Adachi et al.*, 1978; *Ekiel-Jezewska et al.*, 2006; *Machu et al.*, 2001a, b; *Metzger et al.*, 2007; *Nitsche and Batchelor*, 1997] and found that, for unconfined fluids, the cohesiveness of a swarm is strongly dependent on particle concentration, swarm shape, and expansion rate. There is both a critical particle concentration and absolute number of particles below which a swarm will simply break up instead of evolving in time. Most studies of particle swarms have been performed using unconfined systems (i.e., the dimensions of the tank were much greater than the swarm diameter; see Table 5.1). These studies have shown that swarm behavior is highly dynamic and changes with time. Figure 5.1 shows the stages of a typical swarm, as described by *Machu et al.* [2001b]. In an unconfined fluid, immediately after release the swarm is spherical in shape (Figure 5.1a). As the swarm falls under the influence of gravity it flattens into a closed torus that has a slightly larger radius than the initial sphere (Figure 5.1b). The closed torus is so named because the bulk fluid is inhibited from entering the swarm, i.e., the fluid within the swarm is closed off from the bulk fluid. As it continues to fall, the swarm expands and contracts because the particles composing the swarm are constantly in motion. Eventually these oscillations cause the closed torus to transition into an open torus (Figure 5.1c). The open torus is characterized by the ability of the bulk fluid to enter the particle deficient center of the torus. This breaks apart (bifurcates) the swarm into two (or more) separate smaller swarms (Figure 5.1d). Any of the new distinct swarms has the potential to either continue intact, as a spherical drop, or

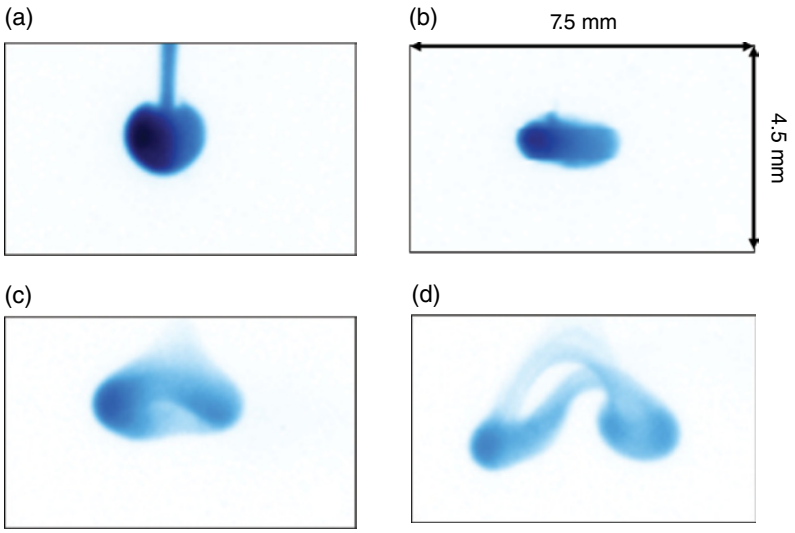

Figure 5.1 Images of the stages of swarm evolution. (a) sphere, (b) closed torus, (c) open torus (destabilization), (d) bifurcation. Bead parameters are given in Table 5.2. False color.

repeat the evolution process. For applications that need to maintain particle swarm cohesiveness in fractures, knowledge of the effect of confinement by rigid boundaries on swarm evolution is required.

Recent investigations have examined the effect of single- and double-wall confinement on swarm stability and behavior [*Mylyk and Ekiel-Jezewska*, 2010; *Mylyk et al.*, 2011]. These studies found that the presence of boundaries tends to reduce the destabilization distance and influence the bifurcation axis. However, they are limited in application to geosciences by the lack of variation in aperture/wall separation as well as the use of glycerin, which is not found in nature.

Approximations for the effect of a single infinite plane wall on single rigid particles in the Stokes regime have existed for over 100 years [*Lorentz*, 1907], resulting in a set of simple equations (Equation 5.5; *Kirby*, 2010) that highlights the important physical parameters affecting the forces acting on particles moving both normally, $\mathbf{F}_{Normal}$, and tangentially, $\mathbf{F}_{Tangential}$ to a boundary.

$$\mathbf{F}_{Tangential} = \frac{-6\pi\mu a\mathbf{v}_p}{1-\frac{9}{16}\frac{a}{d}} \tag{5.5a}$$

$$\mathbf{F}_{Normal} = \frac{-6\pi\mu a\mathbf{v}_p}{1-\frac{9}{8}\frac{a}{d}} \tag{5.5b}$$

Here, d is the distance of the particle from a single planar boundary. It is immediately apparent that particles traveling towards a boundary (Equation 5.5b) experience a stronger force than particles falling parallel to a boundary (Equation 5.5a). This fact will have important implications in the later discussion of swarms in rough fractures. These approximations have since been improved, most notably by *Blake* [1971] and his method of images.

The expansion to parallel plates is a nontrivial problem, requiring far more than simply adding the effects of two plane walls [*Happel and Brenner*, 1965]. Parallel walls induce additional forces and torques that are not observed with a single wall, and their effect on particle motion is still under investigation [*Swan and Brady*, 2010]. An equivalent to Equation 5.5a was calculated numerically by Faxén for particles in the center of two infinite parallel plates (Equation 5.6) [*Happel and Brenner*, 1965].

$$\mathbf{F} = \frac{-6\pi\mu a\mathbf{v}_p}{1-1.004\left(\frac{a}{d}\right)+0.418\left(\frac{a}{d}\right)^3+0.21\left(\frac{a}{d}\right)^4-0.169\left(\frac{a}{d}\right)^5} \tag{5.6}$$

Figure 5.2 provides a comparison of the drag force on a sphere adjacent to a single wall (Equation 5.5a) and between parallel walls (Equation 5.6). In both cases the effect of the boundaries decays quite rapidly, becoming negligible by $\frac{\text{distance from wall}}{\text{particle radius}} \approx 10$.

Equations 5.5 and 5.6 were derived for single spherical particles falling adjacent to a single wall or between two parallel walls. However, swarms are collections of smaller particles and results in behavior that is fundamentally different from single particles in unconfined fluids, as shown in Figure 5.1. A swarm's shape and size evolves over time as it falls. Similarly, if the equations for drag force were applied to the particles in a swarm, a single swarm

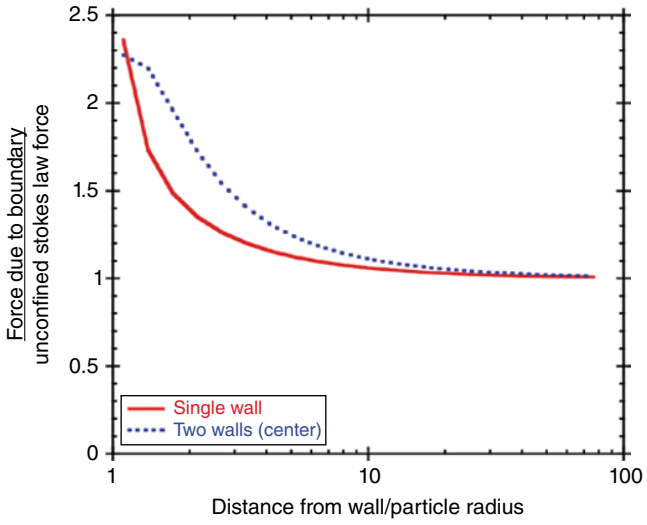

Figure 5.2 The expected forces resulting from a single wall (Equation 5.5a), and a particle located at the center between two parallel plates (Equation 5.6) as a function of distance from the wall normalized by particle radius. The force is normalized by the unconfined Stokes law force (Equation 5.3).

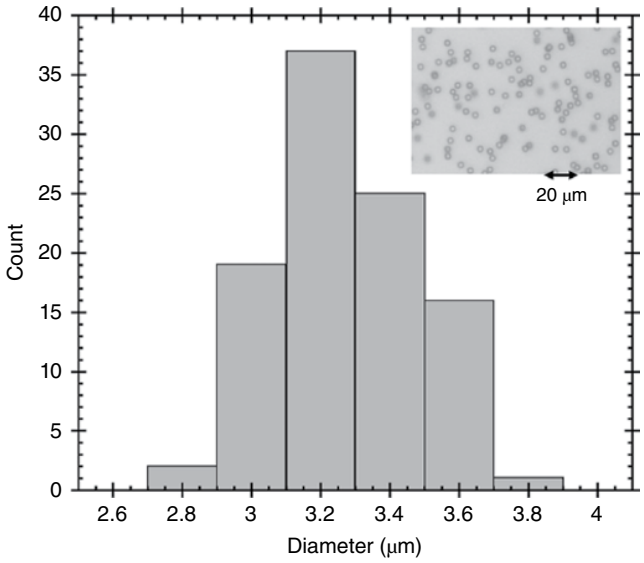

Figure 5.3 Histogram of the diameters of the particles used in swarms. *Inset*: Optical microscopy image of the beads.

particle would most likely be unaffected by the fracture walls because $\frac{\text{distance from wall}}{\text{particle radius}} = \frac{10^{-3}}{10^{-6}} = 1000 \gg 10$. However, in this chapter, we demonstrate experimentally that fracture geometry and aperture strongly affect swarm evolution, speed, and bifurcation. When a swarm is released inside a uniform aperture fracture, tangential drag from the fracture walls affects the speed of descent of a swarm, while confinement forces affect the rate and symmetry of swarm expansion. As a result, an optimal range of fracture apertures exists that suppresses swarm bifurcation and maintains a coherent swarm over longer distances (i.e., increases the destabilization distance). In addition, variations in fracture aperture are shown to influence swarm behavior by inducing and/or suppressing bifurcations.

5.2. EXPERIMENTAL METHODS

Experiments were performed using several fractures with different aperture distributions to determine the effect of confinement from fractures on swarm behavior. In this section, descriptions of the swarm, fracture samples, and experimental approach are given.

5.2.1. Swarm Composition

Particle swarms were created using fluorescent polystyrene beads (Thermo-Scientific, R0300B) in a dilute suspension (~1.0% by mass) with water. The beads were internally dyed and had an absorption wavelength of 542 nm (green) and an emission wavelength of 612 nm (red).

Table 5.2 Properties of the particles and the swarms used in the experiments.

Particle Property	Polystyrene
Particle density (kg/m^3)	1050
Fluid density (kg/m^3)	1000
Fluid viscosity (*mPa•s*)	1.002
Swarm concentration (by mass)	1%
Effective swarm density (kg/m^3)	1010
Swarm particle density (particles/μL)	1,300,000
Mean particle diameter (μm)	3.29 ± 0.02
Median particle diameter (μm)	3.23
Minimum particle diameter (μm)	2.75
Maximum particle diameter (μm)	3.72
Single particle settling speed (mm/s)	0.245×10^{-3}

The size distribution of the beads (Figure 5.3) was obtained from optical microscopy images of the beads taken at a magnification of 20x (e.g., Figure 5.3 inset). Based on 100 measurements, the average bead diameter was 3.29 ± 0.02 μm while the median value was 3.23 μm. Other statistical quantities related to bead size are given in Table 5.2, as well as the particle density and the number of particles per volume of swarm solution.

5.2.2. Fracture Samples

The objective of this study is to determine the effect of confinement by a fracture on the evolution, maintenance, and destabilization of swarms. While the ultimate goal is the investigation of rough-walled fractures (Figures 5.4d and 5.5) similar to those observed in nature, several different

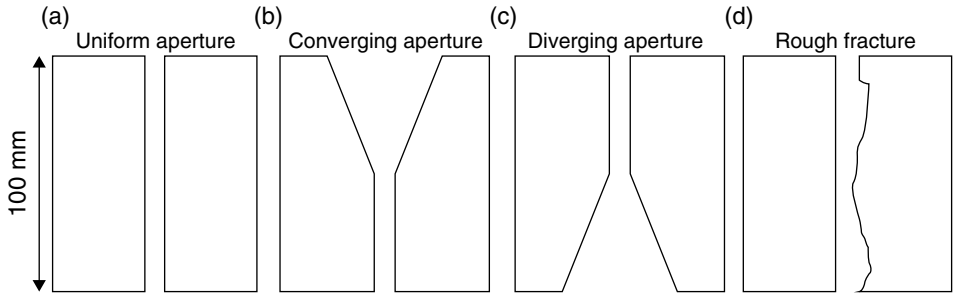

Figure 5.4 Sketches of the various fracture geometries used in the experiments. (a) Uniform aperture fracture, (b) converging fracture, (c) diverging fracture, (d) rough fracture.

Table 5.3 The number of experiments performed for each fracture style and aperture. All apertures are defined as the minimum separation distance in millimeters between the two plates and are displayed in bold text.

	Number of Experiments at Each Fracture Aperture													
Fracture Type	**0**	**0.5**	**1**	**2.5**	**5**	**6**	**8**	**10**	**12**	**15**	**20**	**25**	**30**	**40**
Uniform Aperture		10	10	10	10	10	17	17	17	15	11		10	7
Converging Aperture		10	10	10	10	10	10	9		9	8		10	10
Diverging Aperture		9	8	9	9	14	6	12	11	9	12	10	10	10
Rough Fracture 1	11		10	11	12		13	12	12	11	7			
Rough Fracture 2	10		10	10										

smooth-walled fracture geometries (Figure 5.4a, b, c) were constructed to provide insight into swarm responses to both fracture aperture and aperture variation. The smooth-walled fractures were constructed from two blocks of transparent acrylic with dimensions of 50 mm ×100 mm ×100 mm that were held a fixed distance apart to form an uniform aperture fracture. Table 5.3 lists the apertures used in this study. In all cases the aperture was defined as the minimum separation distance, i.e., 0 mm is the point at which the two blocks touched.

Three different smooth-walled fracture geometries were used in this study, (1) a uniform aperture fracture (Figure 5.4a), (2) a variable geometry fracture with both converging and uniform aperture regions (Figure 5.4b), and (3) a variable geometry fracture with both diverging and uniform aperture regions (Figure 5.4c). The converging/diverging fractures were composed of two rectangular blocks that each had a triangular wedge (25 mm × 100 mm × 50 mm) removed, resulting in converging/diverging fracture apertures with an angle of ~54° and a maximum aperture that is 50 mm greater than the point of minimum separation (the aperture of the uniform portion of the fracture).

Rough fractures were formed by fabricating acrylic casts of an induced fracture in Austin chalk. These casts had the same external dimensions as the smooth-walled fractures and were used in the same experimental setup. The rough surface casts were not fully transparent, so each rough block was paired with a uniform smooth block (Figure 5.4d) to image the swarms through the transparent smooth block. Both halves of the fractured sample were paired in this way, creating two distinct rough fractures (Figure 5.5). Swarms were released at the location marked in the fracture (black circle in Figure 5.5a and b). The maximum asperity height difference of both fracture surfaces was 6 mm.

Laser profilometry was used to measure the asperity height distribution of each rough fracture surface. The sample was placed on a motion-controlled platform (Newport, MTM250PP1) beneath a mounted laser (Keyence, LK-G152). The platform was moved in set increments and was controlled by a custom Labview code. At each increment the laser measured the height of the sample surface. With this profilometry system, variations in height up to 9.969 mm can be measured at a resolution of 0.5 μm. For this study, measurements were taken over the entire fracture surface in 0.25-mm increments along two orthogonal axes. Both rough fractures were profiled using this technique.

The asperity height for both rough fractures varied between 0 and 6 mm (Figure 5.5c). As shown in Figure 5.5, fracture apertures were observed to converge and diverge within the same fracture because the fracture surfaces were rough. This is in contrast to the smooth-walled fractures shown in Figure 5.4b and c which only feature either converging or diverging geometries or the uniform aperture fracture in Figure 5.4a. Additionally, swarm expansion is more limited in the rough-walled fractures than the smooth-walled fractures because of the additional confinement along the fracture plane. If a swarm evolves adjacent to an

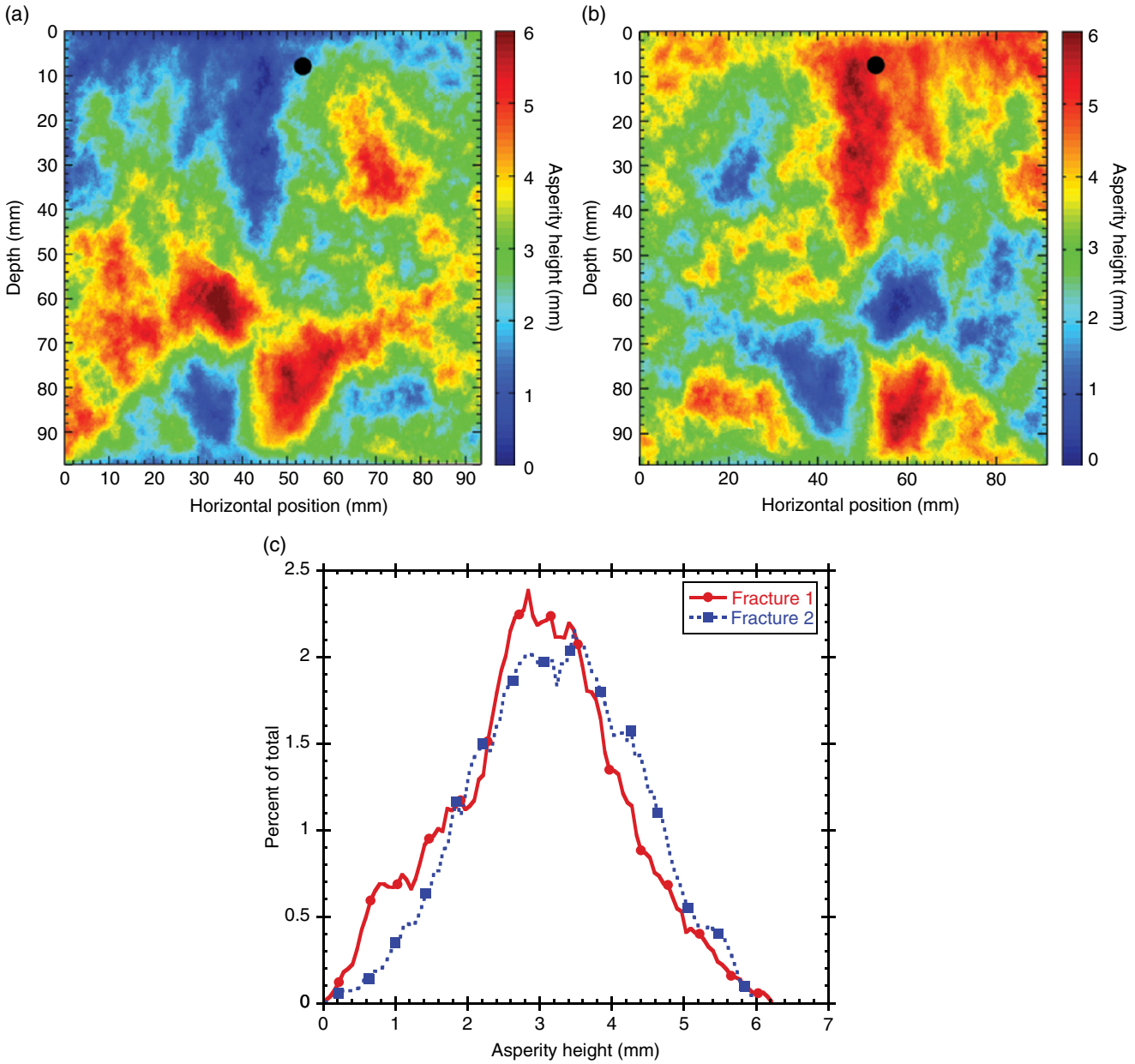

Figure 5.5 The asperity map of (a) Fracture 1, (b) Fracture 2, and (c) the asperity height distribution obtained via laser profilometry. The block dot in (a) and (b) represents the release location of the swarm.

asperity peak it will experience enhanced confinement along the *y* axis (Figure 5.6), as well as increased drag (*z* axis).

5.2.3. Swarm Release

Each block was placed in a holder that was mounted on an optical rail suspended over the center of a tank with dimensions 25 cm × 25 cm × 30 cm (Figure 5.6). Water was added to the tank until the top of each block was ~25 mm below the surface of the water, completely filling the fracture. The optical rail enabled a wide range of apertures to be investigated. Table 5.3 shows the number of experiments performed at each of the investigated apertures for each fracture type.

Swarms were released within a fracture into the water using a 25-gauge hypodermic needle (~0.26 mm inner diameter) that contained ~0.15 mL of the bead suspension. The tip of the needle was placed below the top surface of the block to eliminate the transition from an open tank to a confined region (Figure 5.6). Five-microliter swarms were released using a mechanical syringe pump (Harvard Apparatus, PHD2000) at a rate of 0.5 mL/min.

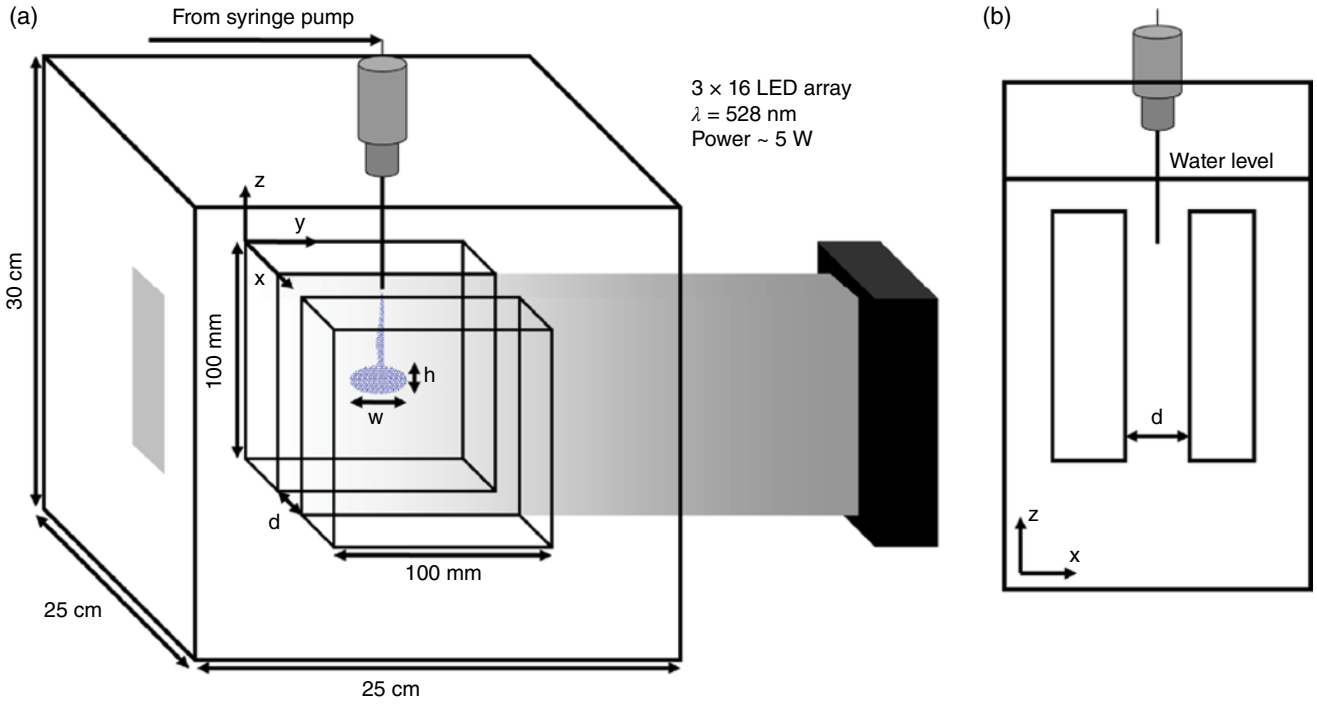

Figure 5.6 A sketch of the experimental set-up for imaging confined swarms (not drawn to scale). (a) Camera view, (b) side view.

A green (528 nm) LED array was used to provide uniform planar illumination along the aperture plane (Figure 5.6), causing the beads to fluoresce. A CCD camera (QImaging, Retiga 2000DC) was placed ~1.2 m from the center of the aperture to capture images of the swarm (y-z plane in Figure 5.6) at a rate of five frames per second during the descent of a swarm. As the swarm fell, an image sequence was recorded and then analyzed to extract properties such as velocity, distance traveled, width, and height of the swarm for each image in the sequence.

5.3. ANALYSIS TECHNIQUES

A custom image analysis code was written in IDL (Interactive Data Language) software to identify a swarm and to determine the location and size of a swarm as function of depth (-z direction in Figure 5.6) and time. A region of interest (ROI) was defined that included only the main body of the swarm (Figure 5.7a). The resulting subset was then thresholded (Figure 5.7b) to remove any background noise and isolate the swarm. The swarm was defined as the largest continuous set of pixels within this region. Sobel edge detection (Figure 5.7c) performed on the ROI enabled the identification of the swarm's edges and returned the height and width of the swarm in terms of the number of pixels. Calibration experiments were performed using an Air Force test chart (MIL-STD-150A, 1951 USAF resolution test chart) to convert these values to SI units. The pixel edge length was 74.4 μm/pixel. This resolution is insufficient to resolve the individual particles in the swarm, which have radii of ~1.5 μm (Table 5.2, Figure 5.3), but is sufficient to measure macroscopic (millimeter scale) swarm attributes such as speed, height, width, and position.

Swarm velocity was obtained by using a moving average method that was performed on the position data prior to calculating swarm speed. The position data extracted from the images was smoothed using the RLOWESS smoothing function in MATLAB. RLOWESS fits a weighted first-order polynomial over a defined region, applying lower weights to outliers. This range was set at 10% of the total number of frames, and was typically 50–60 frames. The velocity quantization of the smoothed data is given by

$$v = \frac{\text{pixel edge length} * N}{10\% \text{ of total time}} = \frac{0.0744\ mm * N}{50\ \text{frames} * 0.2\ spf} = N * 0.00744\ mm/s$$

where N is an integer representing the number of pixels the swarm traveled between two frames and *spf* is the seconds per frame.

While the RLOWESS smoothing was being used as a noise filter, swarms that naturally have highly varying velocities will

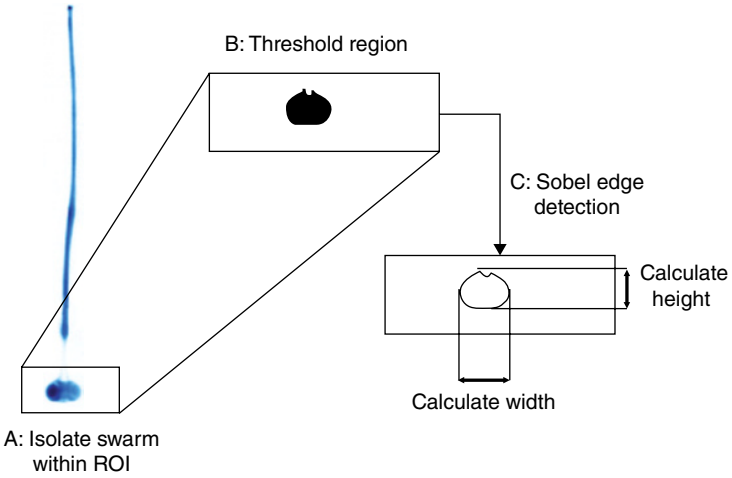

Figure 5.7 A sketch of the process used to analyze an image sequence. (ROI = region of interest)

have this effect reduced by the smoothing function. The smoothed position data was used only for the calculation of swarm velocity. All other experimental results using distance were obtained from the raw, presmoothed distance data.

5.4. RESULTS AND DISCUSSION

Experiments were performed to determine the effect of fracture aperture distribution on swarm evolution. In this section, the experimental results for uniform aperture fractures are discussed first, followed by the results for the converging and diverging fractures. In the last section, particle swarm behavior in rough fractures is presented and examined in terms of the behavior of swarms in the idealized fractures. To facilitate the discussion of results across the different fractures, swarm parameters were normalized by their data from experiments in a wide aperture (40 mm) uniform fracture (Table 5.4).

5.4.1. Uniform Aperture Fractures

The properties of swarms in a uniform aperture fracture (Figure 5.4a) depended on the fracture aperture. Three distinct aperture regimes were observed in the smooth-walled uniform fracture (Figure 5.8): (1) highly confined $\left(\frac{d}{w} \le 1\right)$, (2) optimally confined $\left(1 < \frac{d}{w} < 10\right)$, and (3) unconfined $\left(10 \le \frac{d}{w}\right)$. Here, d is the fracture aperture and w is the width of the swarm along the y axis (Figure 5.6).

In the highly confined region, swarm velocity was less than that observed for an unconfined swarm $\left(\frac{d}{w} \approx 20\right)$. For small apertures the drag force from the walls is quite large (Figure 5.2) as the swarm dimension is comparable to the aperture. In the unconfined region, swarm parameters (size, velocity, bifurcation distance, etc.) tended towards an asymptote (Figure 5.8a, b). This was expected, because the drag force decays as the distance of the swarm from the wall increases (Figure 5.2). If the fracture is sufficiently open (in this case $\frac{d}{w} \approx 15-20$), swarm behavior is indistinguishable from open tank behavior, where the swarm is free to expand in any direction and follow the evolution shown in Figure 5.1.

However, in the optimally confined regime swarms displayed very different behavior than for either of the other two regimes. Swarms that bifurcated had velocities that were a factor of ~2 greater at bifurcation than in the unconfined experiments (Figure 5.8a). In addition, swarms traveled nearly twice as far before bifurcation in the optimal regime than in the open tank (Figure 5.8b). Similarly, swarms in the optimal regime were less likely to bifurcate than swarms in either the highly confined or unconfined regimes (Figure 5.8c).

Table 5.4 Swarm parameters in large-aperture smooth-walled fractures (40-mm aperture). Used to normalize the data in Figures 5.8, 5.13, 5.16, and 5.20.

Parameter	At Bifurcation	At 30-mm Depth	At 60-mm Depth
Swarm Width (w) (mm)	2.296	2.243	1.588
Swarm Height (h) (mm)	1.116	1.084	1.432
Anisotropy (h/w)	0.493	0.497	0.887
Velocity (mm/s)	0.234	0.247	0.138
Distance (mm)	33.929	30	60
Time (s)	124.857	102.8	366.5
Single Particle Reynolds Number	3.5×10^{-4}	3.5×10^{-4}	2.07×10^{-4}

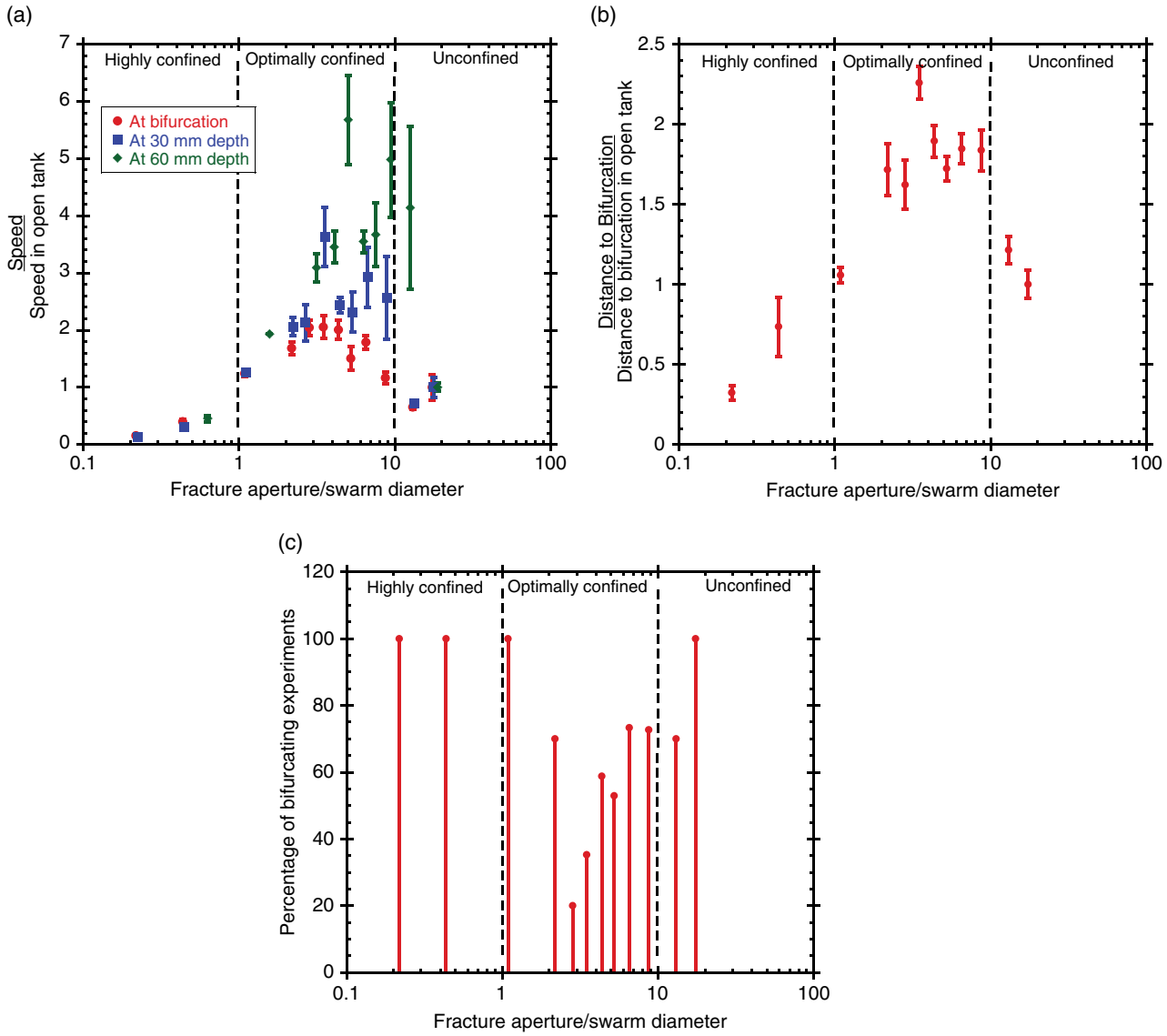

Figure 5.8 Swarm parameters as a function of fracture aperture in the uniform aperture fracture. (a) Speed, (b) distance to bifurcation, (c) percentage of bifurcating swarms.

The optimal regime is also observed at fixed depths in the fracture (Figure 5.8a). At the specified depths of 30 mm ($\sim \frac{1}{3}$ of the fracture) and 60 mm ($\sim \frac{2}{3}$ of the fracture), swarm velocity is enhanced relative to both the highly confined and unconfined regimes. The large error bars on the 60 mm data occur because of the large difference in behavior between swarms that bifurcated and swarms that did not.

An examination of swarm velocity and size as functions of depth (Figure 5.9) reveals insight into swarm behavior in these different regimes. In very small apertures (1 mm aperture, $\frac{d}{w} \approx 0.5$), swarm velocity is nearly constant and is quite small due to the close proximity of the fracture walls, reaching a terminal velocity immediately after release (Figure 5.9a). As a consequence of the close proximity of the fracture walls all swarm expansion is along the fracture plane (y axis in Figure 5.6), resulting in large swarm widths (Figure 5.9b). At larger fracture apertures (2.5 mm aperture, $\frac{d}{w} \approx 1$) the swarm velocity was initially higher; however, the velocity decreased rapidly as a function of depth since the walls were still close. In the open fracture experiments (20 & 40 mm apertures, $\frac{d}{w} \approx 10 \,\&\, 20$), swarm velocity was initially high, but the lack of fracture confinement resulted in free swarm expansion (Figure 5.9b), causing the swarm velocity to decrease and swarm width to increase. However, in the optimal confinement range

(5 & 10 mm apertures, $\frac{d}{w} \approx 2.5 \& 5$), swarm velocities did not significantly decay over the length of the fracture, instead remaining high. This coincided with limited swarm expansion in the optimal range (Figure 5.9b). The size of swarms in the optimal regime only increased ~30% over the length of the fracture as opposed to the doubling in size observed in the other regimes. This difference in expansion rate is a factor in the cause of the enhanced swarm behavior observed in the optimal regime (Figure 5.8). Swarms that do not expand are less likely to bifurcate because the bulk fluid is unable to enter the particle deficient hole in the torus, which inhibits bifurcation. In addition, the increased particle density caused by the lack of expansion results in an enhanced velocity.

In addition to maintaining particle density, the lack of swarm expansion also results in a narrow swarm morphology and a reduced cross section. While it is incorrect to approximate a swarm as a single particle, the hydrodynamic particle interactions depend on the relative positions of the particles. This means that, all else being equal (number of particles, particle properties, fluid properties, etc.), a swarm with a small cross section should travel faster than a swarm with a large cross section. The combination of small cross section and increased particle density results in a high swarm velocity relative to swarms in an open tank.

While the exact confinement mechanism is still under investigation, it is likely that the observed behavior is a result of the different levels of confinement arising from two orthogonal forces similar to those shown in equations 5.5a and b. In very small apertures $\left(\frac{d}{w} \leq 1\right)$ swarm behavior is dominated by the tangential drag from the wall. As the aperture increases a crossover occurs, and the swarm becomes controlled not by tangential drag but by normal confinement. This confinement maintains swarm density and affects swarm geometry as it falls (Figure 5.9b), causing the swarm to fall faster (Figure 5.8a) and maintain cohesion over greater distances (Figure 5.8b). At sufficiently large apertures $\left(10 \leq \frac{d}{w}\right)$ the confinement force has decreased so that the swarm is not influenced by the presence of either force and is able to freely follow an unconfined evolutionary path to bifurcation, as shown in Figure 5.1.

These results show that the presence of a fracture effects particle swarms in ways that are different from the effect on a single particle (Figure 5.2). Instead of transitioning smoothly to an unconfined regime, swarm velocity and evolution are changed by the fracture and are fundamentally different in the optimally confined regime than in the unconfined and confined regimes.

5.4.2. Diverging and Converging Distributions

Variations in fracture aperture were also determined to affect swarm behavior. These effects depended on whether the fracture aperture was increasing or decreasing and resulted in dramatic changes in the evolution of a particle swarm. The confinement effects observed in the uniform aperture fracture still appear to exist, although they are partially masked by additional effects that arise from the variable fracture apertures.

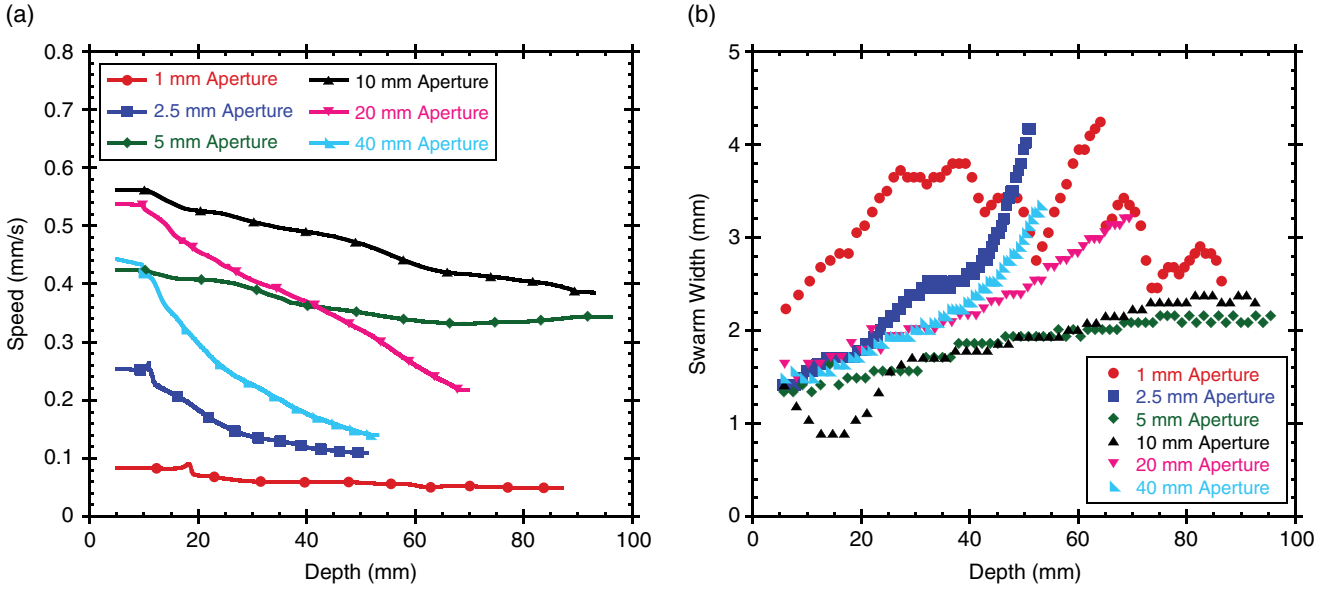

Figure 5.9 Swarm parameters vs. depth for representative swarms in various fracture apertures in the uniform aperture fracture. (a) Speed, (b) swarm width.

5.4.2.1. Converging fracture

In the converging portion (depths from 0 to 50 mm) of the fracture (Figure 5.4b), swarms behaved similarly across all measured fracture apertures. The swarms were observed to travel with similar speeds and topologies (Figures 5.10 and 5.11) because the fracture boundaries were sufficiently far apart that swarms were traveling in a mostly unconfined regime $\left(\frac{d}{w} > 10\right)$. However, as a swarm approached the transition between the converging region and the uniform aperture region, variations in wall separation became important (Figures 5.10 and 5.11).

Swarms in the converging region of the fracture behaved similarly to swarms in the unconfined regime of the uniform aperture fracture. Swarm velocity decayed rapidly and equally across all fracture apertures until the swarms reached the uniform aperture region (Figure 5.10a, compare to Figure 5.9a). This is confirmed by the composite image (Figure 5.11). Figure 5.11 shows swarms from multiple fracture apertures at fixed time intervals (20*s*) in a side-by-side comparison. Swarms in the converging aperture region have similar shapes and speeds across a wide range of fracture apertures.

At very small apertures $\left(\frac{d}{w} \le 1\right)$, swarms began to decelerate dramatically (Figure 5.10a, 1 mm & 2.5 mm apertures) and expand rapidly (Figure 5.10b) approximately 10 mm before the converging/uniform transition and did not enter the uniform portion of the fracture. These swarms bifurcated even though their vertical motion had been greatly decreased. The swarms expanded along the fracture plane (Figure 5.12). At larger apertures $\left(\frac{d}{w} > 1\right)$, swarm motion was not arrested by the transition from converging to parallel walled fracture, and the swarms continued their evolution with most eventually bifurcating deeper in the fracture (Figure 5.13b).

Swarms that entered the uniform aperture region (depths from 50 to 100 mm) of the fracture tended to have velocities that were very similar across fracture aperture (Figures 5.10a and 5.13a) and higher than were observed in the open tank experiments. In the uniform aperture region, the swarm deceleration was less than that observed in the converging region (Figure 5.10a). Swarm velocity (Figure 5.13a) and distance to bifurcation (Figure 5.13b) for these swarms are all higher than those in the unconfined regime and are similar to the optimal regime in the uniform aperture fracture (Figure 5.8a and b). However, nearly all of the swarms in the converging fracture bifurcated (Figure 5.13c), unlike the swarms in the uniform aperture fracture (Figure 5.8c). This occurred because in the converging fracture, swarms formed torii and expanded while in the relatively unconfined upper region. As a result, the confinement from the uniform aperture portion of the fracture merely delayed bifurcation rather than preventing it, as occurred in the uniform aperture fracture. At very large apertures, swarm velocity and distance to bifurcation returned to their unconfined values (Table 5.4).

The results from the converging fracture are significant because it demonstrates that the swarms still respond to the aperture variation even though the initial aperture was large. As noted in Section 5.2.2, the aperture where the swarm was released was 50 mm $\left(\frac{d}{w} \approx 25\right)$ or more for the converging fracture. Consequently, swarms in the converging

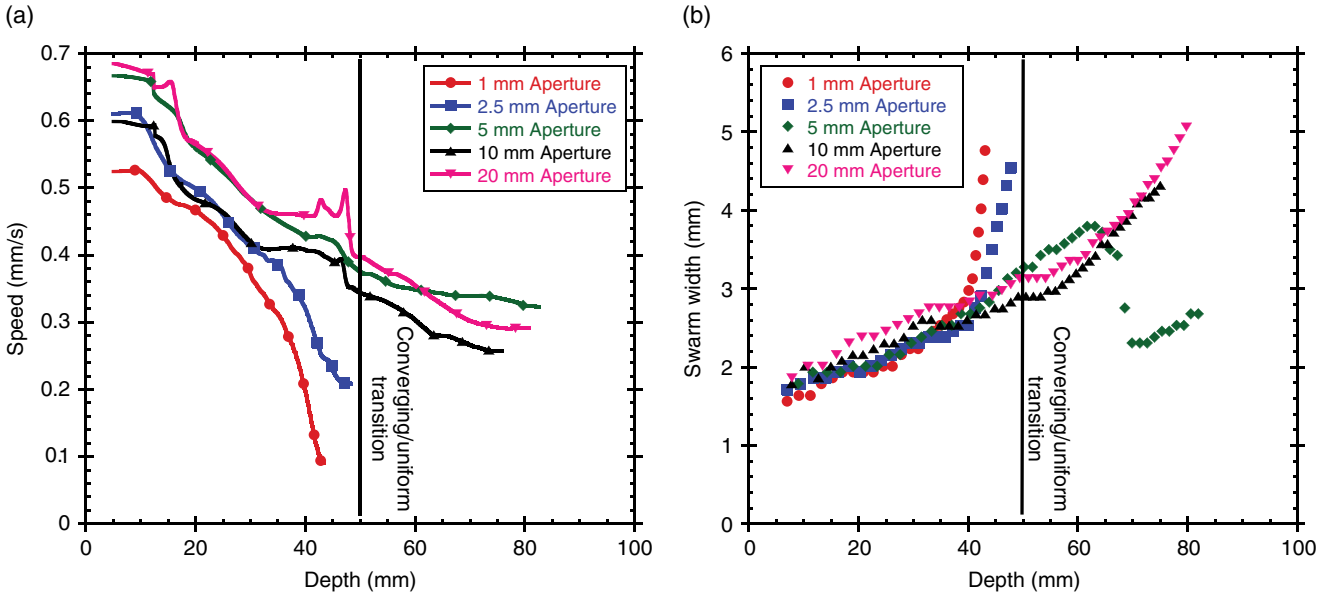

Figure 5.10 Swarm parameters vs. depth for representative swarms in various fracture apertures in the converging fracture. (a) Speed, (b) swarm width.

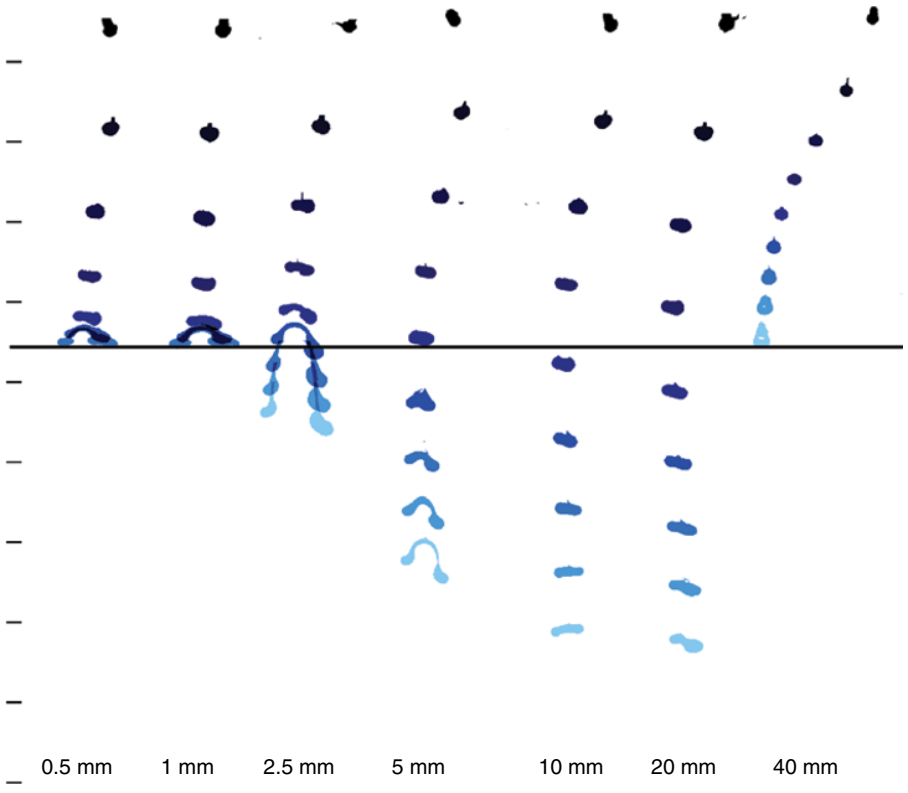

Figure 5.11 A side-by-side comparison showing how swarms traveled through various apertures in a converging fracture at fixed time steps. The horizontal line marks the transition between the converging and uniform aperture portions of the fracture. False color.

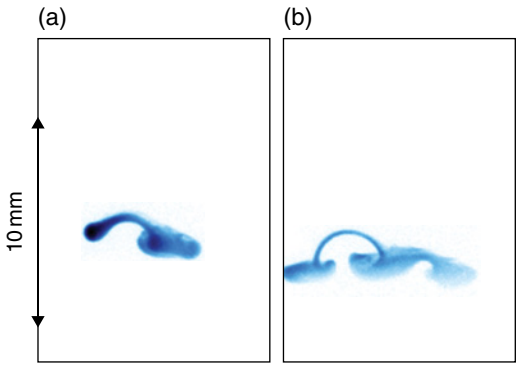

Figure 5.12 Images of swarm expansion along the transition point in the converging fracture taken 50 s apart for the 0.5 mm separation. False color.

region behaved similarly to swarms in the open tank, i.e., with steady deceleration and expansion. However, upon approaching the converging/parallel transition swarm behavior changed; bifurcations were suppressed and velocities enhanced as in the uniform aperture fracture. Swarms sensed the upcoming aperture constriction approximately 10 mm before reaching it and responded by either decelerating and bifurcating (Figures 5.10 and 5.12) or by preventing swarm bifurcation and maintaining swarm cohesion (Figure 5.13b). The dominant effect depends on absolute fracture aperture and is likely also controlled by the rate of aperture decrease.

5.4.2.2. Diverging fracture

In the diverging fracture (Figure 5.4c) the sudden loss of confinement at the transition from uniform to diverging aperture often resulted in dramatic changes in swarm morphology when compared to both the uniform aperture and converging fractures (Figure 5.14). Upon reaching the diverging aperture in the fracture, many swarms would suddenly change shape (Figure 5.14a to b) and accelerate (Figure 5.15a). This change was termed "falling over" because swarms tended to remain tori that rotated with their normal orientation along the y axis rather than the typical z axis (Figures 5.6 and 5.14c). Instead of expanding along the fracture plane (yz plane) like most other swarms (example, Figure 5.12), swarms that fell over expanded along the x axis and contracted along the the y axis (Figure 5.15b). This behavior was captured by placing a second camera on the y axis (Figure 5.6) facing the LED array to image the xz plane. As a result of this different evolutionary path, swarms in the diverging aperture fracture tended not to bifurcate (Figure 5.16c).

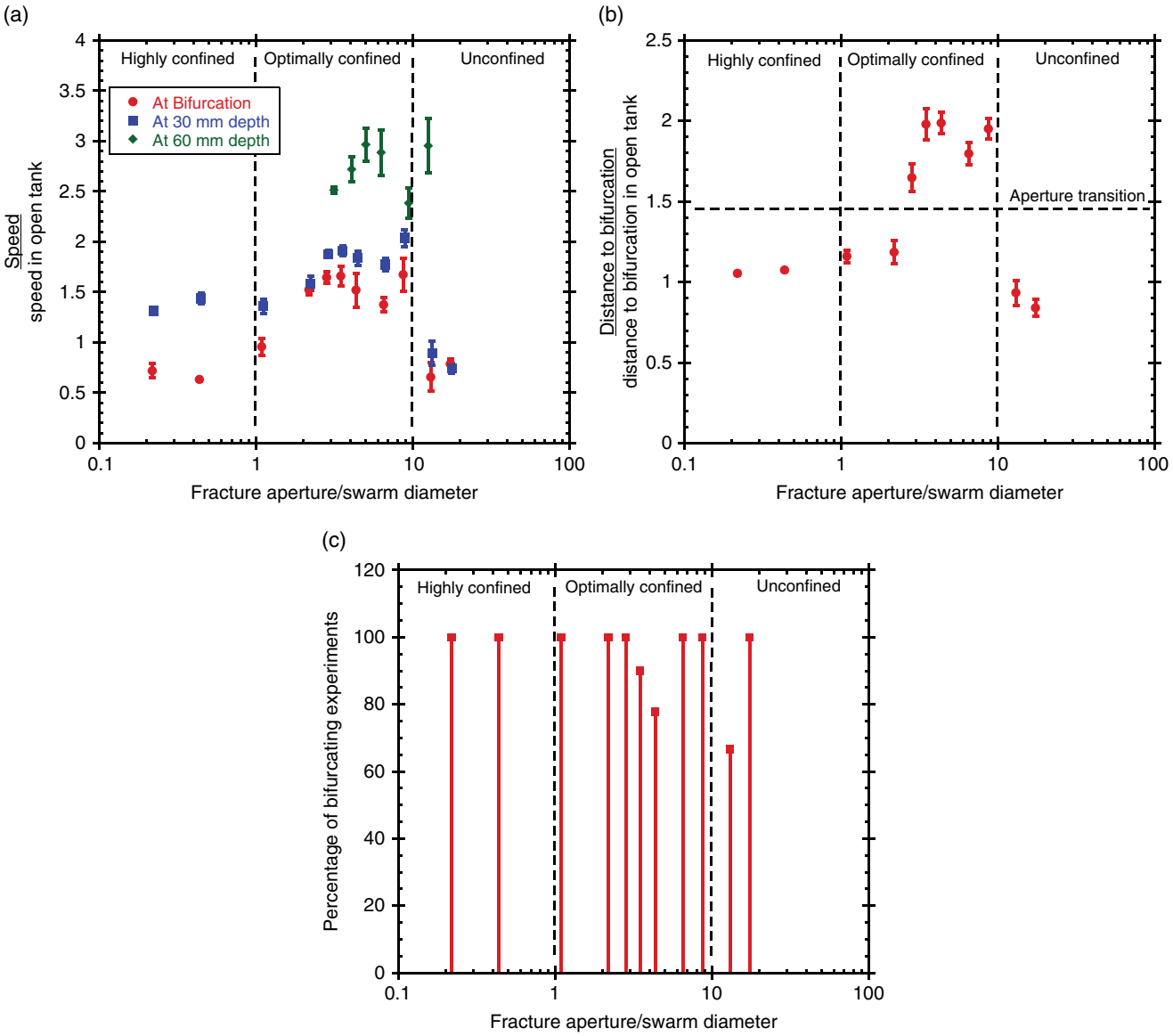

Figure 5.13 Swarm parameters as a function of fracture aperture in the converging fracture. (a) Speed, (b) distance to bifurcation, (c) percentage of bifurcating swarms.

Swarms in the uniform aperture fracture tended to decelerate depending on the aperture (Figure 5.9a). However, swarms traveling through the uniform aperture region of the diverging fracture (depths from 0 to 50 mm) did not decelerate (Figure 5.15a). Instead, swarms either maintained a constant velocity (2.5 & 5 mm apertures, $\frac{d}{w} \approx 1 \& 2.5$) before accelerating, or accelerated over the entire length of the fracture (10 & 15 mm apertures, $\frac{d}{w} \approx 5 \& 7.5$). This indicates that just as swarms in the converging fracture sensed the variation in aperture preceding the uniform aperture region, swarms in the uniform region of the diverging fracture sensed the upcoming diverging region.

An examination of the fixed depth speeds also demonstrates that swarms respond to the entire fracture geometry. The fixed depth of 30 mm is well within the uniform aperture region of the diverging fracture. However, swarms in the diverging fracture (Figure 5.16a) travel faster than swarms in the uniform aperture fracture (Figure 5.8a) by a factor of ~2.

The three smooth-walled "idealized" fractures (Figure 5.4a, b, c) provided insight into the response of a swarm to rigid boundaries. Swarm behavior is greatly modified by the presence of a fracture and its geometry. There is an optimal range of fracture apertures $\left(1 < \frac{d}{w} < 10\right)$ in which the fracture limits swarm expansion (Figure 5.9b), resulting in enhanced speeds (Figure 5.8a)

and suppressed bifurcations (Figure 5.8c). The converging fracture resulted in an enhanced bifurcation rate compared to the uniform aperture fracture (Figure 5.13c), and the transition from converging to uniform region resulted in swarms rapidly decelerating and bifurcating (Figure 5.10a). In the diverging fracture, the sudden loss of confinement resulted in a change in swarm geometry (Figure 5.14) that suppressed swarm bifurcation (Figure 5.16c) and caused swarms to travel faster (Figure 5.15a) than in the uniform aperture case. Finally, swarms "sense" the resistance of the entire travel path responding to aperture variations that are farther down the fracture.

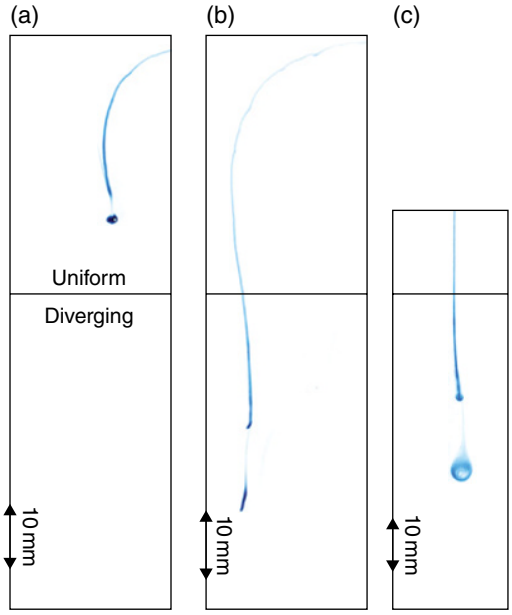

Figure 5.14 A figure showing swarm behavior in the diverging fracture. (a) Swarms in the diverging fracture began as a normal sphere/torus. (b) Upon reaching the diverging portion of the fracture the swarm would rotate. (c) A side view of B is shown in. False color.

5.4.3. Rough-Walled Fractures

The results from the uniform and variable aperture fractures provide a physical understanding of the response of swarms to variations in fracture aperture (i.e., converging/diverging apertures). Swarms react very strongly to variable aperture fractures, responding to transitions even before reaching them. However, real fractures are far more complex, containing regions with both converging and diverging features, nonuniform fracture planes, nonsymmetric topology, optimal flow paths, etc. These features cause swarms to change behavior (i.e., evolve) in response to the highly varied nature of a rough fracture.

With the knowledge gained from the smooth-walled fracture studies, the behavior of a particle swarm as it falls through a rough-walled fracture is understood. At small apertures $\left(0-2.5mm, \frac{d}{w} \leq 1\right)$, swarm behavior is strongly controlled by the fracture roughness (Figures 5.17 and 5.18). Figures 5.17 and 5.18 each contain a graph of velocity vs. depth (left), a contour plot of fracture asperity height with a typical swarm path shown by a black line (center), and a graph of asperity height vs. depth along the marked path (right). Large asperity heights correspond to small apertures. As in the uniform aperture fracture, swarms decelerated while in regions with small

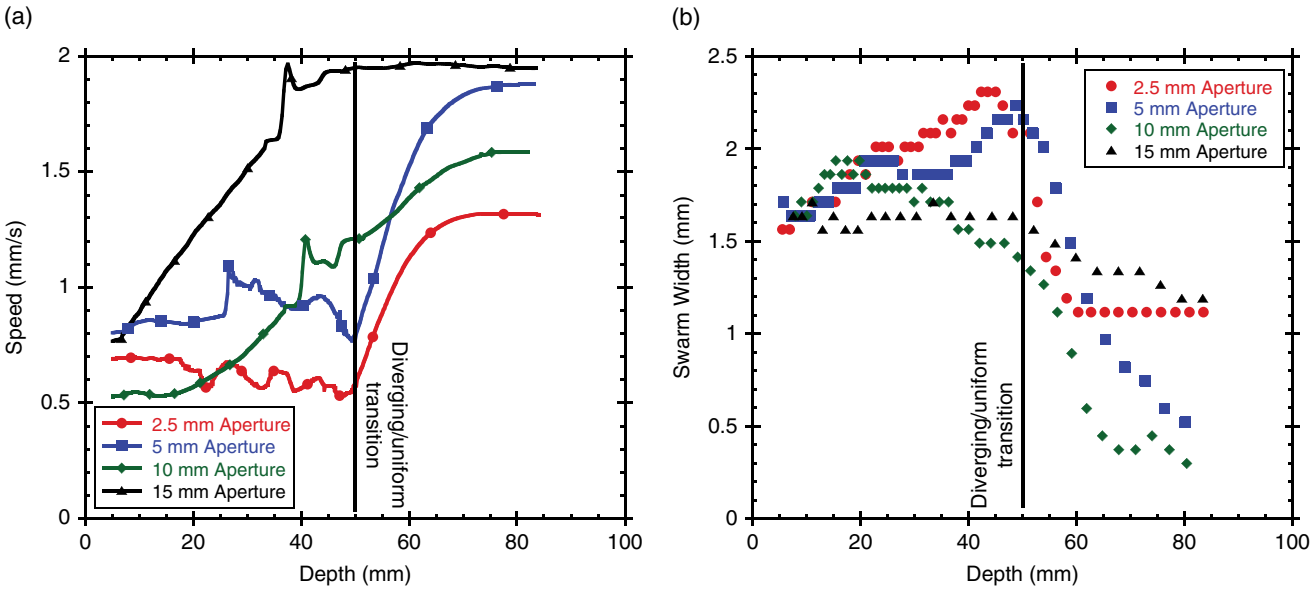

Figure 5.15 Swarm parameters vs. depth for representative swarms in various fracture apertures in the diverging fracture. (a) Speed, (b) swarm width.

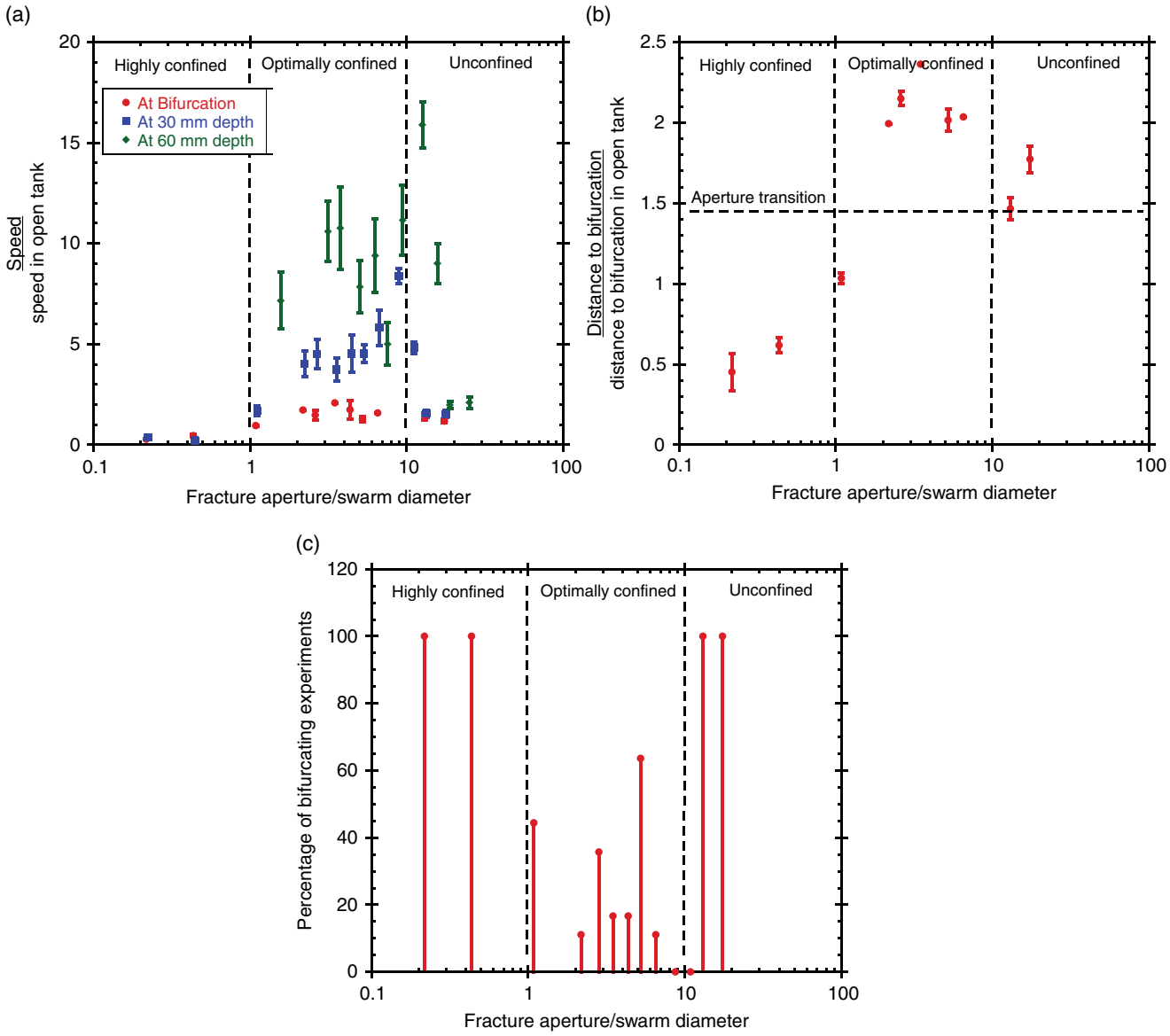

Figure 5.16 Swarm parameters as a function of fracture aperture in the diverging fracture. (a) Speed, (b) distance to bifurcation, (c) percentage of bifurcating swarms.

apertures, for example, between points *b* and *c* in Figure 5.17 and between points *a* and *b* in Figure 5.18. When a swarm moved into regions with increasing fracture aperture (points *b*–*c* in Figure 5.18) they accelerated and changed shape (Figure 5.19 right). Swarms decelerated as they approached asperity peaks (Figure 5.17, points *b*–*c*, and Figure 5.18, points *c*–*d*). At large fracture apertures $\left(>10mm,\ \frac{d}{w}>5\right)$ the asperity variation from the fracture (~6 mm) became less significant and swarms no longer responded as strongly to the fracture roughness (Figure 5.21a), instead transitioning to behavior that was similar to the uniform aperture fracture (Figure 5.9a).

Swarm behavior is controlled by changes in the level of confinement from the fracture wall. Swarms traveling through rough-walled fractures responded to the varying fracture aperture by changing both speed and shape in ways that were consistent with the results observed in the smooth-walled converging and diverging fractures described in the previous section. For example, when the fracture aperture increased, as at point *b* in Figure 5.18, swarms tended to elongate and accelerate (Figure 5.19 right), as was seen in the diverging fracture (Figures 5.14 and 5.15). In Fracture 2, confinement from an asperity ridge over depths of 20–50 mm and horizontal position of 10–20 mm caused the swarm to rotate or "fall over" (Figure 5.19 right). This additional confinement was not present in the smooth-walled diverging fracture.

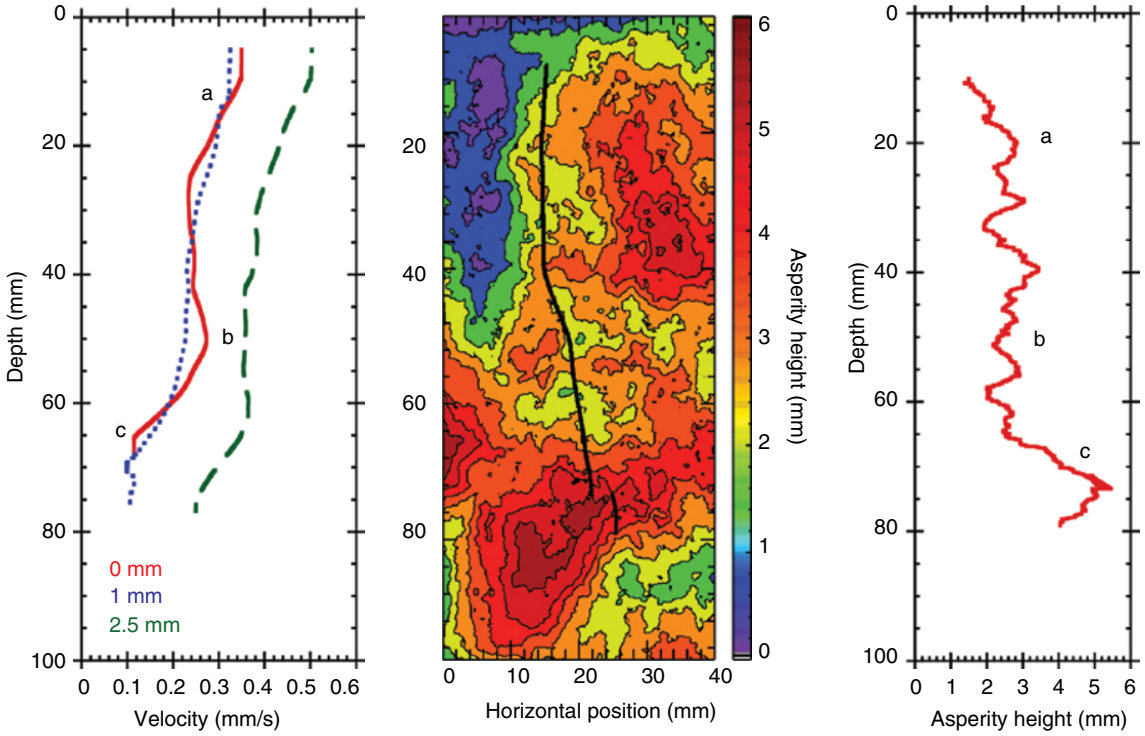

Figure 5.17 A collection of plots pertaining to Fracture 1. (Left) A graph of swarm velocity vs. depth, (Center) a contour plot of fracture asperity height marked with a typical swarm path, (Right) a graph of asperity height along the swarm path. (a) Mild deceleration due to low levels of confinement, (b) deceleration due to approaching asperity peak, (c) swarm bifurcates around the asperity peak.

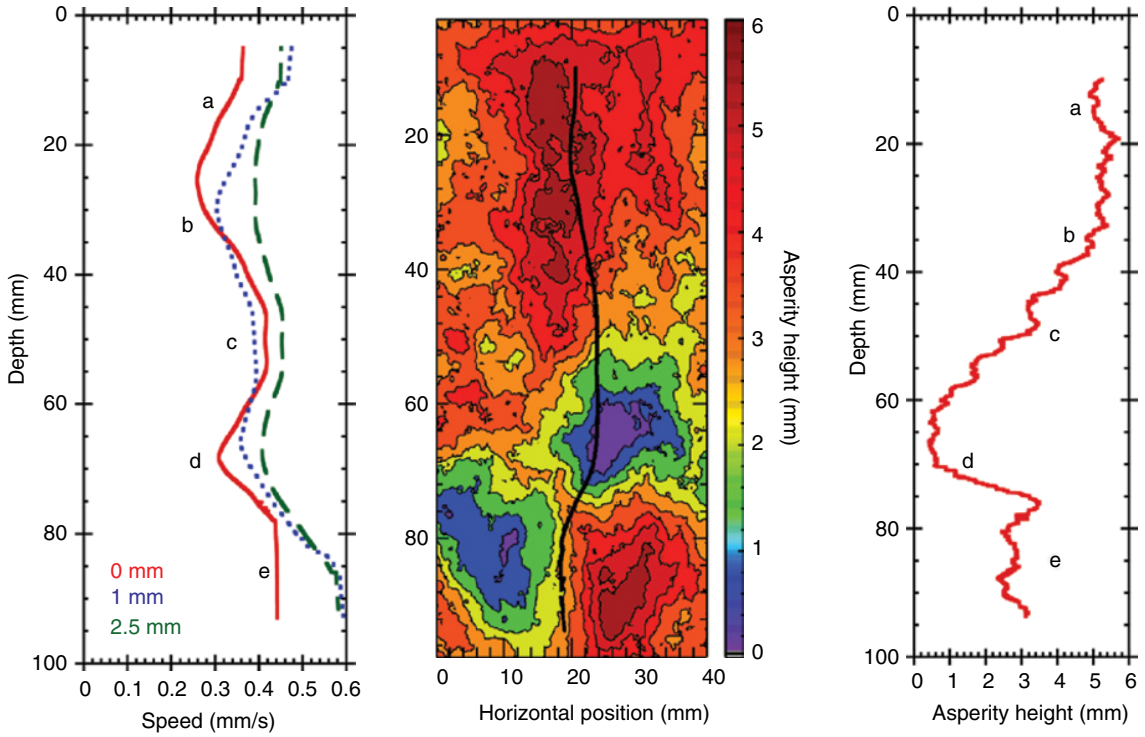

Figure 5.18 A collection of plots pertaining to Fracture 2. (Left) A graph of swarm velocity vs. depth, (Center) a contour plot of fracture asperity height marked with a typical swarm path, (Right) a graph of asperity height along the swarm path. (a) Deceleration due to strong confinement, (b) acceleration due to fracture opening, (c) swarm begins to decelerate due to approaching asperity peak, (d) swarm avoids asperity peak by reorganizing, (e) swarm travels in open region.

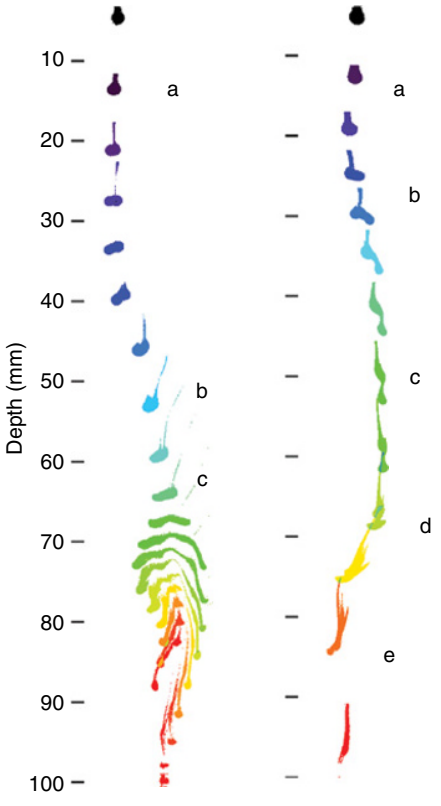

Figure 5.19 Composite image showing the dominant swarm response to Fracture 1 *(left)* and Fracture 2 *(right)*. The fracture aperture in both images is 0 mm. Each tick mark is 10 mm apart. The labels correspond to Figure 5.17 (left) and Figure 5.18 (right).

As in the uniform aperture fracture, swarms in Fracture 1 traveled more slowly in small apertures (Figure 5.20a). However, the asperity height variation (Figure 5.5) complicates direct comparisons between the rough and uniform aperture fractures. On average, the rough fracture has an absolute fracture aperture $\frac{d}{w} \approx 1.5$ greater than the uniform aperture fracture. This has the effect of shifting the optimal and unconfined region to smaller values of $\frac{d}{w}$ than for the uniform aperture graph. The shift eliminates the very small aperture highly confined (high drag) regime $\left(\frac{d}{w} < 1\right)$ because there are few regions in the fracture with sufficiently high asperities (Figure 5.5c) to result in $\frac{d}{w} < 1$.

An examination of swarm speed and size vs. position in Fracture 1 (Figure 5.21) reveals interesting behavior. At small apertures $\left(0{,}1, 2.5\,mm, \frac{d}{w} \le 1\right)$ swarm behavior was dominated by the fracture roughness, decelerating and expanding in response to asperity variations as shown in Figure 5.17. At intermediate apertures $\left(5{,}10mm, \frac{d}{w} = 2.5{,}5\right)$ swarms no longer responded strongly to the fracture asperity "height" and displayed behavior similar to the uniform aperture fractures' optimal regime (i.e., minimal deceleration and lower rates of expansion). In large apertures $\left(20mm, \frac{d}{w} = 10\right)$ swarm velocity behaved similarly to the behavior in the parallel fracture (Figure 5.9a), rapidly decelerating due to the lack of confinement. However, the swarm width did not increase rapidly in the rough fracture (Figure 5.21b) as it did in the uniform aperture fracture (Figure 5.9b). This is likely due to the differences in confinement between the two fractures.

Swarms in Fracture 2 exhibited a very strong relationship between shape, velocity, and asperity height (Figures 5.18, 5.19b, and 5.22). As discussed previously, swarms in rough fractures accelerate and decelerate in response to variations in asperity height. These changes in speed correspond to changes in swarm geometry (Figure 5.22b). Accelerations corresponded to a decrease in swarm widths while decelerations corresponded to increasing swarm widths. This is the same behavior that was observed in the other smooth-walled fractures that were investigated (Figures 5.9, 5.10, and 5.15).

Swarms approaching asperity peaks (aperture minima) decelerated before reaching the obstruction (Figures 5.17b and 5.18c), as was observed in the converging fracture (Figure 5.10a). However, unlike the converging fracture, where the obstruction was uniform across the entire fracture plane, the asperity peaks in the rough fractures had finite extents. As a result, swarms in small-aperture rough fractures avoided the asperity peak and continued without stopping. The shape of the obstruction controlled the swarm's response. In Fracture 1, swarms tended to bifurcate around the relatively large asperity peak, while in Fracture 2 the swarms did not bifurcate and instead reformed before traveling into the open region adjacent to the peak (Figure 5.19).

5.5. CONCLUSIONS

The experimental results presented in the previous section demonstrate that swarm transport in a fracture is affected by the topology of the fracture, specifically the size and spatial variation in aperture. The walls of a fracture exert normal and tangential drag forces on a swarm in addition to the viscous drag that occurs as an object moves through a fluid. For a single solid sphere, the drag forces from the fracture walls would cause the sphere to decelerate as it falls under gravity with the amount of deceleration decreasing monotonically as the aperture of the fracture increased. While a swarm is subjected to the same drag forces, the resulting behavior of the swarm confined by a fracture differs from that for a single solid sphere. An optimal range of fracture apertures $\left(1 < \frac{d}{w} < 10\right)$ were

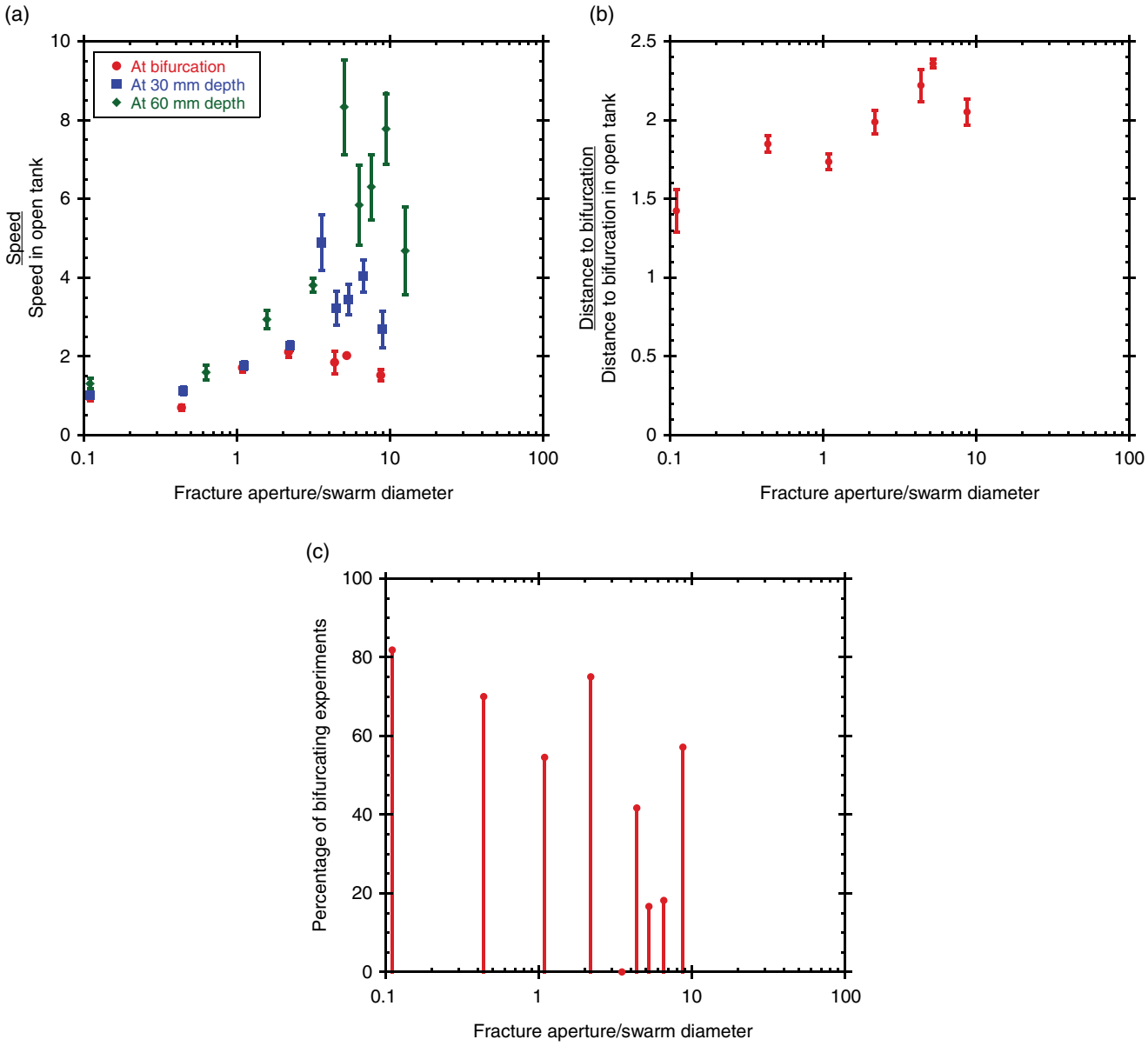

Figure 5.20 Swarm parameters as a function of fracture aperture in rough fracture 1. (a) Speed, (b) distance to bifurcation, (c) percentage of bifurcating swarms.

observed in which swarms traveled faster, farther, and with fewer bifurcations than in fractures with smaller $\left(\frac{d}{w}<1\right)$ or larger $\left(\frac{d}{w}>10\right)$ apertures. This optimal range is not observed for a single solid sphere because solid spheres do not expand or contract as they fall between parallel walls. As described in the introduction, expansion and contraction is a natural part of swarm evolution as it falls under gravity. For large apertures $\left(\frac{d}{w}>10\right)$, swarm width increased by a factor of 2 while in the optimal aperture range a swarm only expanded by 30% of its original diameter. The suppression of expansion by the fracture walls maintains a small cross-sectional diameter of a swarm, thereby decreasing the global drag on the swarm, preventing or delaying the formation of the open torus stage of swarm evolution that leads to swarm destabilization, and maintaining a swarm's particle density which sustains a swarm's velocity. Current models of swarm evolution based on Stokeslets do not capture this observed behavior for several reasons: the drag forces on a single particle from the walls is negligibly small $\left(\frac{a}{d}\sim 10^{-3}\right)$, modeling 1,000,000 or more particles to represent swarms

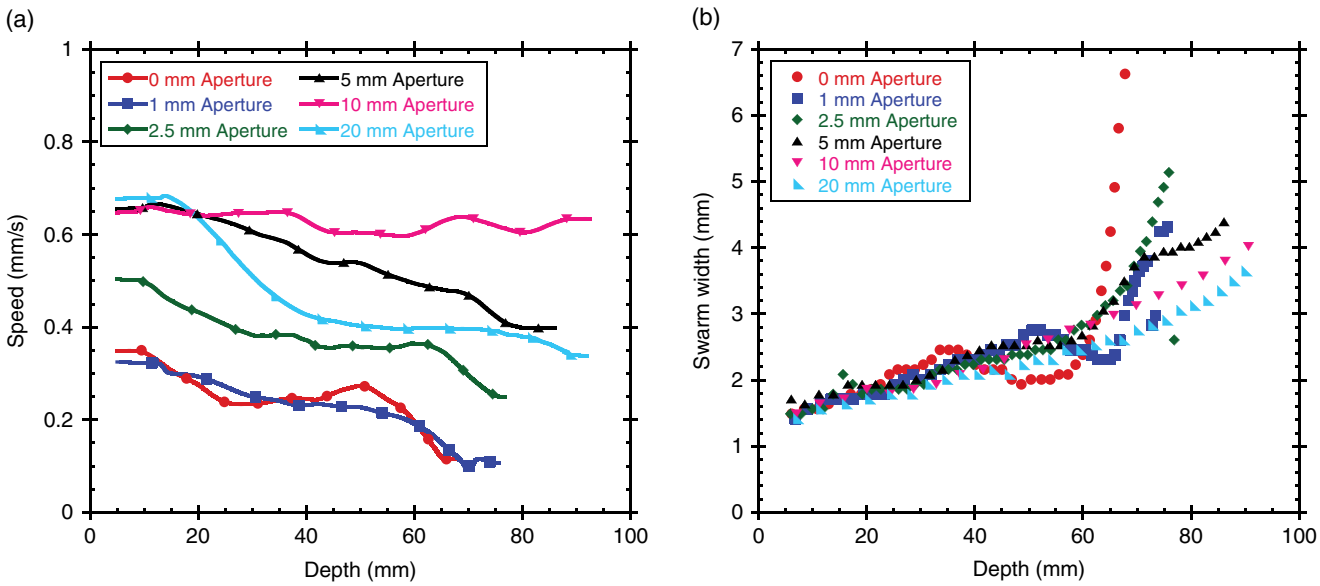

Figure 5.21 Swarm parameters vs. depth for representative swarms in various fracture apertures in rough fracture 1. (a) Speed (b) swarm width.

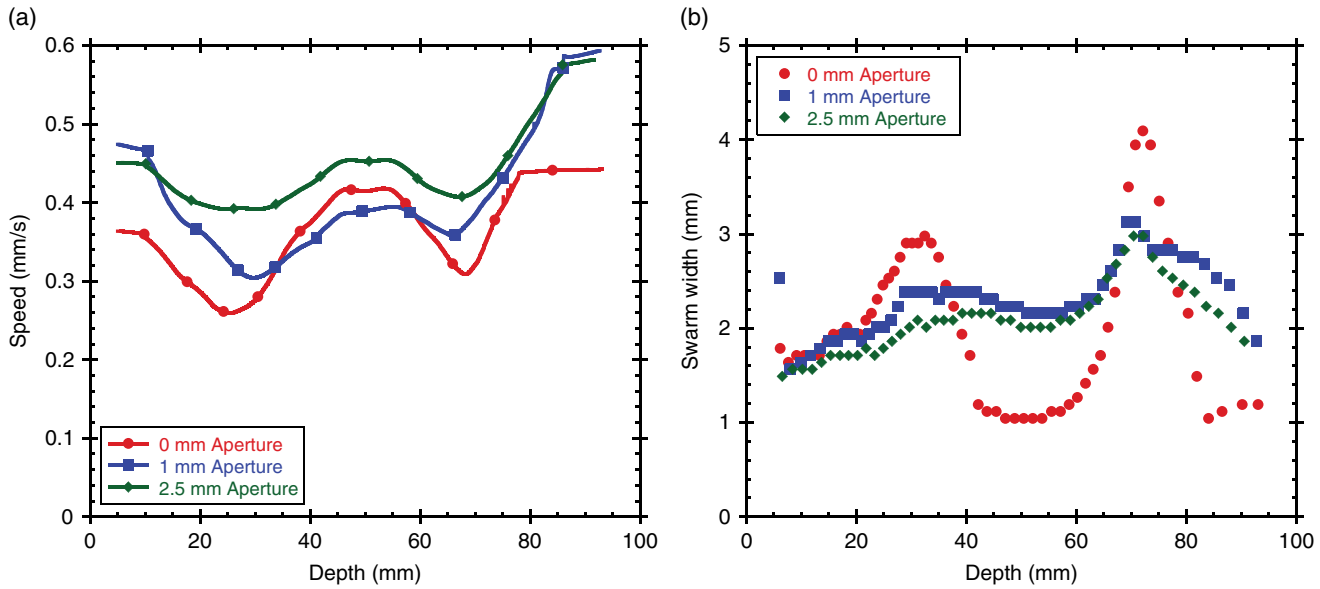

Figure 5.22 Swarm parameters vs. depth for representative swarms in various fracture apertures in rough fracture 2. (a) Speed (b) swarm width.

is computationally intensive, Stokeslets assume a true Stokes regime, which may not be applicable for swarms in low-viscosity fluids where inertial effects arise. Future work must include the development of an approach or theory to model both the individual particle behavior that provides the evolution of swarm topology and the collective behavior of the swarm on the bulk fluids.

The importance of possible inertial effects was observed in the swarm behavior for fractures with a variation in aperture and the rough-walled fractures. Swarms were observed to accelerate or decelerate in response to aperture expansions and constrictions along the transport path prior to the swarm reaching such features. A swarm responded to the resistance of the entire fracture geometry as opposed to only local variations in apertures. For example, swarms were observed to travel faster in the uniform portion of the diverging fracture sample compared to a swarm at the same depth in the uniform aperture fracture sample. The uniform portion of the diverging fracture was half the length of the uniform fracture

sample, while the swarm speed differed by a factor of 2. These results suggests that an induced flow can occur in a fracture as a swarm falls in a low-viscosity fluid, giving rise to possible Poiseuille flow behavior in a fracture. Additional research is needed to confirm this observation.

The cohesive nature of particle swarms is beneficial when quick and localized transport is desired, such as releasing micro- or nanosensors into fractured rock in the subsurface. However, this same behavior is not advantageous for colloidal-scale particulate contaminants that arise naturally or from manufacturing of such diverse products as cosmetics to microelectronics. A swarm of particulate contaminants would travel greater distances more rapidly and with greater localization than a disperse cloud of particles. The swarms in this study traveled 1000 times faster than the settling speed of a single particle. This has important implications in understanding particle sedimentation and contaminant spreading in the subsurface. If particulates are able to self-coalesce into swarms (or are released in a droplike manner), then they will travel farther and faster than a disperse solution, leading to different environmental impacts than sedimentation.

ACKNOWLEDGMENTS

The authors wish to acknowledge support of this work by the Geosciences Research Program, Office of Basic Energy Sciences, U.S. Department of Energy (DE-FG02-09ER16022), and by Nicholas J. Nolte for his assistance with image analysis.

REFERENCES

Adachi, K., S. Kiriyama, and N. Yoshioka (1978), The behavior of a swarm of particles moving in a viscous fluid, *Chemical Engineering Science*, *33*, 115–121.

Blake, J. R. (1971), A note on the image system for a Stokeslet in a no-slip boundary, *Proceedings of the Cambridge Philosophical Society*, *70*, 303–310.

Bosse, T., L. Kleiser, C. Härtel, and E. Meiberg (2005), Numerical simulation of finite Reynolds number suspension drops settling under gravity, *Physics of Fluids*, *17*, 037101.

Durham, L. S. (2011), Nanotech research making strides, *AAPG Explorer*.

Ekiel-Jezewska, M. L., B. Metzger, and E. Guazzelli (2006), Spherical cloud of point particles falling in a viscous fluid, *Physics of Fluids*, *18*.

Happel, J., and H. Brenner (1965), *Low Reynolds Number Hydrodynamics*, Prentice-Hall, Englewood Cliffs, New Jersey.

Kirby, B. J. (2010), *Micro- and Nanoscale Fluid Mechanics Transport in Microfluidic Devices*, Cambridge University Press, New York.

Lorentz, H. A. (1907), *Abhandlungen Uber Theoretische Physik*, Druck und Verlag Von B. G. Teubner, Berlin.

Machu, G., W. Meile, L. Nitsche, and U. Schaflinger (2001a), The motion of a swarm of particles traveling through a quiescent viscous fluid, *Zeitschrift Fur Angewandte Mathematik Und Mechanik*, *81*, S547–S548.

Machu, G. W. Meile, L. C. Nitsche, and U. Schaflinger (2001b), Coalescence, torus formation and breakup of sedimenting drops: Experiments and computer simulations, *Journal of Fluid Mechanics*, *447*, 299–336.

Metzger, B., M. Nicolas, and Élisabeth Guazzelli (2007), Falling clouds of particles in viscous fluids, *Journal of Fluid Mechanics*, *580*, 283–301.

Mylyk, A., and M. L. Ekiel-Jezewska (2010), How walls influence destabilization of a suspension drop settling under gravity in a viscous fluid, *Colloids and Surfaces A-Physiochemical and Engineering Aspects*, *365*, 109.

Mylyk, A., W. Meile, G. Brenn, and M. L. Ekiel-Jezewska (2011), Break-up of suspension drops settling under gravity in a viscous fluid close to a vertical wall, *Physics of Fluids*, *23*, 063302.

Nitsche, J. M., and G. K. Batchelor (1997), Break-up of a falling drop containing dispersed particles, *Journal of Fluid Mechanics*, *340*, 161–175.

Pignatel, F., M. Nicolas, and E. Guazzelli (2011), A falling cloud of particles at a small but finite Reynolds number, *Journal of Fluid Mechanics*, *671*, 34–51.

Prodanovic, M., S. Ryoo, A. R. Rahmani, R. Kuranov, C. Kotsmar, T. E. Milner, K. P. Johnston, S. L. Bryant, and C. Huh (2009), Effects of magnetic fields on the motion of multiphase fluids containing paramagnetic particles in porous fluids, in *2009 SPE Annual Technical Conference and Exhibition*, Society of Petroleum Engineering, New Orleans, Louisiana.

Swan, J. W., and J. F. Brady (2010), Particle motion between parallel walls: Hydrodynamics and simulation, *Physics of Fluids*, *22*, 103301.

Yang, Y., M. Becker, J. Englehart, H. Zhu, V. Colvin, L. M. Abriola, and K. D. Pennell (2011), Stable nanoparticles for high salinity applications, in *242nd American Chemical Society National Meeting and Exposition*, American Chemical Society, Denver, Colorado.

6

The Effect of Chemical Osmosis on Oil and Gas Production from Fractured Shale Formations

Perapon Fakcharoenphol[1], Basak Kurtoglu[2], Hossein Kazemi[1], Sarinya Charoenwongsa[1], and Yu-Shu Wu[1]

ABSTRACT

Shale swelling during drilling is attributed to osmotic pressure, where low-salinity water enters the shale pores to cause swelling. Low-salinity water injected into high-salinity Bakken formation could similarly enter the matrix pores to displace oil by countercurrent flow observed in core experiments. As a result, we believe, low-salinity water can potentially enhance oil recovery from oil-wet Bakken formation.In this chapter, we report on experimental and numerical modeling studies we conducted to evaluate the potential of low-salinity water flooding in Bakken. For laboratory experiments, we used horizontal core plugs drilled parallel to the bedding plane.The mathematical model included osmotic pressure, gravity, and capillary effects. In the mathematical model, the osmotic pressure mass transfer equations were calibrated by matching time-dependent salinities in a published laboratory osmotic pressure experiment. We also modeled oil recovery for a Bakken core using our osmotic pressure mass transport model. The results indicate that osmotic pressure promotes countercurrent flow of oil from both the water-wet and oil-wet segments of the core.

6.1. INTRODUCTION

Osmosis is the transport of water molecules from the low-salinity side of a semipermeable membrane to the high-salinity side to equalize the concentration of the dissolved salts. This causes an increase of pressure on the higher-salinity side, called osmotic pressure (π, Figure 6.1). In subsurface environment, high-clay shale sediments can behave as a semipermeable membrane, thus causing osmotic water transport [*Kemper*, 1961, *Milne et al*., 1964; *Young and Low*, 1965; *Chenevert*, 1970; *Olsen*, 1972; *Greenberg et al*., 1973; *Marine and Fritz*, 1981; *van Oort et al*., 1995; Keijzer, 2000].

Marine and Fritz [1981], *Neuzil* [2000], and *Neuzil and Provost* [2009] reported that high-pressure anomalies in geological formations could be osmotic pressure. Furthermore, high-salinity brine in some formations could be explained by reverse osmosis because during burial, porous rock is continuously compressed by the increasing overburden weight [*De Sitter*, 1947; *Bredehoeft et al*., 1963]. Consequently, water molecules expel from the formation leaving salt behind. Because high-salinity brine (up to 280,000 ppm) is found in shale formations, it may indicate the semipermeable membrane property of the shale [*Kurtoglu*, 2013].

6.2. CLAY AS SEMIPERMEABLE MEMBRANE

The electric double layer (EDL) and diffused layer (DL) could explain the semipermeable membrane property of shale and neutral zone formed between pore body and the negatively charged clay surfaces (Figure 6.2). The DL imposes an electrical repulsive force on anions; and to maintain electro-neutrality outside the DL, cations will remain with their co-ions. As a result, only charge-neutral water molecules can flow through the pore center.

[1] *Colorado School of Mines, Golden, Colorado, USA*
[2] *Marathon Oil Company, Houston, Texas, USA*

Dynamics of Fluids and Transport in Complex Fractured-Porous Systems, Geophysical Monograph 210, First Edition.
Edited by Boris Faybishenko, Sally M. Benson, and John E. Gale.

Additionally, there are uncharged membranes that behave as sieves [*Keijzer and Loch*, 2001]. That is, smaller particles are not restricted when flowing through such a membrane but bigger ones are. *Olsen* [1972] and *Whitworth* [1993] state that kaolinite and chalks may behave as efficient semipermeable membrane based on pore size distribution.

6.2.1. Membrane Efficiency in Shale

Shale is very heterogeneous, composed of fine-grained sediments with a wide range of compositions including kerogen, clay, quartz, feldspar, pyrite, and heavy minerals. Prolific shale formations may contain high clay content up to 80% [*Bohacs et al.*, 2013]. Shale also exhibits a wide range of pore-size distribution (Figure 6.3a). *Kuila and Prasad* [2011] reported three classes of pore size in shale formations. The macro pores (diameter >1000 nm) are predominately fractures, microfractures, and space between aggregates of clay. Mesopores (diameter 10–100 nm, Figure 6.3b) comprise mainly the space between clay particles and within kerogen. Micro-pore (pore diameter <10 nm) is intercrystalline pores between clay platelets.

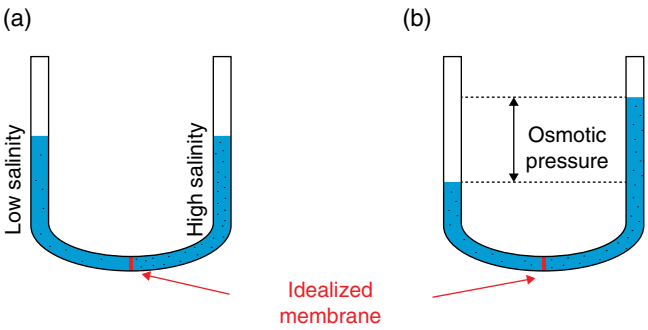

Figure 6.1 Illustration of osmotic pressure: (a) initial condition and (b) equilibrium condition.

Because of the wide pore-size range, shale can act as a non-ideal semipermeable membrane, only restricting the passage of some of the solutes in the solvent. As a result, pressure increase across the membrane does not reach the theoretical high osmotic pressure. For instance, *Neuzil and Provost's* [2009] review of public experimental data revealed a consistent low-membrane efficiency (less than 5%), which was defined as the measured pressure increase across the membrane divided by the theoretical osmotic pressure.

Confining stress increases membrane efficiency. For instance, Rahman et al. [2005] reported an increase in membrane efficiency from 14% at confining pressure of 1,000 psi to 39% at confining pressure of 4,000 psi.

Figure 6.4 illustrates the clay-pore leakage mechanism as the cause of osmotic pressure. Initially, the pore space between clay particles and within the clay structure is

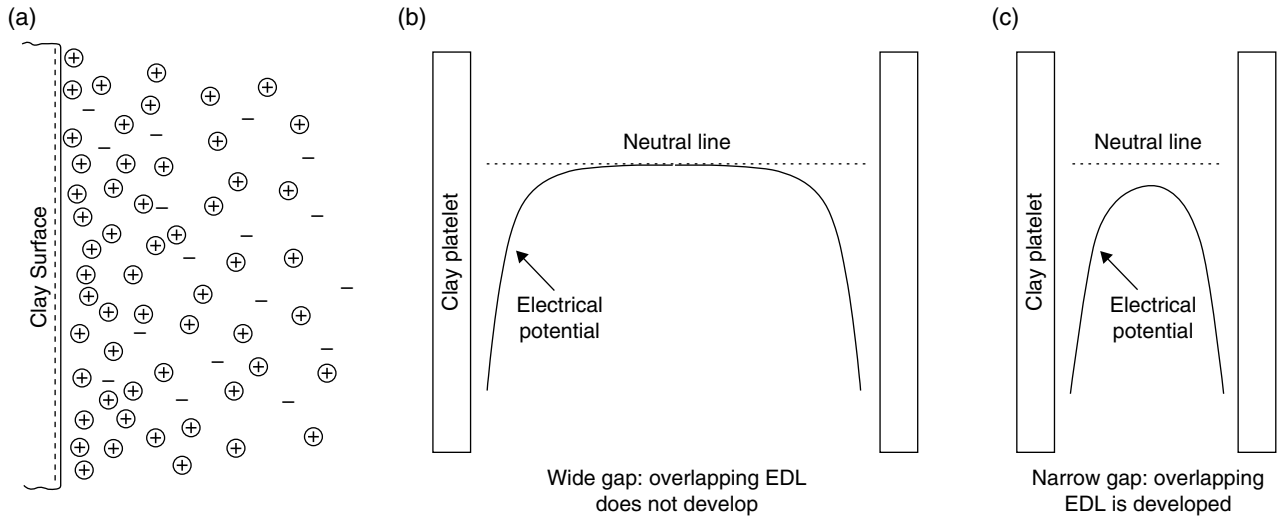

Figure 6.2 Diagram showing the electric double layer (EDL) next to the clay surface, the diffused layer, and the neutral zone (adopted from *Mitchell and Soga*, 2005, and *Keijzer*, 2000): (a) electrical charge distribution near clay surface, (b) electric potential profile of a wide gap between two clay platelets with no overlapping diffused layer, and a neutral zone. The latter portrays pores in conventional reservoirs, which allows charged particles to pass through. (c) Electrical potential profile in a narrow space between two clay platelets, as in an unconventional pore space, having an overlapping diffused layer, which resists passage of charged particles while allowing the neutral particle migration.

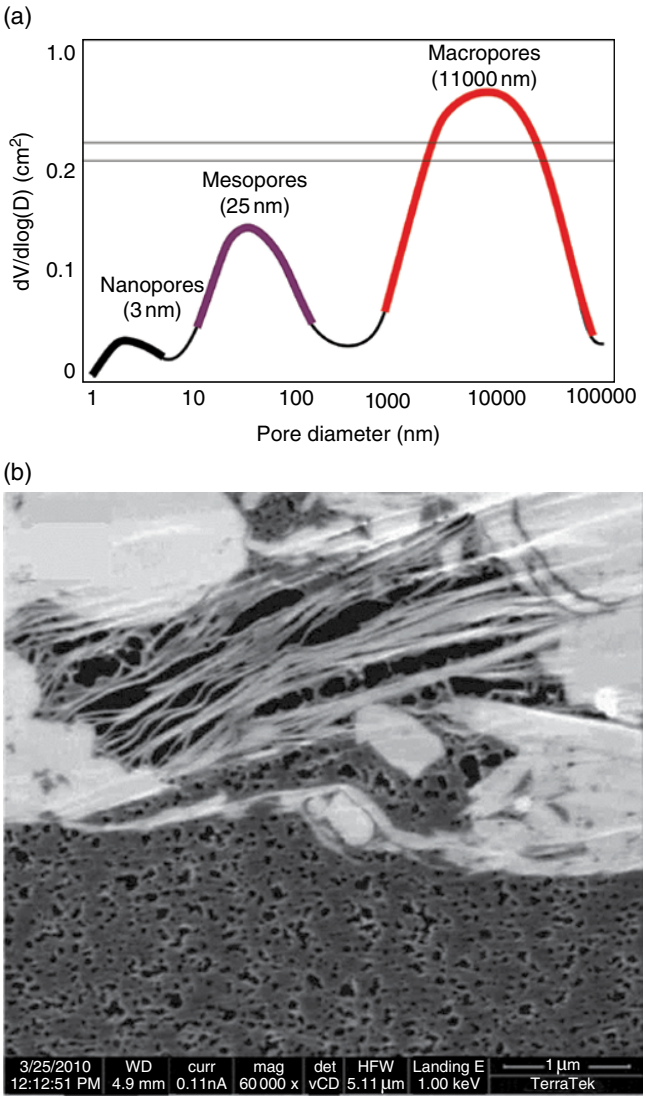

Figure 6.3 Pores in shale formations: (a) Three pore-size distribution for a shale sample [*Kuila and Prasad,* 2011]. (b) Ion-milled SEM image of mesopores in kerogen and in clay for a Barnett shale sample [*Milner et al.,* 2010].

full of high-salinity formation brine. Once low-salinity water contacts the clay particles, osmotic force induces the flow of water molecules into the clay structure through the small mesopore between clay particles to cause EDL overlap and reduction of salinity in the pore. Furthermore, pressure inside the pore increases (osmotic pressure) and expels some of the water and salt through the larger pore. This is why the laboratory-measured osmotic pressure is not as high as the theoretical osmotic pressure of a perfect membrane. Nonetheless, at the nanoscale level, the pressure that causes flow across the overlapping EDLs may be as high as the theoretical osmotic pressure.

6.2.2. Osmotic Pressure-Induced Flow in Multiphase System in Shale Formations

In hydrocarbon-producing shale, the bulk of movable fluids in the shale matrix includes oil and gas, while high-salinity brine is either trapped or bound to clays. Water flowback data indicate that the salinity of formation brine can be as high as 280,000 ppm or 28% by weight in some shale formations such as Bakken [*Kurtoglu*, 2013]. In the Bakken, low-salinity fracturing fluid (e.g., 20,000 ppm) has been used. This salinity contrast can cause a substantial osmotic pressure gradient to drive fracturing fluid into the shale matrix via surrounding fractures.

Figure 6.5 is a schematic of the osmosis-induced flow in shale containing oil and water. Initially, oil occupies most of the pore space while formation water is bound to the clay platelets (Figure 6.5a). Once low-salinity water contacts the clays, low-salinity water molecules enter the nanopore space within the clay structure. As a result, clay swells and pore pressure increases to expel oil through larger mesopores (Figure 6.5b).

Interestingly, shale formations are oil-wet because of Ca^{2+}/Na^{+} bridging of oil molecules to the negatively charged clay surface. The invaded low-salinity water dilutes salt concentration in the formation brine and causes detachment of Ca^{2+}/Na^{+} from the clay surface [*Kurtoglu*, 2013]. As a result, the surface may become water-wet, causing an increase in relative permeability of oil and a reduction of irreducible oil saturation, thus leading to improved oil production.

6.3. OIL RECOVERY EXPERIMENTS IN BAKKEN

A preserved core in Middle Bakken formation was used in the experiment. The mineralogy and pore structure of Middle Bakken are shown in Figure 6.6. The pore space is filled with illite and clay-size grain particle, causing low-permeability rock matrix. The permeability is in the range of micro-Darcy.

We performed low- and high-salinity imbibition experiments using a laminated Middle Bakken core. First, the core was soaking in a 282,000 ppm high-salinity Bakken brine imbibition cell. Then, the same core was placed in a low-salinity imbibition cell, filled with 20,000-ppm KCl brine.

Figure 6.7 shows the experimental results after five and six days of soaking in high- and low-salinity cells, respectively. Minimal oil droplet is observed in the high-salinity brine cell (Figure 6.7a). It indicates that the brine hardly penetrates into the core. In contrast, the low-salinity brine has greater spontaneous imbibition than that of the high-salinity, indicated by more oil droplets forming on the core surface (Figure 6.7b). It is interesting that much of the oil appeared along the core laminations. No clay

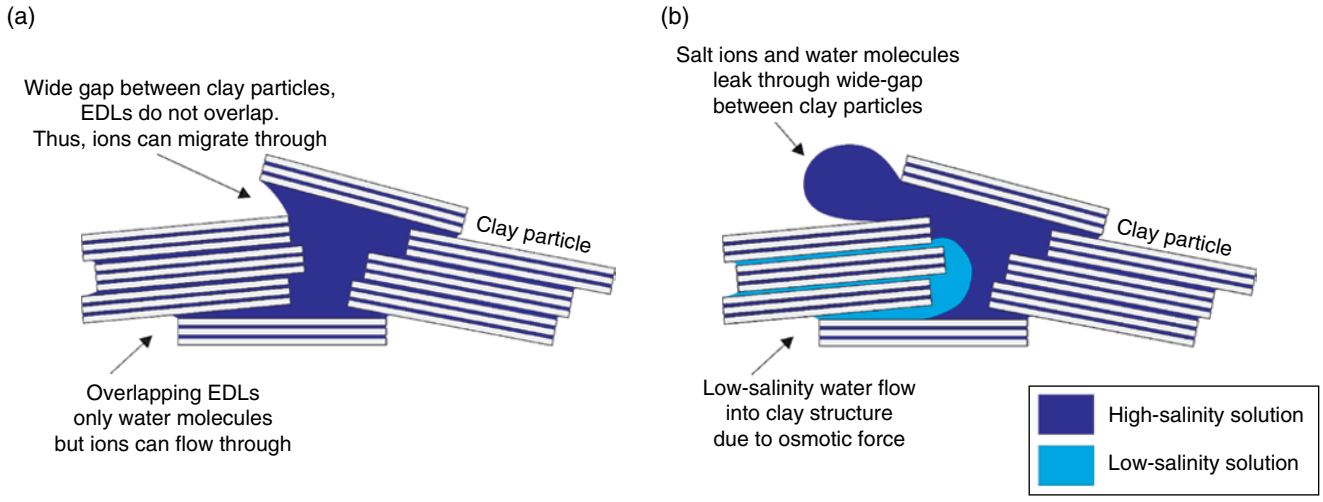

Figure 6.4 Schematic showing membrane leakage mechanism for clays: (a) Pore space initially filled with high-salinity water. (b) Low-salinity water flows into the clay structure due to osmotic force, and high-salinity water leaves through a pore gap larger than clay sheet spacing. (EDL = electric double layer)

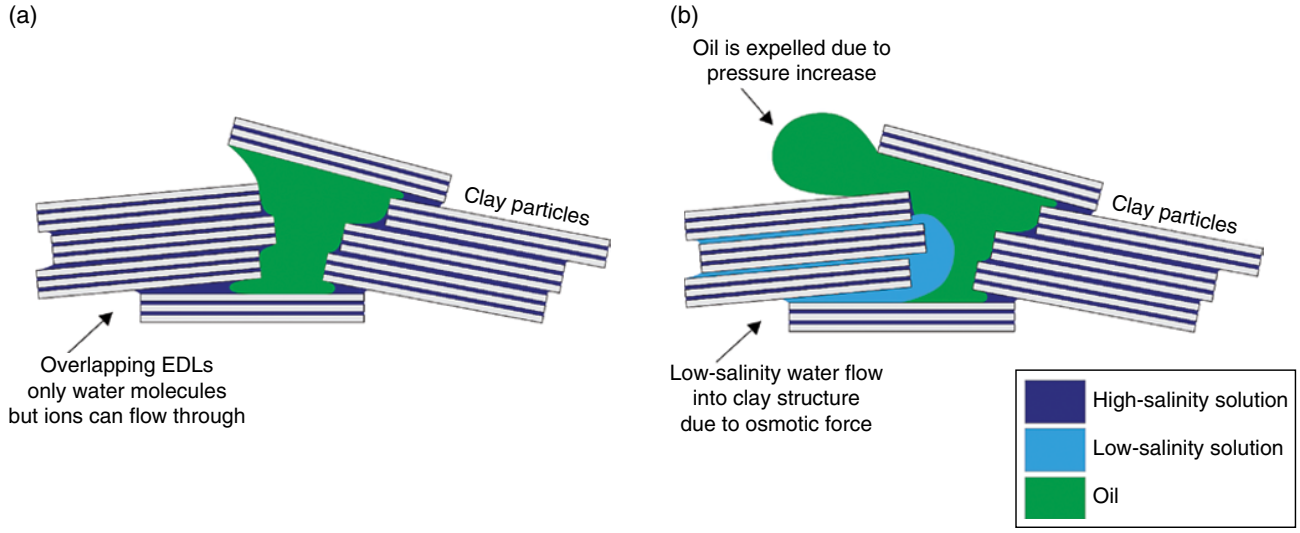

Figure 6.5 Schematic showing oil-water flow in shale: (a) Pore space at the initial condition where the bulk of the movable fluid is oil while high-salinity brine is bound to clay sheets. (b) Clay in contact with low-salinity water, which has broken through some clay structure to push oil out of mesopores. (EDL = electric double layer)

swelling was observed during the experiment because the Middle Bakken is illite-rich formation and the low-salinity brine comprises KCl, a natural clay-swelling inhibitor. The experimental results confirm that chemical osmosis induces oil-water countercurrent flow in the oil-wet Middle Bakken core.

In high-smectite formations, injecting low-salinity brine can cause clay swelling. As a result, it could reduce rock permeability and could demote the effect of chemical osmosis. If NaCl-dominated low-salinity brine is used, a slight increase in the induced osmotic pressure is expected.

6.4. MATHEMATICAL MODEL

The mathematical description of osmosis-induced flow in porous media has been well documented [*Abdel-Aziz and Taylor*, 1964; *Olsen*, 1972; *Neuzil*, 1986; *van Oort*

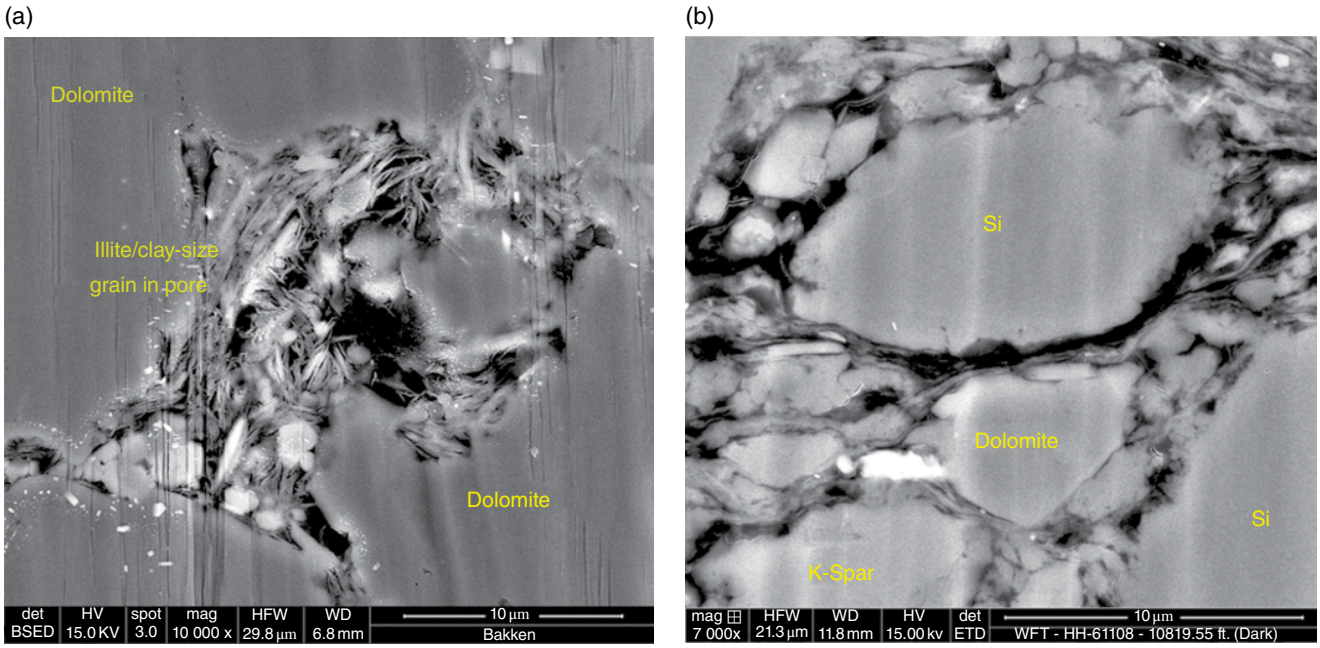

Figure 6.6 Mineralogy and pore structure of Bakken formation: (a) Ion-milled SEM of oil-producing Middle Bakken. (b) Ion-milled SEM of source rock in Lower Bakken [*Kurtoglu,* 2013].

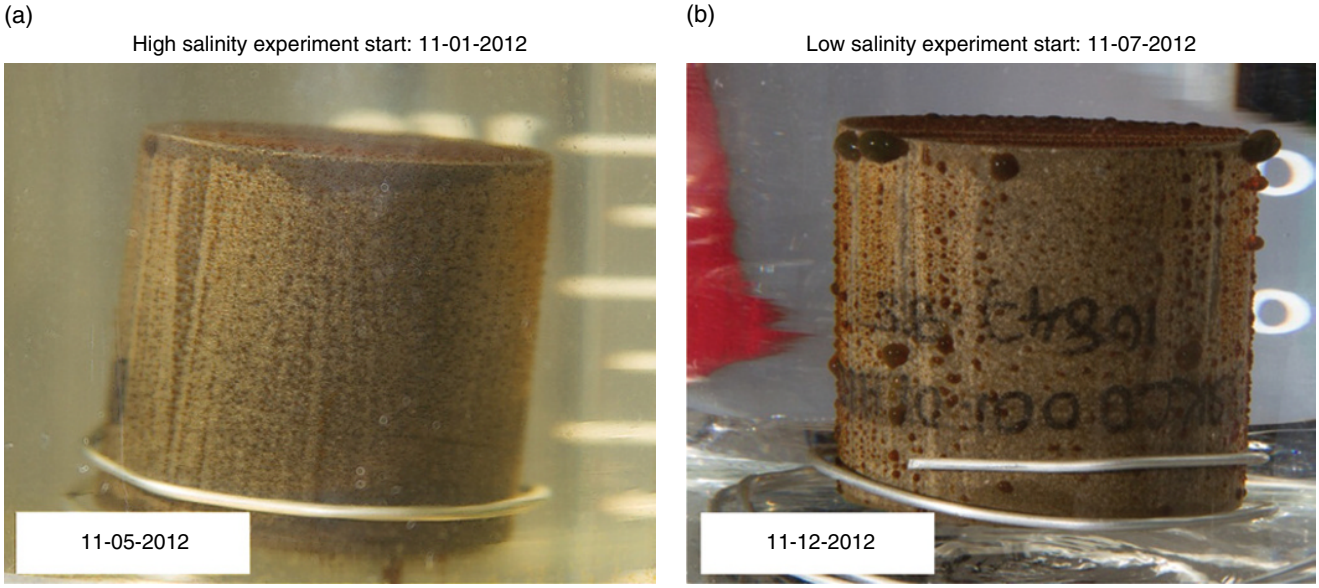

Figure 6.7 Spontaneous imbibition experiments: (a) High-salinity formation water after five days of soaking. (b) Low-salinity brine after six days of soaking [*Kurtoglu,* 2013].

et al., 1995, *Keijzer*, 2000; *Mitchell and Soga*, 2005]. Specifically, *Olsen* [1972] compared chemical and electrical osmosis flow to the pressure-induced flow in a subsurface environment, and *Greenberg et al*. [1973] modeled seawater intrusion in California using chemical osmosis concepts.

In this paper, we present a multiphase chemical-osmosis flow model for hydrocarbon-bearing shale formations. We modeled solute transport by a single component. We created osmotic pressure as a function of salt concentration in the same manner as capillary pressure and relative permeability saturation functionality.

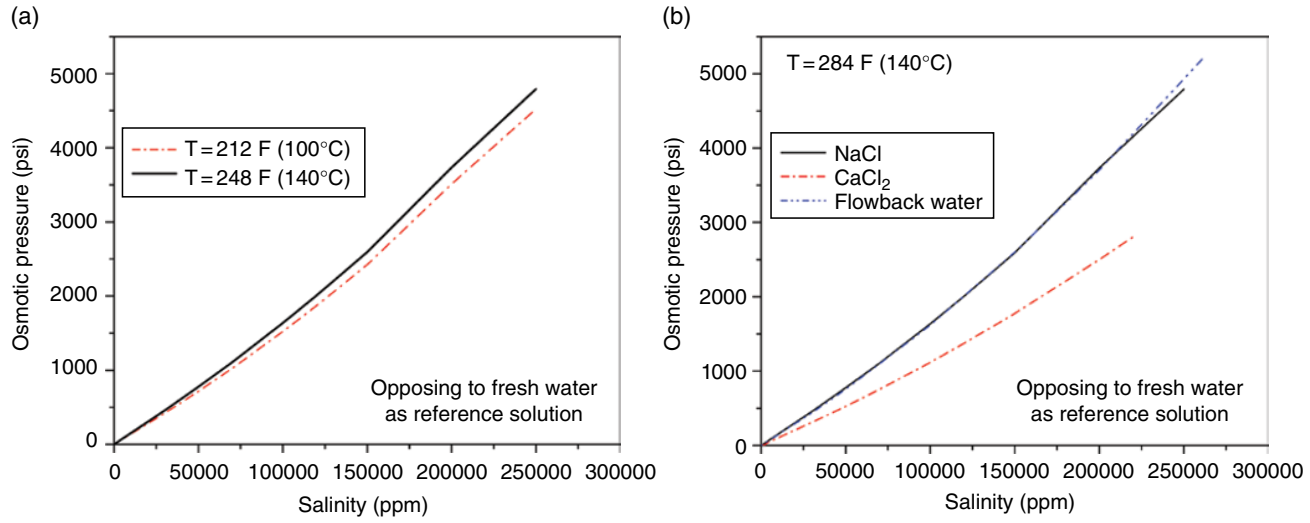

Figure 6.8 Osmotic pressure for Bakken: (a) Reservoir temperature 212°F and 284°F, (b) NaCl brine vs. $CaCl_2$ brine. (Brine composition from *Kurtoglu*, 2013)

6.4.1. Osmotic Pressure Calculation

Marine and Fritz [1981] described osmotic pressure (π) by Equation 6.1:

$$\pi = \frac{RT}{V}\ln\left(\frac{a_I}{a_{II}}\right) \tag{6.1}$$

where a_I and a_{II} are water activities of low-salinity brine I and high-salinity brine II; water activity for freshwater is 1.0; R is gas constant equal to 0.082 (liter.atm)/(g-mol°K); T is temperature in °K; and V is molar volume in liters/g-mol.

Water activity can be calculated from the Helgeson-Kirkham-Flowers equation of state [*Helgeson et al.*, 1981]. In high-solute concentration and high-temperature environments, this calculation is an iterative procedure [*Xu et al.*, 2004]. We used TOUGHREACT simulator to generate brine activity values using a single-grid model. Because water activity of freshwater is one, Equation 6.1 becomes

$$\pi = -\frac{RT}{V}\ln(a_{II}) \tag{6.2}$$

6.4.2. Salt Concentration–Osmotic Pressure Curves

Assuming a perfect semipermeable membrane, we constructed a plot of the salt concentration versus osmotic pressure to investigate the effect of temperature and water composition on osmotic pressure as an input to the flow simulator.

Figure 6.8a presents calculated osmotic pressure of the Bakken flow back brine (Table 6.1) at a temperature of 212°F and 284°F. For comparison, Figure 6.8b is the computed osmotic pressure for sodium chloride (NaCl) and calcium chloride ($CaCl_2$) solutions. The results indicate that water composition significantly affects osmotic pressure. Osmotic pressure of sodium chloride solution is much higher than that of calcium chloride solution.

Table 6.1 Bakken flow-back water composition.

Ion	Concentration (ppm)	Molality (mol/liter)
Ca^{2+}	20,507	0.51
Mg^{2+}	1,491	0.06
Na^{+}	85,994	3.74
Cl^{-}	174,733	4.92
Total salinity	282,725	

Source: *Kurtoglu* [2013].

6.4.3. Single-Phase, Single-Component Transport in Shale

Olsen [1972] described single-phase flow of water in shale by the Darcy flow enhanced by osmotic pressure, Equation 6.3:

$$\vec{v}^{op} = -\frac{k}{\mu}\left[\nabla p - \gamma\nabla D - E_{op}\nabla\pi(C)\right] \tag{6.3}$$

where k is permeability, μ is fluid viscosity, p is pressure, γ is fluid gradient, D is depth (positive downward), π is osmotic pressure (a function of salt concentration C), and E_{op} is osmotic pressure efficiency.

Solute transport through small mesopores is controlled by the semipermeable membrane property of shale as discussed

in the previous section. Thus, solute molecules move by (1) advection pressure gradient through large pores ($\vec{F}^{adv}$) and (2) diffusion concentration gradient ($\vec{F}^{diff}$).

Advection:

$$\vec{F}^{adv} = C^p \rho^p \vec{v}^p \tag{6.4}$$

Where C^p and ρ^p are solute concentration and density, while $\vec{v}^p$ is the Darcy flux vector, Equation 6.5:

$$\vec{v}^p = -\frac{k}{\mu}\left(\nabla p - \gamma \nabla D\right) \tag{6.5}$$

Equation 6.6 describes the net diffusion flux:

$$\vec{F}^{diff} = -(1 - E_{op}) D \nabla C \tag{6.6}$$

Equations 6.7 and 6.8 are the mass-transport equations for water (solvent) and solute (salt) in shale, which we used in our model:

Water:

$$-\nabla \cdot \rho \vec{v} + \rho \hat{q} = \frac{\partial \rho \phi}{\partial t} \tag{6.7}$$

where $\hat{q}$ represents the sink/source term per unit volume, ϕ porosity and t, time.

Solute:

$$-\nabla \cdot \vec{F}^{adv} - \nabla \cdot \vec{F}^{diff} + C \rho \hat{q} = \frac{\partial C \rho \phi}{\partial t} \tag{6.8}$$

6.4.4. Simulating an Osmotic Pressure Mass Transport Experiment

To test the validity of our osmotic pressure mathematical model, we matched osmotic pressures measured on a shale sample experiment, conducted by *Takeda et al.* [2012]. The sample, siliceous shale cut from a core taken at depth of 982 m, was 5 cm in diameter and 1 cm in thickness. Two separated sodium chloride reservoirs were connected to the top and bottom of the sample. The top reservoir contained 0.1 mol/liter salt solution while the bottom reservoir contained 0.55 mol/liter solution. In the experiment, Takeda et al. measured pressure and salt concentration at discrete time intervals, which we used to match the numerical model calculations. The numerical model was a vertical 1-D finite-difference simulator consisting of seven grid cells. The first grid cell represented the sodium chloride reservoirs at the bottom while the seventh cell was the sodium chloride reservoir at the top. The remaining five grid cells represented the shale sample. Table 6.2 contains the details of the model input parameters, while Figure 6.9 parts a and b show the comparison between experiment and modeling results.

The simulation results indicate that the pressure in the bottom cell sharply increases due to flow of low-salinity brine, by osmotic pressure gradient, from the top cell. The countercurrent flow and diffusion of salt molecules decrease salt concentration in the bottom reservoir. To achieve a match, we used an osmotic pressure membrane efficiency of 0.05 (5%).

Table 6.2 Input parameters for the osmotic pressure flow model.

	Bottom reservoir	Rock	Top Reservoir
Rock property			
Volume, ft^3	7.417×10^{-3}	6.923×10^{-3}	3.532×10^{-3}
Initial pressure, psi	42.5	42.5	42.5
Initial concentration, mol/liter	0.55	0.1	0.1
Porosity, fraction		0.28	
Permeability, mD		1.54×10^{-4} *	
Interface area, ft^2	0.021	0.021	0.021
Length, ft		0.032	
Effective diffusion coefficient, ft^2/day		2.487×10^{-5} **	
Grid cell number	1	2, 3, 4, 5, 6	7
Main matching parameter			
Osmotic pressure membrane efficiency, fraction		0.05	

**Takeda et al.* [2012].
***Rahman et al.* [2005].

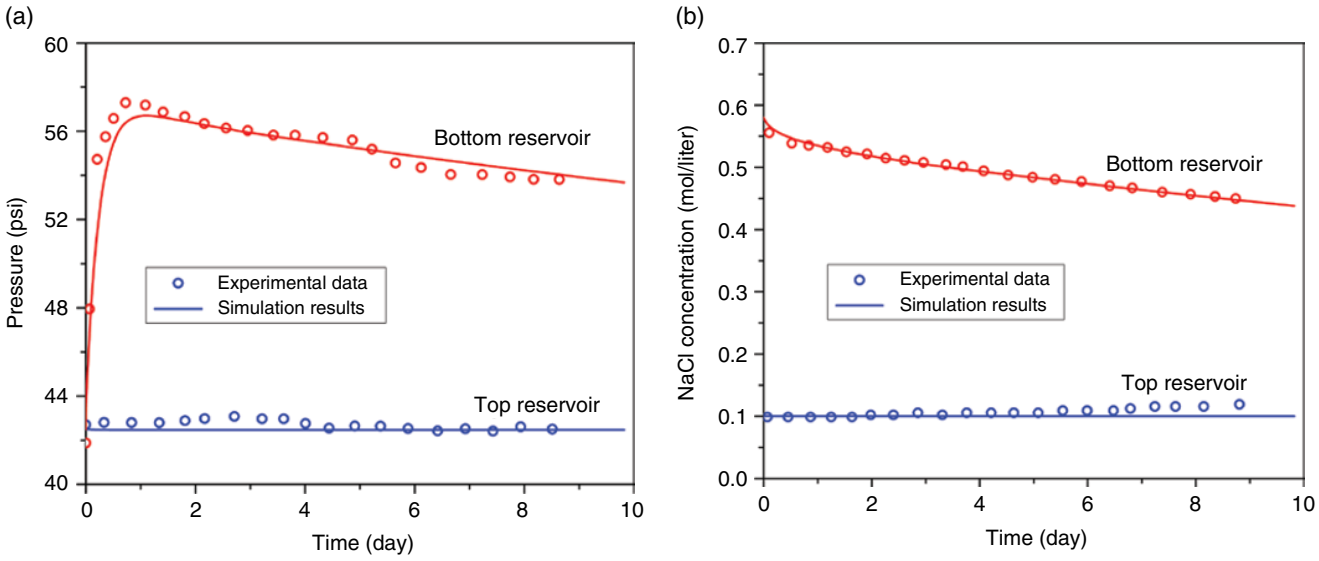

Figure 6.9 Comparison between numerical simulation and experimental data of *Takeda et al.* [2012]: (a) pressure and (b) salt concentration.

6.4.5. Multiphase Flow Mathematical Model of Fractured Shale Formations

Micropore ($d \le 2\ nm$), mesopore ($2nm \le d \le 50\ nm$), and macropore ($d \ge 50\ nm$) are common designations of shale pore-size distribution. The macropores represent predominately fractures and microfractures, while mesopores and micropores represent two main pore classes in the shale matrix (*Kuila and Prasad*, 2011). Consequently, we can formulate fluid flow in shale using a double-porosity model, where fractures form the continuum of interconnected fracture network while the shale matrix becomes the discrete medium embedded in the fracture continuum.

The commonly used transfer function, τ, used to describe mass transport between fracture and matrix in dual-porosity modeling [*Kazemi and Gilman*, 1993] can be extended to chemical osmosis mass transport. The following equations describe the modifications for the water-oil flow:

Water:

$$\tau_{w,f/m} = \tau^{p}_{w,f/m} + \tau^{\pi}_{w,f/m} \tag{6.9}$$

where $\tau^{p}_{w,f/m}$ and $\tau^{\pi}_{w,f/m}$are transfer functions of water induced by pressure and osmotic pressure, respectively. The following equations describe $\tau^{\pi}_{w,f/m}$ and $\tau^{p}_{w,f/m}$:

$$\tau^{\pi}_{w,f/m} = -\sigma_{f/m} k_m \lambda_{w,f/m} E_{op} \left[\pi_f(C_f) - \pi_m(C_m)\right] \tag{6.10}$$

where $\sigma_{flm}$is shape factor for flow between fracture and matrix, k_m is shale matrix permeability, and $\lambda_{w,flm}$ is water mobility.

And,

$$\tau^{p}_{w,f/m} = \sigma_{f/m} k_m \lambda_{wf/m} \left[(p_{of} - p_{om}) - (p_{cowf} - p_{cowm}) + \frac{\sigma_{z,f/m}}{\sigma_{f/m}} \gamma_w (h_{wf} - h_{wm})\right] \tag{6.11}$$

where p_{of} and p_{om} are the oil pressure in fracture and matrix, p_{cowf} and p_{cowm} are the capillary pressure of a water-oil system in fracture and matrix, $\sigma_{z,flm}$ is shape factor for flow in vertical direction, and h_{wf} and h_{wm} are water column height in fracture and matrix [*Kazemi and Gilman*, 1993].

Oil:

$$\tau_{o,f/m} = \sigma_{f/m} k_m \lambda_{of/m} \left[(p_{of} - p_{om}) - \frac{\sigma_{z,f/m}}{\sigma_{f/m}} \gamma_o (h_{wf} - h_{wm})\right] \tag{6.12}$$

Governing equations for a water-oil system in fractured shale formations are given:

Mass balance in fracture:

Water:

$$-\nabla \cdot (\rho_w \vec{v}^{op}_w)_f + \rho_w \hat{q}_w - \rho_w \tau_{w,f/m} = \frac{\partial (\rho_w S_w \phi)_f}{\partial t} \tag{6.13}$$

Oil:

$$-\nabla \cdot (\rho_o \vec{v}_o)_f + \rho_o \hat{q}_o - \rho_o \tau_{o,f/m} = \frac{\partial (\rho_o S_o \phi)_f}{\partial t} \tag{6.14}$$

Salt:

$$-\nabla\cdot\left(\vec{F}^{adv}\right)_f-\nabla\cdot\left(\vec{F}^{diff}\right)_f+C\rho_w\hat{q}_w-F_{f/m}^{adv}-F_{f/m}^{diff}=\frac{\partial(C\rho_wS_w\phi)_f}{\partial t} \tag{6.15}$$

where $F_{f/m}^{adv}$ and $F_{f/m}^{diff}$, defined below, are salt transport between fracture and matrix by advection and diffusion, respectively.

$$F_{f/m}^{adv}=C_{f/m}\rho_w\tau_{w,f/m}^{p}+C_{f/m}\rho_w\tau_{w,f/m}^{\pi} \tag{6.16}$$

$$F_{f/m}^{diff}=(1-E_{op})\sigma\rho_wD_{f/m}(C_f-C_m) \tag{6.17}$$

where C_{flm} is salt concentration in fracture or matrix, σ is shape factor, and D_{flm} is effective diffusion coefficient between fracture and matrix.

Mass balance in matrix:

Water:

$$\tau_{w,f/m}=\frac{\partial(\rho_wS_w\phi)_m}{\partial t} \tag{6.18}$$

Oil:

$$\tau_{o,f/m}=\frac{\partial(\rho_oS_o\phi)_m}{\partial t} \tag{6.19}$$

Salt:

$$F_{f/m}^{adv}+F_{f/m}^{diff}=\frac{\partial(C\rho_wS_w\phi)_m}{\partial t} \tag{6.20}$$

6.5. THE EFFECT OF OSMOSIS PRESSURE ON OIL AND GAS PRODUCTION

We used a 1-D dual-porosity model to simulate the effect of chemical osmosis on oil and gas production in shale formations. The matrix was a sugar cube with a linear dimension of 10 feet. The simulation starting point is after a single-staged hydraulic-fracture stimulation operation. In the simulation, the fracturing fluid has a salinity of 10,000 ppm. Thus, the fracture network also contains low-salinity fracturing fluid with 10,000-ppm salt concentration at all times. The 1-D simulation results were up-scaled to a one-square-mile multistage well pattern. The simulation assumptions are the following:

- Fracture pressure, water saturation, and salt concentration are constant while matrix pressure, water saturation, and salt concentration are changed with time.
- The average matrix block size is 10 ft.
- Oil production from the matrix immediately reaches the producers once leaving the matrix.
- Matrix wettability alteration due to the change in salt concentration is ignored.
- No fracture and matrix permeability change throughout the simulation.

We used the relative permeability data (Figure 6.10a) that a service company had measured on a Bakken core. We also constructed the capillary pressure function (Figure 6.10b) based on numerous published laboratory-measured drainage data. Table 6.3 presents the remaining input parameters for the model. We modeled six simulation scenarios (Table 6.4) with different shale-membrane efficiency and wettability to investigate their effect on well production.

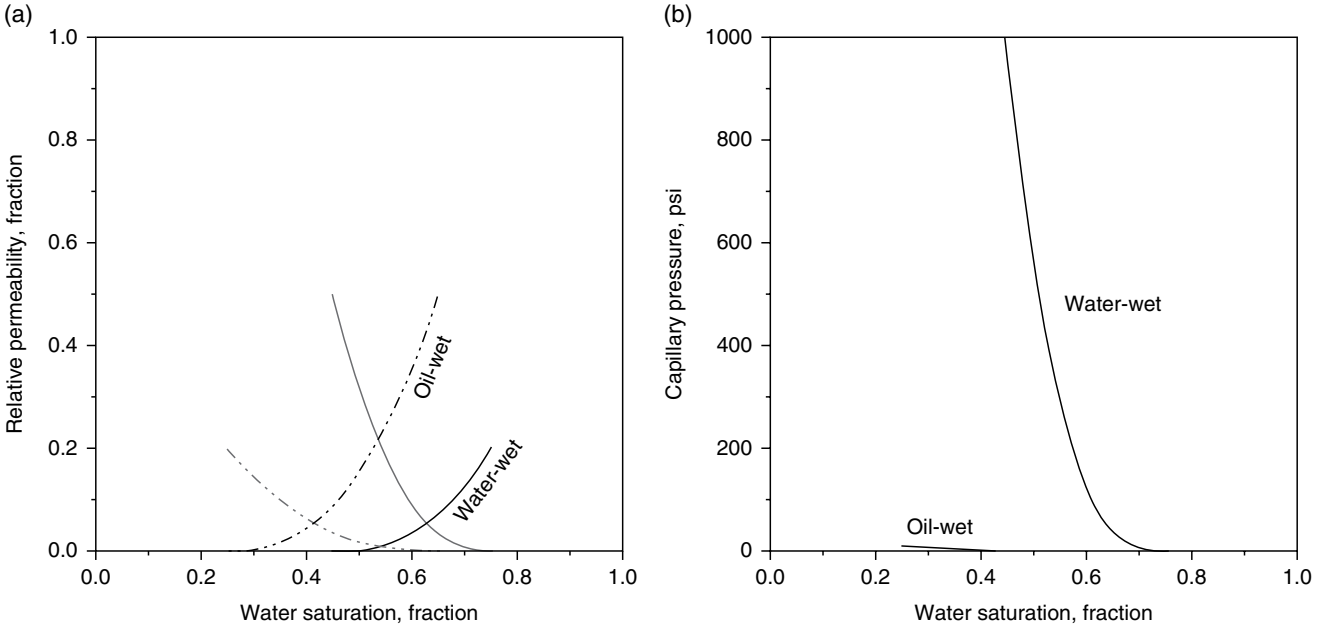

Figure 6.10 Rock properties: (a) relative permeability and (b) capillary pressure.

Table 6.3 Input parameters for the field simulation model.

Parameter	Fracture	Shale Matrix
Initial salt concentration, ppm	10,000	250,000
Initial water saturation, fraction	1.00	0.28 (oil-wet) 0.48 (water-wet)
Irreducible water saturation, fraction		0.25 (oil-wet) 0.45 (water-wet)
Porosity, fraction		0.08
Permeability, mD		1.0×10^{-3}
Shape factor, ft^{-2}		0.12 (10 ft. matrix block)
Effective diffusion coefficient, ft^2/day		1.0×10^{-6}
Osmotic efficiency, fraction		0.05
Drainage area, ft^2	5,280 × 5,280	
Thickness, ft	35	

Table 6.4 Shale wettability and shale membrane efficiency scenarios.

Case	Rock Wettability	Osmotic Efficiency (%)
1	Oil-wet	1
2	Oil-wet	5
3	Oil-wet	10
4	Water-wet	1
5	Water-wet	5
6	Water-wet	10

6.5.1. Simulation Results

The simulation results of the oil-wet rock with a membrane efficiency of 5% (Case 2) are shown in Figure 6.11. Water and oil flow rates are reported in Figure 6.11a. Initially, the flow rate between fracture and matrix is minimal because relative permeability to water in the matrix is low; however, after considerable time water penetrates into the matrix pores to cause higher flow rates.

The osmotic force induces flow from fracture to matrix (negative value). As a result, matrix pore pressure increases (Figure 6.11b). This increase causes flow from matrix to fracture. In turn, the flow reduces matrix pressure; thus, only a 40-psi pressure increase is observed. As the relative permeability to oil is higher than that of water, oil starts to flow from matrix to fracture (positive value) at about 20 years. After 40 years of production, oil recovery factor from shale matrix could reach about 35% (Figure 6.11d).

Low-salinity water flowing from fracture flow into the matrix pores dilutes the matrix salt concentration (Figure 6.11c) and reduces the concentration contrast between fracture and matrix. As a result, it reduces the osmotic force. Thus, the osmotic-induced water flow rate decreases.

6.5.2. Wettability and Shale-Membrane Efficiency

Osmotic force is the only realistic force to overcome the negative capillary pressure of the oil-wet rock to cause countercurrent flow of water from the fracture into the matrix and oil into fractures. Thus, osmotic membrane efficiency could significantly affect economic oil production rates and recovery factor (Figures 6.12 and 6.13) in oil-wet shale.

6.6. CONCLUSIONS

Hydrocarbon-producing shale formations are oil wet because of the abundance of kerogen in the pore structure. Thus, brine should have a difficult time entering the shale pores. However, we have observed brine entering preserved core samples in the laboratory. We believe this is caused by osmotic pressure because of the presence of clays and high-salinity brine in the shale pores. When shale is contacted with low-salinity brine, it enters shale pores by osmotic pressure created because of the salinity contrast of the high-salinity brine in the pores and the low-salinity brine contacting the shale. We built a dual-porosity mathematical model to include this osmotic pressure in the model. In this study, we have arrived at the following conclusions:

1. Because of the presence of clays and high-salinity brine in the shale pores, some hydrocarbon-bearing formations behave as osmotic membranes when contacted with low-salinity brine. Thus, low-salinity brine can potentially displace oil in oil-bearing shale formations. Similarly, in gas-bearing formations, when a gas well is shut in for several months after hydraulic fracturing, the gas rate will increase when the well is reopened. We believe osmotic pressure can imbibe the hydraulic fracturing fluid, the "slickwater," to enhance gas production temporarily.

2. The mathematical model presented in this chapter can simulate the osmotic pressure oil recovery, the underlying principle of the low-salinity water flooding. This oil recovery technique might yield economic amounts of incremental oil in suitable shale formations.

3. The osmotic pressure, caused by salinity contrast, can cause a countercurrent flow of water and oil both in oil-wet and water-wet porous formations. Thus, in conventional reservoirs, low-salinity oil recovery improvements of carbonate formations might be partly because of osmotic pressure induced by salinity contrast.

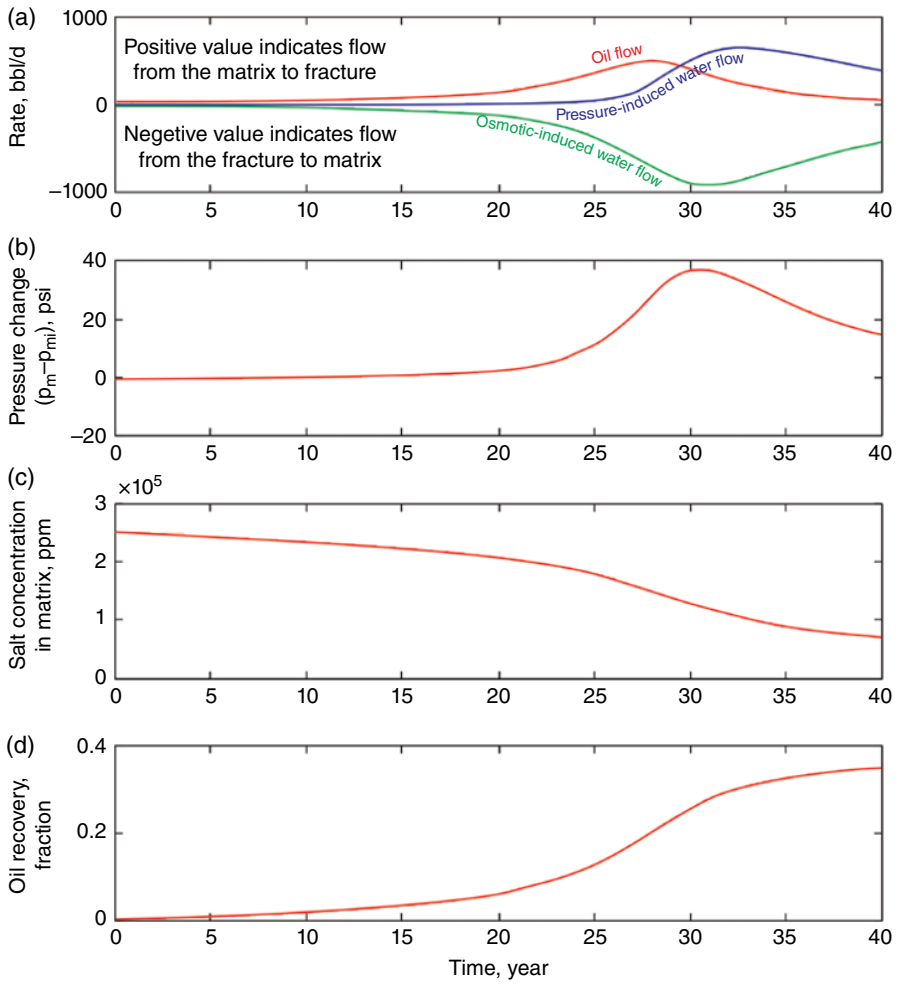

Figure 6.11 Simulation results for Case 2, oil-wet rock and shale membrane efficiency of 5%: (a) water and oil flow rates, (b) pressure change in shale matrix, (c) salt concentration in shale matrix, and (d) oil recovery factor.

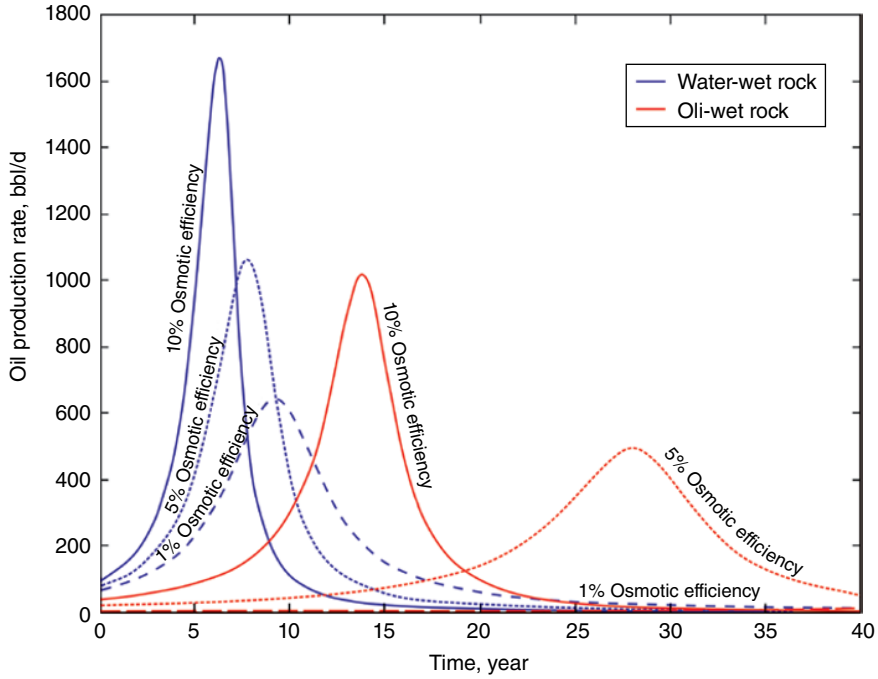

Figure 6.12 Comparison of oil production rates.

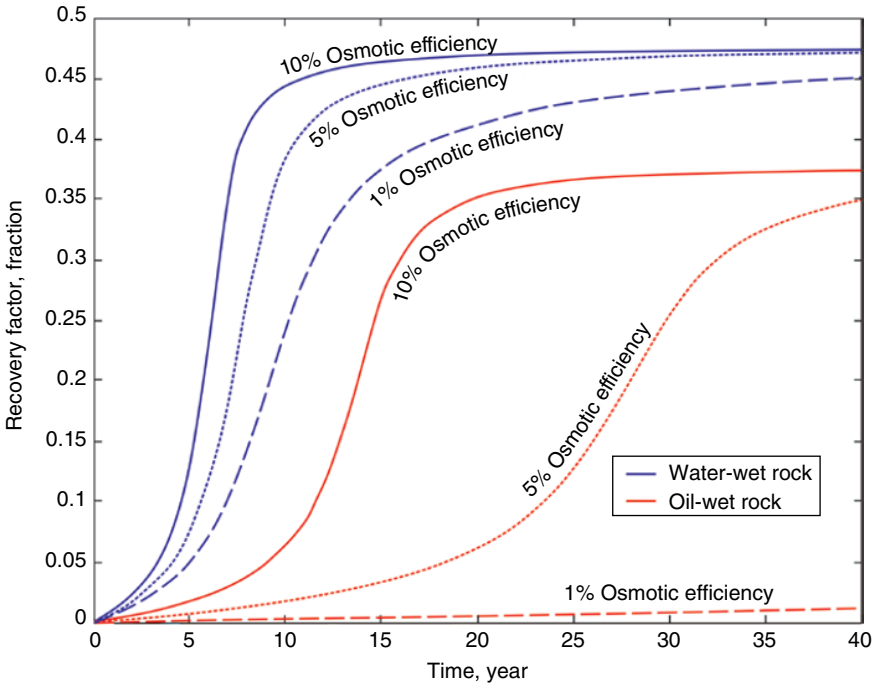

Figure 6.13 Comparison of oil recovery factors.

ACKNOWLEDGMENTS

The authors acknowledge the support received from the Marathon Center of Excellence for Reservoir Studies and the Energy Modeling Group at Colorado School of Mines and Marathon Oil Company. We also extend special gratitude to the following individuals at Marathon Technical Laboratory: Richard Rosen, Tobi Kosanke, and William Mickelson for their help in the experimental studies and interpretation.

NOMENCLATURE (A DASH DENOTES NO UNIT OF MEASURE)

a	water activity [-]
C	salt concentration [-]
D	depth [L]
E_{op}	osmotic efficiency [-]
$\vec{F}$	mass flux rate [M/(L^{2}t)]
h	height of fluid column [L]
k	permeability [L^2]
p	pressure [M/(Lt^2)]
$\hat{q}$	fluid sink and source term per volume [1/t]
R	gas constant [L^2/t^{2}T]
S	fluid saturation [-]
t	time [t]
T	temperature [T]
$\vec{v}$	Darcy velocity [L/t]
V	molar volume [L^3/m]

Greek Letters

ϕ	porosity [-]
γ	fluid gradient [M/(L^{2}t^2)]
μ	viscosity [M/(Lt)]
π	osmotic pressure [M/(Lt^2)]
ρ	density [M/L^3]
σ	shape factor [1/L^2]
τ	transfer function [1/t]

Operators

∇	Gradient operator
$\nabla\cdot$	Divergence operator
$\partial / \partial t$	time derivative [1/t]

Superscripts

adv	induced by advection
diff	induced by diffusion
p	induced by pressure
π	induced by osmotic pressure

Subscripts

cwo	capillary of a water and oil system
f	fracture
f/m	between fracture and matrix
m	matrix
o	oil phase
w	water phase
z	in vertical direction only

REFERENCES

Abdel-Aziz, M., and S. A. Taylor (1964), Simultaneous flow of water and salt through unsaturated porous media, *Soil Sci. Soc. Amer. Proc.*, *29*(2), 141.

Bohacs, K., Q. Passey, M. Rudnicki, W. Esch, and O. Lazar (2013), The spectrum of fine-grained reservoirs from "shale gas" to "shale oil"/tight liquids: Essential attributes, key controls, practical characterization, IPTC-16676, in *6th International Petroleum Technology Conference*. Beijing, China.

Bredehoeft, J. D., C. R. Blyth, W. A. White, and G. B. Maxey (1963), Possible mechanism for concentration of brines in subsurface formations, *AAPG Bulletin*, *47*(2): 257–269.

Chenevert, M. E. (1970), Shale alteration by water adsorption, *JPT*, 1309–1316.

De Sitter, L. V. (1947), Diagenesis of oil-field brines, *Am. Assoc. Pet. Geol. Bull.*, *31*(11), 2030–2040.

Greenberg, J. A., J. K. Mitchell, and P. A. Witherspoon (1973), Coupled salt and water flows in a groundwater basin, *Journal of Geophysical Research, 78*, 6341–6353.

Helgeson, H. C., D. H. Kirkham, and G. C. Flowers (1981), Theoretical prediction of the thermodynamic behavior of aqueous electrolytes by high pressures and temperatures: Part IV, Calculation of activity coefficients, osmotic coefficients, and apparent molal and standard and relative partial molal properties to 600 degrees C and 5kb, *American Journal of Science*, *281*, 1249–1516.

Kazemi, H., and J. R. Gilman (1993), Multiphase flow in fractured petroleum reservoirs, in J. Bear, C.-F. Tang, and B. De Marsily (eds.), *Flow and Contaminant Transport in Fractured Rocks*, Academic Press, New York, 267–323.

Kemper, W. D. (1961), Movement of water as effected by free energy and pressure gradient II, Experimental analysis of porous systems in which free energy and pressure gradients act in opposite directions, *Soil Sci. Soc. Am. Proc.*, *25*(4), 260–265.

Keijzer, T. J. S. (2000), Chemical Osmosis in Natural Clayey Materials, PhD thesis, Utrecht University, Netherlands.

Keijzer, T. J. S., and J. P. G. Loch (2001), Chemical osmosis in compacted dredging sludge, *Soil Science Society of America Journal*, *65*(4), 1045–1055.

Kuila, U., and M. Prasad (2011), Surface area and pore-size distribution in clays and shales, SPE-146869, in *2011 SPE Annual Technical Conference and Exhibition*, Society of Petroleum Engineers, Denver, Colorado.

Kurtoglu, B. (2013), Integrated Reservoir Characterization and Modeling in Support of Enhanced Oil Recovery for Bakken, PhD thesis, Colorado School of Mines, Golden, Colorado.

Marine, I. W., and S. J. Fritz (1981), Osmotic model to explain anomalous hydraulic heads, *Water Resources Research*, *17*(1), 73–82.

Milne, I. H., J. G. McKelvey, and R. P. Trump (1964), Semi-permeability of bentonite membranes to brines, *Am. Assoc. Pet. Geol. Bull.*, *48*(1), 103–105.

Milner, M., R. McLin, and J. Petriello (2010), Imaging texture and porosity in mudstones and shales: Comparison of secondary and ion-milled backscatter SEM methods, SPE-138975, in *Canadian Unconventional Resources and International Petroleum Conference*, Calgary, Alberta, Society of Petroleum Engineers.

Mitchell, J. K., and K. Soga (2005), *Fundamentals of Soil Behavior*, 3rd ed., John Wiley & Sons, Hoboken, New Jersey.

Neuzil, C. E. (1986), Groundwater flow in low-permeability environments, *Water Resources Research*, *22*(8), 1163–1195.

Neuzil, C. E. (2000), Osmotic generation of "anomalous" fluid pressures in geological environments, *Nature, 403*, 182–184.

Neuzil, C. E., and A. M. Provost (2009), Recent experimental data may point to a greater role for osmotic pressures in the subsurface, *Water Resources Research, 45*(3).

Olsen, H. W. (1972), Liquid movement through kaolinite under hydraulic, electric, and osmotic gradients, *AAPG Bulletin, 56*(10), 2022–2028.

Rahman, M. M., S. Chen, and S. S. Rahman (2005), Experimental investigation of shale membrane behavior under tri-axial condition, *Petroleum Science and Technology, 23*, 1265–1282.

Takeda, M., T. Hiratsuka, K. Ito, and S. Finsterle (2012), Development and application of chemical osmosis simulator based on TOUGH2, in *2012 TOUGH2 Symposium*, Lawrence Berkeley National Laboratory, Berkeley, California.

van Oort, E., A. H. Hale, and F. K. Mody (1995), Manipulation of coupled osmotic flows for stabilisation of shales exposed to water-based drilling fluids, SPE 30499, in *1995 SPE Annual Technical Conference and Exhibition*, Dallas, Texas, Society of Petroleum Engineers.

Whitworth, T. M. (1993), Hyper-filtration-induced isotopic fractionation: Mechanisms and role in the subsurface, Ph.D. thesis, Purdue University, West Lafayette, Indiana.

Xu, T., N. Spycher, E. Sonnenthal, G. Zhang, L. Zheng, and K. Pruess (2004), TOUGH-REACT user's guide: A simulator program for non-isothermal multiphase reactive transport in variably saturated geological media, LBNL-55460, Lawrence Berkeley National Laboratory, Berkeley, California.

Young, A., and P. F. Low (1965), Osmosis in argillaceous rocks: Geological notes, *AAPG Bulletin*, *49*, 1004–1007.

7

An Experimental Investigation of Stress-Dependent Permeability and Permeability Hysteresis Behavior in Rock Fractures

Da Huo and Sally M. Benson

ABSTRACT

Stress-dependent permeability in rock fractures has been investigated since the 1960s [*Snow*, 1968]. The consequences of stress-dependent permeability in fractures have implications in oil and gas production, especially in tight oil/gas production [*Abass et al*., 2009] and shale gas production [*Cho et al*., 2012], coalbed methane production [*McKee et al*., 1988], and for CO_2 storage projects. Changes in permeability are attributed to three factors: changes in mean aperture, changes in roughness, and changes in contact area. The relative contribution of each factor and how it depends on the stress history are investigated here using concurrent stress-dependent permeability and aperture measurements using X-ray CT scanning. Saw-cut fractures in two rocks are tested. We find that stress-dependent permeability and hysteretic behavior is influenced by both aperture change and roughness change. For a small aperture fracture tested here, changes in roughness dominate the permeability response to stress changes. The Modified Cubic Law [*Witherspoon et al*., 1980] and models from *Walsh* [1981], *Zimmerman et al*. [1992], and *Sisavath et al.* [2003] are compared with the experimental data, and results show that all four models do not result in sufficiently large permeability variation. Additionally, none of the previous models quantifies the relative contribution of aperture and roughness to permeability change. A new empirical model is proposed based on the Modified Cubic Law [*Witherspoon*, 1980] that provides a better match to the experimental data and accounts for both stress-dependent aperture and roughness.

7.1. INTRODUCTION

Worldwide, fractured carbonates contain 60% of the remaining oil and more than 40% of gas reserves [*Beydoun*, 1998]. The recent shale gas/oil boom also results from the formation of fracture networks generated by hydraulic fracturing. In both cases, resource production would not be possible without the presence of fractures, which provide permeable pathways by which reservoir fluids can flow to the well. In most cases, fracture permeability is treated as constant during production [*Tao et al.,* 2009]. However, oil production from fracture networks in shale reservoirs is impacted by reduced natural fracture conductivity caused by stress effects, resulting in lower recovery, as indicated by *Wan et al*. [2013]. Permeability decline with the reservoir depletion is also found in naturally fractured reservoirs [*Pinzon et al*., 2000].

Fractures are commonly visualized conceptually as parallel plates separated with an aperture e. The most commonly used equation for describing flow through fractures is the Cubic Law [*Boussinesq*, 1868; *Witherspoon et al.*, 1980], which assumes laminar flow (Hagen-Poiseuille flow) between two parallel plates:

$$q = -\frac{e^3}{12\mu}\frac{dp}{dx} \tag{7.1}$$

where q is the flow rate per unit width of the fracture, e is the aperture between separated plate surfaces, $\frac{dp}{dx}$ is the pressure gradient, and μ is the fluid viscosity.

The parallel plate model highly simplifies fracture flow and neglects the tortuosity and roughness of natural fractures. Several other parameters also impact a fracture's permeability, including inertial loss from entrance and

Department of Energy Resources Engineering, School of Earth Sciences, Stanford University, Stanford, California, USA

Dynamics of Fluids and Transport in Complex Fractured-Porous Systems, Geophysical Monograph 210, First Edition.
Edited by Boris Faybishenko, Sally M. Benson, and John E. Gale.

exhaust boundaries, change in flow velocity or direction due to constrictions or obstructions, and initiation of turbulence due to localized eddy formation [*Lomize*, 1951; *Huitt*, 1956; *Romm*, 1966; *Raven and Gale*, 1985; *Parrish*, 1963; *Pyrak-Nolte et al*, 1987]. Modifications of the parallel plate model have attempted to include the effects of roughness and tortuosity. For example, *Witherspoon et al*. [1980] introduced a friction factor, f, to account for the roughness of fracture surfaces:

$$q = -\frac{1}{f}\frac{e^3}{12\mu}\frac{dp}{dx} \tag{7.2}$$

The friction factor is a representation of the tortuosity and roughness of the fracture surface [*Cook et al.,* 1990]. With the increase of roughness, the friction factor will also increase because it becomes harder for fluid to percolate through the fractures. The friction factor will become unity if there is no tortuosity or roughness. The aperture distribution will affect surface roughness and tortuosity; thus, it will affect the friction factor. Rough fracture permeability can be 35 times smaller than the smooth fracture [*Crandall et al*., 2010]. Another modification is to increase the power index. The power index is reported to be between 3.5 and 13.0 for different fracture types [*Pyrak-Nolte et al*., 1987; *Sisavath et al*., 2003; *Qian et al*., 2011].

When effective stress increases, fracture permeability may decrease due both to decreases in aperture and increasing friction factor. The friction factor has been expressed and calculated using different methods. *Walsh* [1981] proposed a relationship of the following form:

$$\frac{K}{K_0} = \frac{1-\alpha}{1+\alpha} \tag{7.3}$$

where K is the permeability of rough fractures, K_0 is the permeability of the fracture with no asperities, and α is the ratio of contact area to total area of the fracture. *Walsh* [1981] also proposed the relationship between permeability and normal stress:

$$\frac{K}{K_0} = \left[1-\sqrt{2}\frac{h}{e_0}\ln\left(\frac{P}{P_0}\right)\right]^3 \frac{1-b\left(P-P_0\right)}{1+b\left(P-P_0\right)} \tag{7.4}$$

where h is the scalar quantity of root mean square asperity heights, b is the change in the ratio of contact area to crack area with pressure, and e_0 is the initial aperture. *Kassis and Sondergeld* [2010] conducted laboratory experiments that showed the Walsh model provides good estimates of effective stress-dependent fracture permeability in most cases. However, the Walsh model simplifies the asperities to be circular cylindrical. To account for more general cases, *Zimmerman et al*. [1992] introduced the elliptical shape and the resulting expression becomes

$$\frac{K}{K_0} = \frac{1-\beta\alpha}{1+\beta\alpha} \tag{7.5}$$

where $\beta = \dfrac{(1+b)^2}{4b}$ and b is the aspect ratio of the ellipse. It is noted that the fracture permeability will not drop down to zero even if high stress is applied. *Esaki et al*. [1998] proposed that there is an initial aperture E_0 that cannot be deformed. Other models between permeability and stress have also been proposed by *Gangi* [1978], *Gale* [1982], and *Swan* [1983]. Of these three models, *Lee and Cho* [2002] argued that Gale's model provides better permeability estimates than do Gangi's and Swan's models. However, none of these models provides a way to quantify the relative contributions of aperture change and roughness change.

Roughness relates two concepts for describing fracture apertures, the hydraulic aperture (the effective mean aperture of the fracture) and the mechanical aperture [*Renshaw*, 1995]. The hydraulic aperture is calculated by equating Darcy's Law and the cubic law with the measured pressure drop for a given flow rate. The mechanical aperture is the real opening between the two fracture surfaces, usually obtained by the arithmetic mean of all aperture data. The relationship between hydraulic aperture and mechanical aperture is defined as [*Barton et al*., 1985]

$$e_h = \frac{E^2}{JRC^{2.5}} \tag{7.6}$$

where E is the mean mechanical aperture, e_h is the hydraulic aperture, and JRC is the joint roughness coefficient, which is primarily defined to characterize the shear fracture surface roughness. Both of the two parameters are expressed in microns. By taking JRC into consideration, the Barton equation presents a simple way to relate the mechanical aperture with the hydraulic aperture. JRC ranges from 0 to 20 [*Barton and Choubey*, 1977]. Rougher fracture surfaces correspond to larger values for the JRC. For higher flow rates and larger apertures, the hydraulic aperture and the mechanical aperture tend to be equal, and using hydraulic methods to measure the mechanical aperture provides a good approximation [*Iwai*, 1976]. As both of the apertures get smaller, generally induced by higher normal stress, laboratory tests show that the hydraulic aperture will be much smaller than the mechanical aperture [*Cook et al*., 1990]. To account for the irregular shape of the fracture surface, *Sisavath et al*. [2003] applied perturbation method to fluid flow through a symmetric fracture with varying walls. For a sinusoidally varying fracture surface, they proposed the hydraulic aperture and the mechanical aperture relates by

$$h_H^3 = \frac{(2H_0)^3\left(1-\tilde{\delta}^2\right)^{\frac{5}{2}}}{1+\frac{\tilde{\delta}^2}{2}}\left[1+\frac{\tilde{\delta}^2}{\tilde{\lambda}^2}\left(\frac{36}{15}\right)\frac{\pi^2\left(1-\tilde{\delta}^2\right)}{1+\frac{\tilde{\delta}^2}{2}}\right]^{-1} \tag{7.7}$$

where H_0 is the mean half-aperture of the fracture, h_H is the hydraulic aperture, $\tilde{\delta} = \frac{\delta}{H_0}$, and $\tilde{\lambda} = \frac{\lambda}{H_0}$, where δ is the amplitude of the constriction and λ is the wavelength. When the mean aperture is small, this model results in large decreases in permeability with increasing stress.

7.1.1. Stress-Dependent Permeability in Fractures

Fractures voids tend to be more cracklike compared with oval or triangular shapes of pores in porous media and thus deform easily and have a higher degree of stress sensitivity [*National Research Council*, 1996]. Changes in normal stress and shear stress can both cause the permeability of a fracture to change [*Brace*, 1978; *Esaki et al*., 1998; *Esaki et al*., 1999]. Joint deformation can take different forms, including normal closure, opening, shearing, and dilation. In this chapter, we discuss only the effect of normal stress on fracture permeability and void geometry change.

Void geometry determines fluid flow paths in rock fractures. The critical neck (the smallest aperture along the path of highest aperture through the fracture) dominates macroscopic flow properties [*Pyrak-Nolte and Cook*, 1988; *Pyrak-Nolte et al*., 1990]. At low to moderate effective stress (effective stress is defined as the difference between the compressive stress and the pore pressure), aperture changes can result in up to three orders of magnitude change in conductivity, which results in conductivity loss at early stages of reservoir depletion [*Abass et al*., 2009]. The highly nonlinear stress deformation curves for fractures must be a result of changes in the geometry of the areas of contact in response to changes in the applied stress [*National Research Council*, 1996]. Increasing compressive stress will increase the number of points of contact between asperities on the fracture surfaces. At low stress levels, natural fracture openings diminish more rapidly than fracture closures. Aperture and tortuosity of those portions of the flow path that impede flow at high stress levels become virtually independent of stress or fracture closure at the highest stress level [*Cook et al*., 1990]. This behavior can be explained by the increase of fracture stiffness with normal stress, described by *Pyrak-Nolte et al*. [1990].

7.1.2. Permeability Hysteresis in Fractures

Another well-observed phenomenon is strain hysteresis in intact and fractured rocks [*Jaegar et al*., 2007]. By interference from the cubic law, similar hysteresis for permeability can be expected. Permeability hysteresis has been observed but not discussed in detail in previous studies [*Witherspoon*, 1980; *Gale*, 1982; *Tsang and Witherspoon*, 1983; *Raven and Gale*, 1985]. When a fracture under high effective stress is decompressed, the permeability increases but not along the compression pathway, and it never returns to the original precompression value. This hysteretic behavior suggests irreversible deformation of fracture asperities and fracture roughness. Repeated cycles of loading and unloading could be anticipated to induce hysteretic behavior in both permeability and fracture apertures.

In this study, we conduct a set of experiments to systematically investigate the relationship between permeability, aperture distributions, and effective stress. We concurrently measure fracture permeability and fracture aperture distribution changes (using X-ray CT) with cycling stress. Permeability changes and aperture changes are compared at the same effective stress. Due to simultaneous measurement of fracture permeability and aperture distribution, roughness change with stress is also investigated using the friction factor and Joint Roughness Coefficient approaches.

7.2. MATERIALS AND EQUIPMENT

7.2.1. Materials

Permeability is measured using a high-pressure core flood apparatus while X-ray computed tomography (CT) scanning is performed to measure fracture aperture distributions that can be correlated with permeability change. Two data sets, including a high-permeability Berea sandstone and a low permeability Israeli Zenifim Formation sandstone, have been measured. Both rocks have a single saw-cut fracture in the middle of the core.

The high-permeability Berea sandstone core is well sorted with submature granular features. The rock is relatively homogeneous with little porosity variation in the core. Before the experiments, the Berea sample is fired at 700°C to stabilize swelling clays. The extremely low permeability sandstone from the Zenifim sandstone formation is obtained from the Ramon-1 well in the central Negev area at a depth of about 1770 m below surface (Precambrian age). The Zenifim sandstone is described as immature feldspathic greywacke. The rock grains are compositionally and texturally immature, with a wide range in grain sizes and a high angularity and low sphericity. The Zenifim sandstone is well cemented, which causes its extremely low permeability. Significant porosity heterogeneity is also

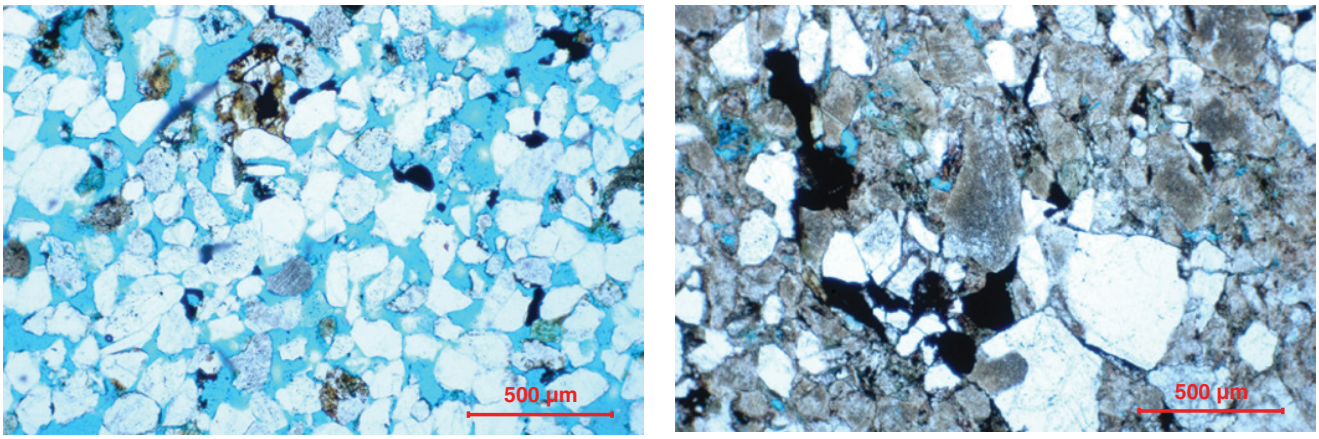

Figure 7.1 Thin section micrographs of Berea sandstone (left) and Zenifim sandstone (right).

Table 7.1 Properties of Berea and Zenifim sandstones.

Rock Samples	Berea Sandstone	Zenifim Sandstone
Length, cm	8	6.7
Radius, cm	5	5
Porosity, %	22	2.5–3.9
Permeability, mD	500	<<1

found. The saw-cut fracture is smoother for the highly cemented Zenifim sandstone compared with the Berea sandstone, where some grains are removed from the surface during sawing. The thin-section micrographs of Berea sandstone and Zenifim sandstone are shown in Figure 7.1. The properties of two rock samples are shown in Table 7.1.

7.2.2. Experimental Setup

7.2.2.1. Core flood apparatus

The core flooding apparatus is a modified version of a facility described by *Perrin and Benson* [2009] shown in Figure 7.2. The rock sample is wrapped in a sleeve with layering from the core outwards of heat-shrinkable Teflon, nickel foil, another layer of heat-shrinkable Teflon, and a viton rubber sleeve, and then placed in an aluminum core holder. Two high-accuracy pressure transducers (oil-filled Digiquartz Intelligent Transmitter, model 9000-3K-101) are tapped into the core holder to measure pressure at the inlet and outlet of the core. A variable displacement pump (Teledyne Isco, model 260D) is used to inject water around the sleeve to create the confining stress. Electric heaters are kept between the sleeve and core holder to maintain the temperature inside the core. A dual pump system is used to inject water or nitrogen into the core (Teledyne Isco, model 500D). The system is composed of two pumps connected with a set of electric valves. The dual pump configuration provides continuous fluid delivery by synchronizing the pump and refill strokes so that one pump is always delivering fluid. The refill and delivery of each pump are automated through a central controller. A pressure-regulating pump (Teledyne Isco, model 1000D) is connected to the outlet of the core through a recirculation pressure vessel to maintain 2.07 MPa at the downstream end of the core throughout the experiment.

7.2.2.2. Permeability measurements

Permeability is measured using the steady state method. Fluid is injected at three different rates while the pressure drop across the core is measured. Based on the core size, the fluid viscosity, the slope of pressure drop, and the fluid injection rate, Darcy's Law is used to calculate the permeability. For gas measurements, upstream pressure and downstream pressure are included to adjust gas volume change [*Ahmed*, 2010]. At 2.07 MPa pore pressure, the slippage effect is highly suppressed and therefore not considered here [*Klinkenberg*, 1941; *Firouzi and Wilcox*, 2013]. The intact core permeability is measured at different stress levels. Using Darcy's Law, we subtract the matrix permeability from the fractured core permeability and obtain the permeability for the fracture itself. The fracture permeability is calculated by

$$K_f(\sigma) = (K(\sigma) - K_m(\sigma)) * \frac{A_m}{A_f(\sigma)} + K(\sigma) \qquad (7.8)$$

where K_m, K_f, and K are the permeability for matrix, fracture and whole core. A_m and A_f are surface areas for matrix and fracture. In Equation 7.8, K_m, K_f, K, and A_f are stress dependent, while A_m keeps constant with changing stress levels. The area of the fracture is calculated using a constant mean aperture of 0.1 mm for the Berea sandstone. For Zenifim sandstone, the fracture area changes with stress and is calculated directly based on aperture measurements obtained from CT scanning.

For the Berea sandstone, water is used to measure the permeability because the pressure drop is not large enough

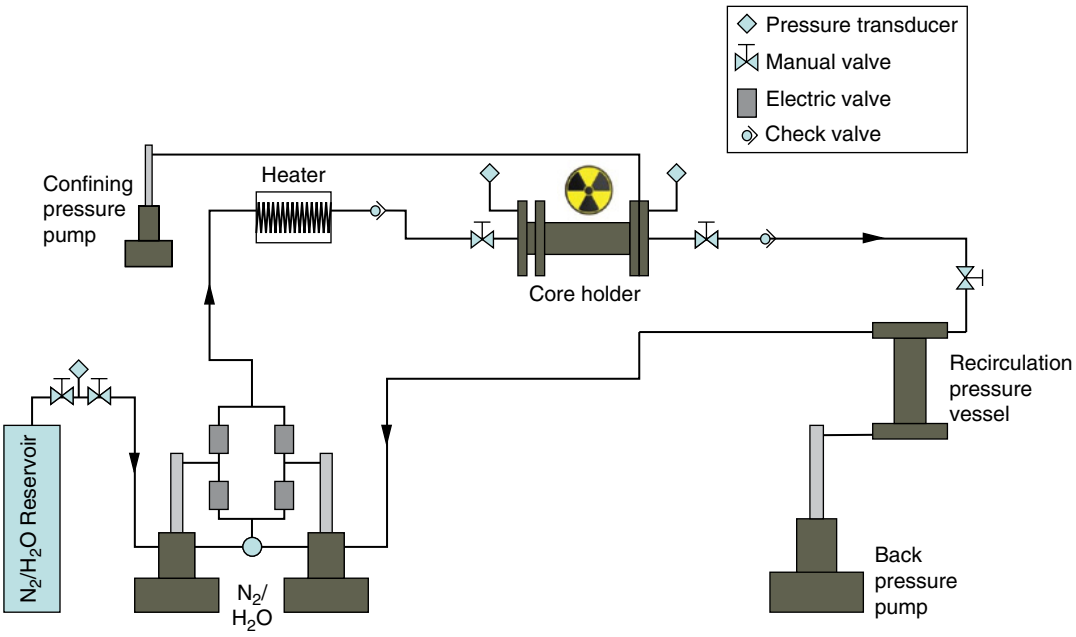

Figure 7.2 Schematic of the core flooding apparatus.

to measure with nitrogen. The aperture and permeability measurements are conducted sequentially. The aperture is first measured in an air-filled core using CT scanning while cycling confining stress. For the Zenifim sandstone, nitrogen is used.

For both cores, a series of permeability and aperture measurements are made for a range of confining stresses. The Berea sandstone's effective stress cycle starts at 0.34 MPa and increases stepwise to 11.03 MPa, then decreases stepwise back to 0.34 MPa. The second effective stress cycle ranges from 0.34 to 22.06 MPa. For the Zenifim sandstone, a single cycle with effective stress changes from 0.69 to 22.06 MPa is performed.

7.2.2.3. Aperture measurement using CT scanner

To measure fracture aperture distributions, the aluminum core holder is placed in a medical X-ray CT scanner (General Electric Hi-Speed CT/i X-ray computed tomography). Apertures are determined using the missing attenuation method based on calibration using spacers of known thickness [*Johns et al.*, 1993; *Keller*, 1997; *Van Geet and Swennen*, 2001; *Ketcham et al.*, 2010; *Vandersteen et al.*, 2003]. For the calibration, the following imaging parameters are applied: a voxel dimension of about $(0.5 \times 0.5 \times 1)$ mm^3, a tube current of 200 mA, an energy level of 120 keV and a display field of view of 25 cm. Five scans are taken and averaged to reduce the uncertainty of the CT scanning. By repeating for five scans, the measurement error can be reduced to less than one twentieth of the voxel dimension or 25 μm [*Huo et al.*, in press].

The missing CT attenuation is defined as

$$CT_{MA} = \sum_{i=1}^{N_{vox}} \left(CT_{mat} - CT_i \right) \tag{7.9}$$

where CT_{mat} represents the average CT value of the rock matrix, CT_i represents the CT values of the line across the trough, and N_{vox} represents the voxel number of the line across the trough. Because CT numbers are discrete, we use the summation in all calculations. The fracture aperture is related to the missing attenuation by

$$d = \frac{CT_{MA}}{C} \tag{7.10}$$

where d is the fracture aperture and C is the calibration coefficient. Calibration coefficients are determined for both rocks using 0.2, 0.3, 0.4, and 0.5 mm spacers between the two rock surfaces. After the sample has been placed into the core holder, a slight confining stress of 0.34 MPa is added to the rock to flatten the spacer. During the calibration runs, twenty scans are taken to reduce the uncertainty of CT scanning even further. The images of scans with different spacers are shown in Figure 7.3.

To calculate the missing attenuation due to the presence of a fracture, data cropping, classification, and identification of fracture features is needed [*Karpyn*, 2009]. In this study, we choose the mean CT number of the matrix as the baseline. Based on the preknown fracture location, the lowest CT number is located. Trough region is identified when CT number stops increasing on both sides of the lowest CT number. Any value that is less than baseline CT value in the trough region is considered to be

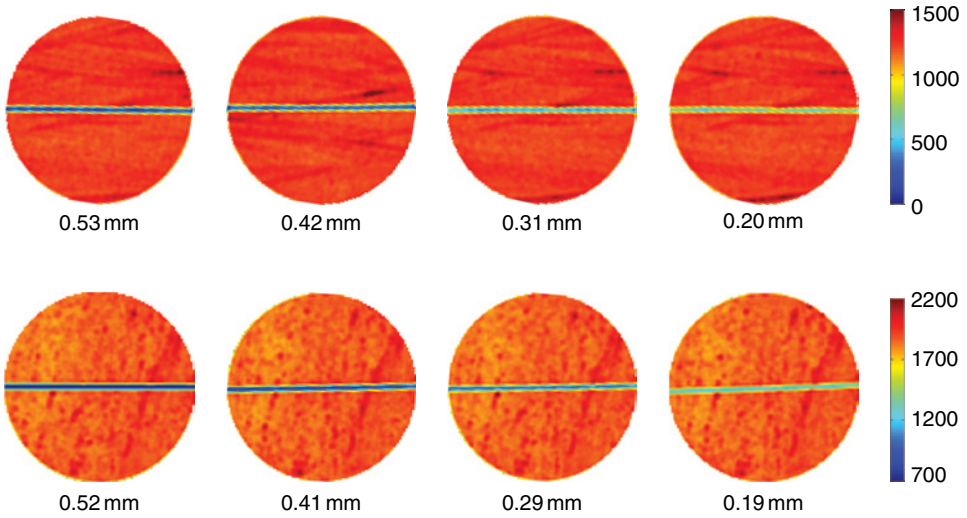

Figure 7.3 Calibration image of Berea sandstone (upper) and Zenifim sandstone (lower) with different spacers. Each image is the average of 20 scans. The color bar represents the CT number.

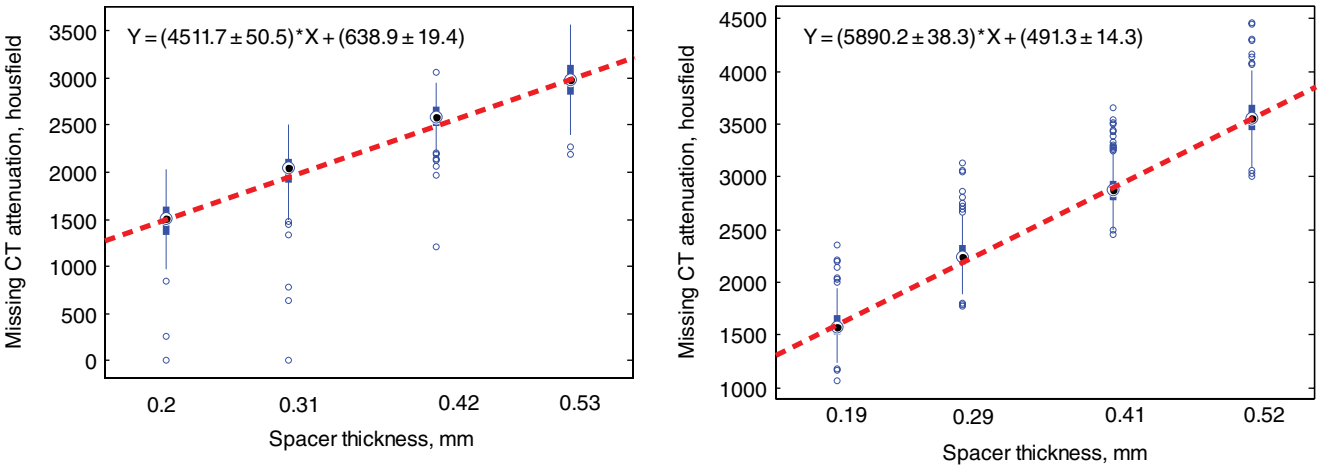

Figure 7.4 Calibration of Berea sandstone (left) and Zenifim sandstone (right). The dotted line corresponds to linear fitting between missing CT attenuation and spacer thickness. The standard deviation of the slope is also calculated. The thick blue lines show the 75% confidence interval while the thin blue line shows the 25% confidence interval. The circles above and below the thin blue lines are outliers.

caused by the fracture. The missing attenuation is calculated using Equation 7.9. For a perfectly smooth fracture, the fracture aperture and missing attenuation are expected to have a linear relationship, and the regression line should pass through the origin. However, in practice, the regression line does not pass through the origin because of the roughness of the fracture. The calibration coefficient C is calculated from the slope of the line fit through the data points.

Calibration curves are shown in Figure 7.4. Linear regression has been done based on all values of missing attenuation, and the standard deviation is calculated both for slope and intercept. Based on this, the calibration coefficients are 4511.7 ± 50.5 and 5890.2 ± 38.3 for the Berea and Zenifim sandstones, respectively. Note that the regression line does not pass through the origin, suggesting that the missing attenuation caused by the roughness of the fracture creates an apparent aperture of 0.14 mm for Berea sandstone and 0.08 mm for Zenifim sandstone.

7.3. EXPERIMENTAL RESULTS

7.3.1. Stress-Dependent Pressure Drops and Hysteresis in Fractured Berea Sandstone

As an example of the stress-dependent permeability and hysteresis, a preliminary experiment is conducted by continuously flowing water through the fractured rock

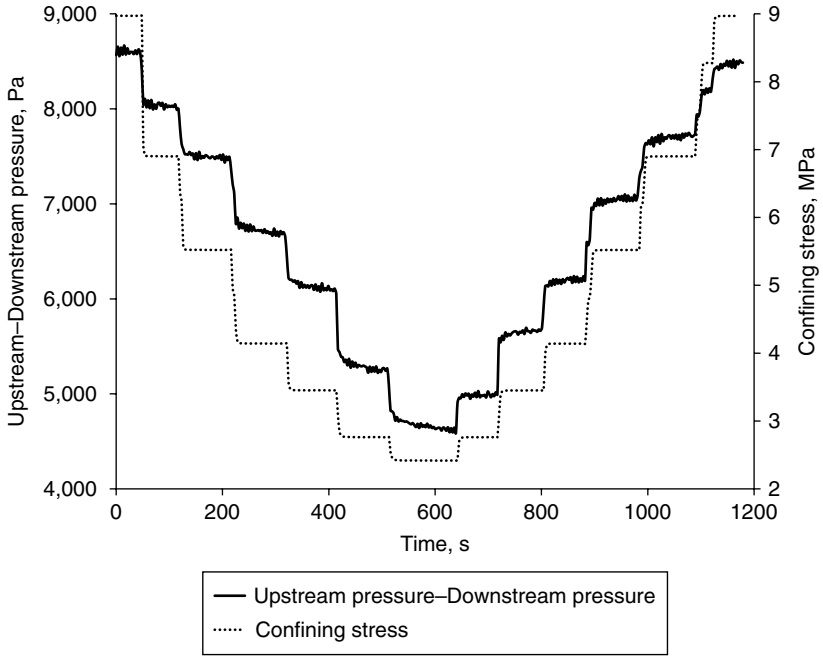

Figure 7.5 Pressure drop showing continuous water injection with change of confining stress for the fractured Berea sandstone.

while changing the confining stress (Figure 7.5). The confining stress first decreases stepwise from 8.96 MPa to 2.41 MPa and then increases back to 8.96 MPa. If the permeability is constant (not stress dependent), the pressure drop across the core should remain constant throughout the entire experiment. The large change in pressure drop across the core clearly demonstrates the stress dependency of fracture permeability. If there is no hysteresis, the pressure drop should be identical for each value of effective stress, regardless of whether it is increasing or decreasing. As shown clearly in Figure 7.5, the pressure drop is slightly larger during decompression than it is during recompression, clearly demonstrating hysteresis.

The hysteresis behavior is caused by the change of the state of meta-stable equilibrium [*Gumbsch and Pippan*, 2011]. Under meta-stable equilibrium, the strength of the asperities supports the applied load, and the equilibrium will break when changing the loading status. Increasing the load will create an unstable state where stress exceeds the asperity strength at the asperity tips. This will result in an increase of the contact area, and possibly crushing of the asperities. A new meta-stable equilibrium will form once the asperity strength reaches the applied load. Since the asperity tips are crushed to a certain extent, the elastic recovery of the fracture aperture is reduced, and hysteresis is produced.

7.3.2. Permeability and Aperture Measurements for the Berea Sandstone

The Berea sandstone experiment includes the two effective stress cycles shown in Figure 7.6. When the fractured rock is compressed, the permeability drops to less than half of the original value due to increasing the effective stress from 0.34 MPa to 11.03 MPa. The permeability has an exponential relationship with effective stress. During the decompression, permeability values are consistently lower. A second cycle exhibits similar changes in permeability, with further permeability reduction when effective stress increases to 22.06 MPa.

The aperture distributions for these compression and decompression cycles are shown in Figure 7.7. An obvious decrease of apertures is observed when stress is applied. At low stress levels, the larger apertures close first. Fracture voids are closed, and the contact area is increased at higher effective stress. When stress is relieved, apertures recover but do not reach the original preloading values. Examination of these images suggests that hysteresis is mostly present in portions of the fracture with larger apertures.

As shown in Figures 7.8 and 7.9, initially, fracture apertures are normally distributed. With increasing effective stress, the distribution becomes lognormal, and the mean value decreases. When effective stress decreases, the distribution remains lognormal. In Figure 7.9, aperture

distributions at the same stress level for different loading-unloading cycles are compared. Most deformation occurs in the first cycle and for the largest apertures. In the second cycle, the deformation and hysteresis are small. For the first compression and decompression cycle, which is shown in the right-hand figure of Figure 7.9, the major aperture changes are found in the range of 0.1 to 0.15 mm, which is typical of the grain size in a Berea sandstone, suggesting that grains are being crushed and roughness is consequently reduced. The mean aperture, the standard deviation of aperture distribution, and the correlation length of x and y directions for Berea sandstone are listed in Table 7.2. The standard deviation and the correlation length do not exhibit a clear stress dependency.

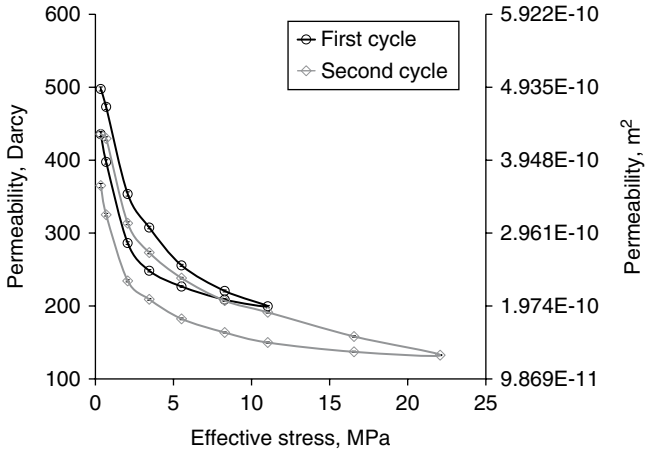

Figure 7.6 Stress-dependent permeability for different cycles of fractured Berea sandstone. The black curve shows the permeability measurement in the first cycle while the grey curve shows the second cycle. Circular or diamond-shaped points on the curves show different measurements, and the error bars on each point show one standard deviation of permeability measurement, caused by the uncertainty of measured pressure drop.

7.3.3. Permeability and Aperture Measurement Using Fractured Zenifim Sandstone

Clear stress-dependent permeability and hysteretic behavior for the fracture in the Zenifim sandstone are shown in Figure 7.10. The permeability of the fracture in the Zenifim sandstone drops to less than 10% of the original value when the effective stress increases from 0.69 MPa to 11.03 MPa. The permeability also exhibits an exponential relationship with effective stress. When the rock is decompressed to the initial effective stress of 0.69 MPa, the permeability is only about half the original value.

Aperture maps and frequency distributions are shown in Figures 7.10 and 7.11. The contact area (fraction of the fracture surface with zero apertures) increases with effective stress (upper right panel of Figure 7.10) and a larger fraction of the apertures remain closed after the

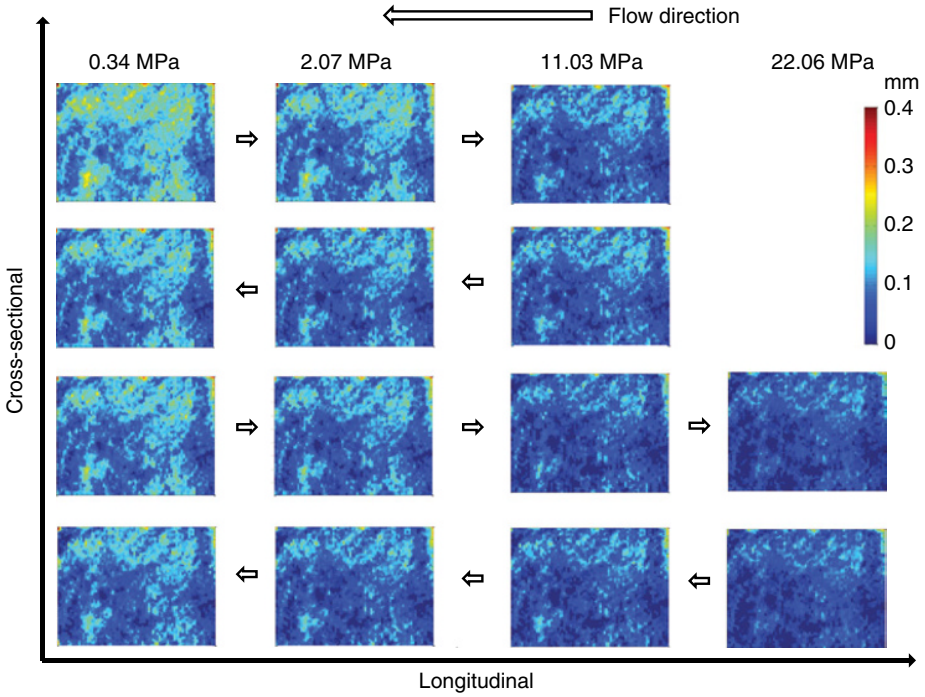

Figure 7.7 Stress-dependent aperture distribution of different cycles of fractured Berea sandstone. The upper two rows of figures show the aperture distributions in the first cycle, and the lower two rows of figures show the aperture distributions in the second cycle. The effective stress is provided at the top of the images.

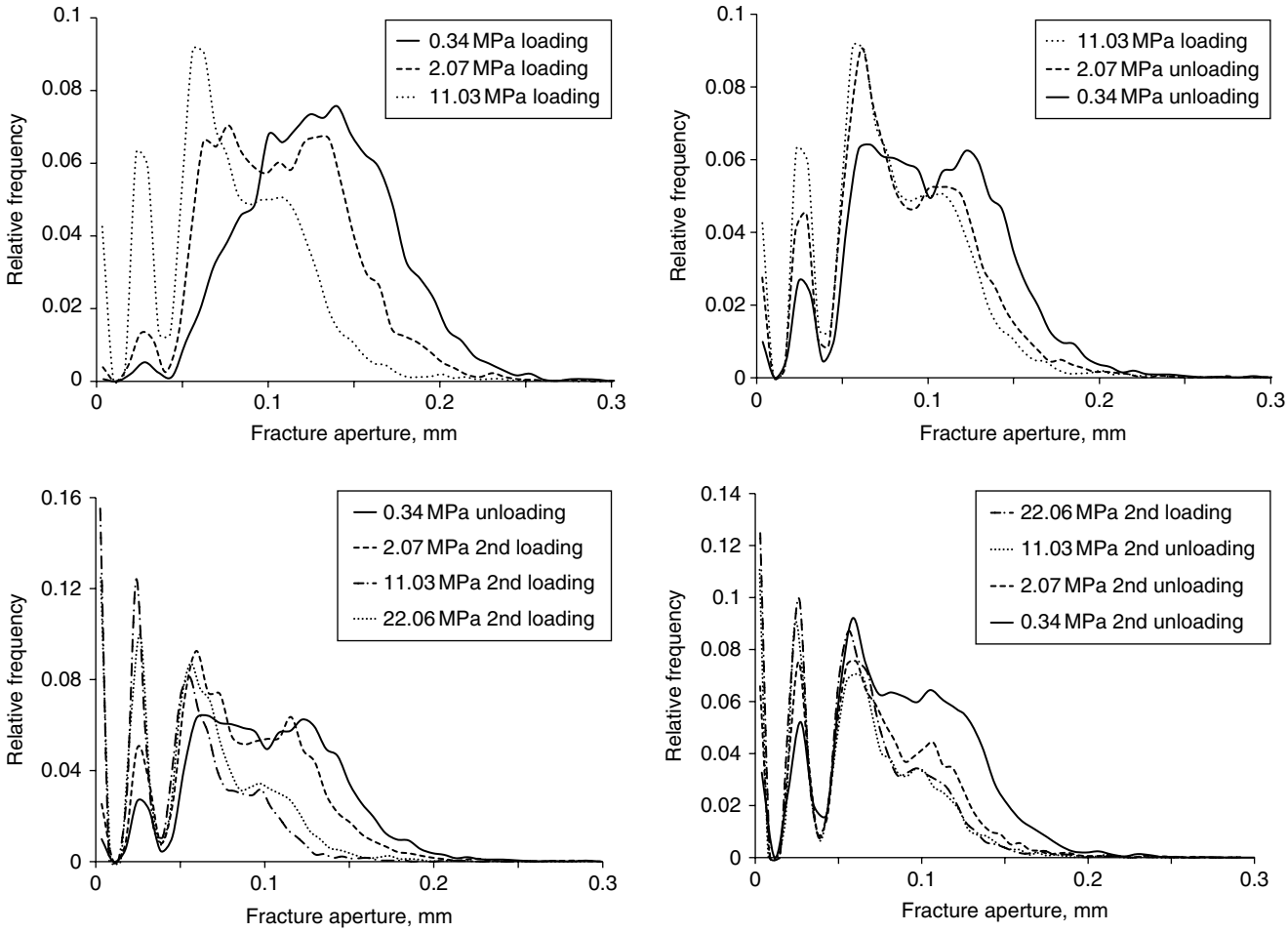

Figure 7.8 Comparison of fracture aperture relative frequency at different stress level for different loading-unloading cycles.

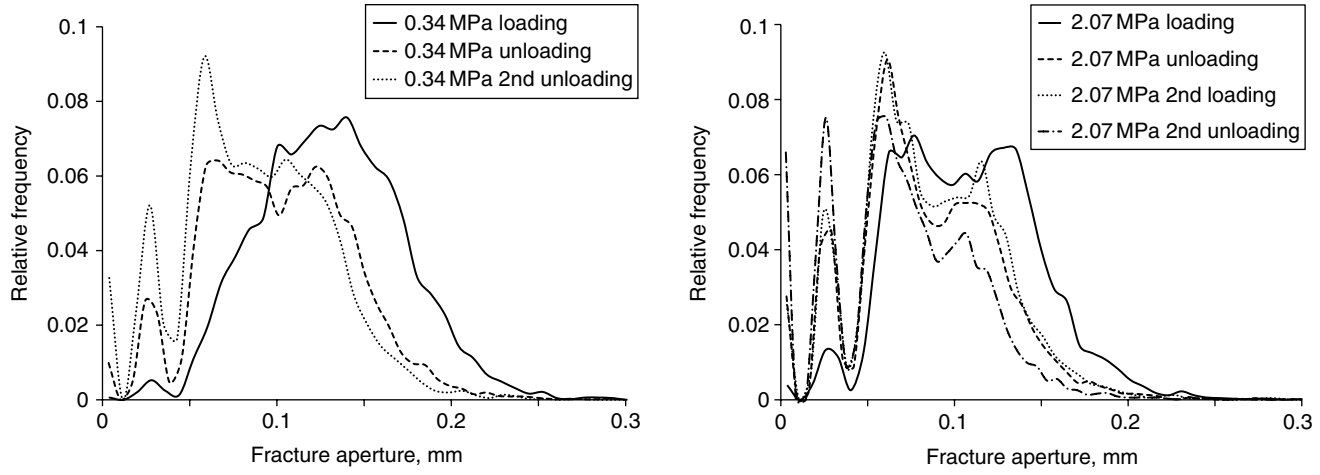

Figure 7.9 Comparison of fracture aperture relative frequency at same effective stress of different loading-unloading cycles (left: 0.34 MPa, right: 2.07 MPa).

Table 7.2 Comparison of statistical analysis of aperture data for Berea sandstone.

Cycle	Effective Stress, MPa	Mean Aperture, mm	Standard Deviation of Aperture Distribution, mm	Spatial Correlation, *x* Direction, mm	Spatial Correlation, *y* Direction, mm
First loading cycle	0.34	0.1619	0.0502	29.00	10.50
	2.07	0.1406	0.0494	29.93	10.07
	11.03	0.1140	0.0481	32.34	11.21
First unloading cycle	2.07	0.1204	0.0486	30.65	10.78
	0.34	0.1349	0.0499	30.41	10.62
Second loading cycle	2.07	0.1210	0.0484	31.06	10.42
	11.03	0.0857	0.0396	31.35	14.19
	22.06	0.1003	0.0453	29.55	10.09
Second unloading cycle	11.03	0.1027	0.0462	29.09	11.48
	2.07	0.1096	0.0482	29.24	10.98
	0.34	0.1230	0.0511	30.32	11.49

compression-decompression cycle. At 22.06 MPa effective stress, a significant fraction of the apertures are closed (Figure 7.11), which explains the low fracture permeability (3.25 D). The statistical parameters for Zenifim sandstone are listed in Table 7.3. The standard deviation and the correlation length also do not exhibit a clear stress dependency for the Zenifim sandstone.

7.4. DISCUSSION

Permeability changes can be attributed to three factors: changes in mean aperture, changes in roughness, and changes in contact area [*Witherspoon*, 1980; *Zimmerman and Bodvarsson*, 1996]. Stress changes affect all the factors [*Tsang and Witherspoon*, 1983]. However, their relative contributions and how they depend on stress history is an open question. By comparing loading to unloading behavior for permeability, mean aperture, friction factor, hydraulic and mechanical apertures, and Joint Roughness Coefficient, we can distinguish the relative importance of aperture and roughness changes.

In the following discussion we focus on the fractured Zenifim sandstone, for which we have simultaneous aperture and permeability measurements. In Figure 7.12, permeability and mean aperture are compared for the loading and unloading cycles. There is no significant difference between the loading and unloading permeability-aperture relationship. To distinguish the relative contributions of aperture and roughness change, the friction-modified version of the Cubic Law is applied to calculate permeability based on the friction factor at the initial loading condition (0.69 MPa) [*Witherspoon et al.*, 1980]. If all of the stress dependence is attributable to changes in the mean aperture, the measured data and permeability predicted from the friction-modified cubic law should be identical. However, the large and increasing gap between the calculated and measured permeabilities demonstrates that changes in aperture alone cannot predict change in permeability and that changes in roughness must occur. Closed aperture percentage data from Figure 7.10 are applied to the *Walsh* [1981] model and *Zimmerman et al*. [1992] to predict changes in permeability and are also shown in Figure 7.12. For the model in *Zimmerman et al*. [1992], the parameter β is estimated to minimize the sum of the squared difference between experimental data and model predictions. Both models fail to replicate the observed permeability decrease with decreasing aperture. By matching the aperture data with sinusoidal curve along the flowing direction, and obtaining the median amplitude (ranging from 0.0043 to 0.0050 mm) and wavelength (ranging from 9.38 to 12.97 mm) at each stress level, the model by *Sisavath et al*. [2003] captures the large permeability drop for small apertures. However, it still underestimates the permeability decrease with large stress change. We also apply power law to fit the permeability and aperture data, and obtain power index of 14.85, which is larger than previous research [*Pyrak-Nolte et al*., 1987; *Sisavath et al*., 2003; *Qian et al*., 2011]. Nevertheless, none of these models provides quantification of the relative contribution of aperture and roughness to permeability change.

By history matching the permeability data with the friction-modified cubic law model and the measured mean aperture, it is possible to calculate how the roughness changes with increasing stress. Unlike *Witherspoon et al*. [1980], the calculated friction factors shown in Figure 7.13 demonstrate that the friction coefficient is highly stress sensitive and is an order of magnitude higher than those reported therein. The relative contributions of mean aperture and roughness can be calculated using these values based on the first data at 0.69 MPa. Aperture change contributes from 20% to 45% of stress-dependent permeability changes. At low stresses during loading, increases in roughness are relatively more important. This is consistent with the observation that contact area increases rapidly at lower stresses, thus rapidly increasing tortuosity or

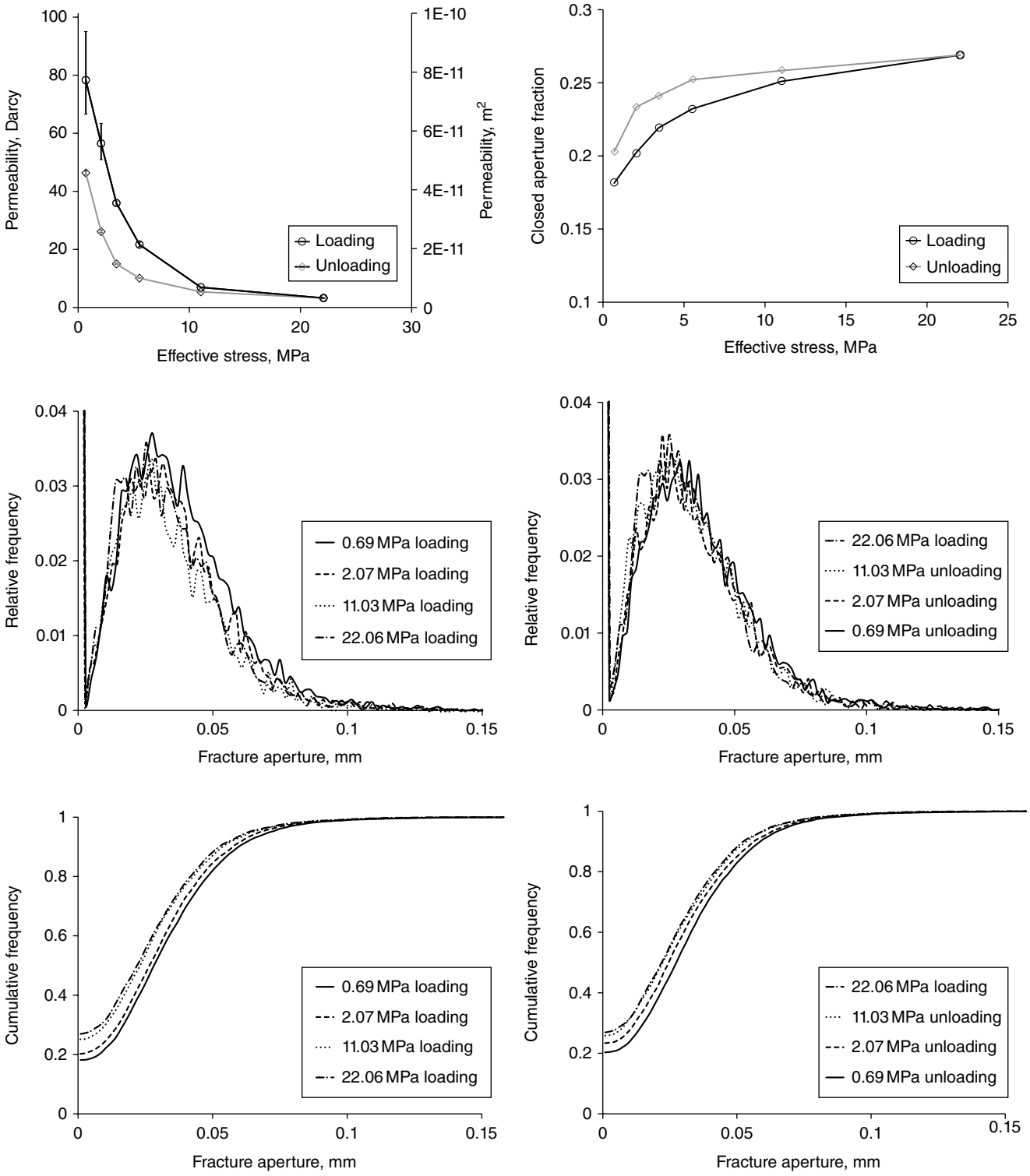

Figure 7.10 Upper left: Stress-dependent permeability for loading and unloading process of fractured Zenifim sandstone. Error bars represent one standard deviation of permeability uncertainty. Upper right: Change of closed aperture percentage (or contact area percentage) with cycled effective stress. Middle left: Relative frequency at different stress levels while loading. Middle right: Relative frequency at different stress levels while unloading. Lower left: Cumulative frequency at different stress levels while loading. Lower right: Cumulative frequency at different stress levels while unloading.

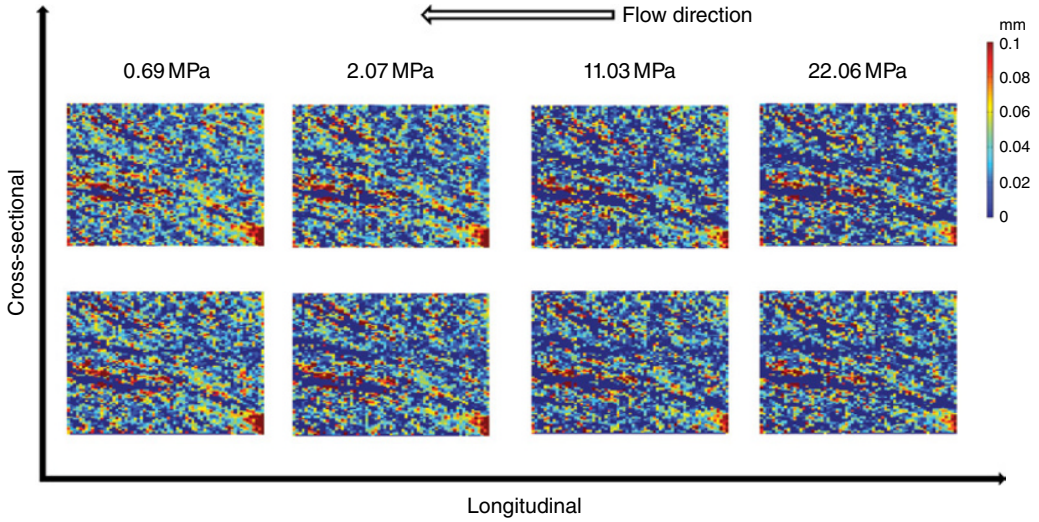

Figure 7.11 Effective stress-dependent aperture distributions for different cycles for the fractured Zenifim sandstone. Effective stress is listed across the top of the images.

Table 7.3 Comparison of statistical analysis of aperture data for Zenifim sandstone.

Cycles	Effective Stress, MPa	Mean Aperture, mm	Standard Deviation of Aperture Distribution, mm	Spatial Correlation, *x* Direction, mm	Spatial Correlation, *y* Direction, mm
First loading cycle	0.69	0.0310	0.0303	2.660	1.346
	2.07	0.0290	0.0298	2.674	1.348
	3.45	0.0279	0.0296	2.617	1.191
	5.51	0.0270	0.0284	2.583	1.172
	11.03	0.0257	0.0293	2.497	1.184
	22.06	0.0249	0.0284	2.433	1.177
First unloading cycle	11.03	0.0254	0.0291	2.424	1.142
	5.51	0.0264	0.0292	2.514	1.277
	3.45	0.0271	0.0292	2.554	1.162
	2.07	0.0274	0.0299	2.530	1.274
	0.69	0.0297	0.0301	2.597	1.308

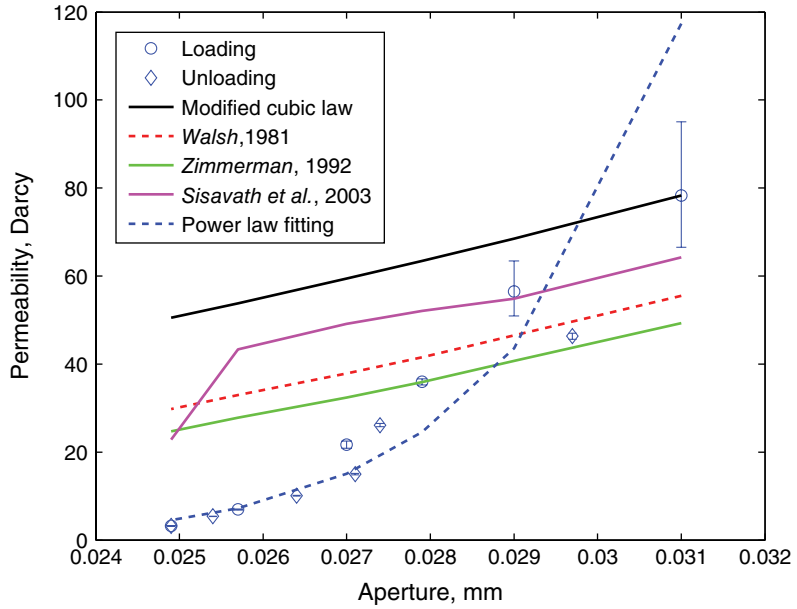

Figure 7.12 Relationship between mean aperture and permeability of fractures in Zenifim sandstone in loading and unloading process. Error bars represent one standard deviation of permeability uncertainty.

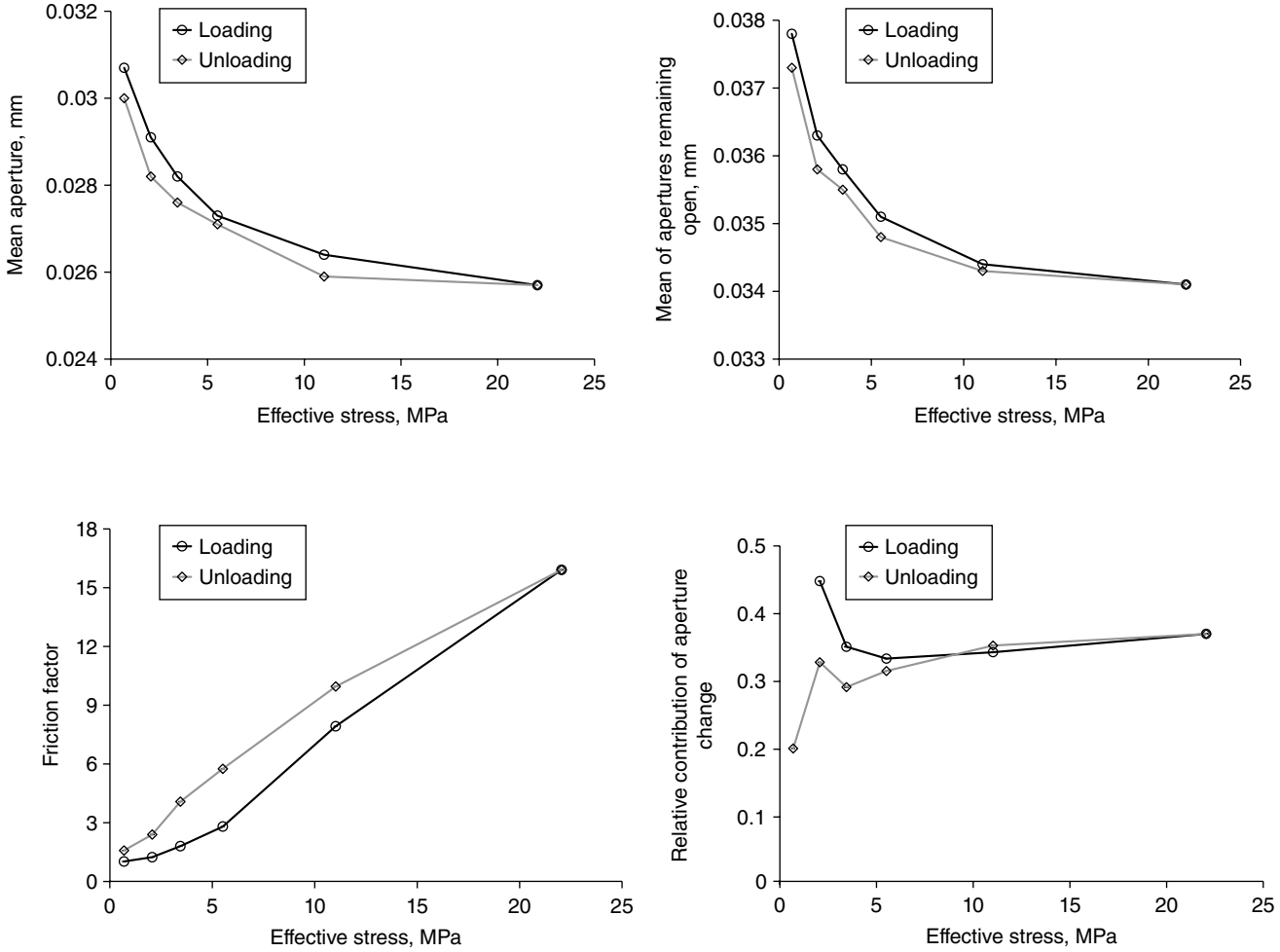

Figure 7.13 Stress-dependent mean aperture and friction factor for loading and unloading process of fractured Zenifim sandstone. Upper left: mean aperture; upper right: mean of apertures that remain open; lower left: friction factor; lower right: the relative contribution of aperture change to permeability change with effective stress.

roughness (Figure 7.10, upper right). This phenomenon can be explained by the fact that larger apertures close first at low stresses, which will cause significant permeability drop. However, because of the lognormal distribution of fracture apertures, mean aperture will not significantly reduce. At an effective stress of 0.69 MPa, aperture change contributes only 20% of permeability change, and roughness contributes 80% of permeability change.

Figure 7.14 shows that the mechanical aperture and the hydraulic aperture follow the same linear trend during loading and unloading with no evidence of hysteresis. The hydraulic aperture is found to be nearly equal to the mechanical aperture with low applied stress but reduces to about 30% of the mechanical aperture at the highest stress. Thus, the hydraulic aperture is about three times more stress sensitive than the mechanical aperture, again supporting the conclusion that roughness change contributes to the observed permeability changes.

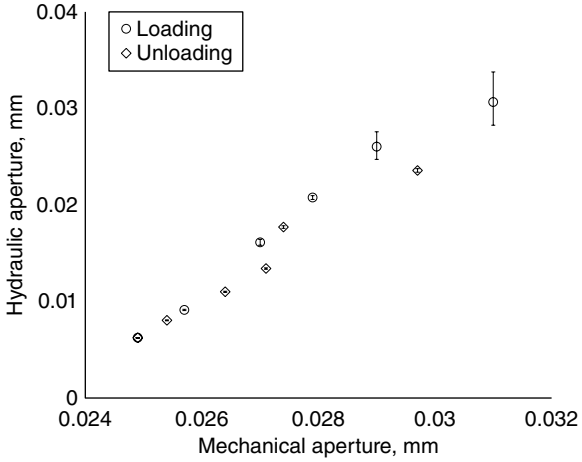

Figure 7.14 Comparison between mechanical and hydraulic apertures during loading and unloading for fractured Zenifim sandstone.

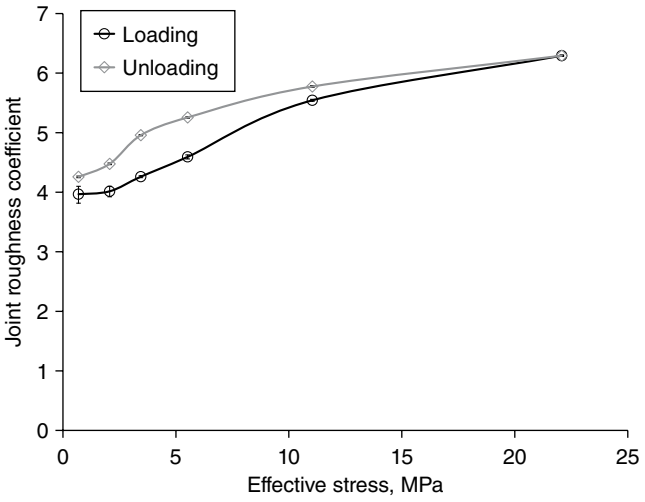

Figure 7.15 Comparison of Joint Roughness Coefficient during loading and unloading for fractured Zenifim sandstone.

Table 7.4 Parameters for fitting between friction factor/aperture and effective stress.

		a_1, a_2	b_1, b_2	c_1, c_2	R^2
Friction factor, f	Loading	−33.73	−0.0257	33.76	0.9752
Friction factor, f	Unloading	−32.85	−0.0282	33.76	0.9981
Aperture, e	Loading	0.0069	−0.2392	0.0250	0.9933
Aperture, e	Unloading	0.0053	−0.2709	0.0250	0.9617

The apparent JRC, calculated from Equation 7.6 and the data in Figure 7.15, is in the range of 3–7, corresponding to low roughness [*Barton and Choubey*, 1977]. It increases over the loading cycle, confirming that the smaller the fracture aperture, the greater the apparent roughness and tortuosity of the fracture (Figure 7.15). A small amount of hysteresis is evident at moderate stress.

Although previous research has provided various methods to relate permeability, aperture, and stress, none of these models quantifies the relative contribution of aperture and roughness to permeability change. Here we propose a modified model based on *Witherspoon et al*. [1980]. In this model, aperture and friction factor both have an exponential relationship with effective stress.

$$q = -\frac{1}{f(\sigma)}\frac{e(\sigma)^3}{12\mu}\frac{dp}{dx} \tag{7.11}$$

where $f(\sigma)$ and $e(\sigma)$ are friction factor and fracture aperture with respect to effective stress σ. Both $f(\sigma)$ and $e(\sigma)$ are expressed as follows:

$$f(\sigma) = a_1 e^{b_1\sigma} + c_1 \tag{7.12}$$

$$e(\sigma) = a_2 e^{b_2\sigma} + c_2 \tag{7.13}$$

where a_1, b_1, c_1, a_2, b_2, and c_2 are fitting parameters, and c_1 and c_2 stand for the irreducible friction factors or apertures. In general, it is not required that c_1 and c_2 be equal for loading and unloading. But for the experiment conducted here, the data suggest they are equal. The fitting parameters are shown in Table 7.4. The last column provides the regression coefficient using these parameters and shows that the model provides an excellent match to the data.

7.5. CONCLUSION

In this chapter, stress-dependent permeability and aperture are measured using core flooding data and CT scanning concurrently. Two distinct cores are used to represent a rough fracture and a smooth fracture. Stress-dependent aperture and permeability hysteresis are found in both experiments. A pixel-based aperture field is measured, and a complex hysteresis relationship both in aperture and permeability has been observed. Aperture change and roughness are respectively analyzed, and roughness change is found to be the dominant factor responsible for stress-dependent permeability change. This work also investigates the heterogeneities of fracture aperture change with stress. Preexisting models have been compared with experimental data and found to be insufficient in predicting large permeability variations. Additionally, these models do not quantify the relative contribution of aperture and roughness to permeability change. A modification of the *Witherspoon et al*. [1980] model that incorporates stress-dependent aperture and roughness is proposed and provides a better match to the observed permeability changes with stress.

ACKNOWLEDGMENTS

This work has been supported by ENI. The authors are grateful to Rani Calvo from the Geological Survey of Israel for providing the Zenifim sandstone sample used in this study.

REFERENCES

Abass, H. H., M. R. Khan, and L. Sierra (2009), Understanding stress sensitive tight gas reservoirs, *Saudi Aramco Journal of Technology*, Summer 2009, 11–21.

Ahmed, T. (2010), *Working Guide to Reservoir Rock Properties and Fluid Flow*, Gulf Professional Publishing, Burlington, MA.

Bandis, S. C., A. C. Lumsden, and N. Barton (1983), Fundamentals of rock joint deformation, *Int. J. Rock Mech. Min. Sci. Geomech. Abstr.*, *20*, 249–268.

Barton, N., S. Bandis, and K. Banktar (1985), Strength, deformation and conductivity coupling of rock joints, *Int. J of Rock Rock Mechanics, 22*(3) 121–140.

Barton, N., and V. Choubey (1977), The shear strength of rock joints in theory and practice. *Rock Mechanics*, *1*/2, 1–54.

Beydoun, Z. R. (1998), Arabian plate oil and gas: Why so rich and so prolific? *Episode 1998*, *21*(6), 74–81.

Boussinesq, J. (1868), Mémoire sur l'influence des frottements dans les mouvements réguliers des fluides (Study of the effect of friction on the laminar flow of fluids), *Journal de Mathématiques Pures et Appliquées, 2e série, tome 13,* 377–424.

Brace, W. F. (1978), A note on permeability change in geologic materials due to stress, *Pure Appl. Geophys., 116,* 627–633.

Calvo, R., and Z. Gvirtzman, (2013), Assessment of CO2 storage capacity in southern Israel. *International Journal of Greenhouse Gas Control, 14*, 25–38.

Cho, Y., O. G. Apaydin, and E. Ozkan, (2012), Pressure-dependent natural-fracture permeability in shale and its effect on shale-gas well production, SPE Annual Technical Conference and Exhibition, San Antonio, Texas.

Cook, A. M., L. R. Myer, G. W. Cook, and F. M. Doyle (1990), The effect of tortuosity on flow through a natural fracture, *Proceedings of the 31st U.S. Symposium on Rock Mechanics*, 371–378.

Crandall, D., G. Bromhal, and Z. T. Karpyn (2010), Numerical simulations examining the relationship between wall-roughness and fluid flow in rock fractures, *Int. J. Rock Mech. Min. Sci. 47*, 784–796.

Esaki, T., S. Du, Y. Jiang, Y. Wada, and Y. Mitani (1998), Relation between mechanical and hydraulic apertures during shear-flow coupling test, *Proc. 10th Japan Symp. Rock Mech.*, 91–96.

Esaki, T., S. Du, Y. Mitani, K. Ikusada, and L. Jing, (1999), Development of a shear-flow test apparatus and determination of coupled properties for a single rock joint, *Int. J. Rock Mech. Min. Sci.*, *36*, 641–650.

Firouzi, M., and J. Wilcox (2013), Slippage and viscosity predictions in carbon micropores and their influence on CO2 and CH4 transport, *J. Chem. Phys.*, *138*, 064705, doi: 10.1063/1.4790658.

Gale, J. E. (1982), The effects of fracture type induced versus natural on the stress-fracture closure-fracture permeability relationships, *Proc. 23rd U.S. Symp. Rock Mech.*, University of California–Berkeley, 290–298.

Gangi, A. F. (1978), Variation of whole and fractured porous rock permeability with confining pressure, *International Journal Rock Mechanics Mining Science, 15*, 249–257.

Gumbsch, P., and R. Pippan (2011), *Multiscale Modelling of Plasticity and Fracture by Means of Dislocation Mechanics*, Springer Science & Business Media, New York.

Huitt, J. L. (1956), Fluid flow in simulated fractures, *AIChE J.*, *2*, 259–264, doi: 10.1002/aic.690020224.

Huo, D., R. Pini, and S. M. Benson (in press),A new method for measuring fracture aperture distributions using X-ray computed tomography, *Geosphere.*

Iwai, K. (1976), Fundamental studies of fluid flow through a single fracture, Ph.D. thesis, University of California–Berkeley.

Jaegar, J. C., N. G. W. Cook, and R. W. Zimmerman (2007), *Fundamentals of Rock Mechanics*, Wiley-Blackwell, Oxford, UK.

Johns, R. A., J. S. Steude, L. M. Castanier, and P. V. Roberts (1993), Nondestructive measurements of fracture aperture in crystalline rock cores using X ray computed tomography, *Journal of Geophysical Research, 98*(B2), 1889–1900.

Karpyn, Z. T., A. Alajmi, F. Radaelli, P. M. Halleck, and A. S. Grader (2009), X-ray CT and hydraulic evidence for a relationship between fracture conductivity and adjacent matrix porosity, *Engineering Geology*, *103*, 139–145.

Kassis, S., and C. Sondergeld (2010), Gas shale permeability: Effects of roughness, proppant, fracture offset, and confining pressure, International Oil and Gas Conference and Exhibition in China, 8–10 June 2010, Beijing, China.

Keller, A. A. (1997), High resolution CAT imaging of fractures in consolidated materials, *International Journal of Rock Mechanics and Mining Science*, *34*(3/4), 358–371.

Ketcham, R. A., D. T. Slottke, and J. M. Sharp, Jr. (2010), Three-dimensional measurement of fractures in heterogeneous materials using high-resolution computed tomography, *Geosphere*, *6*, 499–514.

Klinkenberg, L. J. (1941), The permeability of porous media to liquids and gases, *Drilling and Production Practice*, American Petroleum Inst., 200–213.

Lee, H. S., and T. F. Cho (2002), Hydraulic characteristics of rough fractures in linear flow under normal and shear load, *Rock Mech. Rock Engng.*, *35*(4), 299–318.

Lomize, G. M. (1951), *Flow in Fractured Rocks* (in Russian), Gosenergoizdat, Moscow, 27 pp.

McKee, C. R., A. C. Bumb, and R. A. Koenig (1988), Stress-dependent permeability and porosity of coal and other geologic formations, *Society of Petroleum Engineers Formation Evaluation*, *3*, 81–91.

National Research Council (1996), Rock fractures and fluid flow: Contemporary understanding and applications, National Academies Press, Washington, D.C.

Parrish, D. R. (1963), Fluid flow in rough fractures, *Proceedings SPE-AIME, Prod. Res. Symp.*, *563*, Norman, Oklahoma, April 29–30.

Perrin, J. C., and S. M. Benson (2009), An experimental study on the influence of sub-core scale heterogeneities on CO2 distribution in reservoir rocks, *Transport in Porous Media*, *82*(1), 93–109.

Pinzon, C., H. Y. Chen, and L. W. Teufel (2000), Complexity of well testing analysis of naturally fractured gas condensate wells in Columbia, *SPE, 59013*, presented at the 2000 SPE International Conference, Villahermosa, Mexico.

Pyrak-Nolte, L. J., and N. G. W. Cook (1988), Fluid percolation through single fractures, *Geophys. Res. Lett., 15*(11), 1247–1250.

Pyrak-Nolte, L. J., N. G. Cook, and L. R. Myer (1990), Stratified percolation model for saturated and unsaturated flow through natural fractures, *Proceedings of First Annual International High-Level Radioactive Waste Management Conference*, *1*, 551–558.

Pyrak-Nolte, L. J., L. R. Myer, N. G. Cook, and R. A. Witherspoon (1987), Hydraulic and mechanical properties of natural fractures in low permeability rock, *Proceedings of 6th International Congress of Rock Mechanics*, 225–232.

Qian, J., Chen, Z., Zhan, H., and H. Guan (2011), Experimental study of the effect of roughness and Reynolds number on fluid flow in rough-walled single fractures: A check of local cubic law, *Hydrol. Process.*, *25*, 614–622.

Raven, K. G., and J. E. Gale (1985), Water flow in a natural rock fracture as a function of stress and sample size, *Int J Rock Mech Min Sci Geomech Abstr*, *22*(4), 251–261.

Renshaw, C. E. (1995), On the relationship between mechanical and hydraulic apertures in rough-walled fractures, *J. Geophys Res*, *100*, 24629–24636.

Romm, E. S. (1966), *Flow Characteristics of Fractured Rocks* (in Russian), Nedra, Moscow, 283 pp.

Sisavath, S., A. Al-Yaarubi, C. C. Pain, and R. W. Zimmerman (2003), A simple model for deviations from the cubic law for a fracture undergoing dilation or closure, *Pure Appl. Geophys.*, *160*, 1009–1022.

Snow, D. T. (1968), Fracture deformation and changes of permeability and storage upon changes of fluid pressure, *Colorado School of Mines Quarterly*, *63*, 201.

Swan, G. (1983), Determination of stiffness and other joint properties from roughness measurements, *Rock Mechanics and Rock Engineering*, *16*, 19–38.

Tao, Q., C. A. Ehlig-Economides, and A. Ghassemi (2009), Investigation of stress-dependent fracture permeability in naturally fractured reservoirs using a fully coupled poroelastic displacement discontinuity model, *SPE*, *124745*, presented at 2009 SPE Annual Technical Conference and Exhibition held in New Orleans, Louisiana.

Tsang, Y. W., and P. A. Witherspoon (1983), The dependence of fracture mechanical and fluid flow properties on fracture roughness and sample size, *J. Geophys. Res.*, *88B3*, 2359–2366.

Vandersteen, K., B. Busselen, K. Van Den Abeele, and J. Carmeliet (2003), Quantitative characterization of fracture apertures using microfocus computed tomography, *Applications of X-ray Computed Tomography in the Geosciences*, *215*, 61–68.

Van Geet, M., and R. Swennen (2001), Quantitative 3D-fracture analysis by means of microfocus X-ray computer tomography (μCT): An example from coal, *Geophysical Research Letters, 28*(17), 3333–3336.

Walsh, J. B. (1981), Effect of pore pressure and confining pressure on fracture permeability, *Int. J. Rock Mech. Sci. Geomech.*, *18*, 429–435.

Wan, T., J. J. Sheng, and M. Y. Soliman (2013), Study evaluates EOR potential in naturally fractured shale reservoirs, *American Oil and Gas Reporter*, December 2013 exclusive story.

Witherspoon, P. A., J. S. Y. Wang, K. Iwai, and J. E. Gale (1980), Validity of cubic law for fluid-flow in a deformable rock fracture, *Water Resour. Res., 16*, 1016–1024.

Zimmerman, R. W. and G. S. Bodvarsson (1996), Hydraulic conductivity of rock fractures, *Transport in Porous Media*, *23*, 1–30.

Zimmerman, R. W., D. W. Chen, and N. G. W. Cook (1992), The effect of contact area on the permeability of fractures, *J. Hydrol.*, *139*, 79–96.

8

Permeability of Partially Cemented Fractures

Michael C. Tsenn

ABSTRACT

The effect of amount and pattern of fracture-surface contact to the permeability of a single partially cemented fracture is investigated through numerical modeling. Almost all natural fractures from subsurface cores had some degree of cementation and/or dissolution. These chemical processes could alter the arrangement of contact area. In this study, the amount and the pattern of contact area are randomly selected. The results show that (1) fractional contact area has greater effect on fracture permeability than the contact-area pattern/distribution; (2) a linear relationship exists between fractional contact area and normalized fracture permeability (normalized by parallel-plate fracture permeability) where fractional contact area is low; (3) as fractional contact area increases, the normalized fracture permeability decreases, and the spread of values can be one or more orders of magnitude; and (4) flow percolation through fractures can be blocked when fractional contact area is even higher. The fracture permeability variation and the difficulty of estimating contact area in natural partially cemented fractures make accurate estimation of fracture network permeability extremely difficult. Dynamic data, such as pressure transient tests, are needed to calibrate hydraulic apertures or hydraulic conductivities for fractures in a fracture network. Only with calibration it is possible to estimate hydraulic behavior of natural fracture networks.

8.1. INTRODUCTION

Fractures observed in core from the subsurface generally have some degree of cementation or dissolution. Geologists who study fractures in cores recognize this and believe that the amount and pattern of cementation in fractures affect fluid flow along fractures. Estimating the permeability of natural fracture networks is important when engineers use single- or dual-medium simulation to address questions about nuclear waste repository design [e.g., *Pruess et al.*, 1990; *Wu et al.,* 1999] and hydrocarbon reservoir management strategies [e.g., *Van Golf-Racht*, 1982; *Narr et al.,* 2006].

Fluid flow in a single fracture has been studied by many authors [e.g., *Romm*, 1966; *Bear*, 1972]. The simplest model of fluid flow through a fracture is the parallel plate model, in which a fracture is represented by two smooth, parallel surfaces separated by a gap of constant aperture, b.

ExxonMobil Upstream Research Company, Houston, Texas, USA

For laminar flow with uniform pressure distribution and a nonslip boundary condition, the theoretical parallel-plate fracture permeability k_f is given by

$$k_f = b^2/12 \tag{8.1}$$

[*Zimmerman and Bodvarsson*, 1996]. For a potential (or pressure head, depth-corrected pressure) drop across a vertical fracture in its horizontal direction, ΔP, the volumetric flow rate, Q, is given by Darcy's law as

$$\frac{Q}{\Delta P} = Cb^3 \tag{8.2}$$

where C is a constant that combines fracture dimensions and fluid viscosity [*Witherspoon et al.*,1980]. This relationship is often called the "cubic law" for laminar flow in a fracture.

The surfaces of natural fractures are never perfectly smooth or planar. Fracture surfaces are characterized by local highs and lows. The local relief distorts the flow

Dynamics of Fluids and Transport in Complex Fractured-Porous Systems, Geophysical Monograph 210, First Edition.
Edited by Boris Faybishenko, Sally M. Benson, and John E. Gale.

paths, so that the fracture permeability is less than that estimated from the parallel-plate model [*Tsang*, 1984]. *Pyrak-Nolte et al.* [1987] first documented the heteorgenity of flow paths by injecting molten Wood's metal into *natural* fractures in quartz monzonite (Stripa granite) core samples. In these samples, fracture surface contact area could be up to 40% of total fracture surface area under 30-MPa stress normal to fracture surfaces. In *artificially induced* tensile fractures in granite [*Iwai*, 1976], contact area varies between 10% and 20% under maximum applied normal stress of 20 MPa [*Tsang and Witherspoon*, 1981].

Various models have been proposed to investigate fluid flow through a rough-surfaced fracture. *Witherspoon et al.* [1980] proposed an asperity model to validate the cubic law for fluid flow in a deformable rock fracture. In their experiments, *artificially induced* tensile fractures are generated in basalt, granite, and marble samples. *Tsang* [1984] and *Brown* [1987] used electrical resistor models and computer simulations, respectively, to investigate the effect of fracture-surface roughness on fracture permeability. All models suggest that volumetric flow rate through a rough-surfaced fracture can be fit by a cubic law with an equivalent "hydraulic aperture."

Assuming asperities are circular in shape and randomly distributed on fracture surfaces, *Walsh* [1981] proposed that the fracture hydraulic conductivity <*K*> of such fractures be

$$\langle K \rangle = \frac{1-c}{1+c} K \tag{8.3}$$

where K is conductivity of the idealized smooth parallel-plate fracture and c is the fractional contact area (defined as the ratio of the area of contacts to the total area of the fracture surface). This expression can be reduced to a relationship between the fracture permeability $\langle k_f \rangle$ and parallel-plate fracture permeability k_f as follows,

$$\langle k_f \rangle = \frac{1-c}{1+c} k_f \tag{8.4}$$

where the rough-surfaced fracture and the parallel-plate fracture have the same aperture. *Zimmerman et al.* [1992] proposed a model for which elliptically shaped fracture-surface contacts are randomly distributed. Fracture permeability of such model is

$$\langle k_f \rangle = \frac{1-\beta c}{1+\beta c} k_f \tag{8.5}$$

where $\beta = (1 + \alpha)^2 / 4\alpha$ and the elliptical aspect ratio, α, is defined as the ratio of the minor and major axes. Through numerical simulation, *Zimmerman et al.* [1992] showed that Equation 8.5 is applicable to fractures with irregularly shaped contacts up to fractional contact area of 0.25 if contacts are "replaced" by ellipses with the same areas and perimeters [Figure 5 in *Zimmerman et al.,* 1992]. Therefore, for fractures with small fractional contact area, one can estimate fracture permeability using Zimmerman's model if fracture surface contacts can be converted to equivalent ellipse shapes.

Fracture surface contacts have various forms that result from mechanical and chemical processes (Figure 8.1). *Asperities* are fracture surface features that probably formed during fracture propagation and later deformation (Figures 8.1a and b). When a fracture propagates, it either breaks the mineral grains or the bind between mineral grains and their surrounding at the fracture tip. Fracture surface deformation can happen when two opposing fracture surfaces press together or slide against each other due to stress changes [*Paterson and Wong,* 2005, pp. 205–208]. Fractional contact-area due to asperities within fractures can be as low as 0.1 to 0.2 (such as in granite reported by *Iwai* [1976] and *Tsang and Witherspoon* [1981]). Fracture surfaces may also be modified by chemical processes such as cementation and dissolution (Figure 8.1c through g). Almost all fractures in subsurface cores have some cement either partially or completely filling the opening. *Dissolution* may also modify fracture surfaces by dissolving wall rock or previously formed cements as the fluid becomes undersaturated. Other chemical reactions such as dolomitization may also modify fracture openings. These mechanical and chemical processes change not only the smoothness of fracture surfaces but also the amount, size, and shape of fracture-surface contacts.

Fractures in the subsurface vary from completely "open" without any cement to completely "closed" ("sealed," "cemented") and filled by cement. Cement in partially closed fractures often forms bridges that connect both fracture surfaces [*Laubach*, 2003]. Dissolution, on the other hand, often creates vugs (voids) on fracture surfaces and within cement and rock matrix (Figure 8.1g). It also can create "wormholes" within previously cement-filled fractures and matrix. Geologists use the terms *fill* or *fracture fill* for any cementation in natural fractures, and use the terms *fractional fill* or *fill percentage* to describe how much fill exists in a fracture opening. These chemical processes can create fractional contact area within natural fractures that can be as low as 0, or as high as 1.0 for completely filled fractures.

The *Zimmerman et al.* [1992] model predicts fracture permeability for fractures with fractional contact area up to 0.25. However, the fractional contact area of natural

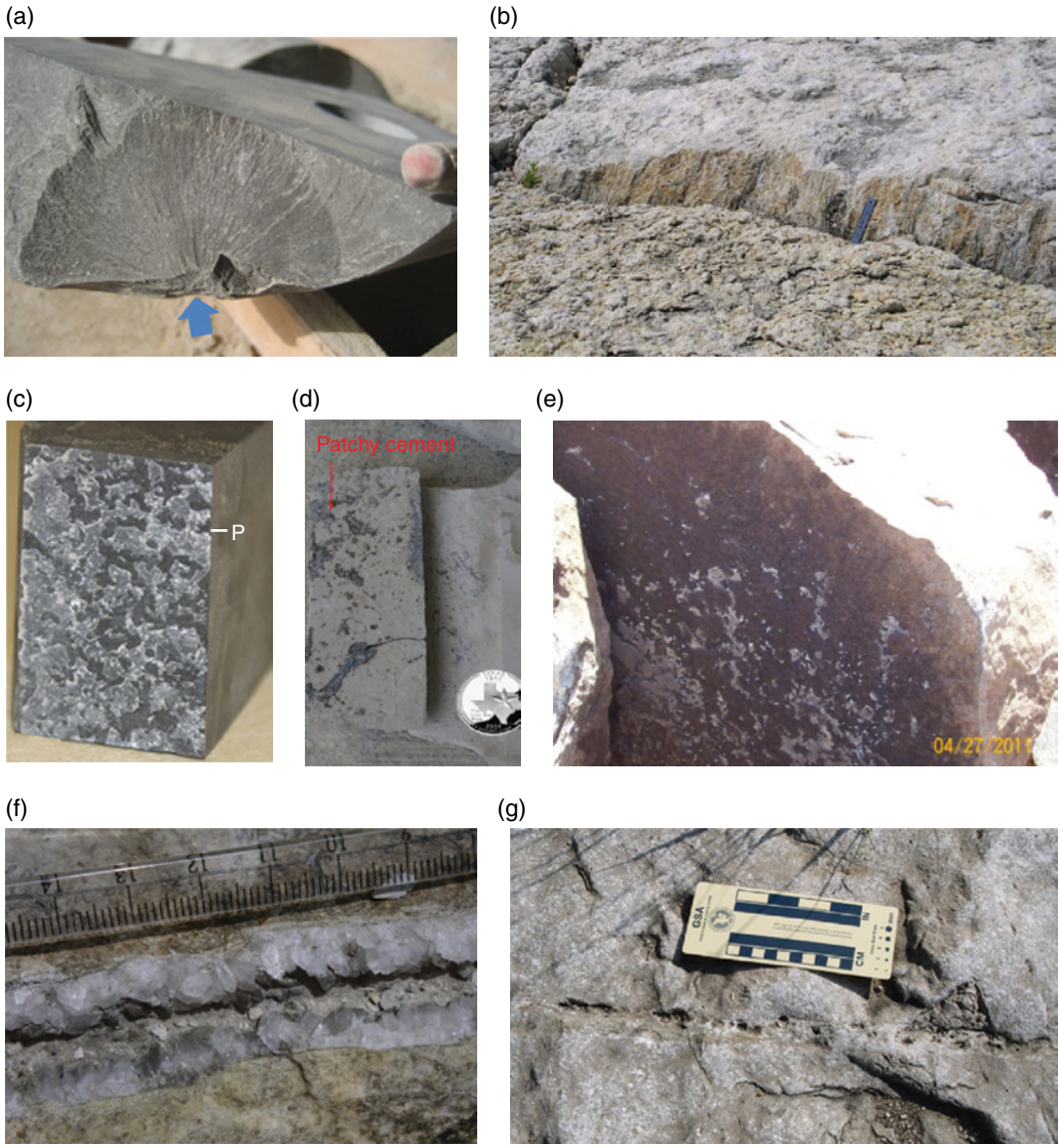

Figure 8.1 Natural fracture surface structures and patterns observed in cores and outcrops. (a) Fracture surface patterns (hackle plumes and rib marks) of an induced fracture in a Mesozoic mid-east carbonate core. The arrow points to the origin of the fracture. (b) Fault slicken lines in Austin chalk outcrop, central Texas. A 15-cm-long ruler was placed on the fault plane parallel to the fault slip direction. (c) Devonian New Albany shale, Indiana, core. Fracture surface is partially filled with calcite; "P" is void. Short dimension of fracture face is about 4 cm (Reprinted with permission from *Laubach et al*. [2010]). (d) Patchy cement pattern on a fracture surface observed in a Mesozoic mid-east carbonate core. (e) Both patchy and salt-and-pepper cement patterns observed in a Jurassic sandstone, Utah. Fracture face is about 50 cm cross. (f) A partially cemented fracture observed in Austin chalk outcrop, central Texas. The ruler is in centimeters. (g) Cement and later dissolution in a fracture, Austin chalk, central Texas. The ruler has both centimeter and inch scales.

fractures could be much higher due to the cumulative effect of asperities, cementation, and dissolution. In this study, I investigate the permeability of partially cemented fractures with larger amounts of fracture surface contact area. The pitfall of using data collected through logging fractures in cores and outcrops to estimate the fracture hydraulic behavior will be discussed.

8.2. METHODS

8.2.1. Conceptual Model

In this chapter, I propose a void-contact model with a constant local aperture, which is a modified version of asperity models in *Tsang and Witherspoon* [1981; Figure 8.2a]

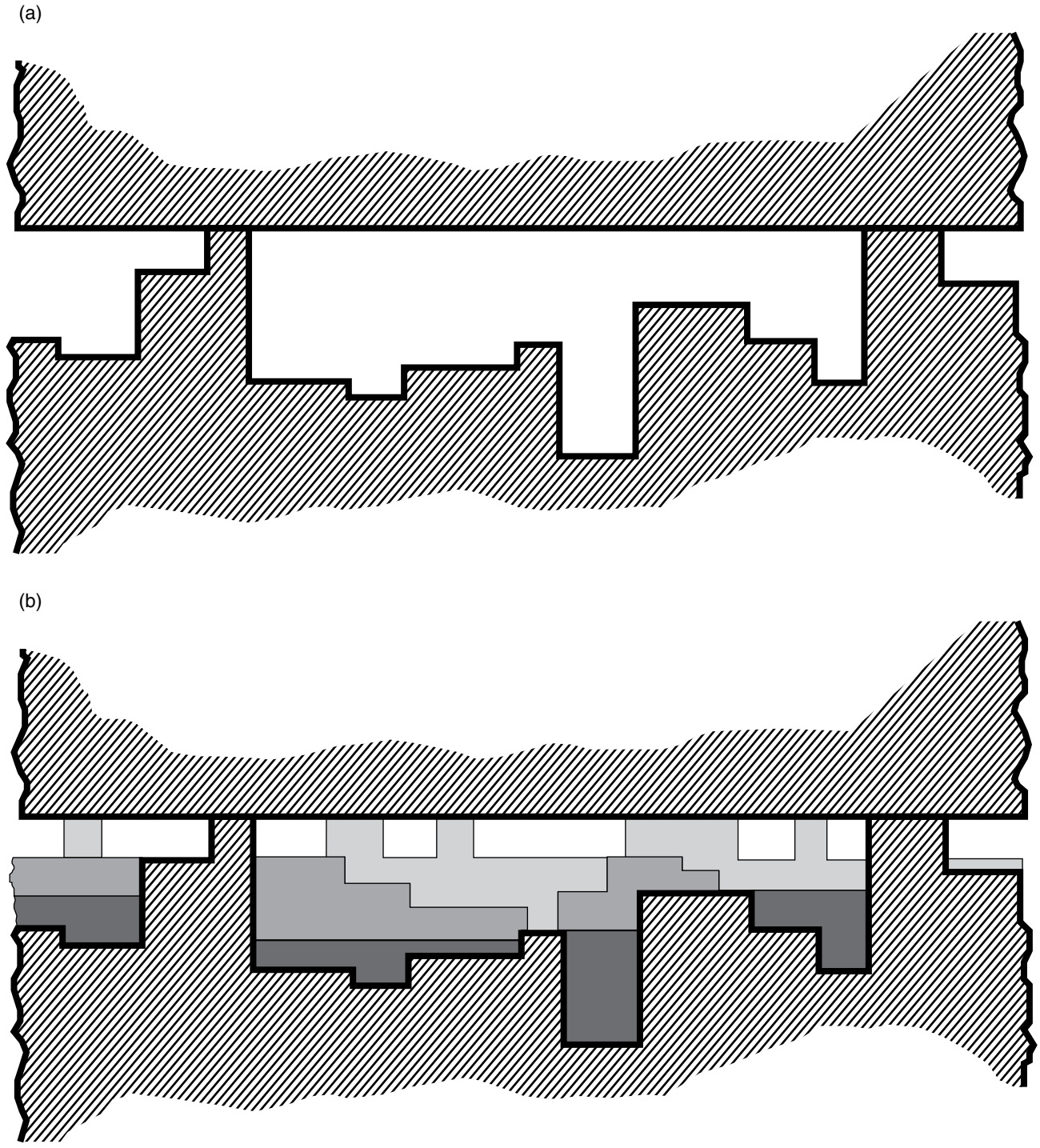

Figure 8.2 (a) Schematic representation of a fracture by an asperity model proposed by *Tsang and Witherspoon* [1981]. (b) The void-contact fracture model proposed in this study. It consists of a smooth fracture surface and a rough fracture surface distributed with asperities and cements. Multiple generations of cementations are shown in different shades. Uneven cements in different generations represent that cements may form and dissolve later during geological time. Combinations of asperities and cements on the rough surface can either contact the smooth surface, forming local barriers to the fluid flow, or have a constant distance (local aperture) to the smooth surface. This final configuration with a constant local aperture is assumed, since only one or two aperture data are collected for each fracture during fracture logging.

and *Zimmerman et al.* [1992]. The model consists of a smooth fracture surface on one side and a rough fracture surface on the side with distributed asperities and cements (Figure 8.2b). Conceptually, local relief on the rough fracture surface may be formed through asperities and multiple generations of cementation and dissolution. Cement may fill in the fracture opening and dissolve later. The distance from the precementation asperities to the smooth surface may be modified by later cementation and dissolution. The final arrangements of asperities and cements on the rough surface can either contact the smooth surface to form local barriers to fluid flow, or have a *constant* distance from the smooth surface (local aperture). This constant local-aperture simplification is assumed, since only one or two aperture data are collected for each fracture during fracture logging.

Even though natural fractures may exist in any geometry, this study is restricted to model rectangular shaped fractures. It is commonly observed in outcrop or in subsurface cores that fractures in sedimentary rocks are bed-bounded. The difference in mechanical properties on two sides of the beds and the strength of the bedding planes cause fractures to propagate easier within beds than across bed boundaries [*Bourne*, 2003]. The lengths of fracture can be measured on the bedding plane (i.e., fracture length) and on the plane that is perpendicular to the bedding plane (i.e., fracture height). From field observation, most bed-bounded fractures have a ratio of fracture length to fracture height greater than one. Although it is very rare to observe a complete three-dimensional geometry of a fracture in the outcrop directly, it is commonly believed that most bed-bounded fractures form approximately a rectangular shape [*National Research Council*, 1996, p. 44].

8.2.2. Contact Distribution Models

Based on my knowledge, there are very few systematic studies of contact distributions on fracture surfaces. *Coakley* [1989] proposed a simple numerical model to represent local contact distributions on fracture surfaces. This model is adopted by *Zimmerman et al*. [1992].

In Coakley's model, the fracture planes are overlaid with grids. Each grid cell is a square, and they are labeled (*i,j*) as indices in a matrix. An independent log-normally distributed random number, X_{ij}, is assigned to each grid cell. X_{ij} can be convolved with a moving-average filter, H_{ij}, to obtain a correlated log-normally distributed random variable, Y_{ij}, as

$$Y_{ij} = \sum_{m=-D}^{D} \sum_{n=-D}^{D} X_{(i-m)(j-n)} H_{mn} \tag{8.6}$$

Filters H_{mn} are radially symmetrical, which decay exponentially as

$$\begin{aligned} H_{mn} &= exp\left(-\lambda\sqrt{m^2+n^2}\right) \quad \text{for } \sqrt{m^2+n^2} \le D \\ &= 0 \qquad\qquad\qquad\qquad\quad \text{otherwise} \end{aligned} \tag{8.7}$$

where D is the size of the filter and λ is a damping factor that determines the rate at which the filter weights decay. A clipping level, Y_o, was then chosen based on the desired fractional contact area as

$$\begin{aligned} Y_{ij} &= contact \quad \text{if } Y_{ij} \le Y_o \\ &= void \qquad \text{if } Y_{ij} > Y_o \end{aligned} \tag{8.8}$$

This procedure generates contact distributions on fracture surfaces. The patterns in Figure 8.3 show that the

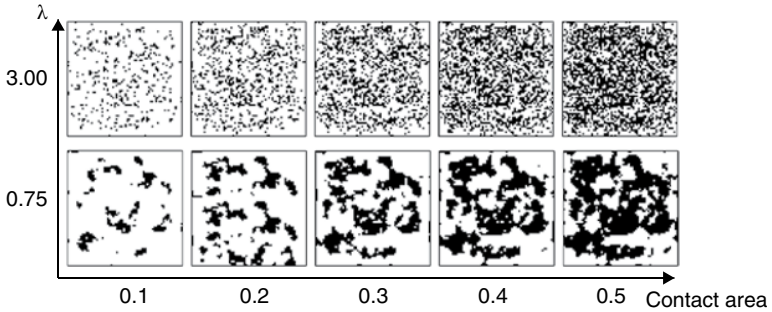

Figure 8.3 Modeled fracture surface contact generated based on *Coakley* [1989]. Contacts are black and voids are white. Fractional contact area, from left to right, is 0.1, 0.2, 0.3, 0.4, and 0.5. The pattern factor, λ, is 0.75 for figures in the bottom row, and 3.0 for the top row. The smaller the pattern factor, the patchier the contacts are. Voids are always in patchy form when fractional contact area is low (e.g., fractional contact area of 0.1 for both contact patterns). At high fractional contact area, voids are less patchy if contacts form a salt-and-pepper pattern.

contacts are in patchy form when λ is smaller, and in salt-and-pepper pattern if λ is larger. Because λ controls the shape and pattern of simulated contacts, we refer it as a "pattern factor" instead. Some simulated patterns are remarkably similar to the cement patterns on the fracture surfaces observed in subsurface cores and outcrops (*cf.* Figure 8.1c and Figure 8.3). Detailed description of the model can be found in *Coakley* [1989].

8.2.3. Mathematical Models

The steady-state potential for a single phase, incompressible fluid within a parallel-plate fracture can be described by

$$\nabla \cdot (K \nabla P) = 0 \tag{8.9}$$

where K is the hydraulic conductivity which is a function of fracture aperture. For the constant local-aperture model proposed in this study, Equation 8.9 reduces to Laplace's equation:

$$\nabla^2 P = 0 \tag{8.10}$$

[*Zimmerman and Bodvarsson,* 1996]. From the velocity described in the system, *Zimmerman and Bodvarsson* [1996] derive the potential gradient normal to the boundaries of contact region (i.e., contact perimeters) to be

$$\frac{\partial P}{\partial n} = 0 \tag{8.11}$$

where n is outward unit normal vector to the contact perimeters. In this case, there is no flow across the contact perimeters.

8.2.4. Numerical Models

The boundary-element method [*Brebbia and Dominguez*, 1992] is adopted in this study to solve the Laplace equation (Equation 8.10). In this method, the domain boundary is discretized, instead of domain discretization methods like finite difference or finite-element methods. This method is chosen because gridded fracture planes used to populate fracture surface contacts naturally become discretized boundaries.

There are two types of external boundary condition used in the model (Figure 8.4). The left and right sides of vertical fractures are potential boundaries (i.e., essential conditions) for which known potentials are assigned. A horizontal potential gradient can therefore be determined based on the potential difference across two vertical sides and

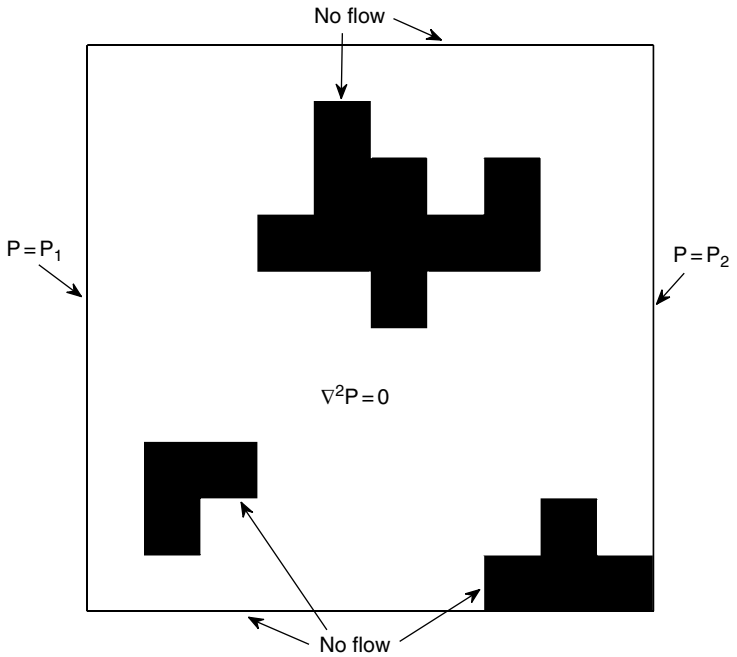

Figure 8.4 Boundary conditions of modeled fractures. They are two types of external boundary condition: (1) the left and right boundaries of fractures are potential boundaries (i.e., essential conditions) for which known potentials are assigned, and (2) the other two sides are flow boundary (i.e., natural conditions) for which zero flow rate is assigned. Contact perimeters are internal boundaries. Because no flow is set through contact perimeters, those contacts are given a zero flow rate.

fracture length. Two horizontal sides are flow boundary for which zero flow rate is assigned (i.e., natural conditions).

Contact perimeters are internal boundaries. A flow condition is assigned to all of them with a zero flow rate across the boundaries. This indicates that there is no fluid flow in and out of these internal boundaries. This satisfies the assumption that contacts are flow barriers as shown in Equation 8.11.

Constant boundary elements [*Brebbia and Dominguez*, 1992] are used in the models. For each element, either potential or potential gradient normal to the element is known. For potential boundary condition, a known potential is assigned, and potential gradient normal to these elements is solved. For flow-boundary condition, zero potential gradient normal to the boundary of each element is assigned to accomplish the no-flow condition. For these elements, the potential for each element is solved.

After solving the Laplace equation (Equation 8.10), flux and volumetric flow rate for each external boundary element are calculated. From the flow rate, the fracture permeability for a given aperture b can be calculated. Mass balance is always checked after equations are solved.

8.2.5. Numerical Simulations

To investigate the permeability of natural fractures, the fundamental problem is that one cannot accurately predict the amount or spatial distribution of contacts on natural fracture surfaces. Therefore, Monte Carlo simulations are conducted. In these simulations, three different fracture geometries with length to height (horizontal to vertical) ratio of 1, 2, and 4, are selected, with 64x64, 128x64, and 256x64 grids, respectively. For a given fracture geometry, a thousand fracture models are randomly generated. For each fracture model, a fractional contact area of 0 to 0.7 and a pattern factor λ of 0.75 to 3.0 are randomly selected (Figure 8.5).

During the early stage of this study, it was found that flow cannot percolate through modeled vertical fractures along their horizontal (length) direction if fractional contact area is greater than 0.6. The maximum fractional contact area of 0.7 therefore is selected. Since the contact area of fractures cannot be directly observed, cement patterns observed on natural fracture surfaces are used as a proxy for contact patterns. Multiple contact distribution models were run, and it appeared that λ in the selected range generated various contact patterns similar to cement distribution patterns observed in core and in outcrop fractures.

8.3. RESULTS

In the following, the dimensionless, normalized fracture permeability is used instead of the absolute fracture permeability. The calculated fracture permeability is normalized by the parallel-plate fracture permeability based on an idealized fracture with the same aperture. Both calculated fracture permeability and parallel-plate fracture permeability contain a b^2 term. Therefore, the normalized fracture permeability is independent of fracture apertures. Fracture fractional contact area is the ratio of the contact area to the total area of a fracture. It is independent to the fracture dimensions (height and length). Consequently, the result is applicable to any fracture aperture and any fracture dimension. However, the discussion is limited to fractures with "relative" small apertures and flow rates to avoid the invalidation of the laminar flow assumption. Because the normalized value is independent of the aperture, the normalized fracture permeability has the same value as the dimensionless normalized fracture conductivity. This is fracture conductivity (defined as the product of fracture permeability times fracture aperture) normalized by parallel-plate fracture conductivity of fractures with the same apertures.

One thousand simulations of each fracture geometry case are generated based on two randomly selected input parameters, the fractional contact area and the pattern factor. The randomness of these two input values plots on fractional contact area and pattern factor space as shown in Figure 8.5. Fracture permeability for some cases cannot be calculated due to the blockage of flow by contacts shown in crosses in Figure 8.5; otherwise, simulations are marked as solid circles in Figure 8.5. In the histograms on the top of Figures 8.5a and b, input values of fractional contact area are binned with size of 0.05. Only a fraction of simulations has the fluid percolates through for each bin. The percentage of these simulations to total number of simulations in that particular bin determines the height of the bars in the histograms.

In all simulations, fluids percolate through fractures when fractional contact area is low. The chances where a flow cannot percolate through fractures increase with increasing fractional contact area. Normalized fracture permeability for those cases which fluids percolated through is plotted against input fractional contact area as shown in Figure 8.6. In these figures, the symbols are color-coded pattern factors that vary from patchy patterns (cold colors) to salt-and-pepper patterns (warm colors). As fractional contact area increases, the normalized fracture permeability decreases. At low fractional contact area, there is an apparent linear relationship between the fractional contact area and the calculated normalized fracture permeability (Table 8.1). This relationship becomes less obvious with increasing fractional contact area, and the spread of normalized fracture permeability for a given fractional contact area could be up to one or more orders of magnitude.

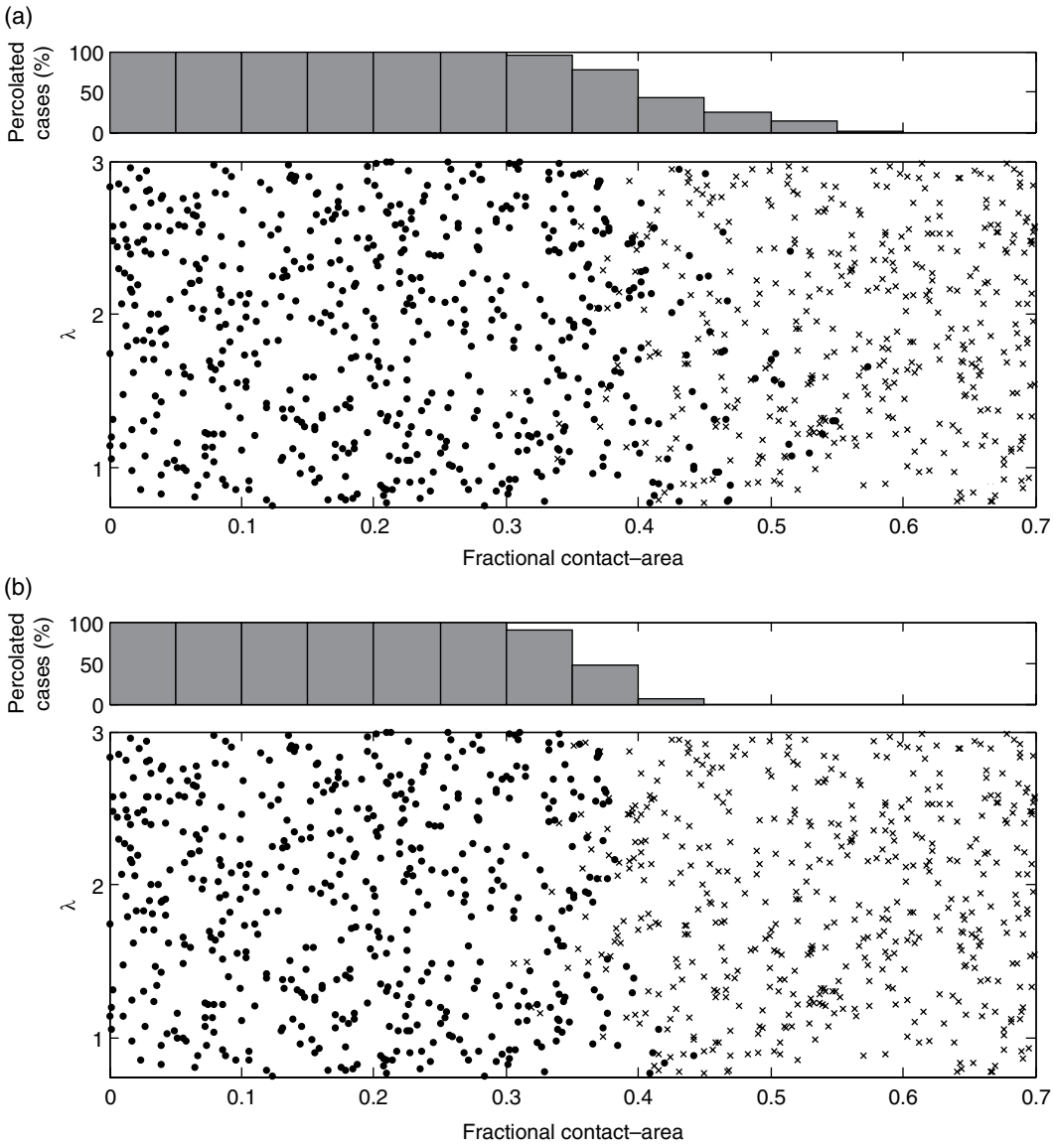

Figure 8.5 The sampling space of models. Two randomly selected parameters (fractional contact area and the pattern factor, λ, which controls contact patterns) are cross plotted to show there is no visible sampling bias in simulations. Solid circles indicate that, for a given fractional contact area and contact spatial distribution, the fluid flows from one side of the fracture to the other side. Crosses show those with no flow, and these have zero fracture permeability. The top histograms represent the percentage of flow-percolated cases, which is calculated based on the ratio of the number of cases with fluid flow through and total number of cases in that particular bin (bin size 0.05). Part a is for fractures with an aspect ratio (length to height) of 1, and Part b is for fractures with an aspect ratio of 4.

8.4. DISCUSSION

Tsang and Witherspoon [1981] and *Pyrak-Nolte et al.* [1987] reported that asperity could make up to 0.3 to 0.4 fractional contact area in samples under normal stress across the fracture planes. Despite this, we observe that subsurface natural fractures in cores are completely "open" (with no cement fill), or completely "closed" (completely cemented up), with any fill amount between these two end members. The tensile fractures in granite, marble, and basalt cited in *Tsang and Witherspoon* [1981] were *artificially* induced opening-mode fractures; cement most likely does not accumulate on these fracture surfaces. These samples probably represent the open natural fractures with no cementation. *Natural* fractures in the Stripa granite were studied by *Pyrak-Nolte et al.* [1987].

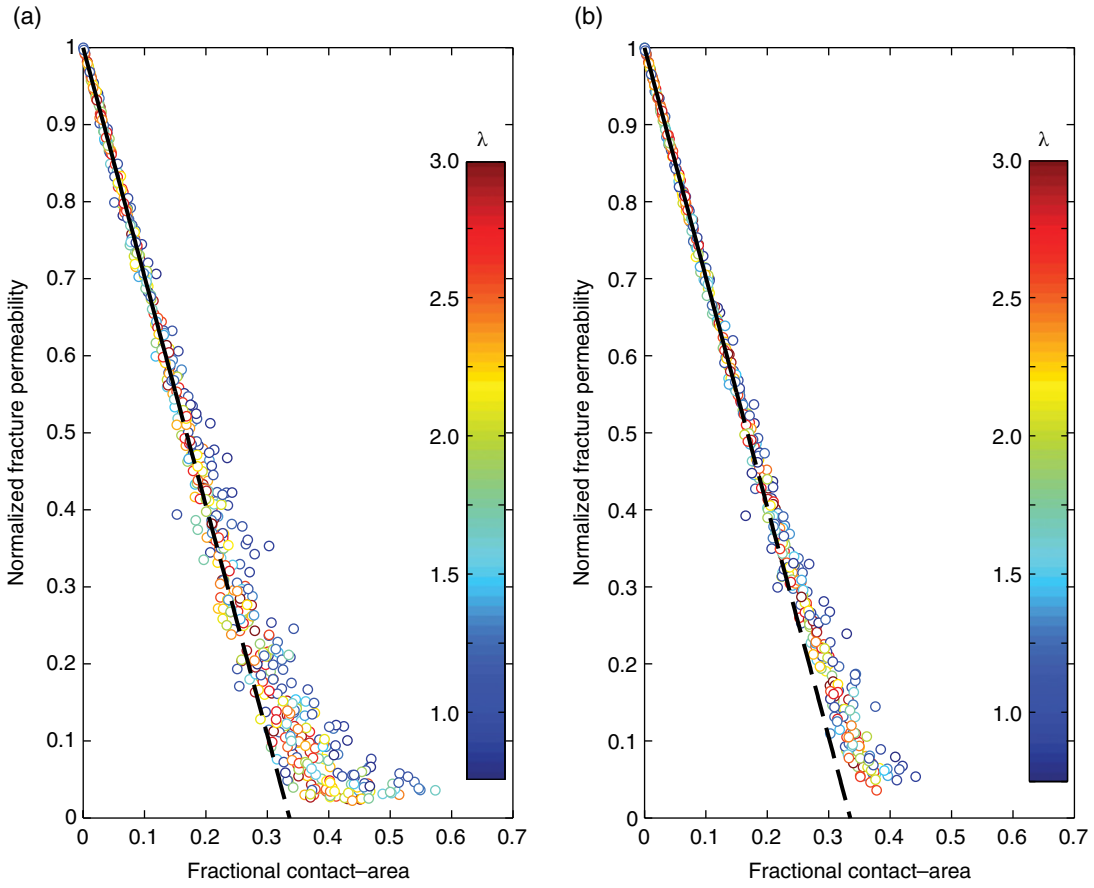

Figure 8.6 Fractional contact area vs. normalized fracture permeability for fractures with aspect ratios of 1 and 4 (Parts a and b, respectively). Data are color coded by the pattern of contacts. Cold colors represent patchy contact patterns and warm colors represent salt-and-pepper contact patterns. Sold lines are statistical fits for data less than 0.15 fractional contact area. Regression lines are forced to pass through the normalized fracture permeability of 1.0 when fractional contact area is 0. The dashed lines are an extrapolation of the regression lines beyond the data range.

Table 8.1 Statistical fit for data with fractional contact area less than 0.15[a].

Fracture Aspect Ratio	Intersect	Slope	R-squared
1	1.0	–2.9743	0.9882
2	1.0	–3.0171	0.9931
4	1.0	–2.9834	0.9999

[a]Normalized fracture permeability = intersect + slope * fractional contact-area. The trend lines are forced to pass through normalized fracture permeability of 1.0 at zero fractional contact area.

Samples were cut from cores drilled for extensometer instrumentation holes in Stripa, Sweden, at a depth of 340 m below the surface [*Pyrak*, 1988, p. 38]. Fracture fills for these samples are not reported. *Olkiewicz et al.* [1979] reported that fractures in extensometer cores are either open or closed. Because the fractional contact area is less than 0.2 under a uniaxial stress of 1 MPa normal to the fracture [Figure 10 in *Pyrak-Nolte et al.*, 1987], it is possible that the natural fractures in the investigation are either without or with a small amount of cement on fracture surfaces. Therefore, one can assume that asperities in fresh fractures could occupy up to 0.3 fractional contact area. The later chemical processes, such as cementation and dissolution, further modify the roughness of fracture surfaces. With these processes combined with existing mechanical-related asperities, fractional contact area of natural fractures could be much higher than 0.3.

In this study, fluids do not always percolate through fractures when the fractional contact area is high. There is a transition zone where chances of fluids percolating through become lower with higher fractional contact area. This transition seems to occur at lower fractional contact area where fractures have a larger ratio of length to height as shown in the histograms in Figure 8.5. Figure 8.5 also suggests that the contact distribution

(i.e., the pattern factor, λ) does not play a major role in terms of percolation as observed by *Zimmermann et al.* [1992]. However, in the transition zone, the patchy contacts (smaller λ) seem to have a better chance to have fluids percolate through.

Fractional contact area and normalized fracture-permeability data for these simulations with fluid percolates through are plotted as shown in Figure 8.6. All three different modeled fracture geometries appear to exhibit a "hockey stick"–shaped relationship between normalized fracture permeability and fractional contact area. At low fractional contact area, normalized fracture permeability is found to be linearly related to fractional contact area. The data deviated from this linear relationship when the fractional contact area was greater than 0.2, and the spread of the data also became larger. However, data from fractures with a high aspect ratio (length-to-height) (Figure 8.6b) are less scattered than those from fractures with a low aspect ratio (Figure 8.6a).

Regression lines (as in Table 8.1) for data with fractional contact area less than 0.15 were calculated by forcing the normalized fracture permeability to be 1.0 at a zero fractional contact area are plotted in Figure 8.6. The regression lines of three different fracture geometries have very similar slopes with a value of −3.0. This suggests that all calculated normalized fracture permeability has the same relationship with the fractional contact area, regardless of fracture geometry (aspect ratios), when the fractional contact area is smaller than 0.15. Inspection of the contact patterns in Figure 8.3 reveals that both patchy and salt-and-pepper contacts produce voids in patchy patterns at low fractional contact area (<0.2), and in very different patterns when fractional contact area is above 0.2. Therefore, for low fractional contact area, flow tortuosity for both types of contact distributions is similar, which results in similar normalized fracture permeability. At high fractional contact area, two contact patterns have different associated void patterns and thus different flow tortuosity and different normalized fracture permeability. *Tsang* [1984] also observed that tortuosity and surface roughness greatly affect the flow, especially for fractional contact area greater than 0.3.

At high fractional contact area, as described earlier, the flow along the modeled fracture may be completely blocked by contacts. However, caution must be made when applying this simulation result to rock fractures. The local aperture in the modeled fracture proposed in this study is fixed to be either zero at contacts or a constant value at voids as shown in Figure 8.2b. In a rock fracture, local apertures could vary on fracture surfaces similar to the asperity model suggested by *Tsang and Witherspoon* [1981], as shown in Figure 8.2a. Therefore, high fractional contact area in the current model could be equivalent to the existence of very small local apertures in a real rock fracture. The normalized fracture permeability could be very small, instead of zero, due to the existence of these small local apertures. *Tsang* [1984] predicted that the flow rate of such fractures could be three or more orders of magnitude lower from idealized parallel-plate fractures.

Even though the *Zimmerman et al.* [1992] model predicts the normalized fracture permeability at low fractional contact area, [Figure 5 in *Zimmerman et al.,* 1992], applying Equation 8.5 to natural fracture permeability prediction has a limitation due to its dependency on the equivalent ellipse aspect ratio. To obtain these ratios, one must convert irregularly shaped contacts to equivalent elliptical contacts. When working with natural fractures, the amount and the shape of contacts cannot be observed directly, and consequently equivalent ellipse aspect ratios cannot be predicted. Even though Equation 8.5 fits for data with the small fractional contact area such as those in fresh induced and natural fractures, it is very difficult to use Equation 8.5 to predict fracture permeability in natural fractures.

Directly applying this study to natural fractures is as difficult as applying Equation 8.5 to natural fractures. When geologists study fractures, they record fracture apertures, fracture fill, and fill percentage, among other observations.

8.4.1. Aperture

Apertures of a single fracture may vary greatly. Some studies therefore record averaged apertures, and others record the minimum and the maximum apertures. The recorded values are only valid within core viewing intervals. For this reason, some researchers record "characteristic" or "representative" apertures at subjectively selected locations along fractures within core viewing intervals. The resolution of aperture measurements is about 100 to 200 μm under 10x magnifier hand lenses with standard grain size charts. Figure 8.6 suggests that permeability for fractures with the same aperture may vary two or three orders of magnitude; consequently, an "accurate" measurement of apertures does not reduce the uncertainty of fracture permeability. Some researchers reported hydraulic apertures that were calculated based on fitting flow rate data to equations following a cubic law [*Brown*, 1987; *Sawada and Sato*, 2010]. Figure 8.7 shows the large variation of the normalized hydraulic apertures (calculated hydraulic aperture normalized by the parallel plate aperture) in the simulations conducted in this study, even though all simulations have the same apertures. This suggests that the hydraulic aperture cannot be correctly estimated based on fractured core logging.

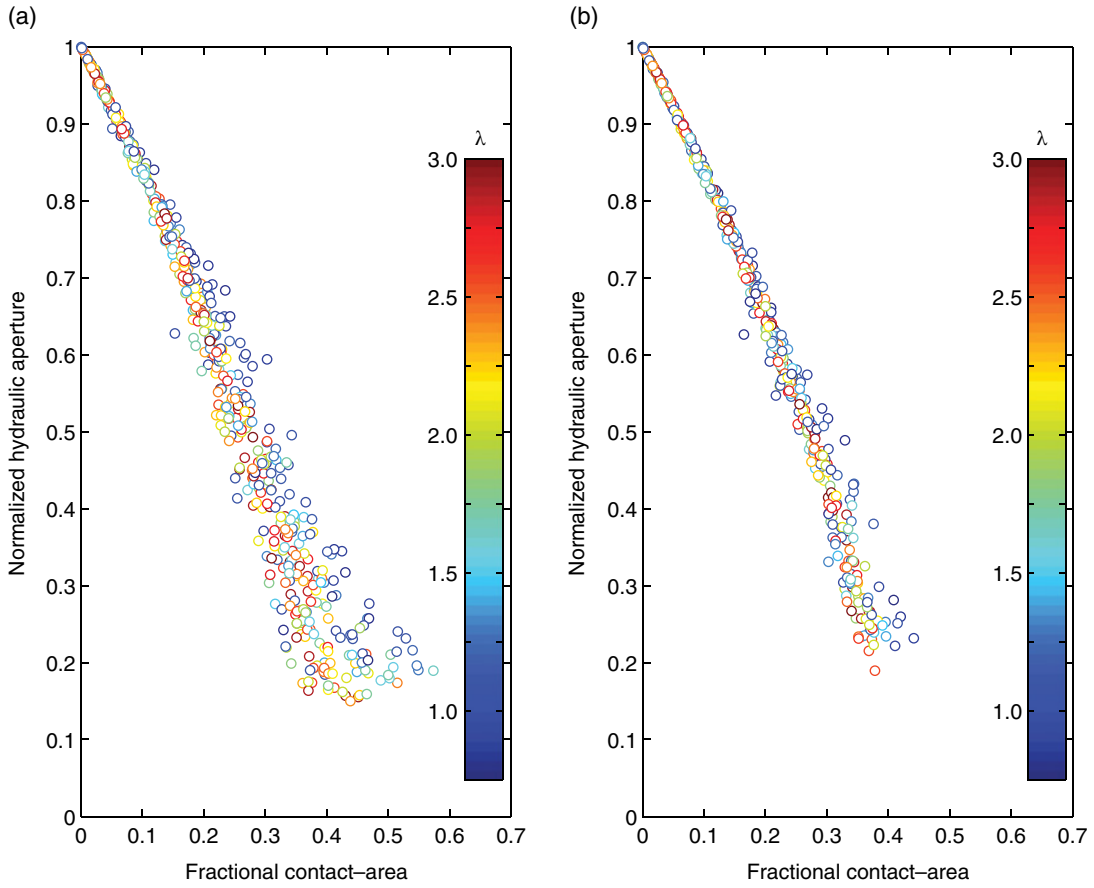

Figure 8.7 Fractional contact area vs. normalized hydraulic apertures for fractures with aspect ratios of 1 and 4 (Figures a and b, respectively). Data are mapped (using the pattern factor, λ) to color through the color bar. Cold colors represent patchy contact patterns and warm colors represent salt-and-pepper contact patterns. Normalized hydraulic apertures are obtained by taking a square root of normalized fracture permeability for each corresponding data point.

8.4.2. Fracture Fill and Fill Percentage

Most natural fractures observed in cores have some amount of cements. Fill percentage is the volumetric ratio of cements to fracture opening. The value is usually obtained by estimating the ratio of cemented area to fracture opening area on the core viewing interval. Occasionally, the fill percentage is estimated directly on both fracture planes when a piece of core breaks off from the core along a fracture. However, one cannot convert fill percentage to fractional contact area. For example, the fracture shown in Figure 8.1f has about 95% space filled with cement, but one cannot estimate the fractional contact area based on the figure. Therefore, the fractional contact area cannot be determined from fracture core logging.

From above discussion, it is concluded that fracture aperture measured in cores cannot be used directly to estimate fracture hydraulic behavior, and the cement fill fraction cannot be converted directly to fractional contact area. The later implies that fractional contact area probably cannot be correctly estimated from core logging. However, from simulations conducted in this study, three observations can be made:

1. There is an apparent linear relationship between the fractional contact area and the normalized fracture permeability when the fractional contact area is low.
2. At high fractional contact area, the normalized fracture permeability for a given fractional contact area could vary up to one or more orders of magnitude.
3. At even higher fractional contact area, flow could be completely blocked by contacts.

With such a large variation of fracture permeability, to estimate it accurately based on fracture logging is a near impossible task unless the fractional contact area is low, such as in induced fractures or natural fractures with minor or no chemical alterations.

However, I emphasize the utility and reliability of quantitative core fracture logging for many important

purposes distinct from fracture permeability estimation. Reservoir fracture spacing and fracture termination information can only be directly obtained from core logging. With oriented core or orientation-calibrated core, one can also obtain fracture orientation and identify fracture sets. One can further identify the timing relationship among different fracture sets, and lithological and structural controls on fracture intensity and orientation. With this knowledge, a geologist can construct a conceptual fracture network model and make predictions of fracture occurrence in reservoirs. Based on my experience, fracture apertures measured during core logging can be used to calculate fracture porosity. It is the fracture hydraulic behavior that cannot be estimated accurately from logging fractures in core.

Geologists are more interested in the fracture network permeability than the fracture permeability for a single fracture. Reservoir engineers use dual-medium simulation to model flow in fractured reservoirs [*Warren and Root*, 1963], which requires fracture-network permeability. To calculate fracture-network permeability, a 3D fracture network must be reconstructed based on the statistical distribution of fracture characteristics. These include features such as the distributions of fracture height, length, density, aperture, and fill fraction as well as the spatial distribution of fracture density [*Long and Witherspoon*, 1985]. Furthermore, it will require a geological understanding (such as controls identified from core logging) or seismic conditioning of fracture density spatial distribution away from wellbores. Caution must be made when excluding long fractures with high fractional contact area. This study's results suggest that fluid may not percolate in such fractures. However, in a fracture network, fluid flows between fracture intersections. Therefore, for highly cemented fractures, fluid could flow through local voids between fracture intersections. A highly cemented fracture, therefore, may still contribute flow in a fracture network.

In order to calculate fracture-network permeability, one important input parameter is fracture permeability for fractures in the fracture network. As was discussed earlier, fracture hydraulic behavior cannot be estimated based on these core-logging measurements. However, the hydraulic properties for fractures in the fracture network can be estimated if the dynamic data, such as pressure transient tests [*Lee*, 1982] and borehole air-injection tests [*LeCain*, 1997], are available. With these measurements, equivalent hydraulic apertures or equivalent hydraulic conductivities of fractures can be estimated, and these values can be used in the reconstructed fracture network to calculate fracture-network permeability in a reservoir.

8.5. CONCLUSION

When using apertures measured from fracture core logging, fracture permeability based on the parallel-plate model always overestimates fracture-network permeability. This overestimation could be one or more orders of magnitude too high. At low fractional contact area (<0.2), for practical purposes, normalized fracture permeability is linearly related to the fractional contact area, but it deviates from linearity at higher fractional contact area. Necessary measurements of fracture hydraulic aperture and fractional contact area cannot be obtained from cores or outcrops to accurately calculate fracture-network permeability. By inference, hydraulic behavior cannot be accurately obtained from core or outcrop fracture logging. To estimate natural fracture-network hydraulic behavior, calibration through dynamic data is needed.

ACKNOWLEDGMENTS

The author appreciates ExxonMobil for granting permission to publish this paper. Thanks to all the individuals who helped in this project: Bruce Chalton, Jim Galbraith, Jim DeGraff, Enru Liu, Mary Jones, Chih-Ping Lu, Ellen Meurer, and two anonymous reviewers. Their many suggestions and comments have helped to clarify details. The author would like to thank the Canadian Society of Exploration Geophysicists for granting permission to republish the image in Figure 8.1c.

REFERENCES

Bear, J. (1972), *Dynamics of Fluids in Porous Media*, Elsevier, New York.

Bourne, S. J. (2003), Contrast of elastic properties between rock layers as a mechanism for the initiation and orientation of tensile failure under uniform remote compression, *J. Geophys. Res., 108*(B8), 2395, doi:10.1029/2001JB001725.

Brebbia, C. A., and J. Dominguez (1992), *Boundary Elements: An Introduction Course*, WIT Press, Ashurst, Southampton, UK.

Brown, S. R. (1987), Fluid flow through rock joints: The effect of surface roughness, *J. Geophys. Res.*, *92*(B2), 1337–1347.

Coakley, K. J. (1989), Spatial statistics for predicting flow through a rock fracture, Ph.D. dissertation, Dept. Statistics, Stanford Univ., Stanford, CA, USA.

Iwai, K. (1976), Fundamental studies of fluid flow through a single fracture, Ph.D. dissertation, Dept. Civil Engineering, Univ. of California, Berkeley, CA, USA.

Laubach, S. E. (2003), Practical approaches to identifying sealed and open fractures, *AAPG Bull.*, *87*(4), 561–579.

Laubach, S. E., J. E. Olson, P. Eichhubl, S. Fomel, and R. A. Marrett (2010), Natural fractures from the perspective of diagenesis, *CSEG Recorder*, *35*(7), 26–31.

LeCain, G. D. (1997), Air-injection testing in vertical boreholes in welded and nonwelded tuff, Yucca Mountain, Nevada, *Water-Resources Investigations Report 96-4262*, U.S. Geological Survey.

Lee, J. (1982), *Well Testing*, Society of Petroleum Engineers, Richardson, TX.

Long, J. C. S., and P. A. Witherspoon (1985), The relationship of the degree of interconnection to permeability in fracture networks, *J. Geophys. Res., 90*(B4), 3087–3098.

Narr, W., D. S. Schechter, and L. B. Thompson (2006), *Naturally Fractured Reservoir Characterization*, Society of Petroleum Engineers, Richardson, TX.

National Research Council (1996), *Rock Fractures and Fluid Flow: Contemporary Understanding and Applications*, National Academies Press, Washington, DC.

Olkiewicz, A., J. E. Gale, R. Thorpe, and B. Paulsson, (1979), Geology and fracture system at Stripa, *Rep. LBL-8907*, Lawrence Berkeley Lab., Berkeley, CA.

Paterson, M. S., and T.-F. Wong (2005), *Experimental Rock Deformation: The Brittle Field,* Springer, New York.

Pruess, K., J. S. Y. Wang, and Y. W. Tsang (1990), On thermohydrologic conditions near high-level nuclear wastes emplaced in partially saturated fractured tuff: 1. Simulation studies with explicit consideration of fracture effects, *Water Resour. Res., 26*(6), 1235–1248.

Pyrak, L. J. (1988), Seismic visibility of fractures, Ph.D. dissertation, Dept. Material Science and Mineral Engineering, Univ. of California, Berkeley, CA, USA.

Pyrak-Nolte, L. J., L. R. Myer, N. G. W. Cook, and P. A. Witherspoon (1987), Hydraulic and mechanical properties of natural fractures in low permeability rock, *Proc. 6th International Congress on Rock Mechanics*, edited by G. Herget and S. Vongpaisal, Balkerna, Rotterdam, the Netherlands.

Romm, E. S. (1966), *Fluid Flow in Fractured Rock*, Nedra, Moscow. Translated by W. R. Blake (1972), Bartlesville, OK.

Sawada, A., and H. Sato (2010), A study of hydraulic properties in a single fracture with in-plane heterogeneity: An evaluation using optical measurements of a transparent replica, *Nuclear Eng. and Tech., 42*(1), 9–16.

Tsang, Y. W. (1984), The effect of tortuosity on fluid flow through a single fracture, *Water Resour. Res., 20*(9), 1209–1215.

Tsang, Y. W., and P. A. Witherspoon (1981), Hydromechanical behavior of a deformable rock fracture subject to normal stress, *J. Geophys. Res., 86*(B10), 9287–9298.

Van Golf-Racht, T. D. (1982), *Fundamental of fractured reservoir engineering*, Development in Petroleum Science, 12, Elsevier Scientific, Amsterdam.

Walsh, J. B. (1981), Effect of pore pressure and confining pressure on fracture permeability, *Int. J. Rock Mech. Min. Sci. & Geomech. Abstr., 18*, 429–435.

Warren, J. E., and P. J. Root (1963), The behavior of naturally fractured reservoirs, *Soc. Petro. Eng. J., 3*(3), 245–255.

Witherspoon, P. A., J. S. Y. Wang, K. Iwai, and J. E. Gale (1980), Validity of cubic law for fluid flow in a deformable rock fracture, *Water Resour. Res., 16*(6), 1016–1024.

Wu, Y. S., C. Haukwa, and G. S. Bodvarsson (1999), A site-scale model for fluid and heat flow in the unsaturated zone of Yucca Mountain, Nevada*, J. Contam. Hydrol.*, *38*, 185–215.

Zimmerman, R. W., and G. S. Bodvarsson (1996), Hydraulic conductivity of rock fractures, *Transport in Porous Media*, *23*, 1–30.

Zimmerman, R. W., D.-W. Chen, and N. G. W. Cook (1992), The effect of contact area on the permeability of fractures, *J. Hydrol.*, *139*, 79–96.

9

An Emergent Conductivity Relationship for Water Flow Based on Minimized Energy Dissipation: From Landscapes to Unsaturated Soils

Hui-Hai Liu

ABSTRACT

Optimality principles have been widely used in many areas. Based on an optimality principle that an evolving flow field will tend toward a minimum in the energy dissipation rate, this work shows that there exists a unified form of conductivity relationship for two different flow systems: landscapes and unsaturated soils. The conductivity, the ratio of water flux to water head (energy) gradient, is a power function of water flux where the exponent value is system dependent. This relationship indicates that to minimize energy dissipation rate for a whole system, water flow has a small resistance (or a large conductivity) at a location of large water flux. Empirical evidence supports validity of the relationship for landscape and unsaturated soils (under gravity-dominated conditions). Especially, it is of interest that according to this relationship, hydraulic conductivity for gravity-dominated unsaturated flow, unlike that defined in the classic theories, depends on not only capillary pressure (or saturation) but also the water flux. Use of the optimality principle allows for determining useful results that may be applicable to a broad range of areas involving highly nonlinear processes and may not be possible to obtain from classic theories describing water flow processes (that are based on local equilibrium assumption).

9.1. INTRODUCTION

Optimality principles refer to the state of a physical process that is controlled by an optimal condition subject to physical and/or resource constraints. These principles have been used in many different areas, including evolution of vegetation coverage under water-limited conditions [*Eagleson*, 2002; *Liu*, 2011a], treelike paths for liquid flow and heat transfer [*Bejan*, 2000], and application of the maximum entropy production principle, in a heuristic sense, to the prediction of steady states of a wide range of systems [e.g., *Tondeur and Kvaalen*, 1987; *Bejan and Tondear*, 1998; *Nieven*, 2010; *Kleidon*, 2009]. However, the theoretical connections between these optimality principles and the currently existing fundamental laws are not fully established. *Bejan* [2000] argued that these principles are actually self-standing and do not follow from other known laws [*Bejan*, 2000]. It is our belief that these principles are probably a result of characteristics of chaotic (nonlinear dynamical) systems. For a chaotic system, details of system behavior on a small scale are not predictable. However, emergent patterns, as a result of self-organization, often occur on macroscopic scales. More importantly, these patterns are self-organized in such a way that they are efficiently adapted to conditions of the relevant environment [*Heylighen*, 2008]. This adaption feature may correspond to the optimality principles. Our argument is supported by an observation that the involved processes are generally highly nonlinear when these principles are found useful. Most recently, *Liu* [2014] made an effort to establish a thermodynamic hypothesis for the related optimality principles, some of which seem to be contradictory. His major argument is that the optimality principle applies to the driving process only when a system involves multiple processes.

Aramco Research Center, Houston, Texas, USA

Dynamics of Fluids and Transport in Complex Fractured-Porous Systems, Geophysical Monograph 210, First Edition.
Edited by Boris Faybishenko, Sally M. Benson, and John E. Gale.

The role of optimality principles in the formation of complex natural patterns has been recognized for many years in the surface hydrology community [*Leopold and Langbein*, 1962; *Howard*, 1990; *Rodriguez-Iturbe et al.,* 1992; *Rinaldo et al*., 1992; *Liu*, 2011b]. For example, *Leopold and Langbein* [1962] proposed a maximum entropy principle for studying the formation of landscapes. *Rodriguez-Iturbe et al.* [1992] postulated principles of optimality in energy expenditure at both local and global scales for channel networks. However, application of these principles in subsurface hydrology has been very limited, probably because flow patterns in the subsurface are difficult to observe and characterize to motivate research activities based on the related emergent patterns.

Most recently *Liu* [2011b, 2011c], based on the optimality principle that energy dissipation rate (or flow resistance) is minimized for the entire flow system, demonstrated that conductivity for water flow is a power function of water flux for both landscapes and unsaturated soils (under gravity-dominated conditions). That development is supported by experimental observations and empirical relations. The conductivity herein is defined as water flux divided by the head (energy) gradient along the flux direction. Water head refers to energy per unit weight of water. This study extends the work of *Liu* [2011b, 2011c] in two aspects. First, the development in *Liu* [2011b] relied on Manning's equation for describing water flow over landscapes. We will show that Manning's equation is not needed for obtaining a conductivity relationship for overland flow. Second, we will extend the results of *Liu* [2011c] for unsaturated flow in homogeneous soils to heterogeneous cases. The ultimate objective of this contribution is to show that power-function relationships between conductivity and water flux, resulting from the optimality principle, seem to be common for different natural flow systems, although the power value is system dependent.

9.2. STEADY-STATE OPTIMAL LANDSCAPE

Liu [2011b] showed that using an optimality principle leads to a conclusion that conductivity for an optimal landscape is a power function of water flux. However, his work is based on the empirical assumption that overland water flow can be described by the well-known Manning's equation. In this section, we demonstrate that the assumption is not needed to derive the conductivity relationship. Thus, a more general expression for water flux is used in this work, as compared to *Liu* [2011b].

Because this chapter describes results for two different systems (landscapes and unsaturated soils), the definitions and physical meanings of the same symbol (denoting a variable or function) may be different in different sections herein unless the same physical meanings are explicitly indicated.

Following *Liu* [2011b], we consider a landscape involving steady-state water flow and a surface evolution process. (The latter refers to a stabilized landscape that does not change significantly with time.) This steady-state assumption has been implicitly employed in previous studies on topological structures of channel networks [*Leopold and Maddock*, 1953; *Howard*, 1990; *Rodriguez-Iturbe et al*., 1992; *Rinaldo et al*., 2006]. A more detailed justification of this treatment can be found, for example, in *Liu* [2011b].

Based on the above simplifications, coupled water-flow (over a land surface) and surface-elevation equations can be derived from the principle that global energy expenditure rate is at the minimum. From the water mass (volume) conservation, the steady-state water flow equation is given by

$$\frac{\partial q_x}{\partial x} + \frac{\partial q_y}{\partial y} = Q \tag{9.1}$$

where x and y are two horizontal coordinate axes, q_x and q_y are the components of water fluxes (vertically averaged water velocity multiplied by water depth) along x and y directions, respectively, and Q is the rainfall rate.

Accordingly, the energy expenditure rate for a unit land-surface area, Δ_E, can be expressed as (based on energy conservation)

$$\Delta_E = \frac{\partial (q_x E)}{\partial x} + \frac{\partial (q_y E)}{\partial y} - QE \tag{9.2}$$

The above equation simply states that for a given unit area, the energy expenditure rate at that location is equal to the energy carried by water flowing into the area minus the energy carried by water flowing out of the area. The rainfall is assumed to have the same energy as water at the location where the rain falls. The head, E (a function of x and y), refers to water energy per unit weight, including both potential (corresponding to elevation z) and kinetic energy, and is given by

$$E = z + \frac{v^2}{2g} \tag{9.3}$$

where g is gravitational acceleration and v is water velocity. Note that the second term is generally small and has been ignored in some previous studies [e.g., *Howard*, 1990; *Rinaldo et al*., 2006]. For completeness, this term is included here.

A combination of Equations 9.1 and 9.2 yields

$$\Delta_E = q_x \frac{\partial E}{\partial x} + q_y \frac{\partial E}{\partial y} \tag{9.4}$$

The water flux is considered to be given by

$$q_x = -K(h,S_*)\frac{\partial E}{\partial x} \tag{9.5a}$$

$$q_y = -K(h,S_*)\frac{\partial E}{\partial y} \tag{9.5b}$$

where

$$S_* = S^2 = \left(\frac{\partial E}{\partial x}\right)^2 + \left(\frac{\partial E}{\partial y}\right)^2 \tag{9.5c}$$

In Equations 9.5a and 9.5b, $K(h,S_*)$ is conductivity and h (m) is water depth. Note that in *Liu* [2011b], the specific formulation of conductivity is given based on the Manning's equation. In this study, we assume h to be a function of local slope S only [*Gupta and Waymire*, 1989]. Many studies indicate that on average a number of hydraulic parameters can be considered as functions of local slope [*Leopold and Maddock*, 1953]. In this case, K is a function of S_* only.

When we combine Equations 9.4 and 9.5, the global energy expenditure rate throughout water-flow domain Ω is given by

$$\iint_{\Omega} \Delta_E dxdy = \iint_{\Omega} (-KS_*)dxdy \tag{9.6}$$

The optimality principle in our problem is to minimize the absolute value of the above integral. To do so, we employ the calculus of variations that seeks optimal (stationary) solutions to a functional (a function of functions) by identifying unknown functions [*Weinstock*, 1974]. For example, the former corresponds to the integral defined in Equation 9.6 and the latter to land-surface elevation distribution $z(x,y)$.

Furthermore, we employ the following constraint for the optimization problem [*Liu*, 2011b]:

$$\iint_{\Omega} E dxdy = C \tag{9.7}$$

where C is a constant. Since E is mainly composed of potential energy z, the above equation essentially states that the average elevation throughout the model domain (or total volume of the landscape under consideration) remains unchanged, which is consistent with the steady-state assumption made in this study. It should be emphasized that the optimality principle corresponds to minimization of the global energy expenditure rate, not the total energy within the model domain. Under steady state conditions, the global energy expenditure is equal to the difference between the latter and energy carried by water flowing out of the system.

Based on Equations 9.5, 9.6, and 9.7, the Lagrangian for the given problem is given by

$$L = -KS_* + \lambda_1^* \left[S_* - \left(\frac{\partial E}{\partial x}\right)^2 - \left(\frac{\partial E}{\partial y}\right)^2 \right] + \lambda_2^* [E - C] \tag{9.8}$$

Note that the first term is from Equation 9.6 and other terms are constraints from Equations 9.5 and 9.7. The Lagrange multipliers λ_1* and λ_2* are a function of location and a constant, respectively. The last term on the right-hand side of Equation 9.8 corresponds to the constraint defined in Equation 9.7. Note that the constraint related to water flow, Equation 9.1, is not included in Equation 9.8 but will be handled later for mathematical convenience.

The following Euler-Lagrange equation is used to determine an unknown function w associated with L to minimize the integral defined in Equation 9.8 [*Weinstock*, 1974; *Pike*, 2001]:

$$\frac{\partial L}{\partial w} - \frac{\partial}{\partial x}\left(\frac{\partial L}{\partial w_x}\right) - \frac{\partial}{\partial y}\left(\frac{\partial L}{\partial w_y}\right) = 0 \tag{9.9}$$

where w_x and w_y are partial derivatives with respect to x and y, respectively. In this study, w corresponds to S_* and E, respectively.

Applying the Euler-Lagrange Equation 9.9 to S_* in Equation 9.8 gives

$$\lambda_1^* = \frac{d(KS_*)}{dS_*} \tag{9.10}$$

Applying the Euler-Lagrange Equation 9.9 to E yields

$$\lambda_2^* + \frac{\partial}{\partial x}\left(2\lambda_1^* \frac{\partial E}{\partial x}\right) + \frac{\partial}{\partial y}\left(2\lambda_1^* \frac{\partial E}{\partial y}\right) = 0 \tag{9.11}$$

For the optimization results to be physically valid, they must satisfy the water flow equation, 9.1. A direct comparison between Equations 9.1 and 9.11 and consideration of 5 reveal that Equations 9.1 and 9.11 are identical under the following conditions

$$\lambda_1^* = \left(\frac{\lambda_2^*}{2Q}\right)K \tag{9.12}$$

Combining Equations 9.10 and 9.12, we can obtain

$$K \propto S_*^{-1+\frac{\lambda_2^*}{2Q}} = S^{-2+\frac{\lambda_2^*}{Q}} \tag{9.13}$$

From Equations 9.5 and 9.13, water flux q and local slope S has the following relationship:

$$q \propto S^{-1+\frac{\lambda_2^*}{Q}} \tag{9.14}$$

where

$$q = \sqrt{q_x^2 + q_y^2} \tag{9.15}$$

The power-function relationship between water flux (or discharge) and local slope has been intensively investigated and validated in the literature [*Rodriguez-Iturbe et al.*, 1992; *Rinaldo et al.*, 2006; *Banavar et al.,* 2001].

Also note that the power value in the power-function relationship varies with different site conditions. However, previous studies [*Leopold and Maddock*, 1953; *Rodriguez-Iturbe et al.*, 1992; *Rinaldo et al.*, 2006; *Banavar et al.*, 2001] indicate that the averaged exponent value is about -2 in Equation 9.14, suggesting that $\frac{\lambda_2^*}{Q}$ is close to -1 in an average sense.

Equations 9.13 and 9.14 lead to a relationship between the flow conductivity K (flux divided by head gradient) and flux:

$$K \propto q^{\frac{2-\frac{\lambda_2^*}{Q}}{1-\frac{\lambda_2^*}{Q}}} \tag{9.16}$$

When $\frac{\lambda_2^*}{Q}$ is close to -1, the exponent value in the above equation is about 1.5. The equation indicates that under optimal conditions, locations where a relatively large water flux occurs correspond to a relatively small resistance (or large conductance). As demonstrated in the sections to follow, that flow conductivity is a power function of water flux seems to be a common rule under optimal flow conditions.

9.3. UNSATURATED FLOW IN POROUS MEDIA

For a homogeneous soil, *Liu* [2011c] reported that unsaturated conductivity, similar to Equation 9.16, is a power function of water flux under gravity-dominant and optimal flow conditions. This section will show that a similar power-function relationship can be applied to heterogeneous soils as well. We also like to emphasize that our mathematical development closely follows *Liu* [2011c] except that conductivity here is spatially variable.

We consider a steady state unsaturated flow system associated with a heterogeneous and isotropic porous medium. From the water mass (volume) conservation, the steady-state water flow equation is given by

$$\frac{\partial q_x}{\partial x}+\frac{\partial q_y}{\partial y}+\frac{\partial q_z}{\partial z}=0 \tag{9.17}$$

where x and y are two horizontal coordinate axes, z is the vertical axis, and q_x, q_y, and q_z are volumetric fluxes of water along x, y, and z directions, respectively.

We use E (a function of x, y, and z) to represent the hydraulic head for unsaturated flow:

$$E=z+\frac{P}{\rho g}=z+h \tag{9.18}$$

Where z is elevation, g is gravitational acceleration, P is capillary pressure, ρ is water density, and h is capillary pressure head. Accordingly, the energy expenditure rate for a unit control volume, Δ_E, can be expressed as

$$\Delta_E=\frac{\partial(q_x E)}{\partial x}+\frac{\partial(q_y E)}{\partial y}+\frac{\partial(q_z E)}{\partial z} \tag{9.19}$$

The above equation simply states that for a given unit volume, the energy expenditure rate at that location is equal to the energy carried by water flowing into the volume minus the energy carried by water flowing out of the volume.

A combination of Equations 9.17 and 9.19 yields

$$\Delta E=q_x\frac{\partial E}{\partial x}+q_y\frac{\partial E}{\partial y}+q_z\frac{\partial E}{\partial z} \tag{9.20}$$

Throughout this development, Darcy's law is assumed to apply to unsaturated flow:

$$q_x=-K\frac{\partial E}{\partial x} \tag{9.21a}$$

$$q_y=-K\frac{\partial E}{\partial y} \tag{9.21b}$$

$$q_z=-K\frac{\partial E}{\partial z} \tag{9.21c}$$

where K is hydraulic conductivity and given by

$$K=K_s(x,y,z)k_r(h^*,S_*) \tag{9.21d}$$

$$S_*=\left(\frac{\partial E}{\partial x}\right)^2+\left(\frac{\partial E}{\partial y}\right)^2+\left(\frac{\partial E}{\partial z}\right)^2 \tag{9.21e}$$

$$h^*=h\sqrt{\frac{K_{s,ref}}{K_s}} \tag{9.21f}$$

In Equations 9.21d and 9.21f, K_s is the saturated hydraulic conductivity that is a function of location and $K_{s,ref}$ refers to the K_s value at a reference location. The relative permeability k_r is assumed to be a function of both normalized capillary pressure head (h^*) and the square of the energy gradient (S_*). To be able to get closed-form results, we further assume that the function form of relative permeability is independent of location. This treatment is based on the widely used Miller-Miller similarity that pore-space geometry is similar at different locations in heterogeneous porous media [*Miller and Miller*, 1956]. When the similarity is satisfied, the functional form of k_r, in terms of normalized variables, remains the same at different locations.

Assuming k_r to be a function of water flux is equivalent to assuming it to be a function of hydraulic head gradient, because water flux, hydraulic head gradient, and K are related through Darcy's law. Our theory here is developed for a macroscopic scale that may include a number of fingering or preferential flow paths. Local scale refers

to the continuum scale within each finger. The unsaturated flow process on a local scale is mainly controlled by pore-scale physics.

It should be noted that Darcy's law was initially developed for water flow in saturated porous media. *Buckingham* [1907] extended Darcy's law to unsaturated conditions, although it is an issue of debate regarding whether he was aware of Darcy's law when developing his relationship. An excellent historic review of Edgar Buckingham and his scientific contributions to unsaturated flow in soils was recently published by *Nimmo and Landa* [2005]. It may be more appropriate to call Darcy's law for unsaturated flow the Darcy-Buckingham law. In his extension, *Buckingham* [1907] used an unsaturated hydraulic conductivity, a function of water saturation or capillary pressure, to replace hydraulic conductivity in the classic Darcy's law. Although not explicitly stated in *Buckingham* [1907], this development is based on a local equilibrium assumption whose limitations will be discussed later.

When we combine Equations 9.20 and 9.21, the global energy expenditure rate is the same as Equation 9.6. The corresponding Lagrangian for the given problem is given by

$$L = -KS_* + \lambda_1\left[S_* - \left(\frac{\partial E}{\partial x}\right)^2 - \left(\frac{\partial E}{\partial y}\right)^2 - \left(\frac{\partial E}{\partial z}\right)^2\right] \quad (9.22)$$

Replacing w with S_* in the Euler-Lagrangian Equation 9.8 yields

$$\lambda_1 = \frac{\partial(KS_*)}{\partial S_*} \quad (9.23)$$

Replacing w with h (or E) in Equation 9.22 and using 9.23 and the continuity equation, we have

$$\frac{\partial\left(\frac{\partial K}{\partial(\log S_*)}\frac{\partial E}{\partial x}\right)}{\partial x} + \frac{\partial\left(\frac{\partial K}{\partial(\log S_*)}\frac{\partial E}{\partial y}\right)}{\partial y} + \frac{\partial\left(\frac{\partial K}{\partial(\log S_*)}\frac{\partial E}{\partial z}\right)}{\partial z} = \frac{S_*}{2}\frac{\partial K}{\partial h} \quad (9.24)$$

To avoid the trivial solution of zero water flux (resulting in zero energy expenditure), we need to consider an additional constrain that the magnitude of water flux that is averaged over the whole flow domain, $\overline{q}$, is nonzero and fixed. In general, it is difficult to obtain an analytical solution to Equation 9.24. To obtain a practically useful closed-form solution, we introduce the following approximation: $\frac{S_*}{2}\frac{\partial K}{\partial h} = \frac{S_*^{1/2}}{2}\frac{\partial(KS_*^{1/2})}{\partial h} \approx \frac{S_*^{1/2}}{2}\frac{\partial \overline{q}}{\partial h} = 0$. Note that in this approximation, we use the magnitude of average water flux to represent the local value in the right-hand side term of Equation 9.24. This approximation should be reasonable for relatively uniform water-flux fields on the macroscopic scale. For more general cases, the effect of this approximation is expected to be absorbed by a fitting parameter in the final solution (Equation 9.30).

A comparison between Equation 9.24 (without the term on the right-hand side) with the continuity equation (Equations 9.17 and 9.21) yields

$$\frac{\partial K}{\partial(\log S_*)} = AK \quad (9.25)$$

where A is a constant.

To get practically useful results, we consider K to be further expressed by

$$K = K_s(x,y,z)k_r(h^*,S_*) = K_s(x,y,z)f(h^*)g(S_*) \quad (9.26)$$

Substituting Equation 9.26 into 9.25 results in (for a given location)

$$g(S_*) \propto S_*^{\,A} \quad (9.27)$$

Based on Darcy's law, Equation 9.27 can be rewritten as

$$g(S_*) \propto \left(\frac{|q|}{K}\right)^{A/2} \quad (9.28)$$

where $|q|$ is the magnitude of water flux given by

$$|q| = \left[q_x^{\,2} + q_y^{\,2} + q_z^{\,2}\right]^{1/2} \quad (9.29)$$

Combining Equations 9.28 and 9.26 gives our final conductivity relationship as follows

$$K = K_s(x,y,z)F(h^*)\left(\frac{|q|}{K_s}\right)^a \quad (9.30a)$$

where a is a constant exponent for the conductivity-flux power law. Equation 9.30a may also be rewritten as

$$k_r(h,S_*) = F(h^*)\left(\frac{|q|}{K_s}\right)^a \quad (9.30b)$$

There may be different interpretations of Equation 9.30. One interpretation is that $F(h)$ is the local-scale relative permeability within the fingering-flow zone and that the power function of flux in the equation represents the fraction of fingering flow zone in an area normal to water flux direction. (Note that the local scale refers to the continuum scale within each finger, as previously indicated.) The validity of Equation 9.30 for homogeneous soils was demonstrated in *Liu* [2011c] with both laboratory-experimental observations of vertical fingering flow [*Wang et al.*, 1998] and field observations [*Sheng et al.*, 2009]. Based on these observations, *Liu* [2011c] also

speculated that parameter a may have a universal value of 0.5, which, however, needs further verification.

Equation 9.30 clearly shows that for a gravity-dominated unsaturated flow, relative permeability is not only a function of water potential (or saturation) but also a power function of water flux. Treating relative permeability as a function of water potential (or saturation) only has been widely used in the literature of vadose zone hydrology. This needs to be revisited, because the treatment is based on a local-equilibrium assumption that capillary pressure is uniform within a representative elementary volume. This is obviously violated at a large scale by the existence of fingering flow. The power-function term in Equation 9.30 largely reflects the self-organization of flow patterns driven by the minimization of total flow resistance.

An analogue of the corresponding relation of our relative-permeability expression with the classic expression is the relation of some parameters for turbulent and laminar water flow processes in a pipe. When water flow in a pipe is laminar, the product of friction factor and average water velocity, corresponding to K in this work, is proportional to water viscosity and independent of the velocity [*Moody*, 1944]. However, when water flow becomes turbulent, the product is related to a Reynolds number that is a function of both viscosity and water velocity. Note that the turbulent-flow case corresponds to our new expression for the relative permeability. This analogue highlights the need to develop different theories for different flow regimes. While the classic unsaturated-flow theory was developed based on the local equilibrium assumption, our theory intends to deal with water flow when the assumption is not valid anymore.

Application of Equation 9.30 to model unsaturated flow can follow the procedure used in the so-called active region model (ARM) [*Liu et al*., 1998, 2003, 2005; *Sheng et al*., 2009]. ARM divides the flow domain into two parts: active and inactive. Water flow occurs within the active region only, and inactive region is simply bypassed. The formulation to calculate the volumetric fraction of the active region can be related to Equation 9.30, as shown in *Liu* [2011b]. Specifically, $F(h^*)$ and the power-function term in Equation 9.30 can be considered as the relative permeability within the active region and the volumetric fraction of that region, respectively. Also note that the derivation of Equation 9.30 does not consider the physics of water flow at the pore scale. To get physically valid results, the relative permeability calculated from Equation 9.30 needs to be constrained by an upper limit of S_e and a lower limit of $k_r^*(S_e)$, where S_e is the effective saturation defined as water volume (excluding residual water) divided by porosity (excluding pore space occupied by residual water) and $k_r^*(S_e)$ is the local relative permeability at saturation S_e. The rationale for these limits and a detailed numerical procedure for the ARM can be found in *Liu et al.* [2003] and *Sheng et al.* [2009].

We also need to emphasize that the theoretical development in this section is based on an assumption that saturated hydraulic conductivity (K_s) is spatially variable, but the relative permeability relation (in terms of normalized variables) is not and can be described by Miller-Miller similarity [*Miller and Miller*, 1956]. While it is an important step forward compared with the work of *Liu* [2011c], future studies are needed to more rigorously explore the impact of heterogeneity within the optimality framework.

9.4. DISCUSSION

Optimality principles have been widely used in different areas. This study is based on a particular optimality principle that energy dissipation rate (or flow resistance) is minimized for the entire flow system. This allows us to unify the conductivity relationships for two seemingly different systems: landscapes and unsaturated soils. (This may partially explain why flow patterns in these systems are similar.) There is a considerable amount of experimental evidence to support the validly of our results [*Liu*, 2011b, 2011c]. This in turn demonstrates the validity of the optimality principle that we have employed. It is of interest to note that the systems under consideration have the similar feature that water flow processes and the formation of flow patterns are strongly coupled in highly nonlinear ways. For example, landscapes are formed by water-flow-induced erosion, and fingering pattern formation in unsaturated soils is also closely related to nonlinear water flow processes. In other words, the existence of strong positive feedbacks between flow pattern formation and the flow process itself may likely be the underlying reason that the optimality principle is valid for these different circumstances. As indicated in the introduction section, it seems to us that these optimality principles may result from the behavior of chaotic systems.

While there are a number of studies on applications of the optimality in the literature, our study is unique in revealing that conductivity is a power function of water flux in two water-flow systems. This interesting finding has several important implications. First, it makes sense within the context of resource (or conductance) allocation. The power-function relationship with a positive power value always gives a small flow resistance at a location with a large flux, such that flow in the whole system is the most efficient. This allocation strategy is also consistent with our daily life experience. For example, in a highway system, locations with high traffic flux are generally wider or have larger conductivities [*Liu*, 2011c]. Second, while complex partial differential equations are involved in our derivation procedure, the form of our results (a power function) is very simple. This form likely

has something to do with fractal patterns that have been observed and studied intensively in the literature [e.g., *Feder*, 1988]. In general, a fractal has many features that can be characterized by power functions and is related to chaotic systems. A detailed exploration of a possible linkage between our finding and fractals is beyond the scope of this chapter and left to future investigations. Third, one grand challenge facing us in the area of hydrogeology is the need to develop physical laws for large-scale multiphase-flow problems. At a local scale, fluid distribution is mainly controlled by capillarity and not sensitive to flow conditions. That is why relative permeability at a local scale can be successfully described as a function of saturation (or capillary pressure) only. At a large scale, this is not the case anymore, although local-scale relationships have been widely used at large scale because alternatives are unavailable. It is fair to say that as a result of the high nonlinearity involved, how to model large-scale multiphase flow is an issue that has not been resolved at a fundamental level. Our results (Equation 30) suggest that functional forms of large-scale relationships to describe multiphase flow are very likely different from their counterparts at local scales, which cannot be resolved by upscaling based on the same functional forms as those at local scales. It is our hope that the optimality approach may provide an important way to obtain such large-scale relationships.

9.5. CONCLUDING REMARKS

Optimality principles have been widely used in many areas. Based on an optimality principle that the water-flow energy dissipation rate is minimal, this work shows that there exists a unified form of conductivity relationship for two different flow systems: landscapes and unsaturated soils. The conductivity is a power function of water flux although the power value is system dependent. This relationship indicates that to minimize energy dissipation for a whole system, water flow has a small resistance (or a large conductivity) at a location of large water flux. Empirical evidence supports the relationship for landscape and unsaturated soils (under gravity-dominated conditions). Especially, according to this relationship, hydraulic conductivity for gravity-dominated unsaturated flow, unlike that defined in the classic theories, depends on not only capillary pressure (or saturation) but also on the water flux. Use of the optimality principle allows for determining useful results that are applicable to a broad range of areas involving highly nonlinear processes and that may not be possible to obtain from classic theories describing water flow processes.

Finally, we need to emphasize that this study represents the first step in developing a unified theoretical framework to describe flow processes in different systems. Since the optimality principle may hold the key to dealing with complex processes related to water flow, more work is highly desirable along the line discussed here, including the further confirmation of results from this study, exploration of the usefulness of our results in other flow systems, and application of the results to modeling flow processes in the relevant systems.

ACKOWLEDGMENTS

We are indebted to Drs. Jim Houseworth and Dan Hawkes at Lawrence Berkeley National Laboratory for their critical and careful review of a preliminary version of this manuscript. This work was supported by the U.S. Department of Energy (DOE), under DOE Contract No. DE-AC02-05CH1123

REFERENCES

Banavar, J. R., F. Colaiori, A. Flammini, A. Maritan, and A. Rinaldo (2001), Scaling, optimality and landscape evolution, *Journal of Statistical Physics*, *104*(1/2), 1–48.

Bejan, A. (2000), *Shape and Structure, from Engineering to Nature*, Cambridge University Press, New York.

Bejan, A., and D. Tondeur (1998), Equipartition, optimal allocation and the constructal approach to predicting organization in nature, *Revue Generale Thermique*, *37*, 165–180.

Buckingham, E. (1907), Studies on the movement of soil moisture, Bulletin 38, USDA Bureau of Soils, Washington, DC.

Eagleson. P. S. (2002), *Ecohydrology: Darwinian Expression of Vegetation Form and Function,* Cambridge University Press, New York.

Feder, J. (1988), *Fractals*, Plenum Press, New York.

Gupta, V. K., and E. Waymire (1989), Statistical self-similarity in river networks parameterized by elevation, *Water Resour. Res*., doi:10.1029/WR025i003p00463.

Heylighen, F. (2008), Complexity and self-organization, in M. J. Bates and M.N. Maack (eds.), *Encyclopedia of Library and Information Sciences*, Taylor and Francis.

Howard, A. D. (1990). Theoretical model of optimal drainage networks, *Water Resour. Res.*, *26*(9), 2107–2117.

Kleidon, A. (2009), Nonequilibrium thermodynamics and maximum entropy production in the Earth system: Application and implications, *Naturwissenschaften*, *96*, 653–677.

Leopold, L. B., and W. B. Langbein (1962), The concept of entropy in landscape evolution, *U.S. Geol. Surv. Prof. Pap. 500-A*.

Leopold, L. B., and T. Maddock (1953), The hydraulic geometry of stream channels and some physiographic implications, *U.S. Geol. Surv. Prof. Pap. 252*.

Liu, H. H. (2011a). Impact of climate change on groundwater recharge in dry area: An ecohydrology approach, *Journal of Hydrology*, *407*, 175–183, doi:10.1016/j.jhydrol.2011.07.024.

Liu, H. H. (2011b), A note on equations for steady-state optimal landscapes, *Geophysical Research Letter*, *38*, L10402, doi:10.1029/2011GL047619.

Liu, H. H. (2011c), A conductivity relationship for steady-state unsaturated flow processes under optimal flow conditions, *Vadose Zone J.*, *10*(2), 736–740, doi:10.2136/vzj2010.0118.

Liu, H. H. (2014), A thermodynamic hypothesis regarding optimality principles for flow processes in geosystems, *Chinese Science Bulletin*, *59*(16), 1880–1884.

Liu, H. H., C. Doughty, and G. S. Bodvarsson (1998), An active fracture model for unsaturated flow and transport in fractured rocks, *Water Resources Research*, *34*, 2633–2646.

Liu, H. H., G. Zhang, and G. S. Bodvarsson (2003), The active fracture model: Its relation to fractal flow behavior and a further evaluation using field observations, *Vadose Zone Journal*, *2*, 259–269.

Liu, H. H., R. D. Zhang, and G. S. Bodvarsson (2005), An active region model for capturing fractal flow patterns in unsaturated soils: Model development, *J. Contam. Hydrol., 80*(1–2), 18–30.

Miller, E. E., and R. D. Miller (1956), Physical theory for capillary flow phenomena, *J. Appl. Phys., 27*, 324–332.

Moody, L. F. (1944), Friction factors for pipe flows, *Trans. ASME*, *66*(8), 671–684.

Nieven, R. K. (2010), Minimization of a free-energy-like potential for non-equilibrium flow systems at steady state, *Phil. Trans. R. Soc. B2010*, 365, 1213–1331, doi: 10.1098/rstb.2009.0296.

Nimmo, J. R., and E. R. Landa, (2005), The soil physics contributions of Edgar Buckingham, *Soil. Sci. Am. J.*, *69*, 328–342.

Pike, R. W. (2001), Optimization of engineering systems, http://www.mpri.lsu.edu/bookindex.html.

Rinaldo, A, J. R. Banavar, and A. Maritan (2006), Trees, networks and hydrology, *Water Resour. Res.*, *42*, W06D07, doi:10.1029/2005WR004108.

Rinaldo, A., I. Rodriguez-Iturbe, A. Rigon, R. L. Bras, E. Ijjasz-vazquez, and A. Marani, (1992), Minimum energy and fractal structures of drainage networks, *Water Resour. Res.*, *28,* 2183–2191.

Rodriguez-Iturbe, I., A. Rinaldo, A. Rigon, R. L. Bras, A. Marani, and E. Hijas-Vasquez (1992), Energy dissipation, runoff production and the three-dimensional structure of river basins, *Water Resour. Res.*, *28*(4), 1095–1103.

Sheng, F., K. Wang, R. D. Zhang, and H. H. Liu (2009), Characterizing soil preferential flow using iodine-starch staining experiments and the active region model, *J Hydrol. 367*(1–2), 115–124.

Tondeur, D., and E. Kvaalen (1987), Equipartition of entropy production: An optimality criterion for transfer and separation processes, *Ind Eng Chem Res*, *26*, 56–65.

Wang, Z., J. Feyen, and D. E. Elrick (1998), Prediction of fingering in porous media, *Water Resour. Res*., *34*, 2183–2190.

Weinstock, R. (1974), *Calculus of Variations*, Dover Publication, New York.

10

Comparison of Simulated Flow in a Discrete Fracture Laboratory Sample Based on Measured Average and Spatially Varying Hydraulic Conductivity

Eunjeong Seok and John E. Gale

ABSTRACT

Fractured rock masses can be characterized by rapid changes in hydraulic conductivity. In this study, the fully characterized pore space geometry for a 0.055 m^2 section of a fracture plane was used to evaluate approaches to developing input parameters for a finite element flow model; average values, random number generated values, and values that reflect the spatial variability of the fracture pore space. Modeled flow rates based on input parameters that reflect the measured spatial variability matched the measured flow rates but not the model flows produced by other input parameters. Clearly, incorporating spatial variability in numerical model inputs provides a more realistic simulation of experimental data than simply assigning averages or random variability to model inputs. The same pore space and flow measurement data were used to demonstrate the scaling-up effect where, for this data set, subsamples, each equal to 0.73% of the total sample area and with a combined area equal to 21.78% of the total sample area, gave the density and scale (i.e., scale effect) of hydraulic conductivity measurements that were required to obtained a close match between the measured and computed flow rates. The numerical model simulations show that with increasing size of the subsamples, the predicted flow rates rapidly converged on the measured flow rates. The spatial variability approach provided in this work applies equally to both fractured and porous media.

10.1. INTRODUCTION

In most geological or natural materials, the hydraulic, geophysical, and physical properties of the material or geological system at field scales exhibit strong variability. This partially reflects factors such as facies changes in sedimentary rocks, structural variations, or variations in the scale of fracturing in igneous or metamorphic rocks. At a smaller scale, laboratory samples taken from one location can also exhibit strong variability in the measured parameters. This observation was described by *Hubbert* [1956] as the representative elementary volume (REV) concept (Figure 10.1). The REV concept proposes that higher variability in the selected parameter exists at the smaller sample size but decreases with increasing sample size as more of the parameter variability is captured and averaged by larger samples. Fractures are pervasive in rock masses and are major contributors to the mechanical, hydro-mechanical, and transport properties of fractured rock masses. Predicting flow and transport properties of the fractured rock mass is one of the main objectives during planning, designing, and constructing underground structures for waste storage or reservoir/aquifer development.

Laboratory and field permeability data compiled and interpreted (Figures 10.2 and 10.3) by *Brace* [1980 and 1984], *Clauser* [1992], *Gale* [1993], and *Neuman* [1994] for both porous and fractured media show that the range of permeability values is greatest for small laboratory samples. Compared to the range of permeability values for the laboratory scale samples, the permeability values

Fracflow Consultants Inc., St. John's, Newfoundland and Labrador, Canada

Dynamics of Fluids and Transport in Complex Fractured-Porous Systems, Geophysical Monograph 210, First Edition.
Edited by Boris Faybishenko, Sally M. Benson, and John E. Gale.

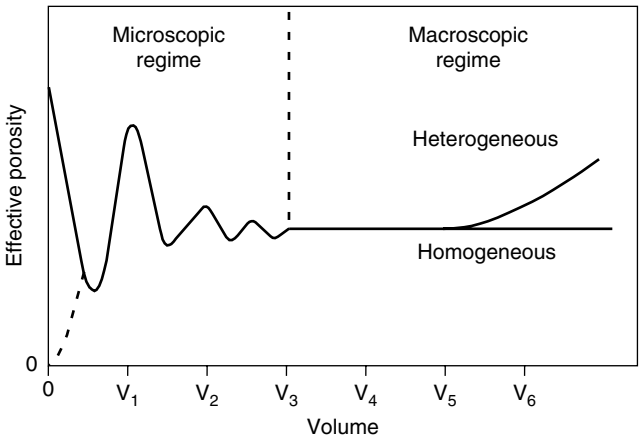

Figure 10.1 The representative elementary volume concept after *Hubbert* [1956].

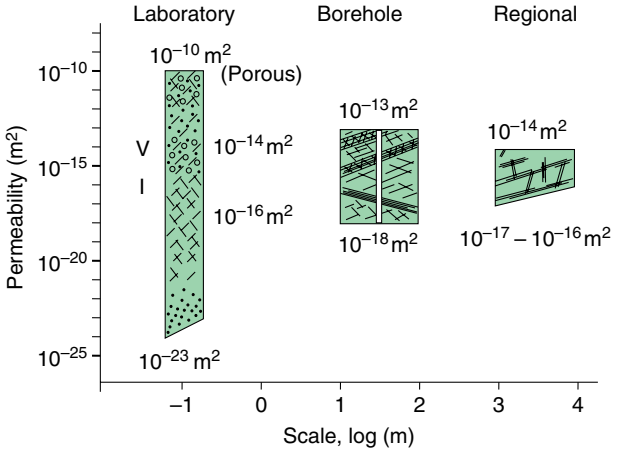

Figure 10.2 Range of permeability values for laboratory, borehole, and regional scales, after *Gale and Seok* [2004], including data from *Brace* [1980, 1984], *Clauser* [1992], *Gale* [1993], and *Neuman* [1994].

measured at the borehole scale show a decrease in the range. In addition, a smaller range in the permeability values was observed at the largest scale (regional aquifer systems) for which the permeability values were measured or inferred using assumed boundary conditions. Obviously, part of this scaling pattern or sample size effect is contributed by small-scale heterogeneities that become more significant as the size of the sample decreases. In addition, boundary conditions and the lower measurement limits are much more precisely defined in small-scale laboratory tests and generally much more poorly defined in borehole tests, with the heterogeneities generally being averaged over significant lengths of the borehole test interval. While it is not directly recognized in the REV concept or sample size effect, spatially

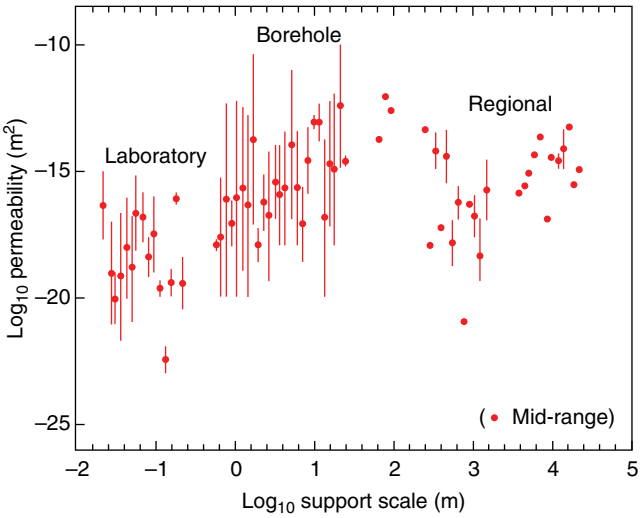

Figure 10.3 Permeability of crystalline rocks and characteristic scale of measurements (after *Clauser*, 1992).

distributed properties or samples frequently show strong spatial variability or structure. Spatial variability may be a key factor that contributes to the observed or assumed sample size effect.

Witherspoon et al. [1979], *Raven and Gale* [1985], and *Gale* [1993] among others addressed the sample size effect using stress-hydraulic conductivity relationship with samples of different sizes ranging from 0.1 m to 0.95 m in diameter. In these experiments, the hydraulic conductivity decreased with increasing normal stress for all the samples regardless of size. However, when the hydraulic conductivities under the maximum stress were compared for different sample sizes, the general trend in sample size-hydraulic conductivity relationship could not be established (Figure 10.4). This may be attributed to comparing experimental data from different rock types and fracture types along with differences in the flow and boundary conditions for each experiment. Therefore, it is imperative to use samples collected from the same rock masses and to conduct tests using similar flow boundary conditions in order to determine if a size effect exists.

Gale [1984] and *Raven and Gale* [1985] conducted laboratory tests on different-sized samples from the same natural fracture plane in a granite and induced fractures from the same granitic rock. Both data sets showed an apparent size effect. *Gale* [1984] compared the results from the different-sized samples by comparing the best fit between the aperture and the normalized flow rate where n is the exponent in the cubic law, $k = (\rho \cdot g)/(12 \cdot \mu) \cdot (2b)^n$ [*Gale*, 1984] (Figure 10.5). The exponent varied as a function of both stress and sample size. For the smaller samples, the exponent ranged from 1.5 to 6.5. With increasing sample size, the exponent generally converged to a value

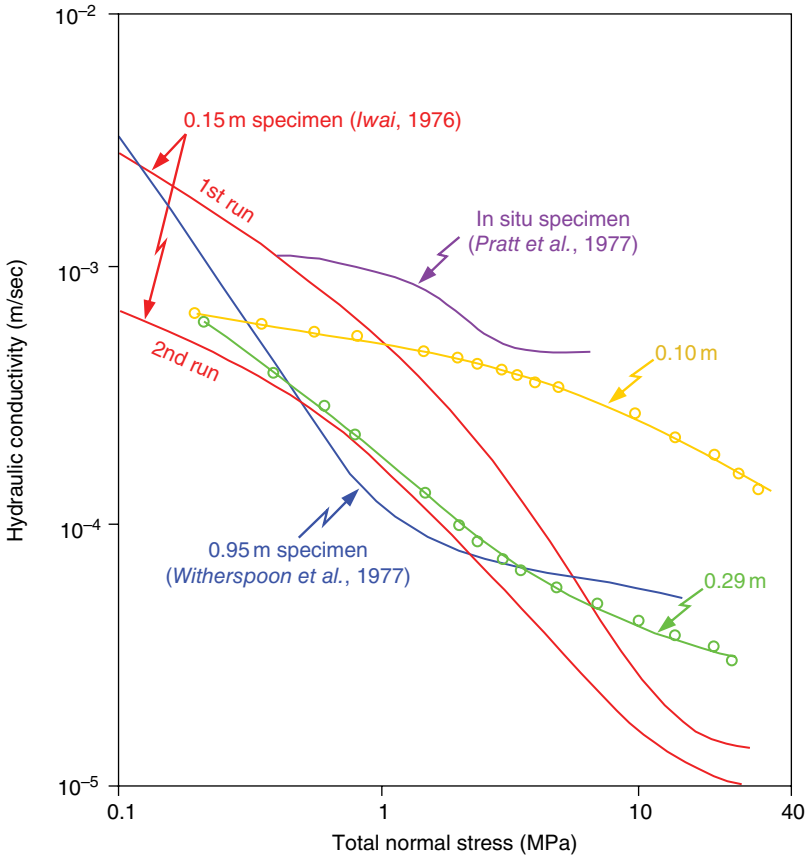

Figure 10.4 Comparison of the effect of sample size on the variation of fracture hydraulic conductivity with normal stress (*Witherspoon et al.*, 1979, with data from *Gale and Raven*, 1980).

of 3 for samples that were approximately 200 mm in diameter or greater. Since the comparison was based on the averaging produced by the hydraulic tests, neither *Gale* [1984] nor *Raven and Gale* [1985] were able to determine if the fracture plane samples exhibited any spatial structure or if there were any significant differences between samples that would account for the variations with sample size. The larger variability in conductivity for the smaller subsamples suggested that there was a spatial variability, since the subsamples were selected from the same fracture plane randomly without overlapping.

Clearly, to determine if a sample size effect exists for discrete fractures, and to determine if a scaling-up relationship can be defined or if the apparent sample size effect is a reflection of variability or spatial variability in key parameters, one needs to develop detailed descriptions or establish databases for the key parameters in the flow system. These databases must include both the flow and transport properties of the fracture plane, or fractured rock mass, or the key parameters that allow one to calculate flow and transport in discrete fractures, such as the fracture pore space geometry. In addition, one must make those measurements that provide the data needed to identify the role of variability and spatial variability of hydraulic conductivity, at all scales, in controlling flow and transport within a fractured rock mass.

Most rock masses or experimental sites are characterized using a series of point measurements, where once a statistically significant sample or description has been obtained it is then extrapolated or extended to describe the entire sample or area of interest. Evaluation of the basic concepts of scale effects and spatial variability and their impact on flow and transport through fractures requires a fully characterized system. With the available technology, fully characterizing a discrete fractured rock mass is not tenable, and if it was feasible, the effort would be very expensive. However, it is feasible to essentially fully characterize a discrete fracture plane at the laboratory or field scale and to use such data sets to evaluate how different approaches to scaling-up, averaging, and/or assigning spatial variability determine the match between measured flow rates and computed flow rates as well as transport within the discrete fracture planes. In this chapter, we present the results of an experimental study [*Seok*, 2001] on a fracture plane sample measuring 190 mm by 290 mm, in which the fracture pore space geometry was

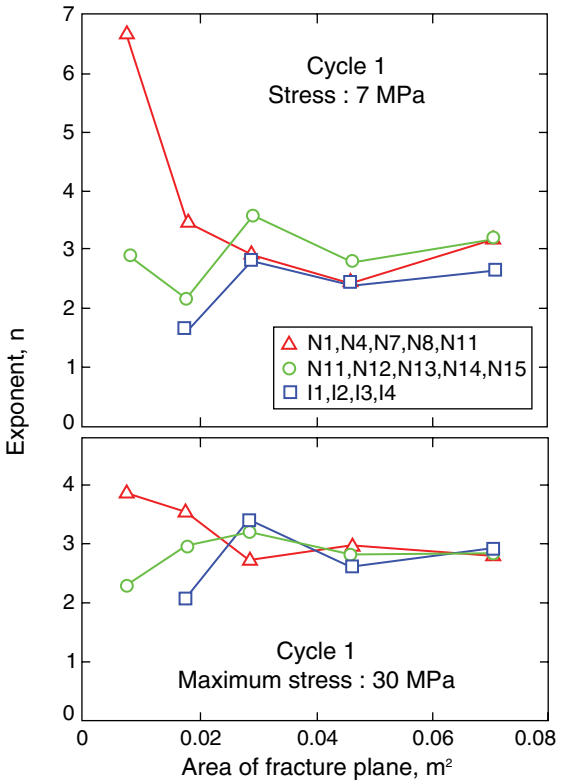

Figure 10.5 Plot of the exponent $(2b)^n$ from cycle 1 data for the 13 samples at two of the reference stresses (7 MPa and 30 MPa) used to calculate the residual aperture (after *Gale*, 1984).

fully characterized for known normal and shear loads, measured fracture closure, and measured flow rates. The experimental data from this experiment were used to conduct a series of numerical experiments to evaluate the use of different procedures for averaging and representing pore space geometry or hydraulic conductivity when developing input parameters for numerical models. These models were then used to compare measured flow rates and computed flow rates for the discrete fracture plane. In addition, a limited number of numerical experiments were conducted to evaluate the role of sample size and data density when simulating flow through discrete fracture planes using detailed fracture pore space geometry for comparison with actual flow measurements.

10.2. MEASURED AND SIMULATED FRACTURE PORE SPACE GEOMETRY AND COMPUTED FRACTURE HYDRAULIC CONDUCTIVITY

10.2.1. Experimental Design and Pore Space Data

As presented in *Seok* [2001], a 190-mm-diameter granitic core sample containing a section of a fracture plane, oriented parallel to the core axis, was recovered from the Svenk Kärnbränslehantering AB (SKB) Underground Hard Rock Laboratory at Äspö, Sweden. Laboratory tests were conducted on this fracture plane sample to determine the coupled hydraulic-mechanical behavior of the fracture plane and to determine the impact of degassing on fracture transmissivity at selected stress levels [*Gale*, 1999]. This sample was subjected to a number of normal loading and unloading cycles followed by a shear loading cycle. Flow and tracer tests were conducted at selected stress levels on the fracture plane. After the final flow and tracer tests were completed at approximately 10 MPa of normal stress, a room-temperature curing resin was injected into the fracture plane. Since the resin was injected under the same stress conditions as those that existed for the final flow and tracer tests, mapping the resin-filled pore space allows one to determine the impact of pore space geometry on the flow and transport properties of this discrete fracture. In addition, the fully characterized pore space geometry allows one to evaluate the flow laws that are applicable to flow and transport through a discrete fracture whose walls are in intimate contact under the applied stress condition.

After the resin had fully cured, the sample was unloaded and a section of the rock sample containing the resin-bonded fracture plane was obtained by making cuts with a diamond saw parallel to and on both sides of the fracture plane. The final dimensions of the slab for the ÄSPÖ2 sample, which contained the resin-impregnated fracture plane, were 290 mm in length, 190 mm in width, and 51 mm in thickness. The pore space mapping procedure consisted of cutting sections perpendicular to the fracture plane, photographing the resin-filled fracture plane using a camera mounted on a microscope, and then digitizing the outline of the resin-filled fracture plane. Analysis of the fracture pore space data in an earlier study [*Fracflow Consultants Inc.*, 1997] from 10-mm-spaced sections showed that the correlation lengths were generally shorter than the 10 mm spacing between the sections that were cut in the previous work. Therefore, additional sections were cut perpendicular to the fracture plane in both the X and Y directions, such that the final section or fracture profile spacing was 5 mm. Photographs of the resin-filled pore space and contact areas within each section were joined together to form a continuous profile of each section. The traces of the fracture pore space and the asperity contacts, or lengths, along each section were digitized to provide data on the spatial distribution of the pore space geometry. The separation distance or aperture between the top wall and the bottom wall of each fracture section was computed at 0.4 mm intervals along each trace by subtracting the bottom profile from the top profile. Asperity contact lengths were mapped separately and recorded as line segments with zero aperture. Similarly, areas of each fracture plane that

were filled with rock and fracture mineral debris impregnated by resin were identified and mapped separately. This fracture or pore space mapping procedure generated a total of 20,152 data points, apertures, contact lengths, and resin-impregnated crushed material for the ÄSPÖ2 fracture plane sample. The detailed experimental and aperture mapping procedures and specifications can be found in *Seok* [2001].

The pore space data for the ÄSPÖ2 sample, which included the contact points and the open pore spaces, enabled one to develop a statistical description of the pore space geometry. These statistics were then used to describe the spatial structure of the fracture pore space. The histogram of the measured pore space data, with 0.04 mm class intervals, is presented in Figure 10.6a. This histogram can be considered bimodal based on the two peaks present in the distribution when one includes contact area as well as the open pore space data; one peak centered on the 0 to 0.04 mm aperture range (contact area) and the other centered on the 0.12 to 0.16 mm aperture range (open pore space data). Key parameters and statistics for the open pore space and contact area distributions are provided in Table 10.1. The pore spaces smaller than or equal to 0.001 mm, based on point measurements, were treated as contact sections/lengths and are included in the 0 to 0.04 mm class interval. The normal stress on the fracture plane, which was maintained at 10 MPa while the resin was being injected, produced a contact area of 24.95%, based on the measured contact lengths. The histograms of the natural logarithm of the open pore space data for the ÄSPÖ2 sample are characterized by lognormal distribution (Figure 10.6b) with a negative skewness (Table 10.1), as shown by the long tail for the smaller pore spaces. An exponential model was fitted to the semivariogram by varying the sill and range in the exponential model to minimize the sum of the differences between the measured and model semivariogram values at the selected lag distances.

A geostatistical model was used with these measured pore space data to generate a regular grid of pore space data for the entire model region (fracture plane); these data were used as numerical model input data for simulating flow and transport through the pore space of the fracture plane sample. The basic statistics and semivariogram properties were compared to ensure that each estimation or simulation result reproduced the bimodal nature of the pore space histogram as well as the spatial structure of the fracture plane pore space geometry that existed when the flow tests were conducted.

10.2.2. Simulation of Pore Space Geometry

To reproduce the spatial structure of the pore space geometry as it existed when the flow and transport tests were conducted, the spatial continuity for the pore space in the sample was evaluated by comparing the semivariogram for the generated pore space with the semivariogram computed using the measured pore space data. Then a pore space geometry with 1 mm by 1 mm regular grid was generated using simulated annealing. The simulated annealing process accepts a spatial structure in the pore space by perturbing one pair of grid cells in the initial image for each perturbation until the specified characteristics in the objective function are met. Since the basic statistics and the bimodal nature of the histogram of the ÄSPÖ2 sample data set had already been reproduced in the initial image, the objective function consisted of only the semivariogram reproduction. Several combinations of annealing schedules and parameters were applied to the initial images to produce several realizations. Then the semivariogram for each realization was compared to that

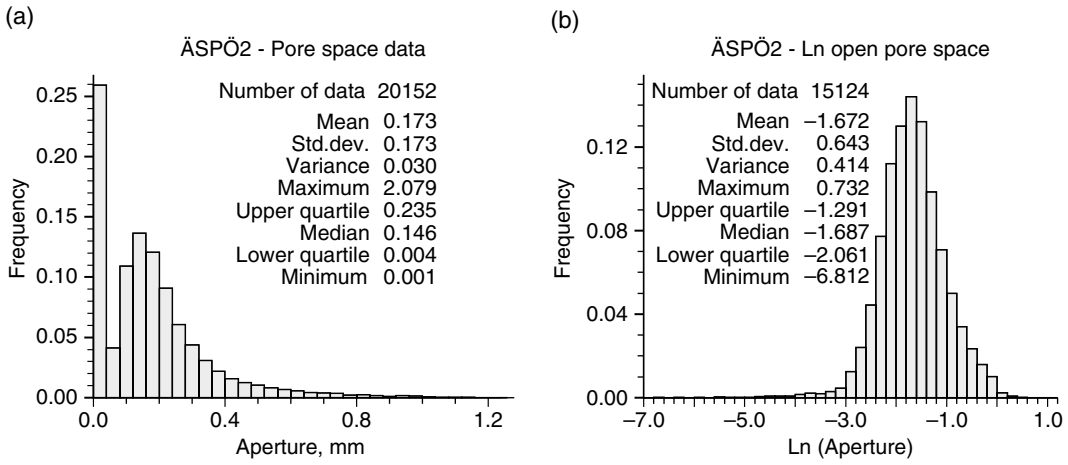

Figure 10.6 Histograms of (a) the total pore space data (open pore space and contact area) for ÄSPÖ2 and (b) the logarithm of open pore space data for the ÄSPÖ2 sample (after *Seok*, 2001).

Table 10.1a Distribution of the open pore space and the contact area for the ÄSPÖ2 samples (after *Seok*, 2001).

	ÄSPÖ2—Measured
Total number of points	20,152
Number of open pore space points	15,124
Number of contact points	5,028
Contact area (%)	24.95

Table 10.1b Basic statistics of the open pore space data (after *Seok*, 2001).

	ÄSPÖ2—Measured
Mean, μ (mm)	0.2298
Std. dev., σ (mm)	0.1638
Max. aperture, σ (mm)	2.0790
μ_{LN}†	–1.6720
σ_{LN}†	0.6434
Skewness	–0.3920
μ_o* (mm)	0.2311
σ_o* (mm)	0.1655

†μ_{LN} and σ_{LN} are the mean and standard deviation of the natural logarithm of the open pore space data.
*μ_o and σ_o are the mean and standard deviation of the original distribution, estimated with the following equation [*Bury*, 1975, p. 279]:

$$\mu_0 = \exp\left(\mu + \frac{\sigma^2}{2}\right);\ \sigma_0 = \left\{\exp(2\mu+\sigma^2)\cdot[\exp(\sigma^2)-1]\right\}^{1/2}$$

of the measured data. At the end of this process, one realization was selected based on the degree of fit of the semivariogram to the data set. Figure 10.7 shows the pore space maps that were generated by the simulated annealing process and the semivariograms that were calculated for the simulated data. The semivariograms of the measured pore space data for the ÄSPÖ2 sample are also plotted in Figure 10.7b for comparison with the semivariograms for the simulated data. Both the semivariogram sill and the range for the annealed pore space map are the same as those of the measured pore space data. However, the semivariograms for the annealed data, for lag distances less than 4 mm, show less variance than those for the measured pore space data. This implies that, for the simulated or annealed pore space data, most data point pairs that have lag distances of less than 5 mm have more continuity than do the measured pore space data.

10.2.3. Computing Fracture Hydraulic Conductivity

Flow through fractures is assumed to be controlled by the friction factor versus Reynolds number relationship (Figure 10.8) with the basic reference being the parallel plate or cubic law for flow between two, open, smooth parallel plates. However, as noted by a number of other researchers and demonstrated by the percentage of contact area for the ÄSPÖ2 sample, most in-situ fracture walls are in intimate contact, pressed together by the applied effective normal stress, and as such, natural fractures in a rock mass do not satisfy the assumptions that are inherent in the derivation of the parallel plate flow and transport law. Based on the published literature (*Gale*, 1999), there appears to be only a few experiments where the friction factor versus Reynolds number relationship has been evaluated or measured (Figure 10.8), and these were cases where the rough fracture surfaces were merely touching and hence not in intimate contact. For laminar flow, at low Reynolds numbers, attempts have been made to correct for the impact of roughness of the fracture walls and the intimate contact between the fracture walls, on the basic flow laws by introducing a relative roughness term. This approach is adopted in this work to allow the flow through the simulated fracture plane pore space to be compared to the measured flows using an equivalent porous media flow and transport model. The obtained or simulated pore space data from the simulated annealing process were converted to fracture hydraulic conductivities using the equation for the modified parallel plate model,

$$K_f = \frac{\rho \cdot g \cdot (2b)^2}{12 \cdot \mu \cdot \left[1 + 8.8(k/dh)^{1.5}\right]}\ \text{[Louis,1969]}$$

where ρ is the fluid density, g is the gravitational acceleration, μ is the dynamic viscosity, $2b$ is the fracture aperture, and k/dh is the relative roughness. For fracture walls that are in intimate contact, the relative roughness (k/dh) is deemed to be 0.5 (see Section 1.3.1 of *Louis* [1969]).

The fracture hydraulic conductivities have to be converted to equivalent porous medium conductivities in order to be used as input parameters in a 3D numerical model that is based on porous media. For the flow model, the volumetric water flow should be the same in the fracture and the model,

$$Q_f = Q_m$$

where Q_f and Q_m are the volumetric flows in the fracture plane and in the model, respectively. The equation can be rewritten as

$$K_f \cdot I \cdot A_f = K_m \cdot I \cdot A_m$$

where, K_f and K_m are the conductivities of the fracture plane and the model, respectively, I is the gradient, and A_f and A_m are the cross-sectional area of the fracture plane

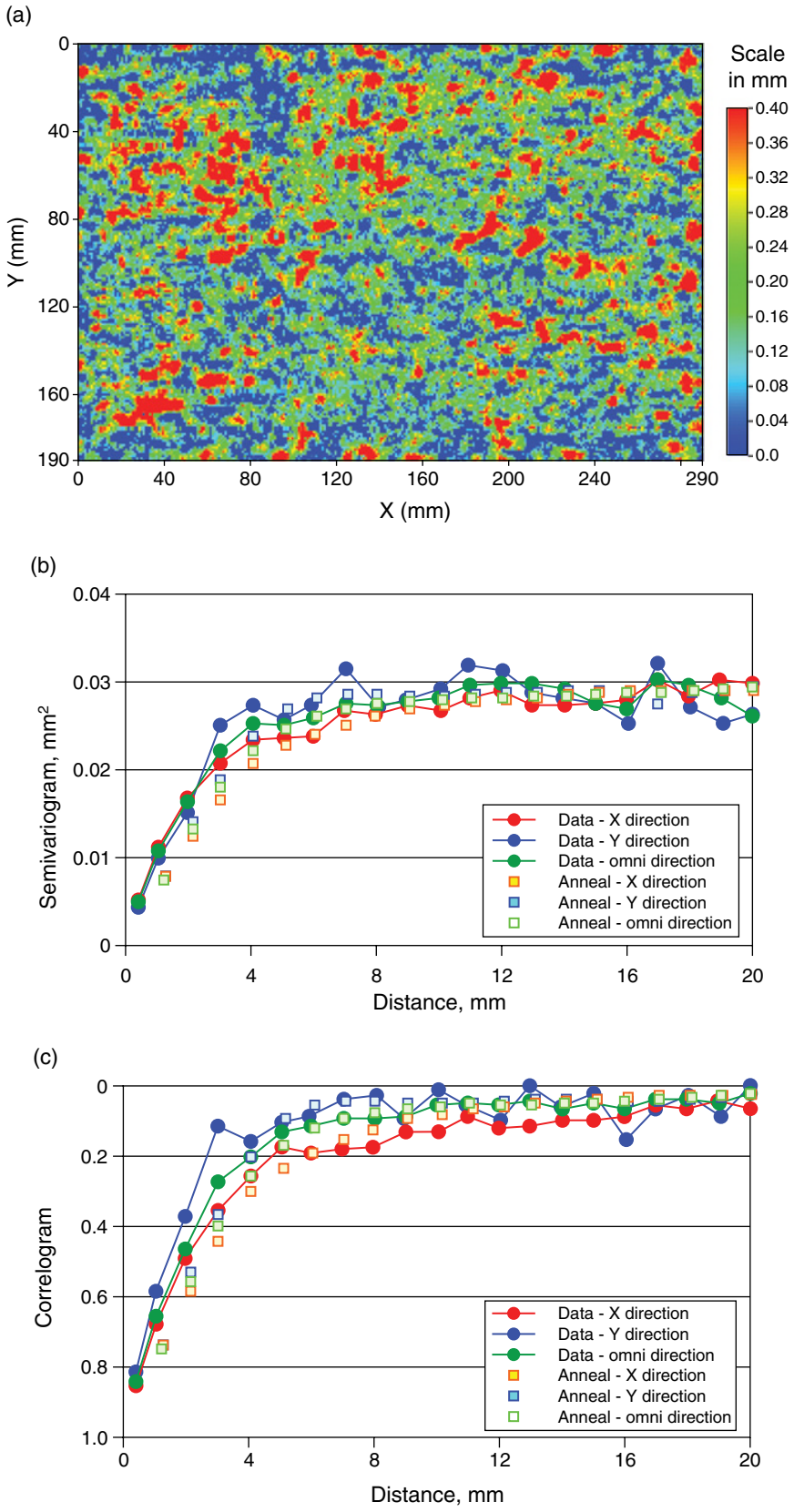

Figure 10.7 (a) Pore space map, (b) semivariogram, and (c) correlogram of the annealed data for ÄSPÖ2 (after *Seok*, 2001).

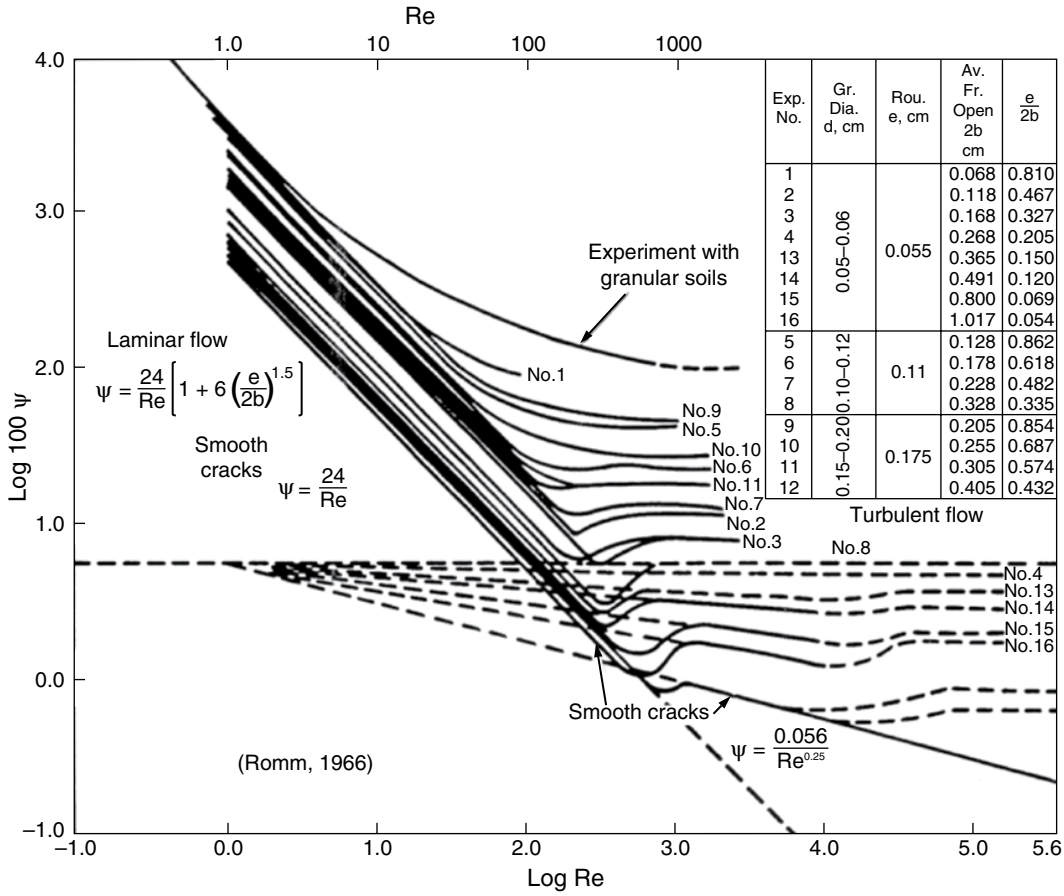

Figure 10.8 Effects of fluid velocity or Reynolds number on friction or head loss (after *Gale,* 1999. Original data from *Romm,* 1966).

and the model, respectively. The fracture conductivity, K_f, is calculated based on the measured apertures, $2b$, from the resin impregnated samples (*Seok*, 2001). Since the gradient must be the same between the flow test and the model, the equation reduces to

$$K_f \cdot 2b \cdot W = K_m \cdot s \cdot W$$

where s is the spacing in the model and W is the width of the fracture and the model. Therefore, the equivalent porous media model conductivity, K_m, can be calculated using the fracture conductivity, as

$$K_m = K_f \cdot \left(2b/s\right)$$

Finally, the fluid velocity in the flow simulation, when transport simulations are being considered, is approximated to that in the fracture by assigning an appropriate porosity value for the equivalent porous media that is computed from the fracture aperture using an assumed fracture spacing, in this case a 1.0-m fracture spacing.

10.3. IMPACT OF FRACTURE PERMEABILITY CHARACTERIZATION ON COMPUTED FLUX

Hydrogeological models are constructed to allow one to analyze laboratory experiments or evaluate field sites for assessment of environmental, water resources, and water management impacts and issues. Because of the size of most sites of interest and even laboratory experiments, models have to be constructed using sparse data sets due to overall costs, site access, and the time frames within which operational and project decisions have to be made.

In laboratory studies, the hydraulic conductivity values are normally computed from the measured flux and one or more measures of the hydraulic gradient across the entire sample or sections of the sample. Similarly, with tracer tests on laboratory samples, the focus is primarily on the boundary conditions with very few, if any, measurements within the flow field.

The input parameters, including hydraulic conductivity, porosity, and hydraulic head, for 3D hydrogeological models of large field sites, are derived from a limited

number of borehole measurements, a limited number of aquifer tests, and in some cases drift inflow data. The challenge is to assign the hydraulic properties to the elements or cells in the model such that the model reflects a reasonable representation of the real hydrogeological system.

In constructing 3D hydrogeological models, with multiple layers and different geological units, it is common for modellers to use one value of hydraulic conductivity and porosity to populate the elements or cells in a geological group or a corresponding layer in the model. For instance, the geometric mean of the hydraulic conductivity measurements that were derived from borehole tests is generally used as the hydraulic conductivities in the model. Applying one representative value for a single layer or geological unit over the entire model area, however, generally presents problems for model calibration and will produce results with a high degree of uncertainty, especially in fractured rock systems where the measured properties can vary with location and borehole direction. In this case, the local variation in hydraulic properties and its impact on flux and transport cannot be captured with the averaged hydraulic property value. Geostatistics represent an approach that can be introduced in an attempt to characterize the spatial variability in key hydraulic parameters for the domain or domains of interest. Constructing 3D numerical models in which this spatial variability is reflected in the model input parameters should provide more robust calibration of the model against measured data and reduction in the uncertainty associated with the model predictions. However, the first requirement to test the improvement in groundwater flow model predictions where spatial variability is reflected in the model input parameters is access to a fully or well characterized database for a well-defined flow system or flow field under field or laboratory conditions.

The pore space data that were generated for the ÄSPÖ2 laboratory sample are considered to represent a complete characterization, from a practical perspective, of the apertures that controlled the flow and transport through this section of the fracture plane. This fully characterized section or sample of a fracture plane provided the opportunity to determine the impact of fracture pore space geometry and the resultant hydraulic conductivity characterization on the fracture flux that is computed using a numerical model. Three hydraulic conductivity input data sets were created from the measured aperture and contact/asperity data and used to assign the hydraulic conductivity values to the 1-mm grid cells in the flow model. The three hydraulic conductivity data sets were constructed using (1) the average or uniform fracture aperture, (2) apertures that were generated from the basic pore space statistics using a random number generator, and (3) apertures that were generated using geostatistics that were computed from the pore space data such that the final aperture or hydraulic conductivity data reflected the underlying spatial variability that had been computed for the fracture plane sample. Since the hydraulic conductivity varies rapidly from cell to cell, the Feflow code [*Diersch*, 2005] was tested using simple geometrical models of a fracture plane to confirm that the code correctly simulated the hydraulic head changes that were associated with abrupt change in apertures.

10.3.1. Data Set 1: Uniform Fracture Aperture or Uniform Hydraulic Conductivity

The ÄSPÖ2 fracture plane is characterized by highly variable apertures. *Duncan et al*. [1972] demonstrated how non-uniform apertures could be converted into equivalent uniform apertures for the one-dimensional case using the measured fracture lengths and apertures to compute an equivalent uniform fracture hydraulic conductivity. No direct procedure, however, exists with which to compute equivalent uniform fracture apertures from fracture pore space data for the two-dimensional case and to convert the computed uniform aperture to an equivalent uniform fracture hydraulic conductivity.

To calculate a uniform equivalent porous media hydraulic conductivity for the uniform aperture case, even in the one-dimensional case, one must first calculate the average aperture. The average aperture (arithmetic mean) can be calculated by finding the average width of the open pore space excluding the contact points. For fractures with a significant percentage of contact area, however, this approach would bias the aperture in terms of the larger pores. To ensure that the computed uniform aperture reflected the contact areas, the average value used in this section was calculated using all the available data points including both open pore space and contact points in order to obtain a representative value. The equivalent uniform porous media hydraulic conductivity was computed from this average aperture following the procedures outlined in the previous section. A second uniform aperture (geometric mean) was calculated by taking the average of the natural logarithm of the same set of apertures that were used to compute the average aperture. In both cases, a minimum aperture of 0.001 mm was assigned to the contact areas so that they could be included in the averaging process.

The average hydraulic conductivity value, computed from the average apertures, was assigned to each cell or element in the flow model, first using the arithmetic mean aperture and then using the mean of the logarithm of the apertures. Table 10.2 shows the arithmetic and logarithmic average values of the measured data points and corresponding equivalent porous media hydraulic conductivities. Two models were run using each hydraulic

conductivity value as the uniform input parameter that was assigned to the entire fracture plane.

10.3.2. Data Set 2: Randomly Distributed Hydraulic Conductivity

The second approach to populating the cells of numerical models when there is limited field data and/or large spatial gaps in the measured data is to use a random number generator, based on the statistics of the original field data distribution, to assign the required hydraulic properties to individual cells or elements. With this approach, the statistics of the input parameters are derived from and match those of the measured data.

In this second approach, the data set that was generated by applying the simulated annealing procedure [*Seok*, 2001] was used as the model input parameters. This data set had the same basic statistics as the measured pore space data set, and the bimodal nature of the measured data set was also maintained (Figure 10.9). However, the data set that was generated using a random number generator did not show any significant spatial distribution (Figure 10.10a). The calculated semivariograms and correlograms shown in Figure 10.10b confirm the lack of spatial distribution in this data set.

10.3.3. Data Set 3: Spatially Distributed Hydraulic Conductivity

The hydraulic conductivity values for fractured rock masses are known to be spatially correlated with the variation in the degree or intensity of fracturing or the underlying structure. For example, in simple layered sedimentary rock structures such as anticlines or synclines, the fracturing is more intense along the crest of anticlines and the trough of synclines than the fracturing along the flanks of both structures. Also, the fracturing appears to be correlated with the overall curvature of the bedrock layers [*Gale et al.*, 1991]. In constructing and executing a 3D model of such structures, assignment of model properties based on either the arithmetic mean, the geometric mean, or the harmonic mean of the measured properties, or assignment of the model properties based on a random number generator using the statistics of the field data, will produce significant calibration errors.

The fracture pore space data for the ÄSPÖ2 sample exhibit spatial variability. The simulated annealing application was applied to this last data set. As described in the previous section, this data set was generated using the modified simulated annealing method, so that the spatial correlation of the measured data set was reproduced in the simulated data set while the basic statistics and the histogram of the measured data set were also maintained. One of the pore space maps is shown in Figure 10.7a for comparison with the randomly distributed pore space map that is shown in Figure 10.10a.

Table 10.2 tabulates the numerical model results for this single fracture case for each of the three different methods used to assign the hydraulic properties. When the measured apertures and contact areas were averaged and the equivalent uniform hydraulic conductivity was computed for this average aperture and then assigned to all elements in the model, the computed flux was 1.4 mL/s, which is much higher than the measured flux (0.5 mL/s). More important, when the individual apertures and contact areas were first converted to equivalent uniform hydraulic conductivities and the arithmetic average of these hydraulic conductivities was calculated and assigned to each element, the computed flux through the fracture plane was 8.4 mL/s. This reflects the weighting that is

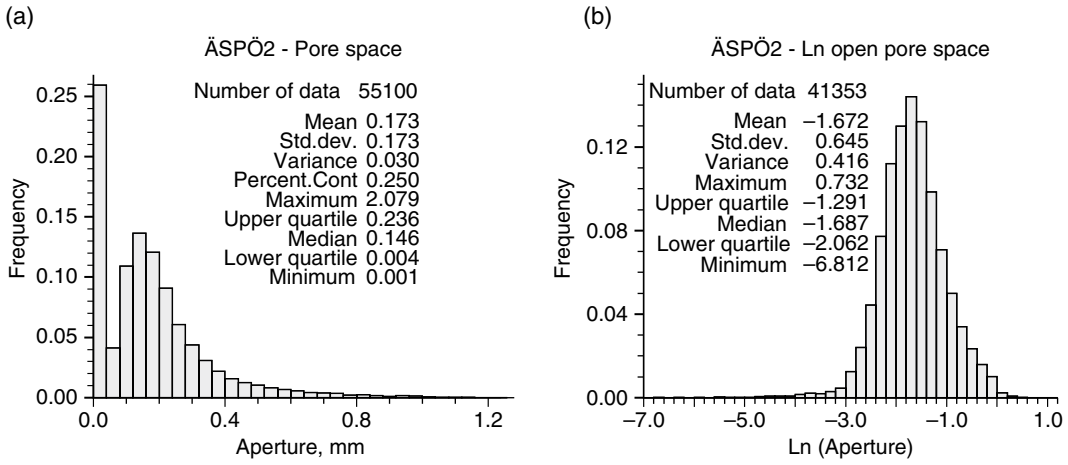

Figure 10.9 Histograms of the (a) cartesian and (b) logarithm values of the initial images for ÄSPÖ2 (after *Seok*, 2001).

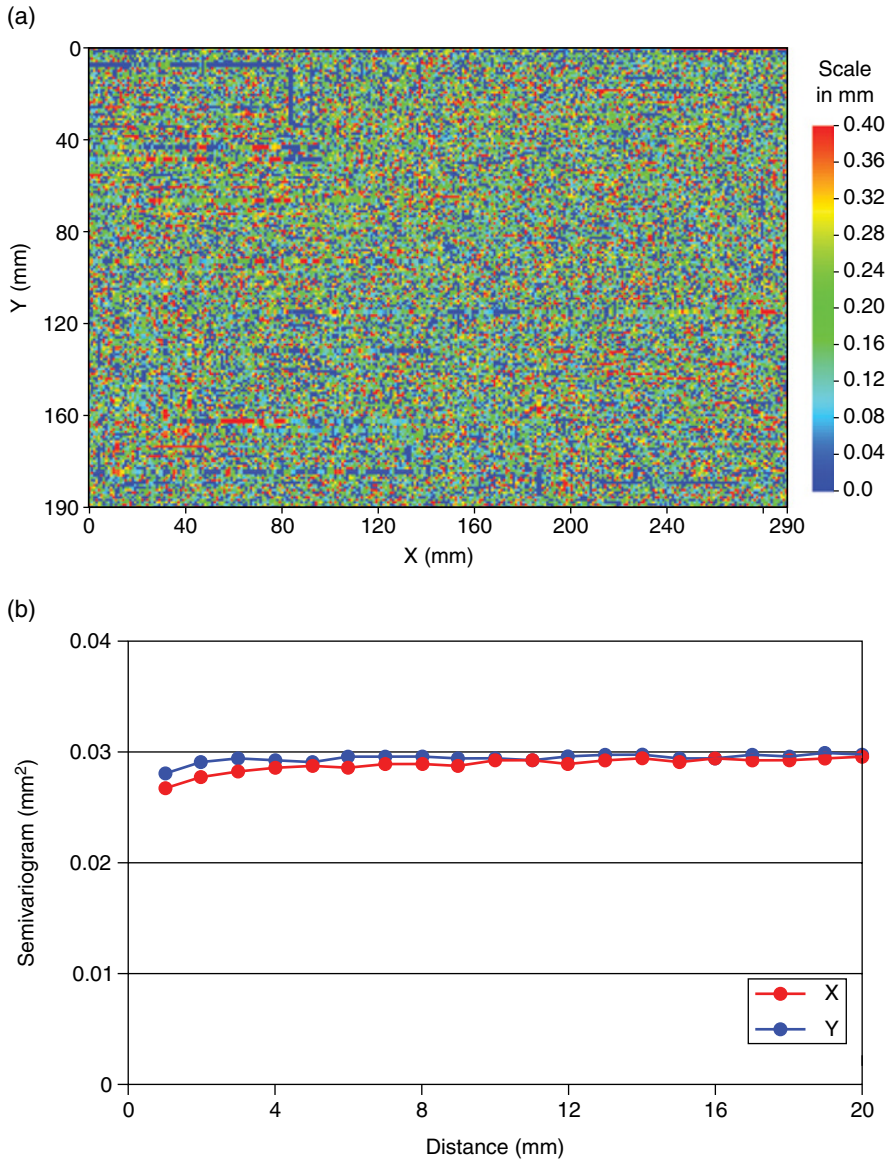

Figure 10.10 (a) Pore space map and (b) semivariogram of the initial image.

provided by the cubic relationship or nonlinear relationship that is assumed to exist between fracture aperture and fracture flow, i.e., the large apertures have a much larger impact on the computed flux.

Overall, the only set of hydraulic conductivity data that clearly brackets the measured flux value is the case where the spatial variability or spatial structure of the hydraulic conductivity distribution has been captured. Obviously, important aspects of the hydraulic conductivity structure of discrete fracture planes that in turn control the flux, and most likely the transport properties as well, are lost if one uses an averaging process.

10.4. HYDRAULIC CONDUCTIVITY SCALE EFFECT

Any review of laboratory- and field-measured flow and transport properties in fractured rocks confirms that these fractured rocks are characterized by a wide range in hydraulic conductivities and fluid/contaminant velocities along with a high degree of anisotropy. This wide range in hydraulic properties presents serious challenges when one is attempting to predict flux and contaminant transport in both saturated and partially saturated fractured rocks systems.

Permeability data (Figure 10.3) compiled and interpreted by *Clauser* [1992] for both porous and fractured

Table 10.2 Average of the apertures and corresponding equivalent porous media hydraulic conductivities used in the numerical modeling and the computed flux.

	Average 2b (mm)	Conductivity (m/s)	Flux (mL/s)
Uniform—2b arithmetic	0.173	2.03 E-4	1.4
Uniform—K arithmetic	—	1.22 E-3	8.4
Uniform—2b geometric	0.051	5.20 E-6	0.03
Uniform—K geometric	—	5.20 E-6	0.03
Random distribution	0.173	Variable	0.33
Spatial distribution	0.173	Variable	Range (0.43—0.56)

media show that the range of hydraulic properties appears to be about 7 to 8 log scales (Log_{10} ranged from -15 to -23 with k in m^2) for small laboratory samples, with the range of the permeability values decreasing as the scale of measurement or sample size increases. However, this reduction in range may be related more to a smaller number of samples for sample sizes greater than 10 cm than to an actual narrowing of the range of permeability values.

Measurements at the borehole scale (Figure 10.3) usually include test sections of the rock mass that are orders of magnitude larger than most laboratory samples. The borehole measurements show a much wider range in measured values than is shown by the laboratory data. In addition, the average or mid-range values reported by *Clauser* [1992] are higher than those presented for the laboratory scale samples. Obviously, borehole test sections capture open fractures and discontinuities that are not captured or not well represented in laboratory samples. The regional scale data tabulated by *Clauser* [1992] are limited in number, and each site or area, in most cases, is represented by only one data point. Where more than one data point is available for a given sample or test size, the range is relatively narrow when compared to either the laboratory or borehole scale data, but this may not be significant.

Overall, there appears to be a trend of increasing hydraulic conductivity with increasing sample size up to the 100-m scale, followed by a poorly defined pattern of decreasing hydraulic conductivity at the regional scale where the interpretation of the hydraulic conductivities for these large regional aquifer systems is based on measured and assumed boundary conditions. Changes with sample size or the size of the area being investigated are normally referred to as the "scale effect," and considerable effort has been devoted to developing scaling-up procedures without fully examining the hydraulic conductivity database from which these scale effects are inferred. *Gale* [1993] added additional laboratory data to the data that were presented by *Clauser* [1992] for a range of porous and fractured samples, and showed that the range for the mid-range values of permeability for laboratory scale samples could be extended to cover approximately 13 log cycles. Using the mid-range values only, *Gale* [1993] showed (Figure 10.2) that the borehole and regional scale values fell within the mid-range of the permeability values that were determined from laboratory data.

Obviously, part of this change with sample size is contributed by small-scale heterogeneities that become more significant as the size of the sample decreases. In addition, test boundary conditions and the lower measurement limits are much more precisely defined in small-scale laboratory samples and generally much more poorly defined or assumed in borehole tests, with the heterogeneities generally being averaged over significant lengths of the borehole test interval.

A comprehensive discussion of how transport properties in porous media are assumed to scale is provided by *Neuman* [1990]. In transport studies, the main focus is usually placed on the dispersivity of the media or how the contaminant spreads with increase in distance traveled and in the time required to travel over the specified distance rather than on the average fluid or contaminant velocity. In fractured rocks, which are characterized by strong anisotropy and rapid changes in fluid velocity from fracture to fracture, very little data exist with which to assess scale effects from a transport perspective.

In low-permeability fractured rocks, it has been assumed by some investigators that flow and transport are controlled by a number of high-permeability pathways, consisting of or within discrete fractures that are not captured by small-scale laboratory samples [*Margolin et al.*, 1998]. However, large-scale field tests, such as the Stripa macropermeability experiment [*Witherspoon*, 2000], did not show any evidence in the measured gradients that would support an interpretation that a few high-permeability pathways were dominating the flux into the mine drift. Furthermore, single-fracture borehole packer tests in the same rock mass [*Gale et al.*, 1987], while indicating a truncated distribution due to the limits on the measurement of low flow rates, did not show a bimodal fracture transmissivity distribution (Figure 10.11).

Given the need to determine how to scale-up from laboratory and borehole data sets to simulate and predict flow and transport in volumes of fractured rock that are of interest to a number of investigators, extensive numerical investigations have been conducted [*Margolin et al.*, 1998, among others] to determine how key parameters scale with an increase in the area of interest. Without

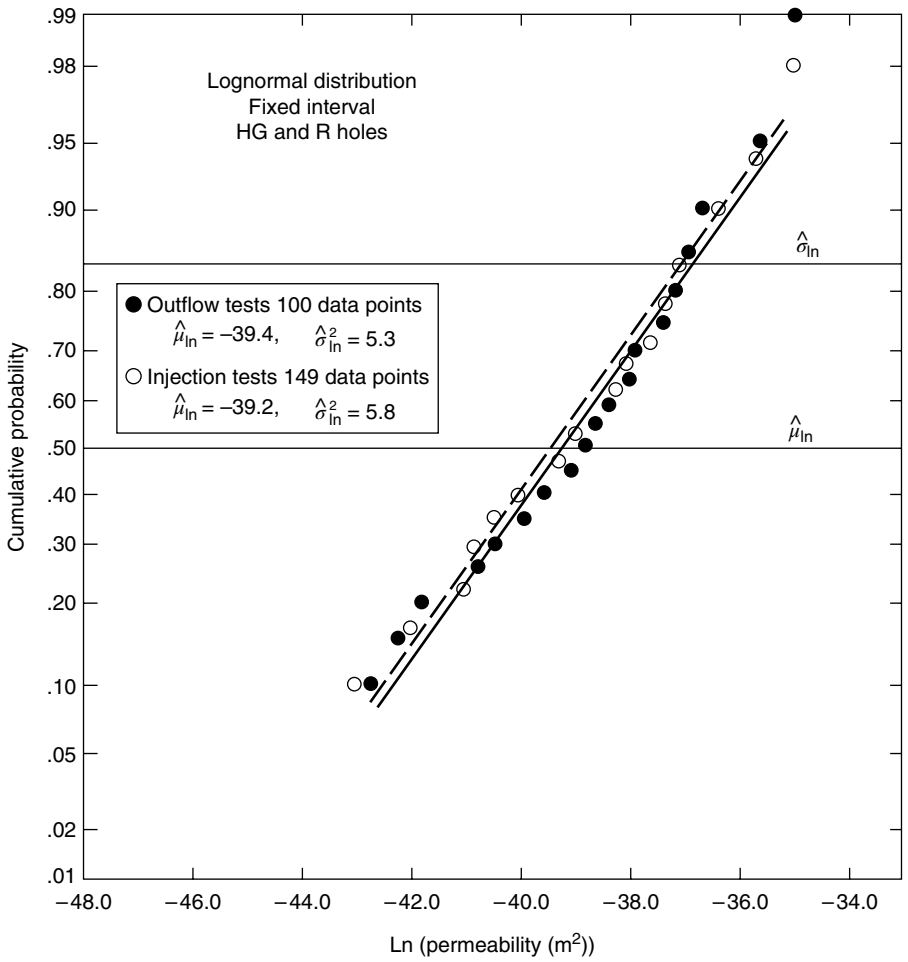

Figure 10.11 Lognormal distribution probability plot for fixed interval outflow and injection test permeabilities in the HG and R boreholes (after *Gale et al.,* 1987).

adequate deterministic fracture-property databases, however, including measured flow and transport properties, with which to calibrate or exercise the available models, it is difficult to validate the various conceptual models of flow in fracture systems along with the appropriate scaling relationships. Databases need to be developed at different scales, and the fracture-pore-space database that is presented here has been used to evaluate scaling relationships at the scale of a single fracture plane.

10.5. ASSESSING SCALING RELATIONSHIPS USING PORE SPACE DATA: SMALL-SCALE FRACTURE

Since the pore space geometry that controls the flow and transport in this fracture plane sample is essentially fully characterized, the concept of scale effect or scaling-up can be evaluated by selecting a number of small but different-sized sections from the fracture plane and determining how these sections contribute to flow through the entire fracture plane. This approach allows one to determine how the prediction of the measured fracture flow rate is affected by the size of the subsample that is used to populate the hydraulic conductivity distribution for the overall fracture plane.

10.5.1. Subsampling of the Fracture Plane

The fracture plane pore-space geometry was divided into 55,100 1-mm by 1-mm grid cells. The overall discrete fracture plane was divided into a series of blocks whose size were the selected sample scale. Each block was numbered sequentially. Thirty block numbers were selected from the entire list of blocks using random number generation for each sample size. This procedure was repeated for each subsample. To demonstrate the role of scale, five different subsample sizes were used (Figure 10.12): 10 mm by 10 mm (100 mm^2 or 100 grid cells), 15 mm by 15 mm (225 mm^2), 20 mm by 20 mm (400 mm^2), 30 mm by 30 mm (900 mm^2), and 40 mm by 40 mm (1600 mm^2).

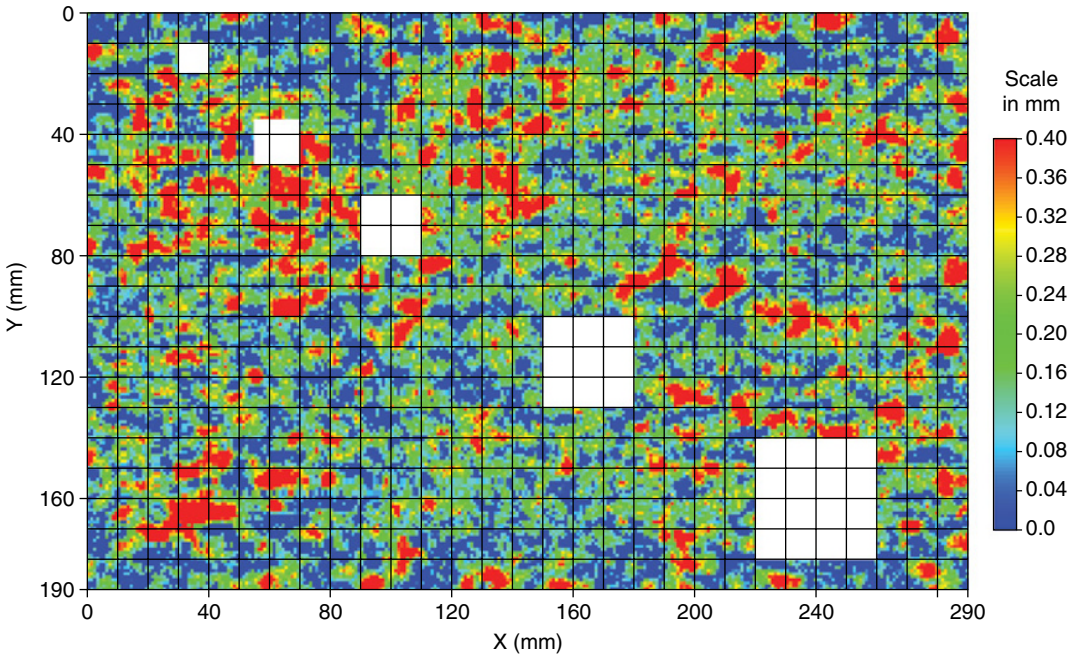

Figure 10.12 Selected sizes for subsampling, 10 mm, 15 mm, 20 mm, 30 mm, and 40 mm rectangular.

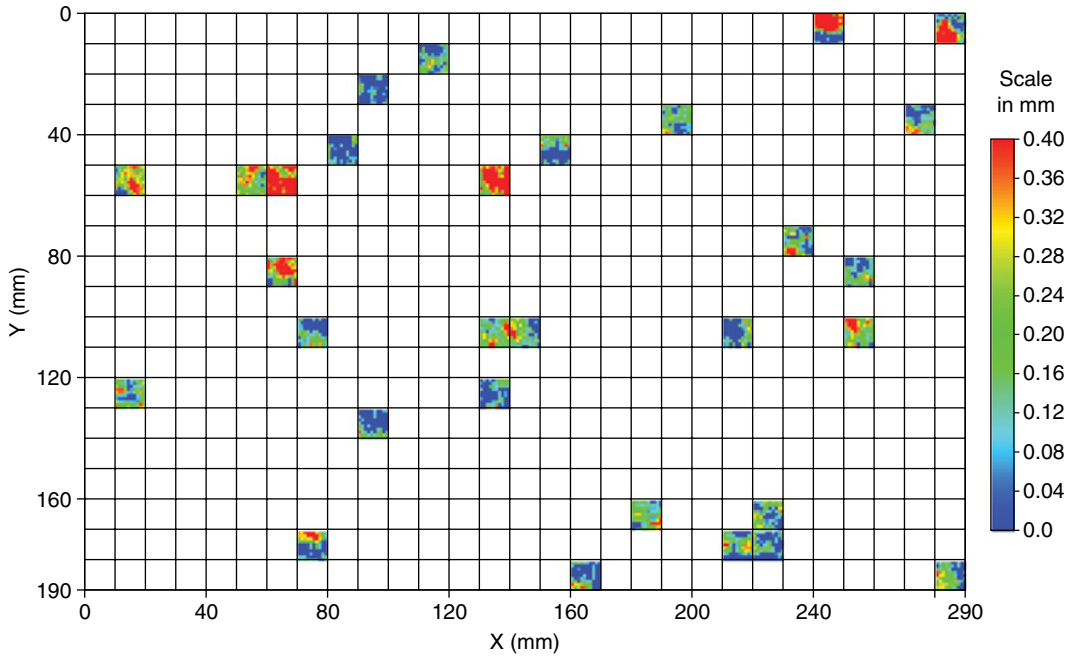

Figure 10.13 Subsamples with 10 mm by 10 mm size.

Figures 10.13 to 10.17 show the randomly selected locations for each group of subsamples. Each group of subsamples consisted of 30 subsamples except for the 40 mm by 40 mm samples, where only 27 subsamples were generated due to the limitations imposed by the size of the original fracture plane.

10.5.2. Flow Simulation

A 3D model using Feflow [*Diersch*, 2005] was set up for each subsample with a corresponding 1 mm by 1 mm grid size and one layer. Flow in both the X direction (Q_x) and the Y direction (Q_y) were simulated for each subsample.

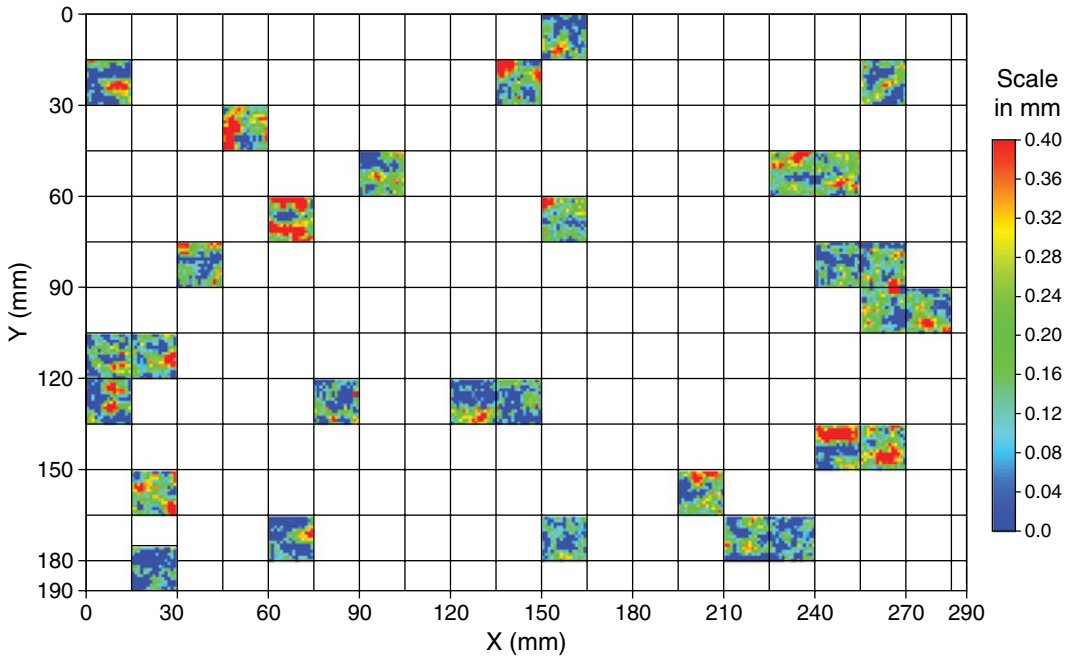

Figure 10.14 Subsamples with 15 mm by 15 mm size.

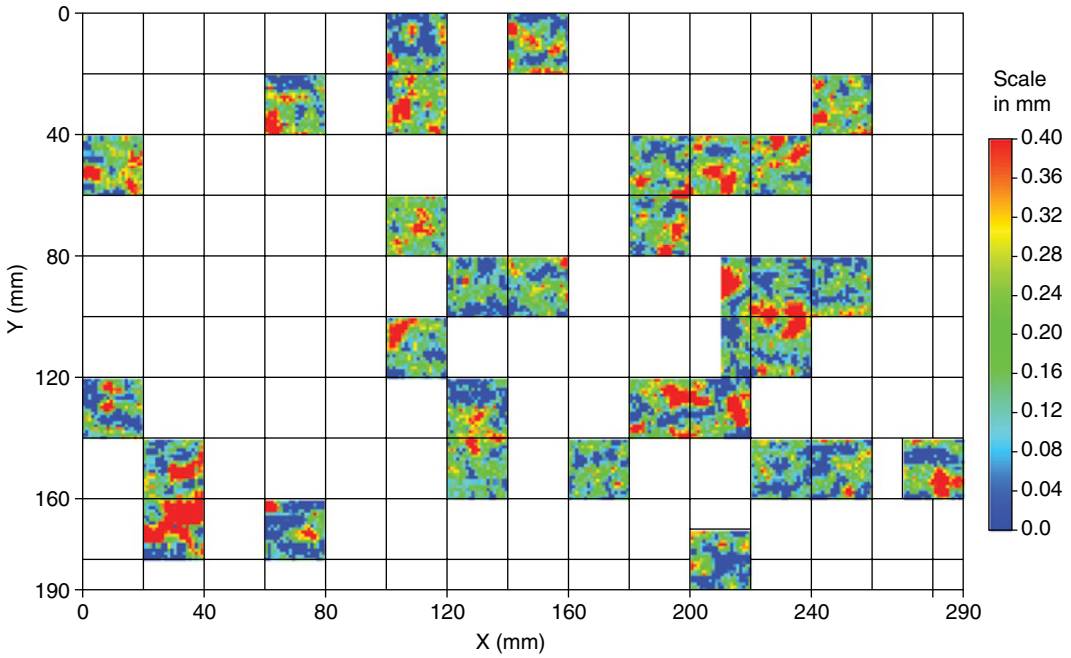

Figure 10.15 Subsamples with 20 mm by 20 mm size.

As discussed above, the measured pore space or aperture data from the simulated annealing process were converted to fracture hydraulic conductivities using the equation for the modified parallel plate model [*Seok*, 2001], with a relative roughness of 0.5. The fracture hydraulic conductivities were converted to equivalent porous medium conductivity and assigned as input parameters in the 3D FEFLOW flow and transport model (*Diersch*, 2005).

Figure 10.18 shows a schematic of the flow boundary conditions used in these simulations. The injection head was increased proportional to the sample size so that the hydraulic gradient for each subsample was the same.

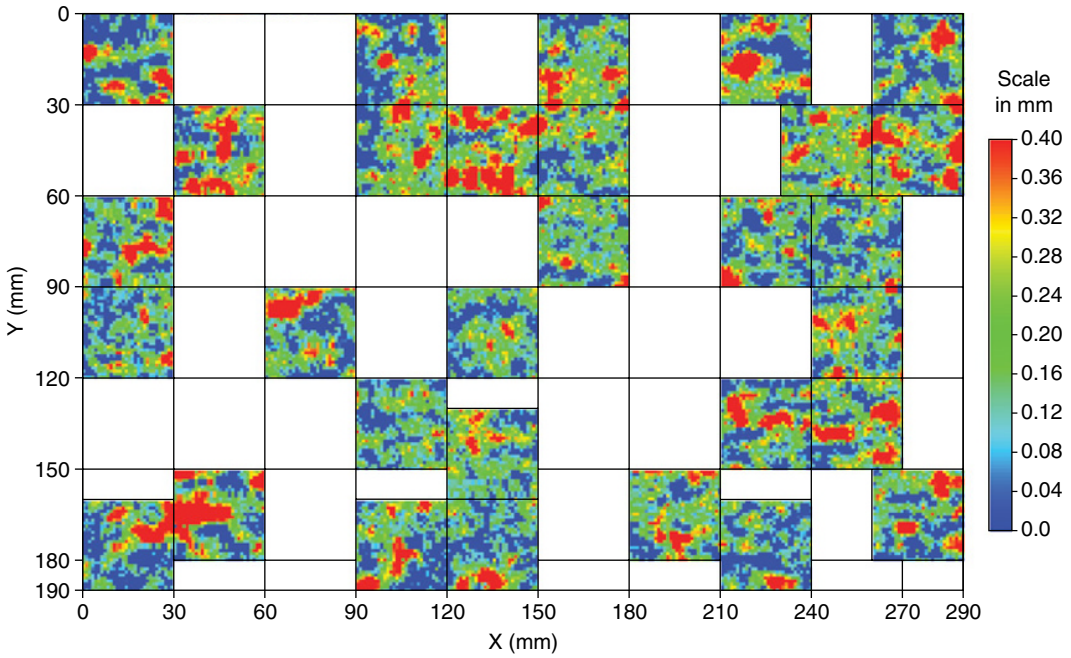

Figure 10.16 Subsamples with 30 mm by 30 mm size.

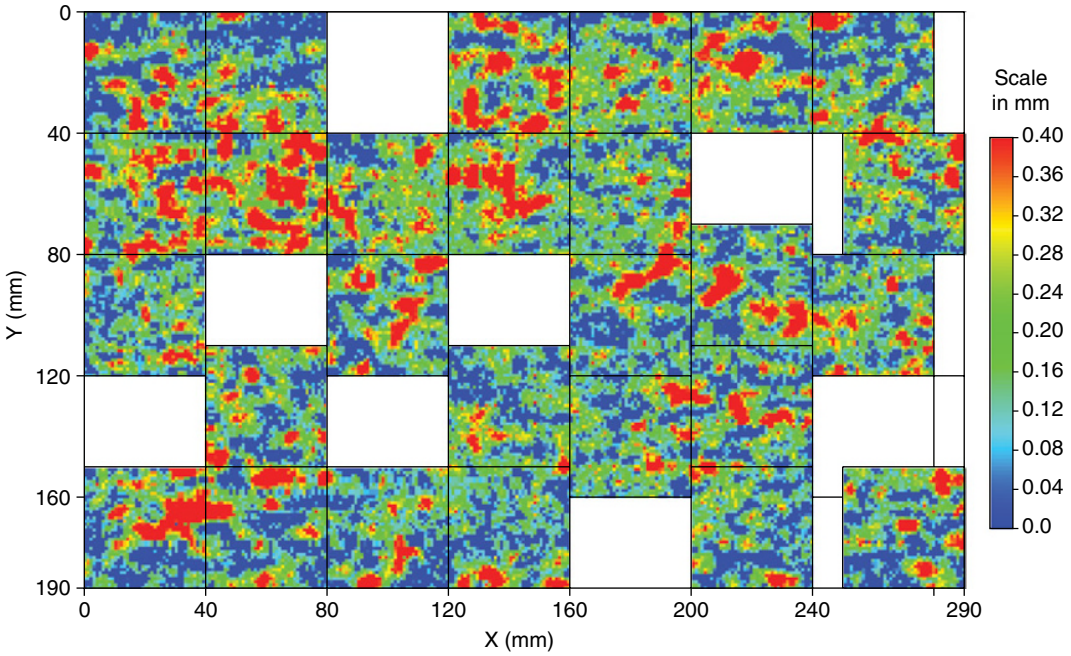

Figure 10.17 Subsamples with 40 mm by 40 mm size.

No-flow boundaries were assigned to two sides of the sample and constant head values were assigned to the other two sides. The hydraulic conductivity for each cell was calculated and assigned based on the corresponding aperture. Table 10.3 shows the basic model geometry and input parameters for each group of subsamples.

The computed flux was normalized to the hydraulic head. Then, the difference in the model size was compensated by dividing the flux by a ratio of the width to 10 mm. The logarithm of the normalized flux in both the X and Y directions, the mean, standard deviation, and variance of the apertures in each subsample, were computed

to enable these five measures to be presented on the same plot (Figure 10.19) with a vertical axis that ranges from -20 to +10 in log units. The horizontal axis shows the individual sample number within each sample size group. In these individual plots, the aperture data along with the computed flux values were sorted and plotted in terms of increasing mean aperture (i.e., decreasing negative values since all of the mean apertures are less than 1 mm). Figure 10.19 shows that the degree of variability in the computed flux values decreases with both increase in sample size and with increase in the mean aperture for each subsample. Clearly, with subsample sizes less than 20 mm by 20 mm, there was a much smaller possibility that the subsample would produce a flux value for this section of the fracture plane that was comparable to the measured flux value for the entire sample. The details of the computed flux for each group are also shown in Table 10.4.

Figure 10.20 shows the box plots of the computed normalized flux for Q_x and Q_y and the range of mean apertures for each group of subsamples. The measured flux value is shown as a solid line for reference. The average and median values for the normalized flux (Q*) and apertures for each group are also plotted and the outliers are indicated for each subsample group.

The mean computed flux values for both the X and Y directions for the 10 mm and 15 mm subsamples are lower than the measured flux. The range of flux, defined by the 25th and 75th percentiles, is wide in the smallest sample size and decreases dramatically with increasing sample size.

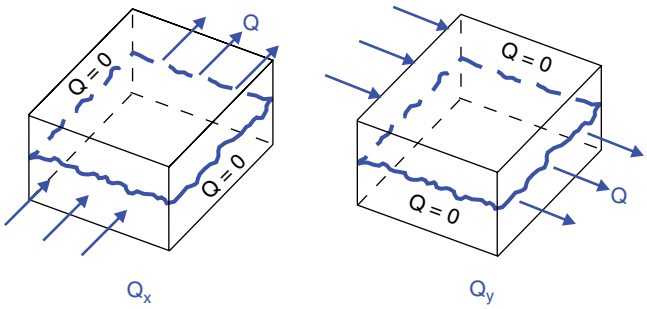

Figure 10.18 Schematic of bidirectional flow measurements, Q_x for X direction and Q_y for Y direction.

10.6. SUMMARY

For the entire fracture plane sample, (1) the simulated flux based on average hydraulic conductivity values and that based on the randomly assigned values did not match the measured value, and (2) the computed flux matched well to the measured flux when the hydraulic conductivities were constrained by the underlying spatial variability over the fracture plane. Characterizing the spatial structure of the underlying hydraulic conductivity data is required if one is to successfully predict flow rates in a given system. Flow rates, predicted using average and/or randomly assigned permeability values to populate an entire model area should not be expected to match the measured flow rates.

Comparison of the computed and measured flux as the subsample size was increased showed that (1) smaller subsamples had greater variability in computed flux, and (2) the computed flux gradually increased with increasing sample size until it converged to the measured flux when the subsample size was 20 mm by 20 mm or 400 mm^2.

Since full data sets for flow in discrete fractures are limited and expensive to obtain, the authors will make available to other researchers the full load and fracture deformation data set as well as the pore space data set and flow measurements for the discrete fracture sample that has been presented in this chapter. An example of part of the pore space data set is presented in the appendix to this chapter. The full data set can be obtained by contacting Fracflow Consultants Inc. or the individual authors (eunjeong_ffc@nfld.net or john_ffc@nfld.net). Additional coupled stress and flow experiments that have been used to demonstrate the importance of using spatial variability data to accurately reproduce measured fracture flow data have included preliminary experiments on a 1 m by 1 m by 1 m fractured rock sample that was supplied by Dr. Alan Shapiro of the United States Geological Survey and simulation of inflow to a large underground mine [*Seok*, 2011]. In both cases the small scale or local variability was constrained by a second or larger scale level of spatial variability. The results [*Seok*, 2011] from

Table 10.3 Model geometry and input parameters.

Group Number	Number of Subsamples	Model Size (each subsample)	Grid Size	Injection Head (m)	Output Head (m)
SS10	30	10 mm × 10 mm	1 mm × 1 mm	2	1
SS15	30	15 mm × 15 mm	1 mm × 1 mm	2.5	1
SS20	30	20 mm × 20 mm	1 mm × 1 mm	3	1
SS30	30	30 mm × 30 mm	1 mm × 1 mm	4	1
SS40	27	40 mm × 40 mm	1 mm × 1 mm	5	1

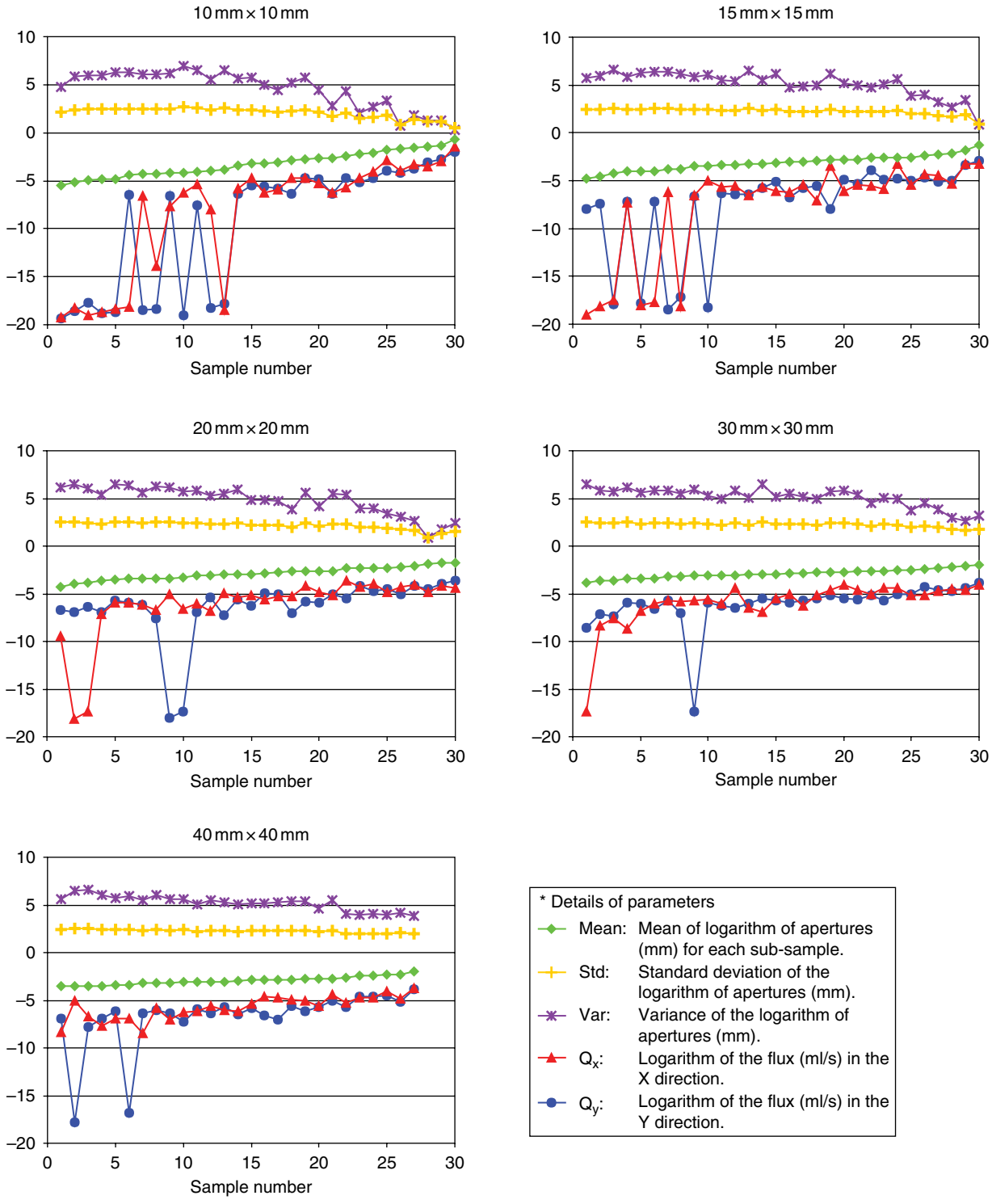

Figure 10.19 Details of simulation results of each group: plot of logarithm of aperture and flux data.

Table 10.4 Simulation results.

Group Number	Mean of Ln(Q_x*)	Min. of Ln(Q_x*)	Max. of Ln(Q_x*)	Mean of Ln(Q_y*)	Min. of Ln(Q_y*)	Max. of Ln(Q_y*)	Mean of Ln(2b) (mm)
SS10	−8.47	−19.27	−1.49	−9.52	−19.33	−1.98	−3.25
SS15	−7.92	−19.04	−3.2	−7.72	−18.44	−2.97	−3.14
SS20	−6.19	−18.09	−3.67	−6.44	−17.97	−3.59	−2.88
SS30	−5.96	−17.39	−4.05	−6.43	−17.35	−3.82	−2.89
SS40	−5.75	−8.45	−3.74	−6.8	−17.76	−3.79	−2.94

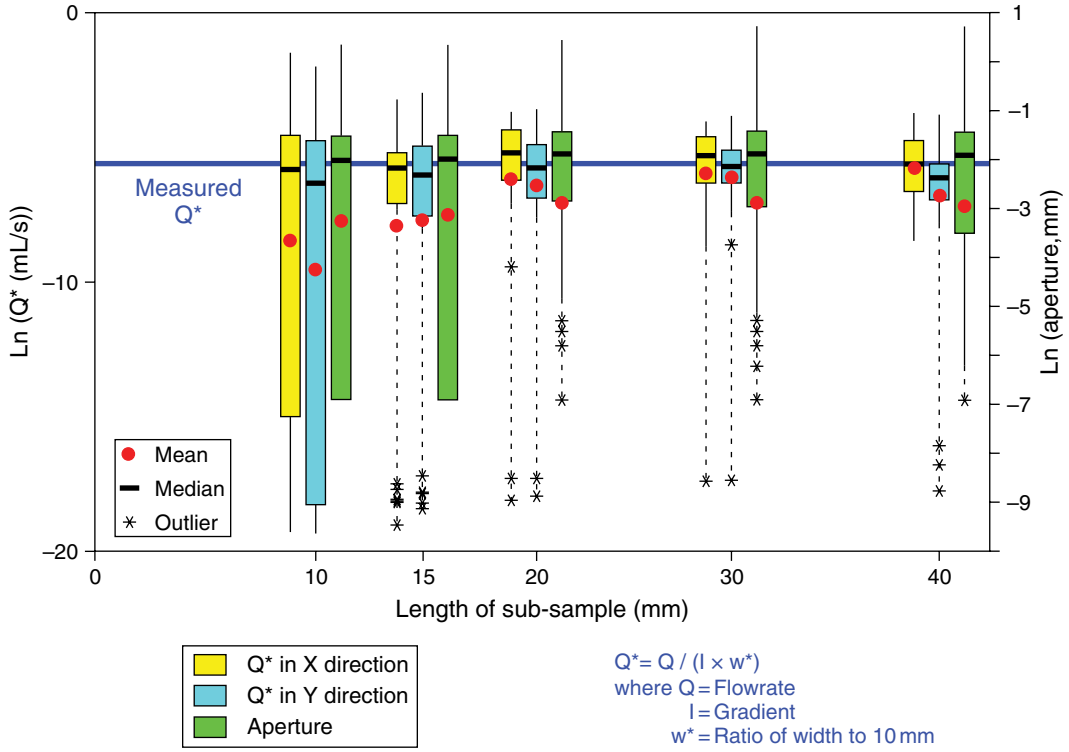

Figure 10.20 Normalized flux and mean of apertures for each subsample.

both the large 1-m-scale fracture sample and the large underground mine inflow simulations demonstrate that modeling of flow measurements can be significantly improved by constructing the hydraulic conductivity input parameters using this spatial variability approach and that this approach is applicable to both small- and large-scale studies or simulations of both discrete fracture media and equivalent porous media.

APPENDIX

Raw Aperture Data Collected from Selected Sections of ÄSPÖ Sample

- Fracture plane sample size: 190 mm x 290 mm
- Total number of section: 107
- Total number of data points: 20,152
- Aperture assigned on contact points: 0.001 mm

X Position mm	Y Position mm	Aperture mm	X Position mm	Y Position mm	Aperture mm	X Position mm	Y Position mm	Aperture mm	X Position mm	Y Position mm	Aperture mm
152	81	0.001	165.647	72.75	0.1442	9	11.185	0.001	16.5	21.457	0.2107
152.792	81	0.001	166.447	72.75	0.001	9	11.989	0.001	16.5	22.262	0.1483
153.584	81	0.001	167.239	72.75	0.001	9	12.793	0.001	16.5	23.046	0.2219
154.376	81	0.001	168.031	72.75	0.001	9	13.597	0.001	16.5	23.852	0.453
155.168	81	0.001	168.848	72.75	0.0652	9	14.401	0.001	16.5	24.657	0.4177
155.96	81	0.001	169.639	72.75	0.0348	9	15.205	0.001	16.5	25.463	0.4797
156.752	81	0.001	170.448	72.75	0.1035	9	16.009	0.001	16.5	26.268	0.7866
157.544	81	0.001	171.256	72.75	0.1324	9	16.813	0.001	16.5	27.074	0.4733
158.336	81	0.001	172.065	72.75	0.1389	9	17.617	0.001	16.5	27.879	0.313
159.128	81	0.001	172.873	72.75	0.063	9	18.421	0.001	16.5	28.684	0.001
159.92	81	0.001	173.665	72.75	0.001	9	19.225	0.001	16.5	29.46	0.0859
160.708	81	0.1052	174.457	72.75	0.001	9	20.029	0.001	16.5	30.266	0.0941
161.507	81	0.0739	175.249	72.75	0.001	9	20.833	0.001	16.5	31.07	0.001
162.305	81	0.1643	176.041	72.75	0.001	9	21.637	0.001	16.5	31.872	0.1193
163.103	81	0.1208	176.854	72.75	0.1278	9	22.441	0.001	16.5	32.677	0.2181
163.901	81	0.0013	177.662	72.75	0.0927	9	23.245	0.001	16.5	33.483	0.1349
164.693	81	0.001	178.471	72.75	0.0459	9	24.049	0.001	16.5	34.288	0.3626
165.485	81	0.001	179.281	72.75	0.0991	9	24.853	0.001	16.5	35.094	0.4385
166.277	81	0.001	180.089	72.75	0.1373	9	25.629	0.001	16.5	35.899	0.3327
167.079	81	0.1006	180.898	72.75	0.1485	9	26.402	0.1059	16.5	36.705	0.094
167.877	81	0.2349	181.706	72.75	0.1641	9	27.205	0.2088	16.5	37.498	0.1452
168.676	81	0.1655	182.515	72.75	0.1002	9	28.008	0.2835	16.5	38.303	0.2904
169.474	81	0.1876	183.323	72.75	0.088	9	28.811	0.2902	16.5	39.109	0.1986
170.272	81	0.1319	184.132	72.75	0.2818	9	29.614	0.2784	16.5	39.914	0.0606
171.053	81	0.0799	184.94	72.75	0.1321	9	30.417	0.2186	16.5	40.725	0.1115
171.832	81	0.0765	185.735	72.75	0.001	9	31.22	0.1153	16.5	41.531	0.0797
172.629	81	0.001	186.552	72.75	0.0834	9	32.023	0.125	16.5	42.336	0.3007

REFERENCES

Brace, W. F. (1980), Permeability of crystalline and argillaceous rocks, *Int. J. Rock Mech. Min. Sci. & Geomech. Abstr., 17*, 241–251.

Brace, W. F. (1984), Permeability of crystalline rocks: New in situ meaurements, *J. Geophys. Res., 89*(B8), 4327–4330.

Bury, K. V. (1975), *Statistical Models in Applied Science*, John Wiley & Sons, New York.

Clauser, C. (1992), Permeability of crystalline rocks, *EOS, Trans. AGU, 73*(21), 233.

Diersch, H.-J. G. (2005), FEFLOW 5.3 Finite Element—Subsurface Flow and Transport Simulation System, WASY GnbH, Institute for Water Resources Planning and Systems Research, Berlin, Germany.

Duncan, J. M., P. A. Witherspoon, J. K. Mitchell, D. J. Watkins, J. H. Hardcastle, and J. C. Chen (1972), Seepage and groundwater effects associated with explosive cratering, Report No. TE-72-2, University of California, Berkeley, 191 pp.

Fracflow Consultants Inc. (1997), Relationship Between Fracture Pore Structure, Roughness, Solute Velocities and MBB1D Model Predictions, Report submitted to AECL Whiteshell Nuclear Research Laboratories, Pinawa, Manitoba.

Gale, J. E. (1984), Changes in fracture permeability as a function of sample size, fracture type, and stress history, IAH Int. Groundwater Symp., Montreal, 44–53.

Gale, J. E. (1993), Fracture properties from laboratory and large scale field tests: Evidence of scale effects, *Proceedings of the Second International Workshop on Scale Effects in Rock Masses*, Lisbon, Portugal, June 1993 (ISRM), 341–352.

Gale, J. E. (1999), Impact of flow geometry, flow regime, two-phase flow and degassing on the transmissivity of rough fractures, SKB IPR-99-08.

Gale, J. E., R. Macleod, J. Welhan, C. Cole, and L. Vail (1987), Hydrogeological Characterization of the Stripa Site, SKB IPR-87-15.

Gale, J. E., and K. G. Raven (1980), Effects of sample size on the stress-permeability relationship for natural fractures, Technical Information Report No. 48, Swedish-American Cooperative Program on Radioactive Waste Storage in Mined Caverns in Crystalline Rock, Lawrence Berkeley Laboratory Report LBL-11865, Berkeley, 111 pp.

Gale, J. E., R. A. Schaefer, A. B. Carpenter, and A. Herbert (1991), Collection, analysis, and integration of discrete fracture data from the Monterey Formation for fractured reservoir simulations, *66th Annual Technical Conference and Exhibition*

of the Society of Petroleum Engineers, Dallas, Texas, October 6–9, 1991, SPE 22741, pp. 823–834.

Gale, J. E., and E. Seok (2004), Using fracture pore space geometry to assess degassing and scaling relationships in fractured rocks, *Proceedings of the Second International Symposium on Dynamics of Fluids in Fractured Rock*, February 10–12, 2004, pp. 25–26.

Hubbert, M. K. (1956), Darcy's law and the field equations of the flow of underground fluids. *Trans. Am. Inst. Min. Met. Engrs., 207*, 222–239.

Iwai, K. (1976), Fundamental Studies of Fluid Flow through a Single Fracture, Ph.D. thesis, Univ. of Calif., Berkeley, 208 pp.

Louis, C. (1969), A study of groundwater flow in jointed rock and its influence on the stability of rock masses, *Imperial College Rock Mechanics Research Report, 10*, London, 88 pp.

Margolin, G., B. Berkowitz, and H. Scher (1998), Structure, flow, and generalized conductivity scaling in fracture networks, *Water Resources Research, 34*(9), 2103–2121.

Neuman, S. P. (1990), Universal scaling of hydraulic conductivities and dispersivities in geologic media, *Water Resources Research, 26*(8), 1749–1758.

Neuman, S. P. (1994), Generalized scaling of permeabilities: Validation and effect of support scale, *Geophysical Research Letters, 21*(5), 349–352.

Pratt, H. R., H. S. Swolfs, W. F. Brace, A. D. Black, and J. W. Handin (1977), Elastic and transport properties of an in situ jointed granite, *Int. J. Rock. Mech. Min. Sci. & Geomech. Abstr., 14*, 35–45.

Raven, K. G., and J. E. Gale (1985), Water flow in a natural rock fracture as a function of stress and sample size, *Int. J. Rock Mech. Min. Sci. & Geomech. Abstr. 22*(4), 251–261.

Romm, E. S. (1966), *Flow Characteristics of Fractured Rocks* (in Russian), Nedra, Moscow, 283 pp.

Seok, E. (2001), Pore space characterization and implications for flow simulation in discrete fracture planes, M.Sc. Thesis, Memorial University of Newfoundland, Canada, 166 pp.

Seok, E. (2011), Impact of variability in laboratory and field fracture permeability data on simulated flux as a function of scale and spatial structure, Ph.D. Thesis, Memorial University of Newfoundland, Canada, 190 pp.

Witherspoon, P. A. (2000), Investigations at Berkeley on fracture flow in rocks: From the parallel plate model to chaotic systems, *Dynamics of Fluids in Fractured Rock, American Geophysical Union Geophysical Monograph 122*.

Witherspoon, P. A., C. H. Amick, and J. E. Gale (1977), Stress-flow behaviour of a fault zone with fluid injection and withdrawal, Report No. 77-1, Department of Materials Science and Mineral Engineering, University of California, Berkeley.

Witherspoon P. A., C. H. Amick, J. E. Gale, and K. Iwai (1979), Observations of a potential size effect in experimental determination of the hydraulic properties of fractures, *Water Resour. Res. 15*(5), 1142–1146.

Part III
Connection to the Surrounding Environment

11

Fractures as Advective Conduits at the Earth-Atmosphere Interface

Maria Inés Dragila[1], Uri Nachshon[2], and Noam Weisbrod[2]

ABSTRACT

Our planet is active and changing. Gas exchange across the earth-atmosphere interface is an essential component, impacting a number of important earth and atmospheric processes, including global water cycle, greenhouse gas emissions, solute precipitation within the vadose zone, and the evolution of karst terrain. Both diffusive and advective mechanisms contribute to net gas exchange at different time and spatial scales. This chapter discusses advective gas transport via vadose zone fractures driven by surface wind and vadose zone thermal gradients.

Two critical aspects of thermal-driven fracture ventilation are evident: (1) Thermal gradients in the top meter of the vadose zone are sufficient to trigger deep penetration of atmospheric air and rapid replacement of fracture air, and (2) Advection by this mechanism occurs only during cooler nighttime hours. On a seasonal scale, deeper vadose zone temperature controls the proportion of the day during which venting is active, with more venting occurring during winter. Wind-driven convection also generates fracture air venting; however, venting does not penetrate as deeply into the vadose zone and its timing and duration depend upon local weather patterns. The work presented here represents the beginning of a quantitative understanding of vadose zone venting via fractures by these two mechanisms.

11.1. INTRODUCTION

Gas exchange between the earth-atmosphere interface is an integral part of earth and atmospheric function. In the uppermost reaches of the vadose zone, diffusive exchange of air between soils and the atmosphere is crucial to maintain soil aeration that provides necessary oxygen concentration for plant growth [*Drew*, 1992] and for soil biogeochemical processes. Soil cracks can facilitate gas exchange deep into the soil profile, and larger, deeper fractures may contribute to larger scale environmental processes. Of most recent interest are exchange rates of water vapor and CO_2, which are important components of the global warming process [*Weihermüller* et al., 2011; *Wickramarachchi et al*., 2011]. In addition, movement of volatile radionuclides, such as ^{3}H, ^{14}C, and Rd from radioactive waste disposal facilities, or emission of Rn from natural sources and industrial volatile organic components [e.g., *Lenhard et al*., 1995; *Conant et al*., 1996; *Smith et al*., 1996; *Choi et al*., 2002; *Kristensen et al*., 2010; *Ronen et al*., 2010] can greatly affect public health when emissions build up in buildings or are emitted into populated areas [*Nazaroff*, 1992; *Scanlon et al*., 2001]. In carbonitic deposits, ventilation via fractures will affect pCO_2 within the karst system, impacting dissolution rates, water quality, and net efflux of CO_2 to the atmosphere [*Liu and Zhao*, 2000]. Because vadose zone fractures potentially impact so many ecosystem processes, it is imperative that we understand the transport mechanisms controlling efflux of these gases across the earth-atmosphere interface.

Historically, diffusion has been considered the main mechanism for gas exchange between the atmosphere and vadose zone [*Hirst and Harrison*, 1939; *Penman*, 1940a, 1940b; *Marshall* 1958, 1959; *Millington and Quirk*, 1961; *Cunningham and Williams*, 1980; *Amali and Rolston*,

[1] *Department of Crop and Soil Science, Oregon State University, Corvallis, Oregon, USA*

[2] *Environmental Hydrology and Microbiology, ZIWR, BIDR, Ben Gurion University of the Negev, Beer-Sheva, Israel*

Dynamics of Fluids and Transport in Complex Fractured-Porous Systems, Geophysical Monograph 210, First Edition.
Edited by Boris Faybishenko, Sally M. Benson, and John E. Gale.

1993], but more recently, several advective gas transport mechanisms have been suggested to also contribute to gas exchange, including (1) wind pumping [*Fukuda*, 1955; *Weeks*, 1991, 1994; *Waddington et al*., 1996], (2) atmospheric barometric changes [e.g., *Pirkle et al*., 1992; *Rossabi*, 2006], and (3) in fractured media, density differences between fracture air and the atmospheric air, that trigger convective motion [*Weisbrod et al*., 2005; *Weisbrod and Dragila*, 2006; *Weisbrod et al*., 2009]. Even though there is broad acceptance that these advective fluxes exist and that they play an important role in our atmospheric processes, quantification of these processes is still in its infancy.

This chapter synthesizes results from a number of experiments aimed at quantifying the effect of two driving forces, wind and thermal gradients on fracture ventilation, and net gas efflux between the earth and atmosphere. Deductions are based on field measurements that have shown the development of venting features, and on laboratory experiments used to quantify venting flux as a function of driving force and fracture aperture.

11.2. THEORY

Diffusion was long considered the dominant process in vadose zone transport due to the high viscous dissipation of motion through small soil pores. Diffusive flux occurs in response to gradients in the partial pressure of gases [*Fick*, 1855],

$$J_D = -D\nabla C \tag{11.1}$$

where J_D is the mass flux, D is the gas diffusion coefficient in free air, and C is the molar gas concentration. The diffusivity of the porous medium will be reduced relative to the free-air diffusivity by the tortuosity and moisture content of the porous medium. Thermal gradients may reduce or enhance diffusivity, and the effect will be gas-species specific. Various groups have investigated the functional relationship of diffusivity with media properties [e.g., *Phillip and deVries*, 1957; *Marshall*, 1958, 1959; *Millington and Quirk*, 1961; *Moldrup et al*., 2000]. As per *Millington and Quirk* [1961], $D_{soil} = Df_a^{4/5}$, where f_a is the air-filled porosity.

In fractured vadose zones where fractures can exhibit very high permeability, small pressure gradients can lead to advective motion of gas that is much higher than diffusive gas fluxes [*Thorstenson and Pollock*, 1989; *Massmann and Farrier*, 1992, *Scanlon et al.*, 2001]. Nonturbulent advective gas transport in porous media can be described by Darcy's law, which correlates gas fluxes (J_a) to media permeability (k), gas dynamic viscosity (μ), and pressure gradient (∇P),

$$J_a = -\frac{k}{\mu}\nabla P \tag{11.2}$$

The expression can be applied to air in fractures where the pressure differences are generated by buoyant forces, resulting from gas density gradients. Fracture permeability can be estimated by $k = (2b)^2/12$, where 2b is the fracture aperture [*Shemin*, 1997].

Diurnal thermal gradients that develop in the upper meter of the vadose zone were first suggested as a triggering mechanism for fracture ventilation by *Weisbrod et al*. [2005] and *Weisbrod and Dragila* [2006]. The thermal profile of the upper meter of the vadose zone at night is such that air at depth within the fracture is warmer (less dense) than air near the surface and also warmer than atmospheric air. The density gradient is in a state of instability. The conditions for onset of convective motion in a fluid with an unstable density gradient are theoretically given by the Rayleigh number (Ra, Equation 11.3), which is a dimensionless number that compares buoyant to viscous forces and thermal dissipation. Onset supposedly occurs when Ra exceeds a critical value of $4\pi^2$ [*Lapwood*, 1948; *Nield*, 1982]. Ra is defined as:

$$Ra = \frac{\Delta T \alpha g k L}{\nu \kappa}. \tag{11.3}$$

In Eq. 11.3, ΔT is the temperature difference between fracture air at the top and bottom of the fracture over the length scale L, ν is the kinematic viscosity, g is the gravitational constant, κ is the thermal diffusivity of the gas within the fracture, and k is the fracture permeability). For example, for a discrete fracture of 1 m depth and 0.5 cm aperture, $Ra = 4\pi^2$ requires a minimum necessary temperature difference of 0.17°C. Temperature differences along the upper 1 m of the vadose zone are typically much greater, in the range of 2–15° [e.g., *Brady*, 1990; *Scott*, 2000], more than sufficient for establishing convective motion.

In the case of a Ra greater than the critical value, any disturbance will trigger convective motion, and fingers of cooler (denser) atmospheric air entering the fracture will force out warm fracture air. Consequently, advective ventilation of fractures should be expected to occur nightly driven by unstable thermal gradient. Diffusive transport will dominate ventilation during the day when stable thermal gradient is established, except when wind or barometric pulses are present. Since movement depends on buoyancy, which is controlled by temperature, gas composition, and vapor pressure, the penetration depth of atmospheric air will depend on the rate at which these properties equilibrate with local fracture air.

The second mechanism studied here is fracture ventilation driven by atmospheric winds that induce pressure fluctuations at the ground-atmosphere interface [e.g., *Kimball and Lemon*, 1971, 1972; *Colbeck*, 1989; *Ishihara et al*., 1992; *Waddington et al*., 1996; *Takle et al*., 2004]. In addition, wind blowing over topographic relief forms

eddies that increase pressure on the windward side of an obstruction and reduce pressure on the leeward side [Scott, 2000]. As a result, advective gas fluxes through porous media are driven by these pressure differences [*Colbeck*, 1989], the Bernoulli effect [*Vogel et al*., 1973;, 1979], and turbulent diffusion [*Kimball and Lemon*, 1971, 1972; *Ishihara et al*., 1992]. These same mechanisms are expected to be even more effective in gas transfer when fractures and other cavities are exposed to the atmosphere because of the much higher permeability of these structures [*Weeks*, 1991].

In spite of the relatively good understanding of the basic principles responsible for wind-induced fracture ventilation, mechanistic models that quantify natural fracture ventilation due to surface winds have not been developed. This manuscript presents an empirical relationship between surface wind strength and fracture ventilation.

The venting effectiveness for the two advective mechanisms presented here is quantified by the Sherwood number, a dimensionless number that conveys the relative dominance of the advective and diffusive mechanism. As defined by *Weast* [1980],

$$Sh = \frac{J_a L}{D} \tag{11.4}$$

where L is the length scale of interest. Advection dominates for Sh > 1.

11.3. MATERIALS AND METHODS

Field data consisted of air temperature measurements at high temporal resolution, within a natural fracture in chalk rock (1–2 cm aperture, 150 cm long and >120 cm deep). A 2D grid of 60 cm × 60 cm with thermistors spaced every 15 cm was installed vertically within the air space, and data were collected every 10 min over a three-year period. Two additional vertical strings of thermocouples were installed in the fracture and within the rock to a depth of 120 cm. Atmospheric wind and temperature were also recorded. For details of field site protocol see *Weisbrod et al*. [2009].

Laboratory experiments were used to constrain parameters and reduce the broad variability found under field conditions. Fracture venting was quantified using a fracture simulator constructed of glass walls with dimension of 50 cm × 50 cm separated by apertures of 1 and 2 cm. Thermocouples were installed along the walls and within the airspace of the fracture. For the experiments exploring thermal gradients, the bottom of the fracture simulator was heated and temperature of the ambient air was controlled. The following temperature differences were tested. The fracture simulator's base was heated to 5, 10, and 13°C over the ambient air temperature for the 1-cm aperture, and to 5, 7, 8, 9, 10, 12, and 13°C over the ambient air temperature for the 2-cm aperture. The fracture was filled with smoke to enable tracing of air movement, with gas motion captured by video camera. A schematic of laboratory setup and procedure details for the thermal gradient experiments are described in *Nachshon et al*. [2008].

The experiments performed to explore the effect of wind used the same fracture simulator with apertures set to 0.5, 1, and 2 cm. Isothermal conditions were imposed. A steady wind was forced across the width of the aperture for a range of wind speeds of 0.25–1.5 m/s, concurring with calculated wind speed at the field site. For details of laboratory protocol for the wind experiments see *Nachshon et al*. [2012].

11.4. RESULTS

11.4.1. Field Results

Field data of air temperature within the fracture give clear evidence of the development of thermal convection cells on a nightly basis (Figure 11.1) as shown by the 60 cm × 60 cm array of thermocouples. Daytime matrix temperature in the upper 60 cm of the vadose zone cools with depth leading to stably stratified air within the fracture (e.g., Figure 11.1 for 1500 or 1700 hrs.). At night the thermal profile in the rock is inverted (warm below and cool above). Convective motion ensues and is sustained by rock temperature. Two distinct convection cells form with a plume of cool atmospheric air moving downward into the fracture space (e.g., Figure 11.1 for 0100 hrs.). While the 2D thermal maps show air motion in the upper 60 cm, the deep string of thermocouples installed to a depth of 120 cm shows significant air disturbance down to its lowest sensor (Figure 11.2). Large differences in temperature between the air space and the rock confirm advective airflow motion within the fracture space (Figure 11.2). While the diurnal cycle seen in Figure 11.1 is repetitive and almost identical each day, the portion of each day during which convection occurs changes with season (Figure 11.3). The daily duration of convection was calculated from the temperature data of the 60 cm × 60 cm thermocouple array, calculated from the time the first convection cell formed (usually around dusk) until the time when a stable temperature profile was reestablished (usually a few hours after dawn). During winter, the vadose zone is warmer than the atmosphere (gray dotted line in Figure 11.3) and convection can proceed all day, with fluxes expected to be higher at night. This relationship may be different in polar regions where diurnal temperature relationships are different, and in some karst terrain where cave ventilation may change the thermal profile within the vadose zone.

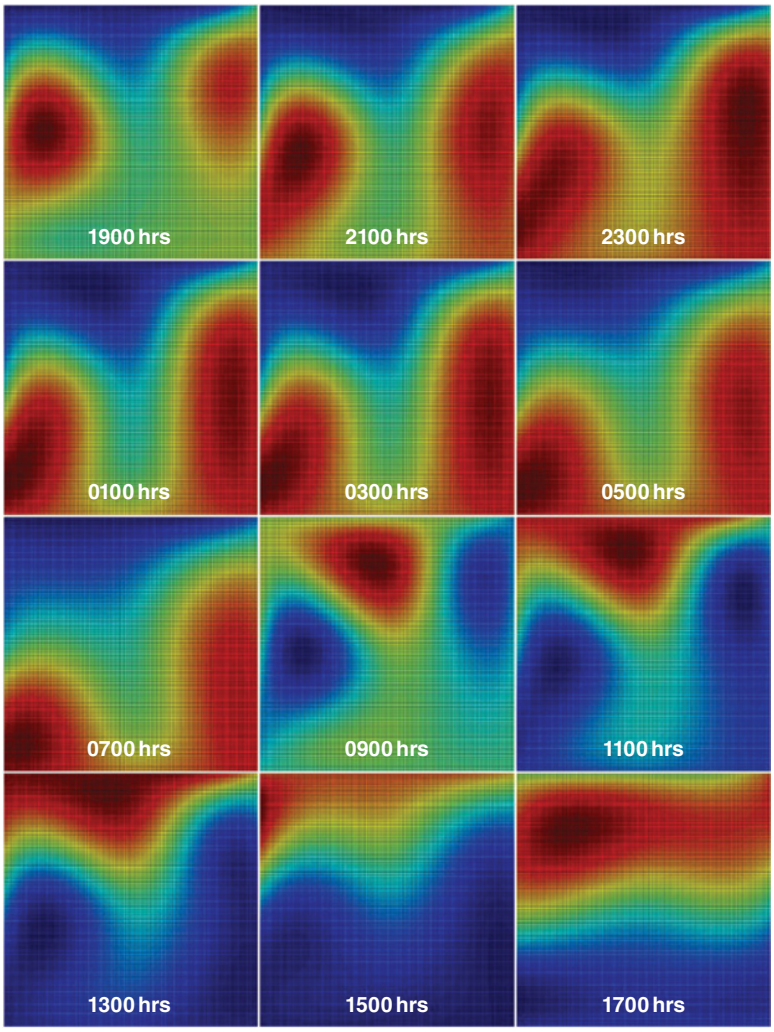

Figure 11.1 Air temperature within a natural fracture over a 24-hr period. Temperature scale is unique to each map to maximize image range: blue (cool) to red (warm): 0100 hrs (8.5–16°C), 0300 hrs (7–16°C), 0500 hrs (8.8–14.7°C), 0700 hrs (10.4–14.5°C), 0900 hrs (13.5–18°C), 1100 hrs (14.6–25.7°C), 1300 hrs (16–28°C), 1500 hrs (16–30°C), 1700 hrs (16–19.8°C), 1900 hrs (14–18°C), 2100 hrs (10.6–17.3°C). Each map is 60 cm wide by 60 cm deep from soil surface. Time is shown on each map (Jan 12, 2006).

11.4.2. Laboratory Results

Heating the bottom of the fracture simulator generated a vertical thermal gradient that led to well-organized convective motion within the fracture. The shape of the convective plumes changed in width and intensity with the magnitude of the thermal gradient. The average speed of each upward plume and the plume width were used to calculate the mass transfer rate. (Details of plume morphology are discussed in *Nachshon et al.*, 2008.) Comparing the mass transfer rate to the Rayleigh (Ra) number permits grouping of the two different apertures and the different thermal gradients. It was found that the mass transfer rate increased with the square of Ra (Figure 11.4). Since Ra is linearly proportional to the imposed thermal gradient, this indicates a dramatic increase in mass transfer efficiency with small changes in temperature differences. To quantify the effectiveness of this venting mechanism relative to diffusive transfer, the Sherwood number was graphed against the Ra number (Figure 11.5). To calculate the Sh number (Equation 11.4), the diffusion coefficient (D) was estimated using Equation 11.1 and the flux (J) and length scales (L) from the experimental data. While for the 1-cm fracture the advective flux is about 10 times more efficient than the diffusive flux, for the 2-cm fracture advection could be as much as two orders of magnitude more effective than diffusion in mixing atmospheric and fracture air.

The wind experiments showed that depth to which the smoke was cleared was linearly correlated to wind speed and aperture (Figure 11.6), with similar slopes for each aperture. The largest depth to which smoke was cleared was <40 cm. Without wind, smoke from the top 10 cm of

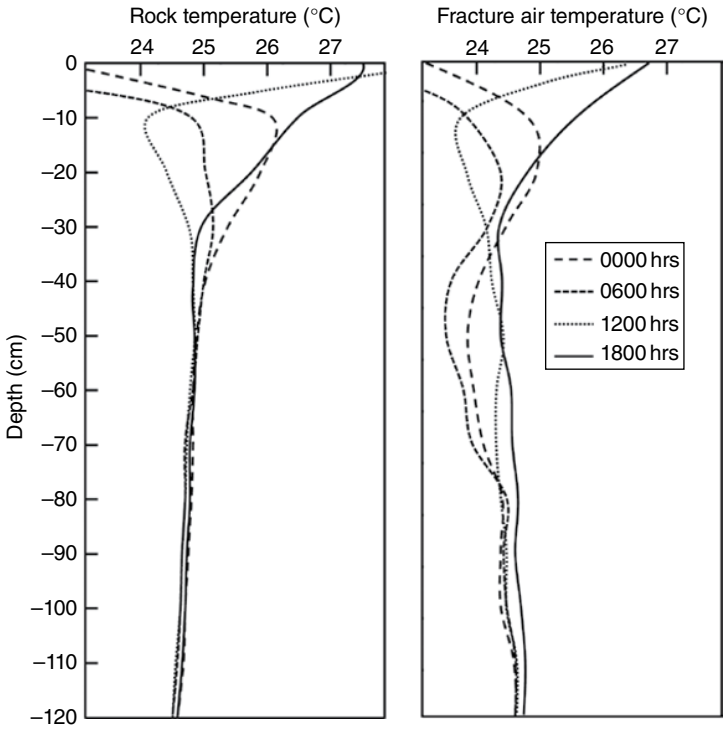

Figure 11.2 Temperature measured at different depths by thermocouples placed in the rock matrix adjacent to the fracture and in the airspace within the fracture.

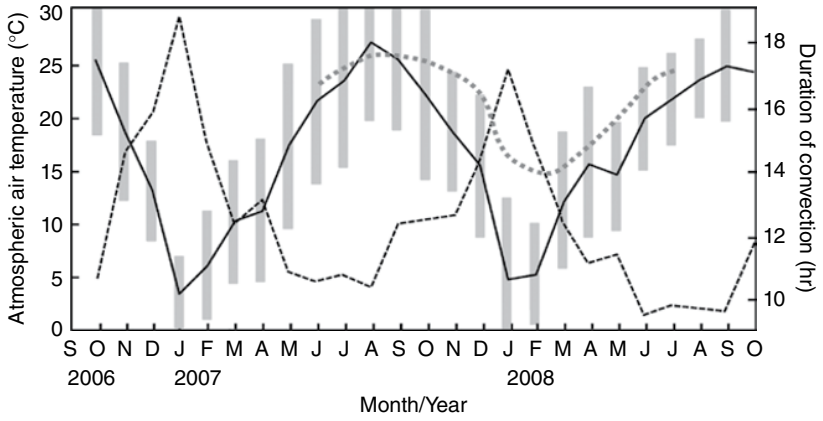

Figure 11.3 Monthly averages of daily duration of convective venting (dashed line), and average monthly atmospheric air temperature (solid line). Gray bars represent the amplitude of diurnal temperature. Gray dotted line is rock temperature data at 120-cm depth from 2005 field season that is superposed onto the graph.

the chamber cleared in ~15 minutes. Under imposed wind, removal time dropped to 5–10 sec. Mean flux rate per unit area of fracture opening ranged from 0.01–0.04 m/s for the range of wind speeds 0.25–1.5 m/s.

11.5. DISCUSSION

Laboratory experiments and field observations yielded evidence of two very important aspects of thermal-driven fracture ventilation. First, commonly occurring near-surface diurnal thermal gradients are sufficient to trigger rapid replacement of fracture air and deep penetration of atmospheric air. Once atmospheric air has entered a fracture system, it will continue to move downward because it is cooler and drier, and therefore denser than surrounding air. The maximum depth will depend on fracture geometry and how rapidly the vapor pressure and temperature equilibrates. In addition, the energy required for evaporation of water from the matrix-fracture interface will slow down convection [*Kamai et al.*, 2009]. Secondly, the advective gate has a time switch: it is open only at night.

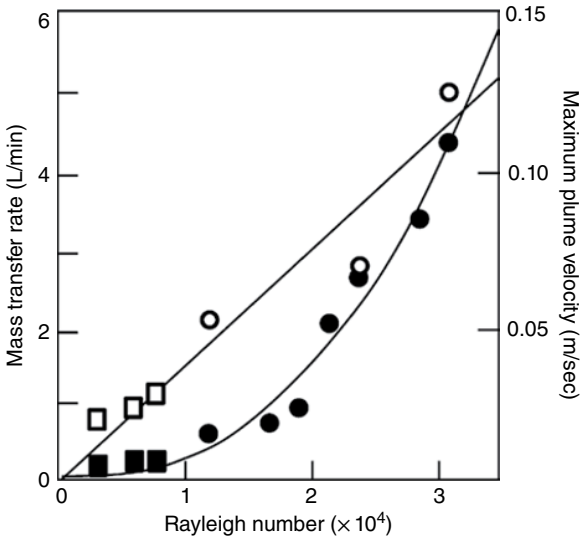

Figure 11.4 Mass transfer rates (solid) from the smoke-replacement experiments increase with the square of the Rayleigh number, while maximum velocity of the plume (open symbols) increase linearly. Squares represent data from 1-cm aperture and circles from 2-cm aperture. Mass transfer rate ~ $(4.3 \times 10^{-9})Ra^2$, $R^2 = 0.97$. Maximum plume velocity = (4×10^{-6}) Ra, $R^2 = 0.94$.

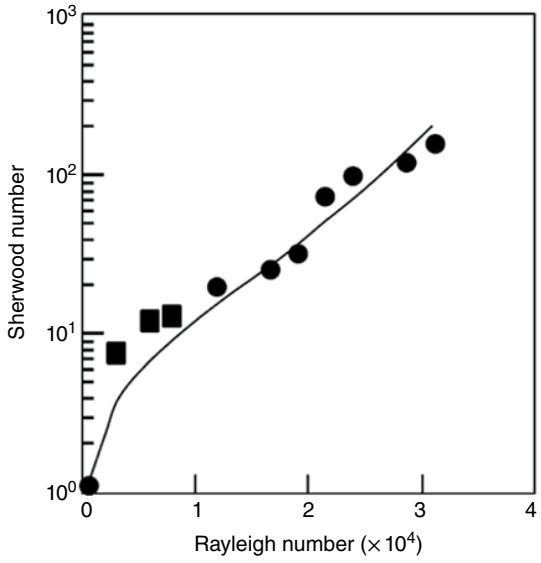

Figure 11.5 Sherwood number (Sh) as a function of Rayleigh number (Ra). Data calculated from thermal gradient experiment using smoke as tracer. Black line is a fitted curve where Sh ~ $(1.5 \times 10^{-7})Ra^2 + 1$.

Wind disturbance under daytime conditions in the lab (stable gas density gradient) did not reach as deeply as thermal venting, with a maximum venting depth of 40 cm for the largest aperture tested (2 cm) and the highest wind speed tested (1.5 m/s). By contrast, it is expected

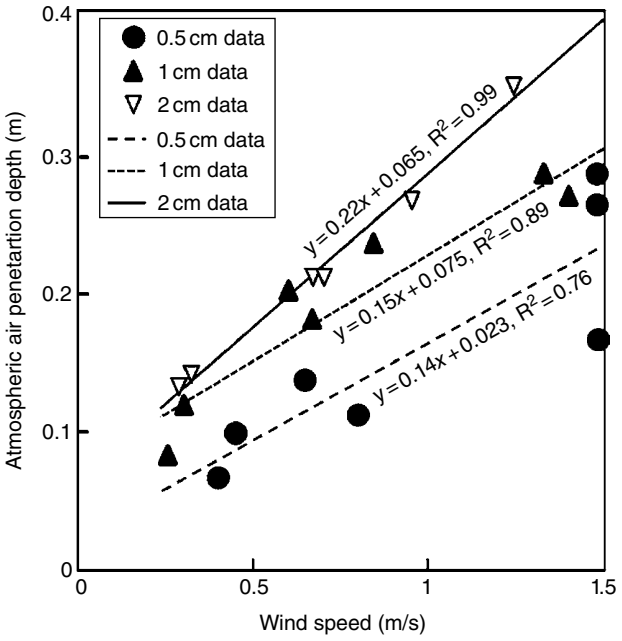

Figure 11.6 Maximum depth of smoke removal for different speeds of imposed crosswind and apertures. Equation of fitted trend lines are shown near respective lines.

that wind disturbance at night may indeed trigger entry of atmospheric air that will dive deeper into the fracture, supported by an unstable density gradient within the fracture. Identifying the exact role of wind in ventilation at night is difficult because it overlaps with venting already occurring by thermal gradients. In both cases, wind and thermal gradients act as a trigger for the initial air disturbance at the top of the fracture. Once triggered, atmospheric air will enter the fracture and move deep into the vadose zone until the density of the downward moving plume equilibrates with local conditions. The maximum ventilation depth will be controlled by the maximum depth of the invading plume, which depends on downward velocity (density difference and fracture aperture); rate of thermal dissipation; and equilibration of gas partial pressures. The maximum depth of plume penetration has not been tested experimentally nor investigated numerically, although the concept of deep atmospheric invasion is supported by field instruments at the fracture site that measured nightly air disturbance at the deepest probe located 120 cm below the surface.

While thermal-driven venting will occur year round, there is a distinct seasonal cycle controlled by the deeper vadose zone's seasonal temperature variability. The deeper vadose zone (>1 m) is warmer in winter than in summer. Field data showed longer duration of ventilation on winter days than on summer days. Also, it is expected that nighttime advective ventilation may

reach to greater depths in winter than during summer months because of the greater difference in subsurface and atmospheric nighttime temperatures.

11.6. CONCLUSIONS

Advective ventilation was shown to be part of the normal function of fractures, producing very high flux rates but with a strong periodic component. Nighttime temperature gradient of the upper half-meter of the vadose zone is sufficient to trigger and sustain convective venting of fracture air. No thermal-driven venting was observed during daytime, and daytime wind-driven venting was suppressed below ~40 cm (for the apertures tested). During daytime, conditions are much less prone to large advective venting fluxes because the stably stratified thermal profile of the upper vadose zone does not produce buoyancy-driven motion. While advective venting fluxes were found to be 1–4 orders of magnitude greater than diffusive venting, the net transport of vadose zone gases will be limited by the much slower diffusion of gas or moisture from the matrix to the fracture. The extreme difference in time constants between the two mechanisms means that convective venting acts to expose the subsurface directly to the atmosphere, thereby increasing the surface area of the earth-atmosphere interface and the potential interactions.

These studies have begun the process of quantifying a relationship between *fracture properties* and *ventilation potential*. Advective venting is much more effective than diffusive venting, and its periodic component could be important for vadose zone processes. Furthermore, because of the rapid turnover of air, the true efflux of vadose zone gases will be limited by transport through the porous media to the fracture system, and water vapor exchange will be limited by evaporation at the matrix-fracture interface. Rapid, diurnal gas ventilation should be considered an integral component of high-permeability systems, impacting normal geochemical and ecological functions of the fractured vadose zone. The operational role of air-filled vadose zone fractures is as an invasive path for the atmosphere, permitting atmospheric air to penetrate deeply into the vadose zone but with a diurnal gate-valve near the surface that forces a specific timescale and rhythm to the exchange process.

ACKNOWLEDGMENTS

The authors are grateful to the reviewers of this manuscript for their insightful comments, and to the U.S. National Science Foundation and the U.S.-Israel Binational Science Foundation for their financial support.

REFERENCES

Amali, S., and D. E. Rolston (1993), Theoretical investigation of multicomponent volatile organic vapor diffusion: Steady-state fluxes, *J. Environ. Qual.*, *22*, 825–831, doi:10.2134/jeq1993.00472425002200040027x.

Brady, C. N. (1990), *The Nature and Properties of Soils*, 10th ed., Macmillan, New York.

Choi, J. W., F. D. Tillman, and J. A. Smith (2002), Relative importance of gas phase diffusive and advective trichloroethene (TCE) fluxes in the unsaturated zone under natural conditions, *Environ. Sci. Technol., 36,* 3157–3164, doi:10.1021/es011348c.

Colbeck, S. C. (1989), Air movement in snow due to wind pumping, *J. Glaciol., 35,* 209–213.

Conant, B. H., R. W. Gillham, and C. A. Mendoza (1996), Vapor transport of trichloroethylene in the unsaturated zone: Field and numerical modeling investigations, *Water Resour. Res., 32*(1), 9–22, doi:10.1029/95WR02965.

Cunningham, R. E., and R. J. J. Williams (1980), *Diffusion in Gases and Porous Media*, Plenum, New York.

Drew, M. C. (1992), Soil aeration and plant root metabolism, *Soil Sci., 154*(4), 259–268, doi:10.1097/00010694-199210000-00002.

Fick, A. (1855), Ueber diffusion, *Annals of Physics, 170*(1), 59–86.

Fukuda, H. (1955), Air and vapor movement in soil due to wind gustiness, *Soil Sci., 79,* 249–256, doi:10.1097/00010694-195504000-00002.

Hirst, W., and G. E. Harrison (1939), The diffusion of radon gas mixtures, *Proc. R. Soc. London, Ser. A, 169,* 573–586, doi:10.1098/rspa.1939.0016.

Ishihara, Y., E. Shimojima, and H. Harada (1992), Water vapor transfer beneath bare soil where evaporation is influenced by a turbulent surface wind, *J. Hydrol., 131*(1–4), 63–104, doi:10.1016/0022-1694(92)90213-F.

Kamai, T., N. Weisbrod, and M. I. Dragila (2009), Impact of ambient temperature on evaporation from surface-exposed fractures, *Water Res. Res., 45,* W02417, doi:10.1029/2008WR007354.

Kimball, B. A., and E. R. Lemon (1971), Air turbulence effects upon soil gas exchange, *Soil Sci. Soc. Am. Proc., 35,* 16–21, doi:10.2136/ sssaj1971.03615995003500010013x.

Kimball, B. A., and E. R. Lemon (1972), Theory of soil air movement due to pressure fluctuations, *Agric. Meteorol., 9,* 163–181, doi:10.1016/0002-1571(71)90020-3.

Kristensen, H. A., A. Thorbjørn, M. P. Jensen, M. Pedersen, and P. Moldrup (2010), Gas-phase diffusivity and tortuosity of structured soils, *J. Contam. Hydrol., 115*(1–4), 26–33, doi:10.1016/j.jconhyd.2010.03.003.

Lapwood, E.R. (1948), Convection of a fluid in a porous medium, *Proc. Cambridge Philological Soc.*, *44*, 508–521.

Lenhard, R. J., M. Oostrom, C. S. Simmons, and M. D. White (1995), Investigation of density-dependent gas advection of trichloroethylene: Experiment and a model validation exercise, *J. Contam. Hydrol., 19,* 47–67, doi:10.1016/0169-7722(94)00055-M.

Liu, Z., and J. Zhao (2000), Contribution of carbonate rock weathering to the atmospheric CO2 sink, *Environ. Geol.* (Berlin), *39*(9), 1053–1058, doi:10.1007/s002549900072.

Marshall, T. J. (1958), A relation between permeability and size distribution of pores, *Journal of Soil Science, 9,* 1–8.

Marshall, T. J. (1959), The diffusion of gases through porous media, *Soil Science Society of America Journal, 10*(1), 79– 82.

Massmann, J., and D. F. Farrier (1992), Effects of atmospheric pressures on gas transport in the vadose zone, *Water Resources Research, 28*(3), 777–791.

Millington, R. J., and J. P. Quirk (1961), Permeability of porous solids, *Trans. Faraday Soc., 57*(7), 1200–1207, doi:10.1039/tf9615701200.

Moldrup, P., T. Olesen, P. Schjonning, T. Yamaguchi, and D. E. Rolston (2000), Predicting the gas diffusion coefficient in undisturbed soil from soil water characteristics, *Soil Science Society of America Journal, 64*(3), 94–100.

Nachshon, U., N. Weisbrod, and I. M. Dragila (2008), Quantifying air convection through surface-exposed fractures: A laboratory study, *Vadose Zone J., 7*(3), 948–956, doi:10.2136/vzj2007.0165.

Nachshon, U., M. Dragila, and N. Weisbrod (2012), From atmospheric winds to fracture ventilation: Cause and effect, *J. Geophys. Res., 117, G02016*, doi:10.1029/2011JG001898.

Nazaroff, W. W. (1992), Radon transport from soil to air, *Rev. Geophys., 30,* 137–160, doi:10.1029/92RG00055.

Nield, D. A. (1982), Onset of convection in a porous layer saturated by an ideal gas, *Int. J. Heat Mass Transfer, 25*, 1605–1606.

Penman, H. L. (1940a), Gas and vapour movements in the soil: I. The diffusion of vapours through porous solids, *J. Agric. Sci., 30,* 437–462, doi:10.1017/S0021859600048164.

Penman, H. L. (1940b), Gas and vapour movements in the soil: II. The diffusion of carbon dioxide through porous solids, *J. Agric. Sci., 30,* 570–581, doi:10.1017/S0021859600048231.

Philip, J. R., and DeVries, D. A. (1957), Moisture movement in porous materials under temperature gradients, *Transactions, American Geophysical Union, 38*(2), 222–232.

Pirkle, R. J., D. E. Wyatt, V. Price, and B. B. Looney (1992), Barometric pumping: The connection between the vadose zone and the atmosphere, *Proceedings of the FOCUS Conference on Eastern Regional Ground Water Issues*, 427–442, Natl. Ground Water Assoc., Dublin, Ohio.

Reimer, G. M., and C. G. Bowles (1979), Soil-gas helium concentrations in the vicinity of a uranium deposit, Red Desert, Wyoming, *U.S. Geol. Surv. Open File Rep*., *79*-975, 9 pp.

Ronen, D., H. L. Wiener, E. R. Graber, O. Dahan, and N. Weisbrod (2010), Simultaneous counter-flow of chlorinated volatile organic compounds across the saturated unsaturated interface region of an aquifer, *Water Res., 44*(7), 2107–2112, doi:10.1016/j.watres.2009.12.016.

Rossabi, J. (2006), Analyzing barometric pumping to characterize subsurface permeability, in C. K. Ho and S. W. Webb (eds.), *Gas Transport in Porous Media*, 279–290, Springer, Dordrecht, Netherlands, doi:10.1007/1-4020-3962-X_16.

Scanlon, B. R., J. P. Nicot, and J. W. Massmann (2001), Soil gas movement in unsaturated systems, in A. W. Warrick (ed.), *Soil Physics Companion*, 297–341, CRC Press, Boca Raton, Fla., doi:10.1201/9781420041651.ch8.

Scott, H. Don. (2000), *Soil Physics: Agricultural and Environmental Applications*, Iowa State University Press, Ames, Iowa.

Shemin, G. (1997), A governing equation for fluid flow in rough fractures, *Water Res. 33*, 53–61.

Smith, J. A., A. K. Tisdale, and H. J. Cho (1996), Quantification of natural vapor fluxes of TCE in the unsaturated zone at Picatinny arsenal, New Jersey, *Environ. Sci. Technol., 30*(7), 2243–2250, doi:10.1021/es950610c.

Takle, E. S., W. J. Massman, J. R. Brandle, R. A. Schmidt, X. Zhou, I. V. Litvina, R. Garcia, G. Doyle, and C. W. Rice (2004), Influence of high-frequency ambient pressure pumping on carbon dioxide efflux from soil, *Agric. For. Meteorol., 124,* 193–206, doi:10.1016/j.agrformet.2004.01.014.

Thorstenson, C. D., and D. W. Pollock (1989), Gas transport in unsaturated zones: Multicomponent systems and the adequacy of Fick's laws, *Water Resources Research, 25*(3), 477-507, doi:10.1029/WR025i003p00477.

Vogel, S., C. Ellington, and D. Kilgore (1973), Wind-induced ventilation of the burrow of the prairie-dog Cynomys ludovicianus, *J. Comp. Physiol. A., 85*(1), 1–14, doi:10.1007/BF00694136.

Waddington, E. D., J. Cunningham, and S. L. Harder (1996), The effects of snow ventilation on chemical concentrations, in E. W. Wolff and R. C. Bales (eds.), *Chemical Exchange Between the Atmosphere and Polar Snow*, NATO ASI Ser., 43, 403–452, Springer, Berlin.

Weast, R. C. (1980), *CRC Handbook of Chemistry and Physics*, CRC Press, Boca Raton, Fla.

Weeks, E. P. (1991), Does the wind blow through Yucca Mountain, in D. D. Evans et al. (eds.), *Proceedings of Workshop V: Flow and Transport Through Unsaturated Fractured Rock-Related to High-Level Radioactive Waste Disposal*, 45–53, U.S. Nucl. Reg. Comm., Washington, D.C.

Weeks, E. P. (1994), Thermal and wind pumping as mechanisms for passive vapor extractions in hilly terrain (Abstract), *Eos Trans. AGU, 75*(44), 263.

Weihermüller, L., M. Lamers, and M. Reichstein (2011), Introduction to production, transport and emission of trace gases from the vadose zone to the atmosphere, *Vadose Zone J., 10,* 151–155, doi:10.2136/vzj2010.0117.

Weisbrod, N., and M. I. Dragila (2006), Potential impact of convective fracture venting on salt-crust buildup and groundwater salinization in arid environments, *J. Arid Environ., 65,* 386–399, doi:10.1016/j.jaridenv.2005.07.011.

Weisbrod, N., M. I. Dragila, U. Nachshon, and M. Pillersdorf (2009), Falling through the cracks: The role of fractures in Earth-atmosphere gas exchange, *Geophys. Res. Lett., 36,* L02401, doi:10.1029/2008GL036096.

Weisbrod, N., M. Pillersdorf, M. I. Dragila, C. Graham, and J. Cassidy (2005), Evaporation from fractures exposed at the land surface: Impact of gas-phase convection on salt accumulation, in B. Faybishenko, P. A. Witherspoon, and J. Gale (eds.), *Dynamics of Fluids and Transport in Fractured Rock*, Geophys. Monogr. Ser., 162, 151–164, AGU, Washington, D.C., doi:10.1029/162GM14.

Wickramarachchi, P., K. Kawamoto, S. M. Hamamoto, P. Moldrup, and T. Komatsu (2011), Effects of dry bulk density and particle size fraction on gas transport parameters in variably saturated landfill cover soil, *Waste Manag., 31*(12), 2464–2472, doi:10.1016/j.wasman.2011.07.008.

12

Quantifying Water Flow and Retention in an Unsaturated Fracture-Facial Domain

John R. Nimmo[1] and Siamak Malek-Mohammadi[2]

ABSTRACT

Hydrologically significant flow and storage of water occur in macropores and fractures that are only partially filled. To accommodate such processes in flow models, we propose a three-domain framework. Two of the domains correspond to water flow and water storage in a fracture-facial region, in addition to the third domain of matrix water. The fracture-facial region, typically within a fraction of a millimeter of the fracture wall, includes a flowing phase whose fullness is determined by the availability and flux of preferentially flowing water, and a static storage portion whose fullness is determined by the local matric potential. The flow domain can be modeled with the source-responsive preferential flow model, and the roughness-storage domain can be modeled with capillary relations applied on the fracture-facial area. The matrix domain is treated using traditional unsaturated flow theory. We tested the model with application to the hydrology of the Chalk formation in southern England, coherently linking hydrologic information including recharge estimates, streamflow, water table fluctuation, imaging by electron microscopy, and surface roughness. The quantitative consistency of the three-domain matrix-microcavity-film model with this body of diverse data supports the hypothesized distinctions and active mechanisms of the three domains and establishes the usefulness of this framework.

12.1. INTRODUCTION

There is much experimental evidence, for example, from *Tokunaga and Wan* [1997], *Su et al.* [1999], and *Dragila and Weisbrod* [2003] that partially filled pores contribute substantially to preferential as well as diffuse flow. Preferential flow is known to be critically important to contaminant-transport and water-resource issues, and its occurrence in unsaturated media is widespread [*Nimmo*, 2012]. An important feature is that because of reduced viscous friction from there being less solid surface in contact with the flowing liquid, flow in partially filled conduits can be faster than in totally filled conduits, as commonly noted in textbooks on fluid dynamics. Various researchers [e.g. *Tokunaga et al.*, 2000; *Tuller and Or*, 2001; *Hincapié and Germann*, 2009; *Nimmo*, 2010] have developed models based on partially filled pores.

Complications arise from the dominance of different physical processes affecting flow in the matrix and the fractures, given that observed hydrologic behavior results from their combination and the interaction between them. This poses a serious challenge to traditional unsaturated-zone flow theory, which emphasizes a binary filled/unfilled state of pores that either are or are not conducting flow. The unsaturated flow properties of a macroscopic medium are traditionally construed to result from the collective effect of those pores that are completely filled with water. *Celia et al.* [1995], *Or and Tuller* [1999], and others have noted that this construct, which neglects the hydraulic effect of partially filled pores, is overused in unsaturated zone hydrology.

In this chapter we discuss and quantify the dynamics of flow, replenishment, storage, and drainage of an unsaturated zone fracture-facial domain. Spatially, it comprises that portion of a fracture's internal volume typically within a fraction of a millimeter of the fracture's internal face, within which water flow and storage occur

[1] *U.S. Geological Survey, Menlo Park, California, USA*
[2] *Bradley University, Peoria, Illinois, USA*

Dynamics of Fluids and Transport in Complex Fractured-Porous Systems, Geophysical Monograph 210, First Edition.
Edited by Boris Faybishenko, Sally M. Benson, and John E. Gale.

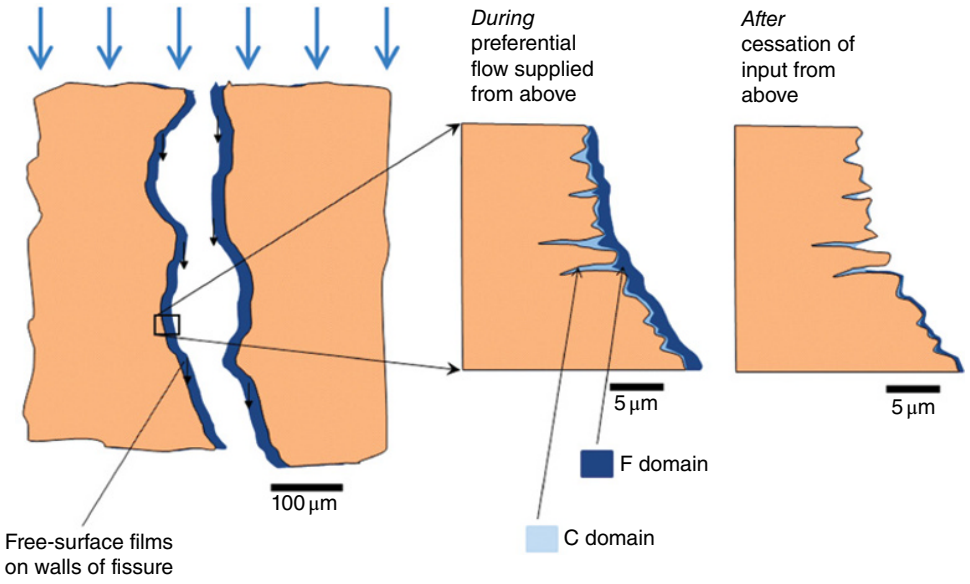

Figure 12.1 Diagram showing the C and F domains within a fissure. The two alternative inset drawings illustrate the configuration of C- and F-domain water during and after a major episode of preferential flow supplied from above.

while the fracture is not completely water filled. The overriding practical question is how can matric potentials, saturation state, and flowing water associated with matrix and fracture domains be reconciled with each other and with observed behavior at timescales of storms, seasons, and unsaturated-zone residence. Although some terminology here pertains primarily to fractured rock, the content may also relate to the analogous case of macroporous soil and other media with the possibility of unsaturated preferential flow. In this chapter we use the term *fracture* to refer to any possible nonmatrix flow conduit, regardless of shape or developmental process.

Objectives of this chapter center on development of a model based on films and microcavities that quantitatively accounts for both water flow and storage in the fracture-facial region. This model must relate to pores in matrix material that may or may not participate in water transport and with which it is not necessarily in equilibrium. We have tested this model with available data from lab experiments and field observations to evaluate whether it can provide a coherent, self-consistent quantification of hydrologically important phenomena associated with unsaturated-zone preferential flow.

12.2. HYDRODYNAMICS OF A FRACTURE-FACIAL DOMAIN

We consider three components that make up total water content. The matrix, or M component, comprises the internal matrix pores. Microcavities on internal fracture faces make up a second component, labeled C. This could include the possibility of dead-end fractures within the matrix that are small enough to fill by capillarity under realistic high (but negative) matric potential, and that open to a fracture face. Free-surface films on internal fracture faces make up the third component, labeled F. The C and F regimes comprise the fracture-facial domain. Figure 12.1 illustrates the spatial relationships of these domains and their dynamics during and after an incidence of preferential flow from a source higher up in the profile.

In the matrix domain, capillary relations govern the moisture state as in traditional unsaturated flow theory, with matric potential as the controlling influence. The M-domain water content may be considered as the diffuse-domain water content θ_D of the source-responsive flux model [*Nimmo*, 2010]. Similarly, the F-domain water content may be considered the source-responsive preferential flow domain of this model. The C domain resembles the M domain in being sensitive to capillarity but differs in the directness of its connection to the F domain.

12.2.1. The C Domain: Roughness Storage in Microcavities

The C domain is a regime of adsorptive and surface-tension influences that resembles traditional diffuse formulations of unsaturated flow. It is typically active on a seasonal timescale. Its wetness is based on water retention in the total volume of microcavities, i.e., crevices, indentations, and other roughness features in faces of fractures, macropores, and other large void spaces of a porous

medium. Such features have been hypothesized by many [e.g. *Buckingham*, 1907; *Dillard et al.*, 2001] to retain a particular amount of water at given energy state. For a particular regular geometry of angular pores, *Tuller et al.* [1999, Appendix B] developed an exact model based on capillarity.

Various terms, such as "irregularities" [*Price et al.*, 2000], have been used for these individual water-containing elements. *Or and Tuller* [2000] discussed "partially filled corner flow," and also used the terms "surface roughness element" and "pit." Here we use the term *microcavities* to emphasize that it is the concave portions of roughness irregularities in which the water is held by capillary force. The concept of unsaturated roughness storage is the collective effect of all such microcavities in an unsaturated medium. *Kibbey* [2013] computed capacity of such a domain as related to surface roughness, for particular grain-surface topographies observed in electron stereomicrographs.

Sensitivity to capillary control causes the function and behavior of the C domain to resemble those of the M domain. The degree of fullness is determined by capillary relations and the matric potential at the fracture face. For several reasons, it can be useful to regard the C domain as distinct from M. One is the possibility of disequilibrium between the fracture face and internal matrix. Another is to accommodate substantial differences in the timescale of interactions with the F domain, which may be very slow for M and essentially instantaneous for C. In mathematical formulation of the C domain, areal concepts are useful in addition to volumetric concepts, whereas the M domain has a more strictly volumetric character.

Retention properties, such as the water content vs. matric pressure relation, of the collective microcavities of a natural surface in general must be determined empirically because the microcavities, like pores in a soil, have individually irregular geometries. Each microcavity has its own such relation, and for macroscopic purposes they have to be effectively averaged within a representative elementary volume.

12.2.2. The F Domain: Flow in Free-Surface Films

The F domain is a free-surface film-flow regime on fracture faces, typically active on an individual-storm timescale. Effective flow channels may sometimes occur in the form of sheets, ribbons, rivulets, etc. The F domain can be quantified using the source-responsive model of preferential flow [*Nimmo*, 2007; *Nimmo*, 2010], extended and supplemented as appropriate.

The physical description of this domain uses free-surface film concepts and quantifications of *Dragila* [1999] and *Dragila and Wheatcraft* [2001]. The mathematical formulation is based on laminar flow of water driven by gravity. Here we take it as vertical; it could be extended to other dimensions. In this chapter we are not explicitly including the possibility of waves, instabilities, or turbulence, though these can have major importance and could be incorporated in further development.

The film may also be considered equivalent to a thick film in the sense used by *Tokunaga and Wan* [2001]. Phenomenologically, the film is thick enough that the net effect of interaction between the solid surface and molecules of the liquid is negligible relative to the net effect of interaction between the liquid molecules themselves. This distinguishes it from adsorbed thin films, dominated by adhesive force between solid and liquid. Other investigators, for example *Tuller and Or* [2001], have made a similar distinction between thin and thick films.

Quantitatively, the upper limit of film thickness is estimated to be 10 to 70 microns [*Tokunaga and Wan*, 1997; *Tokunaga et al.*, 2000]. The thickness is not determined by static relationships but by the dynamic interaction of flow rate, driving force, flow geometry (e.g. slope angle), surface roughness, and properties of the liquid. For steady-state conditions with a given medium and liquid, thickness of these films depends solely on the flux of water flowing in them [*Dragila and Wheatcraft*, 2001], the same principle by which a river's volumetric flow rate determines its depth. This dependence on the inflow of water identifies the flow in such films as a source-responsive concept [*Nimmo*, 2010]. Flux/thickness compensating mechanisms as discussed by *Nimmo* [2007] may keep the thickness within a narrow range. *Su et al.* [2003] provide a well-documented example with measured flow characteristics.

The porosity of the F-domain, ϕ_F, would equal a maximum possible effective film thickness multiplied by the fracture facial area density. This density, symbolized M, is the total area of activatable fracture internal surface area per bulk volume of rock. This porosity would typically be a small fraction of the total fracture porosity since the fracture internal space occupied by air is not part of the F-domain. The water content θ_F would essentially equal ϕ_F multiplied by the fracture active area fraction, f. *Nimmo* [2010] defined f as a number between 0 and 1 that represents the fraction of area potentially available for film flow that is actually occupied by flowing films at the time of observation.

Based on laminar flow theory the thickness of the flowing films can be calculated from

$$L = \sqrt{\frac{3\nu < v_z >}{g \cos \beta}} \tag{12.1}$$

where $< v_z >$ is the average flow rate of water in the film (dimensions LT^{-1}), β is the inclination angle of the fractures from vertical, υ is the kinematic viscosity of the flowing fluid, and g is the acceleration of earth gravity

[*Bird et al.*, 2002, p. 46]. In a porous medium, $<v_z>$ is not normally a quantity that is known or predicted. A formula in terms of q_F, the F-domain flux density at a given depth (i.e., preferential flow) would be more useful. Considering the fracture geometry implied by the macropore facial area density M, this flux density relates to film velocity as

$$q_F = ML_F < v_z > \tag{12.2}$$

so the film thickness can be expressed as

$$L_F = \left[\frac{3\nu \mathrm{q_F}}{M \mathrm{g} \cos\beta} \right]^{1/3} \tag{12.3}$$

For vertical flow of water at the surface of the earth we can use

$$L_F = B \left[\frac{\mathrm{q_F}}{M} \right]^{1/3} \tag{12.4}$$

where B (dimensions $L^{1/3}T^{1/3}$) combines the known constants into one and has a value, in SI units, equal to 6.74×10^{-3} $m^{1/3}s^{1/3}$.

12.2.3. Fracture-Face Model Based on Films and Microcavities

Actual matric potential varies continuously through space and across domain interfaces. The C and F domains, being in direct fluid contact, can be considered to have equal matric potential. The same value would also correspond to the matric potential of the edge of the matrix or fracture face, a boundary condition for the matrix. In various applications, matric potential, like other state variables, for simplicity is often taken to be uniform within matrix material. For example, it is laterally uniform for one-dimensional downward flow. In this case it would be assumed to have a single value, ψ_M. After cessation of input from above causes water to disappear from the F domain, ψ_C would approach equilibrium with the local value of ψ_M at a rate determined by properties and conditions within the bulk matrix and at the fracture face.

Key properties of this domain include the surface roughness and the fracture-facial area per unit volume M (dimensions L^{-1}) [*Nimmo*, 2010]. As mentioned above, storage and flow characteristics notably do not depend on the aperture of fractures.

Total bulk volumetric water content θ, as measurable by a volume-averaging device such as a neutron moisture probe, in principle would be

$$\theta = \theta_M + \theta_C + \theta_F . \tag{12.5}$$

This total water content would fluctuate as the input flux and the matric potential vary. Presently-available volume-average methods for measuring water content in the field are not sufficiently accurate to distinguish differences much less than 1%, so for some purposes the θ_C and θ_F contributions may be locally negligible [*Nimmo and Mitchell*, 2013]. At large scales, however, the total volume of water indicated by small θ_C and θ_F can be significant, which is central to some applications discussed below.

A useful artificial concept is the volume of water per unit facial area of fractures, L_C (dimension L). It can be interpreted as the effective average thickness of equivalent uniform film storage. Because C-domain water has a microscopically irregular distribution on a rough surface, L_C does not represent a film thickness in the way that its counterpart L_F does.

12.3. APPLICATION AND RESULTS

12.3.1. Unsaturated Zone Hydrology of the English Chalk

The materials and setting of the English Chalk formation permit simplifications that clarify the roles played by the M, C, and F domains. In the southeast of England, the Chalk is a fine-grained (generally less than 10 μm), pure (more than 98% CaCO3), soft, white fractured limestone with some marls and flints. The unsaturated zone thickness can be 100 m or more. The region has a humid temperate climate with precipitation throughout the year. With high evapotranspiration in summer, recharging fluxes are greater in winter.

The matrix material typically has porosity of 25% to 40% [*Lewis et al.*, 1993]. Its saturated hydraulic conductivity is typically 2 to 6 mm/d [*Price et al.*, 1976; *Lee et al.*, 2006]. Pore throats of chalk matrix are small, typically less than 1 μm, giving it an extreme air-entry value, about –250 kPa or less [*Price et al.*, 2000]. This air-entry value, in combination with the wet climate and the effect of interspersed impeding layers, allows the matrix water content to be effectively saturated in many circumstances. This high saturation of the fine-pored matrix facilitates studies of fracture flow by minimizing the influence of matrix pore-water dynamics.

The fracture porosity is typically about 1% to 2% [*Lewis et al.*, 1993]. *Price et al.* [2000] present evidence from techniques of resin impregnation coupled with electron microscopy, and acoustic measurements under varying levels of stress applied to samples, that the fracture apertures are in general greater than 30 μm. This criterion chiefly applies to fractures that actively participate in preferential flow; there are known to be smaller fracturelike openings that are dead-ended or otherwise too poorly connected for significant flow.

12.3.2. Recharge During Unsaturated Conditions

There is considerable evidence that recharge by preferential flow mechanisms can occur through unsaturated chalk, observed for example from water table fluctuations. This includes the results of *Lee et al.* [2006], which *Malek-Mohammadi and Nimmo* [in review] treated with a source-responsive flux model. During a five-week interval during the winter of 2006–2007 at East Ilsley, *Gallagher et al.* [2012, their Figure 9] observed a marked increase in water table rise while matric potentials remained negative in the unsaturated zone. *Lewis et al.* [1993], in Chalk catchment water balance studies, combined and compared streamflow, recharge, water-table fluctuation, and unsaturated-zone flow dynamics on a seasonal basis. They found streamflow to be greater, by as much as a factor of 10, than could be accounted for by the recession of the water table. The discrepancy could not be explained by the drainage from the matrix, which stays effectively saturated. They estimated that drainage during one dry season, additional water equivalent to around 0.25% to 0.30% of the volume of rock in the unsaturated zone, would be sufficient to compensate for the unexpectedly small apparent contribution from the aquifer.

Price et al. [2000] showed that irregularities on fracture surfaces provide a storage capacity in the chalk unsaturated zone sufficient to account for volumes of water of the order of those required to explain the findings of *Lewis et al.* [1993]. Their laboratory experiments included water retention measurements, discussed below, that *Low et al.* [1997] presented in detail. Results showed no matrix pores that drain and fill under natural conditions. They also found that large pores (up to about 100 μm diameter, mostly in the form of foram tests) do commonly exist, but their interconnections are very small and so do not allow drainage from the matrix. On fracture faces, however, these large pores constitute microcavities of the C domain.

12.3.3. Conceptual Model

12.3.3.1. Damping depth and continuous flux

When water moves downward by diffusive unsaturated-flow processes combined with gravity, temporal fluctuations of infiltration at the land surface can be damped to the extent that the downward flux, and hence the unsaturated hydraulic conductivity and water content, are constant [*Gardner*, 1964; *Nimmo et al.*, 1994]. In the English Chalk, multiseason tensiometer measurements show the matric potential becoming constant at depths of 2 to 7 m [*Wellings and Bell*, 1980; *Wellings*, 1984]. Given water table depths typically of tens of meters, this allows for a substantial thickness of unsaturated zone to be immune from variation of diffuse fluxes in the matrix. The extreme air-entry value of the Chalk matrix means that the matrix water content would not only be constant but would be effectively saturated, which would likely further enhance its temporal stability. The low matrix hydraulic conductivity of chalk also promotes stability and shallowness of damping depth. This picture implies that preferential flow occurs within fractures and interacts minimally with matrix material, so the English Chalk affords opportunity for investigation of unsaturated preferential flow in isolation from other flow modes.

The distribution of matric potential is likely to follow patterns as observed by *Rutter et al.* [2012]. In winter when the recharging flux is large, matric potential commonly is near zero, especially in the zones just above impeding layers. In particular, matric potential becomes high above marls and may have lower values (but still within AEV) above that region up to the next marl. In drier seasons, it is likely to go to tens of kPa negative. Thus, the matric potential typically undulates with depth, but the gradient on average, from the damping depth to the water table, is essentially zero. Therefore, gravity-driven flow through the effectively saturated matrix creates an ongoing steady component of recharging flux, whose value numerically equals the saturated hydraulic conductivity of the matrix material, typically a few millimeters per year.

12.3.3.2. Flow dynamics on storm and seasonal timescales

During periods when infiltration substantially exceeds ET, downward flux at the damping depth may exceed the steady component of recharge flux through the matrix. This establishes the necessary condition to drive preferential flow by source-responsive processes through the unsaturated zone below this level. This flux in excess of the matrix flux then constitutes the flow rate that determines the thickness L_F of free-surface films in the F domain (Equations 12.1 and 12.2). Evidence from borehole video shows clear evidence of substantial film flow on borehole walls [*Gallagher et al.*, 2012]. Assuming natural fracture faces behave like the observed walls, it is likely that similar films occur in fractures. Tensiometers in boreholes for continuous monitoring have shown the matric potential increases above -5 kPa during the winter wet season, with the matrix, which is saturated at these potentials, unable to absorb water that flows down the fractures to the water table.

12.3.4. Seasonal Storage in Microcavities

Water retention properties of the C domain can be estimated using water retention data of *Low et al.* [1997]. They used a pressure-plate apparatus to measure the water content of chalk samples at a series of matric

potentials. The samples came from two different quarries and varied in size and surface roughness. Some samples had naturally rough faces, being either natural fracture faces or exposed by fracturing. Others had surfaces cut smooth in sample preparation. The interior of the block is the matrix material, while the block's total outer surface area effectively acts as fracture facial area. At the start, the samples were totally saturated with water, and remaining F-domain water was allowed to drain away under gravity. The pressure-plate measurements involved static equilibrium without film flow, so water retained at the block surfaces would be in the C but not the F domain. Over the range of pressures applied, down to -150 kPa or further, the matrix remained above the air-entry value and stayed saturated, so that changes result from the dynamics of the C domain. The measured changes in sample weight during the decreasing sequence of matric potentials then indicate changes in C-domain water content.

Both *Low et al.* [1997] and *Price et al.* [2000] presented results in terms of degree of saturation of the sample volume. We similarly computed θ_C for each sample at each ψ in the measured range, with results shown in Figure 12.2 (top). Equivalent to the results published by *Low et al.* [1997] and *Price et al.* [2000], these are plotted on a relative scale that indicates the change in C-domain water from its amount at −160 kPa.

It is instructive to relate this water content change to what it implies concerning the total water storage in the unsaturated-zone volume of the catchment, as done by *Price et al.* [2000]. In doing so it must be kept in mind that additional factors may become significant when moving from the small and perhaps idealized lab samples to the entire catchment. The relevant calculation is of the amount of water released from a large volume of fractured chalk during a seasonal decline of matric potential. Considering seasonal variations of matric potential in the Chalk between −1 kPa during winter to −50 kPa or less during summer, the average effective storage capacity of the C domain is about 0.4%. This value is consistent with estimates of 0.25% to 0.35% that *Lewis et al.* [1993] had calculated would be needed to permit enough seasonal storage in the deep unsaturated zone to explain the observation of high dry-season streamflow with minimal water table recession.

With additional assumptions we can calculate the water retention on an areal basis, i.e., the volume of water per unit area of sample face, equal to L_C, as a function of matric potential. Like the original investigators, we assume no major internal fractures, though there may be dead-end microfractures that contribute to storage but not rapid flow. We estimate the outer surface area of samples from the reported sample volumes. Geometrically, for a given shape, regardless of size, the ratio of the square root of the area to the cube root of the volume is the same. Thus, the outer area of a block is

$$A = GV^{2/3} \tag{12.6}$$

where V is the bulk volume of the block and G is a geometric factor, the surface area to volume ratio, that has a characteristic constant value for each type of shape. For spheres and cubes, which have known surface area and volume formulas, it is easy to determine that G equals 4.84 and 6, respectively. Its value is greater for more elongated or more irregular shapes. For the somewhat elongated, somewhat irregular shapes of the samples of *Low et al.* [1997], we assume G equals 8. This gives the values in Table 12.1. The facial area per unit volume M is the ratio of the estimated area from Equation 12.6 to the bulk volume in this table. Using the computed M values from Table 12.1 and

$$\theta_C(\psi) = ML_C(\psi) \tag{12.7}$$

we also computed effective L_C for each sample at each ψ in the range (Figure 12.2, bottom). Again considering the change in retained water over a −1 kPa to −50 kPa range, the change in L_C would be about 40 μm for sample SH5/5 and about 20 μ for others. These numbers are approximate, in particular because of uncertainty of L_C at the wet end of the range.

It is interesting to compare L_C with results of *Weisbrod et al.* [2000], who measured root-mean-square roughness about 100 to 200 μm for uncoated chalk surfaces, and *Price et al.* [2000], whose photomicrographs suggest that foram tests cause a similar or somewhat lesser degree of roughness. Note that these values, representing indentations from the fracture face, can be larger than the fracture's aperture. Our L_C estimates of 20–40 μm are consistent with such roughness, given that L_C represents an average equivalent film thickness, as if water from microcavities were evenly spread over the entire surface.

Interpretation of the retention data on the areal basis here differs from some of the volume-based interpretations of *Price et al.* [2000], though it also supports the hypothesis of significant roughness storage. The L_C interpretation allows comparison of D domain water per unit area of fracture face, thus characterizing the material of the different samples. Three samples show very similar C-domain characteristics and the fourth indicates significantly greater retention over the range. Systematic differences on the basis of natural vs. smooth-cut surfaces and small vs. large samples are not apparent. Instead there is a distinction between the three samples from one quarry (PH), and the single one, with greater retention, from the other (SH). Though four samples cannot establish much confidence, this suggests a possible innate material difference in samples from the different chalk formations.

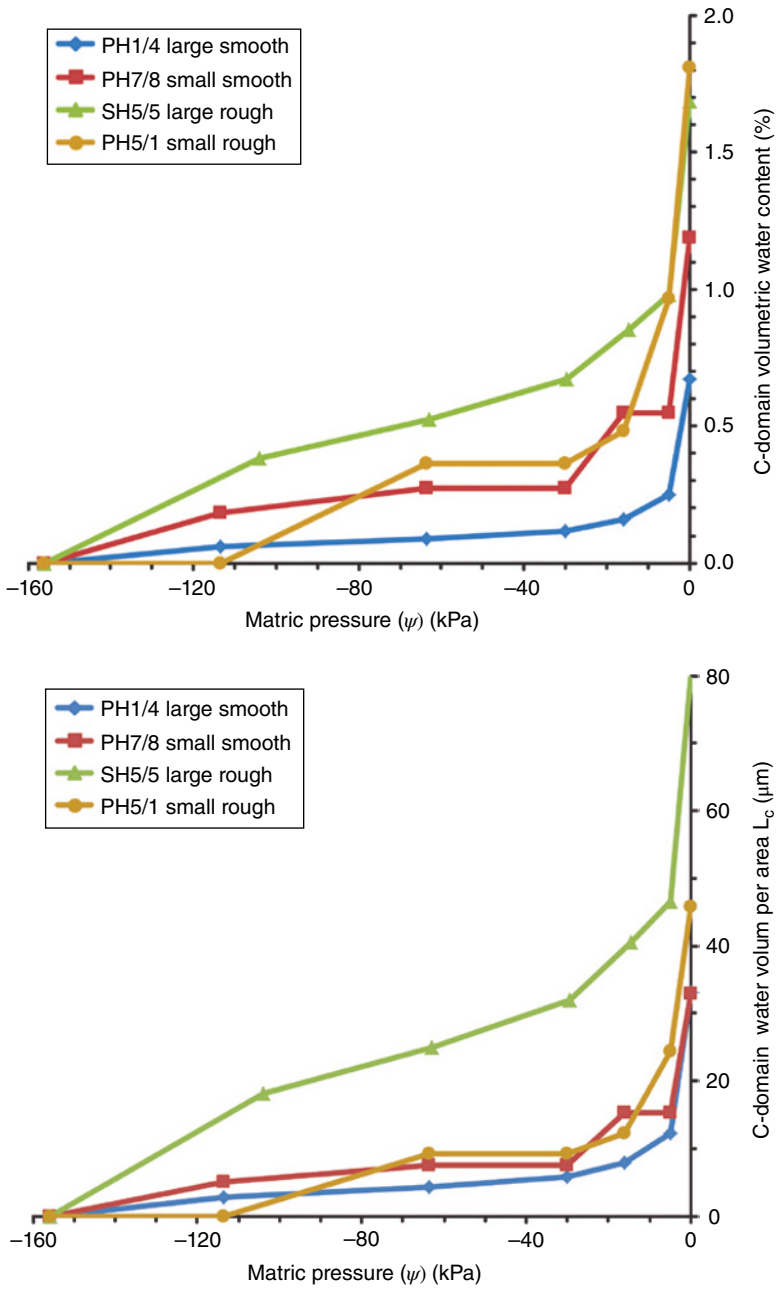

Figure 12.2 Microcavity (C-domain) water retention for four samples measured by *Low et al.* [1997]. Top: Volumetric basis, indicating the volume of C water per bulk volume of material. Bottom: Areal basis, indicating the volume of C water per unit facial area of fracture faces.

Table 12.1 Volumes and areas of four samples used for water retention measurements by *Low et al.* [1997]. The designations "PH1/4" etc. are the published sample labels. The samples are from two different quarries, PH and SH.

Sample	Bulk Volume (cm^3)	Estimated Area (cm^2)	M (m^{-1})
PH1/4 large smooth	68.65	139	203
PH7/8 small smooth	10.93	39	360
SH5/5 large rough	55.18	116	210
PH5/1 small rough	8.29	33	395

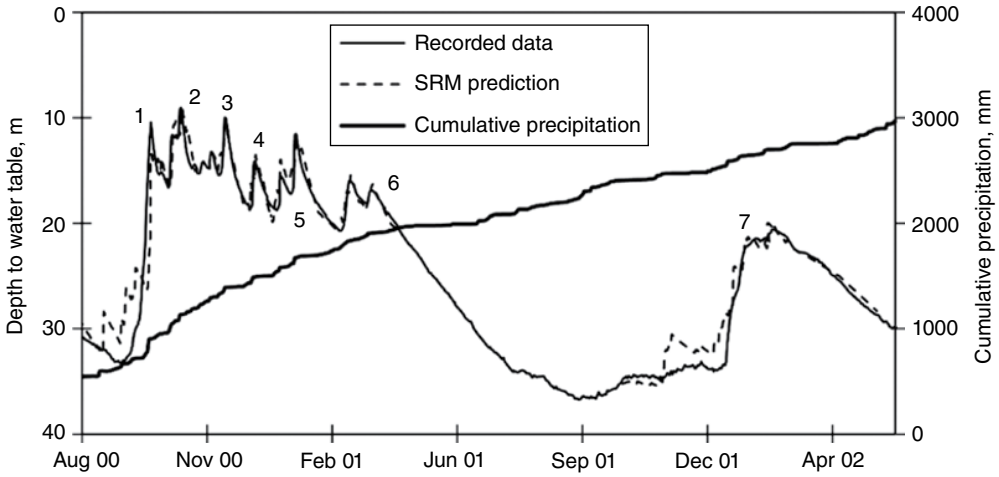

Figure 12.3 Measured and predicted water table and precipitation over a 22-month period at the Houndean site [*Lee et al.,* 2006]. Predictions were made by *Malek-Mohammadi and Nimmo* [in review] using the source-responsive flux model.

12.3.5. Film Flow

Malek-Mohammadi and Nimmo [in review] successfully applied the source-responsive flux model [*Nimmo*, 2010] to predict the fast water-table response at two sites located in the Upper and Middle Chalk, Broadhalfpenny, and Houndean. The simulated water level is compared with the field-recorded data provided by Lee et al. [2006] as shown in Figure 12.3. In most rapid-rise cases, the model predicts the final peak and timing with good accuracy. The model provides a practical tool for estimating a physically reasonable upper bound on possible recharge for the Upper and Middle Chalk. The simulation results also demonstrate that this model can be employed in a continuous mode to quantify the dominant recharge process over annual timescales. Optimized M values from the model calibration were about 300 m^{-1}, in good general agreement with our estimates of M (Table 12.1) from the data of *Low et al.* [1997].

12.4. DISCUSSION

12.4.1. Hydrologic Role of Roughness Storage and Film Flow

The three-domain matrix-microcavity-film model presented here usefully organizes the properties and relationships of the components of an unsaturated fractured-rock system. The collective results of physical property and flux evaluations in the English Chalk unsaturated zone support the model and its applicability.

These results suggest some new directions for thinking about unsaturated flow in fractured rocks. The model conceptually distinguishes (1) a mostly static, capillarity-governed facial storage domain, whose key variable is the matric potential at the fracture face, and (2) a flow domain with water content governed by free-surface film-flow relations, whose key variable is the flux supplied to the domain. Both of these facial domains are distinct from the matrix domain, from which they differ in degree of mobility and timescale of interaction. The model identifies hydraulic properties and relationships for these unsaturated fracture-facial domains and underlines their hydrologic significance.

The domain of microcavities accommodates significant water storage within the unsaturated zone on an intermediate timescale. Water seasonally stored in the unsaturated zone in this way does not fall under the definition of recharge because it is not yet in the aquifer. As hypothesized by *Price et al.* [2000], It may contribute to streamflow in the same manner as aquifer water, though given the possibility of rapid lateral transport, it may have too short a residence time in the saturated zone to register as a measurable rise of water table. This can be responsible for the minimal seasonal decline of streamflow despite the drastically different behavior of water table recession curves during wet and dry seasons as in Figure 12.3.

12.4.2. Reinitiation of Preferential Flow

This model also suggests possible mechanisms for reinitiation of preferential flow after temporary cessation, which would help to explain observations of long-range preferential flow through deep unsaturated zones [*Pruess*, 1999]. It is paradoxical how preferential flow can persist for years, taking tracers to depths of hundreds of meters while the rock remains unsaturated. The source-responsive travel-time model [*Nimmo*, 2007] hypothesizes

pulsed preferential flow when the water source is intermittent, and requires there be a mechanism to reactivate preferential flow. The behavior of marls noted by *Rutter et al.* [2012], in acting to generate seepage and free-surface film flow [*Su et al.*, 2003], suggests analogous processes may occur where there are layers of contrasting impedance. Reactivation after a period of zero flux in the F domain could also be triggered by a pressure pulse that propagates downward with the initial pulse of a new infiltration episode. Such a mechanism could explain how a source-responsive model would apply to deep unsaturated zones as by *Ebel and Nimmo* [2013] and *Mirus and Nimmo* [2013].

12.4.3. Further Possible Extensions

Dynamics of the M, C, and F domains could also enhance understanding of solute transport. C-domain water, which may include contaminants from the land surface brought to depth by flow in the F domain, may remain in the unsaturated zone long enough for diffusion to carry solutes into the matrix. This process might considerably enhance contaminant transport into the matrix at depth compared to what is transported by slow matrix flow or by the fast and temporary F-domain water. Such a mechanism may be responsible for some bypass of matrix material observed by *Smith et al.* [1970], who found 15% of bomb tritium in the matrix pore water to reside at depths lower than was possible by matrix transport alone. The conclusion drawn from this was that while flow in the Chalk is dominated by diffusive flow, 15% of it is transported through fractures. *Foster and Smith-Carington* [1980] suggested that high tritium concentration recorded in pores might occur as a result of diffusion from fractures to matrix domain. The three-domain model presented here can clarify and help resolve such issues.

It is possible to develop models analogous to the capillary-bundle models commonly used for flow describable by Darcy's law or Richards' equation. Similar to the model of *Or and Tuller* [2000], one could postulate a regularized geometry, for example, conical pits varying in diameter or angle, in the way that capillaries are used for soil pores, and from the measured retention curve, calculate a corresponding distribution of diameters or angles that would give that curve.

12.5. CONCLUSIONS

A fracture-facial region of the pore space, with a combination of a flowing phase whose fullness is determined by the availability and flux of preferentially flowing water, and a slower-changing portion whose fullness is determined by the local matric potential, can have explanatory value for the hydrodynamics of a hydrologic system that includes unsaturated fractured rock. Rough fracture surfaces can provide storage that operates on a seasonal timescale, even while its replenishing fluxes operate on an individual-storm timescale. Microcavities on fracture faces and their capability to store the percolating water creates conditions suitable for the water and contaminants to be exchanged between the two domains by diffusion.

While the long-term water table response in the Chalk is controlled by the matrix flow (M domain), source-responsive models can represent the characteristic behavior of rapid water table response during unsaturated conditions (F domain) [*Malek-Mohammadi and Nimmo*, in review]. The model also highlights the importance of C-domain water, stored during winter (near-zero matric potential), which gradually drains to the aquifer during summer (lower matric potentials), reducing the apparent water table recession.

This model should be applicable to other sites and media. These often would have a less uniform or coarser-pored matrix, making it more difficult to identify the specific features involved. However, the same principles can be applied, and the mathematical formulation may be valuable even if the processes are not so easily distinguishable.

Estimated properties and parameter values for the three-domain matrix-microcavity-film model are consistent with quantitative information from diverse sources. The model provides a way to link together in a consistent picture such quantities as recharge estimates, streamflow, water table fluctuation, analysis of surface roughness, imaging by electron microscopy, and surface roughness. The self-consistency of this model, and its consistency with a body of diverse data in the English Chalk, supports the hypothesized active mechanisms of the three domains and establishes the usefulness of this framework.

REFERENCES

Bird, R. B., W. E. Stewart, and E. N. Lightfoot (2002), *Transport Phenomena*, Wiley, New York.

Buckingham, E. (1907), Studies on the movement of soil moisture, *USDA Bureau of Soils Bulletin*, *38*.

Celia, M. A., P. C. Reeves, and L. A. Ferrand (1995), Recent advances in pore scale models for multiphase flow in porous media, *Reviews of Geophysics*, *33*(S2), 1049–1057.

Dillard, L. A., H. I. Essaid, and M. J. Blunt (2001), A functional relation for field-scale nonaqueous phase liquid dissolution developed using a pore network model, *Journal of Contaminant Hydrology*, *48*(1–2), 89–119, doi:10.1016/S0169-7722(00)00171-6.

Dragila, M. I. (1999), A new theory for transport in unsaturated fractures: Free surface film flows, University of Nevada, Reno, Ph.D. Dissertation.

Dragila, M. I., and N. Weisbrod (2003), Parameters affecting maximum fluid transport in large aperture fractures, *Advances in Water Resources*, *26*(12), 1219–1228.

Dragila, M. I., and S. W. Wheatcraft (2001), Free-surface films, in *Conceptual Models of Flow and Transport in the Fractured Vadose Zone*, pp. 217–241, National Academy Press, Washington, DC.

Ebel, B. A., and J. R. Nimmo (2013), An alternative process model of preferential contaminant travel times in the unsaturated zone: Application to Rainier Mesa and Shoshone Mountain, Nevada, *Environmental Modeling and Assessment*, *18*(3), 345–363, doi:10.1007/s10666-012-9349-8.

Foster, S., and A. Smith-Carington (1980), The interpretation of tritium in the Chalk unsaturated zone, *Journal of Hydrology*, *46*(3), 343–364.

Gallagher, A. J., H. K. Rutter, D. K. Buckley, and I. Molyneux (2012), Lithostratigraphic controls on recharge to the Chalk aquifer of Southern England, *Quarterly Journal of Engineering Geology and Hydrogeology*, *45*(2), 161–172, doi:10.1144/1470-9236/09-048.

Gardner, W. R. (1964), Water movement below the root zone, *Transactions, 8th International Congress of Soil Science*, 63–68, International Society of Soil Science, Bucharest, Romania.

Hincapié, I. A., and P. F. Germann (2009), Abstraction from infiltrating water content waves during weak viscous flows, *Vadose Zone Journal*, *8*(4), 891–901.

Kibbey, T. C. G. (2013), The configuration of water on rough natural surfaces: Implications for understanding air-water interfacial area, film thickness, and imaging resolution, *Water Resources Research*, *49*(8), 4765–4774, doi:10.1002/wrcr.20383.

Lee, L. J. E., D. S. L. Lawrence, and M. Price (2006), Analysis of water-level response to rainfall and implications for recharge pathways in the Chalk aquifer, SE England, *Journal of Hydrology*, *330*(3–4), 604–620.

Lewis, M. A., H. K. Jones, D. M. J. Macdonald, M. Price, J. A. Barker, T. R. Shearer, A. J. Wesselink, and D. J. Evans (1993), Groundwater storage in British aquifers—Chalk, *National Rivers Authority R&D Note*, *169*, Bristol, UK.

Low, R. G., C. McCann, and M. Price (1997), Mechanisms of water storage in the unsaturated zone of the Chalk aquifer, *Environment Agency R&D Technical Report*, *W50*, Bristol, UK.

Malek-Mohammadi, S., and J. R. Nimmo (in review), Preferential flow and water storage dynamics in unsaturated fissures: Case study in the English Chalk, *Hydrological Processes*.

Mirus, B. B., and J. R. Nimmo (2013), Balancing practicality and hydrologic realism: A parsimonious approach for simulating rapid groundwater recharge via unsaturated-zone preferential flow, *Water Resources Research*, *49*(3), 1458–1465, 2012WR012130, doi:10.1002/wrcr.20141.

Nimmo, J. R. (2007), Simple Predictions of maximum transport rate in unsaturated soil and rock, *Water Resources Research*, *43*(5), W05426, doi:10.1029/2006wr005372.

Nimmo, J. R. (2010), Theory for source-responsive and free-surface film modeling of unsaturated flow, *Vadose Zone Journal*, *9*(2), 295–306.

Nimmo, J. R. (2012), Preferential flow occurs in unsaturated conditions, *Hydrological Processes*, *26*(5), 786–789.

Nimmo, J. R., and L. Mitchell (2013), Predicting vertically non-sequential wetting patterns with a source-responsive model, *Vadose Zone Journal*, *12*(4), doi:10.2136/vzj2013.03.0054.

Nimmo, J. R., D. A. Stonestrom, and K. C. Akstin (1994), The feasibility of recharge rate determinations using the steady-state centrifuge method, *Soil Science Society of America Journal*, *58*(1), 49–56.

Or, D., and M. Tuller (1999), Liquid retention and interfacial area in variably saturated porous media: Upscaling from single-pore to sample-scale model, *Water Resources Research*, *35*(12), 3591–3605, doi:10.1029/1999wr900262.

Or, D., and M. Tuller (2000), Flow in unsaturated fractured porous media: Hydraulic conductivity of rough surfaces, *Water Resources Research*, *36*, 1165–1177.

Price, M., M. J. Bird, and S. S. D. Foster (1976), Chalk pore-size measurements and their significance, *Water Services*, *80*(968), 596–600.

Price, M., R. G. Low, and C. McCann (2000), Mechanisms of water storage and flow in the unsaturated zone of the Chalk aquifer, *Journal of Hydrology*, *233*(1–4), 54–71.

Pruess, K. (1999), A mechanistic model for water seepage through thick unsaturated zones in fractured rocks of low matrix permeability, *Water Resources Research*, *35*(4), 1039–1051.

Rutter, H. K., J. D. Cooper, D. Pope, and M. Smith (2012), New understanding of deep unsaturated zone controls on recharge in the Chalk: A case study near Patcham, SE England, *Quarterly Journal of Engineering Geology and Hydrogeology*, *45*(4), 487–495, doi:10.1144/qjegh2011-010.

Smith, D. B., P. L. Wearn, H. J. Richards, and P. C. Rowe (1970), Water movement in the unsaturated zone of high and low permeability strata by measuring natural tritium, *Isotope Hydrology*, *IAEA-SM-129*(6), 73–87.

Su, G. W., J. T. Geller, K. Pruess, and F. Wen (1999), Experimental studies of water seepage and intermittent flow in unsaturated, rough-walled fractures, *Water Resources Research*, *35*(4), 1019–1037.

Su, G. W., J. R. Nimmo, and M. I. Dragila (2003), Effect of isolated fractures on accelerated flow in unsaturated porous rock, *Water Resources Research*, *39*(12), 1326, doi:10.1029/2002wr001691.

Tokunaga, T., and J. Wan (1997), Water film flow along fracture surfaces of porous rock, *Water Resources Research*, *33*(6), 1287–1295.

Tokunaga, T. K., and J. Wan (2001), Approximate boundaries between different flow regimes in fractured rocks, *Water Resources Research*, *37*(8), 2103–2111.

Tokunaga, T. K., J. Wan, and S. R. Sutton (2000), Transient film flow on rough fracture surfaces, *Water Resources Research*, *36*(7), 1737–1746.

Tuller, M., and D. Or (2001), Hydraulic conductivity of variably saturated porous media: Film and corner flow in angular pore space, *Water Resources Research*, *37*(5), 1257–1276.

Tuller, M., D. Or, and L. M. Dudley (1999), Adsorption and capillary condensation in porous media: Liquid retention and

interfacial configurations in angular pores, *Water Resources Research*, *35*(7), 1949–1964.

Weisbrod, N., R. Nativ, E. M. Adar, D. Ronen, and A. Ben-Nun (2000), Impact of coating and weathering on the properties of chalk fracture surfaces, *Journal of Geophysical Research: Solid Earth*, *105*(B12), 27853–27864, doi:10.1029/2000jb900295.

Wellings, S. R. (1984), Recharge of the upper chalk aquifer at a site in Hampshire, *England, Journal of Hydrology*, *69*, 259–273.

Wellings, S. R., and J. P. Bell (1980), Movement of water and nitrate in the unsaturated zone of upper chalk near Winchester, Hants., *England, Journal of Hydrology*, *48*, 119–136.

Part IV
Multidisciplinary Research for Different Applications

13

Plutonium Transport in Soil and Plants: An Interdisciplinary Study Motivated by Lysimeter Experiments at the Savannah River Site

Fred Molz[1], Inci Demirkanli[2], Shannon Thompson[3], Dan Kaplan[4], and Brian Powell[1]

ABSTRACT

Understanding reactive transport processes in the vadose zone, with its heterogeneity, nonlinear property relationships, complex boundary conditions, root growth, and associated biochemistry, requires an interdisciplinary approach. Such an approach is illustrated by analysis of 11-year plutonium (Pu) lysimeter experiments at the Savannah River Site, which showed anomalous Pu distributions below the source with significant above-source migration. A conceptual model of the transport process was based on fully transient soil water movement coupled to REDOX reactions between reduced and oxidized Pu species. Initial simulations yielded reasonable below-source transport but little above-source transport. The conceptual model was then modified to include Pu absorption by plant roots and upward movement in the transpiration stream. Resulting simulations in the 51-L lysimeters were then consistent with Pu activity concentrations in the top 20 cm of soil and an observed activity residue on the soil surface. This motivated laboratory experiments on corn that have verified rapid Pu transport in the transpiration stream and the involvement of Pu complexing agents (siderophores) in the transport process. Throughout this study, mathematical models were used to analyze data, a type of computer-aided thinking that when combined with additional experiments can yield new insights. A second lysimeter experiment is underway.

13.1. INTRODUCTION

Plutonium (Pu) is essentially a manmade radionuclide with complex chemical properties, and recent broad overviews of Pu in the natural environment include *Kersting* [2013] and *Geckeis et al*. [2013]. There are 15 isotopes of Pu, some with a half-life of minutes, but the most abundant isotopes (Pu-239, Pu-240 and Pu-241) have half-lives of 14.4, 6,500, and 24,000 years, respectively. So a 24,000-year half-life is a reasonable number to work with. This is a long time by human standards, implying that longer-term experiments are important if one is to develop a reasonable expectation of Pu behavior in the natural environment. (Naturally occurring Pu-244 has a half-life of 80 million years but is found at negligible concentrations in nature [*Lachner et al.*, 2012].)

The biochemical behavior of Pu in soil-plant systems, the main topic of the present chapter, is highly dependent on its oxidation state. In aqueous solutions, Pu can take on oxidation states III, IV, V, or VI, and two or three of these oxidation states are typically present simultaneously at equilibrium [*Choppin*, 2003]. The reduced states III and IV are more stable under acidic conditions, while the oxidized states V and VI are more stable at higher pH levels [*Choppin et al*., 1997; *Silva and Nitsche*, 1995]. In porous media, it is generally observed that the reduced Pu species (Pu(III) and Pu(IV)) are much less mobile, while the oxidized species (Pu(V) and Pu(VI)) are more mobile [*Choppin*, 2003]. The relatively low solubility of Pu(IV) and sorption on sediment surfaces is an important mechanism for limiting the subsurface mobility of Pu, but it is now known that this is only part of the story. Mineral surfaces can mediate the oxidation and reduction of adsorbed

[1] *Environmental Engineering and Earth Sciences, Clemson University, Anderson, South Carolina, USA*

[2] *The Cadmus Group, Inc. Arlington, Virginia, USA*

[3] *US Nuclear Regulatory Commission, Office of Research, Rockville, Maryland, USA*

[4] *Savannah River National Laboratory, Aiken, South Carolina, USA*

Dynamics of Fluids and Transport in Complex Fractured-Porous Systems, Geophysical Monograph 210, First Edition.
Edited by Boris Faybishenko, Sally M. Benson, and John E. Gale.

species. Reduction of Pu(V) to Pu(IV) has been observed on a number of mineral surfaces [*Kenney-Kennicutt and Morse*, 1985; *Sanchez et al*., 1985; *Powell et al*., 2004, 2005, 2006; *Hixon et al*., 2010]. Oxidation of Pu(IV) has been observed on Mn(IV)-bearing minerals such as ranceite, birnessite, and pyrolusite [*Duff et al*., 1999; *Morgenstern and Choppin*, 2002; *Powell et al*., 2006]. However, the oxidation appears to be temporary and reduction to thermochemically stable Pu(IV) sorbed complexes appears to dominate solid phase Pu speciation [*Powell et al.*, 2006]. Especially important to the present study, ligands of biological origin can mobilize Pu, similar to the way that Fe is mobilized and taken up by microbes and plants by secreting chemicals called siderophores [*Neu et a*l., 2002; *Neu et al*., 2003; *Cataldo et al*., 1988]. Collectively, all these biogeochemical phenomena have led to greater than expected Pu subsurface transport at several sites, including Mortandad Canyon at the Los Alamos National Laboratory, the 100K Area at the Hanford Site, the Nevada Test Site, Rocky Flats Environmental Technology Site in Colorado, the Mayak Site in Russia, and the Savannah River Site in South Carolina [*Penrose et al*., 1990; *Marty et al*., 1997; *Dai et al*., 2002, 2005; *Kersting et al*., 1999; *Santschi et al*., 2002; *Xu et al*., 2008; *Novikov et al*., 2006]. It is now clear that a variety of biochemical and geochemical phenomena can greatly influence the sorption and transport of Pu in natural soil systems, but the details of such phenomena are often not understood well. Therefore, further study is needed to understand Pu transport more fully in many natural systems.

With longer-term interests in mind, a series of field experiments were performed at the Savannah River Site (SRS) during the 1980s. A group of lysimeters containing sources of known Pu oxidation states were placed in the shallow subsurface. From 1981 until 1991 all lysimeters were left open to the environment except one, which was capped in 1983 and stored until it was analyzed. During this field period, aqueous leachate samples were collected and analyzed for gross alpha and beta activity; precipitation and climatic variables were recorded also. At the end of the open field period, all lysimeters were covered for an additional five years. Then these lysimeters were cored vertically, through the center, and the cores were stored in a cooler for an additional six years. After this time, various cores were sectioned, and Pu activities measured as a function of depth.

This chapter is devoted to describing the historical, ongoing, and future activities of a research program that was motivated by the SRS lysimeter experiments outlined in the previous paragraph. The original lysimeter project was devoted to studying the (assumed) downward movement of Pu(III), Pu(IV), and Pu(VI) species over a much greater time period than that typical of laboratory studies. However, the results of the field experiments showed unexpected Pu distributions in both the downward and upward directions, so additional research aimed at understanding the cause and dynamics of the observed data was motivated. This recent and ongoing research involved theoretical studies motivated by the original lysimeter data and additional laboratory experiments motivated by the theoretical studies, a good example of the scientific method.

The complete study described in this chapter consisted of four iterations, with each iteration (or objective) motivating the next one. The first objective was to study and simulate the processes that govern the observed downward movement of Pu in the various lysimeters using a steady-state flow model. This was relatively easy to do, because the net water flow was downward during the lysimeter exposure period, and the lysimeter water balances enabled us to calculate an average velocity. However, to match the odd below-source data it was necessary to include surface-mediated redox reactions in the transport portion of the model. This was also done consistently as model complexity increased.

Naturally, a net-downward flow model produced negligible Pu transport above the source, and it was assumed, perhaps naively, that the observed extensive upward transport was due to water moving into the overlying root zone of weed plants (mainly grasses) that were allowed to grow on the lysimeter surfaces. In order to simulate such upward water movement, it was necessary to include fully transient water flow through all climatic periods, which was a laborious task since it required at least a daily water balance including precipitation, transpiration (root water uptake), evaporation from the lysimeter surfaces and lysimeter drainage. After many computer runs and careful consideration of all potential soil-based flow and transport mechanisms, the fully transient model (second iteration) produced the same results as the steady downward flow model: good agreement with the below-source Pu distributions but negligible Pu transport above the sources. So nothing was left to move Pu upward except the plants and their root systems. This led to the third iteration of the Pu flow and transport model to test this hypothesis.

In order to allow root water uptake to move Pu into and through plants, it was necessary to consider root geometry in more detail and to simulate Pu transport (uptake, advection, and dispersion) along the root xylem. It didn't take long to realize that Pu had to be much (orders of magnitude) more mobile in plant tissue than in soil to produce the above-source Pu distributions observed in the lysimeter cores. Previous plant studies also supported this realization. (One can imagine how prejudiced we were after observing a downward movement of a few centimeters through the soil in 11 years!) Finally, with much more mobile Pu species in the root xylem, we were able to produce a Pu distribution above and below the source that agreed well with the lysimeter data, while using consistent climatic data and soil parameter values throughout the study. After "best-fit" parameter values were determined, these values were compared to related laboratory measurements.

Completing the third iteration resulted in a reasonable understanding of what went on in the SRS lysimeters during the extended field study, but it left us wondering about the detailed processes and dynamics of Pu uptake by plant roots and the resulting transport through the root and stem xylem with accumulation in the surrounding tissues. This led to iteration number four, which involved a return to the laboratory to study Pu uptake by corn plants, an easily grown member of the grass family. By this time, it was realized fully that in order to move relatively rapidly in plant tissue, the Pu had to be in a complexed form, perhaps behaving similarly to iron, which is an essential plant nutrient. (Plants have evolved a specialized chemical system for obtaining relatively immobile Fe from soils and moving it into their growing tissues.) After performing a series of experiments using known chelating agents, it became clear that complexed Pu is highly mobile in the cell walls and xylem of corn but more limited in its ability to cross cell membranes. However, the combination of high xylem and limited membrane mobility was consistent with the observed Pu distributions in the lysimeter experiments.

The results outlined in the previous paragraphs has motivated two of us (Kaplan and Powell) to initiate a second round of more extensive lysimeter experiments that are now ongoing at the SRS. A continuing study of Fe versus Pu uptake by plant roots is also ongoing. These new experiments along with selected results from several related studies are outlined at the end of the chapter, and mathematical details of the simulation procedure are presented in the appendix. It is hoped that the overall approach utilized results in a more interdisciplinary description of a research effort than is commonly given in scientific publications.

13.2. LYSIMETER EXPERIMENTS AT THE SRS

As shown in Figure 13.1, lysimeters, used in the field experiments conducted at the SRS during the 1980s, were constructed using 52-liter carboys with the bottoms removed. They were filled with vadose zone sediment recovered from 0.2 to 2 m depth from the Old Burial Grounds at the SRS. During construction, a small disc of filter paper spiked with Pu solutions of selected oxidation states and known amount of activity was placed near each lysimeter center, and the entire lysimeter was filled and buried with the top left open to the natural environment. Lysimeter bottoms were connected by tubing to reservoirs so that any leachate exiting the containers could be collected and analyzed. Weeds, mostly native grasses, were allowed to grow on the lysimeter soil surfaces, and from time to time the weeds were cut and allowed to decay in situ. Further details concerning preparation and execution of the experiments may be found in *Kaplan et al.* [2004, 2006]. Typical soil properties

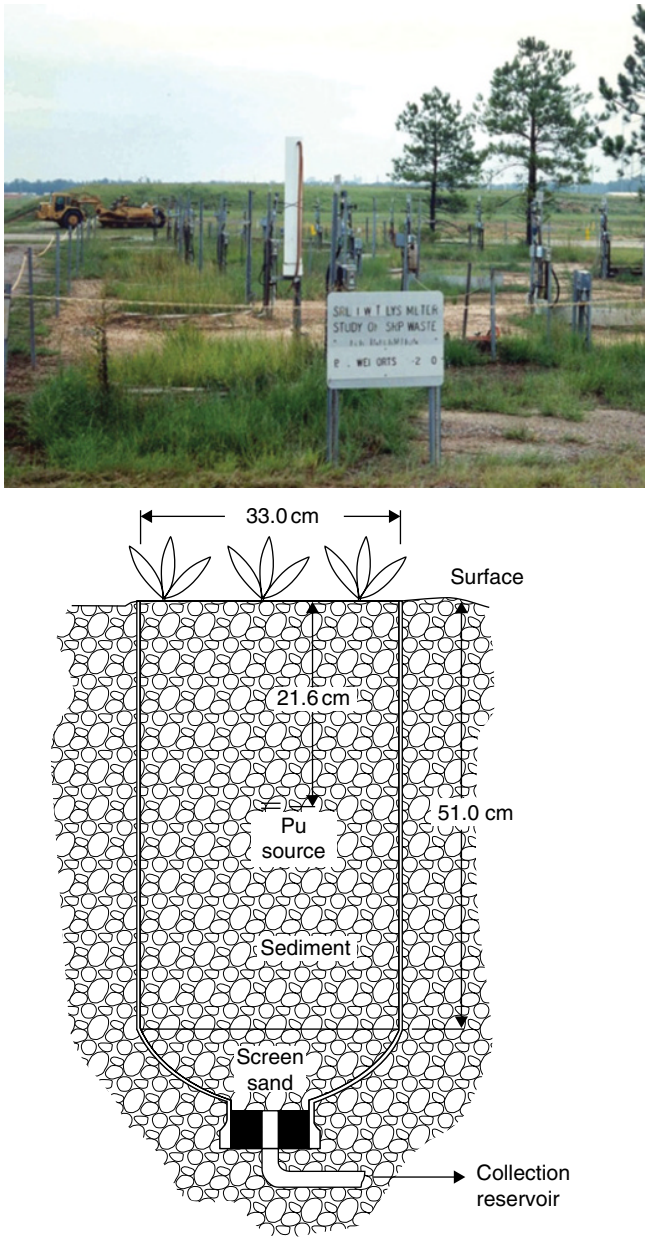

Figure 13.1 A site picture of the SRS lysimeters and a schematic diagram of an individual lysimeter.

were as follows: pH: 6.3; sand/silt/clay (wt. %): 71/10/19; organic matter: <0.01%.

Shown in Table 13.1 is listing the Pu sources used in these field experiments with their oxidation states and initial amount of source activity. The two different durations shown are "field duration", the time the lysimeters were in the field and open to the atmosphere, and "storage duration", the time after the lysimeters were capped until the central cores were analyzed. The relatively short "field duration" associated with the Pu(VI) oxidation state was due to the fact that Pu(VI) moved downward

much faster than Pu(III) or Pu(IV), with the activity front approaching the lysimeter bottom within 2 years.

13.2.1. Results of Experiments

Shown in Figure 13.2 are Pu activities versus depth from the four lysimeters containing Pu sources, with S_o, the measured activity at the source locations. The measurement time associated with the reduced sources (filled symbols) is about 21 or 22 years after emplacement [*Demirkanli et al.*, 2007, 2008, 2009]. Detailed information about transport rate and mechanisms did not result from the lysimeter data directly, because there was only one coring per lysimeter after the long field and storage time period. Developing such information was the major motivation for the mathematical study described herein.

Table 13.1 Data overview of the lysimeter experiments [*Demirkanli et al.*, 2007).

Pu Source in the Experiment	Field Experiment Duration (yr)	Capped (Storage) Duration (yr)	Total Activity in the Sediment (μCi)
$Pu(VI)O_2(NO_3)_2$	~2	0	29.6
$Pu(IV)(NO_3)_4$	~11	~10	152.98
$Pu(IV)(C_2O_4)_2$	~11	~10	89.75
$Pu(III)Cl_3$	~11	~12.4	165.28

The most surprising observation about the collective lysimeter data is the large amount of upward movement of Pu from all the sources. Even given the travel time difference for the Pu(VI), the activity distributions between a depth of about 20 cm and the source locations are quite similar, as they are below the source for the reduced Pu. Above 20 cm the data scatter quite a bit, but nevertheless indicate that some Pu gets all the way to the surface, an upward migration of about 26 cm. In fact, some of the near-surface activity values are higher than others measured in the top 20 cm. Trying to understand and explain this data set initiated the research program described in the remainder of this chapter.

The above-source data correspond to the main portion of the plant root zone, so here we are definitely dealing with the rhizosphere. *McNear* [2013] describes this zone as "roots, soil and everything in between," and for people unfamiliar with the rhizosphere, he presents a nicely outlined overview that helps one appreciate the complexity of this system. Given the plant, microbial, and biochemical processes occurring in this soil region, it is logical to suspect that at least some of them play an important role in the upward Pu movement, and ultimately this was found to be true. With so many interacting phenomena (flow, transport, Pu speciation, coupled chemical reactions, precipitation, transpiration, etc.), an iterative modeling and experimental process was the only hope of untangling the meanings of the data set presented in

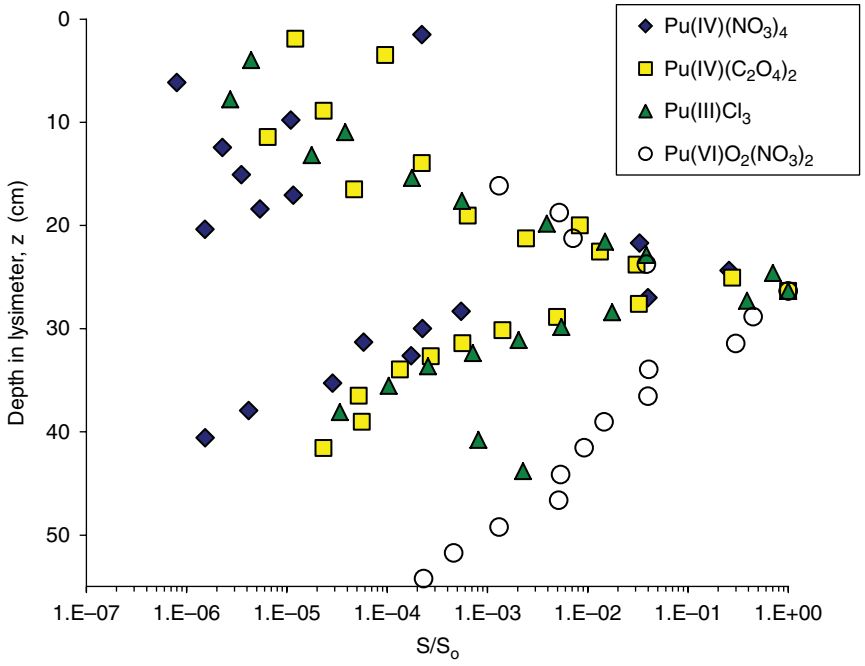

Figure 13.2 Dimensionless Pu activity versus depth from cores through the four lysimeters discussed in Table 13.1. S_o is the activity measured at the elevation of the four sources, and the data have been adjusted so that all sources are at the same vertical position.

Figure 13.2. The performance of this process and the insights obtained are described in the following sections of this chapter.

13.3. MATHEMATICAL MODEL DEVELOPMENT AND APPLICATION

13.3.1. History of Model Development

The overall model development and application is described in three papers [Demirkanli et al., 2007, 2008, 2009]. Three separate models were developed, each of increasing detail and inclusive of the previous model. The first model was based on steady-state, net downward water flow in the soil along with reactive transport of two different groups of Pu based on their oxidation state as oxidized and reduced Pu. Oxidized Pu (Puo) represents Pu(V) and Pu(VI) and reduced Pu (Pur) represents Pu(III) and Pu(IV). So the formulation of this first model employed a combination of steady-state soil hydraulics along with transient reactive transport. The second model generalized the first to include fully transient soil hydraulics, also with transient reactive transport. This model considered uptake of water by plant roots and also the associated upward water movement and Pu transport in the soil (Figure 13.3). The third model allowed for both fully transient hydraulics and transient Pu transport in both the soil and plant xylem (see Figure 13.6). Since the first and second models (Pu transport in the soil only) produced the same results, only the fully transient soil and soil/plant analyses will be discussed further.

Furthermore, the impact of different potential release scenarios from the source was initially evaluated through a number of preliminary simulations performed with different imposed release rates (constant with time, exponentially decreasing with time, etc.) that each produced the measured release amounts. In this way it was shown that release rate did not matter as long as the correct amount of Pu was released within the applicable time period [*Demirkanli et al*., 2007]. Therefore, in the simulations that followed, a constant release rate was utilized. Throughout the analysis we thought of modeling as "computer-aided thinking," not just predicting and fitting data. So an effort was made to identify the important parameters (as shown in Figure 13.3) and to keep parameter values consistent. Each analysis motivated the next more sophisticated analysis, and whenever experiments could be used to further clarify something, such as particular parameter values (e.g., root geometry or plant uptake rates), supporting experiments were performed or reviewed.

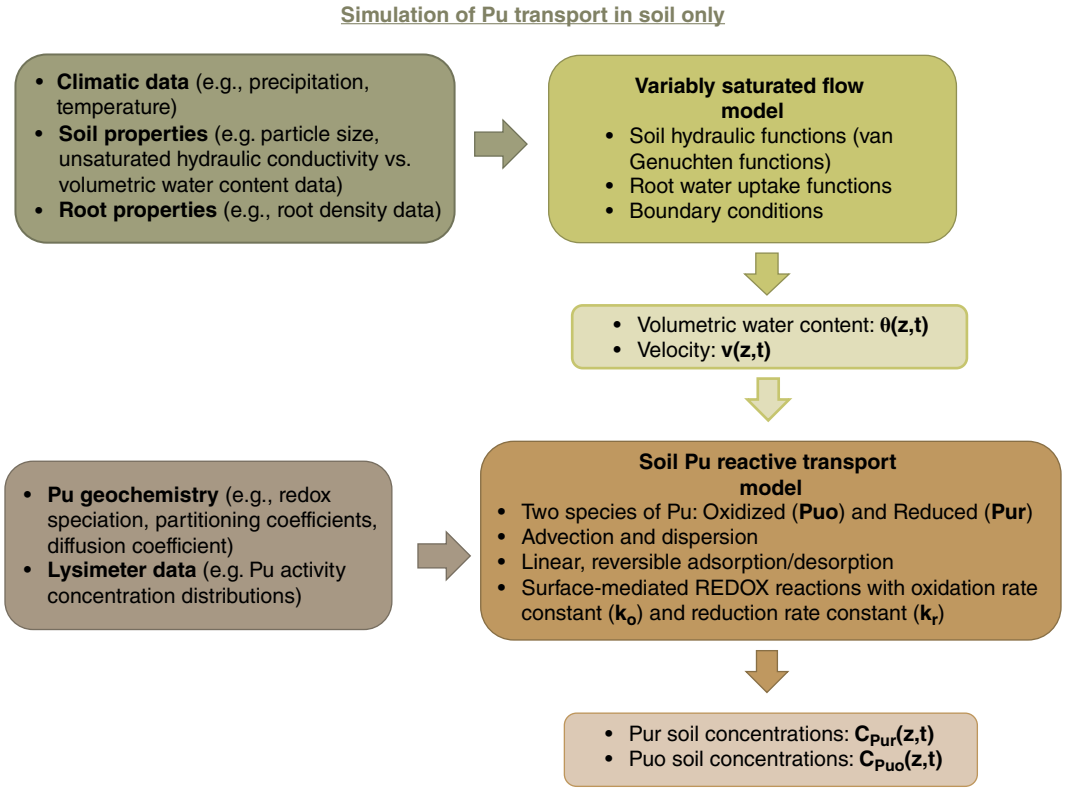

Figure 13.3 Outline of model development for simulating reactive Pu transport in the soil of the SRS lysimeters. Water flow was assumed to be independent of Pu transport, but the transport of oxidized Pu (Puo) and reduced Pu (Pur) were coupled to the water flow and to each other.

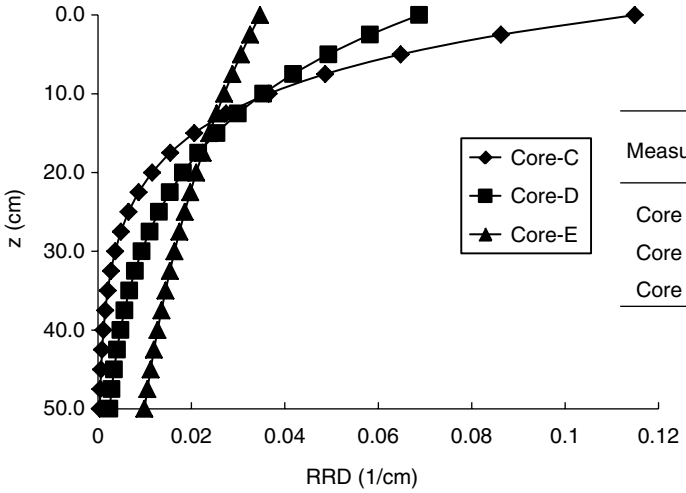

Measured core	Calculated relative root density functions
Core C	$RRD(z) = 0.114902\ e^{-(0.114571 \cdot z)}$
Core D	$RRD(z) = 0.068777\ e^{-(0.066457 \cdot z)}$
Core E	$RRD(z) = 0.034695\ e^{-(0.025 \cdot z)}$

Figure 13.4 Relative root distributions of wild grasses obtained from three soil cores obtained at the SRS. We ended up using the middle core results (squares) in most of our simulations of plant water uptake. The transpiration demand (water uptake rate) was then spread over the root zone in proportion to the selected RRD(z). (See *Demirkanli et al.,* 2008, for details.)

13.3.2. Results for Pu Transport in the Soil Only

Much data gathering went into developing the transient flow and transport model described in Figure 13.3. Unsaturated soil properties had to be developed as well as daily estimates of evapotranspiration and precipitation [*Demirkanli et al*., 2008]. In order to determine the root distributions of grasses common at the SRS, three soil cores were taken from a field adjacent to the SRS lysimeter facility. Root densities, RD(z), in gm root/cc soil were measured on the three cores and normalized so that the area under each root density curve was equal to 1. We call this the relative root density, RRD(z), and the results are shown in Figure 13.4. Exponential functions were then fit to the measurements, with the most typical distribution identified from "Core-D" (Figure 13.4).

The distinct differences between the oxidized and reduced sources had to be accounted for, as well as the "compound shape" of the reduced source distributions shown in Figure 13.2. Essentially, 99+ % of the downward-migrating Pu activity from reduced sources stayed within about 3 cm of the source, but the remaining activity moved an additional 10 cm with a break in the slope of the activity versus depth line. Based on previous studies, we had a potential explanation for the slope change. *Fjeld et al*. (2001, 2003) identified a very small, relatively high-mobility fraction of Pu that was attributed to differences in redox state. Other evidence was developed for the surface-catalyzed oxidation of reduced Pu to oxidized Pu. So the model we developed (see appendix) considered the advection, dispersion, and reversible adsorption of two Pu forms (Pur and Puo), along with the surface transformation of Puo to Pur and vice versa. Oxidation and reduction rate constants (k_o and k_r, respectively) controlled the oxidation state tranformations and were used as fitting parameters along with the partitioning coefficients for oxidized Pu and reduced Pu (K_{d_Puo} and K_{d_Pur}, respectively). Final results are shown in Figure 13.5 for the oxidized and reduced sources, respectively. Notice that these parameters are very similar to those identified in the best fit results for the oxidized source simulations and the reduced source simulations, even though the oxidized Pu exhibited a much higher rate of downward transport. This was one of the main observations that enables us to discount colloid-facilitated transport as an important transport mechanism in the SRS lysimeters. If anything, this mechanism would be expected to transport the highly adsorbing Pu forms more rapidly than the less adsorbing forms.

One of the major outcomes of the the soil-based transport modeling effort is that these mehanisms do not capture the upward transport of Pu documented in the data. To confirm this outcome, additional soil-based mechanisms were considered as a potential explanation and integrated into the modeling effort, including extreme root distribution functions to encourage upward movement of soil water, hysteresis in the soil properties, and concentration-dependent oxidation rates (since oxidized Pu is relatively more mobile). However, the simulated activity distributions resulting from the model with these additional mechanisms were essentially unchanged. Thus, we were led by the theory and data to consider the possibility of Pu absorption by the plant roots and upward movement in the plant xylem. This led to the modeling philosophy described in Figure 13.6; for more detailed information on the derivation of this model, please see the appendix.

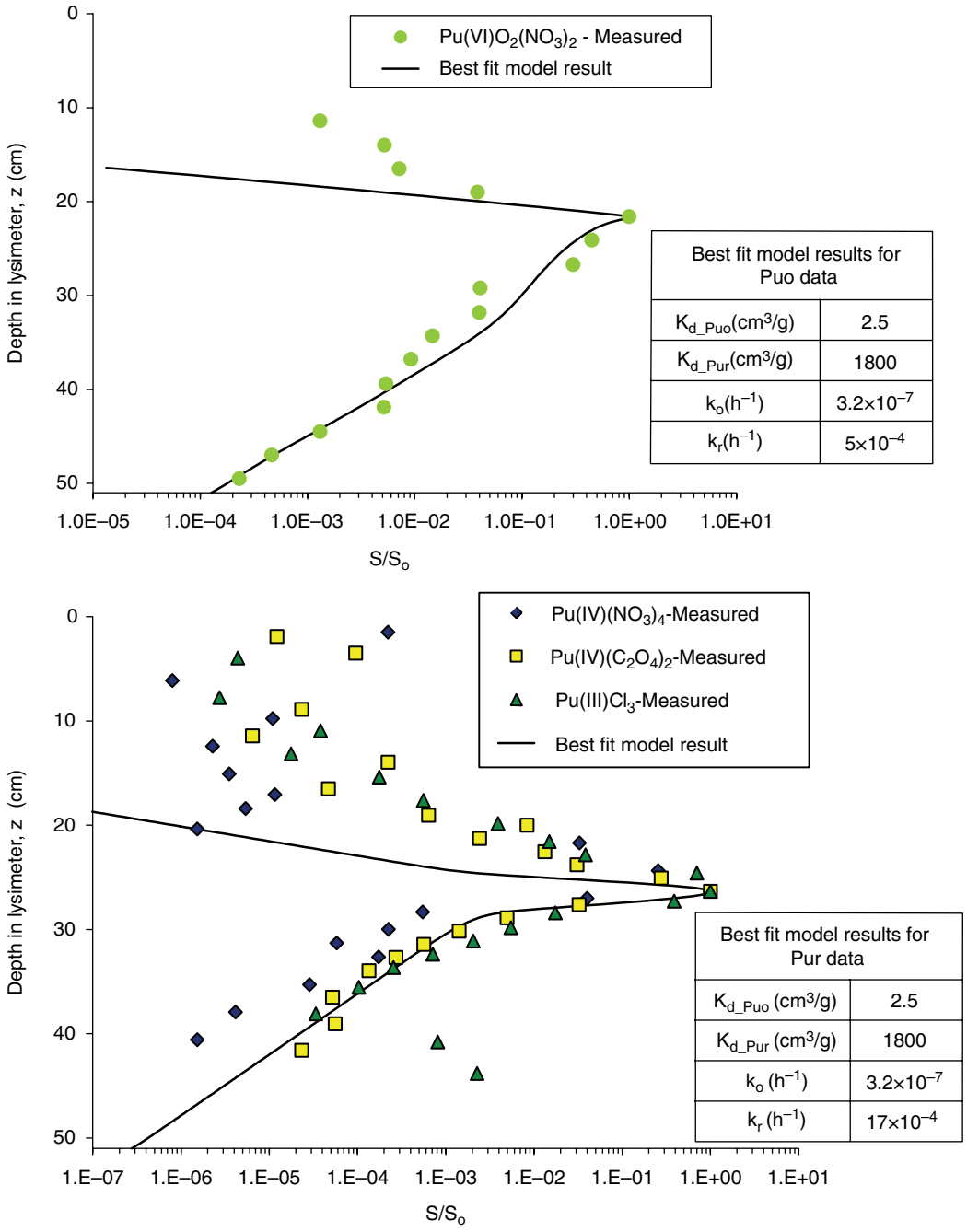

Figure 13.5 Best-fit simulation results of the dimensionless activity distributions in the SRS lysimeters along with the values for the best-fit distribution coefficients for the oxidized and reduced Pu and surface-mediated oxidation and reduction rate coefficients for: (a) the lysimeter containing the oxidized source and (b) the lysimeters containing reduced sources.

13.3.3. Results for Pu Transport in Soil and Roots

Figure 13.6 outlines the integration of the Pu root uptake and transport mechanisms into the previously developed model described in Figure 13.3. Because plant uptake was not considered during the planning phase for the lysimeter experiments, the site-specific plant data necessary to fully parameterize a plant-based Pu transport model were not available. However, existing data on the anatomy of grass roots and rooting density [*Wahl and Ryser*, 2000; *Cook and Kelliher*, 2006] allow a reasonable analysis to be performed. It was known from previous

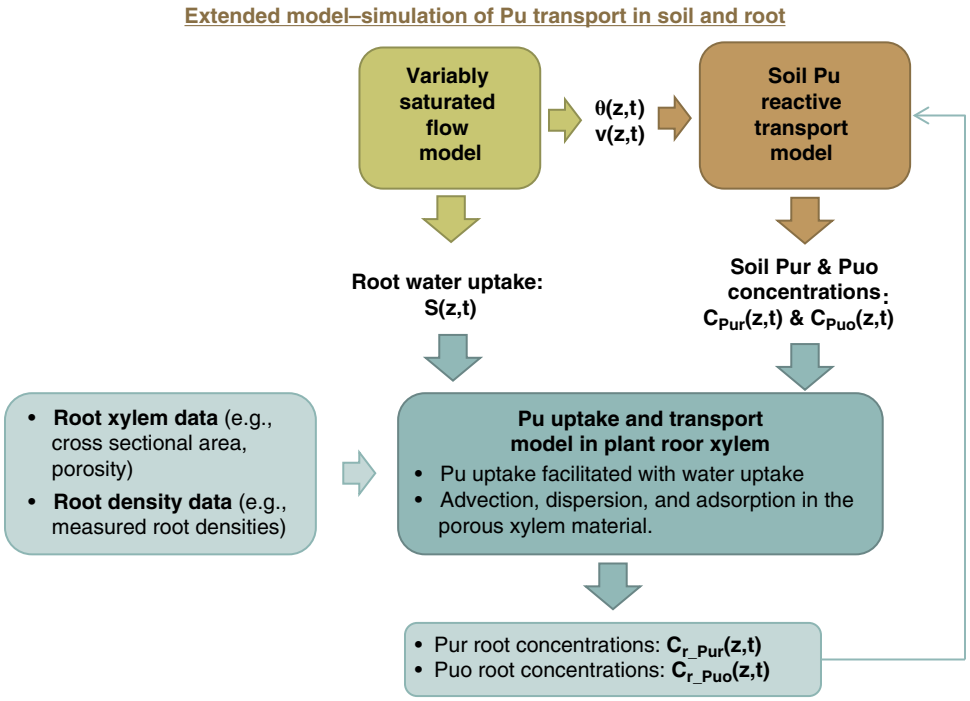

Figure 13.6 A Pu uptake and transport model with the root xylem coupled to the soil system described in Figure 13.3 (*Demirkanli et al.,* 2009; mathematical details shown in appendix).

"whole plant" studies [*Whicker et al*., 1999] that Pu and other actinides could penetrate above-ground plant tissue within one growing season, which implies much faster Pu transport through plants than that observed in the soil below the lysimeter sources. This is consistent with the findings of *Garland et al*. [1981] showing that Pu is not readily immobilized or subject to hydrolysis after uptake by a plant. Later, *Cataldo et al.* [1988] reported that Pu in xylem exudates (fluids extracted at stem cuttings) is present primarily as organic acid complexes, and many metals move rapidly in such complexes (including the essential plant micronutrient Fe).

Figure 13.7 includes three limiting case simulation results with the extended model using the best fitting parameter values from the previous results for the soil system, where simulation 1 indicates no Pu uptake and transport in the root xylem; simulation 2 presents when Pu is relatively mobile in the root xylem and reaches the surface in one season; and simulation 3 occurs when Pu is very immobile in the plant, similar to the soil, with the front not reaching the surface during the field and storage durations.

A large amount of climatic data was necessary to fully parameterize the plant equations as well as xylem area data. However, the new simulations were consistent with the older ones, and a good fluid mass balance was maintained. On average, the net fluid movement in the soil was downward; only in the plant roots was the net fluid movement upward. The maximum xylem water velocity (not the daily average) resulting from the model was 539.7 cm/h during a day in July. Daily xylem velocity averages during the uncapped duration of the experiment are shown in Figure 13.8. A zero value indicates rainfall for that day, since the model assumes no water uptake during rainfall. The observed cycling in xylem velocity was due to the differences in monthly transpiration rates calculated based on the seasonal temperature and rainfall data [*Demirkanli*, 2006; *Demirkanli et al*., 2008]. The maximum and average values produced by the model agree well with experimental values produced previously [*Peuke et al*., 2001].

13.3.4. Confirmation of Pu Source Deposition on the Soil Surface

At this point it was realized that if Pu could penetrate the entire root system, and presumably the above-ground plant parts also, in one growing season, as observed by *Whicker et al*. [1999], then a residue containing source-derived Pu would be expected to accumulate on the surface of the lysimeters. This would be due to annual die-back and intermittent cutting of the local grasses growing in the lysimeters. In fact, in the original processing of the lysimeter cores, such a (low activity) residue was detected, but it was assumed initially to be due to atmospheric deposition from previous site operations [*Kaplan et al*., 2010].

Since the sources were composed of selected weapons-grade Pu, an isotopic signature analysis would determine if the observed surface residue was due to regional fallout or was source-related. Shown in Figure 13.9 are the results of an isotope-ratio test performed on surface sediments scraped from the cores containing the four Pu sources. The lysimeter sample ratios agree well with the weapons-grade Pu control, indicating that the observed Pu on the

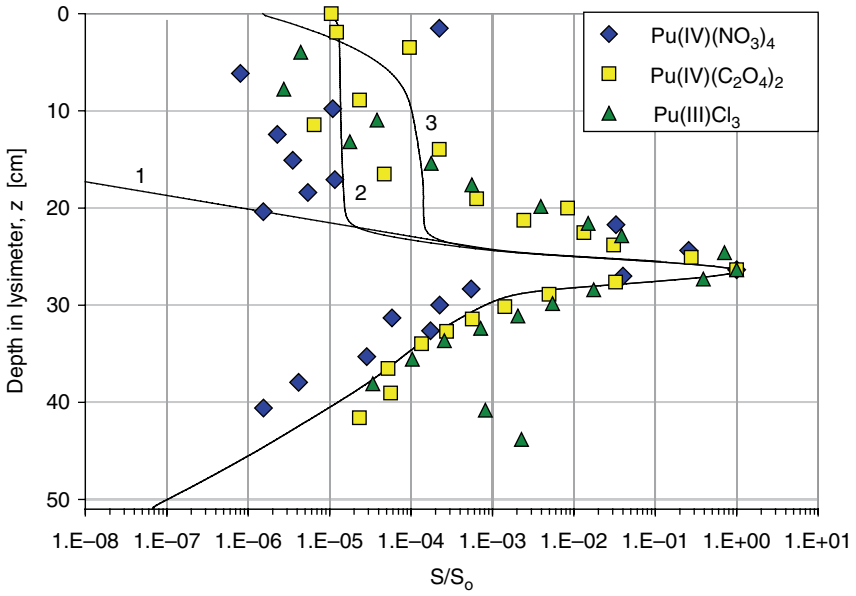

Best fit model results for the soil model	
K_{d_Puo}(cm^3/g)	2.5
K_{d_Pur}(cm^3/g)	1800
k_o(h^{-1})	3.2×10^{-7}
k_r(h^{-1})	17×10^{-4}

	Root model partitioning coefficients	
Simulation #	K_{dr_Puo} (cm^3/g)	K_{dr_Pur} (cm^3/g)
1	-	-
2	1800	1800
3	18000	18000

Figure 13.7 Simulated Pu core activity distributions with and without Pu uptake by roots and upward transport in the root xylem. It was assumed that when the plants died back each winter, the Pu activity that equilibrated throughout the root tissue was simply transferred to the surrounding soil. In this way we could account easily and naturally for the observed activity distribution in the cores, both above and below the sources. The two outliers in one data set (lower green triangles) were ignored.

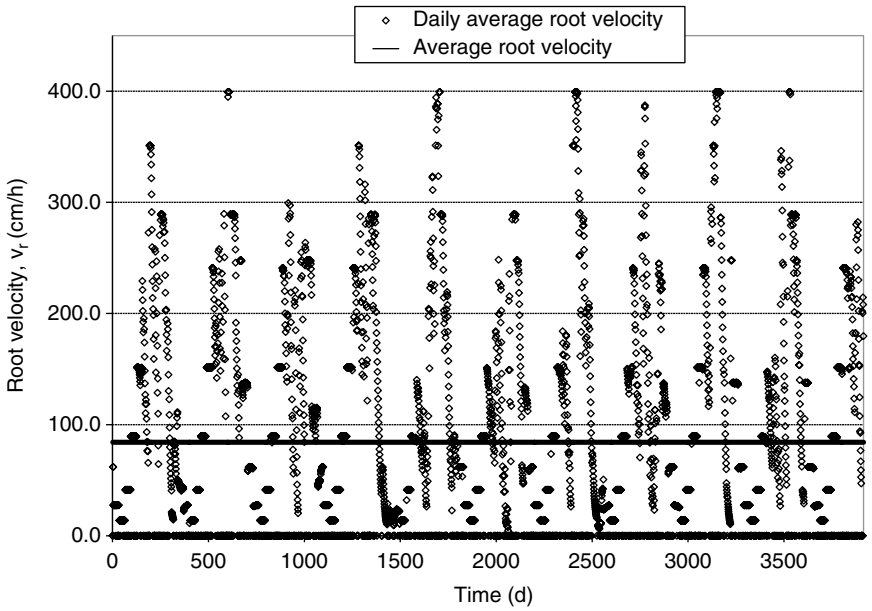

Figure 13.8 Overall average (solid line = 84.4 cm/hr) and daily average pore velocities in the root xylem during the lysimeter field period as simulated by the model.

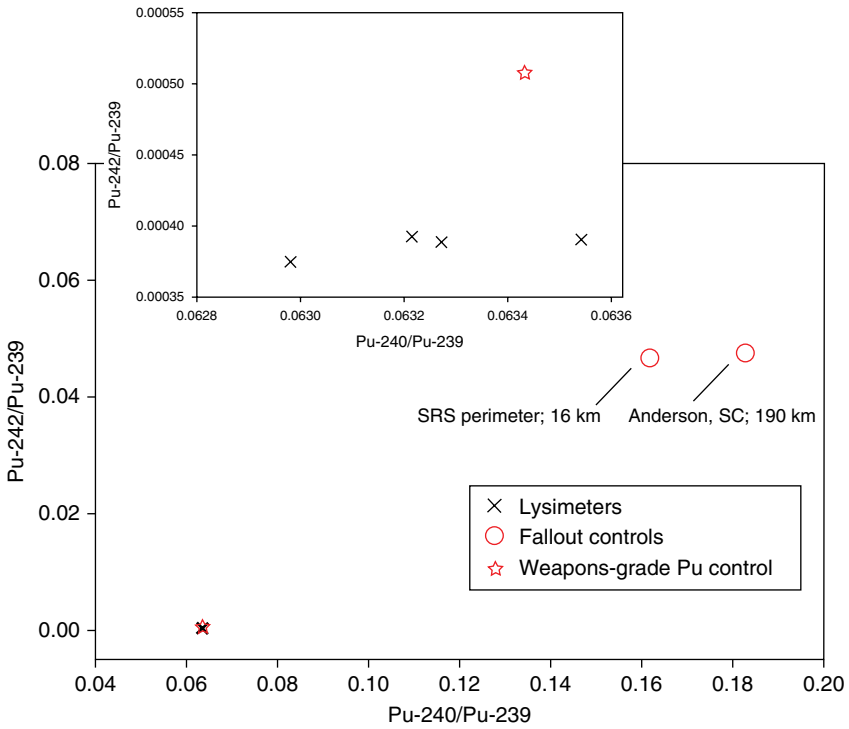

Figure 13.9 Isotope ratio plot for the lysimeter surface samples compared to a weapons-grade control and an atmospheric deposition control collected 16 km and 190 km from the lysimeter site [*Kaplan et al.,* 2010].

sediments' surfaces were derived from the sources used in the experiments and not from atmospheric fallout.

Based on the results of computer simulations compared to data (Figures 13.5 and 13.7, along with the isotopic ratio analysis (Figure 13.9), it was concluded that we had a reasonable understanding of the results of the long-term lysimeter experiments conducted at the SRS [*Demirkanli et al*., 2007, 2008, 2009; *Kaplan et al*., 2010]. Plutonium transport below the source was dominated by the net downward movement of soil water along with adsorption and surface-mediated oxidation and reduction. This continuing redox process along with the Pu source composition (Pur or Puo) was consistent with the very different dynamics of the Pur and Puo sources, along with the odd nature of the Pu distributions below the sources in the three Pur-source lysimeters (99% of the Pu moved only about 3 cm, the remainder moved an additional 10 cm). Because the lysimeter water balances indicated a net downward movement of soil water during the uncapped portion of the experiments, it was not possible to produce significant upward movement of Pu in the soil water. To produce anything like the observed movement of Pu above the sources, it was necessary to include the possibility of Pu uptake by plant roots and the upward movement of Pu in the root xylem. However, since the vast majority of Pu from the Pur sources remained as Pur (>99%), Pu transport in the root xylem had to be much faster than Pu transport in the soil. If it was assumed that Pu in the root xylem was sufficiently mobile to reach the surface and equilibrate with the surrounding root tissue in one growing season, and that this Pu load was transferred to the soil when the roots died back during the winter months, then the model could produce Pu distributions above the sources that were consistent with observations. However, the simulations, which were based on a fixed relative root density function, produced a smooth Pu distribution, while the actual roots, which would die back each year and then regrow in an irregular manner, produced a more erratic distribution with a tendency to increase near the surface.

One data characteristic not produced by our simulations is the more uniform upward migration of Pu within 5 to 10 cm above the sources (Figure 13.7). Data from all lysimeters are in good agreement in this region of the soil, and there is little data scatter, so the phenomenon appears real. Our simulations suggest that this is not a xylem transport phenomenon, because root-derived Pu concentrations at this location are many orders of magnitude below the source concentration. An interesting possibility is that Pu mobility just above the source involves transport mediated by microbial attraction to greater carbon concentrations in the upper root zone, or chemotaxis [*Francis*, 2007]. It might also be due to a multidimensional soil water flow phenomenon that would not be captured in our one-dimensional modeling approach. A type of air-content-dependent Pu oxidation discussed in *Demirkanli et al.* [2008] is also a possibility.

13.4. ARE BEST-FIT PARAMETER VALUES REASONABLE?

Model results indicated that Pu transport in the soil was controlled mainly by Pu oxidation state, adsorption/desorption, and surface-mediated oxidation/reduction, with the best-fit parameter values listed in Figures 13.5 and 13.7. Efforts were made to perform or review additional lab measurements to determine if the main chemical process, surface-mediated redox of Pu(V)/Pu(IV), was a documented phenomenon and if selected values were indeed reasonable. This section describes the performance and results of these experiments.

13.4.1. Measured Pu(V) Reduction Kinetics on Sediment and Pure Mineral Phases

The lysimeter modeling studies discussed above indicate that the downward migration of Pu is controlled by dynamic oxidation and reduction reactions. Rapid surface-mediated reduction of Puo (Pu(V)) is followed by slow oxidation to Puo and subsequent mobilization before reduction occurs again. This dynamic redox cycling must be described using kinetic rather than equilibrium processes. To validate this conceptual model, studies using pure mineral phases representative of the SRS lysimeter soils as well as the actual soils have been undertaken. Direct reduction of Pu(V) on SRS lysimeter soils has been verified by *Kaplan et al*. [2004] and *Hixon et al*. [2010]. Reduction of Pu(V) to Pu(IV) in SRS lysimeter soil suspensions followed pseudo first-order kinetics with a rate constant of 0.112 ± 0.007 hr^{-1} (Figure 13.10).

To gain insights regarding the mechanism of reduction, studies with the iron oxyhydroxide mineral goethite (a primary Fe-bearing phase in SRS lysimeter sediments) were also performed. *Powell et al*. [2005] reported the pH-dependent reduction rate expression:

$$\frac{df_{aq+solid}^{Pu(V)}}{dt} = -k_{rxn} f_{aq+solid}^{Pu(V)} [H^+]^{-0.21\pm0.04} \qquad (13.1)$$

with $k_{rxn} = 3.0 \pm 1.4 \times 10^{-6}$ (mol^{-1}L). At pH 5, reduction of Pu(V) on goethite has a rate of 0.127 hr^{-1}. This compares well with the value of 0.122 ± 0.007 hr^{-1} obtained with whole soils reported by *Kaplan et al*. [2004]. Therefore, it appears that Fe-bearing minerals may be controlling Pu redox speciation. Reduction of Pu(V) by SRS lysimeter soil was measured using an indirect solvent extraction–based technique.

Hixon et al. [2010] directly validated these observations of Pu(V) reduction using X-ray absorption near edge spectroscopy (XANES). As further support of Pu(IV) as the dominant sorbed oxidation state, *Kaplan et al.* [2007] demonstrated that sorbed Pu within the lysimeter sources is dominated by Pu(IV) using XANES and also observed possible preferential association of Pu with Fe phases using micro-XRF (X-ray fluorescence).

While these studies verify that reduction takes place, it remains unclear why reduction of Pu(V) is occurring on a sediment under largely oxidizing vadose zone conditions and little reduction capacity. This observation is further confounded by the observation by many scientists that reduction of Pu(V) occurs on many minerals which contain no obvious electron source such as Fe(II) or Mn(II).

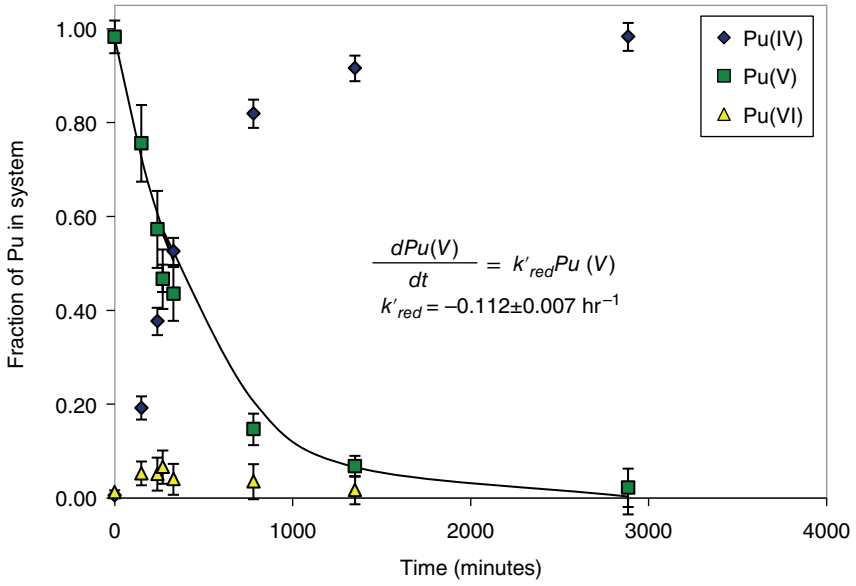

Figure 13.10 Oxidation state of sediment Pu following aqueous Pu(V) addition to lysimeter sediment suspensions (suspended solids = 25,000 mg L^{-1}; pH = 5; background electrolyte = 0.02 M NaCl. Fitted line represents pseudo first order fit to Pu(V) reduction. (Modified from *Kaplan et al.,* 2004.)

Examination of mechanisms that could be responsible for plutonium oxidation state transformations mediated by Fe- and Mn-(oxyhydr) oxides have been the subject of much recent work. It has generally been observed in these studies that the solid phase oxidation state of plutonium is Pu(IV). The thermodynamic favorability of sorbed or precipitated Pu(IV) and the availability of trace Fe(II) as an electron source were proposed to explain the observed Pu(V) reduction on hematite and goethite [*Powell et al.*, 2005]. Despite the oxidizing capacity of MnO_2 oxides, trace levels of Mn(II) were proposed to facilitate reduction of trace Pu(V) to Pu(IV) on pyrolusite (β-MnO_2; *Powell et al.*, 2006). Interestingly, early examination of Pu oxidation state in contact with Mn oxides contained within Yucca Mountain tuff suggested that Pu may be stable as Pu(V) on natural Mn-oxide minerals [*Duff et al.*, 1999]. Examination of these same samples after 2 years of aging indicated that this Pu will eventually reduce to Pu(IV) [*Powell et al.*, 2006]. Similar oxidation at low pH was observed by *Powell et al.* [2006], where Pu(V/VI) was measured in the aqueous phase following addition of Pu(IV) to a pyrolusite suspension. These results indicate that redox active mineral surfaces can control plutonium oxidation states and the redox transformations will be dependent on radionuclide concentrations, solution conditions, and mineral composition. Thus, the conceptual basis for the surface-mediated redox employed in the Pu transport model appears reasonable.

13.4.2. Measured Pu(IV) Oxidation Kinetics on Lysimeter Source Sediments

The conceptual and quantitative model of downward Pu transport includes a slow oxidation step that is relatively difficult to monitor experimentally due to the slow rate. In a series of desorption experiments by *Kaplan et al.* [2004], desorption of Pu was monitored from Pu-amended lysimeter sediments under oxic and anoxic conditions. The results (Figure 13.11) indicated that under oxic conditions, Pu is slowly released, but under anoxic conditions, the aqueous concentration of Pu remains at the detection limit. A pseudo–first order rate constant of 1.4×10^{-6} h^{-1} was determined from these data. This rate constant is considerably larger (reaction faster) than the value of 3.2×10^{-7} hr^{-1} used in the best model fit to the data (Figure 13.7). However, it is notable that the experimentally determined reduction rate of 1.12×10^{-1} hr^{-1} discussed above is also faster than the value of 5.0×10^{-4} hr^{-1} which yielded the best fit to the data. Therefore, the ratio of reduction to oxidizing rates for experimental and modeling studies are ~80,000 and ~1,600, respectively. While these are still over an order of magnitude different, the fact that both predict a reduction rate orders of magnitude faster than the oxidation

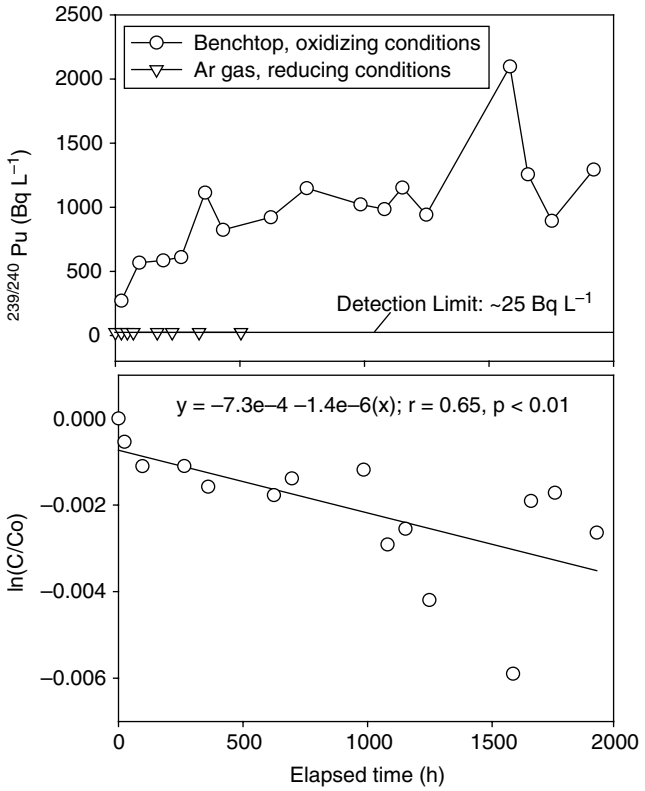

Figure 13.11 Top: Aqueous Pu concentration in contact with Pu(IV)-amended sediment under oxidizing and reducing conditions from lysimeter containing $Pu^{IV}(NO_3)_4$. Under reducing conditions (Ar environment; Eh (SHE) = 323 ± 7mV, pH = 7.2 ± 0.2), no Pu was detected in the aqueous phase. Under oxidizing conditions, aqueous Pu concentrations increased over time. Eh (SHE) generally cycled from 430 to 380 mV and pH from 6.2 to 6.5. Bottom: Pseudo–first order kinetics with respect to solid-phase Pu concentrations; rate constant of 1.4×10^{-6} h^{-1}. (*Kaplan et al.,* 2004; used with permission from the American Chemical Society.)

rate supports the conceptual model underlying the much greater reduction compared to oxidation rates used in the computational model. The difference in the absolute values of these rate terms has been attibuted to differences between the completely mixed experimental systems and the hydraulically controlled field lysimeter system, which experienced long dry periods. Furthermore, additional studies by *Kaplan et al.* [2006] have indicated that desorption of Pu from the lysimeter sediments is drastically influenced by pH and appears to be controlled by solubility of Pu (Figure 13.12). Thus, differences in the local pH environment and mass transfer of Pu may also be responsible for differences in the observed and best-fit rates. These are just some of the problems encountered in interdisciplinary studies involving the field environment and controlled laboratory conditions, where it is hard for a researcher to wait perhaps a decade for a field-relevant result in a highly transient environment.

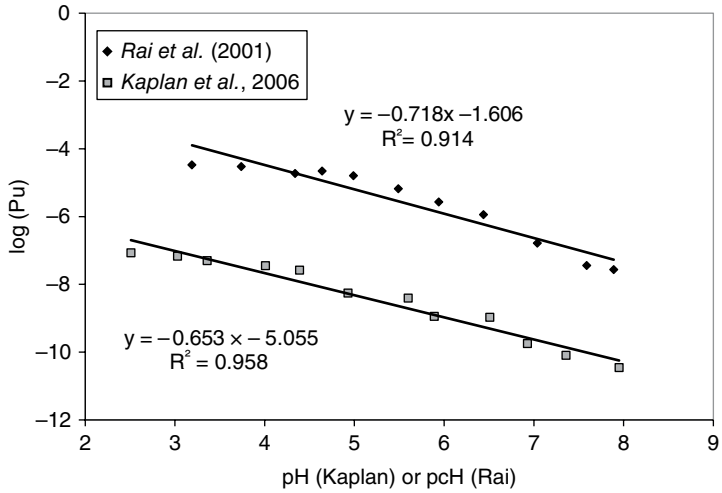

Figure 13.12 Comparison of sediment desorption data and a solubility controlled Pu(V)/PuO_2(am) 0.4 M $NaClO_4$ system (no sediment present, 0.0018-μm filtrates). (Modified from *Kaplan et al.,* 2006.)

13.5. PLUTONIUM UPTAKE AND TRANSPORT IN PLANTS

Simulations and experimental data suggest that in the lysimeters containing reduced sources, a single Pu species (Pur) had to dominate Pu uptake by the plant roots. As mentioned previously, SRS field experiments by *Whicker et al*. [1999] indicate that at least small amounts of Pu is taken up rapidly by many plant species and spreads through the plant tissues, sometimes concentrating in the leaves. To accomplish this in a growing season requires that Pur have a much lower distribution coefficient in the plant xylem than in the surrounding soil. What we consider our most realistic simulation (Figure 13.7, Simulation 2) incorporated a xylem distribution coefficient of 15 and a soil distribution coefficient of 1800. This suggests that soil Pur becomes complexed with a plant-derived compound that leads to much greater mobility in the plant tissue. It is known that grasses in particular have specialized chemical systems for the uptake of strongly sorbed nutrients such as Fe [*Curie and Briat*, 2003], and several researchers have suggested that Pu could be complexed by the same systems [*Adriano et al*., 1986; *Cataldo et al*., 1988; *Neu*, 2000].

Both plant roots and soil microbes require essential nutrients, such as Fe or Zn, that are strongly sorbed to soil surfaces, and a class of biologically produced chelating agents known as siderophores have evolved for specifically obtaining such minerals [*Roemheld and Marschner*, 1986]. The process for synthesizing siderophores has a significant metabolic cost to the plant; thus, the essential metal capture and incorporation benefits from efficiency. In the case of plants, the siderophore would be secreted by the roots, form a chemical complex with the adsorbed metal species of interest (Pur in our case), and return to the root in the transpiration stream. The complex then crosses the cell membrane in the roots to enter the xylem transpiration stream, either in its original complexed form or in combination with still another transport-facilitating chemical, such as citric acid or malic acid [*Namba and Murata*, 2010]. A notable body of research has quantified the partitioning of Pu between the shoot and root tissues of selected plants after exposure times of weeks to years [*Garland et al*., 1981; *Nisbet and Shaw*, 1994; *Adriano et al*., 2000], but a more detailed understanding of the dynamics of Pu movement into living plants is lacking. To better understand the probable details of Pu plant uptake in the lysimeter experiments discussed previously, experiments were performed on corn (*Z. mays, cv. Truckers Favorite*), an easily and rapidly grown member of the grass family. The objective was to measure the uptake and distribution of organically complexed Pu using well-defined and shorter exposure times, which to our surprise turned out to be as short as minutes. Potential plant barriers to Pu transport were identified, and a more refined estimate was made of Pu transport velocity and retardation factor in living corn xylem [*Thompson et al*., 2012]. The complexing agents selected for the experiments were the bacterial siderophore DFOB (Desferrioxamine B) and the chelating agent DTPA (diethylenetriaminepentaacetic acid). DTPA is a Pu complexant used in prior Pu plant uptake studies. DFOB is a bacterial siderophore available commercially, and since we were also interested in root-microbe interactions, most experiments were performed with DFOB. Nothing uniquely different in the response to the two chemicals was observed, although Pu(DFOB) moves more rapidly into corn plants than Pu(DTPA) by a factor of 2–4.

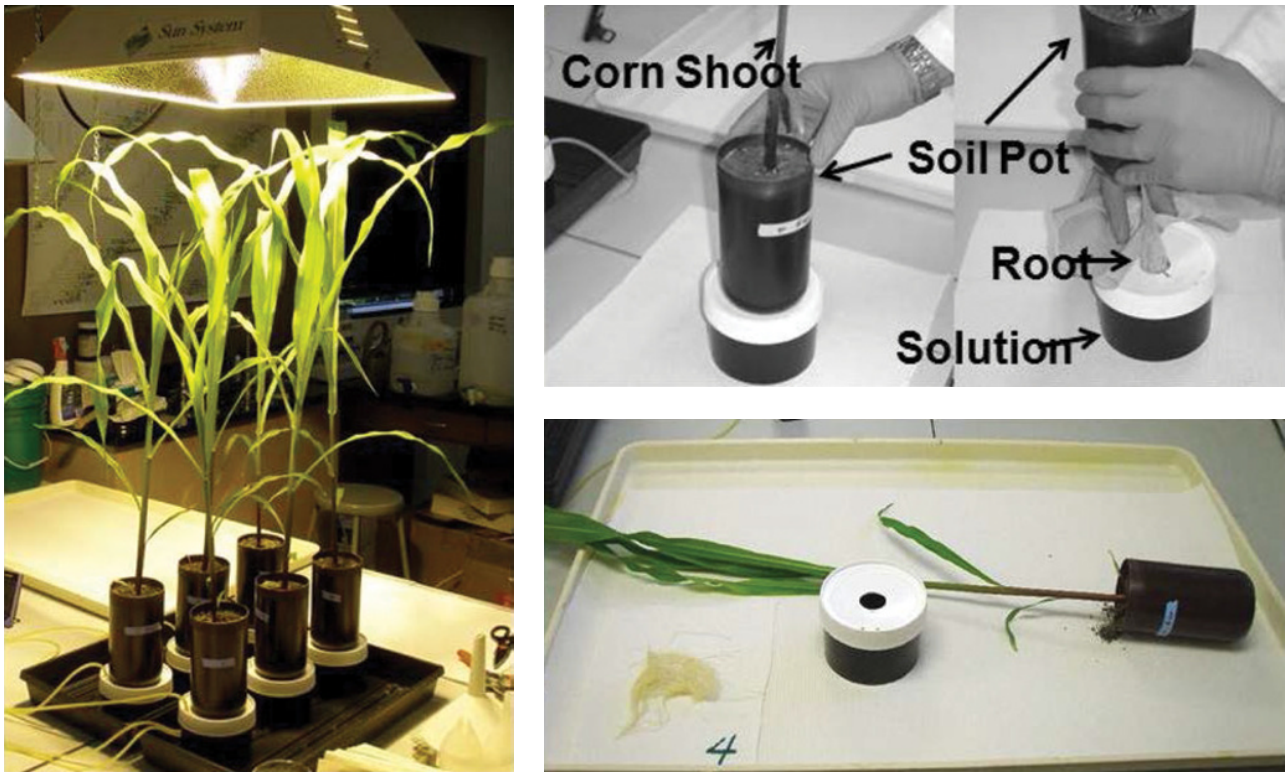

Figure 13.13 Corn plants under a sun lamp with the primary root growing through the upper chamber containing soil, into the lower chamber containing nutrient solution. Tubes and a pump aerated the solutions (Left). The soil pots rested on top of the solution containers (Top Right). Plants were exposed to radionuclides by opening the containers and rapidly replacing nutrient solutions with radiolabeled solutions. At the end of exposure, the roots could then be cut off at the bottom of the soil pot and the stem sectioned for further study (Bottom Right).

13.5.1. Design of the Experiments

As shown in Figure 13.13, corn plants were grown in soil-filled pots placed on top of containers filled with nutrient solution. Matching holes in the bottom of the pots and the top of the containers allowed the primary root of the corn (tap root) to pass through filter paper (to hold back soil) and enter the solution below. To initiate the experiments, seeds were germinated in seed paper for 7 days until their primary roots were sufficiently long to span the soil pot and contact the nutrient solution. This plant growth arrangement allowed a large mass of root to grow throughout the nutrient solution volume of 500 cc. When it was desirable to expose the corn to Pu, Fe, or any other solute, the applicable solution would be placed in the bottom containers, and transpiration demand pulled the solution into the roots and stems of the corn. Each corn plant was grown under a sunlamp, and during the exposure phase the soil was kept dry so that virtually all water was obtained from the solution containers. Transpiration volume versus time was obtained by measuring water loss from the containers at selected times [*Thompson*, 2010; *Thompson et al.*, 2012]. One advantage of this double chamber was that it was possible to introduce the Pu or Fe to the plant roots without competition for the Pu and Fe by soil surfaces. This experimental system also minimized the changes in root morphology (e.g., reduced root hair and greater root branching) that occur in a plant system grown purely in hydroponics.

13.5.2. Detection of Pu

^{238}Pu, the isotope used in our studies, decays by emitting alpha particles; thus, rapid autoradiography cannot be used because the decay products do not have the penetrating power to pass through plant tissue. Therefore, measuring the distribution of radioactive Pu in plants requires destructive tissue analysis and high detection sensitivity. When an experiment was terminated, shoot sections (above-soil plant parts) were cut into specific lengths, chopped finely, dried overnight, weighed, and digested by the method of *Jones and Wallace* [1992] using a mixture of concentrated nitric acid and hydrogen peroxide. Roots were removed from solution, allowed to drip on blotter paper, rinsed in water to remove excess solution, dried, chopped, and processed like the shoot tissues. Digested materials were placed in plastic scintillation vials and counted using a Wallac 1409 liquid sintillation counter [*Thompson*, 2010].

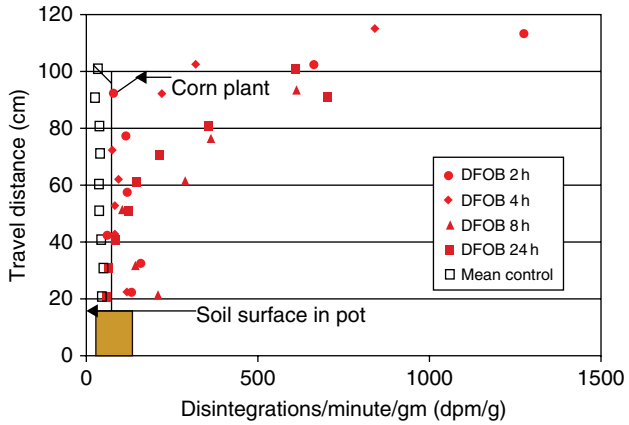

Figure 13.14 Activity concentrations versus distance in 28-day-old corn plants exposed to a ^{238}Pu solution or a nonlabeled control solution. The containers held equal activities of Pu(DFOB), and the exposure times vary from 2 hr to 24 hr. Distance was measured from the bottom of the soil pots to the center of 10-cm stem sections. (Error bars of approximately 10% are not shown for visual clarity.)

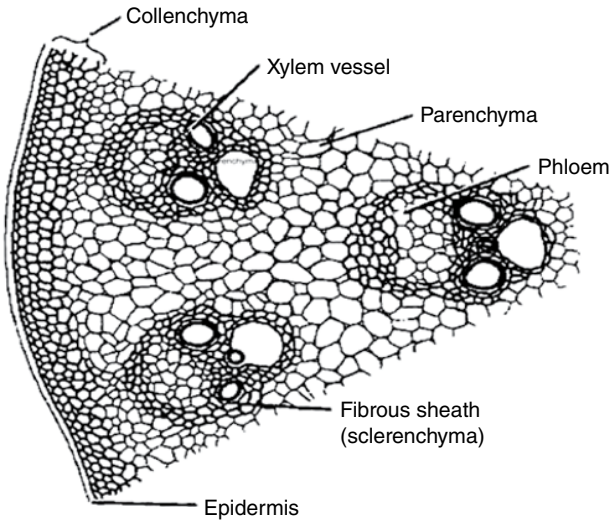

Figure 13.15 Illustrated partial section of a typical corn root. The vascular bundles are scattered throughout the root body (cortex). (Figure from public domain source.)

13.5.3. Distribution and Partitioning of Complexed Pu in Corn

Shown in Figure 13.14 are Pu concentrations versus distance traveled at exposure times of 2, 4, 8, and 24 hrs. Pu is complexed with DFOB, and control activity is due to plant uptake of small amounts of naturally occurring, alpha-emitting radionuclides in the potting soil. The distances are from the bottom of the soil pots to the midpoints of the stem sections, with the corn leaves pulled out straight (vertically upward). Obviously, Pu in its complexed form is much more mobile in corn plants than Pur is in soil. There is an obvious trend of increasing activity with height, and this effect would be expected if the Pu complex in the xylem remained soluble as it moved upward, with the concentration increase due to water loss by evaporation through the leaf stomates.

To enter the root xylem of corn, Pu must cross the epidermis and transverse the cellular structure illustrated in Figure 13.15 [*Beck*, 2005]. Much of this space is occupied by porous cell walls, but the bundle sheath cells surrounding the xylem elements have lignified cell walls, which forces the solution entering the xylem to cross one or more semipermeable cell membranes. These membranes vary in permeability to different solutes but are quite permeable to water molecules. Measured transpiration rates were often 10 cc/hr/plant over 24 hr under constant lighting, with total transpiration volumes over 3 to 10 days averaging between 100 and 500 cc. This is much greater than the total xylem volume in the roots and stem, which we estimate to be less than 2 cc. Thus, when roots are exposed to a new solution, the initial xylem fluid volume is quickly displaced by new transpiration volume. If the complexed Pu molecules in the solution entering the roots are unimpeded by the root tissues relative to water molecules, then the total Pu uptake by the plant shoots (ΣPus) during an extended time period divided by the cumulative transpiration volume (ΣTv) during the same time period should yield an average Pu concentration equal to that in the nutrient solution surrounding the roots. This calculation provides a simple way to quantify Pu discrimination by the applicable cell membranes in the root.

Table 13.2 Partitioning of whole-plant Pu uptake between the roots and shoots of corn.

Plants	Exposure Time	% Pu in Roots	% Pu in Shoots
3	3 days	98.3 ± 0.3	1.7 ± 0.5
3	7 days	97.6 ± 1.3	2.4 ± 1
3	10 days	95.9 ± 1.7	4.1 ± 1.7

To examine the partitioning of Pu in corn tissues, three sets of three plants were each exposed to Pu(DFOB) for 3, 7, or 10 days, respectively. The mean total Pu uptake by the shoots increased with time at the nearly constant rate of 1.27 Bq/d. The ratio of ΣPus/ΣTv at the end of the three time periods was 0.035 Bq/cc, 0.02 Bq/cc, and 0.028 Bq/cc, for an overall average of 0.028 Bq/cc. The Pu concentration in the nutrient solution was 16.5 Bq/cc, which is 580 times greater than ΣPus/ΣTv. Clearly, Pu(DFOB) is excluded from the root xylem relative to water [*Thompson*, 2010].

Further information concerning partitioning of Pu between the shoot and the roots may be obtained by measuring the total Pu uptake by the stems versus that of the roots (ΣPur). This was done for the same three sets of three plants described in the previous paragraph, with the results summarized in Table 13.2. The data imply that Pu is held

up in the root tissue external to the xylem while water flows into the xylem, and this would lead to the Pu concentration in the cortex fluids becoming higher than that in the nutrient solution. We can calculate a lower bound for this concentration increase by simply taking the total root activity divided by the fresh root volume (Root Bq/cc) and dividing it by the initial activity concentration of the nutrient solution (Solution Bq/cc). In an experiment involving 10 plants and 1 day of exposure time, the mean root/solution concentration ratio was 4:1 [*Thompson*, 2010, Table 6.5). Overall, Pu that entered the corn roots was mostly retained in the cortex tissues while quickly entering the xylem in small amounts and moving through the stem in the transpiration stream [*Epstein and Norlyn*, 1973]. Because Pu crosses cell membranes rapidly but in small amounts, after 1 day of exposure most Pu in the root cortex would be in the cell wall material not the cytoplasm, so the concentration here would be higher than four times the solution concentration and would lead to a Pu concentration gradient forcing Pu back toward the nutrient solution.

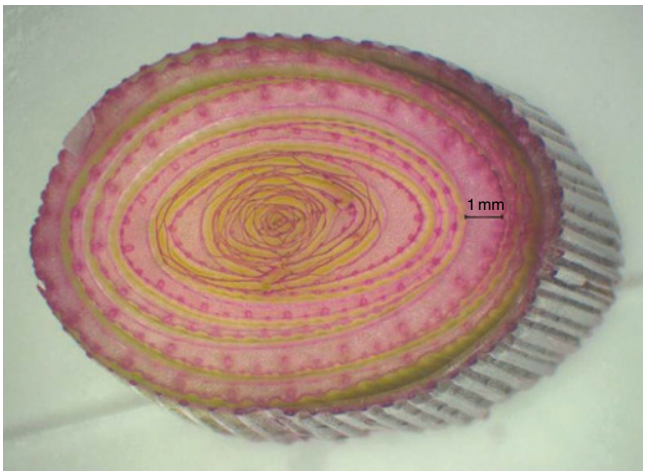

Figure 13.16 Photomicrograph of a control-plant stem cut 5 cm above the soil. The tissue was stained to increase the contrast of the vascular bundles, which are the darker oval structures. Higher resolution portions of such micrographs were studied in order to estimate the fraction of the stem cross-sectional area that was xylem.

13.5.4. The Velocity of Complexed Pu in Corn

The conceptualization, so far, is that complexed Pu enters the corn root cortex relatively rapidly, concentrating in the open (porous) cell wall material but is passed only selectively (small amounts) by the cell membrane(s) surrounding the xylem. It is likely that some particular biochemical pathway is involved in the transport of Pu across cell membranes, similar to the pathways that exist for transporting Fe, and the complexing agent may change at this point. After entering the root xylem, Pu would be expected to move upward in the transpiration stream as a slightly retarded solute and concentrate in the leaves as water is lost through the stomates. This raises the issues of xylem transport velocity and retardation factor [*Sperry et al.*, 2003].

Plutonium velocity experiments were conducted using 23-day-old plants, with the lower roots exposed to nutrient solutions spiked with Pu(DFOB) at time zero. The objective was to time the travel of Pu through the roots and up the stem to an elevation 40 cm above the soil. When the primary root length was added on, the total travel distance was 58 cm. The main objective was to bound the first arrival time of the Pu at the 40-cm elevation, and it took several attempts to select measurement times of sufficiently small duration to actually capture the unexpectedly short travel times. (We were prejudiced by the 3 cm per 11 year soil travel times observed in the lysimeter experiments.) Average water velocity was calculated using measured transpiration rates, based on nutrient solution consumption volumes, and measured xylem cross-sectional areas of corn stems 5 cm above the soil. Using photomicrographs, like that shown in Figure 13.16, xylem area was differentiated from total stem area using iSolution Lite software v. 7.7 [*Thompson*, 2010].

Shown in Figure 13.17 are the results of four travel time measurements made over the 58 cm travel distance using four plants of similar size: two at 10 min. and two at 20 min. Activity was measured in the plant portion above the indicated cut, which we refer to as "the top shoot." Pu is clearly present in the top shoots of the 20 min. plants, with the control plant data plotted at zero exposure time. The 10 min. activity is not significantly different from the control plants. Pu travel velocity is given by the distance traveled divided by the travel time. The data permit bounding the travel time between 10 and 20 min., so we can say that 58 cm/10 min = 5.8 < V_{Pu} < 2.9 = 58 cm/20 min. In hours, the Pu velocity is between 174 and 348 cm/hr, over 5 million times faster than the downward Pur velocity observed below the source in the SRS lysimeter experiemnts.

For short time periods with high transpiration rates, nearly all water moving into the corn is lost to the atmosphere (negligible storage change due to growth). The average water velocity was calculated using measured transpiration rates and estimated total xylem area. The average transpiration rate "Q" on two control plants measured over a 24-hr period under continuous lighting was 9.98 cc/hr. The average stem area of the two control plants was 1.078 cm^2 and the xylem-to-stem area ratio was 0.0115, or about 1% on an areal basis. Thus, the stem

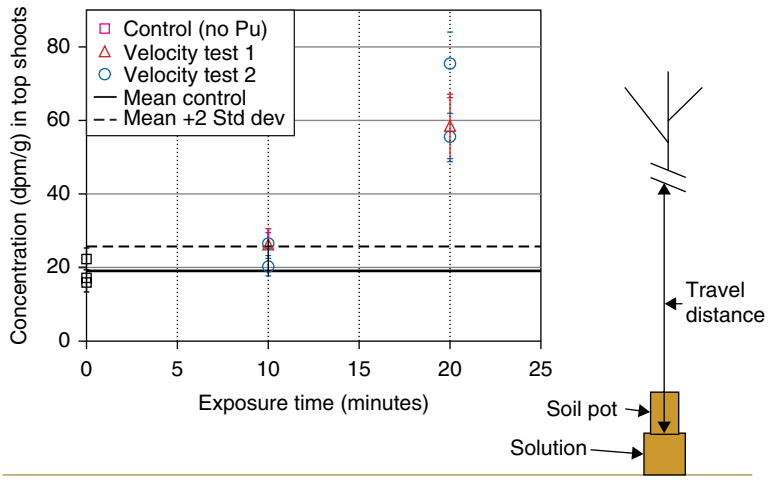

Figure 13.17 A plot of concentration in the top shoot (above cut) versus travel time over the 58 cm travel distance indicated on the figure. The solid horizontal line indicates mean control activity and the dashed line is mean plus two standard deviations. Activity data are from duplicate plants sampled at 10 min. and 20 min.

xylem area "A_x" at 5 cm above the soil is 0.0124 cm^2. This yields an average xylem water velocity at this elevation given by:

$$\bar{V}_W = \frac{Q}{A_X} = \frac{9.98}{0.0124} = 800\ cm/hr \qquad (13.2)$$

The xylem water velocity given in Equation 13.2 has a roughly ±20% error estimate based on the standard deviation of the bundle areas, so the average water velocity could vary between 640 cm/hr and 960 cm/hr. Given that we bounded a "first arrival" time for the Pu over the 58-cm travel distance, the maximum water velocity is needed to estimate an "effective" retardation factor, not the average velocity. (The term *effective* is used because the medium is living, heterogeneous tissue, so an unknown mix of different factors contributes to the observed retardation.) The well-known formula for the laminar velocity distribution in a tube of radius R allows one to calculate the maximum velocity (V_m) from the average velocity (V_a) using the relationship $V_m = 2V_a$ [*Giles et al.*, 1993). So based on this relationship, the maximum water velocity is estimated to be between 1,280 cm/hr and 1,920 cm/hr. From the bounding values for V_{Pu} (174 cm/hr and 348 cm/hr) and the bounding values given for V_m, one can bound the implied Pu xylem retardation factor ($R_{XPu} = V_m/V_{Pu}$) as

$$3.7 \le R_{XPu} \le 11 \qquad (13.3)$$

More detailed information concerning the movement and retardation of Pu in plants is available in *Thompson* [2010] and *Thompson et al.* [2012].

13.5.5. How Do Fe and Pu Enter Corn Roots and Cross Cell Membranes?

Since plants have no known need for Pu, its uptake may occur in response to a requirement for Fe. Fe(III) and Pu(IV) have (1) similar charge to ionic radii ratios of about 47 n/m, (2) similar first hydrolysis constants [Fe(III) LogK = 11.1; Pu(IV) LogK = 12.2], and (3) similar complexation constants with DFOB [Fe(III)DFOB LogK = 30.6; PU(IV)DFOB LogK = 35.8] [*Neu et al.*, 2002]. Previous plant studies by *Garland et al.* [1981] and *Cataldo et al.* [1988] showed that Pu behavior in soybean xylem exudates was quite similar to that of Fe, so one is led to use the uptake of Fe by grasses as an initial model for studying Pu uptake.

Roemheld and Marschner [1986] developed evidence for a specific FE-phytosiderophore uptake system in the roots of grasses, and plants that utilize such a system are called "Strategy II" plants [*Marschner*, 1995; *McNear*, 2013]. Grasses in need of Fe will exude strong Fe(III)-chelating ligands (phytosiderophores) and soil bacteria in need of Fe also secret microbial siderophores such as DFOB. Once formed, these different Fe-siderophore complexes can be used by both plant roots and microbes to obtain Fe, and indirectly Pu, from the soil [*Bar-Ness et al.*, 1992; *Kraemer et al.*, 2006].

While a complex such as Fe-(DFOB) would be expected to move relatively freely through the soil and porous cell walls of corn roots, changes in the transport mechanism would be expected at the cell membranes. As described by *Marschner* [1995], uptake of plant-produced Fe(III)-siderophores is mediated by a specific transport channel in the cell membrane of grass roots. If the channel proteins are damaged, as they are in the mutant corn species

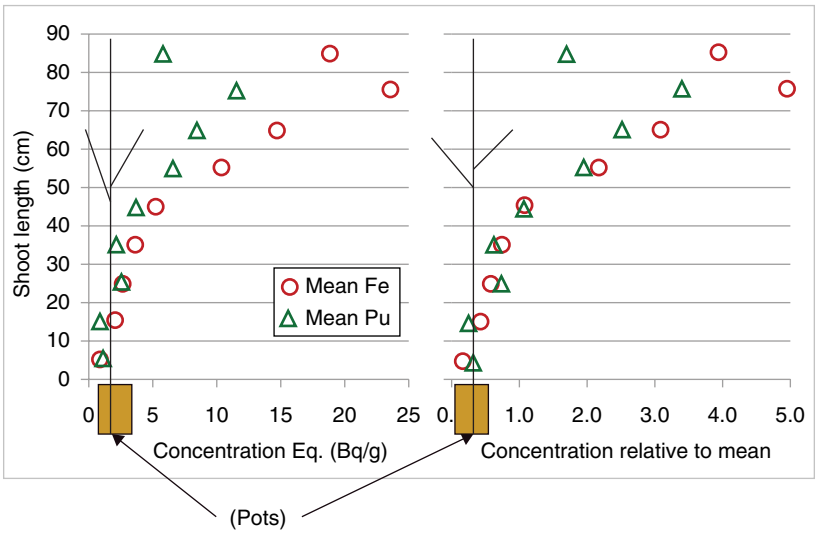

Figure 13.18 Tissue section concentrations of ^{238}Pu and ^{59}Fe versus shoot length. The left-hand plots are mean concentrations over three plants (background concentrations removed), while the right-hand plots are the same points but divided by the mean shoot concentrations. Presented this way, the distributions of Fe and Pu are remarkably similar even though ^{59}Fe accumulation in the shoots was greater overall [*Thompson*, 2010].

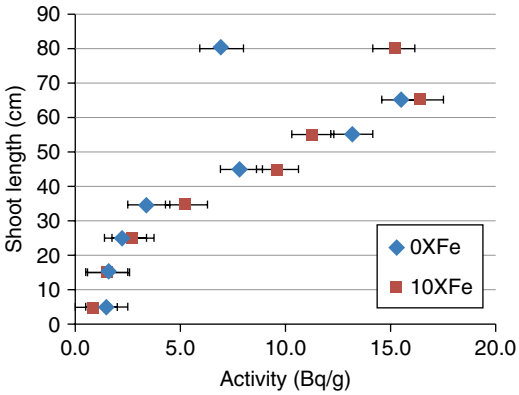

Figure 13.19 Tissue section concentrations of 238Pu versus shoot length, with each set of results averaged over five plants. The Fe:Pu molecular ratio is near zero (0XFe) or 225,000 (10XFe) [*Thompson*, 2010].

called "Yellow-Stripe 1", then Fe uptake is greatly inhibited [*Von Wiren et al.*, 1994; *Curie et al.*, 2001]. John et al. [2001] studied the simultaneous transport of complexed Fe and Pu across the cell membrane of the bacterium *Micobacterium flavescens* and was able to show that Fe interfered with Pu uptake and vice versa.

In tests designed to compare the uptake and distributions of Pu and Fe in corn, three 28-day-old plants were exposed for 2 days to nutrient solutions containing ~37KBq of 238PU (4.71×10^{-10} molar) and ~37KBq of 59Fe (6.68×10^{-13} molar), both metals were complexed with 9.8×10^{-5} molar DFOB. This insured that both radionuclides existed in complexed form during the experiments. Uptake distributions averaged over three plants are shown in Figure 13.18. Even though the number of molecules of Pu and Fe differed significantly, one observes that the uptake pattern is quite similar for both radionuclides.

To look for possible interference between Fe and 238Pu, two additional experiments were done. In these experiments corn was grown in soil pots (two sets of five plants each) above the usual nutrient solutions until 2.5 days prior to exposure. At that time the nutrient concentrations of Fe were changed to have near zero or 1.07×10^{-5} molar Fe. Then at time zero, all plants were exposed to the same solutions but modified to contain 4.75×10^{-10} molar Pu. This resulted in Fe:Pu molecular ratios of near zero or 225,000, with the results shown in Figure 13.19. Surprisingly, in this set of experiments, there is no evidence of Fe molecules interfering with the uptake of Pu molecules. This differs greatly from the microbial results of *John et al.* [2001], where interference was observed at molecular ratios of 1:1 (2×10^{-6} molar Fe and Pu). Clearly, more study is warranted, which is the way research typically ends, or simply pauses, as Paul Witherspoon might say.

13.6. FUTURE WORK: A NEW FIELD LYSIMETER STUDY

While the previous lysimeter and corn plant studies described in this chapter have provided a wealth of information regarding Pu mobility in the SRS vadose zone,

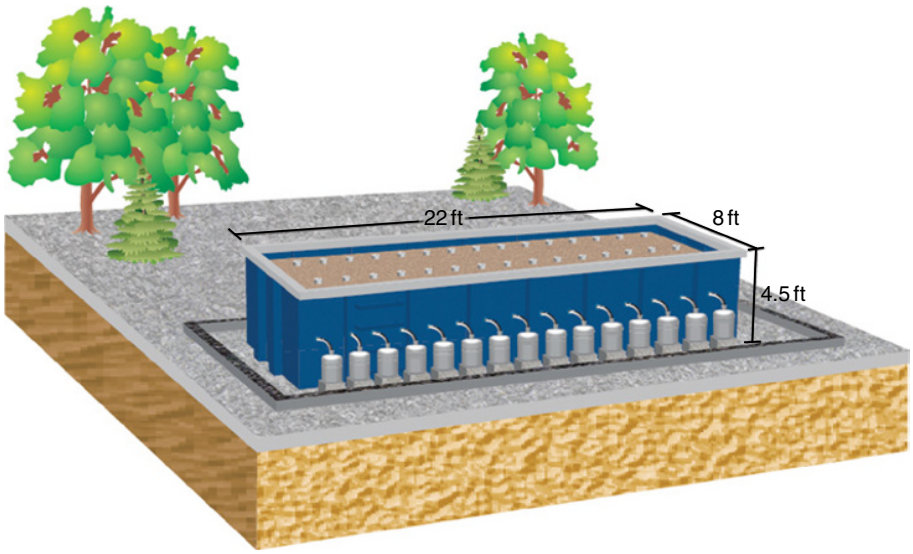

Figure 13.20 Illustrations of the RadFLEx lysimeter facility currently running at SRS.

several unanswered questions remain. Therefore, a new field lysimeter experiment (RadFLEx: Radiological Field Lysimeter Experiment) has been started. The key questions to be addressed in these new experiments are the following:

1. *What are the mechanisms governing downward Pu (and other radionuclide) migration?* In the previous experiments, downward migration of Pu was modeled as a dynamic progression of oxidation and reduction reactions. However, the soil profile was only measured after 2 and 11 years. In the new experiments, sources of Pu(IV)-oxalate, Pu(III)-oxalate, Pu(V)-ammonium carbonate, and Pu(IV)-colloids were prepared in triplicate for analysis of the sediment profile after 2, 4, and 10 years. Furthermore, addition of Np(IV) and Np(V) sources will allow for comparisons of oxidation state chemical analogs.

2. *What is the role of organic matter and/or microbially-mediated solubilization and transport of Pu?* In the new experiment, several lysimeters have utilized soil that has been amended with natural organic matter (NOM). Complexation of Pu with NOM may lead to the formation of mobile Pu(IV) species based on reduced affinity for the sediment and increased solubility of Pu(IV). Furthermore, the microbial community will be monitored in sediment samples in an effort to understand the potential role of direct and indirect interactions with microorganisms on Pu mobility. These measurements are coupled with a series of laboratory experiments examining microbial chemotaxis and sorption of Pu to microbial cell walls.

3. *What is the overall role of grass roots in upward Pu migration?* Modeling and mass spectrometric analysis of the previous lysimeters coupled with laboratory studies has given strong evidence of upward migration of Pu facilitated by grass roots. In the new lysimeter experiments, this will be examined further by running lysimeters with and without grass growing in the surface soil. It is expected that no upward migration of Pu will occur in lysimeters without vegetation on the surface.

In these new experiments, 48 field lysimeters containing radionuclides were installed at the SRS that contain a variety of radionuclides. This is the first large-scale radiological lysimeter program to be established within the DOE laboratory system since 1981, almost 30 years ago. The intent of the RadFLEx lysimeter program, which is funded by SRS Site Operations, is to study long-term geochemical processes of key radionuclide risk drivers under field conditions, with particular attention directed at quantifying input parameters for SRS performance assessment models. Lysimeters were installed in March 2012 and soil hydraulic properties were measured. Sediment cores for vertical activity characterizations will be obtained after 2, 4, and 10 years.

A diagram of the RadFLEx facility is shown in Figure 13.20. The lysimeters consist of 10-cm diameter by 60-cm length PVC pipes filled with SRS vadose zone sediment and contain well-characterized radionuclide sources. The radionuclide amendment was added as a liquid to a filter membrane and permitted

to dry. The amended filter was then buried at a 30-cm depth with clean sediment. One set of 14 lysimeters contains cementitious sources. These are the following:

1. Radionuclide-free cementitious material (control) (Lysimeters 2, 3, 14, and 15)
2. Tc-99 and stable iodine (lysimeters 7, 8, 19, and 20)
3. A suite of gamma emitters, Cs-137, Co-60, Ba-133, and Eu-152 (lysimeters 4–6 and 16–18)

A second set of 29 lysimeters contains soil sources that have been amended with actinides. These include the following:

1. $Pu(V)NH_4(CO_3)$ (lysimeter 21–23 and 41–43).
2. A suite of beta/gamma emitters, Cs-137, Co-60, Ba-133, and Eu-152 (lysimeters 26–28)
3. Np-237 (lysimeters 29–32)
4. Pu(III)-oxalate and Pu(IV)-oxalate (lysimeters 9–11, 33–35, and 38–40)
5. Pu(IV)-colloids (lysimeters 44–46)
6. Sediment controls with no radionuclides (lysimeters 12, 24, 25, and 37)

The lysimeters are located at the A-01 Outfall on the Savannah River Site and are open to natural rainfall. The lysimeters drain directly into collection carboys for periodic sampling of pore-waters for total radionuclide, ultrafiltration-radionuclides, DOC, pH, and routine cation and anion chemistry. Quarterly analyses of radionuclides in the lysimeter effluents have taken place since the start of the experiment, July 5, 2012. As expected, no breakthrough of Pu has been observed in the first four quarters. Monitoring will continue for 10 years and lysimeters will be removed for evaluation of the source term Pu and the nearby soil Pu concentrations and properties after 2, 4, and 10 years.

13.7. CONCLUDING OBSERVATIONS

This chapter describes a decade-long research effort motivated by the Long-Term Lysimeter Experiments started in 1981 at the SRS. Associated studies motivated by the SRS data, as well as future studies, are also described. Fully understanding the original SRS data ultimately required the simulation of flow and transport in the rhizosphere, as well as laboratory studies of Pu uptake by corn roots, a member of the grass family. The overall results of the plant experiments, aimed at characterizing the uptake of Pu complexed with DFOB, were compatible with and supportive of the mathematical model outlined in the early part of this chapter (see appendix for details). Even though a large fraction of the Pu(DFOB) was retained in the corn roots external to the xylem (98.3%–95.9%, decreasing with exposure time), a small fraction of the Pu (1.7%–4.1%, increasing with exposure time) moved rapidly upward in the root and stem xylem, accumulating in the upper leaves as water was lost to transpiration. In one set of experiments, the upward Pu velocity was bounded by 174 cm/hr and 348 cm/hr. By combining this velocity range with the average water velocity and assuming the relationship between average and maximum velocity in small tubes, an effective xylem retardation factor between 3.7 and 11 for corn xylem was estimated. These values are supportive of the earlier modeling efforts and the Pu distributions observed in the SRS lysimeter cores. However, in the plants a small fraction of Pu crossed the root membranes and then moved upward relatively rapidly in the xylem, while in the simulations we had a larger amount of Pu cross the root membranes and then move up relatively slowly in the xylem. So to rigorously simulate the Pu transport observed in the corn, we would have to insert a barrier to Pu transport in the root (selective membrane) and then have the Pu moving upward in the xylem retarded less. Either approach could be adjusted to give the same total Pu uptake by the plant.

A biologically based complexation process appears essential to the vastly accelerated rate of movement of Pur in plant tissue as compared to the SRS soil. This enables plants to be a conduit of rapid upward Pu movement and release to the environment, as evidenced by the accumulation of the source Pu on the lysimeter surfaces. Animals, such as rabbits, could consume grasses containing Pu and move it further into the food chain.

An interesting implication of this and previous studies is that the microbe and plant biochemistry that evolved to obtain Fe from soils may incorporate Pu in place of Fe. There is strong evidence based on joint Pu/Fe interference that this is the case in the microbe *Microbacterium flavescens*, and the distributions of Pu and Fe in soybean xylem exudates and corn roots and shoots are very similar. However, we were unable to document the ability of Fe to interfere with Pu crossing root membranes even when the Fe:Pu molecular ratio was 225,000:1. If a corn-based siderophore (phytosiderophore) took up Pu in place of the desired Fe, one would tend to think that the Pu would follow the usual Fe pathway in crossing cell membranes. But microbes also secrete siderophores, plants have learned to utilize such siderophores, and DFOB is a bacterial siderophore, so could grasses have evolved two or more sets of pathways for transporting Fe across membranes when it is complexed with microbial siderophores, as was the case in our experiments? We hope to further clarify this thought with ongoing experiments.

APPENDIX

13A.1. DERIVATION OF THE MODEL FOR PU TRANPORT IN SOIL AND PLANTS

13A.1.1. The Reactive Transport Model

Based on the findings in the literature and the observations from the data resulted from the lysimeter experiments, discussed within the chapter, the reactive transport model was conceptualized including two classes of Pu, with each exhibiting a different mobility: (1) Reduced class, Pur, (i.e., [Pu(III)] + [Pu(IV)]), considered highly immobile; and (2) Oxidized class, Puo, (i.e., [Pu(V)] + [Pu(VI)]), considered relatively more mobile. The transport of these two classes of Pu in the soil was based on advection and dispersion while geochemical behavior was implemented by using equilibrium, reversible partitioning between aqueous and solid phases, and kinetic oxidation-reduction reactions in the sorbed phase, as can be seen in the conceptual model diagram in Figure A.1. The governing equations for the both Pu classes were derived for a one-dimensional domain as shown in Equations 13A.1 and 13A.2 below. The model parameters are described in Table A.1 (for further details see *Demirkanli et al.*, 2008, 2009)

Fully implicit finite-difference approximations of the governing equations were solved by using Gauss Siedel iterative method for soil aqueous concentrations of Puo and Pur. For coupling of the two equations, Picard iteration scheme was used.

$$\left[1+\frac{\rho}{\theta(z,t)}K_{do}\right]\frac{\partial C_{Puo}(z,t)}{\partial t}+\frac{C_{Puo}(z,t)}{\theta(z,t)}\frac{\partial\theta(z,t)}{\partial t}$$
$$=-\frac{\partial\left[v(z,t)C_{Puo}(z,t)-D(z,t)\dfrac{\partial C_{Puo}(z,t)}{\partial z}\right]}{\partial z}$$
$$+k_o C_{Pur}(z,t)\frac{\rho}{\theta(z,t)}K_{dr}-k_r C_{Puo}(z,t)\frac{\rho}{\theta(z,t)}K_{do} \quad (13A.1)$$
$$+\frac{q_{o,Puo}}{\theta(z,t)}\delta(z-z_{source})$$

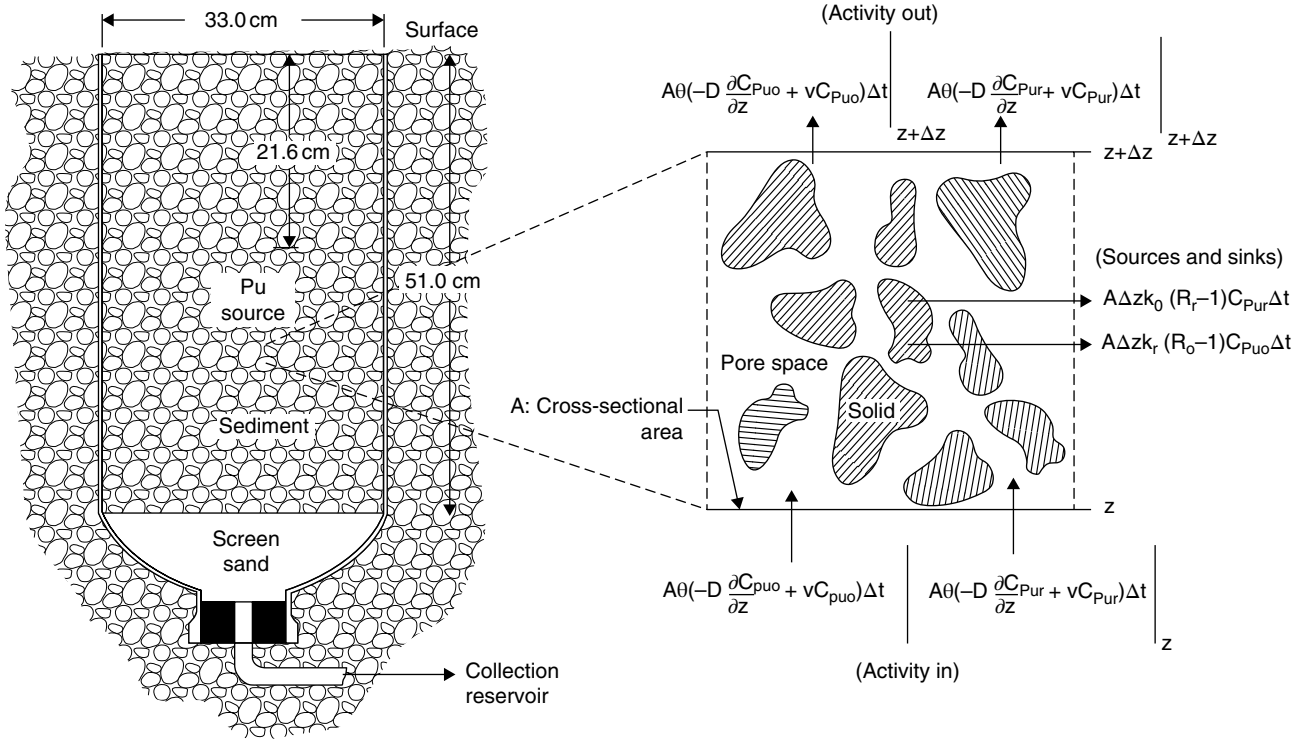

Figure A.1 Schematic representation of the control volume approach and activity balance for both Pu classes that were used to derive the governing equations for the reactive transport model in the soil. C, activity concentrations (μCi cm^{-3}); D, hydrodynamic dispersion coefficient (cm^2 h^{-1}); k_o, oxidation rate constant (h^{-1}); k_r, reduction rate constant (h^{-1}); R_o, retardation factor for oxidized Pu; R_r, retardation factor for reduced Pu; θ, volumetric water content (cm^3 cm^{-3}); z, elevation in lysimeter (cm); δt, time step (h).

Table A.1 Description of the model parameters.

Model Parameter	Descriptions	Unit
C_{Pur}	Pur activity concentration in soil	μCi cm^{-3}
C_{Puo}	Puo Pu activity concentration in soil	μCi cm^{-3}
ρ	Soil bulk density	g cm^{-3}
θ	Volumetric water content	cm^3 cm^{-3}
K_{dr}	Pur partitioning coefficient	cm^3 g^{-1}
K_{do}	Puo partitioning coefficient	cm^3 g^{-1}
v	Advective velocity	cm h^{-1}
D	Hydrodynamic dispersion coefficient	cm^2 h^{-1}
k_o	Oxidation rate constant	h^{-1}
kr	Reduction rate constant	h^{-1}
z	Elevation in lysimeter	cm
t	Time	h

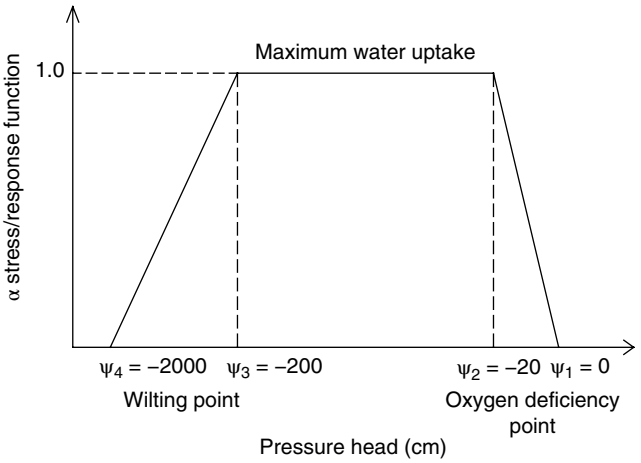

Figure A.2 Schematic representation of the stress-response function versus pressure head.

$$\left[1+\frac{\rho}{\theta(z,t)}K_{dr}\right]\frac{\partial C_{Pur}(z,t)}{\partial t}+\frac{C_{Pur}(z,t)}{\theta(z,t)}\frac{\partial\theta(z,t)}{\partial t}$$
$$=-\frac{\partial\left[v(z,t)C_{Pur}(z,t)-D(z,t)\dfrac{\partial C_{Pur}(z,t)}{\partial z}\right]}{\partial z}$$
$$-k_o C_{Pur}(z,t)\frac{\rho}{\theta(z,t)}K_{dr}+k_r C_{Puo}(z,t)\frac{\rho}{\theta(z,t)}K_{do}$$
$$+\frac{q_{o,Pur}}{\theta(z,t)}\delta(z-z_{source}) \quad (13A.2)$$

13A.2. THE VARIABLY SATURATED FLOW MODEL

To define the variably saturated flow in the vadose zone, a one-dimensional, pressure-head based, mixed form of variably saturated flow equation was used as the governing equation, shown in Equation 13A.3. This equation is proven to provide stable solutions when the system reaches a saturated condition by

$$\frac{\theta(\psi)S_s}{\eta}\frac{\partial\psi(z,t)}{\partial t}+\frac{\partial\theta(\psi)}{\partial t}$$
$$=\frac{\partial}{\partial z}\left[K(\psi)\frac{\partial\psi(z,t)}{\partial z}\right]+\frac{\partial K(\psi)}{\partial z}-S(z,\psi) \quad (13A.3)$$

In the above equation, θ, η, and S_s represent the volumetric water content (cm^3 cm^{-3}), porosity, and the specific storage coefficient (cm^3 cm^{-3} cm^{-1}), respectively. S(z,ψ) is the root water uptake function.

The root uptake function was added to the variably saturated flow model as a volumetric sink term representing the volume of water taken up by the roots per unit bulk volume of the soil per unit time and formulized as shown in Equation 13A.4.

$$S(z,\psi)=\alpha(\psi)*RRD(z)*T_p \quad (13A.4)$$

In the above equation, α(ψ) is the stress-response function, RRD(z) is the relative root distribution as defined by Equation 13A.5, where RD(z) is the measured root distribution in terms of root weight per unit volume of soil, and Z_R is the depth of the root zone. T_p is the potential (maximum) transpiration rate under the prevailing climatic conditions.

$$\int_0^{Z_R}RRD(z)=1 \quad \Rightarrow RRD(z)=\frac{RD(z)}{\int_0^{Z_R}RD(z)dz} \quad (13A.5)$$

As a reasonable approximation, transpiration is assumed to occur at the potential rate unless it is limited by the availability of soil moisture (dry conditions) or oxygen (very wet conditions). Figure A.2 exhibits the general shape of a stress-response function. It is an empirically derived function, where ψ_1 defines an "oxygen deficiency (anaerobiosis) point," and ψ_4 represents a "wilting point." Under conditions wetter than the "anaerobiosis point," root growth is significantly limited due to lack of oxygen in the system. The saturated condition, where the pressure head value is zero, is usually selected as an "anaerobiosis point." Under conditions drier than "wilting point," the water uptake by roots is also assumed to be zero due to the unavailability of enough moisture for roots to survive.

The Thornthwaite equation, shown in Equation 13A.6, is derived for calculating monthly potential transpiration,

Table A.2 Description of the model parameters.

van Genuchten Parameters	Value
Retention Function	
Curve shape parameter, n	1.48013
Curve shape parameter, α (1/cm)	0.027816
Saturated water content, θ_{sat} (cm^3/cm^3)	0.39188
Residual water content, θ_r (cm^3/cm^3)	0.0589
Hydraulic Conductivity Function	
Saturated hydraulic conductivity, K_{sat} (cm/d)	15.984
Tortuosity/connectivity parameter, L	–1.0633

T_{pm} (cm), for especially humid climates like the eastern United States. The equation includes a monthly adjustment factor related to hours of daylight for the location of interest in latitude (N_m), the mean monthly temperature in degrees C (T_m), the heat index for a year (I) calculated by Equation 13A.7, and constant (a) which is a function of the heat index as shown in Equation 13A.8. $\beta_{transpiration}$ is the correction factor estimated from the data and simulation results by trial and error.

$$T_{pm} = \beta_{transpiration} 16 N_m \left[\frac{10 T_m}{I}\right] \qquad (13A.6)$$

$$I = \sum_{m=1}^{12} \left[\frac{T_m}{5}\right]^{1.5} \qquad (13A.7)$$

$$a = 6.7\times10^{-7} I^3 - 7.7\times10^{-5} I^2 + 1.8\times10^{-2} I + 0.49 \qquad (13A.8)$$

Hydraulic parameters, unsaturated hydraulic conductivity, K(ψ), and volumetric water content, θ(ψ), are estimated by using Rosetta with an input of measured average particle size distribution of the soil and the bulk density.[1] van Genuchten parameter values resulted from Rosetta are listed in Table A.2 and the van Genuchten soil hydraulic functions are shown in equations (13A.9) and (13A.10).

$$K(\psi) = K_{sat} S_e^L \left\{1 - \left[1 - S_e^{\,n/(n-1)}\right]^{1-1/n}\right\}^2$$
$$S_e = \left[1 + \left(0.027816|\psi|\right)^n\right]^{1/n-1} \qquad (13A.9)$$

$$\theta(\psi) = \theta_r + \frac{\theta_{sat} - \theta_r}{\left[1 + (0.027816\psi)^n\right]^{1-1/n4}} \qquad (13A.10)$$

A fully implicit, finite difference approximation of the governing equation (Equation 13A.3) was solved for the pressure head by using tri-diagonal algorithm. For nonlinearity caused by the pressure head dependent hydraulic parameters, a Picard iteration scheme is used. Boundary conditions at the top and bottom of the lysimeters are defined numerically by using Neuman (or flux) conditions. In the model, the upper boundary flux value is set equal to the daily rainfall rate (q_I) collected at the site during the experiments.

[1] *Rosetta is a computer program for estimating soil hydraulic parameters with hierarchical pedo-transfer functions, developed by Schaap et al. [2001].[[not in refs]]*

13A.3. THE ROOT PU UPTAKE AND TRANSPORT MODEL

The root Pu uptake and transport model included the typical mechanisms of advective and dispersive transport of Pu within the xylem transpiration stream following Pu uptake with the water from the soil, as shown in Figure A.3. Equations 13A.11 and 13A.12 present the governing equations for transport with the xylem for Pur and Puo, respectively.

$$R_{r\_Pur}\frac{\partial C_{r\_Pur}}{\partial t} = -\frac{\partial}{\partial z}\left[v_r(z,t)C_{r\_Pur}(z,t) - D_r(z,t)\frac{\partial C_{r\_Pur}(z,t)}{\partial z}\right] - \frac{\partial(\ln A_r(z))}{\partial z}\left[v_r(z,t)C_{r\_Pur}(z,t) - D_r(z,t)\frac{\partial C_{r\_Pur}(z,t)}{\partial z}\right] + \frac{C_{Pur}(z,t)S(z,\psi)}{A_r(z)\eta_r} \qquad (13A.11)$$

$$R_{r\_Puo}\frac{\partial C_{r\_Puo}}{\partial t} = -\frac{\partial}{\partial z}\left[v_r(z,t)C_{r\_Puo}(z,t) - D_r(z,t)\frac{\partial C_{r\_Puo}(z,t)}{\partial z}\right] - \frac{\partial(\ln A_r(z))}{\partial z}\left[v_r(z,t)C_{r\_Puo}(z,t) - D_r(z,t)\frac{\partial C_{r\_Puo}(z,t)}{\partial z}\right] + \frac{C_{Puo}(z,t)S(z,\psi)}{A_r(z)\eta_r} \qquad (13A.12)$$

In these governing equations, z is the elevation in the lysimeter and t is the time in hours, C_{r_Pur} and C_{r_Puo} are the aqueous activity concentrations of indicated Pu classes in the root xylem in terms of μCi/cm^3; R_{r_Pur} and R_{r_Puo} are the root retardation factors for Pur and Puo, respectively; η_r is the porosity of the root xylem; D_r is the dispersion coefficient (cm^2/h); and v_r is the average linear fluid velocity (cm/h).

Two key relationships were defined to quantify fluid flow through the plant xylem. The cumulative discharge through the xylem per unit soil area, Qr(z,t), was obtained by summing (integrating) root uptake of water from the bottom of the root zone to the elevation z as

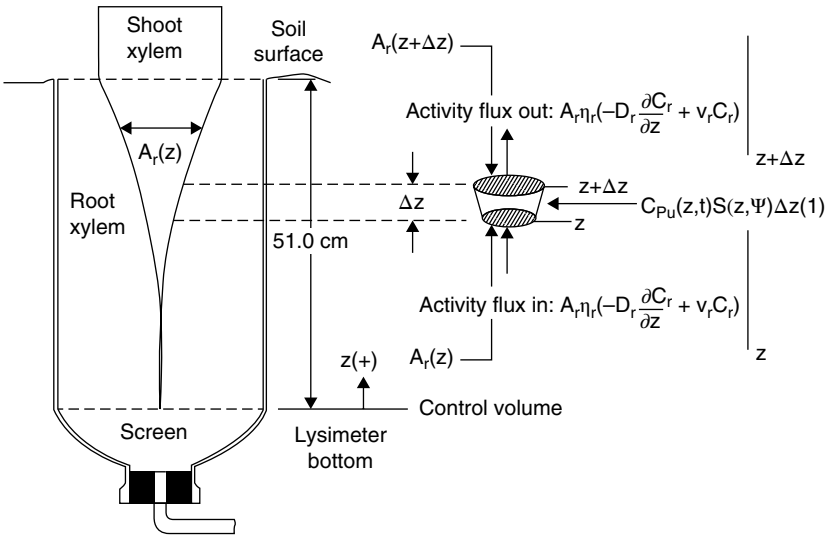

Figure A.3 Schematic representation of the conceptual model for deriving the root uptake and transport equations; Pu; $A_r(z)$, relative xylem area ($cm^2\ cm^{-2}$); z, elevation in lysimeter (cm); ηr, xylem porosity; D_r, dispersion in xylem ($cm^2\ h^{-1}$); Cr, Pu concentration ($\mu Ci\ cm^{-3}$); v_r, velocity in xylem ($cm\ h^{-1}$).

shown in Equation 13A.13. The vertical discharge velocity (average xylem linear velocity), $v_r(z,t)$, was calculated by using the xylem cross-sectional area per unit soil, $A_r(z)$ and the xylem porosity, η_r, as shown in Equation 13A.14.

$$Q_r(z,t) = \int_0^z S(z,\psi)dz \qquad (13A.13)$$

$$v_r(z,t) = \frac{Q_r(z,t)}{A_r(z)\eta_r} \qquad (13A.14)$$

Calculation of xylem cross-sectional area per unit area of soil required identification of a mean root cross-sectional area (0.0021 cm^2) and a mean fraction of xylem area (0.89%) in the literature. Combining this information with the relative root density function derived for the lysimeters yielded a xylem area versus depth function.

Fully implicit, finite-difference approximations of the root model governing equations were solved for the root activity concentration values for Pur and Puo by using a tri-diagonal algorithm for the one-dimensional, second-order, finite-difference grid system.

ACKNOWLEDGMENT

This chapter is based in part upon work supported by the U.S. Department of Energy, Office of Science, Office of Biological and Environmental Research, under Award Number DE-SC0004883.

REFERENCES

Adriano, D. C., A. C. Doswell, T. G. Ciravolo, J. E. Pinder, and K. W. McLeod (2000), Radionuclide content of selected root vegetables as influenced by culinary preparation, *Journal of Environmental Radioactivity, 49*, 307–317.

Adriano, D. C., K. W. McLeod, and T. G. Ciravolo (1986), Long-term availability of Cm and Pu to crop plants, *Health Physics, 50*, 647–651.Bar-Ness, E., Y. Hadar, Y. Chen, A. Shanzer, and J. Libman (1992), Iron uptake by plants from microbial siderophores, *Plant Physiology, 99*, 1329–1335.

Beck, C. S. (2005), *An Introduction to Plant Structure and Development: Plant Anatomy for the 21st Century*, Cambridge University Press, Cambridge, UK.

Cataldo, D. A., K. M. McFadden, T. R. Garland, and R. E. Wildung, (1988), Organic-constituents and complexation of nickel(Ii), iron(Iii), cadmium(Ii), and plutonium(IV) in soybean xylem exudates, *Plant Physiology, 86*, 734–739.

Choppin, G. R. (2003), Actinide speciation in the environment, *Radiochimica Acta, 91*, 645–649.Choppin, G. R., A. H. Bond, and P. M. Hromadka, (1997), Redox speciation of plutonium, *Journal of Radio-Analytical and Nuclear Chemistry, 219*, 203–210.

Cook, F. J., and F. M. Kelliher, (2006), Determining vertical root and microbial biomass distribution from soil samples, *Soil Science Society of America Journal, 70*, 728–735.

Curie, C., and J. F. Briat, (2003), Iron transport and signaling in plants, *Annual Review of Plant Biology, 54*, 183–206.

Curie, C., Z., Panaviene, C. Loulergue, S. L. Delaporta, J. F. Briat, and E. L. Walker (2001), Maize *yellow stripe 1* encodes a membrane protein directly involved in Fe(III) uptake, *Nature Letters*, *409*, 346–349.

Dai, M., J. M. Kelly, and K. O. Buesseler (2002), Sources and migration of plutonium in ground water at the Savannah

River Site, *Environmental Science and Technology*, *36*, 3690–3699.

Demirkanli, D. I. (2006), Modeling Long-Term Plutonium Transport in the Savannah River Site Vadose Zone. Ph.D. Dissertation, Clemson University, Clemson, SC. (www.il.proquest.com, UMI #: 3239606)

Demirkanli, D. I., F. J. Molz, D. I. Kaplan, and R. A. Fjeld (2008), A fully transient model for long-term plutonium transport in the Savannah River Site vadose zone: Root water uptake, *Vadose Zone Journal*, *7*(3), 1099–1109.

Demirkanli, D. I., F. J. Molz, D. I. Kaplan, and R. A. Fjeld (2009), Soil-root interactions controlling upward plutonium transport in variably saturated soils, *Vadose Zone Journal 8*(3), 574–585.

Demirkanli, D. I., F. J. Molz, D. I. Kaplan, R. A. Fjeld, and S. M. Serkiz, (2007), Modeling long-term plutonium transport in the Savannah River Site vadose zone, *Vadose Zone Journal*, *6*(2), 344–353.

Duff, M. C., D. B. Hunter, I. R. Triay, P. M. Bertsch, D. T. Reed, S. R. Sutton, G. Shea-Mccarthy, J. Kitten, P. Eng, S. J. Chipera, and D. T. Vaniman (1999), Mineral associations and average oxidation states of sorbed Pu on tuff, *Environ. Sci. Technol.*, *33*, 2163–2169.

Epstein, E., and J. D. Norlyn (1973), The velocities of ion transport into and through the xylem of roots, *Plant Physiology*, *52*, 346–349.

Fjeld, R. A., T. A. DeVol, R. W. Goff, M. D. Blevins, D. D. Brown, S. M. Ince, and A. W. Elzerman (2001), Characterization of the mobilities of selected actinides and fission/activation products in laboratory columns containing subsurface material from the Snake River Plain, *Nuclear Technology 135*(2), 92–108.

Fjeld, R. A., S. M. Serkiz, P. L. McGinnis, A. Elci, D. I. Kaplan, (2003), Evaluation of a conceptual model for the subsurface transport of plutonium involving surface mediated reduction of Pu(V) to Pu(IV), *Journal of Contaminant Hydrology*, *67*(1–4), 79–94.

Francis, A. J. (2007), Microbial mobilization and immobilization of plutonium*, J. Alloys & Compounds,* 444–445, 500–505.

Garland, T. R., D. A. Cataldo, and R. E. Wildung (1981), Absorption, transport, and chemical fate of plutonium in soybean plants, *Journal of Agricultural and Food Chemistry*, *29*(5), 915–920.

Geckeis, H., J. Lutzenkirchen, R. Polly, T. Rabung, and M. Schmidt (2013), Mineral-water interface reactions of actinides, *Chemical Reviews*, *113*, 1016–1062.

Giles, R. V., J. B. Evett, and C. Liu (1993), *Fluid Mechanics and Hydraulics, Schaums Outline Series*, 3rd ed., McGraw-Hill, New York.

Hixon, A. E., Y. J. Hu, D. I. Kaplan, R. K. Kukkadapu, H. Nitsche, O. Qafoku, and B. A. Powell (2010), Influence of iron redox transformations on plutonium sorption to sediments, *Radiochim. Acta*, *98*, 685–692.

Hu, Y. J., L. K. Schwaiger, C. H. Booth, R. K. Kukkadapu, E. Cristiano, D. Kaplan, H. Nitsche, (2010), Molecular interactions of plutonium(VI) with synthetic manganese-substituted goethite. *Radiochim. Acta 98*, 655–663.

John, S. G., C. E. Ruggiero, L. E. Hersman, C. S. Tung, and M. P. Neu, (2001), Siderophore mediated plutonium accumulation by Microbacterium flavescens (JG-9), *Environmental Science & Technology 35*(14), 2942–2948.

Jones, J. B., and A. Wallace. (1992), Sample preparation and determination of iron in plant tissue samples, *J. Plant Nutr.*, *15*, 2085–2108.

Kaplan, D. I., D. I. Demirkanli, L. Gumapas, B. A. Powell, R. A. Fjeld, F. J. Molz, and S. M. Serkiz (2006), Eleven-year field study of Pu migration from PuIII, IV, and VI sources, *Environmental Science & Technology*, *40*(2), 443–448.

Kaplan, D. I., D. I. Dmeirkanli, F. J. Molz, J. R. Beals, J. R. Cadieux, and J. E. Halverson (2010), Upward monument of plutonium to surface sediments during an 11-year field study, *J. of Eviron. Radioactivity*, *101*, 338–344.

Kaplan, D. I., B. A. Powell, D. I. Demirkanli, R. A. Fjeld, F. J. Molz, S. M. Serkiz, and J. T. Coates (2004), Influence of oxidation states on plutonium mobility during long-term transport through an unsaturated subsurface environment, *Environmental Science & Technology*, *38*(19), 5053–5058.

Kaplan, D. I., B. A. Powell, M. C. Duff, D. I. Demirkanli, M. Denham, R. A. Fjeld, and F. J. Molz (2007), Influence of sources on plutonium mobility and oxidation state transformations in vadose zone sediments, *Environmental Science & Technology*, *41*(21), 7417–7423.

Kaplan, D. I., B. A. Powell, L. Gumapas, J. T. Coates, and R. A. Fjeld (2006), Influence of pH on plutonium desorption/solubilization from sediment, *Env. Sci. Tech., 40*(19), 5937–5942.

Keeney-Kennicutt, W. L., and J. W. Morse, 1985. The redox chemistry of Pu(V)O2+ interaction with common mineral surfaces in dilute solutions and seawater, *Geochimica et Cosmochimica Acta*, *49*, 2577–2588.

Kersting, A. B. (2013), Plutonium transport in the environment, *Inorganic Chemistry*, *52*, 3533–3546.

Kersting, A. B., D. W. Efurd, D. L. Finnegan, D. J. Rokop, D. K. Smith, and J. L. Thompson (1999), Migration of plutonium in ground water at the Nevada Test Site, *Nature*, *397*(7), 56–59.

Kraemer, S. M., D. E. Crowley, and R. Kretzschmar (2006), Geochemical aspects of phytosiderophore-promoted iron acquisition by plants, *Advances in Agronomy*, *91*, 1–46.

Lachner, J., I. Dillmann, T. Faestermann, G. Korschinek, M. Poutivtsev, G. Rugel, C. L. von Gostomski, A. Turler, and U. Gerstmann (2012), Attempt to detect primordial ^{244}Pu on Earth, *Physical Review*, *85*(1), 1–6.

Marschner, H. (1995), *Mineral Nutrition in Higher Plants*, Academic Press limited, London, UK.

Marty, R. C., D. Bennett, and P. Thullen (1997), Mechanism of plutonium transport in a shallow aquifer in Mortandad Canyon, Los Alamos National Laboratory, New Mexico, *Environmental Science and Technology*, *31*, 2020–2027.

McNear, D. H. (2013), The rhizosphere: Roots, soil and everything in between, *Nature Education Knowledge*, *4*(3), 1–20.

Morgenstern, A., and G. R. Choppin (2002), Kinetics of the oxidation of Pu(IV) by manganese dioxide, *Radiochimica Acta*, *90*, 69–74.

Namba, K., and Y. Murata (2010), Toward mechanistic elucidation of iron acquisition in barley: Efficient synthesis of mugineic acids and their transport activities, *Chemical Record*, *10*, 140–150.

Neu, M. P. (2000), Siderophore-mediated chemistry and microbial uptake of plutonium, *Los Alamos Science*, *26*, 416–418.

Neu, M. P., H. Boukhalfa, C. E. Ruggiero, J. G. Lack, L. E. Hersman, and S. D. Reilly (2003), Microbial siderophore influence on plutonium biogeochemistry, *Journal of Inorganic Biochemistry*, *96*(1), 69–69.

Neu, M. P., C. E. Ruggiero, and A. J. Francis (2002), Bioinorganic chemistry of plutonium and interactions of plutonium with microorganisms and plants, in D. C. Hoffman, *Advances in Plutonium Chemistry, 1967–2000*, LaGrange Park, IL, Am. Nucl. Soc, Amarillo, TX University Research Alliance, pp. 169–211.

Nisbet, A. F., and S. Shaw (1994), Summary of a 5-year lysimeter study on the time-dependent transfer of ^{137}Cs, ^{90}Sr, ^{239}Pu, ^{240}Pu and ^{241}Am to crops from 3 contrasting soil types: 2. Distribution between different plant-parts, *Journal of Environmental Radioactivity*, *23*(2), 171–187

Novikov, A. P., S. N. Kalmykov, S. Utsunomiya, R. C. Ewing, F. Horreard, A. Merkulov, S. B. Clark, V. V. Tkachev, and B. F. Myasoedov (2006), Colloid transport of plutonium in the far field of the Mayak Production Association, *Russia, Science*, *314*, 638–641.

Penrose, W. R., W. L. Polzer, E. H. Essington, D. M. Nelson, and K. A. Orlandini (1990), Mobility of plutonium and americium through a shallow aquifer in a semiarid region, *Environmental Science and Technology*, *24*(2), 228–234.

Peuke, A. D., M. Rokitta, U. Zimmermann, L. Schreiber, and A. Haase (2001), Simultaneous measurement of water flow velocity and solute transport in xylem and phloem of adult plants of *Ricinus communis* over a daily time course by nuclear magnetic resonance spectrometry, *Plant Cell and Environment*, *24*(5), 491–503.

Powell, B. A., M. C. Duff, D. I. Kaplan, R. A. Fjeld, M. Newville, D. B. Hunter, P. M. Bertsch, J. T. Coates, P. Eng, M. L. Rivers, S. M. Serkiz, S. R. Sutton, I. R. Triay, and D. T. Vaniman (2006), Plutonium oxidation and subsequent reduction by Mn(IV) minerals in Yucca Mountain tuff, *Environ. Sci. Technol, 40*, 3508–3514.

Powell, B. A., R. A. Fjeld, D. I. Kaplan, J. T. Coates, and S. M. Serkiz (2004), Pu(V)O-2(+) adsorption and reduction by synthetic magnetite (Fe3O4), *Environ. Sci. Technol*., *38*, 6016–6024.

Powell, B. A., R. A. Fjeld, D. I. Kaplan, J. T. Coates, S. M. Serkiz (2005), Pu(V)O2+ adsorption and reduction by synthetic hematite and goethite, *Environ. Sci. Technol.*, *39*, 2107–2114.

Roemheld, V., and H. Marschner (1986), Evidence for a specific uptake system for iron phytosiderophore in roots of grasses, *Plant Physiology*, *80*, 175–180.

Sanchez, A. L., J. W. Murray, and T. H. Sibley (1985), The adsorption of plutonium-Iv and plutonium-V on goethite, *Geochimica Et Cosmochimica Acta*, *49*, 2297–2307.

Santschi, P. H., K. A. Roberts, and L. Guo (2002), Organic nature of colloidal actinides transported in surface water environments, *Environmental Science and Technology*, *36*, 3711–3719.

Silva, R. J., and H. Nitsche (1995), Actinide environmental chemistry, *Radiochimica Acta*, *70/71*, 377–396.

Sperry, J. S., V. Stiller, and U. G. Hacke (2003), Xylem hydraulics and the soil-plant-atmosphere continuum: Opportunities and unresolved issues, *Agronomy Journal*, *95*, 1362–1370.

Thompson, S. W. (2010), Mobility of Plutonium in Zea mays (Corn): Determination of Transport Velocities, Spatial Distribution and Correlations with Iron, Ph.D. Dissertation, Clemson University, Clemson SC (www.il.proquest.com, UMI# 3402559).

Thompson, S. W., F. J. Molz, R. A. Fjeld, and D. I. Kaplan (2012), Uptake, distribution, and velocity of organically complexed plutonium in corn (*Zea mays*), *Journal of Environmental Radioactivity*, *112*, 133–140.

Wahl, S., and P. Ryser (2000), Root tissue structure is linked to ecological strategies of grasses, *New Phytologist*, *148*, 459–471.

Whicker, F. W., T. G. Hinton, K. A. Orlandini, and S. B. Clark (1999), Uptake of natural and anthropogenic actinides in vegetable crops grown on a contaminated lake bed, *Journal of Environmental Radioactivity*, *45*, 1–12.

Xu, C., P. H. Santschi, J. Y. Zhong, P. G. Hatcher, A. J. Francis, C. J. Dodge, K. A. Roberts, C. C. Hung, and B. D. Honeyman (2008), Colloidal cutin-like substances cross-linked to siderophore decomposition products mobilizing plutonium from contaminated soils, *Environmental Science & Technology*, *42*, 8211–821.

14

Experimental and Modeling Studies of Episodic Air-Water Two-Phase Flow in Fractures and Fracture Networks

Thomas Wood[1] and Hai Huang[2]

ABSTRACT

Field tests at various scales (1 to 100 meters) demonstrate that multiphase flow in fracture networks is a highly complex and dynamic process. A series of laboratory experiments indicate that observed behaviors are largely due to the complex interplays among inertial and viscous forces, gravity, surface tension, and wettability of fracture walls, regulated by fracture intersections. The behavior of air-water two-phase flow in fractures has significant implications for contaminant transport in fractured vadose zones. Several equivalent porous-media type numerical models are discussed that have met limited success in these environments. An idealized tipping bucket model appears to mimic many aspects of the episodic dynamics. We present a physics-based modeling approach based on the volume of fluids (VOF) interface tracking method, which overcomes many computational challenges facing equivalent porous media type multiphase flow models. VOF models explicitly represent the fluid-fluid-solid contact line dynamics (advancing and receding angles) and successfully reproduce many interesting multiphase dynamics observed in both laboratory and field fracture flow experiments. Three examples illustrate the importance of a physics-based multiphase flow model for developing a better understanding of the fundamental mechanisms and their interplay that eventually leads to intriguing fluid dynamics in fractured rock systems.

14.1. INTRODUCTION

Developing robust and reliable numerical models that are representative of two-phase fluid flow in variably saturated fractured rocks has been the goal of many studies over the past several decades. Often this work has been driven by both the need to make informed decisions regarding the long-term disposition of buried waste and the need for better scientific understanding on the fate and transport of contaminants released to deep, fractured rock vadose zone environments. However, most predictive models developed so far often fail to reproduce the complex, episodic fluid flow dynamics observed in many field and laboratory fracture flow experiments at various scales, ranging from a few centimeters to ~100 m. The existing models have relied almost exclusively on the concept that the fractured rocks can be treated as some sort of continua, such as equivalent porous media, dual-porosity, or dual-permeability media. These models essentially treat the multiphase flow process as diffusion processes with lumped parameters (such as permeability tensor, hydrodynamic dispersion coefficient) obtained via various volume-averaging and homogenization methods or empirically fitting experimental data (e.g., sorption distribution coefficients). Such simplification of flow and transport processes in fractured rock networks is still widely adopted, not only simply due to our inability to fully characterize the discrete fracture network across all relevant scales and represent them in detail within a field scale model, but it is also a reflection of our limited understanding of these processes. Therefore, despite many advances in the study flow and transport processes in variably saturated fractured rocks over the past few

[1] *University of Idaho, Center for Advanced Energy Studies, Idaho Falls, Idaho, USA*

[2] *Idaho National Laboratory, Idaho Falls, Idaho, USA*

Dynamics of Fluids and Transport in Complex Fractured-Porous Systems, Geophysical Monograph 210, First Edition.
Edited by Boris Faybishenko, Sally M. Benson, and John E. Gale.

decades, there is still a great need for better understanding of the fundamental mechanisms, especially their complex interplays, that ultimately govern multiphase fluid dynamics in fractured rocks, through both well-controlled experiments and more physics-based models.

There are many examples of shortcomings in techniques available for predicting the transport of contaminants in the subsurface [*NRC*, 2000, 2001; *GAO*, 1998]. High levels of uncertainty in model results are often attributed to spatial and temporal heterogeneity and the inability of volume-averaged modeling approaches to adequately represent the full range of dynamical behavior [*Faybishenko*, 2004; *Wood et al.*, 2000a, b]. Common in many studies conducted on a wide variety of fracture rock types, is the observation that fracture networks can facilitate the deep and rapid penetration of dissolved contaminants on short temporal scales, even when the rock matrix is far from saturated [e.g., *Dahan et al.*, 1999; *Faybishenko et al.*, 2000; *Wood and Faybishenko*, 2000; *Wood, Podgorney, et al.*, 2000; *Wood, Stoner, et al.*, 2000; *Glass, Nicholl, Ramirez et al.*, 2002; *Glass, Nicholl, Pringle, et al.*, 2002; *Wood et al.*, 2004]. This common observation in laboratory experiments and field tests leads to the conclusion that this may be typical characteristic behavior of multiphase fluid flow in variably saturated fractured rocks. The question arises of how flow in individual fractures organizes to cause large-scale behavior such as increased focusing of flow with depth, preferential flow, pathway switching, and flow pulsation?

The Department of Energy at its Idaho National Laboratory (INL) has supported field-scale experiments to better understand the fluid flow and contaminant transport processes through deep fractured basalt vadose zones (Figure 14.1). Driving these efforts has been a critical need to more accurately predict contaminant travel times and concentrations from buried waste sites through a fractured basalt vadose zone to the underlying Snake River Plain aquifer [*Wood and Faybishenko*, 2000;

Figure 14.1 Locations of field test sites in Eastern Idaho shown as blue dots.

Faybishenko et al., 2000]. Field experiments began at the 100-meter scale "Large Scale Infiltration Tests" (LSIT) in 1994, followed in 1995 to 1997 by the 10-meter scale "Analog Site for Fractured Rock Characterization," and finally the 1997 to 2000 1-meter scale "Hell's Half Acre Basalt Infiltration Tests." The largest scale experiment was conducted first at the INL because, at the time, it was thought that at a sufficiently large scale of investigation, heterogeneities could be averaged out, and modeling via an equivalent porous media approach (representative elemental volume, REV) was appropriate to capture system behavior at the large scale. It became apparent that infiltration in fractured basalt was not well represented by an REV even at scales of hundreds of meters. Behavior emerged at the large scale that could not be explained by volume averaging or by the summation of small-scale phenomena. Thus, there was a need to reduce the experimental scale to allow for tighter instrumentation and closer scrutiny of multiphase flow behavior. Continuum-based diffusion models for variably saturated fractured rocks could not explain how dynamic episodic behavior at the field scale emerged from small-scale phenomena.

Wood et al. [2002, 2004, 2005] and others [*Draglila and Weisbrod*, 2004; *Glass, Nicholl, Ramirez et al*., 2002; *Glass, Nicholl, Pringle, et al*., 2002; *Glass et al*., 2003; and *Su et al.*, 1999, 2001] have conducted a number of laboratory-scale experiments to further understand the physics of unsaturated flow in fractured rock. Under well-controlled laboratory conditions these experiments suggest that the common continuum-based diffusion models may not be even applicable for such variably saturated fractured rock systems. Side-by-side comparisons of fracture network experiments with common modeling approaches has led to the conclusion that new approaches are needed to model the complex, tightly coupled processes controlling unsaturated flow in fractured rock.

In this chapter we describe a series of field experiments and the behavior that emerges from a number of ponded infiltration tests across a range of scales. This is followed by a description of laboratory experiments conducted to isolate and understand how phenomena at individual fractures organize to create typical field-scale behavior. In the final section, we describe development of a "physics-based" model that accurately represents the influence of inertia, gravity, surface tension, and wettability as water moves through fracture networks. Our modeling approach accurately represents the role of fracture intersections as flow integrators and pathway switches causing pulsed flow. This physics-based modeling approach, when linked with experimental results, enables better fundamental knowledge and understanding of the nonlinear, strongly coupled processes that ultimately determine flow and transport behaviors in deep fractured vadose zones.

14.2. EXPERIMENTS

14.2.1. Large-Scale Aquifer Pumping and Infiltration Test

An early INL experiment with the expectation to collect data at a scale sufficiently large to support prediction of field-scale contaminant fate and transport through the fractured vadose zone was the LSIT [*Wood and Norrell*, 1996]. The infiltration portion of this test consisted of a 182-meter-diameter pond that was created by a 1.5 meter-high earthen berm (see Figure 14.2) and a series of nested wells at various offsets from the center of the pond. The floor of the pond was leveled, exposing basalt over about half of the circular area, and the other half of the pond floor was cover by fine sediment filling low areas in the undulating topography of the basalt flow top. Essentially, the experiment investigated the bulk hydrologic properties on a cylinder of basalt 91 m in diameter and 61 m thick. The lower limit of the basalt volume was defined by an underlying fine-grained sedimentary layer at a depth of approximately 61 m. Infiltration of water and tracers was monitored by 67 wells and a surface geophysical array. The wells were oriented in rings starting from within the basin and radiating outward. Several characteristic well types were constructed, some instrumented with lysimeters and others with well screens for installation of transducers and to provide access for geophysical well logging. Water was pumped from the Snake River Plain Aquifer and discharged to the pond at an average flow rate of 32 L/sec for 36 days. Depth to the static water level of the aquifer in this location is approximately 183 m. Short-lived radioactive tracers were added to the pond water to serve as surrogates for radioactive waste. Water (without tracers) was pumped into the basin for six days. Then the water was spiked with both conservative (Se-75) and reactive (Sr-85 and Tb-160) tracers and the water was allowed to infiltrate subsurface as a slug of water with a constant concentration. No new water was added to the basin for 11 days until the basin was nominally "dry." Afterward, tracer-free water was again added to the basin for a period of 19 days.

Downward water movement occurred primarily within a cylinder defined by the basin; however, the infiltration did not progress as a uniform front. Neutron logging (a method for monitoring moisture content behind well casing) established that preferential and sometimes lateral flow occurred within the cylinder. Moisture changes occurred at discrete depths in wells separated by zones that were dry, indicating that water had to move laterally to get to the wells. The fastest travel times coincided with fracture zones, but not all fractures were infiltrated and some exhibited relatively slow travel times. This is undoubtedly was the result of water flowing in a complex interconnected network of

Figure 14.2 Aerial view of the aquifer pumping and infiltration test site. The basin is shown full of water just after tracers were added. Four docks extend out into the basin for access to nested wells and lysimeters. Radial lines are roads to wells at various offsets from the basin. The diameter of the basins is 182 m; for scale, several vehicles can be seen to the left of center.

fractures and rubble zones (fractured contacts between basalt flow tops and flow bottoms). The focusing of water in only a portion of the available subsurface pathways is also suggested by a low wetted porosity (~0.02) of the vadose zone. The wetted porosity was calculated by dividing the average infiltration rate during the experiment by the average wetting front travel rate. The porosity of small, vesicular basalt cores is about 0.23 [*Bishop*, 1991]. The presence of fractures and rubble zones in the vadose zone undoubtedly would increase the overall porosity of the basalt beyond this value. Thus, less than 10% of the total porosity of the vadose zone conducted the infiltrating water.

Thermal neutron logging and natural gamma logging were used to monitor water movement and track concentrations of gamma-emitting tracers during the experiment. Thermal neutron logs indicated that water reached the top of the underlying sedimentary interbed and was detected in most wells inside the basin within the first week after the initial pond filling. After the fractures became wet, using neutron logs alone to locate active fractures was less useful because the neutron logs only detect water and cannot indicate water movement. However, the natural gamma log could be used to detect tracer(s) in the active fractures after initial wetting. Interpretation of the geophysical well logs suggests that initial wetting and subsequent flow did not necessarily follow the same flow path. It is thought that clean water may have filled "dead-end" fractures before the tracers were introduced to the basin. Or alternatively, once a flow pathway became wet the pathway switched, bypassing the wetted track monitored by the well. Alternatively, active fractures were continually or intermittently flushed, allowing clean water to move past the monitoring point and tracer-containing water to flow in the fracture system and be detected by the natural gamma log. The response of the natural gamma log to changes in gamma wave activity caused by the radioactive tracers was used to locate "active" fractures. Overall, less than half of all fractures were active. The percentage of active fractures within the basalt was determined to be approximately 40%–45% of the total fractures based on core logging, downhole televiewer video logs, and by caliper logging [*Burgess*, 1995].

Nineteen of the 26 wells and lysimeters were found to contain tracer data that was sufficient to construct breakthrough curves (BTCs) for Se-75. Neither Sr-85 nor Tb-160 was detected in any well or lysimeter. Three basic types of BTCs were observed: near-symmetrical BTCs, unexpected BTCs, and bimodal BTCs [*Newman and Dunnivant*, 1995]. The near-symmetrical BTCs are similar to classical BTCs in dual-porosity media with a steep increase in concentration and a long tail. Tailing of BTCs has been reported in other studies of fracture systems [*Abelin et al*., 1991], and this type of BTC might be expected for a large-scale test of fractured rock network. An unexpected type of BTC is where the tracer concentration rapidly increases to a maximum value and then decreases. In these cases, the early time-portion of the BTC is missing and the first water arriving at the sampling location frequently contains tracer. Often the first water to be sampled contained the maximum tracer concentration. This is surprising since the tracer-free water was added to the basin six days before tracers were added, and wells and lysimeters were sampled at least once daily during the period. A first arrival of tracer to a dry sampling point or peak arrival of tracer as a first arrival of a wet sampling point may be explained by pathway switching or a change in flow pathways during the test. The third type of BTC shows a bimodal or double peak in the arrival of Se-75, not an uncommon result for flow in fractured media [*Abelin et al*., 1991]. *Tsang et al*. [1991] proposed based on results from the Streipa-3D study that the number of peaks in a multiple-peak BTC corresponds to the number of primary flow channels. Thus, one interpretation is that a bimodal BTC is the result of at least two primary flow channels. Bimodel BTCs could also be formed where flow pathway switching occurs above the sample point. The fact that BTCs for the same tracer are quite dissimilar between the different wells and lysimeters suggests that flow paths are almost certainly independent. If mixing between flow paths had occurred, the BTCs should have behaved more similarly.

Inverse numerical modeling was applied to the data set from the LSIT in order to calibrate simulations of flow and tracer transport to field results of the infiltration test [*Magnuson*, 1995]. Two hydrogeologic conceptual models were considered, both based on an equivalent porous media approach, a single porosity model where only fractures contributed to flow and a dual porosity model where the matrix and the fractures contributed to flow. A realistic suite of parameters for the fractured basalt were input into the model although the use of a large horizontal to vertical permeability ratio (500:1) in the fractured basalt portion of the domain was required in order to mimic the observed results of the infiltration test. The target rate of infiltration was 5 m/day, which was the average rate calculated from first arrival of water to wells screen immediately above the sedimentary interbed at the depth of 61 m. Reasonable matches to three BTCs for wells outside the basin and immediately above the sedimentary interbed were obtained. The symmetrical nature of the BTCs selected for calibration was attributed to the mixing of waters in the perched water body formed and flowing outward from beneath the infiltration basin. Wells within the footprint of the basin showed varied behavior, as described above, and were not considered for calibration purposes. Essentially, the conventional "equivalent porous media" modeling effort was able to match flow rates and the shape of the BTCs once the infiltrating water had moved through the basalt column and moved laterally along the underlying interbed. The ability to match BTCs and head data at the top of the interbed was probably because of the mixing and flow averaging that occurred as a perched water body developed on top of the interbed being fed by numerous dynamic fracture flow pathways. The model, however, did not match or capture the dynamical behavior observed in the unsaturated basalt beneath the basin and above the sedimentary interbed.

Data collected during the Large Scale Aquifer Pumping and Infiltration Test indicated the presence of a highly complex network of flow paths in the fractured, variably saturated basalt system. Water moved along flow pathways that occupied only a small portion of the subsurface volume and less than half of the observed fractures. Unexpected tracer BTCs suggest a change in flow pathways (switching) during the test. Although the test was highly instrumented, it still lacked sufficient resolution to identify underlying characteristics of fractured basalt to explain the flow and transport behaviors observed. The lack of a uniform explanation for the observed behavior pointed to the need for further refinement of field monitoring at a smaller field scale.

14.2.2. The Analog Site for Fracture Rock Characterization: Box Canyon

A 7 by 8–meter area bounded by a 0.5-meter-high concrete impermeable barrier was constructed at the Box Canyon site, 11 km west of the INL near Arco, Idaho. This site was the subject of many infiltration tests over a period of several years, conducted to develop tools and methods for fractured rock characterization and to improve the understanding of variably saturated flow in fractured basalt. The Box Canyon site was chosen because it is proximal to a vertical cliff along the Big Lost River, providing an exposure of the subsurface fracture system and allowing access to fractures for observation and characterization (Figure 14.3). Over the course of three years (1995–1997), 38 vertical and inclined boreholes were drilled and logged to provide geological, geophysical, geochemical, and hydrogeologic information about the

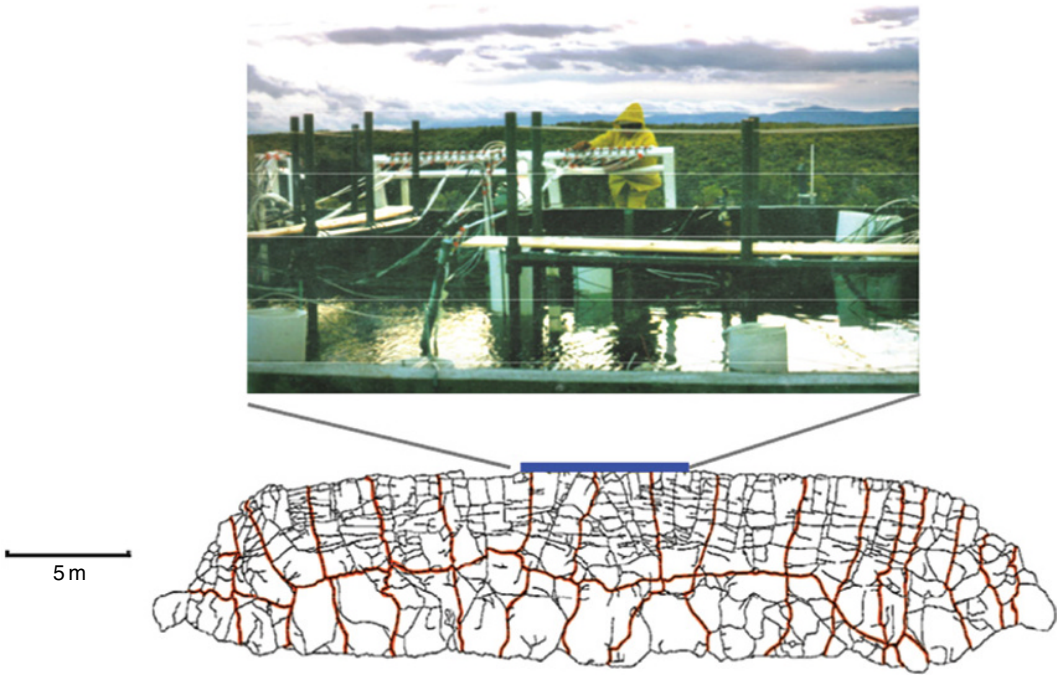

Figure 14.3 Photograph of Box Canyon infiltration pond (7 x 8–m footprint shown in blue) projected to a map of the fractures exposed on the cliff face. Note that the lava flow cooled more quickly on the upper surface and more slowly in the center. This caused a decreasing density of fractures with depth. The red lines show idealized fracture pathways that are connected across the basalt flow.

underlying fractured basalt system [*Faybishenko et al.,* 2000]. A series of ponded and fixed volume infiltration experiments were conducted using a supply of water from the Big Lost River. Preferential flow was observed when deeper tensiometers became saturated earlier than shallower ones. Evidence of pathway switching may have been obtained in some tensiometers after a period of stable water pressure during infiltration; some fractures desaturated despite the continuous operation of the infiltration test. In one test, there was a tendency for a pulse-like infiltration rate to occur. *Faybishenko et al*. [2000] hypothesized that water penetrated into horizontal fractures only if a critical hydraulic pressure was reached, at which point a hydraulic connection between the vertical fractures was established. Once a hydraulic connection was made, water began to flow through the fracture producing a rapid but short-term increase in the infiltration rate. Another observation made during the experiments was called flow funneling by the research team. This phenomenon was attributed to the fracture pattern of the dense basalt flow interiors that causes funneling of flow into progressively fewer flow paths with depth (Figure 14.3). Taken as a whole, the interpretation of the Box Canyon data by *Faybishenko et al*. [2000] was that infiltration is primarily controlled by the characteristics of the fracture system within the basalt flow, leading to strongly preferential, irregular, and "*nonrepeatable*" flow patterns in the subsurface. Flow patterns and zones of saturation were highly variable from test to test.

Doughty [2000] used an unconventional quasi-deterministic numerical approach to model the ponded infiltration test conducted at Box Canyon. The model included a highly simplified representation of the key hydrogeologic features of the fractured basalt vadose zone. The model focused on maintaining fracture network connectivity but omitted many smaller-scale details, such as aperture variation within individual fractures and a rigorous treatment of fracture/matrix interactions. The quasi-deterministic model results were generally consistent with field observations. A recurring theme of the field observations at Box Canyon is that the local lithology alone is not enough to predict what kind of response will be observed at a given point in the subsurface. Rather, *Faybishenko et al*. [2000] stated that local responses depend on the entire flow path from the surface. Under background (low infiltration rate) conditions the largest fractures are drained, leaving the highest effective permeability in the smaller fractures. Under ponded infiltration conditions the largest fractures wet up and provide the primary vertical flow paths. *Fayishenko et al*. [2000] further stated that the tributary structure of the fractures causes the liquid flow to undergo a funneling process with depth.

Unger et al. [2004] modeled the Box Canyon infiltrations using a different approach. A dual-permeability model was constructed using the TOUGH2 code to represent both the matrix and fracture continua. Wetting front arrival times in the fractured continuum were inferred from Br- samples collected from fracture-borehole intersections observed during the infiltrating tests. To calibrate the model, the authors found it necessary to multiply the fracture-matrix interfacial area by a factor between 0.1 and 0.01, using the van Genuchten and Corey relative permeability functions, to reduce imbibition of water from the fracture into the matrix. Furthermore, the porosity of the fracture continuum, as calculated using the fracture aperture inferred from pneumatic-test permeabilities, was increased by a factor of 50 yield porosity values for the upper basalt flow in the range of 0.01 to 0.02. The authors found that the fracture-continuum porosity value was a highly sensitive parameter controlling the arrival times of the simulated infiltration fronts. The matrix-continuum permeability was increased by a factor of 4.5 relative to the core measurements to reflect the influence of highly permeable vesicular zones on the field scale. Calibration had mixed success: identical calibration results were attained for fracture-continuum porosity and matrix-continuum permeability, but interfacial area varied by an order of magnitude, implying a non-uniqueness in the calibration results *or a non-uniqueness in field behavior*. *Unger et al*. [2004] stated that the fracture-continuum porosity and matrix-continuum permeability values were physically justifiable and within the range of measurement error. Flow convergence with depth as noted in the field experiments [*Faybishenko et al*., 2000] was not modeled by *Unger et al*. [2004].

We have noted flow convergence with depth, pathway switching, and pulsating flow in many different types of fracture networks [Glass, Nicholl, Pringle, et al., 2002; Glass, Nicholl, Ramirez, et al., 2002; *Wood et al*., 2004] and in numerical simulations [*La Violette et al*., 2003]. It is likely that this dynamic behavior is characteristic of unsaturated flow in fracture networks of all types and not only caused/forced by the dense flow interiors at the Box Canyon site. Despite the extensive subsurface array of wells and monitoring points at Box Canyon, the data set did not have the resolution to make it possible to clearly identify the causes of the dynamic behavior. A smaller, more tightly instrumented experiment was needed.

14.2.3. Hell's Half Acre

A 1-meter-scale field site was selected in the Hell's Half-Acre Lava Field, 50 km east of the INL (Figure 14.4). A single fracture in an overhanging ledge of basalt approximately 1-meter thick was tightly instrumented to collect a high density of data. Numerous constant head infiltration tests were conducted by ponding water in an open bottom container affixed to the upper basalt surface over the exposed fracture. A constant head was maintained in the container by means of a float valve that allowed water to enter the container from a storage vessel whenever the head dropped slightly. Beneath the basalt ledge a grid of pans was laid out so that water exiting the lower edge of the fracture was captured and conveyed to bottles hanging from weighing load cells so that the mass of water falling into a grid section was measured. Drip counters were constructed from piezo-electric stripes that generated an electrical pulse when struck by a drop of water. Over twenty drip sensors were positioned beneath drip points of the fracture so that drips could be monitored spatially and temporally. In an effort to run the test

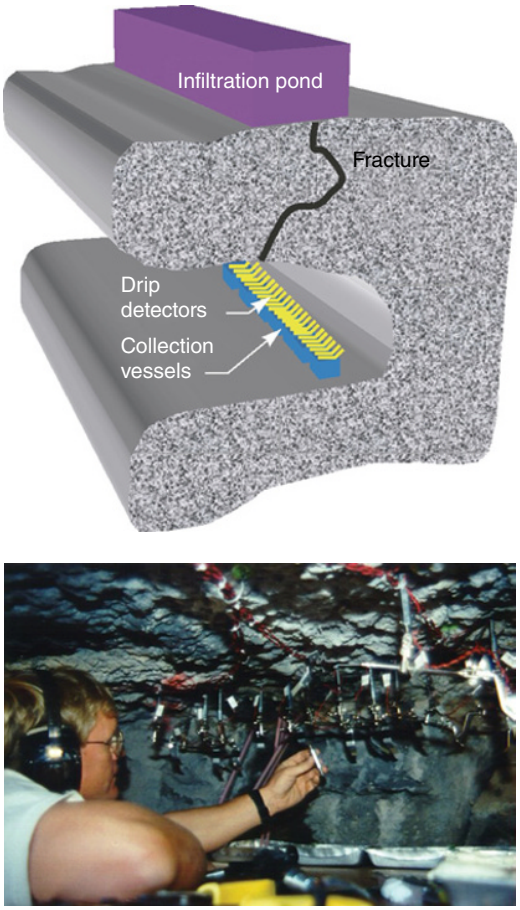

Figure 14.4 Top: Schematic of Hell's Half Acre 1-m infiltration test showing open-bottomed container affixed to an exposed fracture that penetrates an overhanging basalt ledge. Beneath the ledge are drip detectors and collection vessels. Bottom: A worker making adjustments to piezoelectric strips used for monitoring drips. The grid of metal pans is shown in the background, which collected water for determining the spatial distribution of water mass exiting the lower fracture.

until a steady state was achieved, the tests were conducted continuously for up to 20 days. In between tests the rock overhang was allowed to dry to background conditions. Under constant head conditions the tests failed to converge to a steady state in either terms of the rate of flow into the fracture (water entering the fracture spontaneously changed over time) or in the locations of drips along the bottom edge of the fracture (the location of exiting drips and frequency of drips spontaneously changed over time). Even tests conducted under identical conditions were not repeatable due to the dynamical behavior that occurred. Behavior observed included flow path switching (i.e., the drip points spontaneously changed over time) and episodic fluctuations in flow rates (i.e., the flux of water through the fracture changed up or down by a factor of 4).

Because erratic dripping is a central feature of the Hell's Half-Acre experiment, the statistical properties of the flow rate time series was examined employing a careful surrogate data algorithm [*Schreiber and Schmitz*, 2000]. The surrogate data analysis cannot reject the hypothesis that the data are stochastic. Moreover, the observed flow rates in the study are typically less than those reported to be necessary for single dripping faucet chaos. And, finally, the frequency of occurrence of drop intervals of different sizes obeys an approximate power law relationship of the form $\textit{frequency} \propto \textit{interval}^{-p}$. Such a distribution is not characteristic of serial, chaotic dripping faucets [*Peak et al.*, 2002].

Power law behavior of this kind is often symptomatic of an underlying process that lacks a characteristic length or time scale. One circumstance in which power laws can arise is when a spatio-temporal system is decomposable into a network of subsystems with a wide range of sizes. Flow in fractured rock is a natural candidate for being such a system because of the heterogeneity of fractures in basalt media. In particular, flow of liquid through channels in fractured rock can be expected to episodically turn on and off as conditions of channel wetting, channel blockage, entrapped air, and other factors vary. Such fluctuations can result in flow networks with a self-organizing character.

Peak et al. [2002] developed a simple pipe network model that captures the essence of such self-organized fluctuations. The geometry of this simple model is shown in Figure 14.5. Interesting dynamical behavior occurs in this model when the various pipes are allowed to open and close randomly as time goes on. Any fully connected path linking the top of the model to the bottom is assumed to support Poiseuille flow (the pressure is assumed to be known at all top and bottom nodes and calculable at all interior nodes via a relaxation algorithm). If the initial conditions start with a sparse set of open pipes and apply open-closed reversals fairly infrequently,

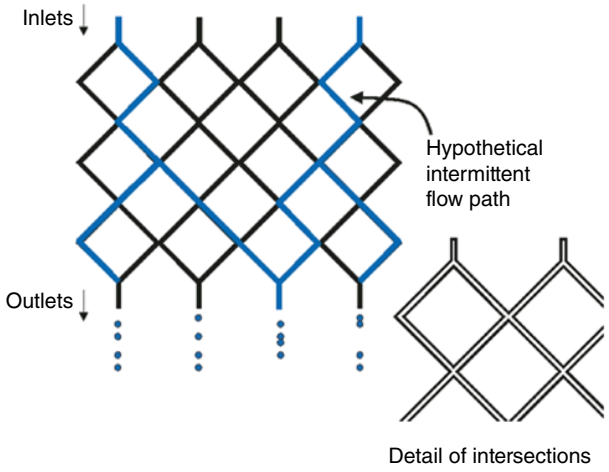

Figure 14.5 Two-dimensional simple pipe network. Various lengths of pipes are allowed to open and close randomly. Blue lines show hypothetical intermittent flow paths.

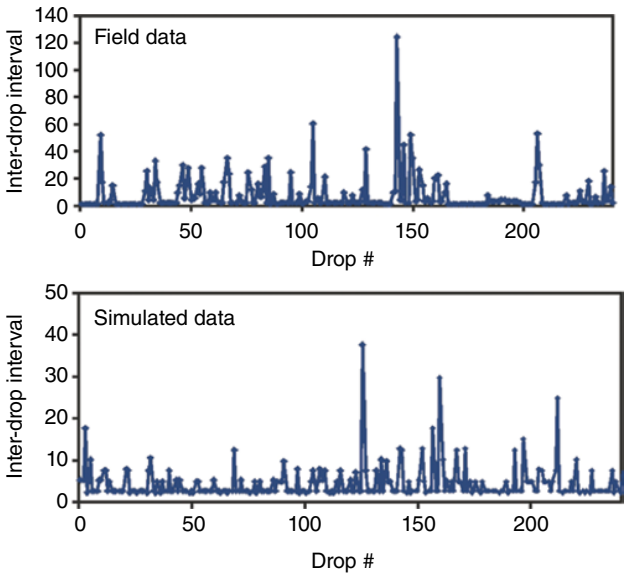

Figure 14.6 Top: Drop interval for the Hell's Half Acre data set. Bottom: Drop interval for the simple pipe network simulation. There is a qualitative agreement between the field data and the simulated data.

flow rates and drop intervals are obtained that are remarkably similar to those seen in the Hell's Half-Acre data (Figure 14.6).

Although the dynamical behavior was qualitatively described with a simple pipe network model, the triggers for opening and closing the gates to flow had not been identified. Furthermore, analyses of the data could not discount that subtle environmental changes or entrapped air

were at play and that they somehow conspired to create the unusual observed behavior. It was determined that bench scale experiments performed on carefully constructed fracture network models under laboratory conditions were required. In the laboratory changes in temperature, vibrations, fluctuations in air pressure, etc. could be controlled or monitored to help isolate and identify the triggers of the dynamic behavior observed under field conditions.

14.2.4. Fracture Network Laboratory Experiments

We constructed a well-characterized fracture network and performed a number of highly instrumented experiments to document flow behaviors [*Wood et. al*, 2004]. A series of experiments were conducted using analogue fracture networks made of limestone blocks stacked into an uncemented wall. The joints between adjacent blocks represented fractures and the limestone blocks represented a rock matrix. An automated system acquired and processed inflow, outflow, and photographic data during each of the tests. The experimental system provided continuous testing for days at a time without human intervention. Figure 14.7 is an illustration of the experimental apparatus and a comparison of wetting front advancement for various tests.

A total of eight experiments were conducted consisting of three different types of tests: (1) random stacking of blocks (Tests 1 through 3); (2) a planned stacking of blocks to focus discharge to a particular outlet (Test 4); and (3) repeated tests using the same stack of blocks (Tests 5 through 8). For all tests, mass flux and points of entry to the model were kept the same (i.e. constant, uniform flux, identical source locations, and a nominal 72-hour test duration). A constant and continuous flux of 1 mL/min was added to the top of each fracture for the

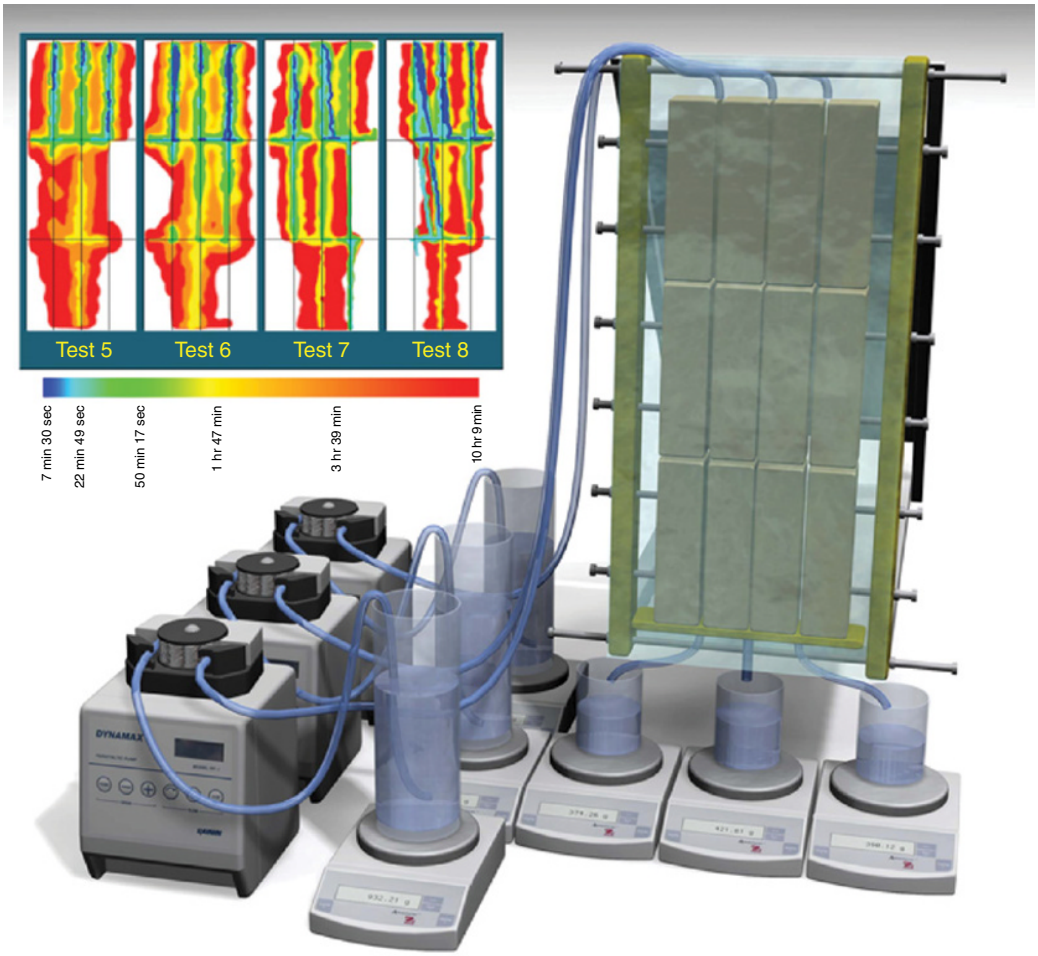

Figure 14.7 Artistic representation (lower right) of experimental system and a comparison of wetted structure development during four tests. The color images (upper left) represent the sequence of wetting development in color composite images. Individual colors (ranging from blue to red on color bar) represent the sequence of wetting at 7 min 30 sec, 22 min 49 sec, 50 min 17 sec, 1 hr 47 min, 3 hr 39 min, and 10 hr 9 min.

duration of all tests. Figure 14.8 shows the discharge rate by fracture versus time for Tests 1 through 7. In most tests there was a tendency for the discharge flow to converge with depth. We observed many instances of pathway switching where discharge from one fracture would increase at the expense of another. Examples of flow path switching can be seen to varying degree in all tests. The switching of flow from one pathway to another occurred either gradually over intervals of hundreds of minutes or abruptly over the period of a few minutes.

Time-lapse images provide a record of the advance of the wetting front through the fracture network. Figure 14.7 shows the development of the wetted structure for each test with each color representing wetted structure at each time step. Focusing of flow into the horizontal fractures and convergence to the middle vertical fracture can be seen in all tests. Variation in the pathways through the middle row of blocks is an example of nonrepeatable, dynamical behavior. Several instances were noted where a finger of water rapidly traverses a large vertical distance

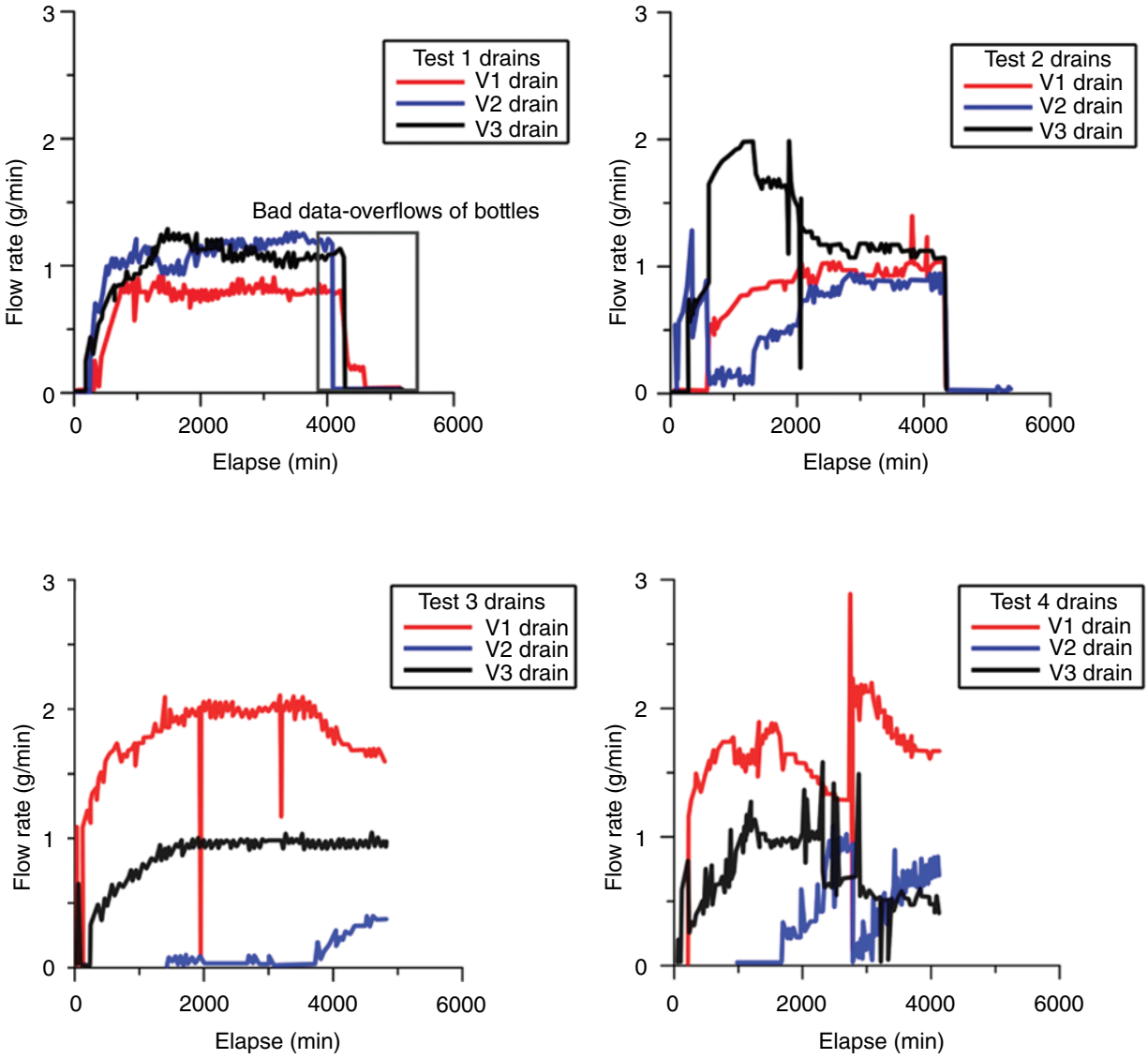

Figure 14.8 Plot of discharge versus time from uniform flux supplied to the top of three vertical fractures in a fracture network having three vertical fractures and two horizontal fractures. A total of eight experiments were conducted consisting of (1) random stacking of blocks (Tests 1 through 3), (2) a planned stacking of blocks to focus discharge to a particular outlet (Test 4), and (3) repeated tests using the same stack of blocks (Tests 5 through 7; Test 8 data was lost). (Source: *Wood et al.*, 2004, Figure 2, reproduced with permission from Alliance of Crop, Soil and Environmental Science Societies)

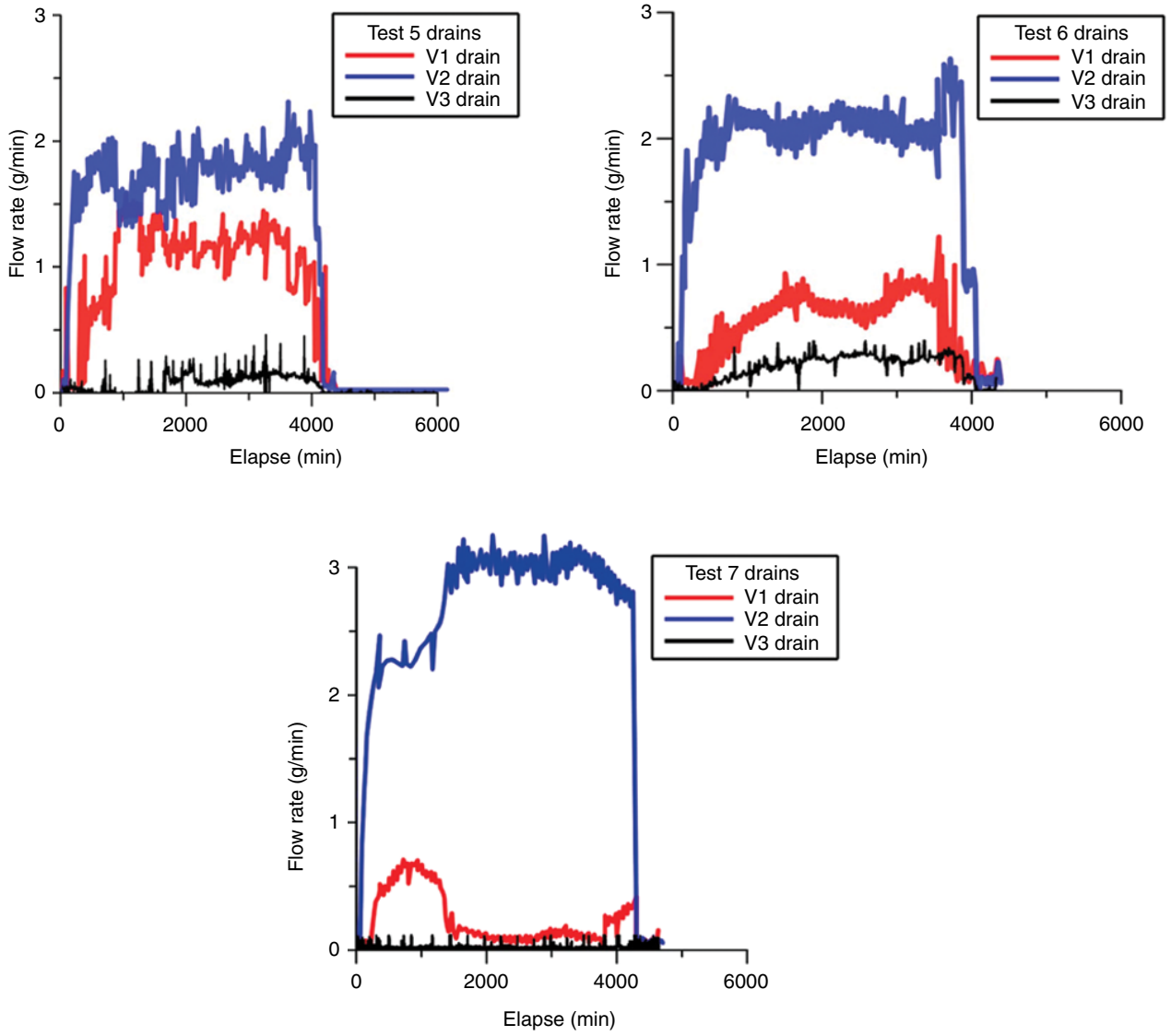

Figure 14.8 (*Continued*)

of a single fracture over a brief period of time. These events or "fluid cascades" were also documented in the experiment of *Glass, Nicholl, Pringle, et al*. [2002]. Fluid cascades are caused by the pooling above a capillary barrier created at a fracture intersection and the subsequent release of water as gravitational force breeches the capillary resistance force of the barrier.

The similarities and differences between experimental observations and behavior predicted with standard modeling approaches [*Fairley et al.*, 2004] were used to show the capabilities and limitations of conventional models in unsaturated fractured rocks. The numerical simulations of flow in the fractured-medium apparatus used three conceptual models: an equivalent continuum model with isotropic properties (iso-ECM), an ECM with anisotropic properties (aniso-ECM), and a discrete fracture model (DFM) with isotropic matrix properties and anisotropic fracture properties. To arrive at hydraulic property sets for the three models, properties were first estimated for the matrix and fracture domains of the experimental apparatus using commonly accepted techniques. Estimates of matrix properties determined from laboratory testing were used without modification. The results of this experiment are presented in Figure 14.9 in a side-by-side comparison to popular modeling approaches. It is apparent that popular modeling approaches cannot reproduce the observed behavior using realistic physical parameters [*Fairley et al*., 2004].

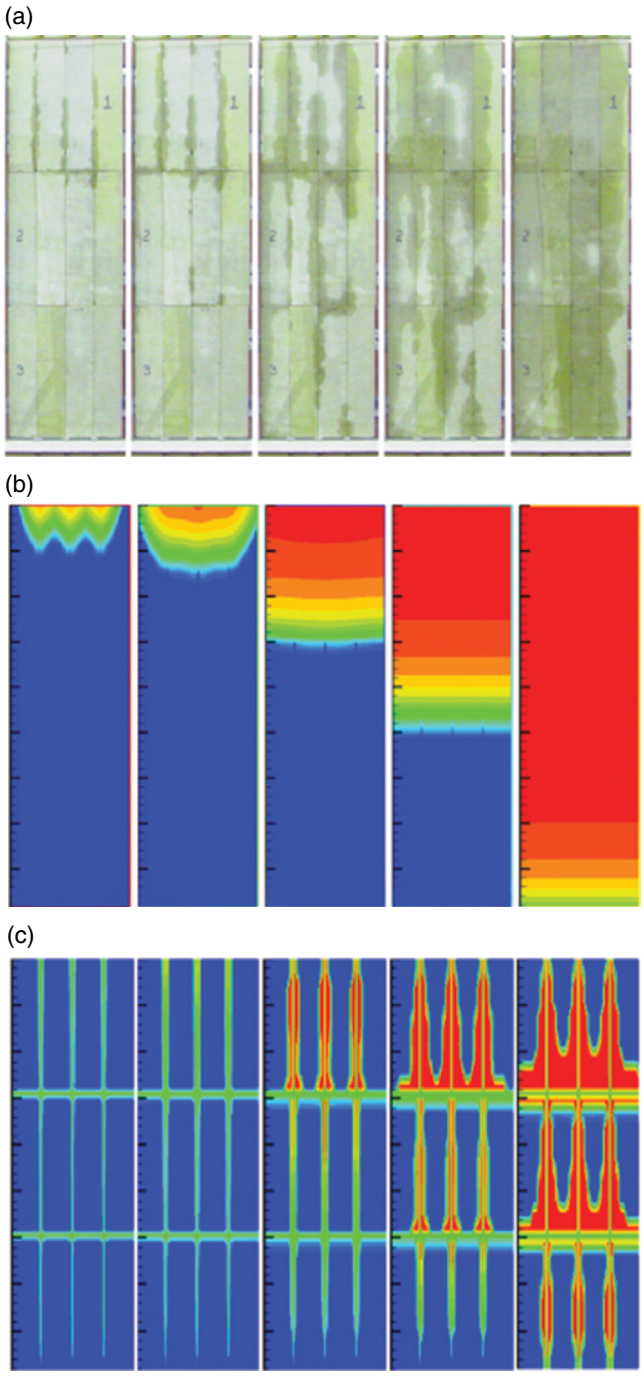

Figure 14.9 Comparison of time-lapse photographs of the experimental observations with selected simulation results, taken (from left to right) 30, 60, 180, 300 and 600 minutes after the onset of injection at the top boundary. (a) Time-lapse of one experiment showing typical behavior. (b) The ECM model results. (c) The "calibrated" DFM model results (mf = 0.8). Note, the blue color in the simulation results indicates the initial liquid saturation of the matrix (~7%) while the red indicates 100% saturation. (Source: *Fairley et al.*, 2004, Figure 2, reproduced with permission from Alliance of Crop, Soil and Environmental Science Societies)

14.2.5. Fracture Intersection Experiments

Following the fracture network experiments, a number of experiments were designed and conducted to better understand the role of fracture intersections in generating the pulsating dynamical behavior observed in field tests and bench scale experiments on unsaturated flow in fractured rock networks. We explored behavior at a simple intersection between a horizontal fracture and a vertical fracture forming an orthogonal cross [*Wood et al.*, 2002]. We also considered three perturbations to this simple geometry, including vertical and horizontal offsets of the intersection and a capillary bridge where detritus was lodged within the intersection to form a local connection [*Wood et al.*, 2005]. At low flows, the intersection formed a capillary barrier that accumulated water in a growing pool. Eventually the retaining meniscus would snap, discharging a pulse of water. The two offset intersections also acted as capillary barriers, while the third formed a capillary bridge across the intersection. At low flow, all of our experimental intersections imposed a temporal signal, with the nature of that signal dependent on intersection geometry and participation by the horizontal fractures in dynamic storage. At high flow, a continuous fluid tendril spanned the system from inlet to outlet with water pooled above the intersection caused by a narrow fluid connection that restricted flow across the intersection. Results from all experiments suggest that pulsation is critically sensitive to small variations in the geometry of fracture intersections and storage in the horizontal fractures. When combined with dependency on supply rate, this sensitivity can generate pulsation of flow across a wide range of time periods and discharge volumes [*Wood et al.*, 2005]. Figure 14.10 illustrates the fluid accumulation and discharge in an orthogonal cross intersection.

The intersection forms a capillary barrier to the slow displacement of air by water. As the fluid pressure increases, the air-water meniscus flattens and eventually invades the intersection. The capillary barrier is breached when the meniscus crosses the intersection contacting the opposite side (Figure 14.10). The pressure jump across the air-water interfaces is related to interfacial curvature by the Laplace-Young relation [*Wood et al.*, 2005]. The volume of water released during discharge (dynamic storage) is a measure of integration by the intersection. Unlike water pooled above the intersection, dynamic storage in the horizontal fractures is not limited by competition between capillary and gravity forces and may thus be substantial. Intersections may act to block downward water flow and divert flow horizontally depending on the fracture geometry.

The fracture intersection experiments demonstrate that fractures have at least two important roles: (1) temporal integrators of flow and (2) spatial integrators of pathways

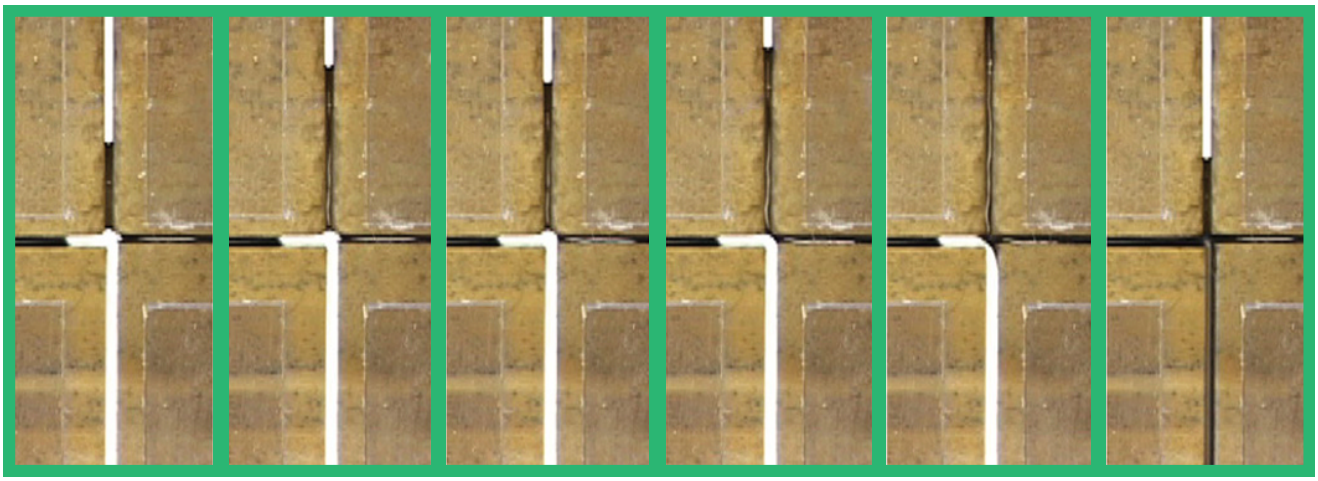

Figure 14.10 Photographic sequence of fluid accumulation and discharge in an orthogonal cross intersection over a ~40-second period at a supply rate of ~1 mL/min. Each photograph shows a 3.5-cm-high by 1.8-cm-wide region about the intersection; dark areas within the fractures are occupied by water, while the light areas are empty.

when connected together into networks. Given the behavior of intersections as maintainers and integrators of pathways, it is also expected that large-scale flow structure will tend toward global convergence with depth. Flow convergence has been identified in both field [*Faybishenko et al.*, 2000, *Wood and Podgorney*, 1999; *Wood and Faybishenko*, 2002; *Wood, Podgorney, et al.*, 2002] and laboratory experiments [*LaViolette et al.*, 2003; *LaViolette and Glass*, 2004; *Wood et al.*, 2004].

Laviolette and Glass [2003] formulated a simple model where fracture intersections can act to accumulate flow from above and to direct flow below within a network. They found that with slow, steady inflow distributed randomly along the top of the network, the system self-organizes to form avalanches of water that can penetrate to great depths. When all intersections split their outflow, flow diverges with depth and develops into a self-organized dynamical state where the distribution of avalanche sizes follows a power-law over many decades. As the fraction of intersections that direct outflow to one direction is increased, spatial structure passes from divergent through braided to a fully convergent, hierarchical flow regime where avalanche size is minimized along one-dimensional slender pathways (Figure 14.11).

Although the laboratory experimental work and the associated modeling described qualitatively a great deal of the observed dynamical behavior, we still lacked a physics-based model to describe system behaviors resulting from complex interplays among various forces. The following section describes the development of numerical models that are based on the physics of multiphase flow occurring at fracture intersections and within fracture networks.

14.3. MODELING

Efforts to develop comprehensive mechanistically based predictive models for multiphase fluid flow and contaminant transport in complex fractured systems, based primarily on the fluid flow behavior observed in experiments, have not been successful. The major barrier to progress in this direction is the complex fluid dynamics in unsaturated fracture apertures, which includes phenomena such as fluid fragmentation, coalescence cascades, highly dynamic rivulets, film flow, and temporally complex dripping (even very simple dripping systems exhibit very complex, flow rate–dependent behavior [Shaw, 1984]). The fundamental equations governing multiphase fluid flow in unsaturated fractures are the well-known Navier-Stokes equations coupled with equations describing the pressure drops across curved fluid-fluid interfaces and the dynamics of fluid-fluid-solid contact lines. One of the major challenges encountered when these equations are applied to practical problems is the difficulty of tracking dynamic interfaces with complex geometries, and these problems are particularly severe when the fluid-fluid interfaces undergo topological changes such as coalescence of droplets, bubble formation, and fluid fragmentation. Large density and viscosity ratios between liquid and gaseous phases, for example, water and air: ≈1000:1 and ≈ 100:1, respectively, also lead to difficulties in the numerical solution of the multiphase Navier-Stokes equations. The surface tension acting on the water-air interface and fluid-fluid-solid contact line dynamics add additional complexity to the physics-based modeling of multiphase flow in fractures and fracture network.

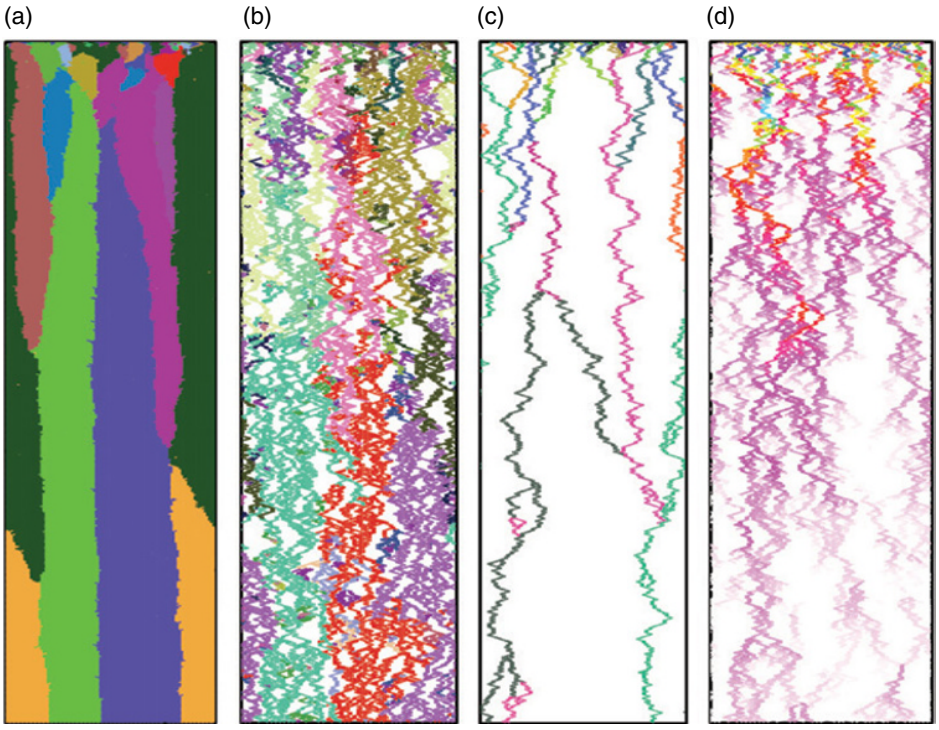

Figure 14.11 Spatial structure regimes: Avalanches are shown with color separation for (a) divergent, (b) braided, (c) convergent - 2% random, and (d) convergent - 20% random. (Source: *Glass and LaViolette*, 2004, Figure 2, reproduced with permission from John Wiley and Sons)

Over the past three decades, multiphase flow simulation has been a challenging topic in computational fluid dynamics and computational physics. In continuum models, the fluid-fluid interface is considered to be a discontinuity in fluid physical properties (density and viscosity) that moves through the computational domain. In simulations of macroscopic multiphase fluid dynamics, this approximation is justified because the thickness of the fluid-fluid interface is on the order of ~1nm. Various interface tracking algorithms have been developed for use in conjunction with finite difference, finite volume, or finite element methods in the discretized computational domain. Generally speaking, interface tracking algorithms can be divided into three main classes: front tracking/distributed force models like that introduced by *Unverdi and Tryggvason* [1992], VOF methods [*Hirt and Nichols*, 1981; *Brackbill et al.*, 1992; *Kothe et al.*, 1991] and level set methods [*Sussman et al.*, 1994, 1998]. Huang and others [*Huang, Meakin, and Li,* 2005; *Huang, Meakin, Liu, et al.*, 2005; *Huang and Meakin*, 2006, *Huang and Meakin*, 2008] are the first to apply the VOF interface tracking method to overcome all previously mentioned computational challenges. These models represent the correct fluid-fluid-solid contact line dynamics (including different advancing and receding angles), and successfully reproduce many interesting air-water two-phase dynamics in fractures and fracture networks observed in both laboratory and field fracture flow experiments mentioned earlier. In this section of the article, we present three numerical examples to illustrate the importance of a physics-based multiphase flow model for developing a better understanding of the fundament mechanisms and their interplay that eventually leads to intriguing fluid dynamics in fractured rocks.

The first example is application of the VOF method to simulate fluid flow in a fracture with a variable aperture as shown in Figure 14.12a. This example does not model any specific INL experiments, but the behavior is expected based on experiments conducted by *Nicholl and Glass* [2005]. We did, however, observe this modeled behavior in both the fracture network and fracture intersection experiments. The computational domain is 3 mm wide (horizontal) and 20 mm high (vertical), and it was discretized with a regular grid of 0.05 mm resolution along both directions. The fracture walls were generated using two cosine functions with the same wavelength but different amplitudes. The fracture aperture varies from 0.4 mm to 1.5 mm, with an average of 1 mm. This simulation used real physical properties (density, viscosity) of air and water and surface tension constant. Water was supplied via a needle of diameter 0.4 mm at a constant speed of 0.3 cm/s (approximated by prescribing the fluid velocity over the needle injection gap). Figures 14.12a through 14.12l show the simulated fluid motion over a period of 10 seconds. More

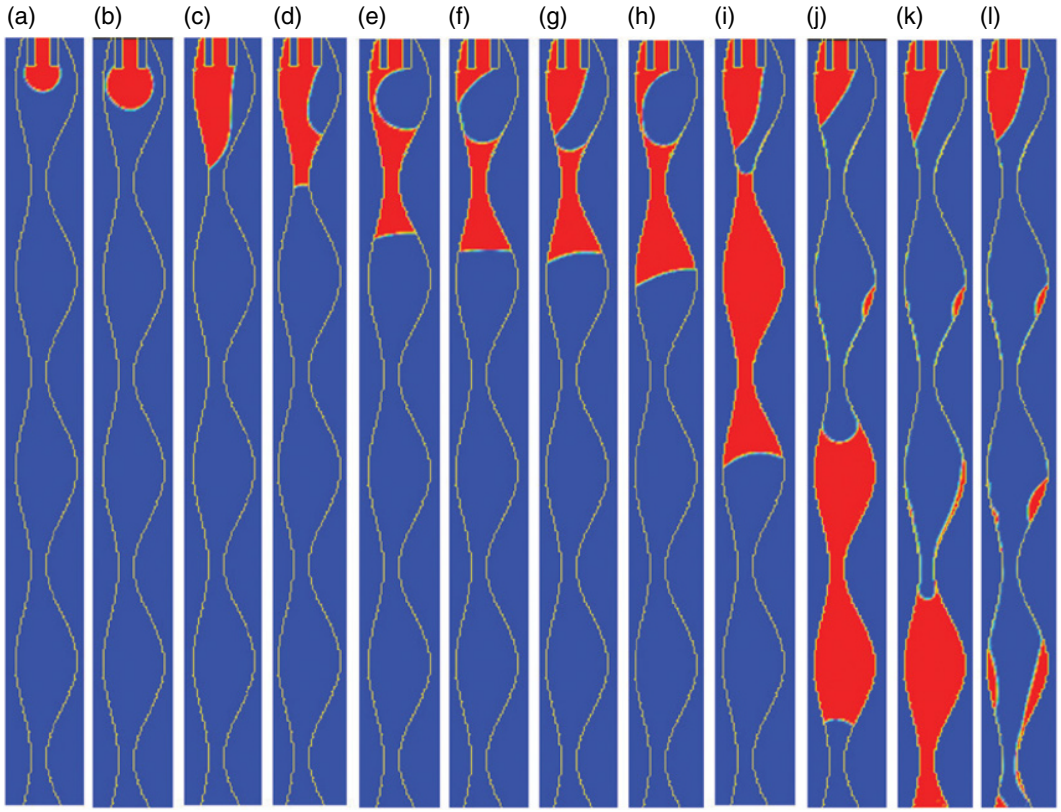

Figure 14.12 Simulated fluid motion in fracture with a constant injection rate.(a) t = 0.5 s; (b) t = 1.0 s; (c) t = 1.9 s; (d) t = 2.0 s; (e) t = 2.1 s; (f) t = 2.2 s; (g) t = 2.9 s; (h) t = 3.0 s; (i) t = 7.5 s; (j) t = 8.2 s; (k) t = 8.3 s; (l) t = 8.5 s.
(Source: *Huang, Meakin, and Liu*, 2005, Figure 5, reproduced with permission from John Wiley and Sons)

specifically, Figures 14.12a through 14.12h illustrate the simulated fluid dynamics during the first 3 seconds. The injected liquid first forms a drop at the bottom of the injection needle and the size of the drop grows steadily as a result of continuous injection of the fluid (Figures 14.12a, b). Because of surface tension, the drop has a nearly circular shape perturbed by gravity acting on the fluid density and forces associated with the flow of fluid within the drop. When the drop touches the left wall of the fracture aperture, the liquid starts to move downward along the left wall (Figure 14.12c), pulled by the wetting force. Then the downward-moving liquid becomes trapped in a narrow gap where the fracture aperture is small enough for the liquid to touch both walls (Figure 14.12d). Once the fluid touches both fracture walls, the liquid fragments (Figure 14.12e) under the influence of capillary forces and gravity, and a small liquid drop is formed and trapped (Figure 14.12f). This trapped liquid drop is called a "capillary island." Because the force of gravity acting on the small droplet is not large enough to overcome the capillary force resisting downward motion of the drop, it becomes essentially stationary. Because of the continuous injection of fluid, the upstream fluid moves downward along the left fracture wall after the first snapping-off (Figure 14.12g). Eventually it reconnects with the trapped droplet and a second fragmentation event (a second snap-off) occurs (Figure 14.12h), adding fluid to the previous trapped droplet (Figure 14.12h). Similar reconnection and snapping-off events occur repeatedly until the trapped droplet accumulates enough volume to overcome the capillary barrier and starts moving downward rapidly (Figures 14.12i–14.12l). It takes some time for the trapped drop to accumulate enough volume to overcome the capillary barrier, depending on injection rate. However, once the sliding starts, the drop moves rapidly downward within the fracture; we referred to this phenomenon as "avalanching." At the same time, the sliding liquid drop leaves behind some residual fluid, which forms a number of disconnected smaller droplets attached to the fracture walls. A new cycle then begins; however, the new cycle might not necessarily repeat exactly the previous one, due to the smaller droplets left behind by the previous cycle.

The simulated fluid dynamics illustrated in Figure 14.12 in general originate from complex interplay among gravity, inertial force, capillary force, contact angle hysteresis, and viscous force. In particular, the modeling was inspired by the experimental work of *Wood et al.* [2002, 2005]. The simulated dynamics also agree qualitatively with the behavior observed directly or indirectly in several laboratory fracture flow experiments conducted by others [*Nicholl et al.*, 1994; *Su et al.*, 1999, 2001; *Weisbrod et al.*, 1999,

2000; *Weisbrod*, 2003; *Persoff and Pruess*, 1995; *Tokunaga and Wan*, 1997; *Dragila and Weisbrod*, 2004]. Even though the fluid is injected at a constant rate, the simulated dynamics are complex and highly non-uniform and may exhibit chaotic behavior similar to that of dripping systems [*Shaw*, 1984]. Complex fluid flow behavior, like that shown in Figure 14.12, is still not well understood even in a single fracture or simple fracture network, and the impact of such non-uniform flow behavior on large-scale flow and transport in the fractured vadose zone is still poorly understood [*NRC*, 2001]. However, a full investigation of this issue is beyond the scope of this work and will be the focus of following work. In our simulation, the fragmentation and coalescence of liquid are handled well by the VOF method.

Our second numerical example is largely motivated by the fracture intersection experiments conducted by *Wood et al*. [2002, 2005], in which the authors found that fracture intersections can function as both barriers to unsaturated flow and flow integrators. Therefore, our second example is a simulation of the gravity-driven penetration of liquid through an unsaturated fracture intersection. Our results qualitatively match the experimental results. Figure 14.13a shows the computation domain and the geometry of the intersection. The intersection is slightly offset to break symmetry. The apertures of the vertical and horizontal fractures are 2 mm and 1.2 mm, respectively. The two ends of the horizontal fracture are treated as no-flow boundaries to mimic the conditions used in the experimental setup of *Wood et al*. [2002]. Parameters used for the simulation, which resemble those of water under normal conditions, include: σ = 52.8 dynes/cm; $\mu = 1.52 \times 10^{-2}$ g/(cm·s); ρ = 1.0 g/cm^3 ; and a gravitational acceleration g = 980 cm/s2. The contact angles were $\theta_a = 50°$, $\theta_r = 10°$ and $\theta_{eq} = 40°$. The liquid was supplied at a constant rate through a "needle" inserted into the top of the upper vertical fracture adjacent to the right fracture wall (see Figure 14.13a).

Figure 14.13 shows several stages in a simulation of fluid flow into an initially unsaturated fracture intersection. These stages are very similar to the behaviors observed by photographic record of a similar laboratory experiment conducted by *Wood et al*. [2005] (Figure 14.10). In the model, the injected fluid moves downward along the right wall of the fracture with a leading bulge connected by a trailing film to the injection needle (Figure 14.13a). When the meniscus reaches the intersection, the bulge swells (Figure 14.13a), because gravity acting on the fluid was not initially sufficient to drive the air-liquid-solid contact point around the corner of the intersection; it contacts the left wall, forming a pool above the intersection (Figure 14.13b). This is equivalent to Steps 1 and 2 in Figure 14.10. As more liquid is injected, the meniscus within the intersection gradually bulges out due to the increasing pressure in the liquid pool (Figure 14.13c) and eventually touches the lower left corner of the intersection (Step 3 in Figure 14.10). Then the capillary force causes

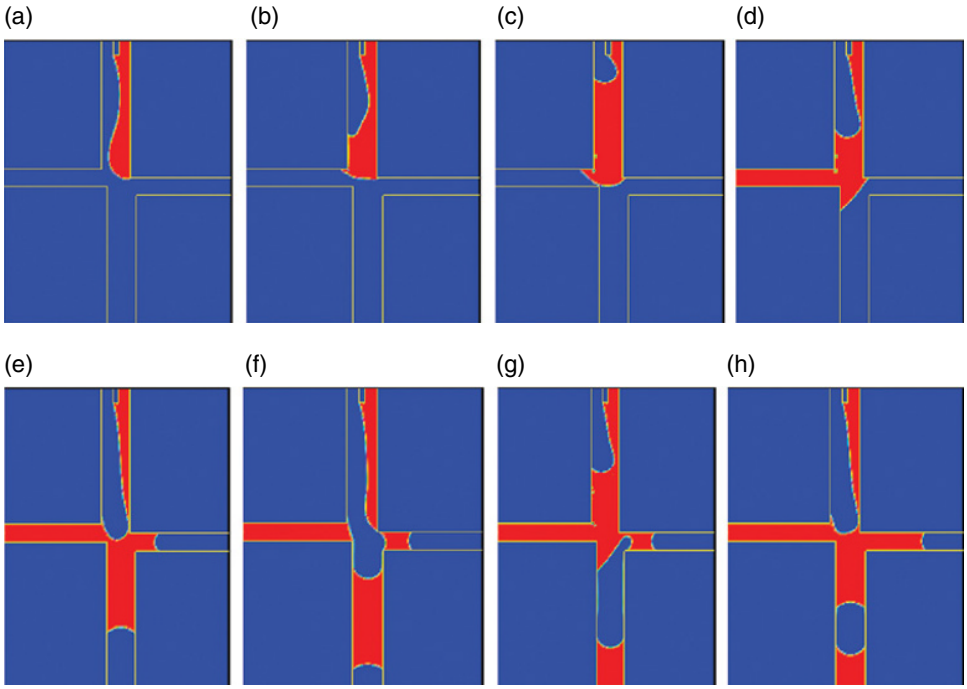

Figure 14.13 Simulated gravity-driven penetration of a wetting fluid through a fracture intersection. Time increases from (a) to (h).

liquid in the pool to rapidly move into and fill the left adjoining fracture (Figure 14.13d), similar to the physical experiment shown as Step 4, Figure 14.10. As the left fracture fills, water pools above the intersection and a portion of the hanging liquid pool moves into the intersection, causing the meniscus to move slowly downward under gravity (as in Step 5 of Figure 14.10). It finally touches the lower right corner of the intersection (Figure 14.13d), causing the liquid to move rapidly into the right fracture and the lower vertical fracture below the intersection (also shown in the physical experiment, Step 6, Figure 14.10). The intersection drains, causing the height of the liquid pool to rapidly decrease (Figure 14.13e). The liquid enters the lower vertical fracture and moves downward and exits at the bottom. Some of the fluid in the right fracture is trapped and is essentially stagnant (Figure 14.13f). Accumulation of liquid above the intersection causes the liquid in the hanging pool to connect to the trapped liquid in the right adjoining fracture, adding liquid to it (Figure 14.13g). Then the hanging liquid pool quickly saturates the intersection and moves rapidly down the vertical fracture under the influence of gravity (Figure 14.13h), emptying the intersection. A new cycle begins. The modeled behavior is very similar, but generally not identical, to the steps identified in the laboratory results presented in Figure 14.10.

Our last example is to simulate the multiphase dynamics in a small fracture network with variable apertures and a number of fracture intersections. This model was inspired by the laboratory work of *Wood et al.* [2004] (see limestone block assembly in Figure 14.7). The purpose of the model was to demonstrate that fracture intersections under the influence of capillarity and gravitational forces can act together to generate pulsed behavior to discharge from a slow steady supply of fluid. Figure 14.14a shows the computational domain and the geometry of the fracture network used in the simulation. All the fractures had an average aperture of 2 mm. The variable apertures were modeled by adding cosine perturbations with small amplitude to the flat fracture walls. The fluid properties used in this simulation were the same as those used in the previous example. The fluid was supplied at a constant rate through a needle inserted into the top of the middle vertical fracture as shown in Figure 14.14a.

The injected liquid initially exhibits dynamics like that in the previous example to invade the initially dry upper intersection and form a liquid pool above the upper intersection (Figure 14.14a) due to a capillary barrier effect. This barrier is breached when the pool accumulates enough volume and the fluid in the pool quickly enters the right horizontal fracture of the upper middle intersection (Figure 14.14b).

Once the wetting front in the horizontal fracture reaches the upper right intersection, a new capillary barrier, the liquid accumulates again in the pool above the upper intersection (Figure 14.14c), while some fluid enters the vertical fracture below the upper intersection

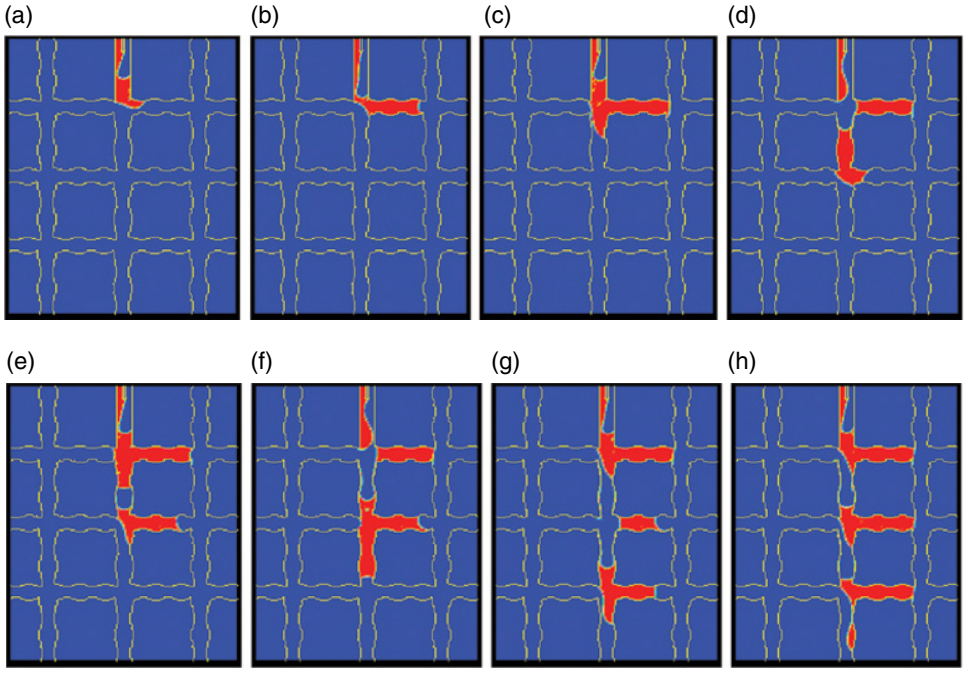

Figure 14.14 Sequential images of simulated fluid distributions during early stages of gravity-driven penetration of a wetting fluid into a small fracture network. (Source: *Huang, Meakin, and McCreery*, 2005, Figure 1, reproduced with permission from John Wiley and Sons)

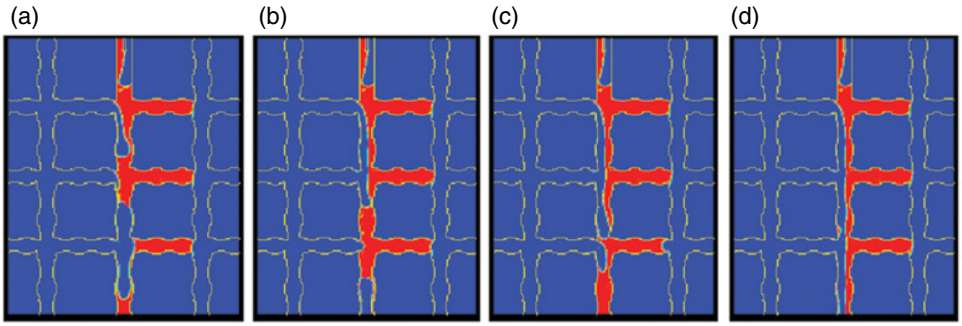

Figure 14.15 Sequential images of simulated fluid distributions during late stage of the simulation. (Source: *Huang, Meakin, and McCreery*, 2005, Figure 2, reproduced with permission from John Wiley and Sons)

due to gravity and wetting of the fracture wall. Once enough liquid accumulates, gravity pulls the liquid pool downward and the liquid pool snaps off again (Figure 14.14d). The downward-moving liquid in the vertical fracture below the upper intersection enters the middle intersection, a new barrier to flow, and repeats the dynamics of the upper intersection when it was invaded by the injected fluid for the first time (Figure 14.14e). At the same time, the injected liquid accumulates again (Figure 14.14e) and starts another cycle to invade the lower intersection (Figures 14.14f and 14.14g). The individual pulsations within all three intersections occurs repeatedly in sequence, forming the vertical ladderlike structure shown in Figure 14.14h.

During the later stages of the simulation, the unsteady dynamics was gradually replaced by a steady, nonpulsating distribution of liquid with a continuous film that conducted the injected liquid to the outlet located at the bottom, as shown in Figure 14.15. This behavior is very similar to that observed in the experiments of *Glass et al.* [2003] in which pulsating dynamics was followed by steady flow through a continuous path in a fracture network. Steady flow was also noted by *Wood et al.* [2005] at higher flow rates. Our simulation reveals in more detail that an essentially stationary distribution of liquid was first established across the upper intersection (Figure 14.15a), while the middle and lower intersections were still pulsating. The stationary behavior then extended across the middle intersection while pulsation continued at the lower intersection (Figures 14.15b and 14.15c). Eventually, the lower intersection was permanently connected to the outlet by a film (Figure 14.15h). Though not shown here, each intersection required a number of pulses before it was connected through the film to the fluid inlet and finally, a continuous, essentially stationary, liquid path connected the inlet to the outlet. In general, the network modeling work is consistent with the fracture network experiments of *Wood et al.* [2004]; however, additional modeling work is required to introduce the dynamical behavior seen in field and laboratory experiments (Figure 14.8).

14.4. CONCLUSIONS AND FUTURE WORK

Our field and laboratory observations and data document that fluid movement in variably saturated fractured networks is complex, even for very simple fracture geometries under constant boundary conditions. We conclude that these systems characteristically have behaviors that are dynamic and often not repeatable under identical initial and operating conditions. The geometry of the fractures, the geometry of the network (particularly the fracture intersections), and the influx of water to the network have important influences on the flow behavior. At the scale of one or two fracture intersections the behavior from one identical test to another is largely repeatable; however, as more fractures are involved, the network behavior becomes less repeatable and more dynamic. Even under controlled laboratory conditions, wide variations in the outcomes of tests can be expected. The variations in discharge locations and flow pathways is probably related to minute variations in air pressure, vibrations, and temperature that were too minor for our monitoring equipment to measure but large enough to affect the delicate menisci formed at air-water contacts. These small variations alter the movement of water across fracture intersections. At the field scale, because of more pervasive environmental "noise," the dynamics of the system are more pronounced and tests repeated under identical conditions are usually unique and often fail to converge to steady state conditions of flow. The body of experimental laboratory and field data presented in this article lead to the conclusion that variably saturated flow in fractured rocks is dynamic, usually exhibiting pulsation, flow pathway switching, and flow convergence with depth. This behavior is largely caused by the competition of gravitational and capillary forces active at fracture intersections and the geometry of the fracture network. The work is not complete. More well-controlled experiments at various scales are needed to develop meaningful scaling across the full range of behavior observed at the laboratory, bench, and field scales.

Significant advances have been achieved in modeling these systems, but further numerical study is needed to more quantitatively investigate the mechanisms that govern the transition of liquid flow modes within unsaturated fracture networks. In this article, we have shown that the VOF method is able to simulate complex fluid dynamics through fractures and across fracture intersections under a variety of conditions. There is a need for greater understanding of the fundamental physics governing unsaturated flow behavior at the fracture network scale. Presently numerical models that can provide physics based representation of the dynamical flow behavior at large laboratory and greater scales do not exist. This area of subsurface science continues to be a fertile area for research.

ACKNOWLEDGMENTS

Funding for this research was provided mostly by the U.S. Department of Energy through the INL Field Office over a period of two decades. We appreciate the help from a host of collaborators (too numerous to list) that have supported the work described in this report. Collaborations with the University of Idaho, Lawrence Berkley National Laboratory, and Sandia Laboratories were a critical component of many of the cited experiments. We are grateful for the review and thoughtful comments by two anonymous reviewers.

REFERENCES

Abelin, H., L. Birgersson, L. Moreno, H. Wden, T. Agren, and I. Neretnieks (1991), A large-scale flow and tracer experiment in granite: 2. Results and interpretations, *Water Resources Research*, *27*, 3119–3135.

Bishop, C.W. (1991), Hydraulic properties of vesicular basalt, M.S. Thesis, University of Arizona, Tucson, AZ.

Brackbill, J., D. B. Kothe, and C. Zemach (1992), A continuum method for modeling surface tension, *J. Comput. Phys.*, *100*, 335–354.

Burgess, J. D. (1995), Results of the neutron and natural gamma logging, stratigraphy, and perched water data collected during a large-scale infiltration test, Engineering Design File, ER-WAG7-60, INEL-95/062.

Dahan, O., R. M. Nativ, B. Adar, B. Berkowitz, and Z. Ronen (1999), Field observation of flow in a fracture intersecting unsaturated chalk, *Water Resources Research*, *35*(11), 3315–3326.

Doughty, C. (2000), Numerical model of water flow in a fractured basalt vadose zone: Box Canyon site, Idaho, *Water Resources Research*, *36*(12), 3521–3534.

Dragila, M. I., and N. Weisbrod (2004), Fluid motion through an unsaturated fracture junction, *Water Resour. Res.*, *40*, W02403, doi:10.1029/ 2003WR002588.

Fairley, J. P., R. K. Podgorney, and T. R. Wood (2004), Unsaturated flow through a small fracture–matrix network: 2. Uncertainty in modeling flow processes, *Vadose Zone J.*, *3*, 101–108.

Faybishenko, B. (2004), Nonlinear dynamics in flow through unsaturated fractured porous media: Status and perspectives, *Rev. Geophys.*, *42*, RG2003, doi:10.1029/2003RG000125.

Faybishenko, B., C. Doughty, S. Steiger, J. Long, T. Wood, J. Jacobsen, J. Lore, and P. Zawislanski (2000), Conceptual model of the geometry and physics of water flow in a fractured basalt vadose zone, *Water Resources Research*, *36*(12), 3499–3520.

General Accounting Office (GAO) (1998), Report to Congressional requesters, nuclear waste: Understanding of waste migration at Hanford is inadequate for key decisions. GAO/TCED-98-80, March 1998.

Glass, R. J., and R. A. LaViolette (2004), Self-organized spatial-temporal structure within the fractured vadose zone: Influence of fracture intersections, *Geophysical Research Letters*, *31*, L15501.

Glass, R. J., M. J. Nicholl, S. E. Pringle, and T. R. Wood, Unsaturated flow through a fracture-matrix network: Dynamic preferential pathways in meso-scale laboratory experiments, *Water Resources Research, 38*(12), 1281, doi:10.1029/2001WR001002.

Glass, R. J., M. J. Nicholl, A. L. Ramirez, and W. D. Daily (2002), Liquid phase structure within an unsaturated fracture network beneath a surface infiltration event: Field experiment, *Water Resources Research, 38*(10), 1199, doi:10.1029/ 2000wr000167.

Glass, R. J., M. J. Nicholl, H. Rajaram, and T. R. Wood (2003), Unsaturated flow through fracture networks: Evolution of liquid phase structure, dynamics, and the critical importance of fracture intersections, *Water Resources Research*, *39*(12), doi:10.1029/2003WR002015.

Hirt, C. W., and B. D. Nichols (1981), Volume of fluid method (VOF) for the dynamics of free boundaries, *J. Comput. Phys.*, *39*, 201–225.

Huang, H., and P. Meakin (2006), Reply to comment by Dani Or and Teamrat Ghezzehei on "Computer simulation of two-phase immiscible fluid motion in unsaturated complex fractures using a volume of fluid method" by Hai Huang, Paul Meakin, and Moubin Liu, *Water Resources Research*, *42*(7).

Huang, H., and P. Meakin (2008), Three-dimensional simulation of liquid drop dynamics within unsaturated vertical Hele-Shaw cells, *Water Resources Research*, *44*(3).

Huang, H., P. Meakin, and M. Liu (2005), Computer simulation of two-phase immiscible fluid motion in unsaturated complex fractures using a volume of fluid method, *Water Resources Research, 41*(12).

Huang, H., P. Meakin, M. Liu, and G. E. McCreery (2005), Modeling of multiphase fluid motion in fracture intersections and fracture networks, *Geophysical Research Letters*, *32*, L19402, doi:10.1029/2005GL023899.

Kothe, D. B., R. C. Mjolsness, and M. D. Torrey (1991), RIPPLE: A computer program for incompressible flows with free surfaces, Technical Report LA-12007-MS, LANL.

LaViolette, R. A., and R. J. Glass (2004), Self-organized spatio-temporal structure within the fractured vadose zone: The influence of dynamic overloading at fracture intersections, *Geophys. Res. Lett., 31*, L18501, doi:10.1029/2004GL020659.

LaViolette, R. A., R. J. Glass, T. R. Wood, T. R. McJunkin, K. S. Noah, R. K. Podgorney, R. C. Starr, and D. L. Stoner (2003), Convergent flow observed in a laboratory-scale unsaturated fractured system, *Geophysical Research Letters, 30*(2), 1083.

Magnuson, S. O. (1995), Inverse modeling for field-scale hydrologic and transport parameters of fractured basalt, OSTI ID:201576.

National Research Council (NRC) (2000), *Research Needs in Subsurface Science*, National Research Council, Board on Radioactive Waste Management Water Science and Technology Board, National Academy Press.

National Research Council (NRC) (2001), *Conceptual Models of Flow and Transport in the Fractured Vadose Zone*, National Academy Press, Washington, DC.

Newman, M. E., and F. M. Dunnivant (1995), Results from the large-scale aquifer pumping and infiltration test: Transport through fractured media, Engineering Design File ER-WAG 7-77, INEL-95/16.

Nicholl, M. J., and R. J. Glass (2005), Infiltration into an analog fracture: Experimental observations of gravity-driven fingering, *Vadose Zone Journal, 4*, 1123–1151.

Nicholl, M. J., R. J. Glass, and S. W. Wheatcraft (1994), Gravity-driven infiltration flow instability in non-horizontal unsaturated fractures, *Water Resources Research*, *30*(9), 2533–2546.

Peak, D., R. Datwyler, N. Rasmussen, P. Simonson, T. R. Wood, and T. Stoops (2002), Giant fluctuations in flow through fractured media: A stochastic, self-organized dynamics model, International Conference on Chaos and Non-linear Dynamics: Dynamics Days, University of Maryland, Baltimore.

Persoff, P., and K. Pruess (1995), Two-phase flow visualization and relative permeability measurement in natural rough-walled rock fractures, *Water Resour. Res., 31*(5), 1175–1186.

Schreiber, T., and A. Schmitz (2000), Surrogate time series, *Physica D: Nonlinear Phenomena*, *142*(3–4), 346–382.

Shaw, R. (1984), *The Dripping Faucet as a Model Chaotic System*, Aerial, Santa Cruz, Calif.

Su, G. W., J. T. Geller, K. Pruess, and F. Wen (1999), Experimental studies of water seepage and intermittent flow in unsaturated, rough-walled fractures, *Water Resour. Res*., *35*(4), 1019–1037.

Su, G. W., J. T. Geller, K. Pruess, and F. Wen (2001), Solute transport along preferential flow paths in unsaturated fractures, *Water Resour. Res*., *37*(10), 2481–2491.

Sussman, M., E. Fatemi, P. Smereka, and S. Osher (1998), An improved level set method for incompressible two-phase flows, *Computers & Fluids*, *27*, 663–680.

Sussman, M., P. Smereka, and S. Osher (1994), A level set approach for computing solutions to incompressible two-phase flow, *J. Comput. Phys*., *114*, 146–159.

Tokunaga, T. K., and J. Wan (1997), Water film flow along fracture surfaces of porous rock, *Water Resour. Res., 33*(6), 1287–1295.

Tsang, C. F., Y. W. Tsang, and F. V. Hale (1991), Tracer transport in fractures, analysis of field data based on a variable-aperture model, *Water Resources Research, 27*, 3095–3106.

Unger, A. J. A., B. Faybishenko, G. S. Bodvarsson, and A. M. Simmons (2004), Simulating infiltration tests in fractured basalt at the Box Canyon Site, Idaho, *Vadose Zone Journal, 3*, 75–89.

Unverdi, S. O., and G. Tryggvason (1992), A front-tracking method for viscous, incompressible, multi-fluid flows, *J. Comput. Phys., 100*, 25.

Weisbrod, N. (2003), Water vapor transport in the vicinity of imbibing saline plumes: Homogeneous and layered unsaturated porous media, *Water Resources Research*, *39*(6).

Weisbrod, N., R. Nativ, E. Adar, and D. Ronen (1999), Impact of intermittent rainwater and wastewater flow on coated and uncoated fractures in chalk, *Water Resour. Res., 35*(11), 3211–3222.

Weisbrod, N., R. Nativ, E. Adar, D. Ronen, and A. Ben-Nun (2000), Impact of coating and weathering on the properties of chalk fracture surfaces, *J. Geophys. Res., 105*(B12), 27853–27864.

Wood, T. R., and B. Faybishenko (2000), Large-scale field investigations in fractured basalt in Idaho: Lessons learned, in B. Looney and R. Falta (eds.), *Vadose Zone Science and Technology Solutions*, Battelle Press, OH, (case study to chapter 3, pp. 396–405).

Wood, T. R., R. J. Glass, T. R. McJunkin, R. K. Podgorney, R. A. LaViolette, K. S. Noah, D. L. Stoner, R. C. Starr, and K. Baker (2004), Unsaturated flow through a small fracture-matrix network: Part 1. Experimental observations, *Vadose Zone J., 3*, 90–100.

Wood, T. R., M. J. Nicholl, and R. J. Glass (2002), Fracture intersections as integrators for unsaturated flow, *Geophys. Res. Lett., 29*(24), 2191, doi:10.1029/2002GL015551.

Wood, T. R., M. J. Nicholl, and R. J. Glass (2005), Influence of fracture intersections under unsaturated, low-flow conditions, *Water Resources Research, 41*, W04017, doi:10.1029/2004WR003281.

Wood, T. R., and G. T. Norrell (1996), Integrated large-scale aquifer pumping and infiltration tests, ground water pathways OU 7-06. Rep. INEL-96/0256. Lockheed Martin Idaho Technologies Company, Idaho Falls, ID.

Wood, T. R., and R. K. Podgorney (1999), Observations of water movement in variably saturated fractured basalt and its possible implications on advective contaminant transport, Dynamics of Fluids in Fractured Rocks: Concepts and Recent Advances, International Symposium in Honor of Paul A. Witherspoon's 80th Birthday, February 10–12, 1999, Berkeley, CA.

Wood, T. R., R. K. Podgorney, and B. Faybishenko (2000), Small scale field tests of water flow in a fractured rock vadose zone, in B. Looney and R. Falta (eds.), *Vadose Zone Science and Technology Solutions*, Battelle Press, OH, (case study to chapter 3, pp. 396–405).

Wood, T. R., D. Stoner, C. Tolle, J. James, D. Peak, B. Faybishenko, and J. Crepeau (2000), Can a fractured basalt vadose zone be characterized as a complex system? *Summit 2000, Abstracts with Programs, 32*(7), Geological Society of America, Annual Meeting and Exposition, November 9–18, 2000, Reno, Nevada.

15

Simulation of THM Processes in Fractured Reservoirs

Philip H. Winterfeld and Yu-Shu Wu

ABSTRACT

We have developed a massively parallel reservoir simulator for modeling thermal-hydrological-mechanical processes in fractured and porous media. We derived, from the fundamental equations describing deformation of thermo-multiporoelastic media, a conservation equation relating mean stress, pore pressure, and temperature, and incorporated it alongside the mass and energy conservation equations of TOUGH2-MP, the basis for the simulator. In addition, rock properties, namely permeability and porosity, are functions of pore pressure and effective stress that are obtained from poroelasticity theories and correlations from the literature. The simulator formulation and numerical implementation were verified using a one-dimensional consolidation problem, which has an analytical solution, and two problems from the literature; CO_2 injection into an aquifer overlain with caprock containing a fractured zone; and an analysis of CO_2 injection and surface uplift in the water leg of a depleting gas field. For both problems from the literature, we compared our results to those from two coupled computer codes, one that simulates fluid flow and heat transport and the other that simulates rock deformation, and obtained good matches. This agreement indicates that our formulation is able to capture THM effects modeled by a coupled simulation with a more detailed handling of rock mechanics.

15.1. INTRODUCTION

THM (thermal-hydrological-mechanical) processes occur in a number of important scientific applications, including recovery from oil and gas reservoirs, geothermal energy production, nuclear waste storage, and carbon dioxide sequestration in deep saline aquifers. These processes arise in porous media that often contain fractures. In this chapter, we describe the development of a fully coupled, fully implicit THM simulator. This simulator is based on Darcy's law for multiphase flow with conservation of mass, Biot's theory of poroelasticity (including thermal effects) with conservation of momentum, and Fourier's law of heat conduction with conservation of energy. Furthermore, we utilize a multiporosity formulation that allows these THM processes to occur in porous and fractured media.

Department of Petroleum Engineering, Colorado School of Mines, Golden, Colorado, USA

Our simulator starting point is TOUGH2-MP [*Zhang et al.*, 2008], the massively parallel version of TOUGH2 [*Pruess et al.*, 1999]. TOUGH2 is a well-known numerical simulator of multicomponent, multiphase fluid and heat flow in porous and fractured media. In the TOUGH2 formulation, fluid advection is described with a multiphase extension of Darcy's law, heat flow occurs by conduction and convection, and phases are in local equilibrium. Physical properties are calculated using modules [*Pruess*, 2005; *Pruess et al.*, 1999] that are designed for specific applications, such as CO_2 sequestration in saline aquifers or geothermal reservoirs. TOUGH2 solves mass and energy balances over the simulation domain using the integral finite difference method on an unstructured grid with multiporosity media modeled using the MINC approach [*Pruess and Narasimhan*, 1985].

The geomechanical formulation is obtained by combining the geomechanical equations relating stresses and displacements to yield an equation for mean stress as a function of pore pressure and temperature, as well as an equation for volumetric strain. These equations, with

Dynamics of Fluids and Transport in Complex Fractured-Porous Systems, Geophysical Monograph 210, First Edition.
Edited by Boris Faybishenko, Sally M. Benson, and John E. Gale.

mean stress as an additional primary variable, are added to the above multiphase flow formulation. Theories of poroelasticity [*Geertsma*, 1957; *Carroll and Katsube*, 1983; *Zimmerman*, 1991] have correlated porosity to effective stress, the difference between mean stress and pore pressure, and experimental studies [*Nur and Byerlee*, 1971] have supported these relations. The dependence of permeability on porosity has had numerous investigators [*Bear,* 1972], and an early example is the Carman-Kozeny hydraulic radius model. We incorporate these dependencies of porosity and permeability into our simulator, obtained from theories of poroelasticity and empirical correlations in the literature.

The highlights of the parallel code are domain partitioning and parallel assembly and solution of the Jacobian matrix. Domains are partitioned using the METIS package [*Karypis and Kumar*, 1998]. Each processor computes Jacobian matrix elements for its own grid blocks, and exchange of information between processors using MPI (message passing interface) allows calculation of Jacobian matrix elements associated with interblock connections across domain partition boundaries. The Jacobian matrix is solved in parallel using an iterative linear solver from the Aztec package [*Tuminaro et al*. 1999]. Aztec solver options include conjugate gradient and generalized minimum residual, among others.

15.2. GEOMECHANICAL EQUATIONS

Our simulator's geomechanical equations are based on the classical theory of elasticity extended to multiporosity nonisothermal media. In the theory of elasticity, the stress-strain behavior of an isothermal elastic material is described by Hooke's law:

$$\tau = 2G\varepsilon + \lambda\left(tr\varepsilon\right)\boldsymbol{I} \tag{15.1}$$

where G is shear modulus and λ is the Lamé parameter. For isothermal fluid-filled porous rocks, the stress-strain behavior is also dependent on pore pressure, and the poroelastic version of Hooke's law is:

$$\tau - \alpha P\boldsymbol{I} = 2G\varepsilon + \lambda\left(tr\varepsilon\right)\boldsymbol{I} \tag{15.2}$$

where α is Biot's coefficient [*Biot and Willis*, 1957]. *Bai et al*. [1993] present a generalization of Hooke's law for a multiporosity medium, a common example of which is the double-porosity medium consisting of a network of fractures and rock matrix:

$$\tau - \sum_j \alpha_j P_j \boldsymbol{I} = 2G\varepsilon + \lambda\left(tr\varepsilon\right)\boldsymbol{I} \tag{15.3}$$

where subscript j refers to a multiporosity continuum such as fracture or matrix. Expressions for the generalized Biot's coefficients, α_j, for a double-porosity medium have been presented by *Wilson and Aifantis* [1982]:

$$\begin{aligned} \alpha_1 &= 1 - \frac{K}{K_*} \\ \alpha_2 &= \frac{K}{K_*}\left(1 - \frac{K_*}{K_s}\right) \end{aligned} \tag{15.4}$$

where K is bulk modulus, K_s is the solid modulus, K_* is the modulus of the porous medium without the fractures, subscript 1 refers to the fractures, and subscript 2 refers to the matrix.

For an elastic material subject to changes in both temperature and stress, the theory of thermoelasticity assumes the resulting strain is the sum of the thermal strain and the stress-caused strain. This theory is mathematically analogous to poroelastic theory [*Norris*, 1992]. For a thermo-poroelastic medium, a porous medium subject to changes in both temperature and stress [*McTigue*, 1986], the pore pressure and thermal strain terms both appear in Hooke's law as:

$$\tau - \alpha P\boldsymbol{I} - 3\beta K\left(T - T_{ref}\right)\boldsymbol{I} = 2G\varepsilon + \lambda\left(tr\varepsilon\right)\boldsymbol{I} \tag{15.5}$$

where T_{ref} is reference temperature for a thermally unstrained state, and β is linear thermal expansion coefficient.

We obtain Hooke's law for a thermo-multiporoelastic medium by adding the Equation 15.5 temperature term to Equation 15.3 for each multiporosity continuum. In addition, since the linear thermal expansion coefficient and bulk modulus apply to the overall porous medium, we weight each multiporosity continuum temperature term by the multiporosity continuum volume fraction, ω_j:

$$\tau - \left[\sum_j \left(\alpha_j P_j + 3\beta K\omega_j\left(T_j - T_{ref}\right)\right)\right]\boldsymbol{I} = 2G\varepsilon + \lambda\left(tr\varepsilon\right)\boldsymbol{I} \tag{15.6}$$

Two other fundamental relations in the theory of linear elasticity are the definition of the strain tensor, in terms of the displacement vector, $\boldsymbol{u}$:

$$\varepsilon = \frac{1}{2}\left(\nabla\boldsymbol{u} + \nabla\boldsymbol{u}^t\right) \tag{15.7}$$

and the static equilibrium equation:

$$\nabla\cdot\tau + \boldsymbol{F}_b = 0 \tag{15.8}$$

where $\boldsymbol{F}_b$ is the body force. We combine Equations 15.6–15.8 to obtain the thermo-multiporoelastic Navier equation:

$$\begin{aligned} &\nabla\left[\sum_j \left(\alpha_j P_j + 3\beta K\omega_j T_j\right)\right] + \left(\lambda + G\right)\nabla\left(\nabla\cdot\boldsymbol{u}\right) \\ &+ G\nabla^2\boldsymbol{u} + \boldsymbol{F}_b = 0 \end{aligned} \tag{15.9}$$

We take the divergence of Equation 15.9 to yield

$$\nabla^2\left[\sum_j\left(\alpha_j P_j + 3\beta K\omega_j T_j\right)\right] + \left(\lambda + 2G\right)\nabla^2\left(\nabla\cdot\boldsymbol{u}\right) + \nabla\cdot\boldsymbol{F}_b = 0 \tag{15.10}$$

The divergence of the displacement vector is the sum of the normal strain components, the volumetric strain:

$$\nabla\cdot\boldsymbol{u} = \frac{\partial u_x}{\partial x} + \frac{\partial u_y}{\partial y} + \frac{\partial u_z}{\partial z} = \varepsilon_{xx} + \varepsilon_{yy} + \varepsilon_{zz} = \varepsilon_v \tag{15.11}$$

The trace of the stress tensor is an invariant, having the same value for any coordinate system. We obtain the following by taking the trace of Equation 15.6, Hooke's law for a thermo-multiporoelastic medium:

$$K\varepsilon_v = \tau_m - \sum_j\left(\alpha_j P_j + 3\beta K\omega_j\left(T_j - T_{ref}\right)\right) \tag{15.12}$$

where τ_m is mean stress, the average of the normal stress components.

Finally, combining Equations 15.10–15.12 yields an equation relating mean stress, pore pressures, temperatures, and body force:

$$\frac{3\left(1-\upsilon\right)}{1+\upsilon}\nabla^2\tau_m + \nabla\cdot\boldsymbol{F}_b - \frac{2\left(1-2\upsilon\right)}{1+\upsilon}\nabla^2\left[\sum_j\left(\alpha_j P_j + 3\beta K\omega_j T_j\right)\right] = 0 \tag{15.13}$$

Equations 15.12 and 15.13 are the governing geomechanical equations for our simulator, and mean stress and volumetric strain are the geomechanical variables associated with those equations. Equation 15.13 is a momentum conservation equation that depends on mean stress and other variables, and Equation 15.12 is a property relation that relates volumetric strain to mean stress and other variables.

15.3. SIMULATOR CONSERVATION EQUATIONS

The simulator conservation equations are based on the TOUGH2 formulation [*Pruess et al.,* 1999] of mass and energy balance equations that describe fluid and heat flow in general multiphase, multicomponent, multiporosity systems. Fluid advection is described with a multiphase version of Darcy's law; in addition, there is diffusive mass transport in all phases. Heat flow occurs by conduction and convection, the latter including sensible as well as latent heat effects. The description of thermodynamic conditions is based on the assumption of local equilibrium of all phases. Fluid and formation parameters can be arbitrary nonlinear functions of the primary thermodynamic variables. We modify this formulation to include geomechanics. In addition to the mass and energy balance equations, we solve a momentum balance equation for mean stress that was derived in the previous section, we add mean stress to the primary thermodynamic variables, and we add volumetric strain to the calculated properties. The conservation equations for mass, momentum, and energy can be written in differential form as:

$$\frac{\partial M^k}{\partial t} = \nabla\cdot\boldsymbol{F}^k + q^k \tag{15.14}$$

where M^k is conserved quantity k per unit volume, q^k is source or sink per unit volume, and $\boldsymbol{F}^k$ is flux.

Mass per unit volume is a sum over phases:

$$M^k = \phi\sum_l S_l\rho_l X_l^k \tag{15.15}$$

where ϕ is porosity, S is phase saturation, ρ is mass density, and X is mass fraction of component k. Energy per unit volume accounts for internal energy in rock and fluid and is the following:

$$M^{N+1} = \left(1-\phi\right)C_r\rho_r T + \phi\sum_l S_l\rho_l U_l \tag{15.16}$$

where ρ_r is rock density, C_r is rock specific heat, T is temperature, U is phase-specific internal energy, and N is the number of mass components.

Advective mass flux is a sum over phases:

$$\boldsymbol{F}_{adv}^k = \sum_l \boldsymbol{F}_l X_l^k \tag{15.17}$$

and phase flux $\boldsymbol{F}_l$ is given by the multiphase version of Darcy's law:

$$\boldsymbol{F}_l = -k\frac{k_{rl}\rho_l}{\mu_l}\left(\nabla P + \nabla P_{c,l} - \rho_l\boldsymbol{g}\right) \tag{15.18}$$

where k is absolute permeability, k_r is phase relative permeability, μ is phase viscosity, P is pore pressure, P_c is phase capillary pressure, and $\boldsymbol{g}$ is gravitational acceleration. Capillary pressure is relative to a reference phase, which is the gaseous phase. Diffusive mass flux is given by:

$$\boldsymbol{F}_{dis}^k = \sum_l \rho_l D_l^k \nabla X_l^k \tag{15.19}$$

where D_l^k is the effective diffusivity. Energy flux includes conductive and convective components:

$$\boldsymbol{F}^{N+1} = -\lambda\nabla T + \sum_l h_l\boldsymbol{F}_l \tag{15.20}$$

where λ is thermal conductivity and h_l is phase l specific enthalpy.

The momentum balance equation (Equation 15.13) can be written as the divergence of a momentum flux:

$$\nabla \cdot \left[\frac{3(1-\upsilon)}{1+\upsilon} \nabla \tau_m + \boldsymbol{F}_b - \frac{2(1-2\upsilon)}{1+\upsilon} \nabla \left[\sum_j \left(\alpha_j P_j + 3\beta K \omega_j T_j \right) \right] = 0 \right] \tag{15.21}$$

Momentum per unit volume is small compared to momentum flux and has been neglected in our formulation.

15.4. MULTIPOROSITY FLOW MODEL

Flow in multiporosity media is modeled using the MINC approach [*Pruess and Narasimhan*, 1985]. The MINC approach is a generalization of the double-porosity concept, originally developed by *Barenblatt et al.* [1960] and *Warren and Root* [1963] among others, to multiple porous continua. The double-porosity approach is used to describe fluid flow in fractured reservoirs, an idealization of which is shown in Figure 15.1. In these reservoirs, the fractures have larger permeability and smaller porosity relative to those of the porous rock matrix. As a result, a pressure change in the reservoir would travel through the fractures much faster than through the rock matrix. The double-porosity approach assumes that global fluid and heat flow occur mostly through the fractures with a quasi-steady exchange between the fractures and matrix that is dependent on pressure and temperature differences between them.

For many systems, such as those with complex, multiphase flow or large matrix volumes, the assumption of quasi-steady exchange between the fractures and matrix is not a good one because the timescale associated with flow through the matrix is too large. We use the MINC approach to describe flow in these systems. In the MINC approach, flow within the matrix is described more accurately by subdividing the matrix into nested volumes, as shown in Figure 15.2, with flow occurring between adjacent nested matrix volumes as well as between the fractures and the outer matrix volume. Flow within the matrix is one-dimensional and transient and the MINC approach reduces to the double-porosity one if there is only one matrix subdivision.

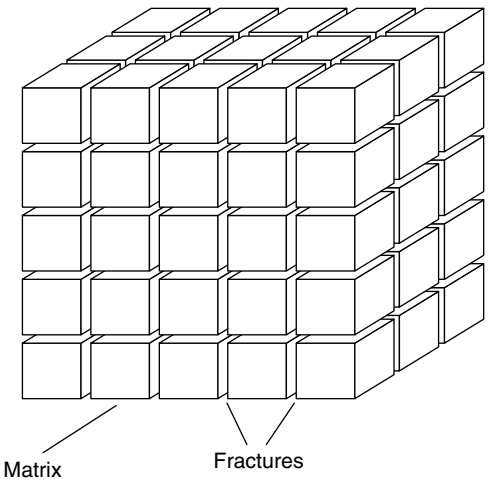

Figure 15.1 Idealized double porosity model of a fractured reservoir showing fractures and matrix blocks, adapted from *Pruess et al*. [1999].

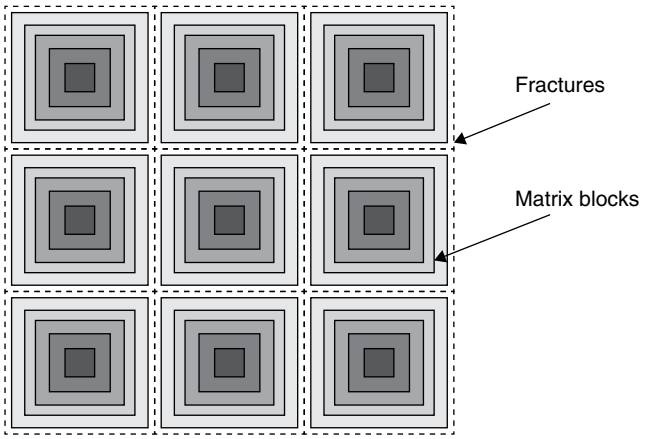

Figure 15.2 Idealized MINC grid showing fractures and nested matrix volumes, adapted from *Pruess et al*. [1999].

15.5. DISCRETIZATION OF CONSERVATION EQUATIONS

15.5.1. Integral Finite Difference Method

The simulator mass, energy, and momentum balance equations are discretized in space using the integral finite difference method [*Narasimhan and Witherspoon*, 1976]. In this method, the simulation domain is subdivided into grid blocks and the conservation equations (Equation 15.14) are integrated over grid block volume V_n with flux terms expressed as an integral over grid block surface Γ_n using the divergence theorem:

$$\frac{d}{dt} \int_{V_n} M^k dV = \int_{\Gamma_n} \boldsymbol{F}^k \cdot \boldsymbol{n} d\Gamma + \int_{V_n} q^k dV \tag{15.22}$$

Volume integrals are replaced with volume averages:

$$\int_{V_n} M^k dV = M_n^k V_n \tag{15.23}$$

and surface integrals with discrete sums over surface averaged segments:

$$\int_{\Gamma_n} \boldsymbol{F}^k \cdot \boldsymbol{n} d\Gamma = \sum_m A_{nm} F_{nm}^k \tag{15.24}$$

where subscript n denotes an averaged quantity over volume V_n, A_{nm} is the area of a surface segment common to volumes V_n and V_m, and double subscript nm denotes an averaged quantity over area A_{nm}. The definitions of the geometric parameters used in this discretization are illustrated in Figure 15.3.

The integrals in Equations 15.22–15.24 apply to a fixed grid block geometry. Because volumetric strain is a variable in our geomechanical formulation, grid block volumes as well as grid block distances and areas are no longer fixed. We introduce volumetric strain dependence into the volumes, areas, and distances that arise when these integrals are evaluated. These dependencies are based on the definition of volumetric strain:

$$V_n\left(\varepsilon_{v,n}\right) = V_{n,0}\left(1-\varepsilon_{v,n}\right) \tag{15.25}$$

where $V_{n,0}$ is grid block n volume at zero strain and $\varepsilon_{v,n}$ is grid block n average volumetric strain. Changes in volumetric strain also cause changes in grid block areas and distances. We account for these by first defining analogs of Equation 15.25 for areas and distances (A and D) in terms of average area and distance strains (ε_A and ε_D):

$$A_{nm}\left(\varepsilon_{A,nm}\right) = A_{nm,0}\left(1-\varepsilon_{A,nm}\right) \tag{15.26}$$

and:

$$D_n\left(\varepsilon_{D,n}\right) = D_{n,0}\left(1-\varepsilon_{D,n}\right) \tag{15.27}$$

where $\varepsilon_{A,nm}$ is the average of area strains $\varepsilon_{A,n}$ and $\varepsilon_{A,m}$. Substituting Equation 15.25 into the volume integral (Equation 15.23) yields:

$$\int_{V_n} M^k dV = M_n^k V_{n,0}\left(1-\varepsilon_{v,n}\right) \tag{15.28}$$

and substituting Equation 15.26 into the surface integral (Equation 15.24) yields:

$$\int_{\Gamma_n} \boldsymbol{F}^k \cdot \boldsymbol{n} d\Gamma = \sum_m A_{nm,0}\left(1-\varepsilon_{A,nm}\right) F_{nm}^k \tag{15.29}$$

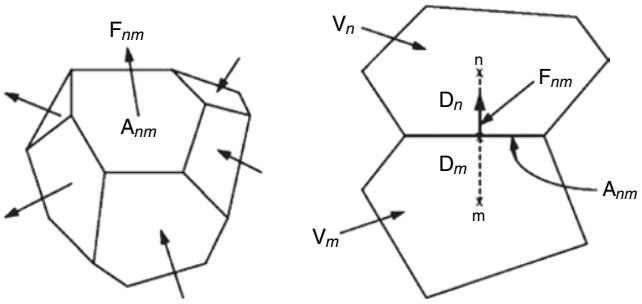

Figure 15.3 Parameter definitions for the integral finite difference method, adapted from *Pruess et al.* [1999].

Next, we relate area and distance strains to volumetric strain. Because our geomechanical formulation is in terms of volumetric strain only, we must make an assumption to do this. Two assumptions are isotropic and uniaxial volumetric strain. For isotropic volumetric strain, area strain and volumetric strain are related by:

$$\left(1-\varepsilon_v\right) = \left(1-\varepsilon_A\right)^{\frac{3}{2}} \tag{15.30}$$

and since strains are small:

$$\varepsilon_{\mathrm{A}} \approx \frac{2\varepsilon_{\mathrm{v}}}{3} \tag{15.31}$$

Distance strain and volumetric strain are related by:

$$\left(1-\varepsilon_{\mathrm{v}}\right) = \left(1-\varepsilon_D\right)^3 \tag{15.32}$$

and since strains are small:

$$\varepsilon_{\mathrm{D}} \approx \frac{\varepsilon_{\mathrm{v}}}{3} \tag{15.33}$$

For uniaxial volumetric strain, distance strain in the strain direction would be equal to volumetric strain and distance strain in other directions would be zero; area strain in the strain direction would be zero and area strain in the other directions would be equal to volumetric strain.

15.5.2. Discretized Mass and Energy Conservation Equations

In the MINC approach, mass and energy conservation apply to each matrix nested volume and the fracture volume. We apply the integral finite difference method to the multiporosity mass and energy conservation equations by integrating over such a porous continuum volume and replacing the time derivative by the standard first-order finite difference approximation to obtain:

$$\begin{aligned}&\left[M_{j,n}^k\left(1-\varepsilon_{v,n}\right)\right]^{l+1} - \left[M_{j,n}^k\left(1-\varepsilon_{v,n}\right)\right]^{l} - \frac{\Delta t}{V_{j,n,0}} \\ &\left[\sum_m A_{nm,0}\left(1-\varepsilon_{A,nm}\right)F_{j,nm}^k + V_{j,n,0}\left(1-\varepsilon_{v,n}\right)q_{j,n}^k\right]^{l+1} = 0\end{aligned} \tag{15.34}$$

where $V_{j,n,0}$ is zero strain volume of porous continuum j in grid block n.

The approximation to the advective mass flux for component k used in the integral finite difference method is the following:

$$\begin{aligned}&A_{nm}F_{nm}^k = \sum_l -k_{nm}\left[\frac{k_{rl}\rho_l X_{lk}}{\mu_l}\right]_{nm} \\ &\left[\frac{P_n - P_m + P_{cl,n} - P_{cl,m}}{D_{n,0}\left(1-\varepsilon_{D,n}\right) + D_{m,0}\left(1-\varepsilon_{D,m}\right)} - \rho_{l,nm}g_{l,nm}\right] \\ &A_{nm,0}\left(1-\varepsilon_{A,nm}\right)\end{aligned} \tag{15.35}$$

where g_{nm} is the component of gravitational acceleration pointing between grid block n and grid block m. The pressure and capillary pressure gradient terms in Equation 15.18 are approximated as their difference divided by grid block distances (D_n and D_m) that depend on distance strain. Analogous expressions can also be obtained for energy and diffusive mass fluxes.

15.5.3. Discretized Momentum Conservation Equation

In the MINC approach, momentum conservation applies to each grid block volume containing the nested matrix volumes and the fracture volume. We apply the integral finite difference method to the multiporosity momentum conservation equation by integrating over a grid block volume, replacing the time derivative by the standard first-order finite difference approximation, and approximating gradients as a difference divided by grid block distances that depend on distance strain to obtain:

$$\sum_m \left[\begin{array}{l} \left(\frac{3(1-\upsilon)}{(1+\upsilon)}\right)_{nm} \frac{\tau_n - \tau_m}{D_{n,0}\left(1-\varepsilon_{D,n}\right) + D_{m,0}\left(1-\varepsilon_{D,m}\right)} + \left(\boldsymbol{F}_b \cdot \boldsymbol{n}\right)_{nm} - \\ \left(\frac{2(1-2\upsilon)}{(1+\upsilon)}\right)_{nm} \sum_j \left(\begin{array}{l} \alpha_j \frac{P_{j,n} - P_{j,m}}{D_{n,0}\left(1-\varepsilon_{D,n}\right) + D_{m,0}\left(1-\varepsilon_{D,m}\right)} + \\ \left(3\beta K \omega_j\right)_{nm} \frac{T_{j,n} - T_{j,m}}{D_{n,0}\left(1-\varepsilon_{D,n}\right) + D_{m,0}\left(1-\varepsilon_{D,m}\right)} \end{array} \right) \end{array} \right] A_{nm,0}\left(1-\varepsilon_{A,nm}\right) = 0 \tag{15.36}$$

where the double subscript *j,n* denotes porous continuum j in grid block n.

15.5.4. Momentum Conservation Equation Boundary Conditions

The momentum conservation equation is the divergence of a momentum flux, and applying the integral finite difference method to it yields an integral of momentum flux over the grid block surface that is approximated as a discrete sum over surface averaged segments. Grid block surface segments are common to another grid block or border the surroundings. The Equation 15.36 summation term as is applies to surface segments that are common to another grid block. For grid block surface segments that border the surroundings, we modify that term by applying the momentum equation boundary conditions.

There are four terms that make up the momentum flux: the body force, and the mean stress, pressure, and temperature difference terms. The body force term is the dot product of the body force, which points in the direction of the gravitational vector, with the vector pointing between grid blocks n and m. We assume the surroundings are at the same elevation as grid block n, so this term is zero. Surface segments bordering the surroundings generally have no fluid flowing through them (fluid loss to the surroundings is represented as a constant pressure sink), so there would be no pore pressure communication between a grid block and the surroundings. Consequently, we neglect the pressure difference term as well. Finally, we assume the temperature and mean stress of the surroundings are the grid block's initial values.

We apply the above boundary conditions to the Equation 15.36 summation term and obtain the form for a surface segment bordering the surroundings:

$$\left[\begin{array}{l} \left(\frac{3(1-\upsilon)}{(1+\upsilon)}\right)_n \frac{\tau_n - \tau_n^0}{2D_{n,0}\left(1-\varepsilon_{D,n}\right)} - \\ \left(\frac{2(1-2\upsilon)}{(1+\upsilon)}\right)_n \sum_j \left(\left(3\beta K \omega_j\right)_n \frac{T_{j,n} - T_{j,n}^0}{2D_{n,0}\left(1-\varepsilon_{D,n}\right)} \right) \end{array} \right] A_{nm,0}\left(1-\varepsilon_{A,n}\right) \tag{15.37}$$

where superscript 0 refers to the grid block initial value.

15.5.5. Solution of Simulator Equations

The simulator mass, momentum, and energy conservation equations, Equations 15.34 and 15.36, are assembled with fluxes and source/sink terms evaluated fully implicitly. The resulting set of nonlinear of algebraic equations in residual form is:

$$\boldsymbol{R}\left(\boldsymbol{x}^{l+1}\right) = 0 \tag{15.38}$$

where $\boldsymbol{x}^{l+1}$ is the primary variable vector at time level *l+1*. These equations are solved by the Newton-Raphson method. The Newton-Raphson method is an iterative procedure used to solve systems of nonlinear equations. Denoting iteration number by subscript p, the following system of equations result from applying the Newton-Raphson method to Equation 15.38:

$$\boldsymbol{J}\left(\boldsymbol{x}_p^{l+1}\right)\left(\boldsymbol{x}_p^{l+1} - \boldsymbol{x}_p^{l}\right) = -\boldsymbol{R}\left(\boldsymbol{x}_p^{l+1}\right) \tag{15.39}$$

where the Jacobian matrix $\boldsymbol{J}(\boldsymbol{x})$ is defined as:

$$\left[\boldsymbol{J}\left(\boldsymbol{x}\right)\right]_{ij} = \frac{\partial R_i\left(\boldsymbol{x}\right)}{\partial x_j} \tag{15.40}$$

The Jacobian matrix is evaluated by numerical differentiation:

$$\frac{\partial R_i\left(\boldsymbol{x}\right)}{\partial x_j} \approx \frac{R_i\left(\boldsymbol{x}\left(\forall i \neq j\right), x_j + \varepsilon_j\right) - R_i\left(\boldsymbol{x}\right)}{\varepsilon_j} \tag{15.41}$$

where ε_j is the increment for primary variable x_j. The iteration is converged when all residuals R_i are less than a prescribed tolerance, ε_{tol}:

$$\frac{R_i\left(\boldsymbol{x}_{p+1}^{l+1}\right)}{M_i\left(\boldsymbol{x}_{p+1}^{l+1}\right)} \le \varepsilon_{tol} \tag{15.42}$$

15.6. ROCK PROPERTY CORRELATIONS

We describe the dependence of permeability and porosity on effective stress and other quantities in this section. Effective stress was initially defined as the difference between average stress and pore pressure by *Terzhagi* [1936] and was generalized by *Biot and Willis* [1957] as:

$$\tau' = \tau_m - \alpha P \tag{15.43}$$

where α is the Biot's or effective stress coefficient. Correlations have been developed for porosity as a function of effective stress and other quantities and permeability as a function of either porosity or effective stress. There are numerous examples of the above correlations, with each developed for a specific set of conditions. We describe those that have been incorporated into our simulator below.

We developed an expression for porosity starting with its definition. Porosity is the ratio of fluid volume to bulk volume, and since fluid volume plus solid volume equals bulk volume, porosity can be written as:

$$\phi = 1 - \frac{V_s}{V} \tag{15.44}$$

where V is bulk volume and V_s solid volume. *Gutierrez and Lewis* [2001] presented expressions for solid volume change with pressure and effective stress. These expressions can be integrated to yield an expression for solid volume:

$$V_s\left(P,\tau'\right) = V_{s,r}\left(1 + \frac{1-\phi_r}{K_s}\left(P - P_r\right) - \frac{1}{K_s}\left(\tau' - \tau_r'\right)\right) \tag{15.45}$$

where subscript r refers to reference conditions. Equation 15.25 relates bulk volume to volumetric strain, and when combined with Equations 15.44 and 15.45, yield porosity as a function of pressure, temperature, and effective stress:

$$\phi = 1 - (1-\phi_r)\frac{\left(1 + \frac{1-\phi_r}{K_s}\left(P - P_r\right) - \frac{1}{K_s}\left(\tau' - \tau_r'\right)\right)}{\frac{(1-\varepsilon_v)}{(1-\varepsilon_{v,r})}} \tag{15.46}$$

An example of reference conditions for Equation 15.46 is the initial conditions for a simulation, where volumetric strain, porosity, mean stress, and pressure are specified.

Rutqvist et al. [2002] presented the following function for porosity, obtained from laboratory experiments on sedimentary rock [*Davies and Davies*, 2001]:

$$\phi = \phi_1 + \left(\phi_0 - \phi_1\right)e^{-\alpha\tau'} \tag{15.47}$$

where ϕ_0 is zero effective stress porosity, ϕ_1 is high effective stress porosity, and the exponent a is a parameter. They also presented an associated function for permeability in terms of porosity:

$$k = k_0 e^{c\left(\frac{\phi}{\phi_0} - 1\right)} \tag{15.48}$$

For fractures, they defined an aperture width b_i for direction i as:

$$b_i = b_{0,i} + \Delta b_i\left(e^{-d\tau'} - e^{-d\tau_0'}\right) \tag{15.49}$$

where subscript 0 refers to initial conditions, Δb_i is the aperture change, and the exponent d is a parameter. Fracture porosity is correlated to changes in b_i as:

$$\phi = \phi_0 \frac{b_1 + b_2 + b_3}{b_{1,0} + b_{2,0} + b_{3,0}} \tag{15.50}$$

and direction i permeability is correlated to fracture aperture of other directions j and k as:

$$k_i = k_{i,0} \frac{b_j^3 + b_k^3}{b_{j,k}^3 + b_{k,0}^3} \tag{15.51}$$

McKee et al. [1988] derived a relationship between porosity and effective stress from hydrostatic poroelasticity theory by assuming incompressible rock grains:

$$\phi = \phi_0 \frac{e^{-c_p(\tau' - \tau_0')}}{1 - \phi_0\left(1 - e^{-c_p(\tau' - \tau_0')}\right)} \tag{15.52}$$

where c_p is average pore compressibility. They also related permeability and porosity using the Carman-Kozeny equation:

$$k \sim \frac{\phi^3}{\left(1-\phi\right)^2} \tag{15.53}$$

These relationships fit laboratory and field data for granite, sandstone, clay, and coal.

Verma and Pruess [1988] presented a power law expression relating permeability to porosity:

$$\frac{k - k_c}{k_0 - k_c} = \left(\frac{\phi - \phi_c}{\phi_0 - \phi_c}\right)^n \tag{15.54}$$

where k_c and ϕ_c are asymptotic values of permeability and porosity, respectively, and exponent n is a parameter.

Permeability and porosity are used to scale capillary pressure according to the relation by *Leverett* [1941]:

$$P_c = P_{c0}\sqrt{\left(\frac{\phi}{k}\right)\left(\frac{k}{\phi}\right)_0} \tag{15.55}$$

15.7. EXAMPLE SIMULATIONS

In this section, we describe three simulations to provide model verification and application examples. The first, a one-dimensional consolidation of a double-porosity medium, is compared to an analytical solution. In the second, fractures are modeled as a region where permeability change with porosity is much greater than that for the surroundings. Finally, a single-porosity analysis of CO_2 injection and surface uplift in the water leg of a depleting gas field illustrates the ability of the parallel code to solve larger problems.

15.7.1. One-Dimensional Consolidation of Double-Porosity Medium

In this one-dimensional consolidation problem, a z-direction stress is applied to the top of a fluid-filled double-porosity (fracture and matrix) porous rock column, instantaneously inducing a deformation and a pore pressure increase. Fluid then is allowed to drain out of the column top and the pore pressure increase dissipates. An analytical solution to this problem was presented by *Wilson and Aifantis* [1982]. In their analysis, strain is uniaxial and z-direction stress is constant throughout the process.

We simulate this problem in two steps. The first step is the load application to produce the pore pressure increase. We start from an unstrained state where pore pressures (fracture and matrix) and mean stress are both equal ($\tau_{m,0} = P_{1,0} = P_{2,0}$) and impose a greater mean stress at the column top ($\tau_{m,1}$) that induces a pore pressure increase ($P_{j,1}$) in the column after the system equilibrates. For uniaxial deformation in an isothermal, double-porosity system, mean stress, z-direction stress, and pore pressures are related by:

$$\tau_m = \frac{1}{3}\frac{(1+\nu)}{(1-\nu)}\left(\tau_{zz} - \sum_j \alpha_j P_j\right) + \sum_j \alpha_j P_j \tag{15.56}$$

and using this equation, we calculate the constant z-direction stress ($\tau_{zz,0}$) from the imposed mean stress ($\tau_{m,1}$) and the equilibrated pore pressures ($P_{j,1}$).

The second step is simulation of fluid drainage. The column is initially at the above equilibrated state. We set the pore pressures at the column top to the initial pore pressures ($P_{j,0}$). Because z-direction stress is constant, the mean stress at the column top must set as well, calculated from Equation 15.56 using $\tau_{zz,0}$ and $P_{j,0}$. Fluid then drains out of the column top as the pore pressures return to the initial values, $P_{j,0}$.

Our simulated column was 100 m long with properties shown in Table 15.1. The column was subdivided into 1000 grid blocks, each of which contained two porous continua, fracture and matrix.

Fracture and matrix porosity vary with pore pressure according to:

$$\phi_j = \phi_{0,j}\left(1 + c_{\phi,j}\left(P_j - P_{j,0}\right)\right) \tag{15.57}$$

where $c_{\phi,j}$ is continuum j pore compressibility. Initial pore pressures and mean stress were 1.0 MPa and the imposed mean stress was 4.0 MPa. The resulting equilibrium pore pressures were 2.165 MPa and the calculated z-direction stress was 5.835 MPa. We ran the drainage portion of the simulation for 300 seconds with 0.1-second time steps. The imposed mean stresses at the column top were 3.418 MPa. Comparison of simulated fracture pressure with the analytical solution is shown in Figure 15.4, with excellent agreement.

15.7.2. CO_2 Injection into a Hypothetical Aquifer-Caprock System

Rutqvist and Tsang [2002] simulated CO_2 injection into a hypothetical aquifer-caprock system covered by semipermeable shale. They coupled two computer codes, TOUGH2 for multiphase flow and heat transport and FLAC3D [*Itasca Consulting Group, Inc.,* 1997] for rock deformation, to study the hydraulic, mechanical, and hydromechanical changes during injection, including the spread of the CO_2 plume, effective stress and permeability changes, and ground surface uplift.

The aquifer is 200 m thick and is bounded above by 100-m-thick caprock. Above the caprock is a homogeneous formation that extends 1200 m to the surface and below the aquifer is additional caprock 1500 m thick. The aquifer properties are those of sandstone and the caprock's are those of shale. The system is two-dimensional and effectively infinite in lateral extent, and the injector was located at the aquifer bottom and at the lateral midpoint.

We reran their simulation of a vertical fractured zone in the caprock. We introduced a fractured zone in the

Table 15.1 Properties for double-porosity column.

	Fracture	Matrix
Young's modulus, GPa	8.0	8.0
Poisson's ratio	0.2	0.2
Initial porosity	0.004	0.032
Pore compressibility, Pa^{-1}	10^{-10}	10^{-10}
Permeability, m^2	8.9×10^{-13}	8.9×10^{-17}
Biot's coefficient	0.1	0.9
Volume fraction	0.5	0.5

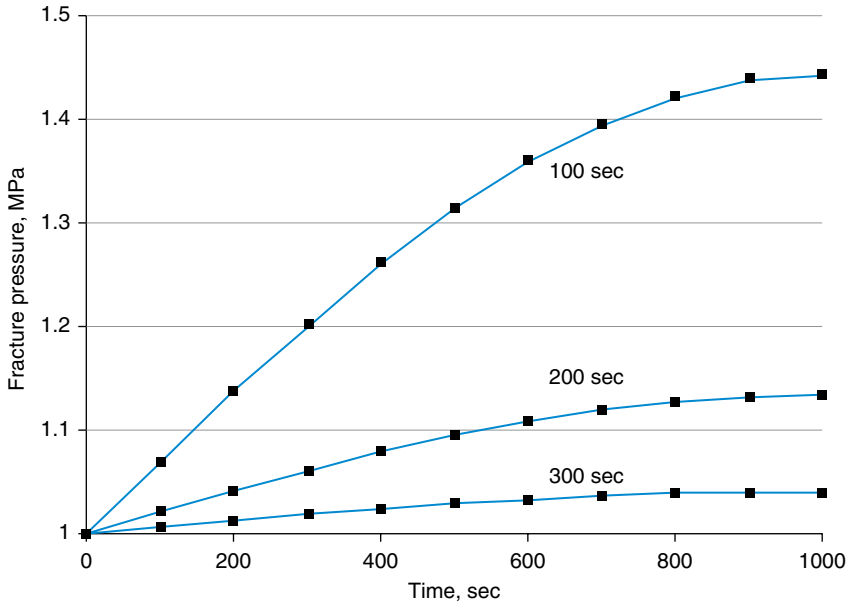

Figure 15.4 Comparison of fracture pressure analytical solution (solid lines) to simulation (points) for one-dimensional consolidation of double-porosity column.

Table 15.2 Input properties for aquifer-caprock system.

	Upper	Caprock	Aquifer	Base	Fractured Zone
Young's modulus, GPa	5	5	5	5	2.5
Poisson's ratio	0.25	0.25	0.25	0.25	0.25
Zero stress porosity	0.1	0.01	0.1	0.01	0.002
Residual porosity	0.09	0.009	0.09	0.009	0.001
Zero stress perm., m^2	10^{-15}	5.0×10^{-18}	10^{-13}	10^{-17}	10^{-16}

vicinity of the injector that spans the caprock thickness. Initially, the fractures are closed and the fracture zone has the permeability of the surrounding caprock. During CO_2 injection, pressure increases and effective stress decreases, causing the fractures to open and allow more flow through them. Fracture opening is modeled using Equations 15.47 and 15.48, with parameters resulting in greater permeability increase for a given effective stress decrease than that for the rest of the caprock. Input properties for this simulation are contained in Table 15.2.

The *xz* simulation grid was 201x100. Grid block thickness (*z*-direction) was smallest around the aquifer and increased away from it. Grid block width (*x*-direction) was smallest in the vicinity of the injector and also increased away from it. Grid block dimensions are shown in Table 15.3.

The fractured zone was located 100 m to the right (column 53) of the injector (column 51, layer 60). CO_2 was injected at 0.05 kg/sec-m for 10 years. Figures 15.5 through 15.7 show the CO_2 plume at 1, 3, and 10 years, respectively. At 1 year, the CO_2 plume ends just below the caprock and there are no visible effects from the fractured zone. At 3 years, the fractured zone has opened and the CO_2 is flowing through it. Finally, at 10 years, the CO_2 has broken through the caprock and has entered the upper zone. These results generally agree with those of *Rutqvist and Tsang* [2002], which are shown in Figure 15.8. Our simulation has a wider fractured zone than *Rutqvist and Tsang* [2002] (50 m versus 10 m), and due to the resulting larger fractured zone volume, less CO_2 has broken through the caprock after 10 years. The permeability increase at 10 years is shown in Figure 15.9 and the increase from *Rutqvist and Tsang* [2002] is shown in Figure 15.10. The magnitiude of the permeability increase in the fractured zones both agree. The permeability increase is not felt as much in the upper portion of the fractured zone as in *Rutqvist and Ts*ang [2002] because of our larger fractured zone volume.

15.7.3. In Salah Gas Project Simulation

The In Salah Gas Project, located in central Algeria, is a CO_2 storage project. Natural gas produced nearby is high in CO_2 and this CO_2 is injected back into the water

Table 15.3 Grid block dimensions.

Column (x)	Lateral Width, m	Layer (z)	Thickness, m
1–10	1600	1–10	60
11–20	800	11–20	40
21–30	400	21–30	20
31–40	200	31–60	10
41–50	100	61–70	20
51–151	50	71–80	40
152–161	100	81–100	45
162–171	200		
172–181	400		
182–191	800		
192–201	1600		

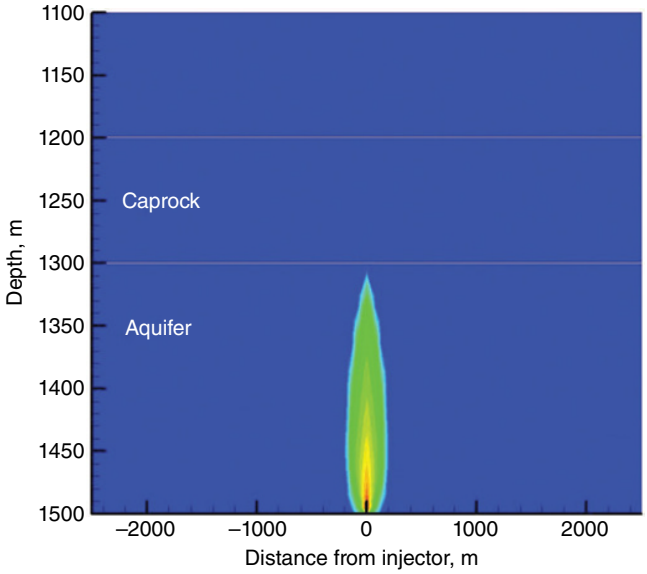

Figure 15.5 CO_2 plume after one year of injection.

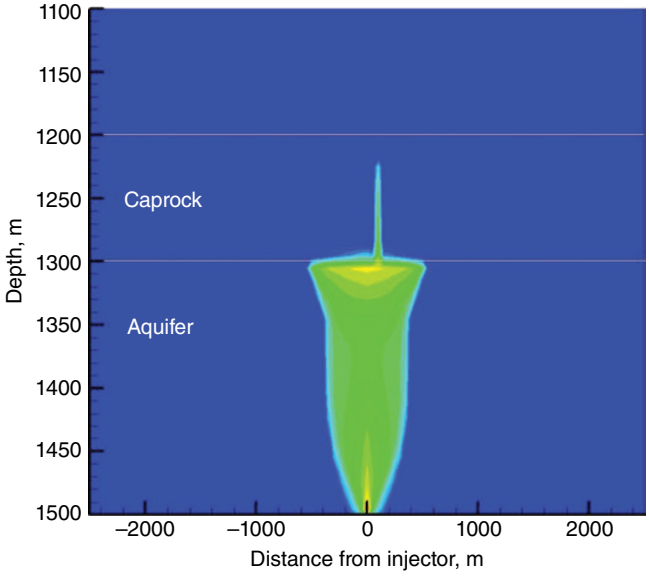

Figure 15.6 CO_2 plume after three years of injection.

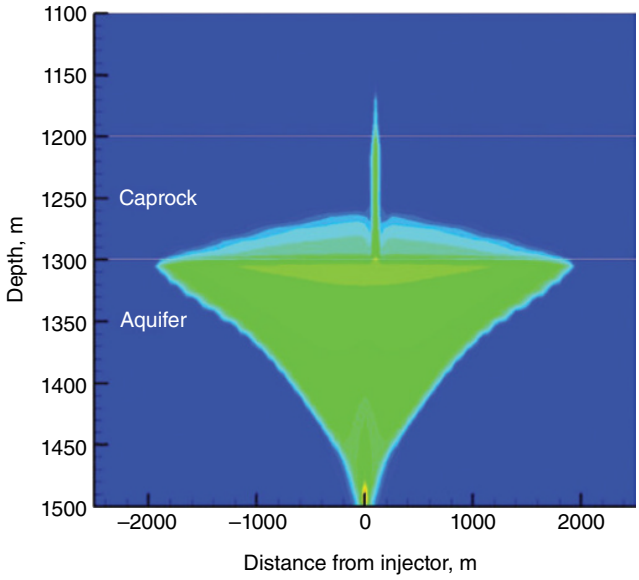

Figure 15.7 CO_2 plume after 10 years of injection.

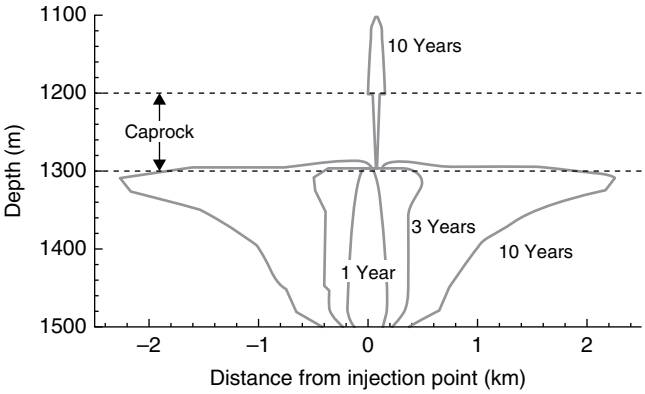

Figure 15.8 CO_2 plume after 1, 3, and 10 years, from *Rutqvist and Tsang* [2002].

leg of a depleting gas field for geological storage. Surface uplift from CO_2 injection has been measured by satellite-based inferrometry, and *Rutqvist et al.* [2010] did a reservoir-geomechanical analysis of In Salah CO_2 injection and surface uplift using the coupled TOUGH2-FLAC3D numerical simulator, described in Section 15.7.2, in order to determine if the uplift can be explained by pressure changes and deformation in the injection zone only.

We reran their analysis and we used a cluster computer to demonstrate our parallel code's ability to simulate larger problems. Our cluster computer contains 16 nodes; each node has 24 GB of memory and two Intel 5620 2.4GHZ 4-core processors. The simulation used the entire processing power of the cluster.

The simulated domain was 10x10x4 km with one 1.5-km horizontal injection well at 1810 m depth and in the domain center. The domain consisted of four geological

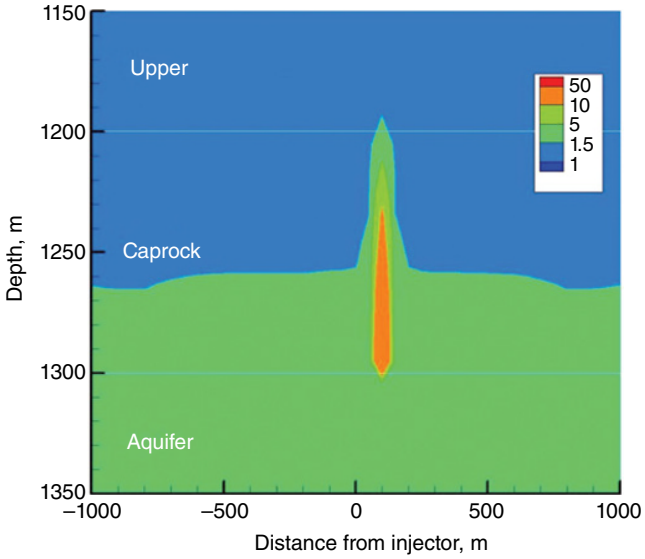

Figure 15.9 Permeability increase in vicinity of fractured zone (caprock, 100 m from injector), at 10 years.

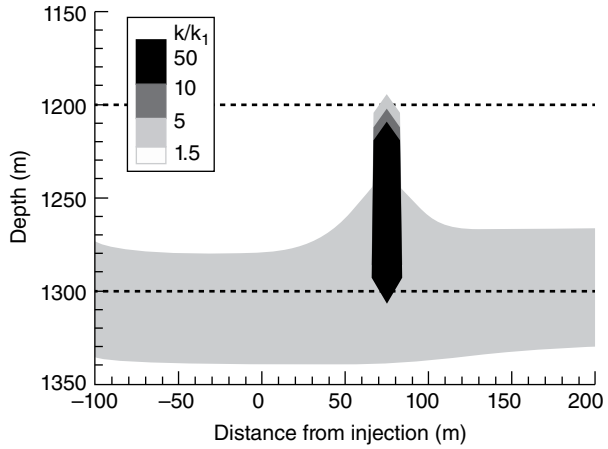

Figure 15.10 Permeability increase at 10 years, from *Rutqvist and Tsang* [2002].

layers, shallow overburden, caprock, injection zone, and base, whose properties are shown in Table 15.4.

The reservoir initially contained water and the initial temperature and pressure at the injection well were 90°C and 17.9 MPa, respectively. The lateral reservoir boundaries were maintained at constant pressure and CO_2 was injected at 9.734 kg sec^{-1} for three years.

CO_2 injection causes surface uplift, a change in reservoir height. Reservoir height is the sum of grid block height over a *z*-direction column of grid blocks. Applying the definition of linear strain from Equation 15.27, we express grid block *l* height, Δz_l, as:

$$\Delta z_l = \Delta z_{l,0}\left(1-\varepsilon_z\right) \tag{15.58}$$

where ε_z is *z*-direction linear strain and $\Delta z_{l,0}$ is grid block height at zero strain. Given initial grid block height $\Delta z_{l,i}$ and linear strain $\varepsilon_{z,i}$, we can write Equation 15.58 as:

$$\Delta z_l = \Delta z_{l,i}\frac{\left(1-\varepsilon_z\right)}{\left(1-\varepsilon_{z,i}\right)} \tag{15.59}$$

and surface uplift, Δz_{uplift}, then becomes:

$$\Delta z_{uplift} = \sum_l \left(\Delta z_l - \Delta z_{l,i}\right) = \sum_l \Delta z_{l,i}\frac{\left(\varepsilon_{z,i}-\varepsilon_z\right)}{\left(1-\varepsilon_{z,i}\right)} \tag{15.60}$$

where the sum over index *l* refers to a z-direction column of grid blocks. Finally, we express linear strain in terms of volumetric strain by assuming isotropic strain, as shown in Equation 15.33:

$$\varepsilon_z = \frac{\varepsilon_v}{3} \tag{15.61}$$

and calculate surface uplift using Equations 15.60 and 15.61.

We simulated a 5x5x4-km quarter symmetry element of their system with a 1000x1000x60 grid (60 million grid blocks). The areal grid was uniform. Layers 1–5 were

Table 15.4 Geological layer properties for InSalah CO_2 injection.

	Shallow Overburden (0–900 m)	Caprock (900–1800 m)	Injection Zone (1800–1820 m)	Base (>1800 m)
Young's modulus, GPa	1.5	20.0	6.0	20.0
Poisson's ratio	0.2	0.15	0.2	0.15
Biot's coefficient	1.0	1.0	1.0	1.0
Porosity	0.1	0.01	0.17	0.01
Permeability, m^2	1.0×10^{-17}	1.0×10^{-19}	1.0×10^{-14}	1.0×10^{-21}
Residual CO_2 saturation	0.05	0.05	0.05	0.05
Residual liquid saturation	0.3	0.3	0.3	0.3
van Genuchten [1980], m	0.457	0.457	0.457	0.457
van Genuchten [1980], P_0, kPa	19.9	621.0	19.9	621.0

Table 15.5 Layer thicknesses for In Salah simulation.

Layer	Thickness, m	Layer	Thickness, m	Layer	Thickness, m
1–5	180.00	17	15.21	48	6.46
6	181.64	18	12.14	49	9.55
7	144.97	19	9.69	50	14.12
8	115.71	20	7.74	51	20.88
9	92.36	21	6.17	52	30.86
10	73.72	22	4.93	53	45.63
11	58.84	23	3.93	54	67.45
12	46.96	24	3.14	55	99.72
13	37.48	25	2.51	56	147.42
14	29.92	26–45	2.00	57	217.94
15	23.88	46	2.96	58	322.19
16	19.06	47	4.37	59	476.30
				60	704.14

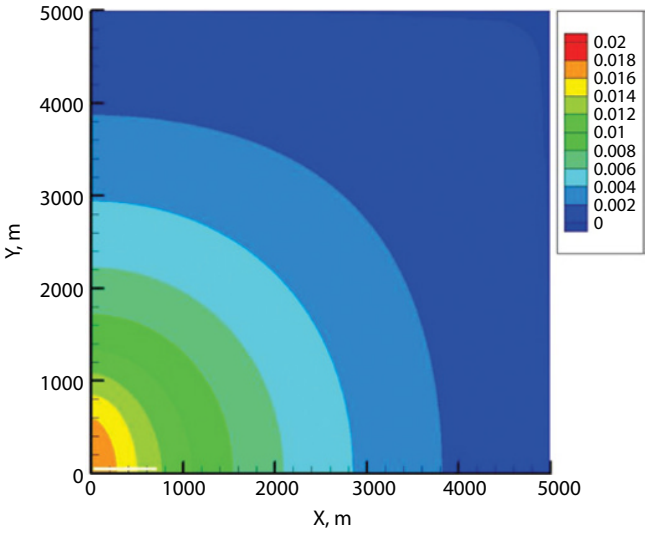

Figure 15.11 Surface uplift, m, for TOUGH2-CSM In Salah CO_2 injection simulation; injection well shown by thick horizontal line at origin.

shallow overburden, 6–30 were caprock, 31–40 were injection zone, and 41–60 were base. The injection zone layers were 2 m thick and layer thickness gradually increased away from there, as shown in Table 15.5.

The simulation took 21.9 days to run with 97.6% of the time used for linear equation solution. The Jacobian matrix had four variables per grid block, resulting in a total of 240 million equations.

Figure 15.11 shows surface uplift after three years of CO_2 injection. The maximum uplift occurs in the vicinity of the injection well, centered at the origin, and is about 0.02 m. This is in agreement with the value shown in *Rutqvist et al.* [2010] for caprock permeability of 10^{-19} m^2.

15.8. SUMMARY AND CONCLUSIONS

We developed a massively parallel reservoir simulator for modeling THM processes in fractured and porous media. We derived, from the fundamental equations describing deformation of porous and fractured elastic media, a momentum conservation equation relating mean stress, pressure, and temperature, and incorporated it alongside the mass and energy conservation equations from the TOUGH2-MP formulation, the starting point for the simulator. In addition, rock properties, namely permeability and porosity, are functions of effective stress and other variables that are obtained from the literature.

We verified the simulator formulation and numerical implementation using an analytical solution and two example problems from the literature. We matched the analytical solution for a one-dimensional consolidation problem in a double porosity medium. For the first problem from the literature, we ran a simulation of CO_2 injection into a hypothetical aquifer-caprock system with a fractured zone in the caprock and found good agreement in saturation profiles and fractured zone permeability increase. For the second, we ran a simulation of CO_2 injection into the water leg of a depleting gas field and obtained a good match of surface uplift after three years of CO_2 injection.

Our first two example problems illustrate two approaches to simulating fractured media. In the first, we used the double-porosity model and in the second we represented the fractured zone as a porous medium with properties representative of fractures. Both approaches are applicable for simulating THM processes in fractured media. Finally, for the two example problems from the literature, we compared our results to those from two coupled computer codes, one that simulates fluid flow and heat transport and the other that simulates rock deformation, and obtained good matches. This agreement indicates that our formulation is able to capture THM effects modeled by a coupled simulation with a more detailed handling of rock mechanics.

ACKNOWLEDGMENTS

This work was supported by the CMG Foundation and by the Assistant Secretary for Fossil Energy, Office of Coal and Power R&D through the National Energy Technology Laboratory under U.S. DOE Contract Number DE-FC26-09FE0000988.

REFERENCES

Bai, M., D. Elsworth, and J.-C. Roegiers (1993), Modeling of naturally fractured reservoirs using deformation dependent flow mechanism, *Int. J. Rock Mech. Min. Sci. & Geomech. Abstr.*, *30*(7), 1185–1191.

Barenblatt, G. E., I. P. Zheltov, and I. N. Kochina (1960), Basic concepts in the theory of seepage of homogenous liquids in fractured rocks, *J. Appl. Math. (USSR)*, *24*(5), 1286–1303.

Bear, J. (1972), *Dynamics of Fluids in Porous Materials*, Elsevier, New York.

Biot, M. A., and D. G. Willis (1957), The elastic coefficients of the theory of consolidation, *J. Appl. Mech*., *24*, 594–601.

Carroll, M. M., and N. Katsube (1983), The role of the Terzaghi stress in linearly elastic deformation, *ASME J. Energy Res. Technol*., *105*, 509–511.

Davies, J. P., and D. K. Davies (2001), Stress-dependent permeability: Characterization and modelling, *SPE Journal*, *6*(2), 224–235.

Geertsma, J. (1957), The effect of fluid pressure decline on volumetric changes of porous rock, *Trans. AIME*, *210*, 331–339.

Gutierrez, M., and R. W. Lewis (2001), Petroleum reservoir simulation coupling fluid flow and geomechanics, *SPE Reservoir Evaluation & Engineering*, June, 164–172.

Itasca Consulting Group, Inc. (1997), *FLAC3D Manual: Fast Lagrangian Analysis of Continua in Three Dimensions—Version 2.0*, Itasca Consulting Group, Inc., Minnesota.

Karypis, G., and V. Kumar (1998), A parallel algorithm for multilevel graph partitioning and sparse matrix ordering, *Journal of Parallel and Distributed Computing*, *48*, 71–85.

Leverett, M. C. (1941), Capillary behavior in porous media, *Trans. AIME, 142*, 341–358.

McKee, C. R., A. C. Bumb, and R. A. Koenig (1988), Stress-dependent permeability and porosity of coal and other geologic formations, *SPE Formation Evaluation*, *3*(1), 81–91.

McTigue, D. F. (1986), Thermoelastic response of fluid-saturated porous rock, *Journal of Geophysical Research*, *91*(9), 9533–9542.

Narashimhan, T. N., and P. A. Witherspoon (1976), An integrated finite difference method for analysis of fluid flow in porous media, *Water Resources Res*., *12*, 57–64.

Norris, A. (1992), On the correspondence between poroelasticity and thermoelasticity, *J. Appl. Phys*., *71,* 1138–1141.

Nur, A., and J. D. Byerlee (1971), An exact effective stress law for elastic deformation of rock with fluids, *J. Geophys. Res*., *76*, 6414–6419.

Pruess, K. (2005), *ECO2N: a TOUGH2 fluid property module for mixtures of water, NaCl, and CO2,* Research Report LBNL-57952, Lawrence Berkeley National Laboratory, Berkeley, CA.

Pruess, K., and T. N. Narasimhan (1985), A practical method for modeling fluid and heat flow in fractured porous media, *Soc. Pet. Eng. J*., *25*(1), 14–26.

Pruess, K., C. Oldenburg, and G. Moridis (1999), *TOUGH2 user's guide, version 2.0*, Report LBNL-43134, Lawrence Berkeley National Laboratory, Berkeley, California.

Rutqvist, J., and C. F. Tsang (2002), A study of caprock hydromechanical changes associated with CO2-injection into a brine formation, *Environ. Geol*., *42*, 296–305.

Rutqvist, J., D. W. Vasco, and L. Myer (2010), Coupled reservoir-geomechanical analysis of CO2 injection and ground deformations at In Salah Algeria, *Int. J. of Greenhouse Gas Control*, *4*, 225–230.

Rutqvist, J., Y.-S. Wu, C. F. Tsang, and G. A. Bodvarsson (2002), Modeling approach for analysis of coupled multiphase fluid flow heat transfer and deformation in fractured porous rock, *Int. J. Rock Mech.& Min. Sci.*, *39*, 429–442.

Terzaghi, K. (1936), The shearing resistance of saturated soils and the angle between the planes of shear, *Proceedings of International Conference on Soil Mechanics and Foundation Engineering*, Harvard University Press, Cambridge, MA, 54–56.

Tuminaro, R. S., M. Heroux, S. A. Hutchinson, and J. N. Shadid (1999), *Official Aztec User's Guide Version 2.1*, Massively Parallel Computing Research Laboratory, Sandia National Laboratories, Albuquerque, NM.

van Genuchten, M. T. (1980), A closed-form equation for predicting the hydraulic conductivity of unsaturated soils, *Soil Sci. Soc.*, *44*, 892–898.

Verma, A., and K. Pruess (1988), Thermohydrological conditions and silica redistribution near high-level nuclear wastes emplaced in saturated geological formations, *J. Geophys. Res.*, *93*, 1159–1173.

Warren, J. E., and P. J. Root (1963), The behavior of naturally fractured reservoirs, *Society of Petroleum Engineers Journal, Transactions AIME*, *228*, 245–255.

Wilson, R. K., and E. C. Aifantis (1982), On the theory of consolidation with double porosity, *Int. J. Eng. Sci.*, *20*(9), 1009–1035.

Zhang, K., Y. S. Wu, and K. Pruess (2008), *User's Guide for TOUGH2-MP: A Massively Parallel Version of the TOUGH2 Code,* Report LBNL-315E, Lawrence Berkeley National Laboratory, Berkeley, CA.

Zimmerman, R. W. (1991), *Compressibility of Sandstones*, Elsevier, Amsterdam.

INDEX

Dynamics of Fluids and Transport in Complex Fractured-Porous Systems, Geophysical Monograph 210, First Edition.
Edited by Boris Faybishenko, Sally M. Benson, and John E. Gale.

WILEY END USER LICENSE AGREEMENT

Go to www.wiley.com/go/eula to access Wiley’s ebook EULA.